

ADVANCED STEEL CONSTRUCTION

An International Journal

Volume 15 Number 1

March 2019

CONTENTS

Technical Papers

Residual Stress of Welded I Sections Fabricated from High Performance Steel: Experimental Investigation and Modeling
Yong-Lei Xu, Yong-Jiu Shi, Yi-Ran Wu and Ling-Ye Meng

Research on Influence of Member Initial Curvature on Stability of Single-Layer Spherical Reticulated Domes
Yang Ding and Tian-Long Zhang

The Structural and Construction Performances of a Large-Span Half Steel-Plate-Reinforced Concrete Hollow Roof

Meng-Zhu Diao, Yil Li, Xin-Zheng Lu, Hong Guan and Yun-Lun Sun

Failure Test of a Suspendedome due to Cable Rupture

Zhi-Hua Chen, Xiao-Xiang Wang, Hong-Bo Liu and Yu-Jie Yu

Developments and Behaviors of Slip-Released Novel Connectors in Steel-Concrete Composite Structures
Yang Ding, Xiao-Meng Dai and Jia-Bao Yan

Experimental and Theoretical Investigations of Spigot Connections under Cyclic Loading
Mutasim Abdel-Jaber, Robert G Beale, Nasim Khalil Shatarat and Muqeasem A Shehadeh

Behavior of CFST-Column to Steel-Beam Joints in the Scenario of Column Loss

Shan Gao, Man Xu, Lan-Hui Guo and Su-Mei Zhang

Experimental VS Theoretical Design Approaches for Thin-Walled Cold-Formed Steel Beam-Columns
Nadia Baldassino, Claudio Bernuzzi and Marco Simoncelli

Determination of the Buckling Loads of Irregularly Shaped Plates using a New Design Approach
Hesham Ahmed, John Durodola and Robert G. Beale

Study on Dynamic Behaviors and Vibration Reduction Techniques on Cable-Supported Ribbed Beam Composite Slab
Wen-Tao Qiao, Dong Wang, Qi An and Hai-Ying Zhang

Turbulent Wind Field Simulation of Wind Turbine Structures with Consideration of the Effect of Rotating Blades
Tao Huo, Le-Wei Tong and Fidelis R. Mashiri

Influence of Random Geometrical Imperfection on the Stability of Single-Layer Reticulated Domes with Semi-Rigid Connection
Zhong-Wei Zhao, Hai-Qing Liu, Bing Liang and Ren-Zhang Yan

Seismic Optimization Analysis of Vertical Stiffener Connection to L-CFST Column
Wang Zhang, Zhi-Hua Chen, Qing-Qing Xiong and Ting Zhou

Method for Evaluating the progressive Collapse Resistance of Long-Span Single-Layer Spatial Grid Structures

Li-Min Tian, Jian-Peng Wei and Ji-Ping Hao

Behaviour of Steel-Concrete-Steel Sandwich Plates under Different Ice-Contact Pressure
Jia-Bao Yan, Zhe Wang and Xuan Wang

Copyright © 2019 by :

The Hong Kong Institute of Steel Construction

Website: <http://www.hkisc.org>

ISSN 1816-112X

Science Citation Index Expanded, Materials Science Citation Index and ISI Alerting

Cover. Macao Athletic Training and Development Centre

e-copy of IJASC is free to download at "www.ascjournal.com" in internet and mobile apps.

ADVANCED STEEL CONSTRUCTION

VOL.15, NO.1 (2019)

ADVANCED STEEL CONSTRUCTION

an International Journal

ISSN 1816-112X

Volume 15 Number 1

March 2019



Editors-in-Chief

S.L. Chan, The Hong Kong Polytechnic University, Hong Kong

W.F. Chen, University of Hawaii at Manoa, USA

R. Zandonini, Trento University, Italy



ISSN 1816-112X

**Science Citation Index Expanded,
Materials Science Citation Index
and ISI Alerting**

EDITORS-IN-CHIEF

**Asian Pacific, African
and organizing Editor**

S.L. Chan
*The Hong Kong Polyt. Univ.,
Hong Kong*

American Editor

W.F. Chen
Univ. of Hawaii at Manoa, USA

European Editor

R. Zandonini
Trento Univ., Italy

ASSOCIATE EDITORS

Y.P. Liu
The Hong Kong Polyt. Univ., Hong Kong

S.W. Liu
Sun Yat-Sen Univ., China

**INTERNATIONAL
EDITORIAL BOARD**

F.G. Albermani
Central Queensland Univ., Australia

I. Burgess
Univ. of Sheffield, UK

F.S.K. Bijlaard
Delft Univ. of Technology, The Netherlands

R. Bjorhovde
The Bjorhovde Group, USA

M.A. Bradford
The Univ. of New South Wales, Australia

D. Camotim
Technical Univ. of Lisbon, Portugal

C.M. Chan
Hong Kong Univ. of Science & Technology, Hong Kong, China

T.H.T. Chan
Queensland Univ. of Technology, Australia

T.M. Chan
The Hong Kong Polyt. Univ., Hong Kong, China

Z.H. Chen
Tianjin Univ., China

S.P. Chiew
Nanyang Technological Univ., Singapore

W.K. Chow
The Hong Kong Polyt. Univ., Hong Kong, China

G.G. Deierlein
Stanford Univ., California, USA

L. Dezi
Univ. of Ancona, Italy

D. Dubina
The Politehnica Univ. of Timisoara, Romania

R. Greiner
Technical Univ. of Graz, Austria

L. Gardner
Imperial College of Science, Technology and Medicine, UK

Y. Goto
Nagoya Institute of Technology, Japan

Advanced Steel Construction

an international journal

L.H. Han
Tsinghua Univ. China

S. Herion
University of Karlsruhe, Germany

G.W.M. Ho
Ove Arup & Partners Hong Kong Ltd., Hong Kong

B.A. Izzuddin
*Imperial College of Science, Technology and
Medicine, UK*

J.P. Jaspart
Univ. of Liege, Belgium

S. A. Jayachandran
IIT Madras, Chennai, India

S.E. Kim
Sejong Univ., South Korea

S. Kitipornchai
The Univ. of Queensland, Australia

D. Lam
Univ. of Bradford, UK

H.F. Lam
City Univ. of Hong Kong, Hong Kong, China

G.Q. Li
Tongji Univ., China

J.Y.R. Liew
National Univ. of Singapore, Singapore

E.M. Lui
Syracuse Univ., USA

Y.L. Mo
Univ. of Houston, USA

J.P. Muzeau
CUST, Clermont Ferrand, France

D.A. Nethercot
*Imperial College of Science, Technology and
Medicine, UK*

Y.Q. Ni
The Hong Kong Polyt. Univ., Hong Kong, China

D.J. Oehlers
The Univ. of Adelaide, Australia

J.L. Peng
Yunlin Uni. of Science & Technology, Taiwan, China

K. Rasmussen
The Univ. of Sydney, Australia

J.M. Rotter
The Univ. of Edinburgh, UK

C. Scawthorn
Scawthorn Porter Associates, USA

P. Schaumann
Univ. of Hannover, Germany

Y.J. Shi
Tsinghua Univ., China

G.P. Shu
Southeast Univ. China

L. Simões da Silva
*Department of Civil Engineering, University of
Coimbra, Portugal*

J.G. Teng
The Hong Kong Polyt. Univ., Hong Kong, China

G.S. Tong
Zhejiang Univ., China

K.C. Tsai
National Taiwan Univ., Taiwan, China

C.M. Uang
Univ. of California, USA

B. Uy
University of Western Sydney, Australia

M. Veljkovic
Univ. of Lulea, Sweden

F. Wald
Czech Technical Univ. in Prague, Czech

Y.C. Wang
The Univ. of Manchester, UK

Y.L. Xu
The Hong Kong Polyt. Univ., Hong Kong, China

D. White
Georgia Institute of Technology, USA

E. Yamaguchi
Kyushu Institute of Technology, Japan

Y.B. Yang
National Taiwan Univ., Taiwan, China

Y.Y. Yang
China Academy of Building Research, Beijing, China

B. Young
The Univ. of Hong Kong, Hong Kong, China

X.L. Zhao
Monash Univ., Australia

X.H. Zhou
Chongqing University, China

Z.H. Zhou
The Hong Kong Polyt. Univ., Hong Kong, China

S.Y. Zhu
The Hong Kong Polyt. Univ., Hong Kong, China

R.D. Zieman
Bucknell Univ., USA

General Information

Advanced Steel Construction, an international journal

Aims and scope

The International Journal of Advanced Steel Construction provides a platform for the publication and rapid dissemination of original and up-to-date research and technological developments in steel construction, design and analysis. Scope of research papers published in this journal includes but is not limited to theoretical and experimental research on elements, assemblages, systems, material, design philosophy and codification, standards, fabrication, projects of innovative nature and computer techniques. The journal is specifically tailored to channel the exchange of technological know-how between researchers and practitioners. Contributions from all aspects related to the recent developments of advanced steel construction are welcome.

Disclaimer. No responsibility is assumed for any injury and / or damage to persons or property as a matter of products liability, negligence or otherwise, or from any use or operation of any methods, products, instructions or ideas contained in the material herein.

Subscription inquiries and change of address. Address all subscription inquiries and correspondence to Member Records, IJASC. Notify an address change as soon as possible. All communications should include both old and new addresses with zip codes and be accompanied by a mailing label from a recent issue. Allow six weeks for all changes to become effective.

The Hong Kong Institute of Steel Construction

HKISC

c/o Department of Civil and Environmental Engineering,

The Hong Kong Polytechnic University,

Hunghom, Kowloon, Hong Kong, China.

Tel: 852- 2766 6047 Fax: 852- 2334 6389

Email: ceschan@polyu.edu.hk Website: <http://www.hkisc.org/>

ISSN 1816-112X

Science Citation Index Expanded, Materials Science Citation Index and ISI Alerting

Copyright © 2019 by:

The Hong Kong Institute of Steel Construction.

ISSN 1816-112X

**Science Citation Index Expanded,
Materials Science Citation Index and
ISI Alerting**

EDITORS-IN-CHIEF

**Asian Pacific, African
and organizing Editor**

S.L. Chan

*The Hong Kong Polyt. Univ.,
Hong Kong*

Email: ceslchan@polyu.edu.hk

American Editor

W.F. Chen

Univ. of Hawaii at Manoa, USA

Email: waifah@hawaii.edu

European Editor

R. Zandonini

Trento Univ., Italy

Email: riccardo.zandonini@ing.unitn.it

Advanced Steel Construction

an international journal

VOLUME 15 NUMBER 1

MARCH 2019

Technical Papers

Residual Stress of Welded I Sections Fabricated of High Performance Steel: 1
Experimental Investigation and Modeling
Yong-Lei Xu, Yong-Jiu Shi, Yi-Ran Wu and Ling-Ye Meng*

Research on Influence of Member Initial Curvature on Stability of Single-Layer 9
Spherical Reticulated Domes
*Yang Ding and Tian-long Zhang**

The Structural and Construction Performances of a Large-Span Half 16
Steel-Plate-Reinforced Concrete Hollow Roof
Meng-Zhu Diao, Yi Li, Xin-Zheng Lu, Hong Guan and Yun-Lun Sun*

Failure Test of a Suspendome due to Cable Rupture 23
Zhi-Hua Chen, Xiao-Xiang Wang, Hong-Bo Liu and Yu-Jie Yu*

Developments and Behaviors of Slip-Released Novel Connectors in 30
Steel-Concrete Composite Structures
*Yang Ding, Xiao-Meng Dai and Jia-Bao Yan**

Experimental and Theoretical Investigations of Spigot Connections under Cyclic 37
Loading
Mutasim Abdel-Jaber, Robert G. Beale, Nasim Khalil Shatarat and Mutasem A. Shehadeh*

Behavior of CFST-Column to Steel-Beam Joints in the Scenario of Column Loss 47
Shan Gao, Man Xu, Lan-Hui Guo and Su-Mei Zhang*

Experimental VS. Theoretical Design Approaches for Thin-Walled Cold-Formed 55
Steel Beam-Columns
*Nadia Baldassino, Claudio Bernuzzi and Marco Simoncelli**

Determination of the Buckling Loads of Irregularly Shaped Plates using a New 66
Design Approach
*Hesham Ahmed, John Durodola and Robert G. Beale**

Study on Dynamic Behaviors and Vibration Reduction Techniques on 73
Cable-Supported Ribbed Beam Composite Slab
Wen-Tao Qiao, Dong Wang, Qi An and Hai-Ying Zhang*

Turbulent Wind Field Simulation of Wind Turbine Structures with Consideration 82
of the Effect of Rotating Blades
Tao Huo, Le-Wei Tong and Fidelis R. Mashiri*

Influence of Random Geometrical Imperfection on the Stability of Single-Layer 93
Reticulated Domes with Semi-Rigid Connection
*Zhong-Wei Zhao, Hai-Qing Liu, Bing Liang and Ren-Zhang Yan**

Seismic Optimization Analysis of Vertical Stiffener Connection to L-CFST 100
Column
*Wang Zhang, Zhi-Hua Chen, Qing-Qing Xiong and Ting Zhou**

Method for Evaluating the progressive Collapse Resistance of Long-Span 109
Single-Layer Spatial Grid Structures
Li-Min Tian, Jian-Peng Wei and Ji-Ping Hao*

Behaviour of Steel-Concrete-Steel Sandwich Plates under Different Ice-Contact 116
Pressure
*Jia-Bao Yan, Zhe Wang and Xuan Wang**

RESIDUAL STRESS OF WELDED I SECTIONS FABRICATED FROM HIGH PERFORMANCE STEEL: EXPERIMENTAL INVESTIGATION AND MODELLING

Yong-Lei Xu¹, Yong-Jiu Shi^{1*}, Yi-Ran Wu¹ and Ling-Ye Meng¹

Key Laboratory of Civil Engineering Safety and Durability of China Education Ministry, Department of Civil Engineering, Tsinghua University, Beijing 100084, P.R. China

* (Corresponding author: E-mail: shiyj@tsinghua.edu.cn)

ABSTRACT

An experimental study was presented to investigate the magnitude and distribution of residual stresses in welded I sections fabricated from a new type of high performance steel with high strength as well as improved fire and corrosion resistance. The residual stress of three I sections with various width-thickness ratios was measured by using sectioning method and more than 2000 original readings were obtained. The effects of width-thickness ratio and interaction of residual stress in the flange and web were clarified. It was found that compressive residual stress was strongly correlated with sectional dimensions, while tensile residual stress at the weld region or flange edge was less correlated with them. In addition, no interaction between the residual stress in the flange and web was identified. Based on the test results, a distribution model of residual stress was proposed which could well represent the experimental results. Finally, the magnitude of residual stresses in welded I sections fabricated from this new type of high performance steel was compared with that of high strength steel.

Copyright © 2019 by The Hong Kong Institute of Steel Construction. All rights reserved.

ARTICLE HISTORY

Received: 01 October 2017
Revised: 21 November 2017
Accepted: 13 December 2017

KEY WORDS

WGJ steel;
Residual stress;
Welded I sections;
Sectioning process;
Modeling

1. Introduction

Residual stress in structural steel members is induced by non-uniform heat input during manufacturing, fabricating and welding process [1]. As one of the most important initial imperfections for welded steel members, it has significant effects on the loading capacity, especially the buckling capacity, because of premature yielding and reduction of section stiffness.

In order to understand the magnitude and distribution of residual stresses, extensive investigations were conducted on conventional strength steel (CSS) sections [2–7], including rolled or welded sections and plates. Based on previous investigations, steel structural design specifications such as Eurocode 3 [8, 9], ANSI/AISC 360-10 [10], and Chinese code GB 50017-2003 [11, 12] have specified some models or calculation methods to represent the residual stress.

However, the models proposed by previous investigations and existing design specifications may not be applicable to high strength steel (HSS) or high performance steel (HPS) members, which have been increasingly applied in recent years [13]. The main considerations are as follows: (1) The material properties and the manufacturing process for HSS or HPS members are different with CSS; (2) Since the yield strength of HSS or HPS is higher, the ratio of tensile residual stress at the welding region to the yield strength of steel material may be less than that of CSS; (3) Most of the current models has not taken into account the effects of section dimensions.

Since the effect of residual stress on mechanical performance is more important for welded sections than rolled ones, and I sections are widely adopted in steel buildings, numerous researches on residual stress of HSS and HPS welded I sections have been carried out.

Rasmussen and Hancock [14, 15] conducted a series of experiments to obtain the compressive residual stress of 4 welded I sections fabricated of 690 MPa HSS. Then 4 welded I sections fabricated of 700 MPa HSS, designated as D and B, were examined by Beg and Hladnik [16]. It was found that the compressive residual stress in the flange was $0.09f_y$ for section B and $0.14f_y$ for section D.

In 2012, Wang et al. [17] investigated the magnitude and distribution of residual stresses of 3 flame-cut welded I-section columns with a nominal yield strength of 460 MPa and different section dimensions. Test results showed that the compressive residual stress in the flange would decrease and tensile residual stress at the flange edge would increase when the width-thickness ratio of the flange increased. Ban et al. [18] conducted an experimental investigation to quantify the residual stress in 460 MPa steel welded I sections by using sectioning method. The magnitude and distribution of both compressive and tensile residual stresses were obtained, and a distribution model for the residual stress of 460 MPa HSS welded I sections was proposed based on test data obtained from 8 different sections. Ban [19] proposed a versatile model to estimate the magnitude and distribution of residual stresses, which was applicable to welded I sections and box sections fabricated from steel with various strength.

Chen [20] applied the blind-hole method to test the residual stress of flame-cut welded I sections fabricated from a new type of HPS designated as GJ steel, which was widely used in landmark buildings like National Olympic Stadium (Birds Nest) and new CCTV Headquarters in China. Yang et al. [21] presented an experimental investigation on the residual stress in welded I sections made of 345 MPa GJ steel by using sectioning method. The test results indicated that the distribution of residual stresses for 345 MPa GJ steel members had a similar profile with that for CSS, but the peak tensile and compressive residual stresses in the flange were much lower than those given by existing models. Qiu et al. [22] designed and manufactured 7 flame-cut welded I-section columns fabricated from 550 MPa GJ steel plates. It was found that tensile residual stress at welding regions was less than actual yield strength of GJ steel (624 MPa), and compressive residual stress in flanges and webs decreased as the width-thickness ratio increased. Yang et al. [23] focused on the residual stress of flame-cut welded I sections made of 460 MPa GJ steel. 8 full scale I sections welded by flame-cut 460 MPa GJ steel plates including 5 doubly symmetric sections and 3 singly symmetric sections were tested. Li et al. [24, 25] proposed a numerical procedure for sectional analysis and suggested a method to account for residual stress and geometric imperfections separately and independently. The approach could be applied to design HSS members.

A new type of HPS, designated as WGJ steel, with high strength as well as improved fire and corrosion resistance, was recently developed by Wuhan Iron and Steel (Group) Company. This type of steel will be widely used in the near future because of its excellent mechanical properties, especially under fire and corrosion conditions. Though there were some research publications and design guides on the loading capacity of columns and beams under fire or corrosion conditions, residual stress in welded I sections made of fire-resistant and weather-resistant steel with higher yield strength was not investigated yet. The magnitude of residual stresses in welded I sections fabricated from WGJ steel may not be precisely obtained by applying traditional models presented before, because of its special material properties.

This paper presents an experimental program to investigate the residual stress distribution of welded I sections fabricated from flame-cut WGJ steel plates. The sectioning method was employed to quantify longitudinal residual stress. I sections were characterized by various width-thickness ratios of flanges and webs. Based on the experimental results, a model to identify the magnitude and distribution of residual stresses was proposed and validated for WGJ steel welded I sections. This model will provide supportive information to the design and analysis of columns and beams fabricated of WGJ steel.

The distinct feature of this investigation is establishing a model to identify the magnitude and distribution of residual stresses in welded I sections fabricated from a new type of high performance steel. In addition, the magnitude of residual stresses in WGJ steel I sections was compared with that in HSS I sections. The comparison indicated that the negative effect of residual stress in steel members could be reduced by applying WGJ steel.

2. Experimental program

2.1. Test specimens

3 welded I-section specimens fabricated from WGJ steel in this experimental program, were summarized in Table 1. Sectional geometric parameters are illustrated in Figure 1, where b_f/t_f and h_0/t_w denote the width-thickness ratios of the flange and the web respectively. Specimens were all 1000mm in length and had different width-thickness ratios of the flange and web. All components of WGJ steel plates were flame-cut and built-up by automatic submerged arc welding with H08MnMoA welding wire and SJ101 welding flux. The fillet weld size (h_f) was 8mm for all specimens.

Before the automatic submerged-arc welding process, the welding flux was pre-heated for one hour at about 300°C in order to remove the water in it. As is known, water (H_2O) is decomposed into hydrogen (H_2) and oxygen (O_2) under high temperature, which results in weld defect.

Based on practical experience and design specifications, 10 mm steel plates in this investigation did not need pre-heating because of small thickness and large coefficient of thermal conductivity. In contrast, when the thickness of a steel plate is over 40mm, it needs pre-heating before welding to reduce non-uniform heat input during the welding process, which leads to inhomogeneous crystalline structure of steel and residual stress in structural steel members.

Post-heating was conducted after welding in order to relieve residual stress and reduce the deformation of I sections. The temperature of post-heating was under 800°C.

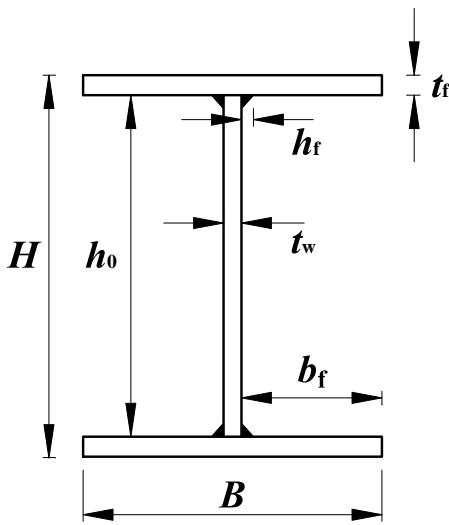


Fig. 1 Schematic diagram of the I section specimen

Table 1

Specimen section dimensions

Specimen label	H (mm)	B (mm)	t_f (mm)	t_w (mm)	b_f/t_f	h_0/t_w
RI1	120	80	10	10	3.5	10
RI2	220	125	10	10	5.75	20
RI3	300	200	10	10	9.5	28

2.2. Main sections

To obtain the mechanical and fire-resistant properties of WGJ steel, material tests at ambient temperature and elevated temperature were conducted. The elastic modulus of WGJ steel at ambient temperature obtained from material tests would be used to calculate the residual stress, after the residual strain was measured.

As is known, the yield strength and elastic modulus of steel reduce significantly under high temperature during welding process, especially for steel near the junction of the flange and web. WGJ steel was manufactured to be fire-resistant, so mechanical properties of WGJ steel under high temperature would be quite different from those of CSS. In addition, the residual strain and stress in structural steel members after welding may be related to the mechanical properties under high temperature during welding process. Thus, residual stress of WGJ steel I sections may be different from that of CSS I sections. Material properties of WGJ steel at elevated temperatures were tested in this study.

Tension coupons were prepared and tested according to Chinese standard

GB/T 228.2-2015 [26]. Temperature conditions in the tests were 20°C, 100°C, 200°C, 300°C, 400°C, 500°C, 600°C, 700°C, 800°C. Once specimens were heated to the specified temperature, a duration of 10 minutes was maintained for the temperature to stabilize. Three coupons were tested under each temperature condition, while the yield strength, ultimate strength, initial elastic modulus and entire stress-strain curves were measured.

Material test results showed that the 0.2% offset yield strength of WGJ steel at ambient temperature ($f_{0.2}$) was 433.8 MPa, and the initial elastic modulus (E) was 196533 MPa, which will be used to determine the residual stress of welded I sections. The stress-strain curves shown in Figure 2 indicate that there are no visible yielding plateaus for WGJ steel under any temperature, which shows typical nonlinearity[27].

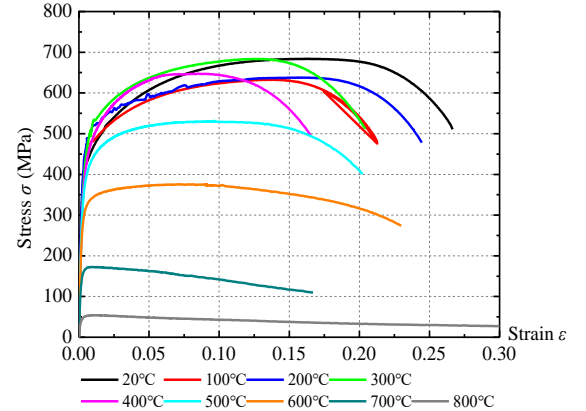


Fig. 2 Stress-strain curves of the tension coupon at different temperatures

Reduction factors can be used to describe the effect of temperature on the strength and elastic modulus of steel. For yield strength, the reduction factor $f_{0.2,T}/f_{0.2,\text{normal}}$ is defined as the ratio of 0.2% offset yield strength at different temperatures ($f_{0.2,T}$) to that at ambient temperature ($f_{0.2,\text{normal}}$). Similarly, the reduction factor E_T/E_{normal} is defined as the ratio of initial elastic modulus at different temperatures (E_T) to that at ambient temperature (E_{normal}).

The 0.2% offset yield strength at 600°C was 301.0 MPa (i.e. $f_{0.2,600}/f_{0.2,\text{normal}} = 0.694$), which was more than 2/3 of that at ambient temperature, so WGJ steel was proved to be fire-resistant. At the same time, initial elastic modulus at 600°C was 162411 MPa (i.e. $E_{600}/E_{\text{normal}} = 0.826$), which was far more than 2/3 of that at ambient temperature.

Reduction factor curves of 0.2% offset yield strength ($f_{0.2,T}/f_{0.2,\text{normal}}$) obtained from this test program were compared with the formula recommended in AISC 360-10 [10], ASCE Manual [28], Australian Standard AS4100 [29] and Chinese Standard CECS 200:2006 [30], as shown in Figure 3. It can be seen that WGJ steel has higher yield strength than CSS at elevated temperatures, especially at temperature around 600°C.

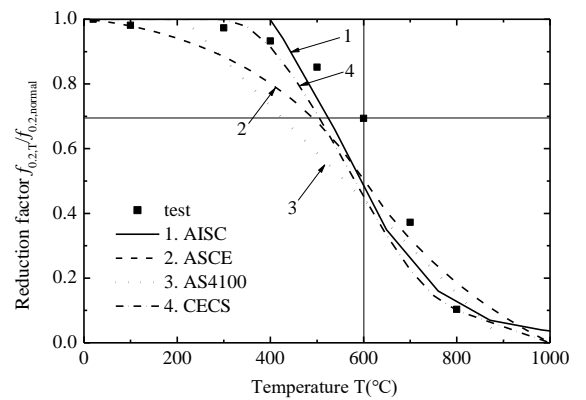


Fig. 3 Reduction factors of 0.2% offset yield strength in the test and specifications at different temperatures

Reduction factor curves of initial elastic modulus (E_T/E_{normal}) were also compared, as shown in Figure 4. It can be seen that WGJ steel has higher initial elastic modulus than CSS at elevated temperatures as well.

Since this paper emphasizes on the residual stress distribution of welded I sections, the material property and structural performance of WGJ steel under fire and corrosion conditions will not be discussed further.

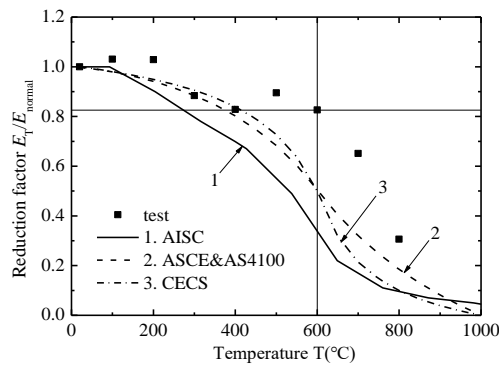


Fig. 4 Reduction factors of initial elastic modulus in the test and specifications at different temperatures

2.3. Measuring residual stress by sectioning process

The sectioning process was conducted following the guidance of Tebedge et al. [3]. A Wire-cut Electronic Discharge Machining (WEDM) was employed to reduce thermal effects. The strain values were calculated based on the deformation of strips which was measured by using YB-25 strain gage (as shown in Figure 5) before and after the sectioning process. The gauge length of YB-25 strain gage was $L_0=250\text{mm}$ and the tolerance was 0.001mm.

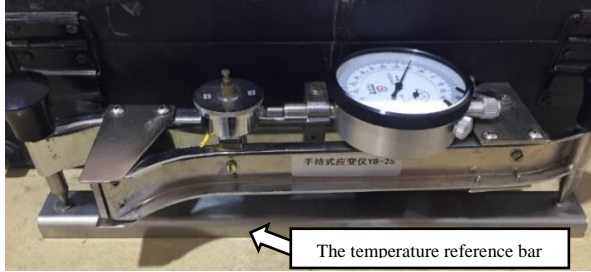


Fig. 5 YB-25 strain gage and the temperature reference bar

According to Tebedge et al. [3], tested segments should be selected more than 1.0 times of the section height (H) away from both ends of members to reduce the end effects. In this experimental program, since the length of all specimens and strips was the same, the distances from the test segments to the ends were taken as 365mm, which was more than 1.0H for all three specimens RI1, RI2, RI3, respectively.

An example was given in Figure 6 for specimen RI1 to show the sectioning arrangement. The length of strips was 270mm and the distance of YB-25 gage holes was 250mm. As shown in the section view in Figure 6, the top and bottom flanges of RI1 were both cut into 15 strips with a width of 5mm each, and the web was cut into 10 strips with a width of 10mm.

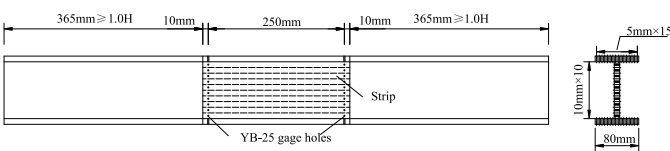


Fig. 6 Sectioning arrangement of RI1

The sectioning process consisting of 3 steps is illustrated in Figure 7. Before sectioning, holes were drilled based on the arrangement shown in Figure 6, except some holes at the junction of the flange and web. Then the YB-25 strain gage was placed on each couple of holes to measure the initial gage length r_1 . After that, the specimen was cut into segments by using the WEDM and the middle part was 270mm long. The flanges and web were sliced further, and the holes had not been prepared before sectioning process could be drilled at this time. YB-25 strain gage was used to measure the distances of the holes drilled just now, and these values were also designated as r_1 . The flanges and web were cut into strips and the distance between each couple of holes on the strip was measured by YB-25 strain gage and it was designated as r_3 . The distance of holes on both sides of each strip was measured and recorded, and the average

was taken for the subsequent analysis and modeling. The strips obtained from sectioning process are shown in Figure 8.

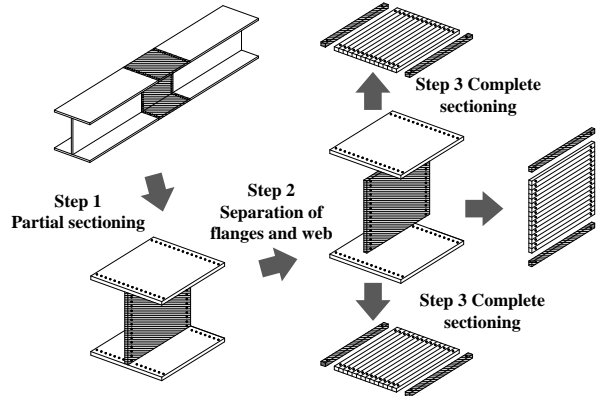


Fig. 7 Process of sectioning

In addition, bending deformation of strips should be measured and used to calibrate the results obtained from YB-25 strain gages. The bending deformation measurement is shown in Section 2.4. A reference bar for temperature compensation was applied to eliminate the error resulting from the temperature change during the test process.

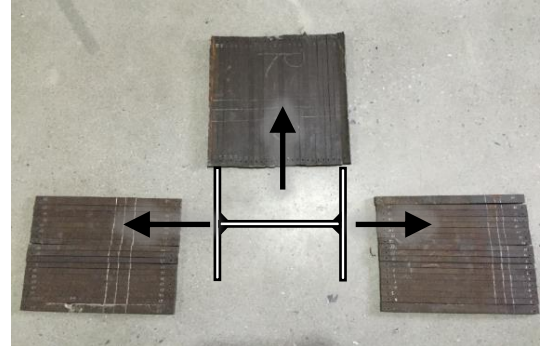


Fig. 8 Strips of RI3 after sectioning process

Residual strain can be obtained by comparing the initial reading r_1 prior to the sectioning process and the final reading r_3 after sectioning. The residual strain can be calculated according to Eq. 1.

$$\varepsilon = \frac{(r_3 + \Delta r_{t3}) - (r_1 + \Delta r_{t1})}{L_0 + r_1 + \Delta r_{t1}} \quad (1)$$

where L_0 is the gauge length of YB-25 strain gage and equals 250mm, $\Delta r_{ti}(i=1, 3)$ is the reading of the temperature reference bar.

2.4. Bending deformation measurement

After sectioning, it was observed that some strips cambered out of straightness, especially those close to flame-cut edges and welding regions. Therefore, the measured value was the chord length rather than the arc length between two holes, so corrections should be incorporated in the calculation of residual strain.

As shown in Figure 9, a highly flat marble was employed as the reference plane, and a type of vertical caliper was applied to measure the offset of the strip.

Tebedge et al. [3] suggested a bending correction equation as given in Eq. 2. By moving the strip, the maximum offset was measured and designated as δ in this paper.

$$\varepsilon_r = \varepsilon + \frac{(\delta/L)^2}{6(\delta/L)^4 + 1} \quad (2)$$

where ε_r is the residual strain incorporating bending correction, and L is the

gauge length of YB-25 strain gage and equals ($L_0+r_1+\Delta r_{tl}$).

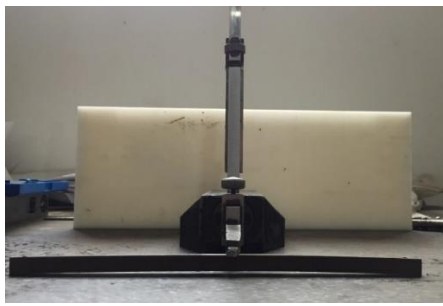


Fig. 9 Deformation measurement of a bending strip

Following the Hooke's Law, residual stress at the measured surface can be calculated as follows:

$$\sigma_r = -E \cdot \varepsilon_r \quad (3)$$

where E is the Young's modulus of WGJ steel and taken as $E=196533$ MPa obtained from the material test results in this paper.

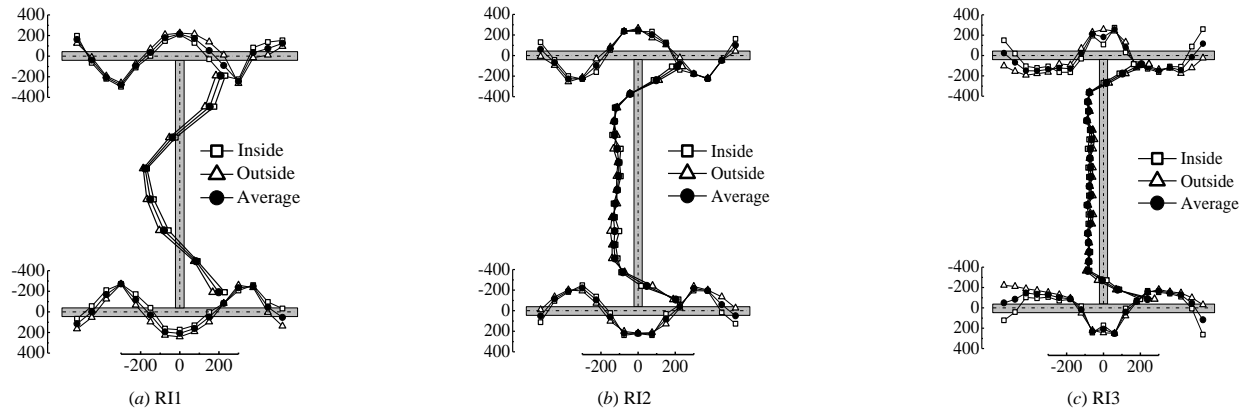


Fig. 10 Residual stress for all sections (MPa), compressive stress in negative and tensile stress in positive

Table 2

Characteristic values of residual stress at typical locations

	Results in flanges (MPa)						Results in web (MPa)						
	σ_{frc1}	σ_{frc2}	σ_{frc3}	σ_{frc4}	σ_{frt1}	σ_{frt2}	σ_{frt1}	σ_{frt2}	σ_{frt3}	σ_{frt4}	σ_{wrc}	σ_{wrt1}	σ_{wrt2}
RI1	-278.7	-245.9	-270.1	-247.3	215.8	207.8	160.8	123.7	116.3	53.2	-177.3	199.1	208.6
RI2	-228.4	-224.0	-219.3	-215.0	249.1	225.4	60.6	101.4	51.7	51.1	-132.9	203.5	210.2
RI3	-151.0	-150.0	-145.4	-166.5	256.2	252.2	23.8	116.8	-48.9	117.1	-89.5	238.6	206.1

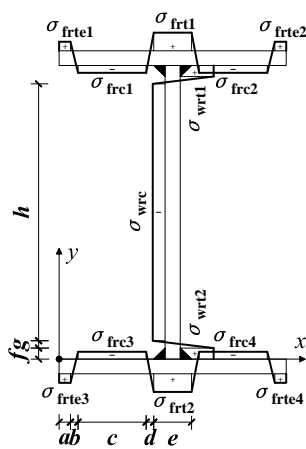


Fig. 11 Distribution and characteristic values of residual stress

3. Residual stress and analysis

3.1. Residual stress results

In this experimental program, 3 specimens were cut into 155 strips in all and then more than 2000 data were recorded. Figure 10 summarizes the magnitude and distribution of residual stresses for each specimen. In these figures, compressive stress is negative while tensile stress is positive. Test results include measurements from both inside and outside surface of each strip and the average values are taken and presented in Figure 10.

The distribution pattern of residual stress for WGJ steel welded I sections is simplified as shown in Figure 11, which is similar to the distribution pattern for CSS as discussed in Section 1. Tensile residual stress was observed at weld regions and flange edges in Figure 11, while compressive residual stress was observed at middle regions of the steel plates. σ_{frt1} and σ_{frt2} represent the maximum values of tensile residual stress at welding regions of two flanges, while σ_{wrt1} and σ_{wrt2} represent the maximum stresses in the web. σ_{frci} ($i=1,2,3,4$) respectively denotes the maximum compressive residual stress in one of the four outstand flanges, while σ_{wrc} denotes the maximum one in the web. At last, σ_{frtei} ($i=1,2,3,4$) respectively denotes the maximum tensile residual stress at each flame-cut edge in the flange. These characteristic values are summarized in Table 2.

3.2. Effects of width-thickness ratio

Magnitude of compressive and tensile residual stresses are given in Figure 12, where compressive stresses both in flanges and webs decrease monotonously as width-thickness ratios increase. This is because the residual stress after cooling process can be dispersed more effectively when the width-thickness ratio is larger. Compressive stresses in flanges reduce more rapidly than those in webs.

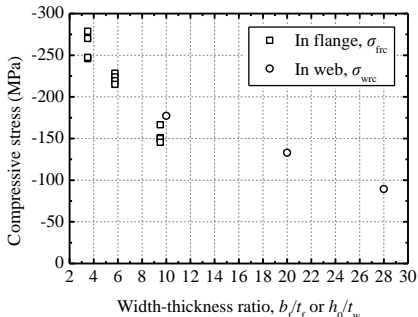
Tensile stresses at welding regions in flanges vary slightly from 215.8 MPa to 256.2 MPa ($256.2/215.8=1.19$), and have no clear correlation with width-thickness ratios. On the other hand, tensile stresses at flame-cut edges in flanges change more irregularly from -48.9 MPa to 123.7 MPa.

3.3. Closing error

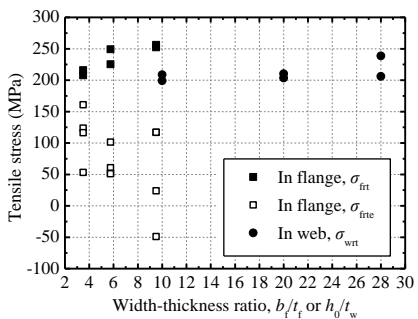
Since there is no external force applied on tested segments, the closing error of residual stress over the whole cross section should be equal to zero to satisfy stress equilibrium. Thus, the closing error, defined by Eq. 4, can be used to verify the accuracy of test results.

$$\sigma_{\text{err}} = \left[\sum_{i=1}^n A_i \cdot \sigma_{ri} \right] / \sum_{i=1}^n A_i \quad (4)$$

where n is the number of strips, A_i is the sectional area of each strip, σ_{ri} is the residual stress magnitude of one strip.



(a) Compressive residual stresses



(b) Tensile residual stresses

Fig. 12 Relationship of residual stresses and width-thickness ratios

So as to investigate the relationship between residual stress in the flange and web, the closing error in each individual steel plate was obtained and shown

in Figure 13. Figure 13 illustrates that the closing error of the whole section for RI1, RI2, or RI3 is no more than ± 30 MPa (around 7% of $f_{0.2}$). It indicates that sections of all specimens are in stress equilibrium, and the test results of residual stress are correct.

With regard to the closing error in flanges, the maximum closing error is -27.2 MPa in top flanges, while -29.7 MPa in bottom flanges. In specimen RI2, the closing error in the web is -55.9 MPa (around 13% of $f_{0.2}$), which is the greatest value of closing error both in individual plates and in whole sections.

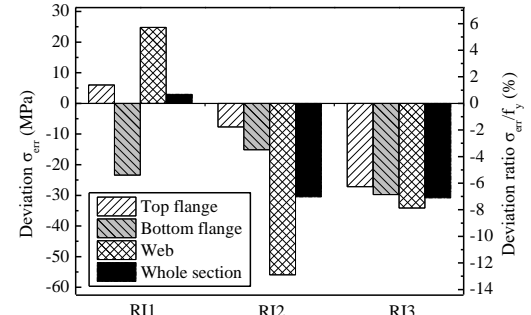


Fig. 13 Residual stress closing error of whole sections and individual parts

In summary, the stress equilibrium assumption is valid with the individual flanges and web for each specimen. In other words, residual stress in the flange is independent of that in the web.

4. Modeling of residual stress for WGJ steel welded I sections

4.1. Existing residual stress distribution models

Many distribution models of residual stress were proposed by other researchers, as shown Figure 14. Model (a) was proposed by Li et al. [31] and Model (b) [12] was adopted in Chinese standard for the steel structure design GB 50017-2003 [11]. These two models are suggested for residual stress when designing steel columns under axial compression. Chernenko and Kennedy [6] proposed Model (c) by studying former experimental data of CSS sections. These 3 models can be adopted when investigating flame-cut welded I sections fabricated from CSS, but may not be appropriate for HSS or HPS sections.

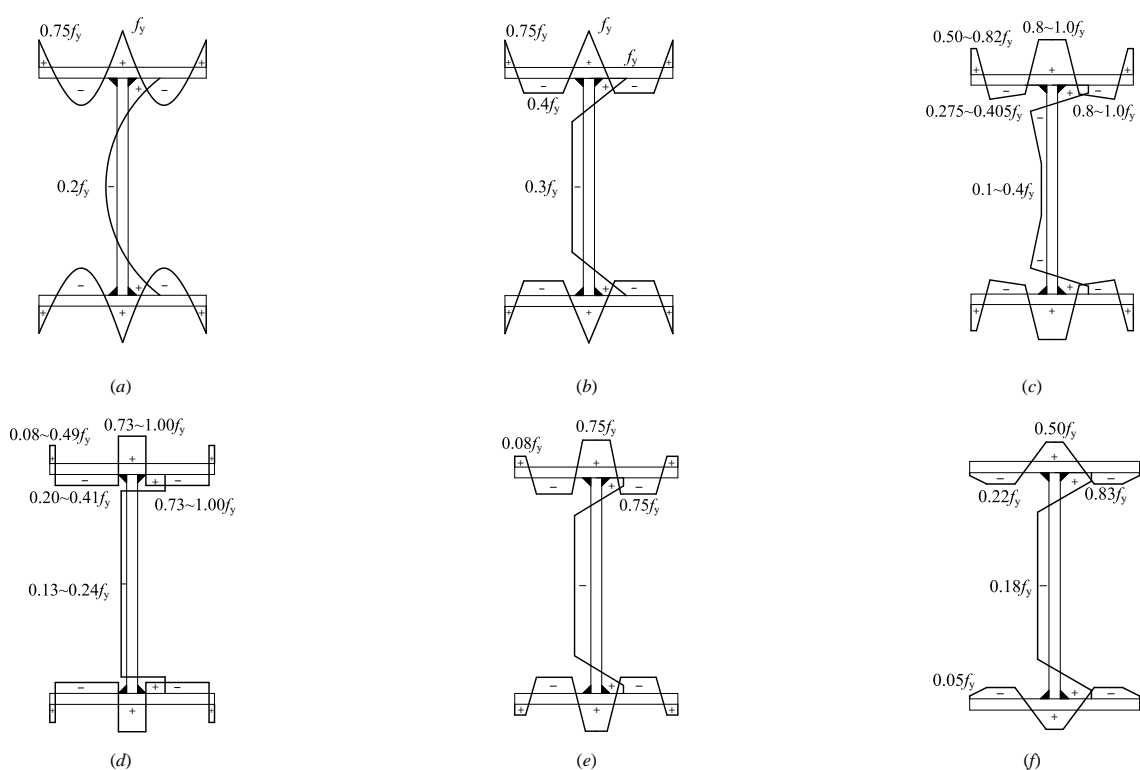


Fig. 14 Existing residual stress distribution models for flame-cut welded I sections

Model (d) was presented in 2012 [17] based on the test of 3 flame-cut welded I section columns with a nominal yield strength of 460 MPa. Ban et al. [18] summarized previous research and proposed Model (e) in 2013 based on original data measured from 8 I sections made of 460 MPa steel. In Model (e), tensile stresses remain constant and compressive stresses are calculated according to the function of plate thickness and width-thickness ratio (b_f/t_f , or h_0/t_w). As for HPS sections, Yang et al. [23] suggested Model (f), which could be applied to describe the residual stress distribution of 460 MPa GJ steel I sections.

Considering the special mechanical properties of WGJ steel, the distribution model of residual stress for WGJ steel I sections may be different from the existing models mentioned above.

4.2. Proposed model

WGJ steel is a new type of HPS with high strength, so Model (d), (e) or (f) may be possible solutions, while Model (a), (b) and (c) are suggested for CSS sections. However, tensile stresses at flange edges turn into compressive stresses discontinuously in Model (d), which does not match the test results. In addition, in Model (f), residual stresses at flange edges are negative, which does not match the test results observed in Section 3.1, either.

After examining the existing distribution models and the test results of residual stress, the distribution pattern characterized in Figure 11 or Model (e) in Figure 14 was adopted in this paper to describe the residual stress of flame-cut welded I sections fabricated of WGJ steel.

In Figure 11 or Model (e), tensile stresses and compressive stresses in some regions remain constant (σ_{fr} , σ_{frte} , σ_{frc} , σ_{wrt} , σ_{wrc} are constant values), and change linearly and continuously in other regions. Since the section referred in this paper is doubly symmetric and the section is in stress equilibrium, the residual stress distribution should be doubly symmetric as well. Thus, the characteristic values of residual stress at symmetric positions are the same ($\sigma_{fr1,2}=\sigma_{fr}$, $\sigma_{fr1,4}=\sigma_{frte}$, $\sigma_{fr1,4}=\sigma_{frc}$, $\sigma_{wrt1,2}=\sigma_{wrt}$).

According to the above discussion, the equations employed to quantify the residual stresses of welded I sections with WGJ steel are recommended as below.

$$\sigma_{fr}(x) = \sigma_{fr}(B-x) = \begin{cases} \sigma_{frte} & 0 \leq x \leq a \\ \sigma_{frte} + \frac{\sigma_{frc} - \sigma_{frte}}{b}(x-a) & a < x \leq a+b \\ \sigma_{frte} & a+b < x \leq a+b+c \\ \sigma_{frte} + \frac{\sigma_{frc} - \sigma_{frte}}{d}[x-(a+b+c)] & a+b+c < x \leq a+b+c+d \\ \sigma_{frte} & a+b+c+d < x \leq a+b+c+d+e/2 \end{cases} \quad (5)$$

$$\sigma_{wrt}(y) = \sigma_{wrt}(h_0-y) = \begin{cases} \sigma_{wrc} & 0 \leq y \leq f \\ \sigma_{wrc} + \frac{\sigma_{wrc} - \sigma_{wrt}}{g}(y-f) & f < y \leq f+g \\ \sigma_{wrc} & f+g < y \leq f+g+h/2 \end{cases} \quad (6)$$

where σ_{fr} is the residual stress at certain position (x) in the flange, while σ_{wrt} is the residual stress at certain position (y) in the web. Independent variable x is the coordinate along the flange while y is the one along the web, as shown in Figure 11. The geometrical symbols of a to h are illustrated in Figure 11 as well.

As shown in Figure 11, the following equations need to be met:

$$a+b+c+d+e/2=B/2 \quad (7)$$

$$f+g+h/2=h_0/2 \quad (8)$$

Since individual flanges and web for each specimen are in stress equilibrium, stresses in flanges σ_{fr} and stresses in the web σ_{wrt} should comply with Eq. 9 and Eq. 10.

$$\iint_{A_f} \sigma_{fr} dA = 0 \quad (9)$$

$$\iint_{A_w} \sigma_{wrt} dA = 0 \quad (10)$$

where A_f and A_w are areas of the flange and web respectively.

In this paper, only sections made of thin plates were investigated, so the

variation of residual stress along thickness direction was not concerned. Thus, equations below can be derived from Eq. 9 and Eq. 10.

$$\int_B \sigma_{fr}(x) dx = 0 \quad (11)$$

$$\int_{h_0} \sigma_{wrt}(y) dy = 0 \quad (12)$$

4.3. Parameters for tensile residual stress

The experimental results of residual stresses in flanges and webs are summarized in Figure 15 and Figure 16 where the outstand plate is divided into 10 portions to describe the relative position of the measured data. According to the experimental results shown in Figure 10 and Table 2, maximum tensile residual stress σ_{frt} ranges from 207.8 MPa to 256.2 MPa, corresponding to 48% to 59% of 0.2% offset yield strength ($f_{0.2}$), which is 433.8 MPa as obtained in Section 2.2. Therefore, σ_{frt} is suggested as 260.3 MPa, 60% of $f_{0.2}$, to cover all the measurement.

The tensile residual stress at the flame-cut edge varies from -48.9 MPa to 160.8 MPa, corresponding to -11% to 37% of 0.2% offset yield strength ($f_{0.2}$). Tensile stress at the flange edge is considered favorable for the stability of steel structure. Therefore, σ_{frte} is suggested as the average value of the measurement, which is 75 MPa, or 17% of $f_{0.2}$.

Distribution parameters in the flange (a , b , c , d , e) are identified based on Figure 15 and given in Table 3. The parameters a , b and e are constant, while c and d are determined according to Eq. 7 and Eq. 11.

In Figure 16, maximum tensile residual stress σ_{wrt} varies from 199.1 MPa to 238.6 MPa, corresponding to 46% to 55% of 0.2% offset yield strength ($f_{0.2}$). σ_{wrt} is suggested as 238.6 MPa, or 55% of $f_{0.2}$, to cover all the measurement. Distribution parameters in the web (f , g , h) are identified based on Figure 16 and given in Table 3. The parameter f is constant, while g and h are determined according to Eq. 8 and Eq. 12.

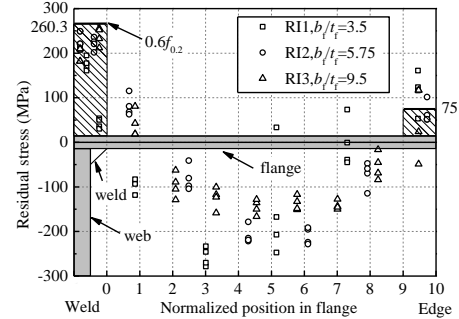


Fig. 15 Magnitude and distribution of residual stresses in the flange

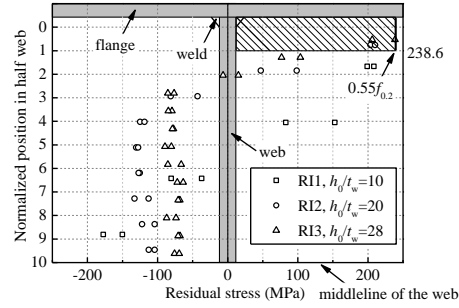


Fig. 16 Magnitude and distribution of residual stresses in the web

Table 3
Distribution parameters of the residual stress model

a	b	c	d
0.1(b_f-h_f)	0.2(b_f-h_f)	Eq. (7), (11)	Eq. (7), (11)
e	f	g	h
t_f+2h_f	$h_f+0.05(h_0-2h_f)$	Eq. (8), (12)	Eq. (8), (12)

4.4. Parameters for compressive residual stress

As discussed in Section 3.2, the magnitude of compressive residual stresses

is affected by the width-thickness ratio (b_f/t_f , or h_0/t_w). It was also concluded by Ban et al. [18] that the magnitude of compressive residual stresses is also affected by the steel plate thickness (t_f , or t_w). Therefore, two empirical fitting equations are proposed here and can be used to determine the compressive residual stress of welded I sections with WGJ steel:

$$\begin{cases} \sigma_{\text{fr}} = \sigma_{\text{fr}0} + K_{\text{fr}1} (b_f / t_f)^{\alpha_{\text{fr}}} + K_{\text{fr}2} (t_f)^{\beta_{\text{fr}}} \\ \sigma_{\text{wr}} = \sigma_{\text{wr}0} + K_{\text{wr}1} (h_0 / t_w)^{\alpha_{\text{wr}}} + K_{\text{wr}2} (t_w)^{\beta_{\text{wr}}} \end{cases} \quad (13)$$

The coefficients in Eq. 13, including $\sigma_{\text{fr}0}$, $\sigma_{\text{wr}0}$, $K_{\text{fr}1}$, $K_{\text{fr}2}$, $K_{\text{wr}1}$, $K_{\text{wr}2}$, α_{fr} , β_{fr} , α_{wr} , β_{wr} , were obtained from nonlinear fitting by using the general software Origin, based on the test results given in Table 2. The fitting result was shown in Eq. 14. It should be noted that the calculated results of compressive residual stress from the fitting equation Eq. 14, where both σ_{fr} and σ_{wr} , may be larger than 0.2% offset yield strength ($f_{0.2}$) when width-thickness ratios are small. In case of this situation, the maximum magnitude of compressive residual stress should be limited to $f_{0.2}$.

$$\begin{cases} \sigma_{\text{fr}} = 1100 - 2890(b_f / t_f)^{-0.04} + 170(t_f)^{0.9} \geq -f_{0.2} = -433.8 \\ \sigma_{\text{wr}} = 1790 - 5190(h_0 / t_w)^{-0.015} + 43500(t_w)^{-1.16} \geq -f_{0.2} = -433.8 \end{cases} \quad (14)$$

However, Eq. 14 is still too complex for engineering application, and it is further simplified to Eq. 15, which can clearly describe the increasing trend of compressive residual stresses as width-thickness ratios (b_f/t_f , h_0/t_w) and steel plate thickness (t_f , t_w) decrease.

Coefficients α_{fr} , β_{fr} , α_{wr} , β_{wr} are taken as -1.0 in Eq. 15. The other coefficients in Eq. 15, including $\sigma_{\text{fr}0}$, $\sigma_{\text{wr}0}$, $K_{\text{fr}1}$, $K_{\text{fr}2}$, $K_{\text{wr}1}$, $K_{\text{wr}2}$ are determined in the similar way through nonlinear fitting based on the test results given in Table 2.

$$\begin{cases} \sigma_{\text{fr}} = 50 - 570 \times \frac{1}{b_f / t_f} - 1570 \times \frac{1}{t_f} \geq -f_{0.2} = -433.8 \\ \sigma_{\text{wr}} = 120 - 1140 \times \frac{1}{h_0 / t_w} - 1840 \times \frac{1}{t_w} \geq -f_{0.2} = -433.8 \end{cases} \quad (15)$$

Table 4

Compressive residual stresses obtained from proposed equations and comparison with test results

Label	$\sigma_{\text{fr},f}$ (MPa)	$\sigma_{\text{fr},f}/\sigma_{\text{fr},t}$	$\sigma_{\text{fr},fs}$ (MPa)	$\sigma_{\text{fr},fs}/\sigma_{\text{fr},t}$	$\sigma_{\text{wr},f}$ (MPa)	$\sigma_{\text{wr},f}/\sigma_{\text{wr},t}$	$\sigma_{\text{wr},fs}$ (MPa)	$\sigma_{\text{wr},fs}/\sigma_{\text{wr},t}$
RI1	-298.4	1.145	-269.9	1.036	-214.3	1.209	-178.0	1.004
RI2	-244.3	1.102	-206.1	0.930	-162.5	1.223	-121.0	0.911
RI3	-190.8	1.245	-167.0	1.090	-137.5	1.537	-104.7	1.171

where $\sigma_{\text{fr},f}$ and $\sigma_{\text{wr},f}$ denote compressive residual stresses in flanges and webs determined by the fitting equation Eq. 14 respectively. $\sigma_{\text{fr},t}$ and $\sigma_{\text{wr},t}$ represent the test results of compressive residual stresses in flanges and webs, respectively. $\sigma_{\text{fr},fs}$ and $\sigma_{\text{wr},fs}$ denote compressive residual stresses in flanges and webs determined by the simplified fitting equation Eq. 15 respectively.

4.5. Model validation

Based on the model given in Section 4.2 and parameters determined in Section 4.3 and Section 4.4, the modeling results of residual stress are obtained and illustrated in Figure 17 with black solid lines. Notice that the compressive stresses (σ_{fr} and σ_{wr}) applied in this model are identified by the simplified fitting equation Eq. 15 and shown in Table 4. It is found that the modeling results are in good agreement with the test results. The validation indicates that the proposed model in this paper can be employed to identify the magnitude and distribution of residual stresses for WGJ steel flame-cut welded I sections.

It should be noted that the results of this investigation are only applicable to steel members with special material properties, limited shape and dimensions of the section, and specific welding and manufacturing process. More theoretical and experimental researches are in need to confirm and improve the proposed modeling approach.

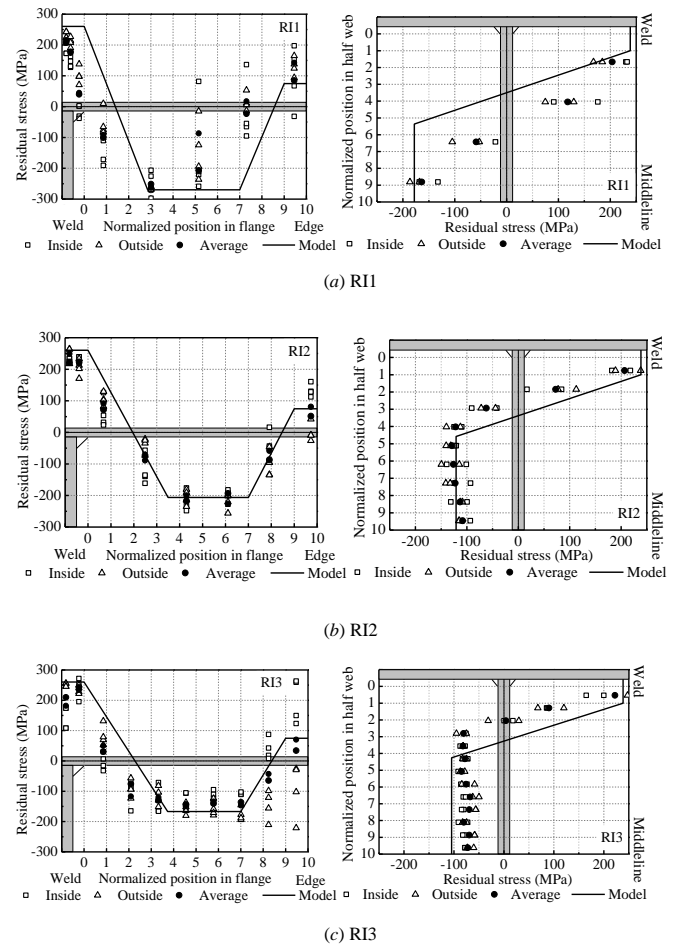


Fig. 17 Comparison of proposed model with experimental results

4.6. Analysis of the magnitude of residual stress

Ban [19] proposed a versatile model to estimate the magnitude and distribution of residual stresses, which was applicable to welded I sections and box sections fabricated from steel with various strength. Table 5 and Figure 18 compared the calculating results of residual stresses for specimen RI1, RI2 and RI3 based on the proposed model by Ban and the proposed model in this paper, respectively.

It is observed that for every specimen, the magnitude of tensile stress (i.e. $\sigma_{\text{fr},t}$, $\sigma_{\text{wr},t}$) and compressive stress (i.e. $\sigma_{\text{fr},f}$, $\sigma_{\text{wr},f}$) given by Ban's model are larger than those given by the proposed model in this paper. This is mainly because these two models are applicable to different types of steel. Ban's model is for HSS sections, while the proposed model in this paper is for WGJ steel sections. So it can be concluded that when applying WGJ steel in manufacturing flame-cut welded I sections, the residual stresses can be reduced to some extent.

Table 5

Characteristic values of residual stress obtained from Ban (2012) and this paper

Label	Proposed model by Ban (2012)				Proposed model in this paper			
	$\sigma_{\text{fr},t}$ (MPa)	$\sigma_{\text{wr},t}$ (MPa)	$\sigma_{\text{fr},f}$ (MPa)	$\sigma_{\text{wr},f}$ (MPa)	$\sigma_{\text{fr},t}$ (MPa)	$\sigma_{\text{wr},t}$ (MPa)	$\sigma_{\text{fr},f}$ (MPa)	$\sigma_{\text{wr},f}$ (MPa)
RI1	345	345	-386.2	-266.0	260.3	238.6	-269.9	-178.0
RI2	345	345	-282.2	-156.0	260.3	238.6	-206.1	-121.0
RI3	345	345	-218.4	-124.6	260.3	238.6	-167.0	-104.7

Residual stress is associated with the non-uniform plastic deformation in a rather narrow weld zone which is restrained by the rest of the plate. During the welding process, the welding region is heated while strength and elastic modulus of steel decrease rapidly, so the plastic deformation is more likely to happen. As shown in Figure 19, because of the higher strength and stiffness of WGJ steel at high temperature when welding (detailed mechanical properties can be observed in the test results mentioned in Section 2.2), plastic strain at weld regions of the WGJ steel section under certain thermal stress σ_{T0} (caused by non-uniform heat) is less than that of the HSS or CSS section. As a result,

the residual deformation and residual stress at welding regions of the WGJ steel section after cooling may be much less. Since the tensile residual stress is reduced, the compressive residual stress decreases as well because of stress equilibrium.

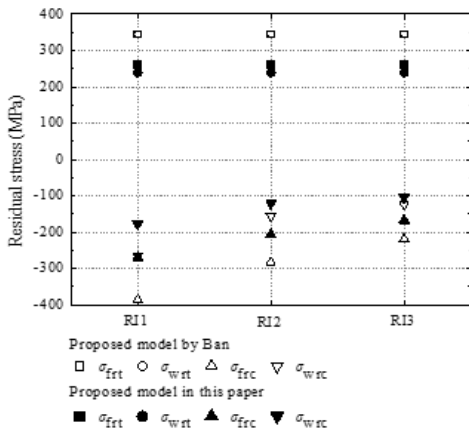


Fig. 18 Comparison of residual stresses obtained from Ban (2012) and this paper

The explanation above just gives one possible reason why residual stresses are reduced when applying welded I sections fabricated of WGJ steel. Further study should be conducted on this topic.

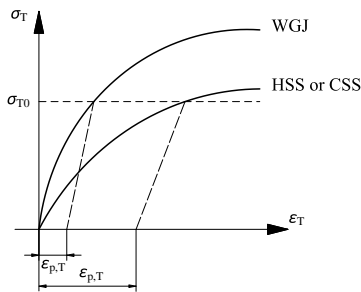


Fig. 18 Stress-strain curves for HSS, CSS and WGJ steel at high temperature

5. Conclusions

The residual stress in flame-cut welded I sections fabricated from a new type of HPS, designated as WGJ steel, were investigated in this experimental program. The sectioning method was applied to cut the plates into strips. Residual strain was measured by using YB-25 strain gage. Based on the experimental measurement and analysis on the effects of sectional dimensions and interactions between flanges and webs, a distribution model of residual stress was proposed and validated through experimental results. Based on this work, the following conclusions can be drawn:

1. The distribution pattern of residual stress for WGJ steel welded I sections was similar to that for HSS or HPS I sections, but the magnitude of tensile residual stresses and compressive residual stresses was quite different.

2. Compressive stresses both in flanges and webs decreased monotonously as the width-thickness ratios increased. In addition, the residual stresses in flanges were not related to those in webs.

3. Maximum tensile residual stresses at welding regions in both flanges and webs for WGJ steel were much lower than the steel yield strength (for WGJ

6. Acknowledgement

The authors gratefully acknowledge the financial supports from the National Natural Science Foundation of China (No. 51578313). Thanks are also extended to Beijing Innovation Center for Metropolitan Transportation for the research facilities provided. The test material and specimens provided by Wuhan Iron and Steel (Group) Company are highly appreciated.

References

- [1] Wang G.Z. and Qu L.Q., "Steel Structure: Principle and Design", Tsinghua University Press, Beijing, China, 1993. (in Chinese).
- [2] Alpsten G.A. and Tall L., "Residual stresses in heavy welded shapes", Welding Journal, 49(3), 93-105, 1970.
- [3] Tebedge N., Alpsten G. and Tall L., "Residual-stress measurement by the sectioning method", Experimental Mechanics, 13(2), 88-96, 1973.
- [4] Fukumoto Y. and Itoh Y., "Statistical study of experiments on welded beams", Journal of the Structural Division, ASCE, 107(1), 89-103, 1981.
- [5] Wang G.Z. and Zhao W.W., "Residual stress measurement for welded and hot-rolled I section steels", Industrial Construction, 16(7), 32-37, 1986. (in Chinese).
- [6] Chernenko D.E. and Kennedy D.J.L., "An analysis of the performance of welded wide flange columns", Canadian Journal of Civil Engineering, 18(14), 537-555, 1991.
- [7] Goto Y. and Kawanishi N., "Change of weld residual stresses due to loss of material", Journal of Structural Engineering, 132(12), 1940-1947, 2006.
- [8] British Standards Institution, Eurocode 3: Design of Steel Structures: Part 1-1: General Rules and Rules for Buildings, EN 1993-1-1, 2005.
- [9] European Convention for Constructional Steelworks, Manual on Stability of Steel Structures: Part 2.2: Mechanical Properties and Residual Stresses, Second Edition. ECCS Publ., 1976.
- [10] American Institute of Steel Construction, Specification for Structural Steel Buildings, ANSI/AISC 360-10, Chicago, 2010.
- [11] Ministry of Housing and Urban-Rural Development, Code for Design of Steel Structures, GB 50017-2003, China Planning Press, China, 2003 (in Chinese).
- [12] Code for Design of Steel Structures Committee, Application Construal of Code for Design of Steel Structures in China, China Planning Press, China, 2003 (in Chinese).
- [13] Shi G., Ban H.Y., Shi Y.J. and Wang Y.Q., "Recent research advances on high strength and high performance steel structures in Tsinghua University", Proceedings of the 6th International Symposium on Steel Structures (ISSS-2011), Seoul, Korea, 984-991, 2011.
- [14] Rasmussen K.J.R. and Hancock G.J., "Plate slenderness limits for high strength steel sections", Journal of Constructional Steel Research, 23(1), 73-96, 1992.
- [15] Rasmussen K.J.R. and Hancock G.J., "Tests of high strength steel columns", Journal of Constructional Steel Research, 34(1), 27-52, 1995.
- [16] Beg D. and Hladnik L., "Slenderness limit of class 3 I cross-sections made of high strength steel", Journal of Constructional Steel Research, 38(8), 201-217, 1996.
- [17] Wang Y.B., Li G.Q. and Chen S.W., "Residual stresses in welded flame-cut high strength steel H-sections", Journal of Constructional Steel Research, 79(12), 159-165, 2012.
- [18] Ban H.Y., Shi G., Bai Y., Shi Y.J. and Wang Y.Q., "Residual stress of 460 MPa high strength steel welded I section: Experimental investigation and modeling", International Journal of Steel Structures, 13(4), 691-705, 2013.
- [19] Ban H.Y., "Research on the Overall Buckling Behavior and Design Method of High Strength Steel Columns under Axial Compression", PhD thesis, Tsinghua University, Beijing China, 2012 (in Chinese).
- [20] Chen J., "Measurement and Analysis on Residual Stress in Welded I-shaped Cross-sectional Member", MS thesis, Chongqing University, Chongqing, China, 2010 (in Chinese).
- [21] Yang B., Nie S.D., Kang S.B., Xiong G., Hu Y., Bai J.B., Zhang W.F. and Dai G.X., "Residual Stress Measurement on Welded Q345GJ Steel H-Section by Sectioning Method and Method Improvement", Advanced Steel Construction, 13(1), 78-95, 2017.
- [22] Qiu L.B., Xue S.D., Hou Z.X., Liu Y. and Shu G.P., "Experimental study of residual stresses in Q550GJ high-strength steel welded H-type sections", Journal of Beijing University of Technology, 41(7), 1035-1042, 2015. (in Chinese).
- [23] Yang B., Nie S.D., Xiong G., Hu Y., Bai J.B., Zhang W.F. and Dai G.X., "Residual stresses in welded I-shaped sections fabricated from Q460GJ structural steel plates", Journal of Constructional Steel Research, 122, 261-273, 2016.
- [24] Li T.J., Liu S.W. and Chan S.L., "Cross-sectional analysis of arbitrary sections allowing for residual stresses", Steel & Composite Structures, 18(4), 985-1000, 2015.
- [25] Li T.J., Liu S.W. and Chan S.L., "Direct analysis for high-strength steel frames with explicit-model of residual stresses", Engineering Structures, 100, 342-355.
- [26] Standardization Administration of China, Metallic materials - tensile testing - Part 2: Method of test at elevated temperature, GB/T 228.2-2015, Beijing, Standards Press of China, 2015. (in Chinese).
- [27] Wang Y.Q., Wang Z.X., Hu X.G., Han J.K. and Xing H.J., "Experimental study and parametric analysis on the stability behavior of 7A04 high-strength aluminum alloy angle columns under axial compression", Thin-Walled Structures, 108, 305-320, 2016.
- [28] American Society of Civil Engineers, Structural Fire Protection, ASCE Manual and Reports on Engineering Practice No. 78, New York, 1992.
- [29] Australia Standards, Steel Structures, AS 4100:1998, Sydney, Australia, 1998.
- [30] China Association for Engineering Construction Standardization, Technical Code for Fire Safety of Steel Structure in Buildings, CECS 200:2006, China Planning Press, China, (in Chinese).
- [31] Li K.X., Xiao Y.H., Nao X.F., Cui J. and Zhu W., "Column curves for steel compression member", Journal of Chongqing Architecture University, 1, 24-33, 1985. (in Chinese)

RESEARCH ON INFLUENCE OF MEMBER INITIAL CURVATURE ON STABILITY OF SINGLE-LAYER SPHERICAL RETICULATED DOMES

Yang Ding^{1,2} and Tian-long Zhang^{1,*}

¹ School of Civil Engineering, Tianjin University, Tianjin, China

² Key Laboratory of Coast Civil Structural Safety of the Ministry of Education, Tianjin University, Tianjin, China

* (Corresponding author: E-mail: ztl1019@126.com)

ABSTRACT

The distribution modes and magnitudes of member initial curvature significantly influence the stability of single-layer reticulated dome. Based on the deflection curvature of a compression bar with unequal end moments, a numerical simulation method for member initial curvature considering end moment effects is proposed using multi-beam methods based on ABAQUS. The approach is verified through a comparison of experiments using different systems. Using Kiewitt-8 dome as an example, the extent of the member initial curvature's effect on the stability bearing capacity of these dome for different structure parameters is studied. The results show that the bending moments at the bar's ends can affect the deflection shape of a compression bar and that the most unfavorable condition occurs when the member initial curvatures are coordinate with the deflection shapes. The reduction degree of the stability load-bearing capacity of such dome modelled using member initial curvatures considering end moments is greater than that for curvatures without considering end moments. The influence of different member initial curvature amplitudes on the stability of these dome varies significantly, and a reasonable maximum value of the member initial curvature is proposed for performing stability analysis based on the structure response and realistic construction conditions.

Copyright © 2019 by The Hong Kong Institute of Steel Construction. All rights reserved.

ARTICLE HISTORY

Received: 13 February 2017
Revised: 16 December 2017
Accepted: 17 December 2017

KEY WORDS

Single-layer spherical reticulated dome;
Nonlinear stability;
Bearing capacity;
Member Initial curvature;
End Moment

1. Introduction

The single-layer reticulated dome is a structure formed with slender compression members and rigid joints. Traditional design procedures for long-span space reticulated structures assume that the shape of each member is a straight line and that the stability analysis of reticulated structures considering the effect of geometric nodal imperfections is conducted without accounting for the effects of member initial defects under normal conditions [1,2]. As a principal factor, the range of geometric nodal imperfections is required and controlled by structural construction codes and technical specifications [3,4]. However, prefabricated bars of these dome may unavoidably become bent during production and transport, resulting in member initial curvatures. The member initial curvatures may reduce the buckling strength of the bars under axial compression load, due to the $P\text{-}\delta$ effect, leading to a redistribution of forces among members in the neighboring regions and to an interaction between individual member buckling and global instability of the dome, which may adversely affect the stability bearing capacity of the dome [5,6].

To investigate the influence of the $P\text{-}\delta$ effect on the stability bearing capacity, adopting shell element to model thin-walled members based on the finite element (FE) method is a direct approach. Kumar *et al.* [7] and Lotfollahi *et al.* [8] proposed shell elements in FE models to investigate the post-buckling performance of steel braces. However, it is extremely complicated to model and analyze a single-layer reticulated dome using shell elements due to the demanding computational requirements. Another possible solution is using beam elements. A plastic hinge model was developed by Liew *et al.* [9] based on the buckling of members without physically altering the member geometry, although this approach is not practical for simulating the cyclic hysteresis behaviour of struts due to the lack of unloading curves. Qi *et al.* [10] introduced a phenomenological model, the Marshall model [11], to consider this interaction. However, the applicable strain range is too narrow to simulate the large deformation of the strut. A theoretical strut model was proposed in Reference [12] using the one-element-per-member method to account for the interaction between individual member buckling and global structural instability, which requires an assumption for the effective length first. Chan *et al.* [13] presented a single-imperfect-element-per-member method that need not assume the effective length and that includes the effects of initial imperfections in the element stiffness. However, this method is based on the underlying assumption that the element is prismatic and elastic.

When a design load induces plasticity in a single-layer spherical reticulated dome, the multi-element-per-member method can accurately simulate the plastic non-linear behavior by dividing one member into more straight elements to study second-order effects on the non-linear stability of the dome. The multi-element-per-member method can present the $P\text{-}\delta$ effect under different end-constraint conditions and avoid the limitations of the effective length assumption. Plastic hinges at different locations in each member can be captured

by the multi-beam method rather than the one-element method [14,15]. Zhou *et al.* [16] proposed initial bending 3D link elements and initial bending 3D beam elements assuming that the initial bending shape of the members is a half-period sine curve, and studied the effects of the bearing capacity of the cable-arch structures. Yan *et al.* [17] adopted the multi-beam method to model the initial curvature of members based on FE analysis and investigated the influence of the direction angle and the amplitude of random variables of the initial curvature of members on the stability of a reticulated shell structure. Wang *et al.* [18] established multi-beam elements with an initial curvature by combining a half-period sine curve and a full-period sine curve to determine the effects on the buckling capacity and seismic response. In the Hong Kong Steel Code [19,20], a second-order analysis method uses a length-free assumption by introducing a half-period sine curve as the member initial curvature. However, this member-only initial bow function is too simple to consider the end moment effect.

In practice, the joints of single-layer reticulated dome are nearly rigid or semi-rigid, and the axial forces as well as the bending moments are transmitted directly by the joints. The bending moments at the bars' ends may affect the buckling shapes of compression bars in single-layer reticulated dome. The existing functions of member initial curvatures do not consider the end moment effect. In this paper, the deflection equilibrium equation for a compression bar with end moments is derived; the results indicate that member initial curvature with a half-period sine curve is not the most unfavorable condition. According to the deflection equilibrium equations, two types of member initial curvatures are proposed that consider the end moment effect to avoid the limitations of the existing curvature functions. A numerical modelling method for determining the member initial curvature in single-layer reticulated dome is proposed via the multi-beam method based on the ABAQUS finite-element program. In addition, the approach is verified through comparison with experiments on different systems. Taking Kiewitt-8 dome as an example, the extent of the member initial curvature's influence on the stability bearing capacity of single-layer reticulated dome with different structure parameters is studied. The influence of different member initial curvature amplitudes is discussed to inform the selection of a reasonable maximum value of the member initial curvature for stability analysis of single-layer reticulated dome.

2. Member initial curvature of compression bar

2.1. Member initial curvature of compression bar with hinged joints

A compression bar with pinned supports balances against bending deformation as soon as it reaches a critical equilibrium state under an axial compression load, as shown in Fig. 1.

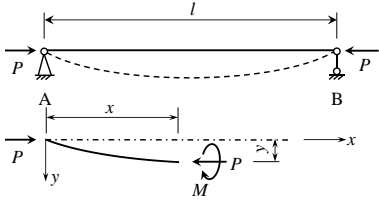


Fig. 1 Deflection shape of compression bar with hinged joints

Given distance x from the left end, the force equilibrium equation and approximate deflection differential equation of the bar are specified as

$$Ely'' = M = -Py \quad (1)$$

where l is the length of a single bar or member; E is the elastic modulus of material; I is the inertia moment of bar section; y is the deflection of a node in the local normal direction; M is the bending moment of bar section; P is the stability load-bearing capacity of compression bar. Let $k^2 = P/EI$ such that Eq. 1 becomes

$$y'' + k^2 y = 0 \quad (2)$$

The general solution of Eq. 2 is obtained as

$$y = C_1 \sin kx + C_2 \cos kx \quad (3)$$

where C_1 and C_2 are coefficients. Eq. 3 is solved by substituting the boundary conditions of the compression bar at the two ends: $y(0)=0$, $y(x)=0$. The result is $C_1 \sin kl = 0$, where $kl = n\pi$ ($n=\pm 1, \pm 2, \dots$). Therefore, the deflection curve of a compression bar with hinged joints under the most unfavorable condition when $n=1$ is obtained as follows

$$y = C_1 \sin(\pi x/l) \quad (4)$$

Eq. 4 accounts for the fact that the deflection shape of the compression bar with hinged joints is a half-period sine curve, which is the most unfavorable buckling mode. Therefore, the lowest stability bearing capacity is obtained when taking a half-period sine curve as the member initial curvature of a compression bar with pinned supports. The member initial curvature of a compression bar with hinged joints is specified as

$$\delta = \delta_{\max} \sin(\pi x/l) \quad (5)$$

where δ is the node imperfection considering the member initial curvature in the local normal direction; δ_{\max} is the amplitude of a member initial curvature imperfection.

2.2. Member initial curvatures of compression bar with end moments

When simulating the initial bending of members, the effect of end moments transmitted by rigid joints or semi-rigid joints should be considered in long-span space structures. The deformation shape of a compression bar under unequal bending moments at the two ends, M_A and M_B , is shown in Fig. 2.

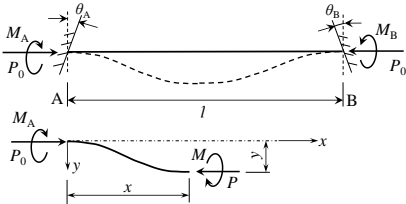


Fig. 2 Deflection shape of compression bar with end moments

M_A and M_B are positive if the synclastic curvature deformation is generated by M_A and M_B . Otherwise, the coefficient with the larger absolute value is positive and the other coefficient is negative if the anticlastic curvature deformation is generated by M_A and M_B . The deflection differential equation of a compression bar under unequal bending moments at the two ends is as follows

$$y'' + k^2 y = \frac{M_A + M_B}{EI} x - \frac{M_A}{EI} \quad (6)$$

where $k^2 = P_0/EI$. The general solution of Eq. 6 is

$$y = C_1 \sin kx + C_2 \cos kx + \frac{M_A + M_B}{k^2 EI} x - \frac{M_A}{k^2 EI} \quad (7)$$

where C_1 and C_2 are coefficients. Eq. 7 is solved by substituting the boundary conditions of the compression bar at the two ends: $y(0)=0$, $y(x)=0$. The coefficients of Eq. 7 are

$$C_1 = -\frac{M_A \cos kl + M_B}{k^2 EI \sin kl} \quad (8)$$

$$C_2 = \frac{M_A}{k^2 EI} \quad (9)$$

The deflection curve result of Eq. 7 for a compression bar under unequal bending moments at two ends when substituting Eq. 8 and Eq. 9 into the equation is

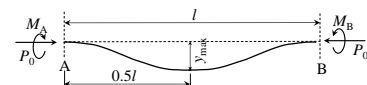
$$y = -\frac{M_A \cos kl + M_B}{k^2 EI \sin kl} \sin kx + \frac{M_A}{k^2 EI} \cos kx + \frac{M_A + M_B}{k^2 EI l} x - \frac{M_A}{k^2 EI} \quad (10)$$

Eq. 10 shows that the deformation curve of compression members under unequal bending moments is the combination of a cosine curve and a sine curve, which are related to both the values and directions of the bending moments bearing at the bar's ends. Because the most unfavourable situation is that in which the initial bending of the bar is in accord with its deformation shape, the member initial curvature should be determined by the distribution of moments at both ends.

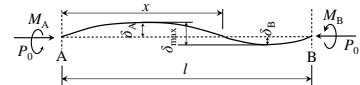
Through the foregoing analysis, an advanced method for determining the member initial curvature is presented considering the distribution of moments at the bar's ends. First, a nonlinear full-range analysis of structures without any member defects is performed to obtain the moment distributions of all member ends in the critical state. Then, different initial bending functions are selected to modify the corresponding coordinates of the internal nodes in each member. To simplify the calculation, two types of member initial curvatures are established based on the different signs of the end moments, as shown in Fig. 3.

The first type of member initial curvatures (MIC 1st) considers that the moments at both ends are positive when the member deformation is a synclastic curvature shape. To simplify the analysis, it is assumed that the member deflection equation is a half-period sinusoid curve similar to the initial bending function, as shown in Fig. 3 (a). Hence, the initial bending amplitude of the middle of the member is considered to have a maximum value δ ; meanwhile, the initial bending direction should agree with the deflation direction of the compression bar. The MIC 1st is specified as

$$\delta = \delta_{\max} \sin(\pi x/l) \quad (11)$$



(a) Identical moment signs



(b) Opposite moment signs

Fig. 3 Two types of member initial curvatures based on end moments

The second type of member initial curvature (MIC 2nd) considers that the bar deformation takes on an anticlastic curvature shape with moments of different signs at the bar's two ends. To simplify the analysis, it is assumed that the member deformation shape consists of two half-period sinusoid curves in opposite directions, as shown in Fig. 3(b), and that the deformation value of the point where the moment equals zero is zero as well. Simultaneously, the maximum value δ of the initial bending amplitude is specified at the middle of the half-period sinusoid curve, where the end moment's absolute value is greater. MIC 2nd is specified as

$$\delta = \begin{cases} \delta_{\max} \left(\frac{M_A}{M_A - M_B} \right) \sin \left[\frac{\pi x(M_A - M_B)}{M_A l} \right] & , x \leq \frac{M_A}{M_A - M_B} l \\ -\delta_{\max} \left(\frac{M_B}{M_A - M_B} \right) \sin \left[\frac{\pi \left(x - \frac{M_A}{M_A - M_B} l \right) (M_A - M_B)}{-M_B l} \right] & , x > \frac{M_A}{M_A - M_B} l \end{cases} \quad (12)$$

Eq. 12 shows that the amplitude of the initial bending equals zero at the point $x = M_A l / (M_A - M_B)$, and the maximum value δ of the initial bending amplitude is obtained at the point $x = M_A l / (2M_A - M_B)$, where $M_A > M_B$. The direction of this part of the half-period sinusoid curves, where $x < M_A l / (M_A - M_B)$, should agree with the deflation direction of the compression bar. The amplitude of the initial bending is $(-M_B \delta / M_A)$ at the point $x = (M_A + 0.5M_B) l / (M_A - M_B)$ in the other part of the half-period sinusoid curves, the direction of which is opposite to the direction at the point $x = M_A l / (2M_A - 2M_B)$.

The modelling of steel space structures is conducted using the ABAQUS finite-element program, and beam B31 elements, 3D linear finite strain beam elements based on Timoshenko beam theory, are selected to simulate the members of the structures. Fig. 4 shows that each bar is meshed with 8 B31 elements using the multi-beam method.

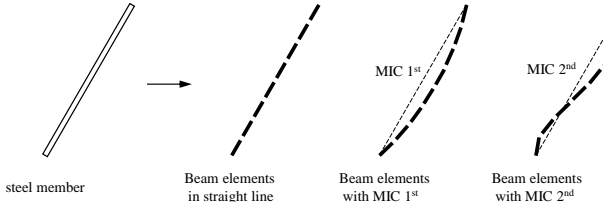


Fig. 4 Meshing rules of bars

The process of establishing structure models with member initial curvature considering the moments at the bars' ends is shown in Fig. 5. The modelling process is divided into end moment analysis and MIC computation. First, we extract the value and the direction of each bar's end moments based on the stability analysis results of the original structural model with straight members. Second, we select the MIC function and calculate the parameters according to Eq. 11 and Eq. 12. Finally, we modify the internal nodes coordinates of each bar to revise the structural model. All of the results are extracted and computed using the MATLAB program.

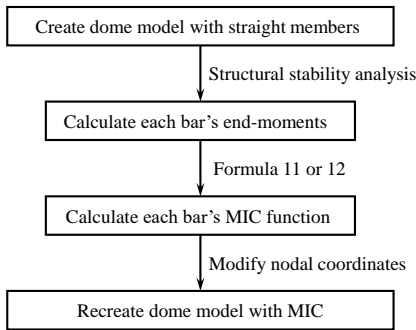


Fig. 5 Flow chart of structure modelling with MIC

3. Model verification

3.1. Single-bar system

To verify the method for establishing a structure model with member initial curvature considering end moments, the analysis single-bar experiment conducted by Sherman with both ends fixed under axial compression, relative

to Reference [21], is analyzed. The single bar is made of steel circular pipes and measures 5.72 m in length, 114 mm in outer diameter and 2.3 mm in thickness, as shown in Fig. 6.

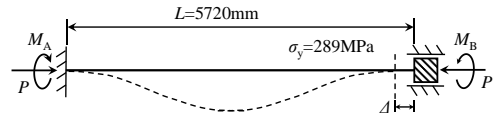


Fig. 6 Sherman's experiment on steel pipe under axial load

Two types of member initial curvatures are chosen to simulate the full-range compressive buckling process under Sherman's test. The maximum value of the initial bending amplitude δ_{\max} is specified as $l/500$, where l is the length of the bar and σ_y is the yield strength of steel. The load factor of the stability load-bearing capacity of the model considering different member initial curvatures is specified as

$$C_0 = P / P_0 \quad (13)$$

where P is the stability load-bearing capacity of the model without any member initial defects and P_0 is the stability load-bearing capacity of the model established using member initial curvatures. The load-displacement curves and load-bearing capacity factor C_0 of the system using different MIC functions are shown in Fig. 7.

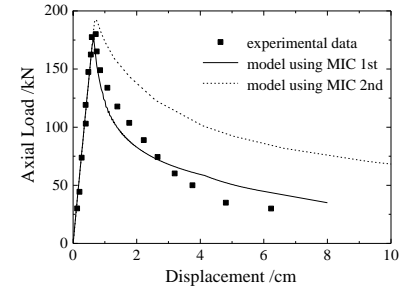


Fig. 7(a) Load-displacement curves

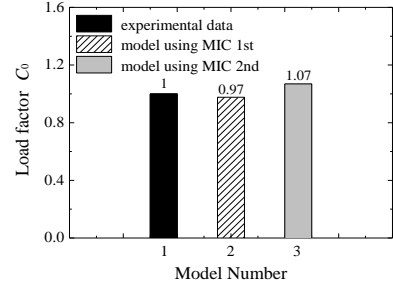


Fig. 7(b) Load-bearing capacity factors

Fig. 7 shows that the load-displacement curve of the model established using the first type of member initial curvature is closer to the test result. The compressive bearing capacities of the test sample, MIC 1st and MIC 2nd are 180.4, 176.1, and 192.8 kN, respectively. These results are obtained because the signs of the moments at the two ends are the same in the single-bar experiment. The first type of initial bending function agrees better with the test case; thus, the compressive bearing capacity is the lowest, proving that the most unfavourable condition occurs when the signs of the end moments are the same.

3.2. Double-bar system

To verify the method for establishing a structure model with member initial curvature considering end moments, a numerical simulation of the double-bar experiment with fixed ends under vertical load reported by Shen in Reference [22] is conducted. The double-bar system is composed of steel circular pipes with strong nonlinear mechanical properties, as shown in Fig. 8. The external diameter and thickness of the pipe sections are 114 mm and 4 mm, and two types of member initial curvatures are chosen to compare the full-range

compressive buckling process of the system without member initial curvature. The maximum value of the member initial curvature amplitude δ_{\max} is specified as $l/500$, where l is the length of each bar; E is the elastic modulus of steel; σ_y is the yield strength of steel. To compare the influence of semi-rigid joints on end moments, the bending stiffness of rigid joints is reduced to produce a semi-rigid joint system. The load-displacement curves and the bearing capacity factor C_0 of the rigid system and the semi-rigid system using different MIC functions are shown in Fig. 9.

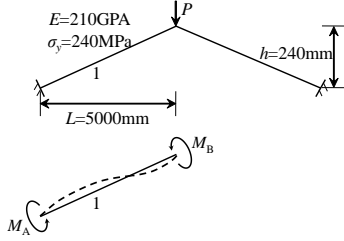
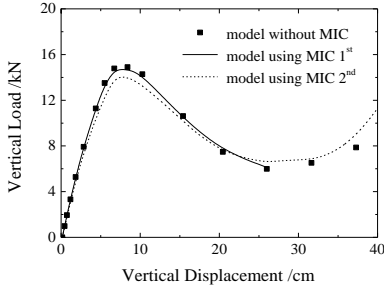
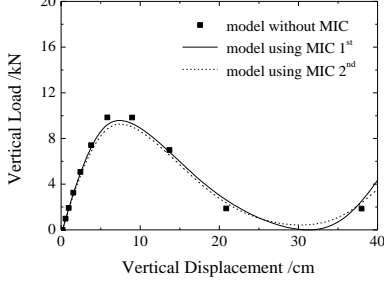


Fig. 8 Double-bar system under vertical load



(a) Load-displacement curves with rigid joints



(b) Load-displacement curves with semi-rigid joints

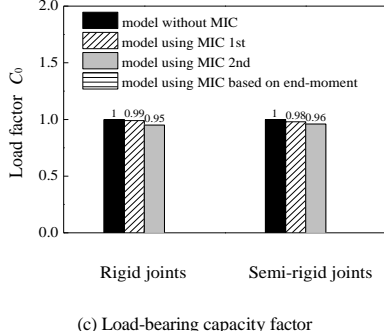


Fig. 9 Model results for the double-bar system

Fig. 9 (a) shows that the stability bearing capacities of the three types of rigid joints models are 14.8, 14.7, and 14.1 kN, and the capacity of the model using the second type of member initial curvature is the lowest. Fig. 9 (b) shows that the stability bearing capacities of the three types of semi-rigid joints models are 9.84, 9.63, and 9.47 kN, and the capacity of the model using the second type of member initial curvature is also the lowest. These results are obtained because the signs of the moments at the bars' ends transmitted by rigid or semi-rigid joints are opposite in the critical state, and the deformation shape of each bar is the anticlastic curvature under vertical load, proving that the second type of member initial curvature represents the most unfavourable condition when the end moments are opposite.

3.3. Hexagon frame system

To verify the method for establishing a structure model with member initial curvature considering end moments, a numerical simulation of the hexagon frame system experiment with hinged supports under vertical load reported by Papadrakakis in Reference [23] is conducted, as shown in Fig. 10. The six bars around the middle loading point are compression bars; two types of member initial curvature are chosen to compare the full-range compressive buckling process of the system without member initial curvature. The maximum value of the initial bending amplitude δ_{\max} is specified as $l/500$, where l is the length of each bar; I is the inertia moment of a pipe section; J is the torsional constant of a circular section; E is the elastic modulus of steel; G is the shear modulus of steel; σ_y is the yield strength of steel. To compare the influence of semi-rigid joints on end moments, the bending stiffness of rigid joints is reduced to produce a semi-rigid joint system. The load-displacement curves and the bearing capacity factor C_0 of the rigid system and the semi-rigid system using different MIC functions are shown in Fig. 11.

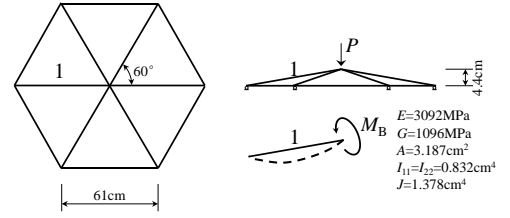
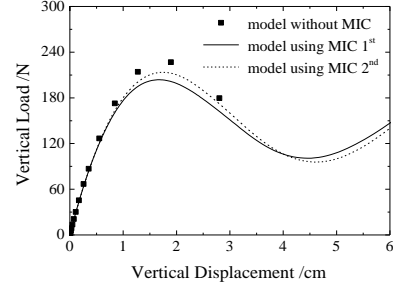
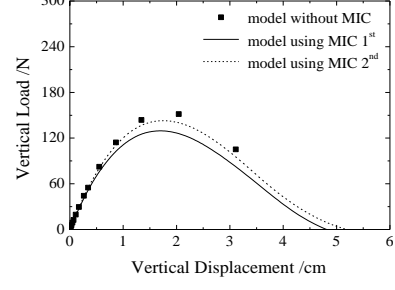


Fig. 10 Hexagon frame system under vertical load



(a) Load-displacement curves with rigid joints



(b) Load-displacement curves with semi-rigid joints

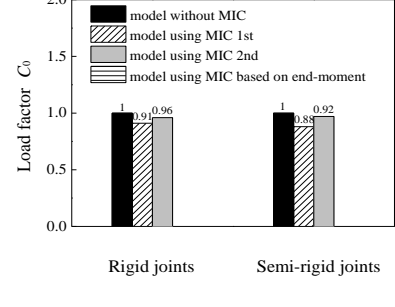


Fig. 11 Model results for the hexagon frame system

Fig. 11 (a) shows that the stability bearing capacities of the three types of rigid joints models are 226.8, 206.6, and 218.3 N, and the capacity of the model using the first type of member initial curvatures is the lowest. Fig. 11 (b) shows that the stability bearing capacities of the three types of semi-rigid joints models

are 151.0, 133.1, and 146.0 N, and the capacity of the model using the first type of member initial curvatures is also the lowest. These results are obtained because the moment of each compression bar's supporting end is zero. In this one-end hinged situation, the deformation shape of each compression bar presents synclastic curvature under load, proving that the first type of member initial curvature represents the most unfavourable condition when one end-moment is zero.

3.4. Hexagon star dome system

To verify the method for establishing a structure model with member initial curvature considering end moments, a numerical simulation of the hexagon star dome system experiment with hinged supports under vertical loads reported by Meek and Tan in Reference [24] is conducted, as shown in Fig. 12. Three types of dome system models considering different member initial curvatures are established for comparison with models with no member initial curvatures. The first type consists of all the member initial curvatures as function 12 (MIC 1st), the second type consists of all the member initial curvatures as function 13 (MIC 2nd), and for the third type, function 12 (MIC 1st) or function 13 (MIC 2nd) is chosen for each bar based on the bars' moments at both ends. The maximum value of the initial bending amplitude δ_{\max} is specified as $l/500$, where l is the length of the bar; I is the inertia moment of a pipe section; J is the torsional constant of a circular section; E is the elastic modulus of steel; G is the shear modulus of steel; σ_y is the yield strength of steel. To compare the influence of semi-rigid joints on end moments, the bending stiffness of rigid joints is reduced to produce a semi-rigid joint system. The load-displacement curves and the bearing capacity factor C_0 of the rigid system and the semi-rigid system using different MIC functions are shown in Fig. 13.

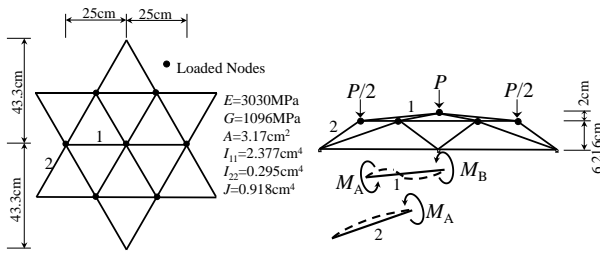
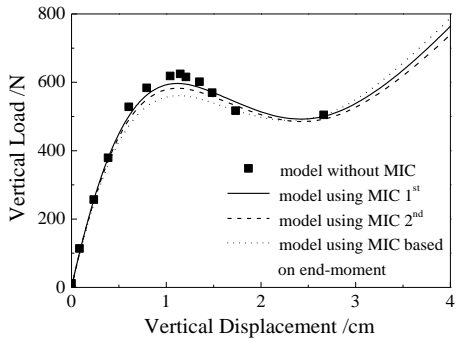
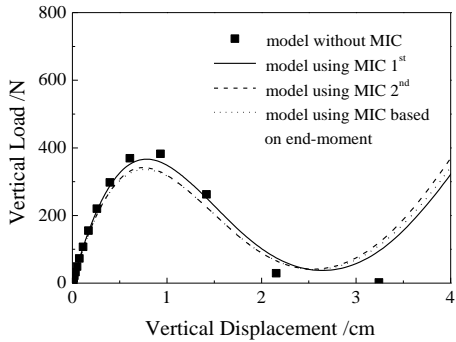


Fig. 12 Hexagon star dome system under vertical load



(a) Load-displacement curves with rigid joints



(b) Load-displacement curves with semi-rigid joints

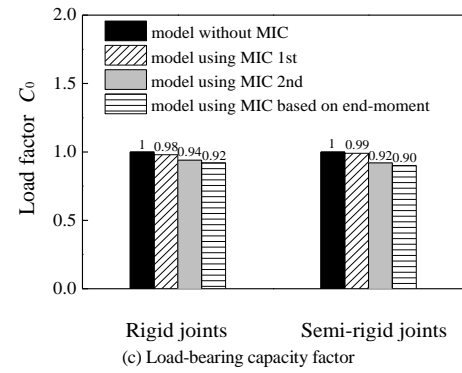


Fig. 13 Model results for the hexagon star dome

Fig. 13 (a) shows that the stability bearing capacities of the four types of rigid joints models are 617.2, 601.9, 577.1, and 572.6 N, and the capacity of the model using the type of member initial curvature based on the bars' end moments is the lowest. Fig. 13 (b) shows that the stability bearing capacities of the four types of semi-rigid joints models are 382.2, 377.1, 351.0, and 342.5 N, and the capacity of the model using the type of member initial curvature based on the bars' end moments is also the lowest. These results are obtained because, in this system, the end moments of the compression bars around the middle loading point are opposite, and the supporting end moments of the compression bars around the supporting points are zero. The deformation shapes of the compression bars may present synclastic curvature or anticlastic curvature accordingly under load, proving that the model featuring different member initial curvatures based on the bars' end moments represents the most unfavourable condition for this dome system.

The analyses of the above mentioned systems verify that the stability load-bearing capacity of structures decreases if the model established considers member initial curvature. The extent to which the stability load-bearing capacity of the models considering different member initial curvatures decreases varies. The model established with member initial curvatures considering the bars' end moments represents the most unfavourable condition, and the extent to which the stability load-bearing capacity decreases in this case is the lowest. Moreover, the degrees to which the rigid or semi-rigid joints decrease the structural stability capacity are nearly the same, because the joint stiffness differences between the rigid and semi-rigid joints do not affect the direction of the end moments or the selected type of MIC functions.

4. Application to single-layer spherical reticulated domes

Through a full-range nonlinear analysis of single-layer spherical reticulated dome under a full-span vertical load, the influence of the structure stability load-bearing capacity considering different member initial curvatures is discussed. The analytical models of single-layer reticulated dome shown in Fig. 14 are employed in this study, including Kiewitt-8 dome. The analytical parameters are the span (L) and the rise-to-span ratio (f/L), as listed in Table 1. For each dome, three types of dome models considering different member initial curvatures are established for comparison with models with no member initial curvatures. For each model, five types of member initial curvature amplitudes (δ_{\max}/l) are selected, as shown in Table 1. The boundary conditions include fixed hinge support, and the material is Q235 steel, with a yield strength of 235 MPa and an elastic modulus of 2.06×10^5 MPa. The steel stress-strain model of the single-layer reticulated dome is a combined-hardening model that possesses the characteristics of both isotropic and kinematic hardening models, as shown in Fig. 15. The material parameters of the steel constitutive model are obtained from experimental results [25].

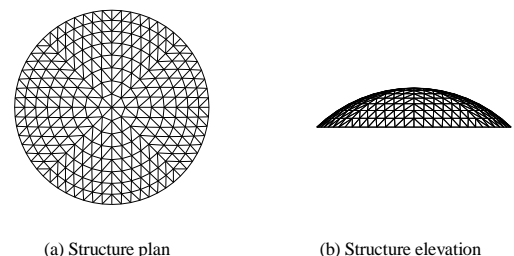


Fig. 14 Analytical models of the single-layer reticulated dome

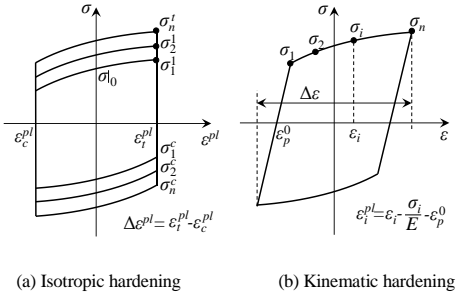


Fig. 15 Steel stress-strain curves

Table 1

Example of a table Parameters of single-layer reticulated domes

Span L/m	Rise-to-span ratio f/L	Numbers of circles	Radial and circular bars	Diagonal bars	MIC amplitude δ/l
40		6	Φ133×4	Φ114×3	1/1000, 1/500,
60	1/4, 1/5, 1/6	8	Φ152×5.5	Φ140×5	1/300, 1/200,
80		10	Φ203×6	Φ194×6	1/100

The three types of dome models using member initial curvatures are MIC 1st only, MIC 2nd only, and different functions based on the bars' end moments. The load factors of the stability load-bearing capacity C_0 of the different dome models using different types of member initial curvatures with the same amplitude of $\delta_{\max} = l/500$ are shown in Fig. 16.

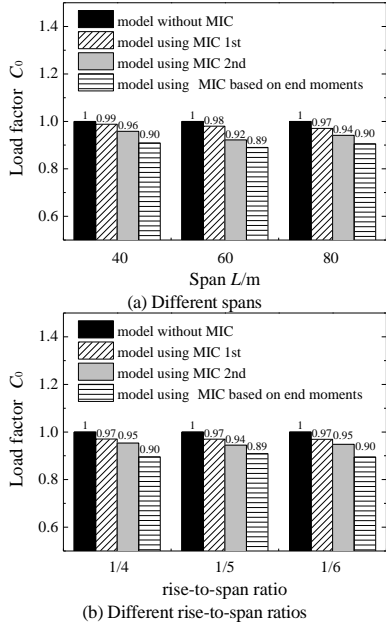


Fig. 16 Model results for single-layer reticulated dome

Fig. 16 verifies that the stability load-bearing capacity of the dome decreases if the model is established considering member initial curvature. The degree to which the stability load-bearing capacity of models considering different member initial curvatures decreases varies. The model established with member initial curvatures considering the bars' end moments represents the most unfavourable condition, and the degree to which its stability load-bearing capacity decreases is the lowest. The average load reduction factor C_0 of the different models using member initial curvatures considering end moments with the same amplitude of $\delta_{\max} = l/500$ is 0.90. This result demonstrates that neither a change in span nor a change in the rise-to-span ratio has a significant influence on C_0 for the different types of models using the same amplitude of member initial curvatures considering end moments.

The reduction factors of the stability load-bearing capacity C_0 of the different dome models using different amplitudes of the member initial curvatures are shown in Fig. 17. Fig. 17 shows that an increase in the amplitude of the member initial curvatures results in a decrease in C_0 . The average C_0 of the models with different spans or rise-to-span ratios using the same member initial curvature amplitudes of $l/1000$, $l/500$, $l/300$, $l/200$ and $l/100$ are 0.96, 0.91, 0.85, 0.81 and 0.72, respectively.

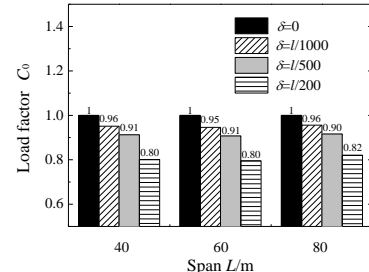


Fig. 17 Amplitude results for single-layer reticulated dome

To choose a reasonable amplitude for the member initial curvature considering end moments, the relationships between the member initial curvature amplitudes and the load factor C_0 are plotted in Fig. 18 with the relationships between the member initial curvature amplitudes and the maximum displacements U_{\max} in the dome's elastic ultimate state. Fig. 18 shows that the stability load-bearing capacity of the single-layer reticulated dome decreases linearly with increasing MIC amplitude. The maximum displacement U_{\max} in the elastic limit state of the single-layer reticulated dome decreases precipitously when the member initial curvature amplitude exceeds $l/500$, this result suggests that a critical state is reached by the single-layer reticulated dome when the member initial curvature amplitude equals $l/500$. It is observed that the amplitude of MIC proposed in this paper is equal to that of Section Type A in the Hong Kong Steel Code [19] when adopting a hot-finished pipe section and greater than the value prescribed by the Chinese code [26], as shown in Table 2. These discrepancies occur because member residual stress and member initial eccentricity must be considered when the amplitude of member imperfection at $l/1000$ does not meet the specified requirements [20]. Considering the internal force state of the structure and the existing code specifications, a member initial imperfection value of $l/500$ is applicable for hot-finished structural hollow sections, which are commonly used in single-layer reticulated dome due to the equivalent biaxial cross-section stiffness, such as that of the pipe and box sections. Other types, such as H and I sections, which are seldom used in these domes due to the large difference of bending stiffness about the strong and weak cross-section axes, are not considered in this paper.

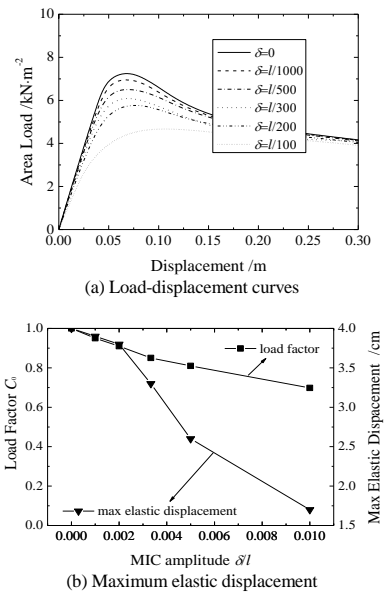


Fig. 18 The relationships of the MIC amplitudes and structure responses

5. Conclusions

(1) The stability bearing capacity of single-layer reticulated dome decreases when the associated numerical model considers the influence of the member initial curvature of each bar. The influence of the end moments transmitted by rigid joints or semi-rigid joints should be considered when numerical models of compression members are established using member initial curvatures.

Table 2

MIC amplitude of single-layer reticulated domes

Representative specification	Type section	Amplitude δ_{\max}/l
Eurocode3		1/300
Hong Kong code	Hot-finished	1/500
Chinese code	hollow section	1/1000
Value recommended in this paper		1/500

(2) The most unfavourable condition occurs when the member initial curvature of the compression bar corresponds to the deformation shape at the critical state. There are two types of deflection shapes of compression bars considering end moments: one in which the signs of the moments at the two ends are the same and the other in which the signs are opposite. According to the two types of deflection curves, two forms of member initial curvatures are proposed: synclastic curvature and anticlastic curvature.

(3) Using the ABAQUS finite-element program, each bar of a single-layer reticulated dome is meshed using B31 elements by the multi-beam method to establish new analytical models considering member initial curvatures based on end moments. The approach performs a full-range nonlinear analysis of a perfect structure without any member defects first to obtain the moments of each bar at both ends in the critical state. Then, the coordinates of the internal nodes in each bar are modified by choosing different types of member initial curvatures depending on the bar's end moments and the bar deflection direction to obtain a new numerical model.

(4) The reduction degree of the stability load-bearing capacity of single-layer reticulated dome when modelling using member initial curvatures based on end moments is greater than that of functions that do not consider end moments. The influence of the same amplitude of the member initial curvatures considering end moments is small when the single-layer reticulated dome's span and rise-to-span ratio vary. Varying the amplitude of the member initial curvatures considering end moments has a strong effect on the stability load-bearing capacity of single-layer reticulated dome. Based on the response of the structure and realistic construction conditions, 1/500 is proposed as a reasonable maximum value of the member initial curvature for hot-finished structural hollow sections.

Acknowledgements

This work was sponsored by the National Key Research and Development Program of China (Grant NO. 2016YFC0701103), the Major Research Plan of the National Natural Science Foundation of China (Grant NO. 91315301-06) and the Natural Science Foundation of Tianjin (Grant NO. 13JCZDJC35200). The financial support from the open project fund of the Key Laboratory of Coast Civil Structural Safety of the Ministry of Education of Tianjin University was also greatly appreciated.

References

- [1] Chen X. and Shen S.Z., "Complete load-deflection response and initial imperfection analysis of single-layer lattice dome", International Journal of Space Structures, 1993, 8(4), 271-278.
- [2] Gioncu V., "Buckling of reticulated shells: state-of-the-art." International Journal of Space Structures, 1995, 10(1), 1-46.
- [3] BSI, "EN 1993-1-6. Eurocode 3: Design of steel structures-Part 1-6: Strength and stability of shell structures", European Committee for Standardization: Brussels, 2007.
- [4] Mohurd "JGJ 7-2010: Technical specification for space frame structures", Beijing: China Architecture Industry Press, 2010. (in Chinese)
- [5] Adman R. and Afra H., "Exact shape functions of imperfect beam element for stability analysis", Advances in Engineering Software, 2007, 38(8), 576-585.
- [6] Li G.Q. and Liu Y.S., "A nonlinear beam element considering initial imperfection", Chinese Journal of Computational Mechanics, 2005, 22(1), 69-72. (in Chinese)
- [7] Kumar P.A., Sahoo D.R. and Kumar N., "Limiting values of slenderness ratio for circular braces of concentrically braced frames", Journal of Constructional Steel Research 2015, 115, 223-235.
- [8] Lotfollahi M., Alinia M.M. and Taciroglu E., "Validated finite element techniques for quasi-static cyclic response analyses of braced frames at sub-member scales", Engineering Structures, 2016, 106, 222-242.
- [9] Liew J.R., Punniyakottay N.M. and Shanmugam N.E., "Advanced analysis and design of spatial structures", Journal of Constructional Steel Research, 1997, 42(1), 21-48.
- [10] Qi L., Shao Y. and Huang Z., et al. "Dynamic damage criterion and damage mode for single layer lattice shell", Journal of Constructional Steel Research, 2014, 99, 102-110.
- [11] Marshall P.W., Gates W.E. and Anagnostopoulos S.W., "Inelastic dynamic analysis of tubular offshore structures", Proceedings of Ninth Annual Offshore Technology Conference Offshore Technology Conference, Houston, USA, 1977, 235-246.
- [12] Ding Y., Chen Z.T. and Zong L., et al, "A theoretical strut model for severe seismic analysis of single-layer reticulated dome", Journal of Constructional Steel Research, 2017, 128, 661-671.
- [13] Chan S.L. and Zhou Z.H., "Second order analysis of frame using a single imperfect element per member", Journal of Structural Engineering, ASCE, 1995, 121(6), 939-945.
- [14] Fan F., Yan J. and Cao Z., "Stability of reticulated shells considering member buckling", Journal of Constructional Steel Research, 2012, 77, 32-42.
- [15] Yan J.C., Qin F. and Cao Z., et al, "Mechanism of coupled instability of single-layer reticulated dome", Engineering Structures, 2016, 114, 158-170.
- [16] Zhou Z., Wu J. and Meng S.P., "Nonlinear stability bearing capacity analysis for a suspended dome based on the initial curvature elements", Chinese Journal of Computational Mechanics, 2010, 27(4), 721-726. (in Chinese)
- [17] Yan J., Fan F. and Cao Z., "Research on influence of initial curvature of members on elasto-plastic stability of reticulated shells", Journal of Building Structures, 2012, 33(12), 63-71. (in Chinese)
- [18] Wang Q., Deng H. and Huang L., "Effect of member's initial curvature on the static and dynamic bearing capacity of suspended dome", Spatial Structures, 2013, 19(4), 18-24. (in Chinese)
- [19] Code of Practice for the Structural Use of Steel 2011.. Buildings Department of the Government of the Hong Kong Special Administrative Region, Hong Kong, China, 2011.
- [20] Pang P.T.C., Kwan K.K., and Chan S.L., "Hong Kong code of practice for the structural use of steel 2005—second-order analysis and design method with effective-length-free assumption", Progress in Steel Building Structures, 2007, 9(5), 57-62. (in Chinese)
- [21] Chan S.L., "Geometric and material non-linear analysis of beam-columns and frames using the minimum residual displacement method", International Journal for Numerical Methods in Engineering, 1988, 26(12), 2657-2669.
- [22] Shen S.Z. and Chen X., "Stability of reticulated shells", Beijing: Science Press, 1999, 69-70. (in Chinese).
- [23] Papadakakis M., "Post-buckling analysis of spatial structures by vector iteration methods", Computers & structures, 1981, 14(5-6), 393-402.
- [24] Meek J.L. and Tan H.S., "Geometrically nonlinear analysis of space frames by an incremental iterative technique", Computer methods in applied mechanics and engineering, 1984, 47(3), 261-282.
- [25] Shi Y.J., Meng W., Wang Y.Q., "Experimental study of structural steel constitutive relationship under cyclic loading", Journal of Building Materials, 2012, 15(3), 293-300. (in Chinese)
- [26] Ministry of Construction of the People's Republic of China, "GB 50017-2003: Code of design of steel structures", Beijing: China Planning Press, 2003. (in Chinese).

THE STRUCTURAL AND CONSTRUCTION PERFORMANCES OF A LARGE-SPAN HALF STEEL-PLATE-REINFORCED CONCRETE HOLLOW ROOF

Meng-Zhu Diao^{1,2}, Yi Li^{1,*}, Xin-Zheng Lu³, Hong Guan² and Yun-Lun Sun⁴

¹ College of Architecture and Civil Engineering, Beijing University of Technology, Beijing, China

² School of Engineering and Built Environment, Griffith University Gold Coast Campus, Gold Coast, Australia

³ Department of Civil Engineering, Tsinghua University, Beijing, China

⁴ Chinergy Co., Ltd., Beijing, China

* (Corresponding author: E-mail: yili@bjut.edu.cn)

ABSTRACT

This paper proposes a new large span half steel-plate-reinforced concrete (H-SC) hollow roof structure for nuclear power plants. The roof composes of 23 I-shaped H-SC beams. Each H-SC beam consists of a steel plate assembly (a bottom plate, a web plate and a short top plate), which is cast inside an I-shaped reinforced concrete beam. This novel system not only has an equivalently high bearing capacity, stiffness and lower gravity load comparing with conventional RC roof, but also can be conveniently constructed by using the bottom plates as formworks. The numerical simulation was conducted to demonstrate its mechanical capacities and the influence of construction process. Firstly, a finite element (FE) model for the H-SC composes was built and a one-third scaled 12 meters large-span H-SC beam was tested to validate the proposed FE model and analyze the steel-concrete-interface bond-slip. Then, the numerical simulation was conducted to assess the effect of the construction process on the mechanical performance of the entire roof structure, in which the deactivation element and trace element techniques were used to simulate the deformation induced by the construction process. The results show that the deflection induced by the construction process accounts for 87% of the final deflection.

Copyright © 2019 by The Hong Kong Institute of Steel Construction. All rights reserved.

ARTICLE HISTORY

Received: 9 April 2017

Revised: 8 October 2017

Accepted: 17 December 2017

KEY WORDS

Half steel plate-reinforced concrete (H-SC) roof; Numerical simulation; Experimental test; Construction process, deactivation element technique; Trace element technique

1. Introduction

The roofs for nuclear power plants usually have large span to bridge over nuclear islands. Therefore, truss and shell grid structures are commonly used in the large span roofs of the nuclear power plants due to their light self-weight, such as Dayawan and Linnan nuclear power plants. After the Fukushima incident, the safety of nuclear power plants has been much widely concerned. Comparing with the steel structures, steel-plate-reinforced concrete (SC) structures have higher stiffness and better integrity as well as good fire, blast, impact and seismic resistances [1,2,3,4]. Such advantages can significantly improve the disaster prevention ability of nuclear power plants. However, the conventional SC structures cannot be directly used as the large span roof due to their heavy self-weight. In this work, a new large span half steel-plate-reinforced concrete (H-SC) hollow roof is proposed and its mechanical performance is analyzed by using the numerical simulation.

The conventional SC structure is composed of a concrete core and steel plates on both sides of the core. Mechanical connectors have been developed for improving the steel-concrete bond, such as the shear connectors [5,6,7,8,9] shown in Fig. 1(a)-(c).

significantly reduce the weight when being used on long-span structures, in which steel plates and concrete can work together very well using appropriate shear connections and suitable anchorage length demonstrating a very good level of ductility [10,11,12,13]. In addition, the SC and H-SC composites exhibit high capacity and ductility thereby providing adequate protections against earthquake and extreme loads such as impact and blast [14,15]. Specially, comparing with the conventional concrete structures, the need of formworks and exposed concrete crack can be completely eliminated during construction, which significantly shortens construction period and reduces maintenance costs.

The new large span H-SC hollow roof is proposed based on the conventional H-SC structure (see Fig. 2). This roof structure features a bottom steel plate, on top of which a set of vertical steel plates is welded at required spacing as the web plates, and shear studs are installed in between the web steel plates. A short-leg plate is also perpendicularly welded on the top of the web plate. In addition, minimum reinforcement and stirrups are arranged in the beam in accordance with the Chinese code [16]. Each I-shaped assemblage of these steel plates is manufactured on the ground. Subsequently, three or four assemblages are joined by welding and hoisted on the top of shear walls (i.e. the location of the roof). Finally, a total of 23 I-shaped steel assemblages are linked by welding and four lateral steel braces (see Fig. 2(b)) are fitted below the top steel plates. After that, the concrete can be cast on the bottom steel plates. During this stage, the bottom plates perform as formworks while all the steel assemblages provide a large bending capacity to carry construction and gravity loads. These features result in the bottom steel plates in tension and the top steel plates in compression (the compressive buckling being resisted by the lateral steel braces). Note that hollow concrete sections are made around their neutral axis to reduce the self-weight of the whole roof structure. Light-weight materials like aerated concrete blocks can be used as the temporary filler in the hollow sections during the construction process and can be left behind after the construction is completed. All these improvements introduced into the proposed roof facilitate large sectional dimensions to satisfy the requirement of the strength and stiffness of the large-span roofs, with marginally increased self-weight. Moreover, the construction cost can be reduced by using the steel plates as formworks without requiring additional time and materials to build the formworks. All these advantages enable feasible and effective application of the H-SC composites in large-span roofs for nuclear power plant construction.

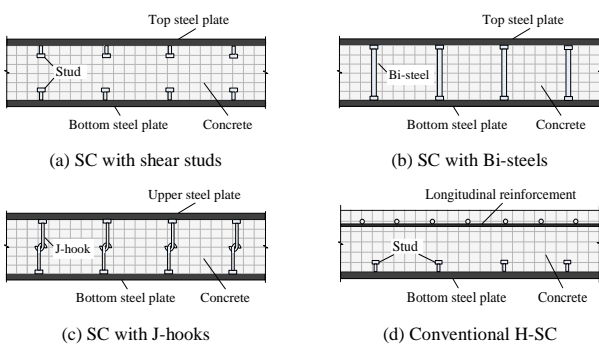


Fig. 1 Typical sections of steel plate reinforced concrete (SC) structures

To facilitate the construction and reduce the internal defects within the concrete, conventional half steel plate-reinforced concrete (H-SC) composites (see Fig. 1(d)) were also introduced in which the top steel plates are replaced by the normal steel reinforcement [5]. The existing experiments on SC and H-SC beam and slab composites indicate that the SC and H-SC composites can

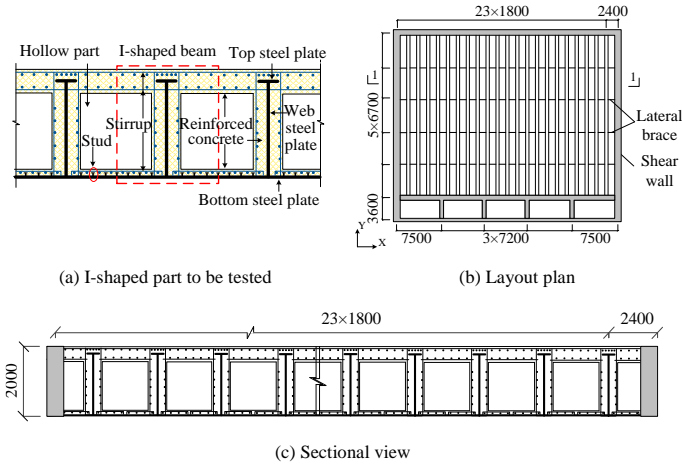


Fig. 2 Proposed H-SC hollow roof structure (unit: mm)

Current researches on the construction mechanics of SC and H-SC composite structures are mainly based on the time varying mechanics theory, in which the construction process is divided into several construction stages. The ‘birth’ and ‘death’ element technology is often used in the analysis of the construction process [17]. However, the ‘death’ element may float after being activated which usually causes the large deviation, resulting in an unconvolved solution. The so-called step by step modeling method can also be used for the construction analysis, in which the stress state of each construction step must be reloaded in the consequent construction step as the initial stress state [18]. This results in the large computational workload. Therefore, accurate and efficient construction modeling methods are still needed.

Considering the limitations of the laboratory test on such a large roof specimen, the numerical simulation was used to analyze the mechanical behavior of the proposed H-SC roof structure. Given the structural characteristics of the roof and the construction process, two issues were studied. Firstly, a one-third scaled 12m large-span H-SC beam isolated from the roof structure (enveloped by the red-colored rectangle, as shown in Fig. 2(a)) was tested to validate the numerical model for the composite structure, in which the bond slip between the concrete and steel plates was also investigated. Secondly, the whole roof structure was numerically simulated, in which the deactivation element and trace element techniques were used, to evaluate the deformation induced by the construction process.

2. Experimental test

To study the mechanical behavior of the proposed H-SC composite and validate the accuracy of the finite element (FE) models, a static test on the one-third scaled 12m large-span H-SC beam was conducted.

2.1. Details of the test specimen

Details of the specimen are shown in Fig. 3(a) and the material properties are given in Table 1. The specimen was 12 m long, with a clear span of 11.2 m (see Fig. 3(c)). The cross-sectional area was 600 mm and 667 mm in width and depth, respectively. All steel plates used were 8mm thick and connected to each other by welding. The bottom steel plate was connected to the concrete through welded studs which served as shear connectors. The specimen was reinforced with 8 diameter bars and the concrete cover was 25 mm. Fig. 3(c) shows the loading arrangement and the test setup. The specimen was placed on the roller bearings to simulate the simply supported boundary condition. A four-point loading system was used: four identical forces were applied to the specimen by two rigid steel beams, on which two equal forces were loaded by two jacks.

2.2. Construction process

During the actual construction process of the H-SC roof, the bottom steel plates are used as formworks. Hence, the initial deformation is produced by the dead-weight of the steel plates, which continuously increases with the gravity load of subsequently casted concrete. The deformation reaches a stable stage until the concrete is hardened. Hence, the bearing capacity and stiffness of the roof also increases in stages. As such, the H-SC beam constructed in the real situation is named as multi-step forming (MSF) H-SC beam. However, it is rather challenging to replicate the actual construction process in the laboratory due to the sheer size of the specimen. In the proposed experiment, the specimen

was fabricated on the floor (see Fig. 3(b)), by which no deformation has occurred because the gravity of the steel plates and concrete was directly supported by the floor itself. For this reason, the potential deformation resulted from the actual construction process was not considered in the present test. The test specimen is thus named as one-step forming (OSF) H-SC beam specimen. The test results were used to validate the accuracy of the FE model in the following.

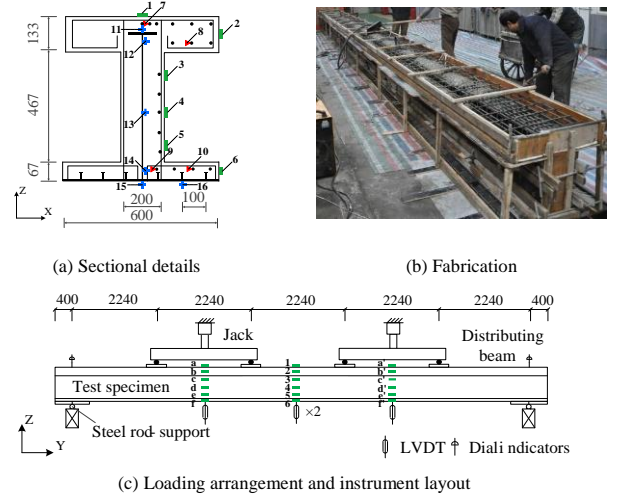


Fig. 3 Schematic diagram and fabrication of test (unit: mm)

Note: ■ denotes the strain gauges on concrete (No. 1-6 represent the gauges at mid-span, No. a-f and No. a'-f' represent the gauges at 2240mm left and right from the mid-span, respectively); ▶ denotes the strain gauges on steel bars (No. 7-10); + denotes the strain gauges on steel plates (No. 11-16). Strain gauges are symmetrically arranged with respect to the Z-axis. For clarity, left-hand side strain gauges are not shown in Fig. 3.

Table 1
Material Properties

Steel bar (HRB335)	f_y / MPa	360
	f_u / MPa	661
	Elongation / %	15
Steel plate (Q345B)	f_y / MPa	408
	f_u / MPa	544
	Elongation / %	25
Concrete (C35)	Cubic compressive strength f_{cu} / MPa	27

3. Test results

3.1. Overall load-displacement curve

The load-displacement curve of the specimen is presented in Fig. 4. The specimen underwent the following three stages: (1) elastic stage (OA), (2) elasto-plastic stage (AB), and (3) unloading stage (BC).

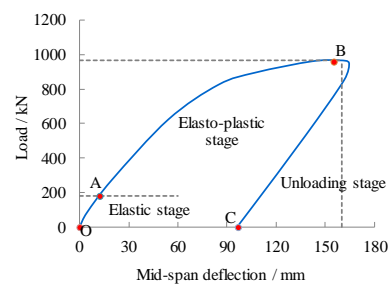


Fig. 4 Load and mid-span displacement relationship

In the elastic stage (OA), all material strains of the specimen at the mid-span section were less than the yield strains of steel and concrete before the mid-span displacement exceeding 12mm. In the elasto-plastic stage (AB), concrete cracks started to form and gradually developed as the load increased. The load-displacement curve tended to level off (at around Point B) indicating the deterioration of the stiffness of the specimen. In the vicinity of the peak load, the specimen maintained a high capacity (95% of peak load) within a large range of vertical deformation (122mm -165mm), indicating a good level

of ductility. At this stage, the concrete in the tension zone began to lose its capacity, and subsequently the bottom steel plate and reinforcing steel bars in the tension area started to yield successively. When the load reached the level of 965kN and the mid-span deflection went up to 165mm, the bearing capacity of the specimen no longer increased but became stable. Concrete crushing in the compression zone caused failure of the beam, showing a typical flexural failure mode. Following on from this point, the unloading stage (BC) commenced, where the load-displacement curve snapped back until reaching 95mm when the unloading stage was terminated.

3.2. Strain distribution in mid-span steel plate cross-section

At five load levels, Fig. 5(a) illustrates the strain of the steel plate distributing along the depth of the mid-span section (strain gauges No. 11-15 in Fig. 3(a)), where the Y-axis denotes the section height. It can be seen from Fig. 5(a) that the strains went up gradually as the load increased. The strain distribution remained largely linear when the load was at 100kN. When the load exceeded 200kN, only the central area of web plate satisfied the plane section assumptions. However, both the steel flanges entered into a plastic phase when the load reached 700kN. In addition, the bottom steel plate, having a large cross section, was able to provide a large tensile force. Meanwhile, the ductility increased as the neutral axis moved up steadily during the loading process. Fig. 5(b) presents the strains at three locations of the bottom steel plate, in which the strain at the middle region is greater than those on the left- and right-hand sides, indicating that the tensile stress in the middle is larger due to its connection to the steel web.

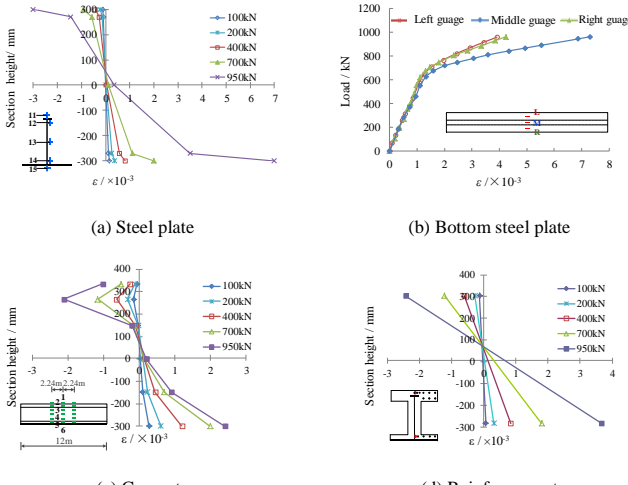


Fig. 5 Load and mid-span displacement relationship

3.3. Strain distribution in mid-span concrete cross-section

At five load levels, Fig. 5(a) illustrates the strain of the steel plate distributing along the depth of the mid-span section (strain gauges No. 11-15 in Fig. 3(a)), where the Y-axis denotes the section height. It can be seen from Fig. 5(a) that the strains went up gradually as the load increased. The strain distribution remained largely linear when the load was at 100kN. When the load exceeded 200kN, only the central area of web plate satisfied the plane section assumptions. However, both the steel flanges entered into a plastic phase when the load reached 700kN. In addition, the bottom steel plate, having a large cross section, was able to provide a large tensile force. Meanwhile, the ductility increased as the neutral axis moved up steadily during the loading process. Fig. 5(b) presents the strains at three locations of the bottom steel plate, in which the strain at the middle region is greater than those on the left- and right-hand sides, indicating that the tensile stress in the middle is larger due to its connection to the steel web.

3.4. Strain distribution in mid-span reinforcement

Fig. 5(d) shows the strain development in a top reinforcement ($Y=304\text{mm}$) and a bottom reinforcement ($Y=-284\text{mm}$) as shown in Fig. 3(a) (strain gauge No. 7 and 9). By comparing Fig. 5(a), 5(c) and 5(d), the steel strain was found to be close to the concrete strain at the same height, indicating a modest slip occurred at the concrete and steel interface. Despite this, the strains in concrete and steel bars increased significantly during the entire loading process, suggesting that the shear connectors and stirrups played an effective

role in providing adequate confinement. It can be concluded that the steel bars, the concrete, and the steel plate collectively and effectively contributed to the loading process. According to the experimental observation, only a minor shear slip gap had occurred in the bottom steel-concrete interface, which also validated the conclusion above.

4. Finite element modelling

4.1. Geometric modelling

A 3D model was developed based on the finite element software MSC.MARC [19] in accordance with the actual dimensions of the specimen to analyze the load-deflection behavior and the beam deformation during the construction process (as shown in Fig. 6). The concrete, the steel plates and the steel bars were simulated, respectively, using 8-node solid elements, 4-node thick shell elements and 2-node truss elements. Four identical forces were applied through four rigid blocks to the top flange to avoid stress concentrations and closely replicate the actual situation in the experimental test. The spring elements were used to simulate the bond and slip between the concrete and the steel plate flanges. According to the mechanical characteristics of the specimen, the bond-slip relationship along the span direction was defined whilst those along the other two directions were neglected.

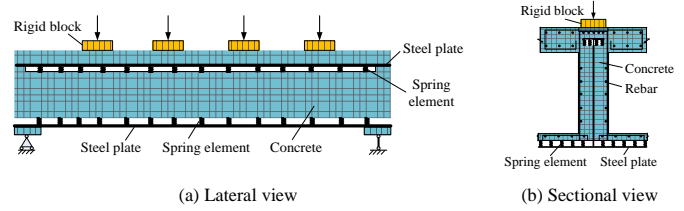


Fig. 6 Finite element model

4.2. Material model

The material models recommended by the Chinese code [20] were adopted as shown in Fig. 7. In Fig. 7(c), f_u and f_y are the ultimate and yield strengths of steel, respectively; ε_y , ε_u and ε_{uy} are the yield and ultimate strains of steel and the strain at the starting point of hardening respectively; and k is the slope of stress vs. strain during strain-hardening stage. The values of f_u , f_y , ε_y , ε_{uy} , ε_u and k for steel bars are 661 MPa, 360 MPa, 0.0019, 0.00567, 0.0438 and 7.89 GPa, respectively, and those values for steel plates are 544 MPa, 408 MPa, 0.0022, 0.00625, 0.0514 and 3.01 GPa, respectively.

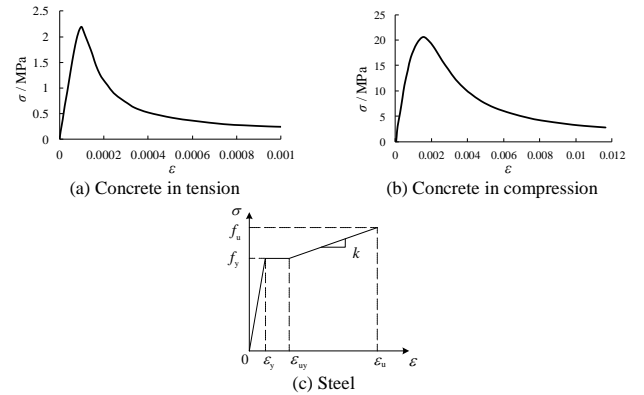


Fig. 7 Material constitutive relationships

4.3. Shear-slip model

The analytical model for the shear behavior of the shear stud connectors proposed by Luo [21] was adopted in this study, which is expressed by

$$\tau = 0.026 + 0.144s - 0.1003s^2 + 0.0373s^3 - 0.0056s^4 \quad (s \leq 2.35) \quad (1)$$

$$\tau = -0.0053s + 0.1363 \quad (2.35 \leq s \leq 10) \quad (2)$$

Where τ is the longitudinal shear stress (MPa) and s is the longitudinal slip (mm).

Consequently, the shear-slip relationship of the springs simulating the interface between the concrete and the steel plates can be expressed as:

$$F(s) = \tau(s) \times A_i \quad (3)$$

Where $\tau(s)$ is the bond slip constitutive relationship given by (4) and (5), A_i is the area represented by each spring at the interface. Note that the shear forces in the springs are different at different locations, which are marked in Fig. 8 by four distinctive areas. For accurate simulation of the spring properties in the finite element model, four shear-slip relationships were specified for the four affiliated areas.

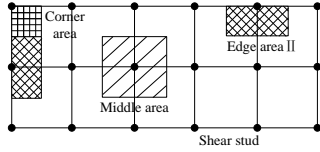


Fig. 8 Affiliated areas of typical springs

4.4. Experimental validations

This section compares the results of the models with different bond-slip conditions, namely: (1) without considering the slip between the steel plates and concrete; (2) considering the steel-concrete interface slip. The second condition covered two kinds of slips occurring at the interfaces between: a) only the bottom steel plate and concrete; b) all steel plates (including the bottom, web and top plates) and concrete.

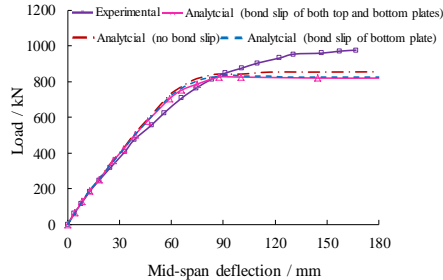


Fig. 9 Comparison between simulation and test

The load-deflection curves under different bond-slip conditions are given in Fig. 9. It can be seen that the numerical and experimental curves are in good agreement. Note that when the deflection exceeded 110mm, the simulated bearing capacity converged at 855kN. In contrast, the test bearing capacity continuously increased until the load reached 965kN. This is because the horizontal friction forces existing in the actually hinged supports partially restricted the longitudinal deformation of the beam specimen which improved the bearing capacity of the specimen. In addition, the load-deflection curves of the numerical models considering different bond-slip conditions are very close indicating that only a modest slip occurred due to the strong confinement provided by the shear studs. For this reason, the impact of bond slip between the steel plates and concrete can be neglected in the numerical analysis. Therefore, the bond slip between the steel plates and concrete would not be considered in the numerical analysis of the whole H-SC roof structure.

5. Simulation of construction process

Since the test of the H-SC beam did not take into consideration of construction process, the numerical analysis of the beam specimen and the whole H-SC roof structure was performed in this work to study the influence of the construction process on the deformation development of the MSF H-SC roof structure.

5.1. Deactivation element technique

During the construction process of the H-SC roof, welding steel plates, assembling reinforcement and casting concrete were performed in sequence, in which the deformation of the beam increased continuously. Deactivation element technique was used to simulate such a process. The entire model of the roof including the steel plates, rebars and concrete was established first.

Then all elements were deactivated, and consequently the steel plate elements, steel rebar elements and concrete elements were activated in turn to simulate the staged construction process. The strength and stiffness of the elements were ignored when deactivated and were being considered when activated. By doing so, the contributions of different structural components at different construction stages were considered by this technique.

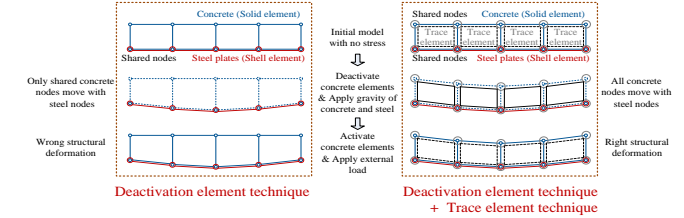


Fig. 10 Simulation of construction process based on the deactivation element and trace element techniques

5.2. Trace element technique

A problem still exists in the deactivation element technique: elements were activated only at the initial position where the entire model was built as shown in

Fig. 10. During the actual construction, concrete was cast on the deformed steel plates and consequently hardened with an initial displacement and a low level of stress and strain. This phenomenon cannot be considered by only using the deactivation element technique. Therefore, the trace element technique was also introduced in this study. Trace elements are equivalent to the host structural elements by having the same element mesh and sharing the same nodes with the structural elements but having a very small elastic modulus and mass density. The trace elements for the rebars and concrete deformed together with the structural elements for the steel plates, while the structural elements for the rebars and concrete remained deactivated. As a result, the nodal coordinates of the trace elements were able to provide the correct positions for the subsequent activation of the structural elements for the rebars and concrete, as described in

Fig. 10. Note that the impact of the trace elements on the deformation and stress of the steel plates can be ignored due to its small elastic modulus and mass density.

5.3. Analysis process

Deactivation and trace element techniques can be fully implemented using the software MSC.MARC, without resorting to any other program or programming work. The simulation of the construction process includes the following steps:

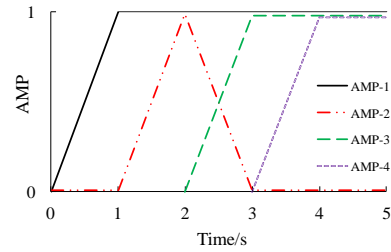


Fig. 11 Relationship of amplitude and time

Deactivation and trace element techniques can be fully implemented using the software MSC.MARC, without resorting to any other program or programming work. The simulation of the construction process includes the following steps:

STEP1: The structural elements (including steel plate, rebar and concrete elements) and trace elements (including the host elements of rebar and concrete elements) were established. Then the structural elements for rebars and concrete were deactivated, and the structural elements for steel plates and the trace elements for rebars and concrete were activated. The gravity load of steel plates was slowly increased in the static analysis (from 0 to 1 g in 0 to 1 sec, where g is the gravity acceleration, as shown in Fig. 11) to simulate the equilibrium state of the steel plates under their self-weight. The amplitude-time relationship of the gravity load was named as AMP-1. Note that the time used in the static analysis had no physical meaning and was only

used for determining the loading stage;

STEP2: The gravity load of concrete and rebars, equivalent to a uniform load, was applied to the bottom steel plate to simulate the gravity load of unhardened reinforced concrete. The amplitude-time relationship of the equivalent uniform load was named as AMP-2;

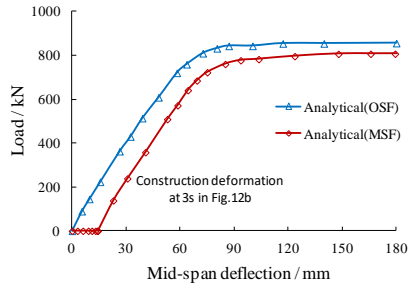
STEP3: The structural elements for rebars and concrete were activated, and in the meantime their gravity load was gradually increased. The corresponding amplitude-time relationship was named as AMP-3. Simultaneously, the equivalent uniform load in STEP2 decreased gradually. At the end of this step, the equivalent uniform load was completely replaced by the gravity load of concrete and steel. The steel plates, rebars and concrete worked together at this stage;

STEP4: The external load was applied to the beam, which was resisted by the steel plates, rebars and concrete. The corresponding amplitude-time relationship of the external load was named as AMP-4.

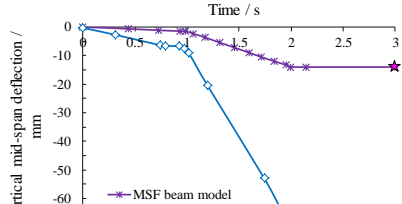
5.4. Simulation results

5.4.1. Beam specimen

Fig. 12(a) compares the load-deflection curves of the MSF and OSF beam models. While the ultimate strengths of the two simulations were different, the trends of the two curves were almost the same. The deformation of the MSF model considering the construction process was equal to that of the OSF model plus the elastic deformation generated during the construction process. In addition, the bearing capacity of the MSF model was about 6% smaller than that of the OSF model (reduced from 855kN to 805kN) due to the initial deflection of the steel plates. This is because an initial rotational deformation in the cross-sections of the beam was generated by the initial deflection, and this caused a larger elastic-plastic deformation in the steel plates during the loading process.



(a) Mid-span deflection of OSF and MSF beam models



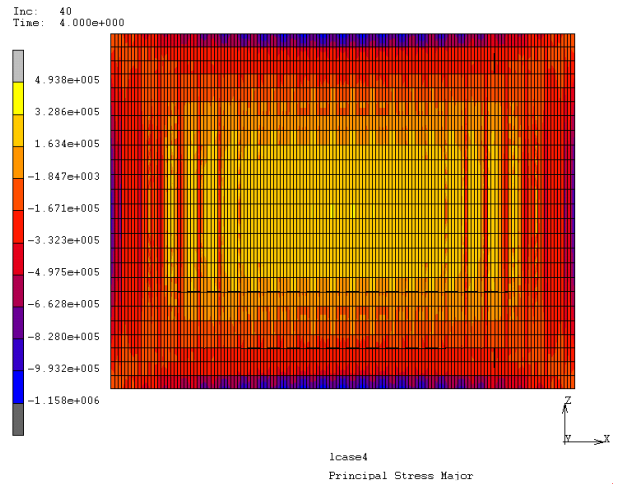
(b) Mid-span deflection development of the beam and roof models during construction process

Fig. 12 Simulated results of beam and roof models

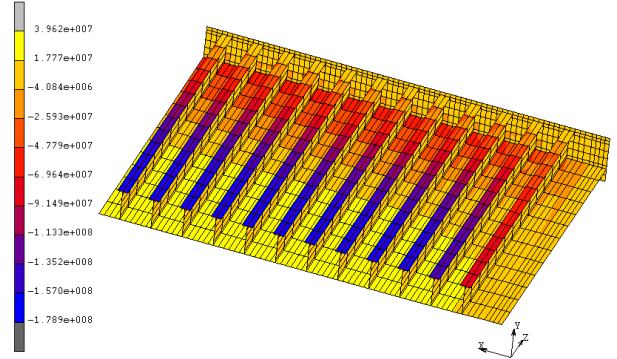
Fig. 12(b) demonstrates the change of the mid-span deflection of the MSF beam against the time during the construction process: (1) from 0s to 1s, a small deformation was found in the steel plates under their self-weight, the maximum deflection was 1.6mm at the end of 1s; (2) from 1s to 2s, the equivalent load of rebars and concrete applied to the bottom steel plate contributed to the further deformation of the steel plates; at the end of 2s, the mid-span deflection reached the maximum of 13.9mm; (3) from 2s to 3s, the gravity load of rebars and concrete increased gradually and the equivalent uniform load of rebars and concrete on the bottom decreased gradually, therefore the mid-span deflection of the steel plates remained almost unchanged, successfully achieving the replacement of the equivalent gravity load and the actual self-weight of rebars and concrete.

5.4.2. Proposed roof structure

The numerical model of the proposed roof structure is also built by the same modeling techniques being used for the beam specimen. Considering the snow load, wind load and the gravity load of ancillary equipment pipeline etc. given by the owner and recommended by the regulation [22], the design external load is 30% of the self-weight of the roof. The develop mode of the deflection of MSF roof model in Fig. 12(b) is similar to that of the beam model indicating the effectiveness of the simulation on the construction process. Fig. 13 demonstrates the stress distribution of concrete and steel plates in the roof model after external loading. The maximum compressive stress of concrete appeared at the bottom of the four side supports due to the effect of the negative bending moment. To be more specific, the stress of the most floor area in the middle part is unidirectional, while the part of the floor close to the corner were under two-way stress, which resulted in a smaller compressive stress in the bottom of the concrete closed to the corner, as seen in Fig. 13(a). It can be seen from Fig. 13(b) that the stress in lower steel plate was relatively smaller due to its large cross section. On the other hand, the middle part contributed in bearing larger compressive stress because of the smaller cross section of the upper steel plate. The deformation and strain of the roof model before concrete casting and after concrete forming are compared in Table 2. The maximum stress of different materials in Table 2 shows that the materials were still in elastic phase after construction completed, which means the redundancy of the roof structure is very large.



(a) Compressive stress in concrete (From the bottom view)



(b) Tensional stress in steel plates (1/4 model)

Fig. 13 Roof model after external loading

Table 2
Mechanical Responses of the H-SC Roof in Different Phases of Construction Process

	Before concrete casting	After concrete forming	After external loading
Maximum deflection of roof (mm)	8	69	70
Maximum compressive stress in concrete (MPa)	-	0.3	1.2
Maximum tensional stress in steel plates (MPa)	21.6	175.7	178.2
Maximum axial force of lateral braces (kN)	64	48.9	55.2

Two key factors are much concerned for the proposed roof. The first one is the deformation of such a large span concrete steel composite roof. The final maximum deflection of the H-SC roof considering the effect of the construction process, i.e., 70 mm, is much smaller than 10/300, i.e., 112 mm, which is the limiting deflection value for roof structure (l_0 is the calculated span of the roof) [20]. The maximum deflection of OSF roof model demonstrating the process without considering the construction influence is only 9mm, which indicates the deflection induced by the construction process accounts for 87% of the ultimate deflection.

The second factor is the safety of the roof during the construction process. Before concrete is hardened, the gravity of the roof is only supported by the steel assemblage in which the short upper flange is in compression. The compressive buckling of these flanges will lead to the collapse of the roof. Hence, four lateral steel braces (2L160×100×10) are connected to the upper flanges by which the compressive buckling of the upper steel flanges is prevented.

According to the Chinese code [23], the axial strength of lateral braces considering buckling N can be calculated by the following equation:

$$\frac{N}{\varphi A} \leq f \quad (6)$$

Where N is axial compression force, A is the net sectional area, f is the design value of compressive strength of steel, φ is the stability factor of the axially loaded compressive member. The calculated axial strength of the lateral braces is 1820kN, which is significantly larger than the axial forces in the braces during the construction process, i.e., 48.9kN (as seen in Table 2), indicating that the lateral braces will not be buckled. Both two factors confirm that the proposed roof is safe during the construction process and under the service state.

6. Carrying capacity and stiffness calculation

6.1. Deactivation element technique

To validate the carrying capacity of H-SC beam, an analysis was carried out in terms of the strain diagram shown in Fig. 14 and the calculation was based on the following assumptions: 1) strain of section remains plane; 2) tensile strength of concrete is disregarded; 3) the distribution of concrete stress is simplified to an equivalent rectangular, the depth of equivalent rectangular stress block equals to the depth of neutral axis multiplied by a factor 0.8; 4) the actual distribution of steel web stress is trapezoid which is also replaced by an equivalent rectangular in calculation; 5) the stress contribution of longitudinal reinforcement in flanges shall be considered and that in steel web shall be neglected.

Based on the above assumptions, the ultimate flexural strength of H-SC beam can be calculated by means of a simplified plastic method, the formulas are as follows:

$$M \leq f_c b h_t (h_0 - \frac{h_t}{2}) + f_c b_0 (0.8x - h_t)(h_0 - 0.4x - \frac{h_t}{2}) + f_y A'_s (h_0 - a'_s) + f_a A'_af (h_0 - a'_a) + M_{aw} \quad (7)$$

$$f_c b h_t + f_c b_0 (x - h_t) + f_y A'_s + f_a A'_af - f_y A_s - f_a A_af + N_{aw} = 0 \quad (8)$$

The notations used in the above equations are given as follows: f_c is the design value of concrete compressive strength; b is the width of concrete flange; b_0 is the width of concrete web; h_0 is the effective depth of section; x is the depth to neutral axis of section; h_t is the depth of flange in compressive zone; h_b is the depth of flange in tension zone; f_y and f'_y are the design values for tensile and compressive strengths of steel bars, respectively; f_a and f'_a are the design values for tensile and compressive strengths of steel plates, respectively; A_s and A'_s are the sectional areas of longitudinal steel bars in tension and compressive zones, respectively; A_af and A'_af are the sectional areas of steel plates in tension and compressive zones, respectively; a'_s is the distance from the point for resultant of forces of longitudinal steel bars to extreme fiber of section in compression zone; a'_a is the distance from the point for resultant of forces of steel plate to extreme fiber of section in compression zone; M_{aw} is the moment for the axis force of steel plate web to the point of longitudinal tension steel reinforcements and steel plate; N_{aw} is the axis force of steel plate web. In which, the calculation of M_{aw} and N_{aw} are completely

followed the formulas in the code [16].

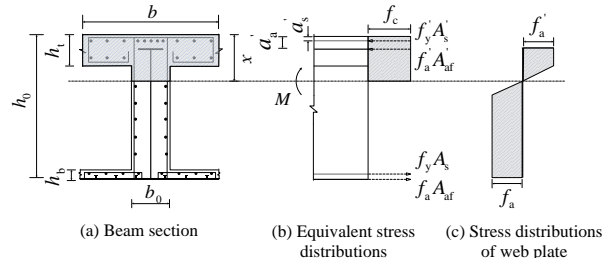


Fig. 14 Diagrammatic sketch of calculation

Theoretical values of ultimate load-bearing capacity can be obtained according to

$$M \leq f_c b h_t (h_0 - \frac{h_t}{2}) + f_c b_0 (0.8x - h_t)(h_0 - 0.4x - \frac{h_t}{2}) + f_y A'_s (h_0 - a'_s) + f_a A'_af (h_0 - a'_a) + M_{aw} \quad (5)$$

And

$$f_c b h_t + f_c b_0 (x - h_t) + f_y A'_s + f_a A'_af - f_y A_s - f_a A_af + N_{aw} = 0 \quad (6)$$

It is 7.7% greater than the test value, as shown in Table 3. Considering that the theoretical method does not take into account the intensification of steel bars and steel plate, so a relatively conservative flexural strength can be obtained using this method.

Table 3

Comparison between the experimental and theoretical strength and stiffness results

-	Experimental results	Theoretical values	Relative error
Flexural capacity (kN·m)	1694	1563	7.7%
Short-term stiffness (kN·m ²)	2.22×10 ⁵	2.12×10 ⁵	4.5%

6.2. Stiffness validation

The theoretical and experimental stiffness values are listed in Table 3. According to the code [16], the short-term theoretical stiffness B_s can be calculated by the following equation:

$$B_s = \left(0.2210^{-3} + 3.75 \frac{E_s}{E_c} \rho_s \right) E_c I_c + E_a I_a \quad (9)$$

Where E_s , E_c , E_a represents modulus elasticity of steel bar, concrete, steel plate respectively. ρ_s is the reinforcement ratio of longitudinal tensile steel bar. I_c is the moment of inertia of concrete section, I_a is the moment of inertia of steel section.

The short-term experimental stiffness B_{st} ($B_{st} = EI = 0.01575 Pl^3 / \Delta$ (11)) can be derived from the structural mechanics formula ($\Delta = \int \frac{M \overline{M}}{EI} dl$ (10)), which reflects the relationship between stiffness, applied load and deflection in linear phase.

$$\Delta = \int \frac{M \overline{M}}{EI} dl \quad (10)$$

$$B_{st} = EI = 0.01575 Pl^3 / \Delta \quad (11)$$

Where M is the internal moment due to loads acting on the specimen, \overline{M} is the internal moment caused by an assumed unit load $P=1$, EI is the flexural rigidity of a cross section, Δ is the test displacement, B_{st} is the testing values of the bending stiffness, P is the applied load, l is the specimen span.

Theoretical values of the bending stiffness in the linear phrase can be obtained by bring the inflection point values (80.9mm, 810.3kN) into Eq. 9. It can be seen from Table 3 that the stiffness of the beam bending theoretical values are in good agreement with the test values.

7. Conclusions

In this study, the mechanical behavior and construction process of a large-span H-SC roof system were studied. A large scaled beam was tested and the numerical simulations of the beam specimen and whole roof structure were carried out to investigate the mechanisms of the H-SC roof and the impact of the construction process on the H-SC roof structure. The main findings are summarized below:

(1) Under ultimate load, concrete crushing occurred in compression and yielding of the steel plate and tension reinforcement was found in the H-SC composite beam, showing a typical flexural failure mode. Minor slippage occurred between the steel plates and concrete in the bottom flange until the load exceeded 700kN, and no debonding failure was observed. It can be concluded that with appropriate shear connections, the steel plates and concrete were able to effectively work together in full composite action.

(2) The comparison between the experimental and numerical results revealed that the finite element model developed in this study was capable of accurately reproducing the mechanical characteristics of the H-SC roof. In addition, the bond slip was found to be small due to the adequately anchored shear connections.

(3) The deactivation element technique and trace element technique were used to simulate the construction process of the H-SC roof. The numerical results indicated that the two techniques can simulate the development of deformation in the process of construction. The deflection induced by the construction process accounts for 87% of the ultimate deflection.

(4) The numerical simulation shows that the proposed H-SC composite roof has enough bearing capacity and stiffness to meet the requirement for the large span structure. And the lateral braces can effectively prevent the compressive buckling of the steel plate assemblage during the construction process. In addition, the comparison between the theoretical and experimental results confirms that the proposed method could accurately calculate the ultimate flexural strength and stiffness of H-SC beam and provides a reference for the design of H-SC structures.

Acknowledgements

This work was financially supported by the National Key Research and Development Program of China (No. 2016YFC0701400), the National Natural Science Foundation of China (No. 51578018), Beijing Nova Program (No. xx2017093) and the International Research Cooperation Seed Fund of Beijing University of Technology (No. A04).

References

- [1] Ma K.J., Xiao J.C., Zhang H.A., Zhang H.P., Zhang Ha., Qi X. and Bai F.J., "A new type of steel-concrete composite plate", Proceedings of 6th Pacific Structural Steel Conference, Beijing, China, 1070-1075, 2001.
- [2] Teng J.G., Wong H.T., Wang Z.C. and Dong S.L., "Steel-concrete composite shell roofs: structural concept and feasibility", Advances in Structural Engineering", 8(3), 287-308, 2005.
- [3] Shanmugam N.E. and Lakshmi B., "State of the art report on steel-concrete composite columns", Journal of Constructional Steel Research, 57(10), 1041-1080, 2001.
- [4] Andrews A. and Folger P., "Nuclear power plant design and seismic safety considerations", Congressional Research Service Report, Report R41694, Washington D.C., USA, 2012.
- [5] JEAC 4618-2009, Technical Code for Seismic Design of Steel Plate Reinforced Concrete Structures: Buildings and Structures, Japanese Electric Association Nuclear Standards Committee (JEAC), Tokyo, Japan, 2009.
- [6] Bowerman H., Coyle N. and Chapman J.C., "An innovative steel/concrete construction system", The Structural Engineering, 80(20), 33-38, 2002.
- [7] Liew J.Y.R. and Sohel K.M.A., "Lightweight steel concrete-steel sandwich system with J-hook connector", Engineering Structure, 31(5), 1166-1178, 2009.
- [8] Liew J.Y.R. and Sohel K.M.A., "Structural performance of steel-concrete-steel sandwich composite structures", Advances in Structural Engineering, 13(3), 453-470, 2010.
- [9] Liu J.B., Liew J.Y.R. and Zhang M.H., "Shear-tension interaction strength of J-hook connectors in steel-concrete-steel sandwich structure", Advanced Steel Construction, 11(1), 73-94, 2015.
- [10] Oduyemi T.O.S. and Wright H.D., "An experimental investigation into the behavior of double-skin sandwich beams", Journal of Constructional Steel Research, 14, 197-220, 1989.
- [11] Nie J.G. and Zhao J., "Flexural behavior of steel plate-concrete composite beams", Key Engineering Materials, 400-402, 37-42, 2009.
- [12] Li G.Q., Liang L. and Li X.H., "Experimental and theoretical study on the behavior of the steel-concrete composite beam with notched web of inverted T-shaped steel section at construction stage", Advanced Steel Construction, 7(4), 376-386, 2011.
- [13] Li G.Q., Liang L. and Li X.H., "Experimental study on behaviors of the trapezoid connectors of the inverted T-shaped steel with notched web for a novel composite beam", Advanced Steel Construction, 7(1), 48-63, 2014.
- [14] Liew J.Y.R. and Wang T.Y., "Novel steel-concrete-steel sandwich composite plates subject to impact and blast load", Advances in Structural Engineering, 14(4), 673-687, 2011.
- [15] Kong S.Y., Remennikov A.M. and Uy B., "An experimental investigation of the performance of non-composite steel-concrete-steel protective panels under large impact loading", Advances in Structural Engineering, 16(7), 1163-1174, 2013.
- [16] JGJ 138-2001, Technical specification for steel reinforced concrete composite structures, The Ministry of Housing and Urban-Rural Development of the People's Republic of China (MOHURD), Beijing, China, 2001.
- [17] Fang S.W. and Yuan X.F., "Construction analysis of the chimney of solar thermal power station", Applied Mechanics and Materials, 283, 41-46, 2013.
- [18] Zhang Q.L., Luo X.Q., Gao Z.F., and Li Z.X., "Numerical tracing and graphic simulation for construction processes of large span pre-tensioned steel structure", Journal of Tongji University, 32(10), 1295-1299, 2004.
- [19] MSC. Marc 2007, "User documentation volume A: Theory and user information", MSC. Software Corporation, www.mscsoftware.com, 2007.
- [20] GB50010-2010, Code for Design of Concrete Structures, The Ministry of Housing and Urban-Rural Development of the People's Republic of China (MOHURD), Beijing, China, 2010.
- [21] Luo H.X., "Longitudinal shear resistant problem about the steel deck-concrete composite slabs", Ph.D. Thesis, Chongqing University, Chongqing, China, 2004.
- [22] GB50009-2012, Load Code for the Design of Building Structures, The Ministry of Housing and Urban-Rural Development of the People's Republic of China (MOHURD), Beijing, China, 2012.
- [23] GB50017-2003, Code for Design of Steel Structures, The Ministry of Housing and Urban-Rural Development of the People's Republic of China (MOHURD), Beijing, China, 2003.

FAILURE TEST OF A SUSPENDOME DUE TO CABLE RUPTURE

Zhi-Hua Chen^{1,2}, Xiao-Xiang Wang^{2,3}, Hong-Bo Liu^{1,2,*} and Yu-Jie Yu²

¹ State Key Laboratory of Hydraulic Engineering Simulation and Safety, Tianjin University, Tianjin 300072, China

² School of Civil Engineering, Tianjin University, Tianjin 300072, China

³ Department of Civil Engineering and Engineering Mechanics, Columbia University, New York 10027, NY, USA

* (Corresponding author: E-mail: hbliu@tju.edu.cn)

ABSTRACT

Suspendome integrates a lower cable–strut tensegrity system below the upper single-layer latticed dome for long span overlapping. Cable rupture, especially hoop cable failure, is an important failure mode that involves transient cable failure with significant impact. In this study, two kinds of cable rupture tests were conducted on a suspendome model to investigate the dynamic responses, failure modes, and mechanical changes. One was cable rupture at static loading state for simulating the practical cable break condition during the in-service period. The other was single hoop cable tension and rupture for exploring the influence of pretension level and cable–strut joint resistance. Results indicated that the stiffness and robustness of the suspendome were good such that no apparent deflection or failure phenomenon was observed. Cable rupture involved sudden tension failure, which led to the oscillatory response to adjacent strut members. Cable sliding occurred under large tension gaps, and it caused extensive tension loss throughout the entire hoop, thereby leading to different cable tension recovery patterns from non-slip numerical simulations. Cable rupture at the outmost ring had a larger impact and tension loss effect than that at the inner rings, and the extent of its influence on the suspendome was closely related to the tension levels and cable–strut joint characteristics.

Copyright © 2019 by The Hong Kong Institute of Steel Construction. All rights reserved.

1. Introduction

Suspendome is a type of hybrid structure that integrates a lower cable–strut tensegrity system below the upper single-layer latticed dome, thereby strengthening the upper shell for long span overlapping. Since the proposal by Kawaguchi, this structure system has been quickly studied and used in many large-span roof systems for public gymnasiums and stadiums due to its high structural efficiency (Kawaguchi et al. [1]; Guo et al. [2]; Liu et al. [3]). Suspendome involves high tension cable systems for improved structural rigidity. Previous experimental studies have indicated that the tensegrity systems in the lower part of the structure significantly influence the boundary reaction and internal force of the upper shell members (Chen [4]; Wang et al. [5]). Therefore, given the importance of cable force in suspendome, many studies have been conducted on force finding, optimism design, and construction control theory. Kang et al. [6] proposed a simplified pretension design method based on static equilibrium and found that the outmost ring-stiffened suspendome is the most efficient. Subsequently, Cao and Zhang [7] found that the outmost ring generally exhibits the highest tension level and the greatest influence on structural performance after a series of force finding analyses. The cable stretching process imposes a considerable influence on the upper shell due to the hybrid construction of suspendomes, and the effect in turn affects the pretension introduction in sub cable systems. Chen et al. [8] indicated that the pretension force of latterly stretched cables influences previously finished cables, and the influencing pattern differs from the comparative locations of hoop cables. Liu and Chen [9] studied the hoop cable stretching process and found that the pre-stressing loss induced by sliding friction during pre-stressing construction exerts a remarkable effect on the mechanical behavior of suspendomes. These findings were validated by the construction process of the Badminton Stadium suspendome for the 2008 Beijing Olympics (Wang et al. [10]). Further studies on form findings and construction control have greatly helped in evaluating and guiding structural designs (Zhang et al. [11]). However, the structural degradation or failure evaluation is crucial because of the wide application of suspendome in public buildings. The structural response under cable rupture requires special consideration, especially for the cable incorporated hybrid type. However, this area remains in the preliminary stage.

In suspendomes, tensioned cables may experience accidental damages or rupture scenarios during their service period due to construction errors or human factors. In addition, cable failure will not only result in the sudden failure of structural components but also involve a considerable unloading effect on the remaining structure owing to the high-tension state (Wang and Bai [12]; Gerasimidis and Baniotopoulos [13]). Chen and Sun [14] explored the internal force distribution pattern and the nonlinear stability behavior of suspendomes before and after cable failure by directly running static simulation with or without ruptured cable pieces. Their results indicated that a ruptured hoop introduces its load bearing share to the upper shell and surrounding members, and the outmost ring exerts the largest influence on internal force redistribution.

ARTICLE HISTORY

Received: 12 April 2017
Revised: 8 August 2017
Accepted: 17 December 2017

KEY WORDS

Suspendome;
Cable rupture;
Robustness;
Cable–strut joint;
Oscillatory response

Zhu et al. [15] performed a cable rupture failure analysis of a cable dome and a suspendome and found that hoop cable rupture in a cable dome leads to large nodal displacements and structural slacking, whereas the suspendome does not experience collapse because of the restraint of the rigid upper shell. However, member forces that surround the rupture point present dramatic variations, with the oscillation extent exceeding three times that of the original stress state. Wang et al. [16] studied the cable breaking problems during construction and operation stages and then evaluated the vulnerable cable parts. Considerable discussion on cable rupture effect has been mainly numerical explorations. Liu et al. [17] recently performed a rupture test on annular crossed cable-truss and found an obvious deflection increase in cable-truss under cable rupture. However, related experimental data are rare as a result of the operation difficulties in suspendome failure tests under cable rupture and the high dynamic reaction measurement requirements.

In this study, the cable rupture response of a suspendome model was experimentally investigated. The experiments were designed to identify the effect of cable loss and the safety of suspendomes under the condition of sudden breakage of critical cables and study the effect of cable sliding on the internal force redistribution behavior. Two impact cases were considered, namely, single hoop cable breaking under normal service conditions and rupture responses with only one tensioned hoop cable under self-weight. The strain histories, dynamic deformations, and member-moving procedures were recorded and identified to study the dynamic reactions and cable rupture effects.

2. Experimental preparation

2.1. Experimental background and general conditions

The tests were performed on a suspendome model, which was designed based on the 10:1 scaled-down design of a real stadium roof with a 108 m span (Fig. 1(a)). The real structure, Chiping Gymnasium (Liu and Chen [9]), adopted the suspendome design with a stacked arch (Fig. 1(b)), whereas the test model only retained the dome part that comprised a K6 lamella single-layer reticulated shell and a sub-tensegrity system with seven hoop cables (Fig.s 1(c) and (d)). The dome span was 10.8 m, and the rise was 2.55 m. The roof model was supported on two circular platforms made of H section beams. Each ring was seated on 24 evenly distributed 3.25 m-high inner columns and 2.4 m-high outer columns.

The dimensions of the model members were designed based on axial stress consistency with the real structure under static loading conditions, and the availability of practical member size in the market was also considered. The specifications of the model members are listed in Table 1. The Chiping Stadium adopted the hoop-cable-stretching method, which can save on tensioning equipment and improve the stretching consistency. A new type of rolling cable–strut joint was proposed to overcome the cable loss from the friction in the cable–strut joint as shown in Fig. 2(a). Therefore, a simplified rolling joint was

designed and utilized in the test model (Fig. 2(b)). Detailed information and the effect of this rolling joint were presented by Chen et al. [8]. The cable–strut joint in the model consisted of a center roller for convenient cable sliding during the tensioning process. After tensioning, U-shaped clips were fastened to both sides of the roller to prevent the continuous cable from sliding. Previous static tests have proved the effectiveness of this joint model in resisting the unbalanced cable force under static loading cases. However, the clip may fail to prevent the cable from sliding under significant dynamic disturbance. This effect was carefully monitored during the current failure test.

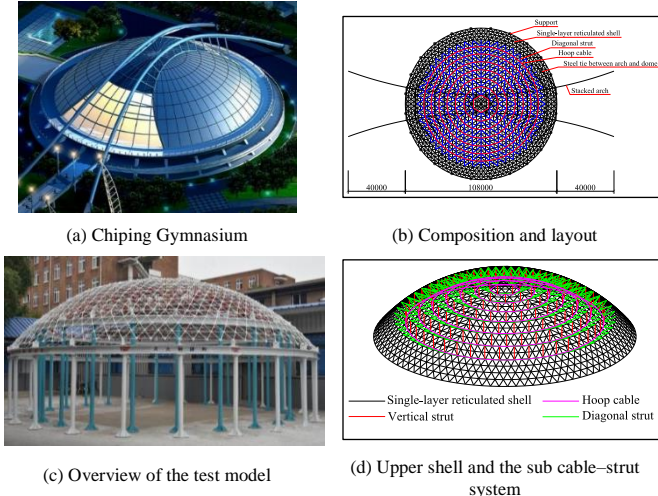


Fig. 1 Chipping Gymnasium and scaled-down suspedome test model

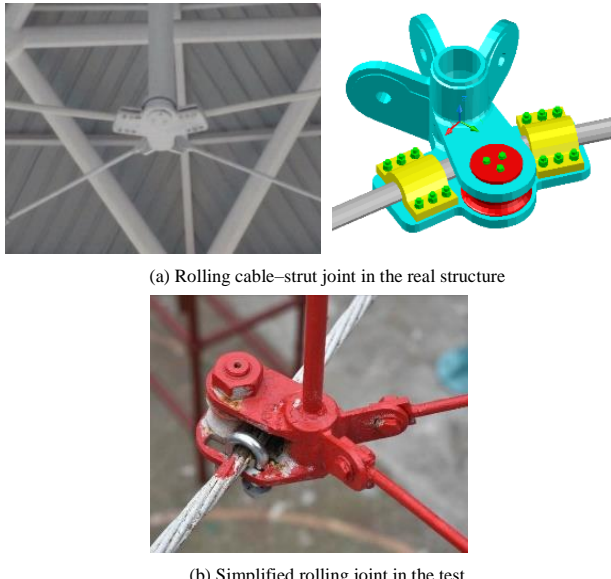


Fig. 2 Rolling cable-strut joint to reduce pretension loss

Table 1
Specification of the experimental model

Items	Prototype members	Prototype section area (cm^2)	Model members	Model section area actual/theoretical (cm^2)
Single-layer reticulated shell	P203×6	37.130	P12×2.5	0.746 / 0.7426
	P219×7	46.620	P13×3	0.942 / 0.9324
	P245×7	52.340	P16×2.5	1.06 / 1.0468
	P273×8	66.600	P17×3	1.319 / 1.332
	P299×8	73.140	P19×3	1.508 / 1.463
6 th to 7 th hoop cable	Φ7×73	28.090	Steel wire rope (Φ12)	0.5688 / 0.5618
1 th to 5 th hoop cable	Φ7×121	46.570	Steel strand (Φ15.24)	1.4000 / 0.9314
Strut	P219×7	46.620	P13×3	0.942 / 0.9324
Radial cable	Φ80	50.240	Φ11.5	1.039 / 1.0048

2.2. Experimental apparatus

The entire testing procedure involved tensioning the hoop cables, applying full-span loads to simulate the working state of the roof, and activating the cable rupture. Therefore, this test required several special apparatuses, which included tensioning devices for applying the pretension, cable-force-measuring devices for obtaining the internal tension state, and a rupture device for simulating the sudden break of the tensioned cable. Fig. 3(a) shows the tension device utilized in the test. The device comprised a pair of channels and long screws, and pretension was applied by tightening the bolts at the long screws. The internal force of the shell members and struts was measured with strain gauges. However, this strain-measuring method could not be directly utilized to obtain the cable tension owing to the multi-wire composition and uneven surface of the cables. A cable force measuring device was then designed (Chen et al. [8]), as shown in Fig. 3(b). The hoop cable was interrupted at the measuring point and then anchored to the two clamps. Therefore, cable tensions were transmitted through measuring devices, and force was obtained through strain measuring at the side plates.

The rupture tests aimed to explore the dynamic effect under cable break impact and suspend dome safety with cable break at different circles. Therefore, a rupture device was designed to ensure a cable break at the desired time and location, as shown in Figs. 3(c) and (d). The device mainly consisted of a handle, a cam, and a pair of clips that could clamp the anchorage. The piles and handle were connected by the cam. When pulling the handle, the cam would turn over and open the clips. At the same moment, the clamped anchorage was released, thereby creating a sudden breaking effect.

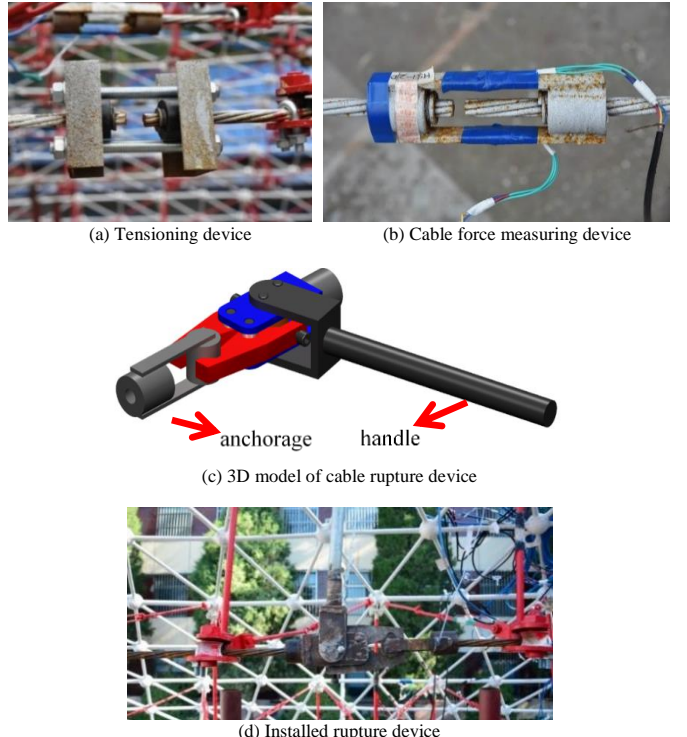


Fig. 3 Special apparatuses in the test

2.3. Cable tensioning, loading, and measuring

The full-sized roof was designed to bear 0.4 kN/m² of dead load during the service period. The real dome has more than a thousand joints. According to load similarity and loading practicability, only 80 nodes were selected as the loading points, and 0.6 kN of vertical load was applied at each node (Fig. 4(c)). Prior to each cable break, the suspedome needed to experience cable tensioning and loading to reach the service state. Similar to the Chipping Stadium, the model employed the hoop cable stretching method, and multiple-point simultaneous stretching with joint lubrication was adopted to reduce frictional loss and achieve a uniform cable force distribution (Figs. 4(a), (b), and (d)). During cable stretching, the internal forces were recorded by the static strain indicator to control the loading extent and verify the measuring effectiveness. Before the rupture, the strain gauges were shifted to a dynamic strain amplifier (type TST5912, Fig. 5(a)) to capture the dynamic signals. When the cable ruptured, the internal force reactions were transient, with member forces experiencing a dramatic change within a short time. The rupturing region was also filmed by a Y-SERIES high-speed video camera with a recording speed of 500 frames per second during the break stage (Figs. 5(b) and (c)).

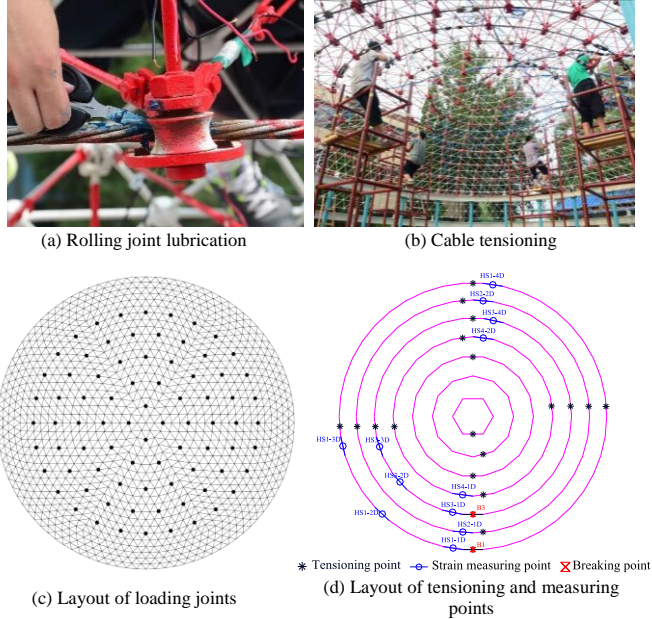


Fig. 4 Cable Tensioning and Loading

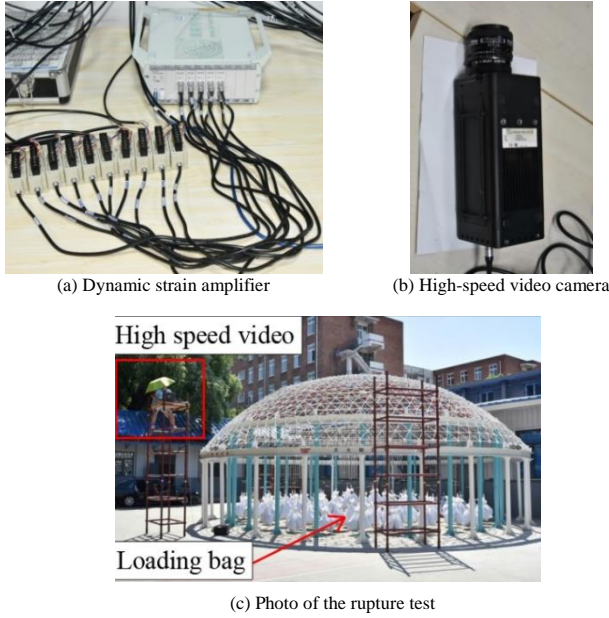


Fig. 5 Measuring device for dynamic reactions

2.4. Testing of cable force

The suspendome model had seven hoop cables, and each ring was numbered first to seventh from outside to inside. The layouts of the tensioning points, rupturing locations, and measuring spots at the hoop cables are shown in Fig. 4(d). Four tensioning points were arranged at the four outer circles (first to fourth hoop), two points at the fifth ring, and one point at the inner sixth and seventh circles. The measuring spots were denoted as HS1-2D, where “HS” represents hoop strands, the first number (e.g., 1) is the number of hoop cable, the second number (e.g., 2) is the sequence number of the measuring spots, and “D” means dynamic.

2.5. Referencing finite element simulation

Construction and cable stretching simulations were performed beforehand in ANSYS for the guidance of pretension introduction. In the finite element simulations, pretension introduction was exerted by changing the initial strain of the cable element. However, for cable rupture problems, loss of cable piece and possible sliding behavior involve variation on structural stiffness matrices. Traditional methods of designing and analyzing suspendomes always simplify cable pieces as multi-segment bar or link elements without bending and compression-resisting capabilities. Therefore, common simulations cannot realize the sliding behavior and dynamic effect. In this study, static loading analysis of the suspendome model without the ruptured cable piece was

performed to obtain the ultimate interforce distribution in the non-sliding cable case as reference. Then, cable sliding behavior and its effects, dynamic oscillatory response evaluation, and failure extents could be deduced from the comparison between the static simulation and test results. In the referencing simulation, the BEAM188 element was applied to the upper shell members and the supporting column. The LINK8 element was applied to the vertical and diagonal struts, and the LINK10 element was applied to the hoop cables.

3. Cable rupture during the service state

3.1. Break at the third hoop cable

Fig. 6 shows the variation in cable forces during tensioning. In this rupture case, the stretching strategy adopted an inward tensioning sequence that started from the first circle to the seventh circle. The tensioning spot (B3) became the ruptured location, and two cable ends were connected by the rupture device at this point. The B1 point was an ordinary stretching spot in this case. The inward tensioning strategy was performed in ANSYS, and the values of which were represented by black dash lines. The results showed that cable force measuring devices could effectively reflect the internal forces and their varying trends. For the measured cable pieces close to the stretching end, the cable forces could be controlled well. On the contrary, for the points located between tensioning ends, such as HS1-2D, HS3-1D, and HS3-2D, the obtained forces were comparatively low due to the tension loss at each turning node. The varying trends of cable tension after each stretching step were not exactly the same with the finite element analysis (FEA) curves owing to the effect of friction.

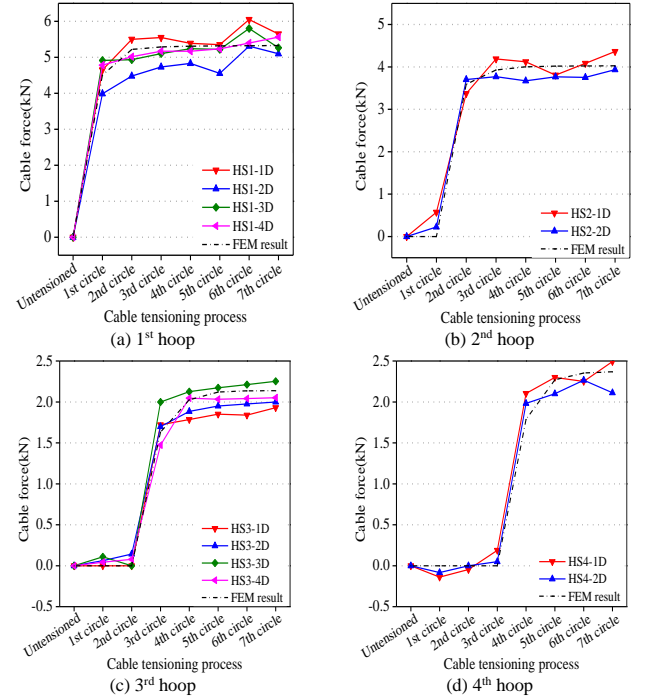


Fig. 6 Variation in cable force during tensioning

The cable break at the third circle did not induce visible deflection or shaking behavior, except for a slight shrink back effect on the ruptured ends. Fig. 7 shows the dynamic reaction of the selected hoop cables, marking the static simulation results with and without ruptured cable piece as reference (dash lines). For the ruptured cable (third hoop), the segments (HS3-1D) near the break point exhibited an immediate and dramatic decrease in internal force. By contrast, the farthest cable pieces (HS3-4D) experienced insignificant variation, the trends of which were consistent with those in the static simulations. Meanwhile, the measured cable tension for the two other spots was different from the FEA results. HS3-2D presented a small decrease instead of an increasing trend (Fig. 7(c)). Being a certain distance away from the break, the tension force of HS3-3D did not suffer much from cable failure in the static simulation. However, the measured data still displayed tension loss, indicating that tension loss spread to more than half of the circular region. The rupture at the third hoop also led to some tension loss at the second circle (HS2-1D).

The different cable force distributions indicated that the non-sliding assumption was no longer suitable for this model, and the adopted rolling joint failed to completely prevent the continuous cable from sliding. In the non-sliding cable suspendome condition, the hoop cable was separated and no sliding was allowed at the cable-strut joints. Therefore, adjacent cable pieces

acted as individual segments, with their tension following the force equilibrium principle. When any cable piece ruptured, the remaining cable could be effectively pulled by the diagonal struts, with the absent tension quickly regained. The quick recovery even induced tension increase in the 45°–90° angle regions, which correspond to the breaking spot. While in the test, the measured data presented cable slackening behavior with the gradual recovery of cable tension from the break spot to the farthest side.

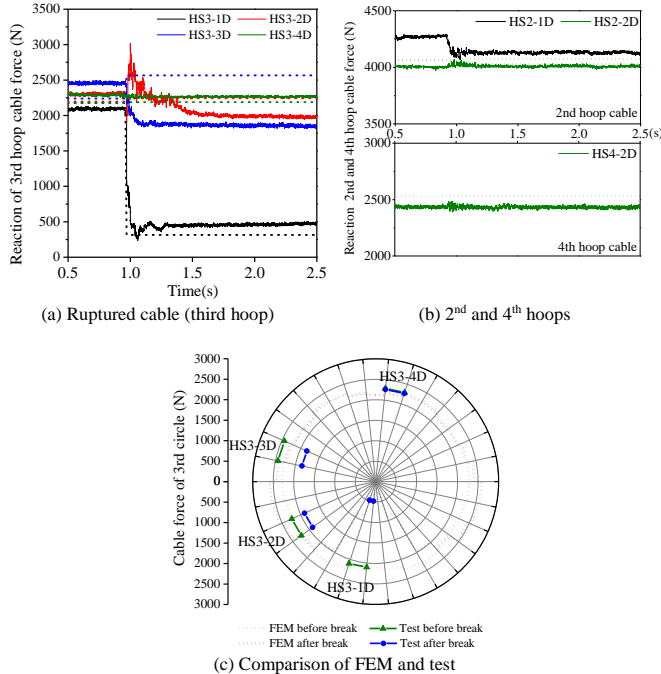


Fig. 7 Variation in cable force during the third circle cable rupture

Fig. 8 shows the filmed images of the ruptured region, and the distance between the ruptured device and the adjacent joints is marked to indicate the cable sliding behavior. Cable broke at time $t = 0.80$ s. When the clamp was opened, the hoop cable was released suddenly. The distance from the rolling joint to the cable end narrowed from time $t = 0.80$ s to $t = 0.92$ s and then reversed slightly at time $t = 0.98$ s. This micro-displacement change, together with the cable force redistribution pattern, indicated that, although fixed with U-shaped clips, cable slip still occurred under a huge tension gap that was induced by the break.

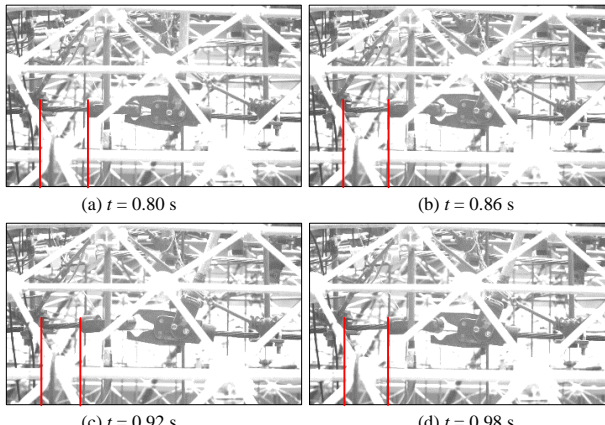


Fig. 8 Typical pictures obtained by the high-speed video camera

Fig. 9 plots the dynamic reactions of the diagonal struts (Fig. 9(b)), vertical struts, and shell members (Fig. 9(c)) close to the ruptured spot. History reactions at critical moments (0.80–1.20 s, gray dot region) were also added separately to present the transient reaction at the rupture moment better. The results indicated that cable slip could also influence the oscillatory response and the force-changing pattern of adjacent struts. During breaks, induced tension gap caused a significant pulling impulse, thereby leading to sudden tension decrease at DS1. Then, the internal force of DS1 rebounded rapidly and vibrated at a high-tension state (from -18 MPa to 20 MPa) to follow the mechanical equilibrium owing to cable sliding and joint friction resistance. The internal force at DS3 exhibited a dramatic increase (from 1.2 MPa to 38.2 MPa). The measured force redistribution patterns could also reveal the cable sliding behavior at the two

adjacent joints. The significant tension increase at DS3 proved its effective roles in resisting cable sliding and in the pulling trend of the remaining cable.

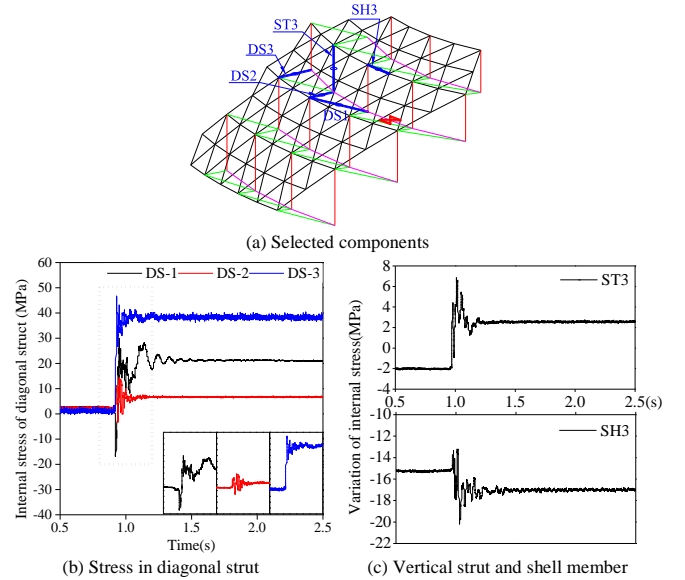


Fig. 9 Internal stress variation at struts and shell members during cable rupture

3.2. Break at the first hoop cable

After the first rupture case, the dome was unloaded and the cables were loosened to prepare for the subsequent break test. In this case, the break occurred at the first circle. The entire testing process was similar to the previous one but with a different tensioning sequence that started from the seventh circle to the first circle. Fig. 10 shows the cable force variation at the outmost four circles during the entire tension process. The tested result demonstrated a consistent pattern with the FEA simulation results. The tension gradient and variation in the same circle were attributed to the slight friction loss at the cable-strut joint.

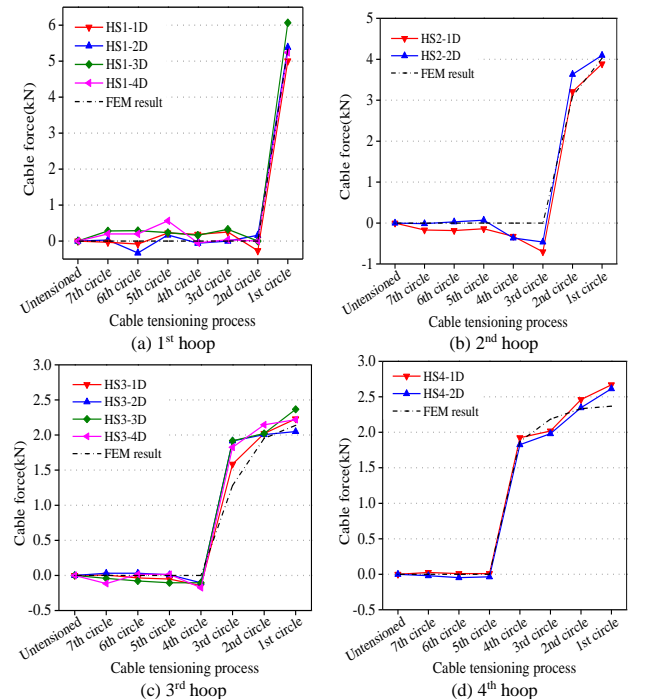


Fig. 10 Change in cable force during the tensioning process

The break initiation of the first hoop rupture case was harder than that of the previous third hoop break as a result of the high-tension state. The sudden rupture induced a strong perceivable vibration, but no visible deflection or shaking behavior was observed. Given that the outmost ring had the highest tension in the suspensome, the excellent stiffness and robustness performance of this hybrid structure was confirmed. Therefore, single member or cable rupture would not lead to global failure or progressive collapse behavior during the service state. Fig. 11 presents the dynamic response of cable force at the first (ruptured circle), second, and fourth circles, with corresponding static

simulation data as reference. The tension of HS1-1D decreased with the sudden release of the clamped end and then reversed back at approximately 2500 N. HS1-2D and HS1-3D presented abrupt decreases without significant oscillation contrary to the slight increase in FEA.

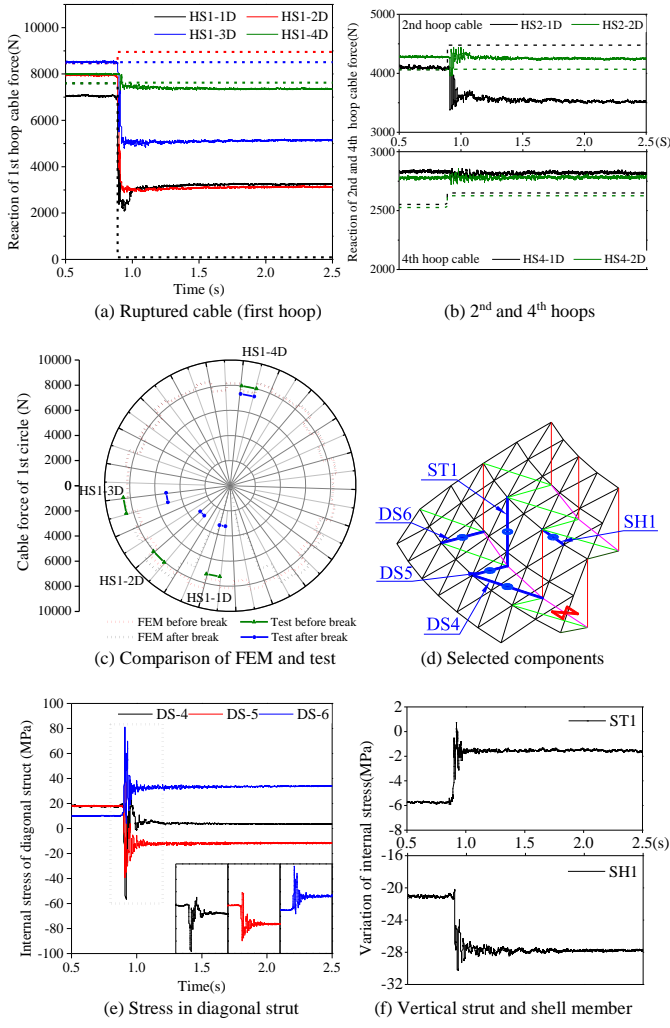


Fig. 11 Variation in member force during the first hoop cable rupture

If no sliding was allowed at the cable–strut joint, then the absent tension at the rupture spot would be recovered within a comparatively small region. However, the test data showed that even the cable piece (HS1-3D) located at nearly 90° away from the break still presented a significant tension loss, indicating a wide range of cable slackening and absent tension recovery behavior. Therefore, the comparison indirectly indicated that joint sliding also occurred at the first hoop break and the influencing range was wider than the third hoop break case due to a high pretension level. In this break case, the rupture not only led to tension force redistribution at the ruptured circle but also caused a strong vibration (HS2-2D) and internal force change at adjacent circles (HS2-1D). The cable tension in the fourth circle did not express significant oscillation behavior, representing a comparatively small influence from the rupture.

The friction resistance and frictional energy dissipation at the cable–strut joints led to weak and quickly dissipating oscillatory response, which subsequently changed the tension state and force redistribution at adjacent cable pieces. Therefore, HS2-1D had an obvious tension decrease instead of increase in the non-slip simulation. DS5 turned into a compression state, and only a slight internal force change was exhibited at DS4 and DS6. The shell member (SH1) presented a large decrease, indicating an unloading effect on the upper shell around the ruptured region.

3.3. Discussion of the dynamic effect

The previous discussion showed that the dynamic effects involved in the hoop cable rupture played a significant role in the internal force redistribution of the suspendome structures. For members located far from the ruptured spot or at the low joint–slip exposure region, the dynamic responses were typically high-frequency oscillation. For the struts or cable pieces (such as DS1, DS5, and ST3) that suffered from cable rupture and slight joint shaking influence, the dynamic response exhibited a dramatic and asymmetric change at the ruptured

moment. For members around the ruptured spot (such as HS3-1D, DS1, HS1-1D, and DS4), the significant impact led to a shaking response at the surrounding rolling joints via cable pulling and frictional sliding, thereby resulting in a low-frequency oscillation part embedded in the dynamic responses.

According to references (Wolff and Starossek [18]; Mozos and Aparicio [19]), the dynamic effect from rupture incidents is generally considered with a dynamic amplification factor (DAF) in design and analysis processes, that is,

$$DAF = \frac{S_{dyn} - S_0}{S_{rest} - S_0} \quad (1)$$

where S_{dyn} represents the extreme dynamic responses in time history, S_{rest} is the rested internal force after the oscillatory effect dissipated, and S_0 is the initial mechanical state before breaking. In typical design cases, rupture tests are seldom implemented because of the high equipment requirements, and dynamic simulations are not always available. Static member removal analysis is usually performed instead, and a factor of 2.0 is applied as the DAF to account for the dynamic effect. This value is based on the behavior of a linear elastic system with no damping and instantaneous removal and theoretically represents the worst-case scenario (Russell et al. [20]). However, given that it is incapable of considering the damping effect and the cable sliding influence, traditional non-slip static simulation cannot reflect the realistic condition, such as the internal force redistribution at diagonal struts and hoop cables. On the basis of the tested data and the comparison with referencing static simulation, two sets of DAFs were calculated and compared (Eqs. 2 and 3), and they are shown in Fig. 12.

$$DAF(test) = \frac{S_{dyn}(test) - S_0(test)}{S_{rest}(test) - S_0(test)} \quad (2)$$

$$DAF(FEA) = \frac{S_{dyn}(test) - S_0(test)}{S_{rest}(FEA) - S_0(FEA)} \quad (3)$$

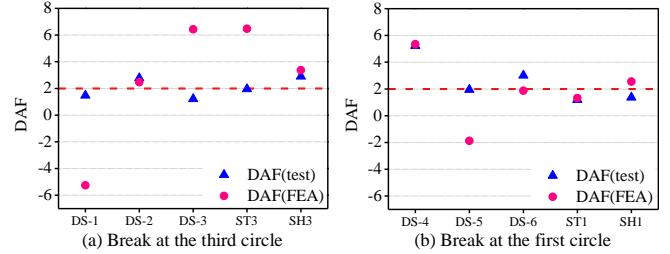


Fig. 12 DAF of selected members

The majority of DAF (test) data fluctuated at approximately 2.0, supporting the reason for this design guidance. However, DAF (test) was calculated on the basis of the test results, the data of which were quite hard to obtain, whereas DAF (FEA) values were more scattered, and some spots were significantly larger than 2.0 or even had negative values (Fig. 12). The difference between the two DAF values and their locations indicated that the scattered spots in both break conditions were mainly diagonal struts directly influenced by cable force redistributions. Like DS1 in the third hoop break and DS4 in the first hoop break case, sudden rupture and induced cable sliding led to different cable force recovery patterns, which then resulted in different denominator variations in Eq. 3 compared with the test data. When analyzing or designing suspendome with rolling joints, special attention or significant safety insurance should be considered for diagonal struts. In addition, further investigations and advanced models are required to account for the dynamic sliding and friction energy dissipation at the rolling joints.

4. Rupture in the single tensioned cable case

The preceding discussion indicated that structural dynamic reactions were closely influenced by the tension level of ruptured cables. The results also indicated that the joint sliding behavior and its effect could affect the oscillation response and internal force redistribution patterns. To further investigate the effect of cable frictional sliding on the dynamic response of the suspendome, a series of rupture tests under the single tensioned cable condition was performed. In this case, only the third circle was tensioned, while the rest of the circles were slackened. The friction-resisting capability of the rolling joints was controlled through the tightening of the U-shaped clips in the rolling joints at different

extents. Different pretension levels and joint-tightening conditions were considered in the test. No external loads were applied. The detailed testing information is listed in Table 2.

Table 2

Parameters of the single cable ruptured test

Case Number	Tightening Condition	Pretension (N)
A1500	All fully tightened	1500
A3000	All fully tightened	3000
A6000	All fully tightened	6000
H3000	Half tightened	3000
N3000	Non-tightening clips	3000

The tests could be divided into two parts. The first three cases, A1500, A3000, and A6000, were all fully fastened conditions, in which all rolling joints were fully fastened under 1500 N, 3000 N and 6000 N pretension levels at the third hoop cable. The last two cases had 3000 N cable tension but H3000 was loosely fastened at the cable-strut joints (half tightened), whereas N3000 had no clips at all. A3000, H3000, and N3000 could be compared to understand the joint effect on the overall dynamic behavior of the suspedome.

In the A1500 and A3000 cases, cable rupture did not produce a perceivable vibration effect. In the A6000 case, the adjacent joints expressed slight oscillation and a separating trend with the release of the cable ends. For the H3000 and N3000 tests, the breaking of hoop cable led to obvious cable sliding, accompanied by slight vibrations at the rolling joints and diagonal struts.

Fig. 13 shows the typical behavior of the ruptured region at the initial state and the largest response moment. Fig. 14 displays the residual sliding conditions after the test. No apparent sliding was observed in the fully fastened condition, even for the A6000 test. Slight member vibrations were observed as the cable tension increased to a high level. In the H3000 and N3000 tests, the remaining cable shrank obviously and slid across the rolling joints with the release of the cable end. The joint friction also induced a slight oscillation effect at the adjacent members during the rupturing period. N3000 had a larger sliding extent and a more violent perceivable shaking behavior at the dome than those of H3000.

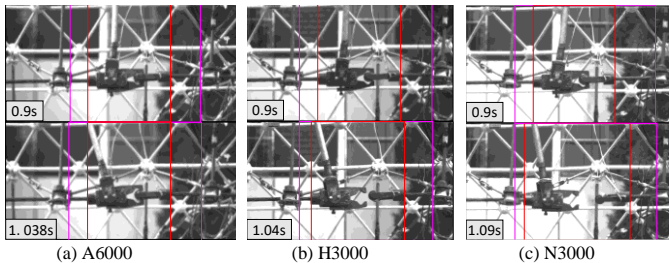


Fig. 13 Typical photos captured by the high-speed camera before and after cable rupture

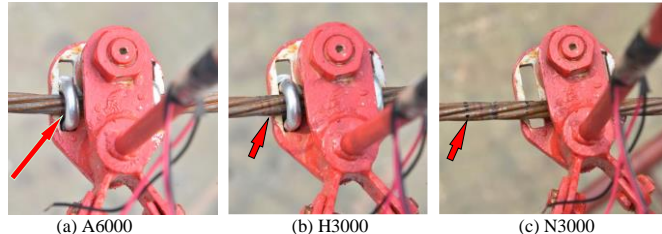
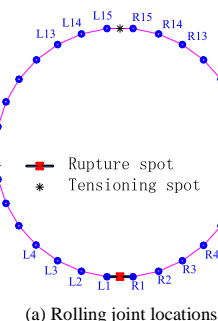
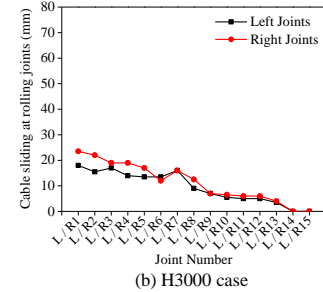


Fig. 14 Residual joint slip after the test

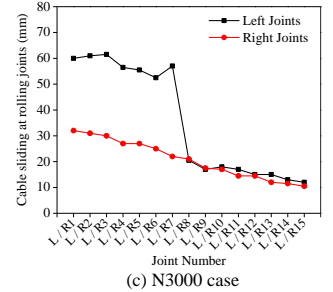
Prior to each test, the clip locations were marked at the ruptured hoop cable. Then, the cable sliding extent could be obtained as the relative distance between the marks and the joint clips. Subsequently, careful examination revealed that H3000 and N3000 exhibited cable sliding at nearly every joint along the cable. Fig. 15 plots the measured sliding extent at each joint and shows that the slip had a gradual decreasing trend from the rupture spot to the farthest side. In the N3000 case, the left-side joints had a larger effect than that of the right-side joints. In addition, the slip extent showed an obvious decreasing trend between L7 and L8 joints in the N3000 test. This change was attributed to the tensioning point located between the joints. Under the sudden impact, the tensioning device slackened, which accounted for the majority of the sliding displacements.



(a) Rolling joint locations



(b) H3000 case



(c) N3000 case

Fig. 15 Residual slip distribution at the rolling joints

Fig. 16 shows a comparison of the internal force reactions at the hoop cable, diagonal struts, and shell members (the component locations are the same as in Figs. 4(d) and 9(a)). In the fully fastened tests, the tension variations at the hoop cable increased with pretension level, but the changing extents were comparatively small. Only in the high-pretension case (A6000) did HS3-1D express an obvious transitory oscillation; this dynamic response was mainly a high-frequency type that dissipated rapidly. H3000 and N3000 showed a dramatic force change at all the four measuring pieces during the rupture, representing a global slackening impact on the entire cable. N3000 also expressed a considerably low-frequency vibration, which might be attributed to the frictional sliding and induced shaking at the rolling joints or related members.

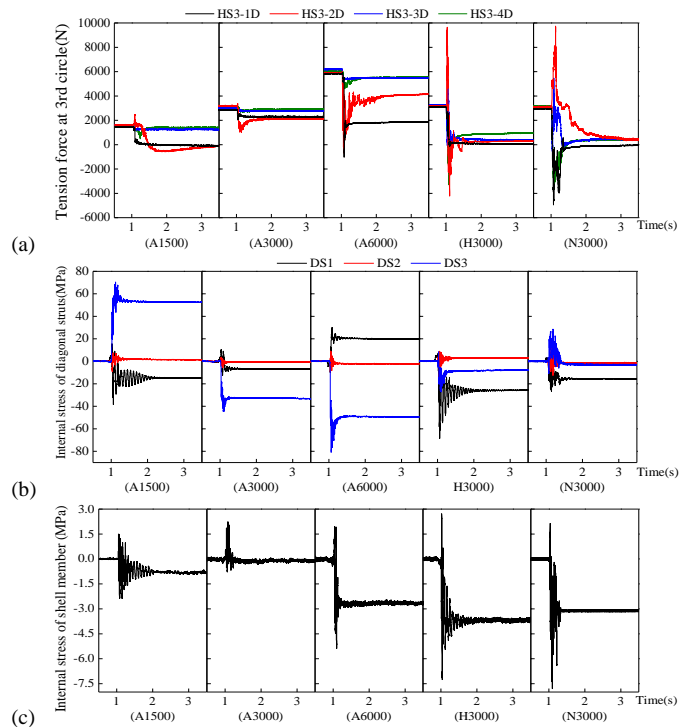


Fig. 16 Dynamic reaction at the structural members: (a) ruptured hoop cable, (b) diagonal struts, and (c) shell member

Given that the stress level at the struts and shell members was small, the initial stress states were greatly affected by the testing or measuring errors, which made distinguishing the real state after cable tensioning difficult. Therefore, as presented in Figs. 16(b) and (c), only the internal force changes were compared, and the initial state of the dynamic responses were set to zero for improved comparison. In the fully fastened group, the internal force

response at DS1 changed from a tension drop reaction to a tension increase reaction as the pretension level increased. Meanwhile, the internal force response at DS3 varied from an increasing to a decreasing trend. The time duration of the oscillation response was shortened in the high-pretension case. In H3000 and N3000, the shrinking and pulling effects of the ruptured cable could not be efficiently resisted by adjacent members because of the weak friction resistance at the rolling joints, thereby leading to a comparatively small inequivalent forces and thus small amplitudes in the oscillatory responses (H3000 and N3000 in Fig. 16(b)). DS2 did not present significant force variation after cable rupture for all test cases, and the oscillatory effects were small.

The slip conditions and cable force varying patterns revealed that sudden rupture and tension failure would be limited to a comparatively small region if the cable-strut joints could effectively resist cable sliding, thereby leading to local failure mode. In this condition, the sub cable-strut system could still effectively support the upper shell, thereby causing only a slight unloading effect and internal force change in the upper shell (A1500 and A3000 in Fig. 16(c)). This unloading effect became intense and led to large amplitude in the dynamic response and an obvious tension decrease at the upper shell member (A6000) as the pretension level increased. However, cable slackening would propagate to a large scope and even to the entire hoop cable range if the cable-strut joints fail to resist the sliding behavior. Large-scale stiffness loss would cause an overall unloading effect on the upper shell, which was reflected as a violent dynamic vibration and internal force loss at the upper shell members (H3000 and N3000 in Fig. 16). Therefore, in practical projects, rolling joints should be fixed and tightened well upon the completion of stretching.

5. Conclusions

In this study, experimental tests were conducted on a suspensdome to investigate the dynamic responses, failure modes, and mechanical changes under cable rupture failure. Two types of failure conditions were considered. One was the cable break at the static loading state for simulating practical breaking during the in-service period. The other had a single hoop tensioned and ruptured for exploring the presence and effect of cable sliding behavior. From the results and discussion, the following key conclusions could be obtained.

1) The proposed tensioning, measuring, and rupturing devices were suitable for rupture tests on suspensdomes. The use of high-speed camera and dynamic strain amplifiers could effectively monitor the transient breaking process and dynamic responses.

2) The suspensdome had excellent stiffness and robustness, and therefore no obvious deflection or shaking were observed. The reactions caused by cable rupture at the outmost circle (the first hoop) were more obvious than that at the inner circle (the third hoop). Rolling joints could effectively reduce joint friction loss during the stretching process and could resist unbalanced cable tension during static loading. However, under cable rupture, cable sliding still occurred and could influence the oscillatory response and cable tension recovery patterns. The DAFs of struts connected to the rupture cable ends were scattered and high. Thus, special attention or significant safety insurance should be considered for diagonal struts.

3) The single hoop-tensioned and ruptured tests indicated that, when joint frictional resistance was certain, the oscillation intensity and impact-affected region increased with the initial tension levels. If cable-strut joints could effectively fix the hoop cable, then cable breaking effect would be limited to a comparatively small region, thereby creating a local failure mode. If the friction-resisting capability of the cable-strut joints was weak, then cable slackening would propagate to a large scope, thereby creating an overall unloading effect.

Acknowledgments

This research was sponsored by the National Natural Science Foundation of China (Grant No. 51478310) and Project of Tianjin Urban & Rural Construction Commission (2014-1). The authors also appreciate the financial support provided by the China Scholarship Council (File No.201606250065) that enables the Visiting Scholar Research at Columbia University at New York, United States.

References

- [1] Kawaguchi M., Abe M. and Hatato T., "On a Structural System 'Suspension-dome' System", Proceedings of the IASS-MSU International Symposium, Istanbul, Turkey, May 24-28, 1993.
- [2] Guo J.M., Dong S.L. and Yuan X.F., "Research on static property of suspensdome structure under heap load", Advanced Steel Construction, 8(2), 137-152, 2012.
- [3] Liu H.B., Han Q.H., Chen Z.H., Wang X.D., Yan R.Z. and Zhao B., "Precision control method for pre-stressing construction of suspensdome structures", Advanced Steel Construction, 10(4), 404-425, 2014.
- [4] Chen Z.H., "Beam String Structure System", Beijing, China, Science Press, 2013. (in Chinese)
- [5] Wang X.X., Yu Y.J. and Yan X.Y., "Theoretical model of symmetric wire breaks in semi-parallel wire cables", Journal of Tianjin University (Science and Technology), 49(S1), 34-40, 2016.
- [6] Kang W.J., Chen Z.H., Lam H.F. and Zuo C.R., "Analysis and design of the general and outmost-ring stiffened suspensdome structures", Engineering Structures, 25(13), 1685-1695, 2003.
- [7] Cao Q.S. and Zhang Z.H., "A simplified strategy for force finding analysis of suspensdomes", Engineering Structures, 32(1), 306-318, 2010.
- [8] Chen Z.H., Yan R.Z., Wang X.D., Liu H.B. and Xiao X., "Experimental researches of a suspensdome structure with rolling cable-strut joints", Advanced Steel Construction, 11(1), 15-38, 2015.
- [9] Liu H.B. and Chen Z.H., "Research on effect of sliding between hoop cable and cable-strut joint on behavior of suspensdome structures", Advanced Steel Construction, 8(4), 359-365, 2012.
- [10] Wang S., Zhang G.J. and Zhang A.L., "The prestress loss analysis of cable strut joint of the Badminton Gymnasium for 2008 Olympic Games", Journal of Building Structures, 6, 39-44, 2007.
- [11] Zhang Z.H., Cao Q.S., Dong S.L. and Fu X.Y., "Structural design of a practical suspensdome", Advanced Steel Construction, 4(4), 323-340, 2008.
- [12] Wang F. and Bai J.T., "Dynamic effects on a pre-stressed multi-story plane steel frame caused by sudden failure of a cable", Advanced Materials Research, 671, 441-445, 2013.
- [13] Gerasimidis S. and Baniotopoulos C.C., "Disproportionate collapse analysis of cable-stayed steel roofs for cable loss", International Journal of Steel Structures, 11(1), 91-98, 2011.
- [14] Chen Z.H. and Sun G.J., "Research on the stability of suspensdome after cables failure", Spatial Structures, 18(1), 46-50, 2012.
- [15] Zhu M.L., Dong S.L. and Yuan X.F., "Failure analysis of a cable dome due to cable slack or rupture", Advances in Structural Engineering, 16(2), 259-271, 2013.
- [16] Wang H.J., Fan F., Qian H.L., Zhi X.D. and Zhu E.C., "Analysis of pretensioning construction scheme and cable breaking for megastructure suspensdome", Journal of Building Structures, S1, 247-253, 2010.
- [17] Liu R.J., Li X., Xue S.D., Mollaert M. and Ye J., "Numerical and experimental research on annular crossed cable-truss structure under cable rupture", Earthquake Engineering and Engineering Vibration, 16(3), 557-569, 2017.
- [18] Wolff M. and Starossek U., "Cable loss and progressive collapse in cable-stayed bridges", Bridge Structures, 5(1), 17-28, 2009.
- [19] Mozo C.M. and Aparicio A.C., "Parametric study on the dynamic response of cable stayed bridges to the sudden failure of a stay. Part I: bending moment acting on the deck", Engineering Structures, 32(10), 3288-3300, 2010.
- [20] Russell J.M., Owen J.S. and Hajirasouliha I., "Experimental investigation on the dynamic response of RC flat slabs after a sudden column loss", Engineering Structures, 99, 28-41, 2015.

DEVELOPMENTS AND BEHAVIORS OF SLIP-RELEASED NOVEL CONNECTORS IN STEEL-CONCRETE COMPOSITE STRUCTURES

Yang Ding^{1, 2}, Xiao-Meng Dai¹ and Jia-Bao Yan^{1, 2*}

¹ School of civil engineering, Tianjin University, Tianjin 300072, China

² Key Laboratory of Coast Civil Structure Safety of Ministry of Education, Tianjin University, Tianjin 300072, China

* (Corresponding author: E-mail: ceyyanj@163.com)

ABSTRACT

Effective connection between steel beam and concrete slab is the key issue for steel-concrete composite structures. The slip-released connectors were developed to overcome cracking of the concrete in the hogging moment region of a continuous beam. A full-scale push-out test with two specimens was conducted to investigate the slipping behaviors of the connectors. Test results offered useful information on the slipping behaviors of the connectors in terms of load-slip behaviors and failure modes. FE models were developed for the slip-released connectors and the accuracy of the FE simulation was checked by the reported test results. Two concepts of the connectors, i.e., an improved version with foamed plastic blocks covered by protecting shell and the sliding connectors were developed to improve the structural performances of the slip-released connectors. Numerical simulations results showed that both concepts could effectively release the shear force within their slipping allowed limit and could achieve the performance requirement of releasing slip.

Copyright © 2019 by The Hong Kong Institute of Steel Construction. All rights reserved.

1. Introduction

Steel-concrete composite structure became popular in recent several decades since it was initially developed in the 1920s and substantially used in the 1950s. Steel-concrete composite structure usually consists of a concrete slab and an underneath steel beam. The effective connection between steel beam and concrete slab is essential to steel-concrete composite structure since it governs its flexural resistance.

Many types of connectors, e.g., headed stud connectors, have been widely used in the steel-concrete composite structure. Slipping and uplift behaviors of the stud connectors were investigated by researchers, e.g., Spremici et al. [1], Han et al. [2] Lin et al. [3] and Ju [4]. Related connectors were also developed, tested and compared. Chu et al. [5] investigated the shear resistance behaviors of a newly puzzle shape of crestbond rib shear connector by experiments. Chung et al. [6] performed push-out tests with numerous parameters on T-type Perfobond rib shear connector for steel concrete composite bridges. Henderson et al. [7-8] investigated and compared the behaviors of different types of shear connectors by tests and theoretical derivation. Dai et al. [9] focused on the effects of concrete strength and stud collar size on the shear strength of the demountable shear connectors by experimental studies. Yan et al. [10, 11] investigated the mechanical behavior of J-hook connectors by push-out tests. He et al. [12] tested the behaviors of the perfobond strip connector by experimental study. All these connectors above restrain the slipping and uplifting displacements between steel and the concrete slab and can be named as slip-restricted connectors [13]. In the sagging moment region of composite beams or girders, the slip-restricted connectors ensure the steel and concrete work compositely to achieve full utilization of the steel and concrete materials. However for continuous composite beams or bridges, tensile stress occurs in the hogging moment region, causing the cracking of concrete slab [14]. Pre-stressed techniques are usually adopted to solve this cracking problem. However, the stress loss will be high due to the compatible deformation between steel and concrete.

Another way to solve this cracking problem is to release the steel-concrete interfacial slip. The flexible shear (FS) connectors (see Fig. 1) developed by Abe and Hosaka [15] are in H- or T-section with web covered by soft foaming polystyrol plate. Since the top flange of the connector is not covered by foaming polystyrol and directly anchored to the concrete, the web of the steel connector will be bent under shear force. Thus, slip between the steel beam and the concrete slab is allowed and the interfacial shear force is partially released. However, the stiffness of the connector's web can not be ignored, and its shear resistance still needs to be accounted. Nie et al. [16] proposed an improved version of the flexible connector namely Uplifted-Restricted and Slip-Permitted (URSP) connector as shown in Fig. 2. The main improvement from the FS to the URSP connector is that the flange of the connector is covered

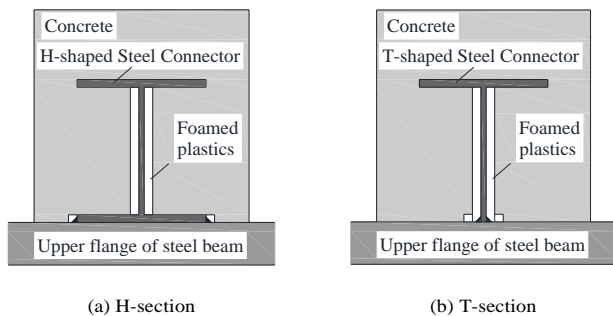
ARTICLE HISTORY

Received: 12 June 2017
Revised: 28 October 2017
Accepted: 17 December 2017

KEY WORDS

Composite structures;
Slip-released connectors;
Push-out test;
Finite element analysis;
Shear resistance

with foamed plastic blocks. Thus the steel-concrete interfacial slip is released through the compressive deformation of the foamed plastic blocks. However, the slipping behaviors of the slip-released connector have not been fully investigated. Improvements and optimizations of this type of connector are still required to improve the slipping behavior of the composite structures.



(a) H-section (b) T-section

Fig. 1 FS connector

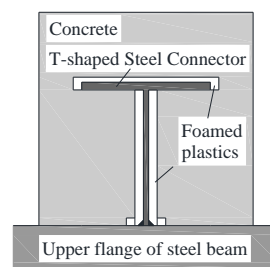


Fig. 2 URSP connector

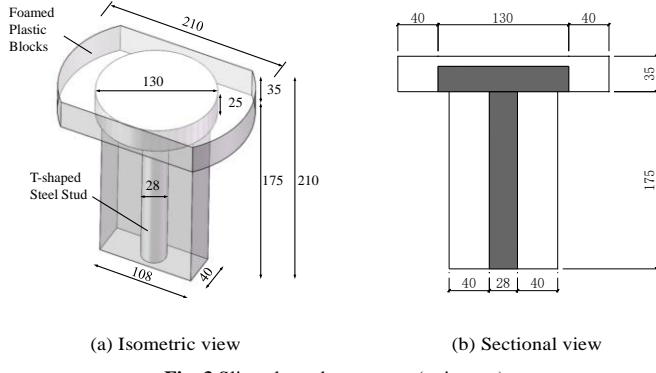
This paper focused on the slipping behaviors of the slip-released connectors. A full-scale push-out test program consisting of two specimens was reported. Test results offered useful information on the ultimate strength, the shear force-slip curves and failure mode. The experimental results showed that the flange of the T-shaped connector was anchored in the concrete that makes sure the direct transformation of the shear force from the connector to the concrete without deformations in the foamed plastic blocks. A finite element model (FEM) was also developed for USRP connectors using general commercial software ABAQUS. The accuracy of the developed FE model was checked through validations against the reported test results. To fully release the steel-concrete interfacial shear force, two concepts, i.e., an improved version with foamed plastic blocks covered by a protecting shell and the sliding connectors were developed to improve the structural performances of the slip-released connectors. Numerical simulations results showed that both concepts could effectively release the shear force within their slipping allowed limit and could achieve the performance requirement of releasing slip.

protecting shell and sliding connectors were developed to improve the structural performances of the slip-released connectors. The slipping behaviors of these concepts were studied through numerical simulations.

2. Full-scale push-out test on ursp connectors

2.1. Test specimens

To investigate the slipping behavior of the slip-released connectors, a full-scale push-out test was carried out. As shown in Fig. 3, the slip-released connector consisted of a T-shaped steel stud and covering Ethylene-Vinyl Acetate (EVA) foamed plastic blocks. The diameters of the shank and the flange were 28 mm and 130 mm, respectively. The slipping limit of the connector was determined by the thickness of the side foamed plastic blocks under compression, i.e., 40mm in this case. Fig. 4 shows the details of the push-out test specimens. Six slip-released connectors were welded on the top surface of steel base with 8 mm fillet weld. A concrete slab was casted on the top surface of the steel base. The concrete slab measures 1200×110×350 mm³ in length×width×depth and reinforced by 16mm-diameter steel bars.



(a) Isometric view (b) Sectional view

Fig. 3 Slip-released connector (unit: mm)

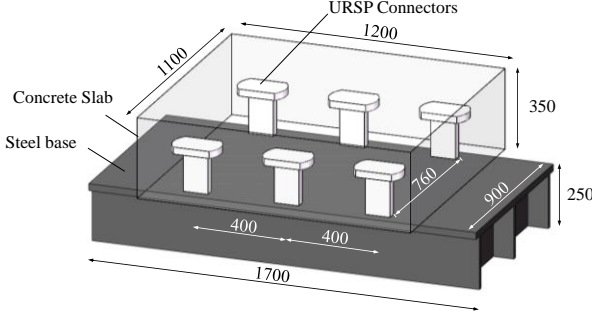


Fig. 4 Specimen of push-out test (unit: mm)

2.2. Material properties

The T-shaped steel studs were fabricated with U20452 (45#) steel while the steel base was processed with Q235B steel. Tensile test was performed on these steel reinforcements according to Chinese standard GB/T 228.1-2010 [17]. The results are listed in Table 1 and the engineering tensile stress-strain curves of steel are shown in Fig. 5.

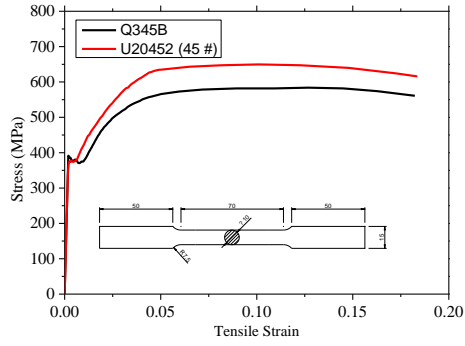


Fig. 5 Engineering tensile stress-strain curves of steel

The concrete slabs adopted C60 normal weight concrete. The mechanical

properties of the concrete as listed in Table 2 were obtained through compressive test at 28 days after casting according to Chinese standard GB/T50081-2002 [18]. Three 150×150×150 cubes (No. 1-3) were prepared for compressive strength test which determined the concrete strength grade. According to Chinese standard, axial compressive strength test must be done before elastic modulus test. Six 150×150×300 prisms (No. 4-9) were prepared for axial compressive strength and elastic modulus tests. Half of the six prisms (No. 4-6) were tested for axial compressive strength. The other prisms (No. 7-9) were tested for elastic modulus.

Table 1
Mechanical properties of steel

Material prop- erty	Steel grade	Yield strength (MPa)	Ultimate strength (MPa)	Elastic modulus (GPa)	Elongation
T-shaped steel stud	U20452 (45#)	370.4	649.4	204.1	21.6
30mm steel plate	Q345B	393.1	576.3	201.3	23.8

Table 2
Mechanical properties of concrete

No	Size (mm)	Compressive strength (MPa)	Axial compressive strength (MPa)	Elastic mod- ulus (GPa)
1	150×150×150	67.6	-	-
2	150×150×150	62.1	-	-
3	150×150×150	63.4	-	-
4	150×150×300	-	39.3	-
5	150×150×300	-	37.8	-
6	150×150×300	-	39.7	-
7	150×150×300	-	-	36.1
8	150×150×300	-	-	35.5
9	150×150×300	-	-	36.6
Average	-	64.4	38.9	36.1

2.3. Test setup and measurements

Fig. 6 shows the setup for push-out test. The steel base was fixed to the ground by six bolts. To simulate the loads acting on the actual structure, 25 kN vertical load of was applied on the top surface of the concrete slab to simulate the certain pressure (36.5 kPa) on the interface between the steel base and the concrete slab of Haihe Bridge in Tianjin, China [19]. Horizontal displacement controlled type of loading was applied on the side surface of the concrete slab by a hydraulic servo loading system. One specimen was applied by horizontal monotonic load and the other was applied by horizontal cyclic load. Slip between the concrete slab and the steel base was measured by two Linear Variable Differential Transformers (LVDTs).

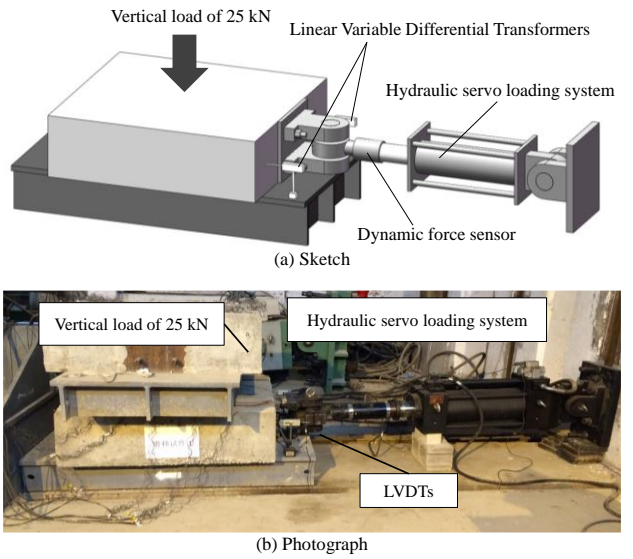


Fig. 6 Test setup

2.4. Experiments results and discussion

2.4.1. General behavior

Fig. 7(a) and (b) show the shear force-slip curves of the tested two specimens. These curves showed that the shear force-slip curve of the specimen under monotonic load, as shown in Fig. 7 (a), can be divided into four working stages:

(a) At the first stage, i.e., curve OA in Fig. 7(a), the shear force increases

with micro slip. The interfacial shear force was taken by the steel-concrete interface bonding and static friction; the connectors were not subjected to the shear force. At the end of this stage, i.e., point A in Fig. 7(a), the initial bonding failed and slip between the concrete slab and I-beam occurred. This initial bonding stress usually consists of mechanical, chemical bonding and static friction. Fig. 8(a) shows the slip traces on the top surface of the steel base.

(b) At the second stage, i.e., curve AB in Fig. 7(a), the interfacial shear force increases almost linearly with the increase of the slip. The connectors were subjected to the shear force and the T-shaped steel studs deformed meanwhile the foamed plastic blocks were compressed. The shear force was taken by the connectors and the interfacial dynamic friction.

(c) At the third stage, i.e., curve BC in Fig. 7(a), the interfacial shear force increases nonlinearly with the increase of the slip and achieved its ultimate resistance at the end of the stage. The T-shaped steel studs deformed further and the weld was in the material hardening stage. At the end of the stage, the weld toes at the root of the T-shaped steel studs failed in shear mode. The sound of metal fracture was heard that accompanied with the failure of the connector.

(d) At the fourth stage, i.e., curve CD in Fig. 7(a), the weld at the root of the T-shaped steel studs failed successively and the interfacial shear force reduces in a steps. At the end of the stage, all the connectors in the specimen failed and the applied shear force was only taken by the friction. Spalling of the concrete took place near the bottom surface of the concrete slab as shown in Fig. 8(b).

The shear force-slip curve of the specimen under cyclic load is shown in Fig. 7(b) and the skeleton curve of the specimen under cyclic load is compared with the curve of the specimen under monotonic load in Fig. 7 (a). These two curves exhibit similar behaviors, though the cyclic one decreases more rapidly than the monotonic one because more damage accumulated in the cyclic load.

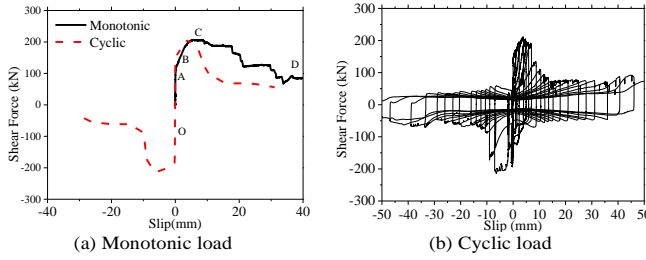


Fig. 7 Shear force-slip curves derived from push-out test

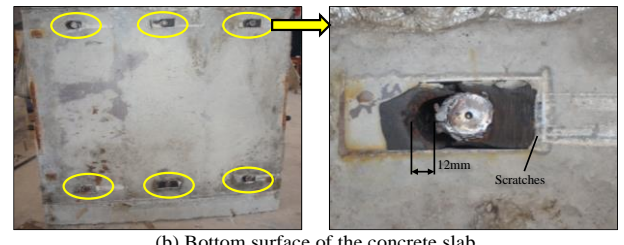
The main failure mode of the push-out test was the welding toes fracture at the root of the T-shaped steel studs. This type of failure mode usually occurred to the large-diameter stud shear connectors [20, 21]. Fig. 9(a) shows the welding fracture at the weld toe on the top surface of the steel base. As shown in Fig. 9(b), the bottom surface of the concrete slab was scratched by the remains of the fillet weld during the slip process after fracture of the weld, and the scratches were about 5mm in depth. The shanks of the connectors were tilted during the push-out test, and a 12 mm-width gap was observed between the shank of the connector and the foamed plastic blocks. The compressive deformation was about 12 mm while compared with the thickness of the compressive side of the foamed plastic was 40mm. The side of the plastic foam was only compressed by 30% before final failure of the specimen.



Fig. 8 General Behaviors of the test



(a) Top surface of the steel base



(b) Bottom surface of the concrete slab

Fig. 9 Weld fracture between slip-released connectors and steel base

2.4.2. Failure mode

The test results in this paper are compared with existing connectors, including URSP connector [16, 22], welded and demountable stud connectors (result in C30 concrete) [9], blind bolt connector (specimen PBB-RT) [23] and PBL connector (standard PBL specimen) [12]. Fig. 10 shows comparison of the load-slip curves in these tests. The shear forces are normalized as P/P_u . P_u is the ultimate strength of a curve. The comparison shows that the initial stiffness of the curve in this paper is greater than that of URSP connector and demountable connector. The P/P_u at ultimate strength in this paper (0.10) is significantly lower than URSP connector (0.55) and the curve decreases more rapidly after the peak. The comparison indicates that the foamed plastic blocks are not significantly compressed. The behavior of the connector is similar to welded stud shear connectors. The connector in this paper can not fully release the slip between the concrete and the steel. Stiffness of the connector is not ignorable. The reason of the unexpected behavior can be conclude: During the casting, the foamed plastic blocks suffered pressure by fresh concrete. Localized deformations were generated at the concrete-foam interfaces as shown in Fig. 11. This greatly reduced the slipping allowance between the concrete and the connector. Thus, the shear force will be directly transferred from the connector to the concrete without deformations in the foamed plastic blocks.

The idealized slip-released connectors should pose low initial shear stiffness and allow slipping. However, from the experimental shear force-slip curves, the structural performances of these connectors are still not satisfactory. Further improvements are still necessary.

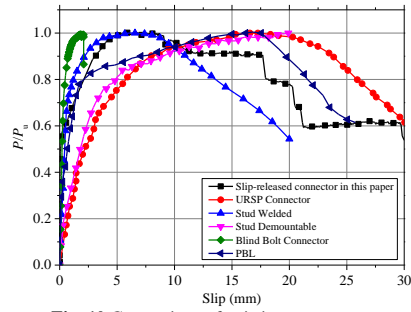


Fig. 10 Comparison of existing connectors

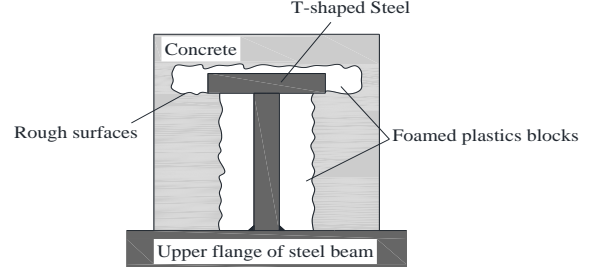


Fig. 11 Rough surfaces generated between the flange and the concrete

3. Finite element analysis

3.1. Geometry, elements and mesh size

A FE model was developed by general finite element program ABAQUS/CAE. Considering the symmetry of the geometry and loading pattern, half of the connector (1/12 of a test specimen) was modeled. The FE model consisted of four parts, i.e., steel plate base, T-shaped steel studs, fillet weld and concrete slab. Considering the elastic modulus and strength of the plastic foam is 3.0 MPa, 0.25 MPa that are much smaller compared with those of steel and concrete, it is thus not modeled in the FEM. To simulate the rough surfaces and the anchored-flange, the interfaces between the bottom surface of the flange of the T-shaped steel stud and the concrete were tied.

The FE model shown in Fig. 12 mainly utilized three-dimensional eight nodes continuum elements in the ABAQUS element library with hourglass control (C3D8R). The C3D8R element is an eight-node linear brick element with reduced integration and three translation degrees of freedom at each node. The concrete slab in vicinity of the connector was modeled by three-dimensional ten-node continuum elements (C3D10I) due to its complex shape.

Different mesh sizes were used in the FE model for the balance between accuracy of the analysis and computing processing cost. The concrete mesh sizes in and out the vicinity of connector were $25 \times 25 \times 30$ mm³ and $30 \times 30 \times 30$ mm³, respectively. The mesh sizes for T-shaped steel stud and fixed steel base were $10 \times 10 \times 10$ mm³ and $40 \times 40 \times 40$ mm³, respectively. The mesh size for the weld toe at the root of the T-shaped steel stud was $2 \times 2 \times 2$ mm³.

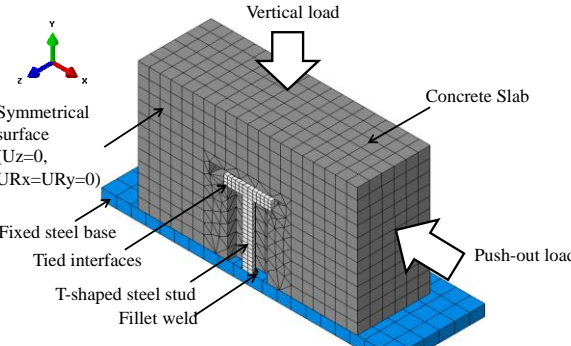


Fig. 12 FE model of slip-released connector

3.2. Material model

The concrete damage plasticity model was used for the concrete slab in the FE model. The strain-stress curves in Chinese code GB50010-2010 [23] were adopted as the input data for the definition of the CDPM model as the following:

$$\sigma_c = (1-d_c) E_c \varepsilon \quad (1)$$

$$d_c = \begin{cases} 1 - \frac{\rho_c n}{n-1+x^2} & x \leq 1 \\ 1 - \frac{\rho_c}{\alpha_c (x-1)^2 + x} & x > 1 \end{cases} \quad (2)$$

$$\rho_c = \frac{f_{ck}}{E_c \varepsilon_{ck}} \quad (3)$$

$$n = \frac{E_c \varepsilon_{ck}}{E_c \varepsilon_{ck} - f_{ck}} \quad (4)$$

$$x = \frac{\varepsilon}{\varepsilon_{ck}} \quad (5)$$

where, σ_c is the compressive stress of the concrete, ε_c is the compressive strain of the concrete, f_{ck} is the compressive stress of standard concrete cubes, ε_{ck} is the strain at f_{ck} , d_c is the parameter for axial compressive damage evolution of concrete. Tensile stain-stress curve was set similarly as the compressive curves:

$$\sigma_t = (1-d_t) E_t \varepsilon \quad (6)$$

$$d_t = \begin{cases} 1 - \rho_t [1.2 - 0.2x^5] & x \leq 1 \\ 1 - \frac{\rho_t}{\alpha_t (x-1)^{1.7} + x} & x > 1 \end{cases} \quad (7)$$

$$\rho_t = \frac{f_t}{E_t \varepsilon_{tk}} \quad (8)$$

$$x = \frac{\varepsilon}{\varepsilon_{tk}} \quad (9)$$

Other plasticity parameters were set including dilation angle of 30° , flow potential eccentricity of 0.1, ratio of biaxial/uniaxial compressive strength of 1.15.

The plastic model was used for steel of the connector according to the engineering tensile stress-strain curves of steel in Fig. 5. Plasticity parameters were set, i.e., the yield strengths of 370 MPa (Q345B) and 393 MPa (U20452), the elastic modulus of 206 GPa and the Poisson ratio of 0.3.

3.3. Load and boundary condition

A displacement controlled type of loading was applied on the side surface of the concrete slab as shown in Fig. 12. A constant vertical load was applied on the top surface of the concrete slab to simulate the pressure in the normal direction to the steel-concrete interface.

The T-shaped steel stud was welded connected to the top surface of the steel base by fillet welding. On the bottom surface of the steel base, both translational and rotational freedoms of the nodes were restrained. Considering symmetry of the geometry and loading pattern, translational freedom Uz and rotational freedoms URx and URy of the nodes on the symmetrical surface were restrained.

Surface-to-surface contact was used to model the interactions among interfaces of different parts. In the normal direction to the contact surface, the hard contact algorithm was used that could transfer the pressure under compression and allow separation under tension. In the tangent direction to the contact surface, friction algorithm was used to describe the interfacial frictions.

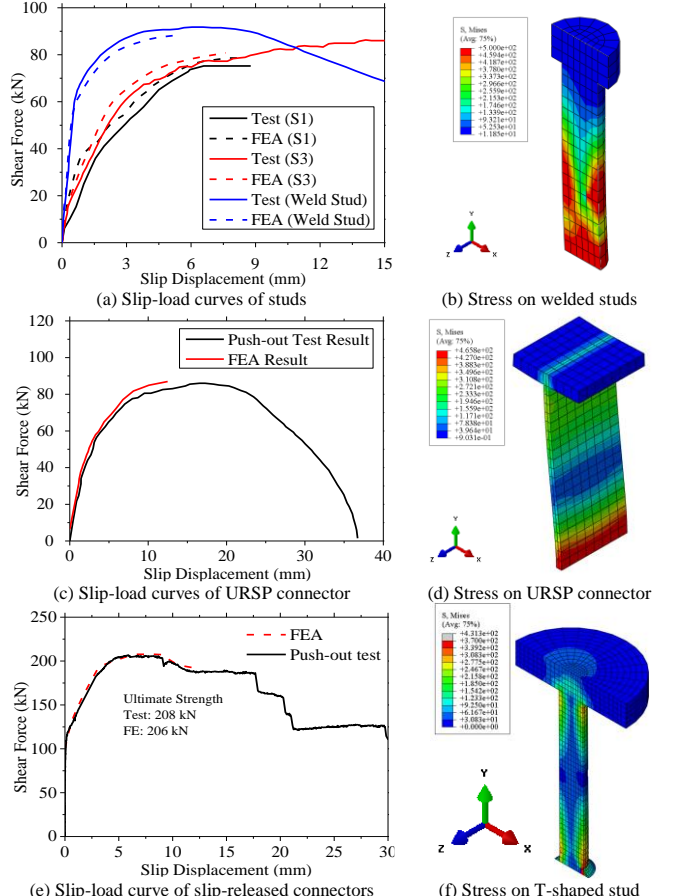


Fig. 13 Validation of FE models

3.4. Validation

The accuracy and feasibility of the FE models was verified through comparison the shear force-slip displacement curves and failure modes. For better validation the FE models, four more comparisons with existing push-out tests' results were made along with the slip-released connector's test. The corresponding FE models were developed and the validations were made. The

geometry and material properties was set according to corresponding references. Fig. 13 (a) and (b) shows the test and predicated curves and Mises stress of three studs, i.e., two types of demountable studs (S1 and S3) and one welded studs in reference [9]. Fig 13 (c) and (d) shows the curves and Mises stress of URSP connector in reference [20]. A good agreement is seen in the comparisons and the effectiveness of the FE models was verified.

The predicted curve of the slip-released connector was compared with test one in Fig. 13 (e). The curves are in good agreement in the first three stages. Mises stress on T-shaped steel stud before failure was shown in Fig. 13 (f), the failure mode of the connector was fracture of the welding toe at the root of the T-shaped steel stud. The FE predicted elastic stiffness and ultimate strength are 23.95 kN/mm and 208 kN compared with experimental value of 24.13 kN/mm and 206 kN.

4. Development of URSP connectors

Since the experimental studies showed that the current existing slip-released connectors could not provide the satisfactory structural performances, two concepts of the slip-released connector were developed that offered alternative forms of slip-released connectors.

4.1. Concept I: Protecting Shell

Concept I slip-released connector adopts the Polyvinyl chloride (PVC) shell to cover the connectors. This protecting shell is about 1-2 mm thick that forms a required gap between the stud and the concrete slab as shown in Fig. 14. Due to the enough stiffness of the PVC shell, it could avoid the rough surfaces produced by the pressure of fresh concrete.

4.2. Concept II: Slidable Connector

Concept II sliding connector adopts square holes to release the interfacial slip. As shown in Fig. 15, the sliding connector consists of three parts, i.e., an H-shaped steel connector, multiple pairs of bolts and nuts and two foamed plastic blocks. Square holes are set on one side of the H-shaped steel connector and each square hole matches with a set of bolt and nut. The bolts are welded on the upper flange of the steel beam and each bolt is sheathed with a sleeve. The height of the sleeve is 0.5 mm higher than the thickness of the connector flange plate to avoid over-tightening. The bolts, sleeves and nuts are sealed with the foamed plastic blocks. The lower side of each foamed plastic block is slotted, the bolts and nuts could move smoothly. The foamed plastic blocks protect the bolts and square holes from fluid concrete as seals during the concrete casting. This type of connector allows slip along the square holes and avoids separation of the steel beam from the concrete slab.

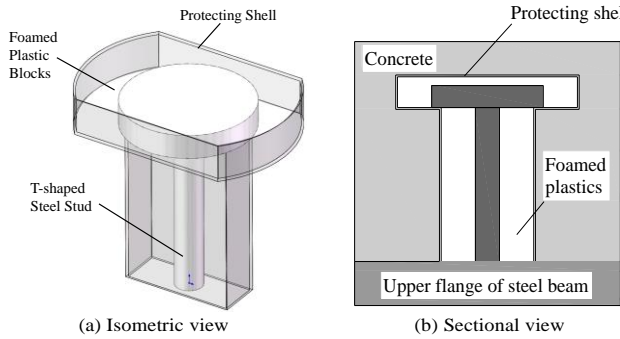


Fig. 14 Concept I: covering the foamed plastic blocks with protecting shell

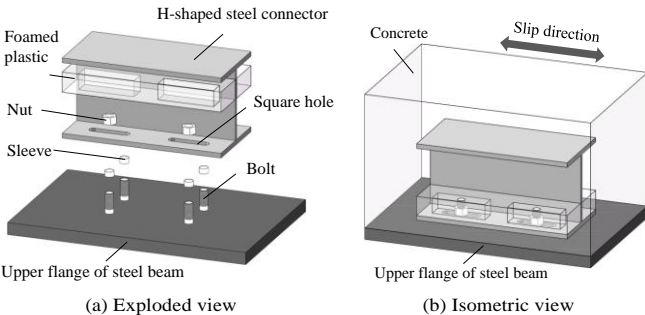


Fig. 15 Concept II: Slidable connector schematic

4.3. Evaluation of structural performance on the novel connectors by FEA

In order to investigate the slipping behaviors of these concepts, the FE model developed in section 3 was used. Considering the symmetric geometry and loading pattern, half of the connector was modeled to save computational cost. The boundary and loading conditions were the same as the previous model. A displacement controlled type of loading was applied on the side surface of the concrete slab and a constant vertical load was applied on the top surface of the concrete slab.

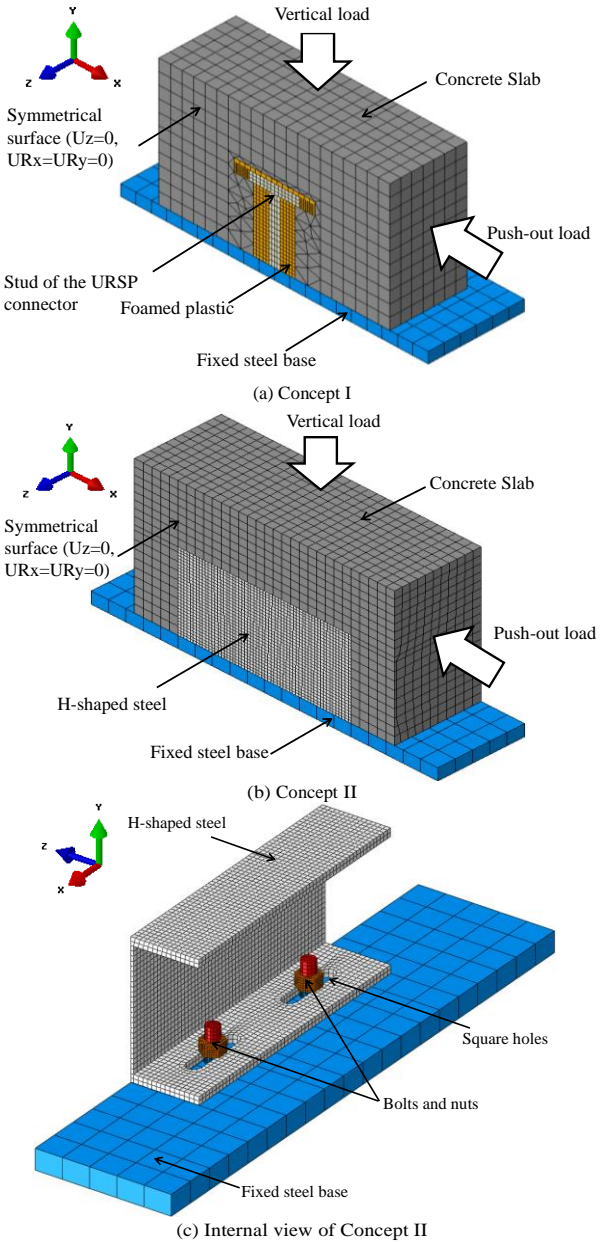


Fig. 16 FE models of the developed concepts

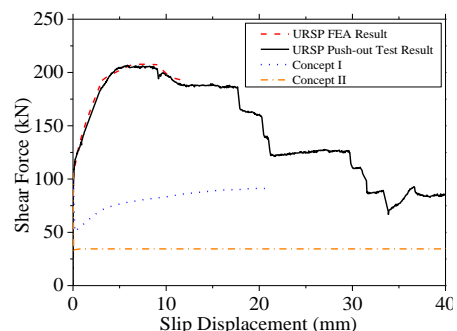


Fig. 17 Comparison of FEA result of Concept I and II

Fig. 16 (a) shows the FE model for Concept I. Fig. 16 (b) and Fig. 16(c) show the FE model of Concept II. The diameter of the bolts was set as 20 mm; the length of the square hole in this model was set as 80mm. Thus, the allowed sliding distance on both sides is 40mm. In this model, the flange of the connector was not anchored and could move smoothly along the square holes. Considering that the interfacial shear force could not be transferred directly between the connector and the concrete, the effects of the foamed plastics could not be ignored. The comparison of the result of these FE models against the experimental result was shown in Fig. 17.

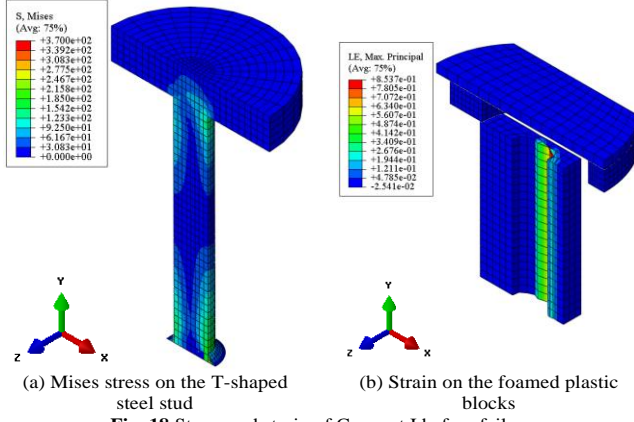


Fig. 18 Stress and strain of Concept I before failure

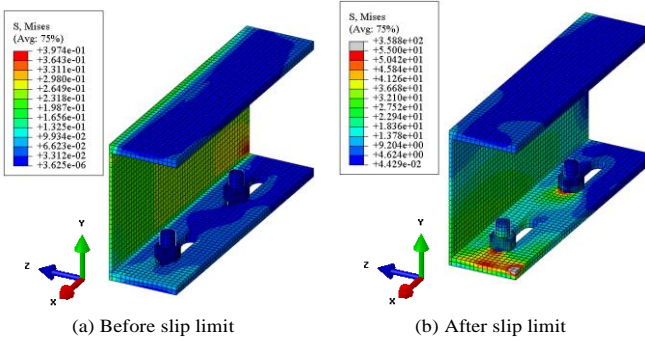


Fig. 19 Mises stress on the H-shaped steel and bolts

4.3. Evaluation of structural performance on the novel connectors by FEA

The shear force-slip curves of these developed concepts were significantly different from those of the slip-released connectors. In the shear force-slip curve of Concept I, after the initial bonding failed and the concrete slab started to slide, the shear force decreased rapidly to 50.8 kN and then increased slowly. The failure mode was fracture of the welding toe, as shown in Fig. 18(a). The foamed plastic blocks were significantly compressed by 50% and the maximum shear force of this FE model was 56% lower than those of the test and the FEA results at the same slip, as shown in Fig. 18(b). This indicated that the slipping behavior of the slip-released connector could be improved after the protecting shell was added.

In the shear force-slip curve of Concept II, after the initial bonding failed, the concrete slab started to slide, the shear force decreased rapidly to 34.5 kN and maintained at this value which equals the friction force between the steel beam and the concrete. That indicated that the shear force was taken by the friction and connectors were not subjected to the shear force within the slipping limit. Once the slip reached its limit allowance of 40 mm, the shear force was taken by the connector and increased significantly to 180.5 kN (see Fig. 19(b)). Under this boundary condition, the sliding connector performed closely to the bolted connectors.

Thus it can be concluded that these two developed concepts could effectively release the shear force within their slipping allowed limit and could achieve the performance requirement of releasing slip.

5. Conclusions

This paper presented a study of the slipping behaviors of slip-released connectors in composite structures by push-out test and finite element analysis. A full-scale push-out test on slip-released connectors was carried out to evaluate their slipping behaviors. Finite element model was developed and the accuracy of the FE simulation was checked by the reported test results. Two concepts of

slip-released connectors were developed and the structural performances were studied by numerical simulations. Based on these tests and numerical studies, the following observations and conclusions can be drawn;

- The test results showed the flange of the T-shaped steel stud was anchored in the concrete, the shear force was directly transferred from the connector to the concrete without deformations in the foamed plastic blocks. Localized deformations which greatly reduced the steel-concrete interfacial slipping allowance were generated at the concrete-foam interfaces. The shear resistance of the connector reduced at the slip of 6.0 mm and the connectors failed successively. The failure mode of the connector fracture of the welding toes at the root of the T-shaped steel studs.

- A FE model was developed for the slip-released connectors and the results was checked by the test results. The numerical simulation result showed that predicted failure mode of the connector was fracture of the welding toe at the root of the T-shaped steel stud, the same as the push-out result. The FE predicted elastic stiffness and maximum resistance are 23.95 kN/mm and 208 kN compared with experimental value of 24.13 kN/mm and 206 kN.

- Two concepts of slip-released connectors were developed, i.e., an improved version with foamed plastic blocks covered by protecting shell and a new type of connectors named as sliding connectors. Numerical simulations were carried out and the results showed that both concepts could effectively release the shear force within their slipping allowed limit and could achieve the performance requirement of releasing slip.

This paper only presented limited experimental and numerical studies on slip-released connectors. Further experimental studies and FE simulations are still required to develop the corresponding design guidelines on slip-released connectors.

Acknowledgment

This study was funded by National Natural Science Foundation of China on a project (grant number 51608358). The authors gratefully express their gratitude for the financial support.

References

- [1] Spremec M., Markovic Z., Veljkovic M., et al., D. "Push-out experiments of headed shear studs in group arrangements", Advanced Steel Construction, 9(2), 139-160, 2013.
- [2] Han Q.H., Wang Y.H., Xu J., et al., "Static behavior of stud shear connector in elastic concrete-steel composite beams", Journal of Constructional Steel Research, 113, 115-126, 2015
- [3] Lin Z.F., Liu Y.Q. and Roeder C.W., "Behavior of stud connections between concrete slabs and steel girders under bending moment", Engineering Structures, 117, 130-144, 2016
- [4] Ju X.C. and Zeng Z.B., "Study on uplift performance of stud connector in steel-concrete composite structures", Steel Composite Structures, 18(5), 1279-1290, 2015.
- [5] Chu T.H.V., Bui D.V., Le V.P.N., et al., Ahn, J.H. and Dao, D.K., "Shear resistance behaviors of a newly puzzle shape of crestbond rib shear connector: An experimental study", Steel Composite Structures, 21(5), 1157-1182, 2016.
- [6] Chung C.H., Lee J. and Kim J.S., "Shear strength of T-type Perfobond rib shear connectors", KSCE Journal of Civil Engineering, 20(5), 1824-1834, 2016.
- [7] Henderson I.E.J., Zhu X.Q., Uy B., et al., "Dynamic behavior of steel-concrete composite beams with different types of shear connectors, Part I: Experimental study", Engineering Structures, 103, 198-307, 2015.
- [8] Henderson I.E.J., Zhu X.Q., Uy B., et al., "Dynamic behavior of steel-concrete composite beams with different types of shear connectors. Part II: Modelling and comparison", Engineering Structures, 103, 308-317, 2015.
- [9] Dai X.H., Lam D. and Saveri E., "Effect of concrete strength and stud collar size to shear capacity of demountable shear connectors", Journal of Bridge Engineering, 14(11), 04015025, 2015.
- [10] Yan J.B., Liew J.Y.R. and Zhang M.H., "Shear-tension interaction strength of J-hook connectors in steel-concrete-steel sandwich structure", Advanced Steel Construction, 11(1), 72-93. 2015.
- [11] Yan J.B., Liew J.Y.R., Sohel K.M.A., et al., "Push-out tests on J-hook connectors in steel-concrete sandwich structure", Materials and Structures, 47, 1693-1714, 2014.
- [12] He S.H., Fang Z., Fang Y.W., et al., "Experimental study on perfobond strip connector in steel concrete joints of hybrid bridges", Journal of Constructional Steel Research, 118, 169-179, 2016.
- [13] Zona A. and Ranzi G., "Shear connection slip demand in composite steel-concrete beams with solid slabs", Journal of Constructional Steel Research, 102, 266-281, 2014.
- [14] Lin W.W. and Yoda T., "Experimental and numerical study on mechanical behavior of composite girders under hogging moment", Advanced Steel Construction, 9(4), 309-333, 2013.
- [15] Abe H. and Hosaka T., "Flexible shear connectors for railway composite girder bridges", Composite Construction in Steel and Concrete IV, ASCE, Reston, VA, 71-80, 2002.
- [16] Nie J.G., Lin Y.X., Tao M.X., et al., "Uplift-Restricted and Slip-Permitted T-Shape

- Connectors”, ASCE, Journal of Bridge Engineering, 20(4), 04014073, 2015.
- [17] GB/T 228.1-2010, Metallic materials-Tensile testing-Part 1: Method of test at room temperature. 2010, General Administration of Quality Supervision, Inspection and Quarantine of the People's Republic of China, Beijing, China.
- [18] GB/T50081-2002, Standard for test method of mechanical properties on ordinary concrete, Ministry of Construction of China, Beijing, China, 2002.
- [19] Luo G.L., “Numerical Simulation of Haihe Bridge Based on Multi-scale Model”, Tianjin University, Tianjin, China, 2015.
- [20] Lee P.G., Shim C.S. and Chang S.P. “Static and fatigue behavior of large stud shear connectors for steel-concrete composite bridges”, Journal of Constructional Steel Research, 61, 1270-1285, 2005.
- [21] Shim C.S., Lee P.G. and Yoon T.Y., “Static behavior of large stud shear connectors”, Engineering Structures, 26, 1853-1860, 2004.
- [22] Nie X., “Study on the structural behavior of key components in steel-concrete composite rigid frame bridge”, 2013, Tsinghua University, Beijing, China.
- [23] Pathirana S.W., Uy B., Mirza O., et al., “Strengthening of existing composite steel-concrete beams utilizing bolted shear connectors and welded studs”, Journal of Constructional Steel Research, 114, 417-430, 2015.
- [24] GB50010-2010, Code for design of concrete structures, Ministry of Construction of China, Beijing, China, 2010.

EXPERIMENTAL AND THEORETICAL INVESTIGATIONS OF SPIGOT CONNECTIONS UNDER CYCLIC LOADING

Mutasim Abdel-Jaber¹, Robert G. Beale^{2,*}, Nasim Khalil Shatarat¹ and Mutasem A. Shehadeh³

¹Professor, Department of Civil Engineering, School of Engineering, The University of Jordan, Amman, Jordan

²Visiting Research Fellow, Faculty of Design, Technology and Environment, Oxford Brookes University, Wheatley, Oxford, UK

³Associate Professor, Department of Mechanical Engineering, American University of Beirut, Beirut, Lebanon

*(*Corresponding author: E-mail rgbeale@brookes.ac.uk)*

ABSTRACT

Cyclic load tests were conducted on the spigot connections for a system scaffold. Two different connections were tested, one where both ends of a spigot were bolted to tubes and the other where one end was bolted and the other end welded. The tests were conducted by applying a series of different fixed axial loads together with a variable side load which was increased until failure occurred. The objective of undertaking cyclic tests was to not only obtain the rotational stiffness of the connection but also the looseness in the connection as looseness has been shown to reduce the performance of frames, and previous research and experiments involving spigots have ignored these effects.

The tests and accompanying finite element calculations showed that the looseness was 0.009 radians for the double bolted spigot and 0.005 radians for the welded connection. The connections proved to be relatively unstable at high axial loads showing considerable scatter in the results. The results were in agreement with the stiffness results obtained by André that for a range of axial loads a single rotational stiffness could be applied but that for low and high axial loads different stiffnesses must be used.

Copyright © 2019 by The Hong Kong Institute of Steel Construction. All rights reserved.

ARTICLE HISTORY

Received: 30 June 2017
Revised: 18 November 2017
Accepted: 11 January 2018

KEY WORDS

Cyclic loading;
Spigots;
Tubular scaffolds;
Failure

1. Introduction

Following a series of bridge falsework and scaffold failures in the early 1970s the UK government commissioned the Bragg Report [1] which ultimately led to the development of BS 5975 [2]. It was known that the traditional UK procedures of analysing temporary works structures by only considering the effective lengths of the columns did not allow for the interaction between horizontal beams and the columns which could precipitate failure. Therefore, the UK Science Research Council funded Lightfoot and co-workers [3, 4] to develop a theoretical model of scaffold structures. They used a finite element program where the beam and column elements were modelled using stability functions. Due to the limited capacity of computers in the early 1970s all the joints were modelled as either pinned or fixed connections and joint and member eccentricity was excluded. The models also analysed simple tower structures with only one or two lifts. Experimental scaled models were constructed and tested. Both the experimental and theoretical models failed by buckling with the theoretical buckling loads being between 10% and 15% higher than the experimental values. Lightfoot and his co-workers accounted for the difference between their analytical and experimental models by the use of rigid connections and the non-inclusion of eccentricities.

Since that time research into scaffold and temporary works structures has been extensive. The emphasis of the research has been into the structural analysis of the components- the beams, columns and connections. The research has been summarised by Beale in a review paper [5] and in a book (with André) [6]. The tubular sections are usually made of steel or aluminium, except in Asia and Central America where bamboo is sometimes used [6]. In the UK the vertical members are called standards and the horizontal beams are called ledgers and transoms for access scaffold structures. There are two principle types of scaffold structure, namely tube and fitting scaffolds (UK name) and system or proprietary scaffolds (which includes modular scaffolds). In the case of tubular scaffolds connections are made by using external components called couplers such as ‘right-angled couplers’ or ‘putlog couplers’. In system or proprietary scaffolds the tubes have a part of the spigot connection welded to one end of the tube and the horizontal members are attached with additional tongues or wedges welded to their ends so that connections can be easily made. As the connections are not rigid but have different rotational stiffnesses about each axis tests must be made to determine these stiffnesses. A common test is simply to fix a section of the standard to an external rig and attach a small section of the horizontal member by the connection in a cantilever and then apply a load to the end of the cantilever. This applies a moment to the joint and by increasing the applied load the moment-rotation curve can be determined. The European codes BS EN 12811 [7] and BS EN 74-1 [8] require the load to be cycled through zero to get both the positive

and negative rotational characteristics of the connection as well as obtaining an estimate of the looseness of the connection. Note that the use of BS in European code references is to show that the standard is the English Language version. Unfortunately, many analyses and tests conducted on scaffolds increase the loads monotonically to failure and do not consider looseness or the differences in rotational stiffness or capacity for rotations if alternative directions which could occur under wind-load conditions. All connections contain looseness. For example, Abdel-Jaber et al [9] determined the rotation capacity of tube and fitting scaffold connections determining looseness in all of them. Prabhakaran et al [10] showed that for unbraced scaffolds a small rotational looseness of 0.01 rad makes a significant difference to the structural behaviour but that for braced scaffolds the effects are smaller. This was particularly important when the effect of erecting standards out-of-plumb was considered. Prabhakaran also showed that the traditional assumption in design that a small out-of-plumb (less than 2%) could be modelled by applying a side load of the same order gave different answers for unbraced frames. In the case of the frame analysed by Prabhakaran the looseness reduced the capacity of single bay scaffold frame by 8%. Recent papers by Cimellaro and Domianeschi [11], Sevim et al [12], Peng et al [13,14] and Liu et al [15] investigate the capacity of both system and tubular scaffolds by loading their trial scaffolds monotonically to failure and ignore looseness or any cyclic loading. In addition, a common mistake that is made is to assume that linear buckling analyses ignore the self-weight of the scaffold and only increase the live load at the top of the scaffold. This assumption is valid for scaffolds with only a few lifts or levels but in multi-storey scaffolds the dead load can often be over 50% of the total load applied to the structure and alternative procedures must be adopted to obtain correct buckling patterns [18, 19].

The columns, which are called standards in the UK for a large scaffold or falsework structure, are made of multiple vertical elements connected together by spigots or couplers. Lightfoot assumed that the coupler could be considered a rigid connection. This assumption is still used for traditional tube-and-fitting scaffolds joined by external sleeved couplers or by parallel couplers (A parallel coupler places the two standards side by side with an offset). Tests on these connections in the European codes (BS EN 12811 and BS EN 74-1) are simple pull-out tests to obtain the ultimate tensile failure load of the connection (for parallel couplers only) or the slipping load (for both sleeved and parallel couplers) [7, 8]. For sleeved couplers four-point bending tests are conducted as shown in Fig. 1 to get the moment-rotation curves. In Fig. 1, P is the applied side load and L the length of the specimen with a maximum length of 500 mm. Commonly the looseness found in couplers is ignored for these connections. An assumption is also made for these couplers that the axial force acting on the coupler has no effect on the moment-rotation characteristic curve of the connection.

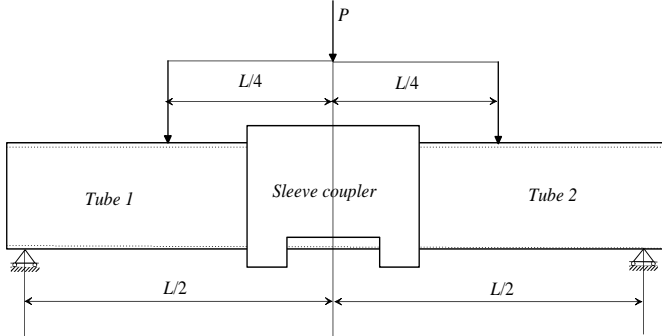


Fig. 1. Schematic of a four-point bending test for sleeved connections.

In proprietary and modular scaffolds the end of one tube has a spigot welded or bolted into the inside of the tube. The second tube is then bolted onto the spigot connection. In these cases, the spigot has a smaller outside diameter than the internal diameter of the standards. According to the European code BS EN 74-1 [8] the total length of the spigot should be equal to or greater than 300 mm. The spigot can be connected to the upper (and lower) standard(s) by pins, by bolts inserted through centred holes or by locking the upper standard to a special connector welded to the spigot wall. See Fig. 2 for a schematic of two tubes joined by a welded spigot and a photograph of the spigot connection analysed in this research. Note the looseness within the connection which cannot be removed.

A prototype proprietary scaffold (Cuplock®) consisting of three bays and three sets of horizontal members, was tested at Stuttgart during the development of BS EN 12811 [7]. The prototype structure was analysed by Beale and Godley [18]. They showed that 2-D and 3-D nonlinear analyses ignoring spigot looseness give results where the maximum deflection was only half that observed in the tests, although the failure loads were predicted accurately. Only when contact elements at spigot joints were added to the analysis, allowing for the rotation within the connection of 0.1 radians before a rigid contact was assumed, was a good correlation between theory and experiment obtained. Note that the use of 0.1 radians is high but the Cuplock® scaffold used had a slightly conical shape which meant that its looseness was greater than those reported in the tests in this paper. The maximum loads in all the analyses were approximately the same as there were no appreciable side loads. See Fig. 3. Prabhakaran [10] shows the effects of a small rotational looseness on scaffold frames, particularly when side loads, such as wind or effects of standards out-of-plumb are taken into account.

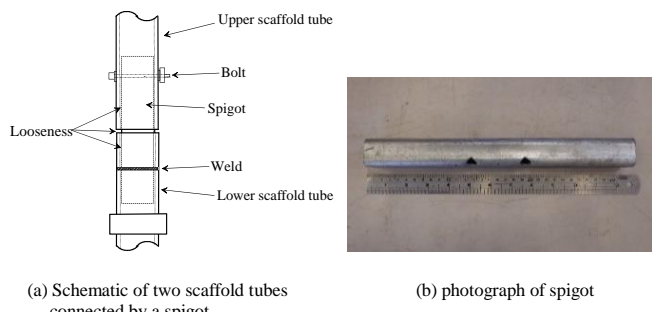


Fig. 2. Spigot arrangement

In racking structures, it is well known that the moment-rotation characteristic curve for a baseplate to column connection not only depends upon the applied moment to the connection but also upon the axial force being transmitted through the column to the baseplate and tests have been conducted to develop curves for different applied moments [19, 20]. Similar results relating moment-rotation stiffness to axial force were found in tests on components of proprietary scaffolds containing spigots [21-24].

A detailed study of the Cuplok® proprietary fasework was undertaken at the University of Sydney, Australia, starting with an investigation of the spigot joint by Enright et al [25] using tests and nonlinear computer models. The Sydney research team then tested the individual components to determine connection and material properties followed by tests on falsework assemblies [23, 24].

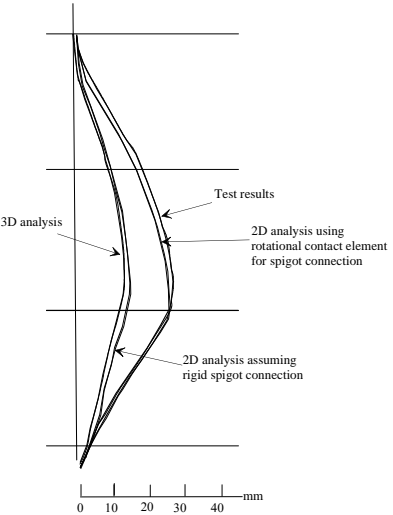


Fig. 3. Comparison between the deflection of the prototype scaffold structure calculated using different analysis models

In the Enright model [25], the spigot is considered to be rigid (300 mm long) and is connected to the top and bottom standards by short elements with high rigidity (EI) and high axial stiffness (EA) which can only transfer lateral force into the spigot. The vertical load is transferred directly from the top standard to the bottom standard. See Fig. 4. The pinned connections between the standards and the spigot ensure that no vertical forces are applied to the spigot and only lateral forces are transferred via the spigot which cause the standards to bend, the amount of bending depending upon the amount of out-of-plumb of the standards and the value of the load being transmitted from the top to the bottom standard. This model does not model the contact problem between the standard and spigot. Eccentricity at the connection due to lateral displacement had to be included explicitly and was a fixed size for a given analysis and therefore could not be used for models where the rotation changed as the scaffold was loaded. The model was found by André [21] not to give consistent results.

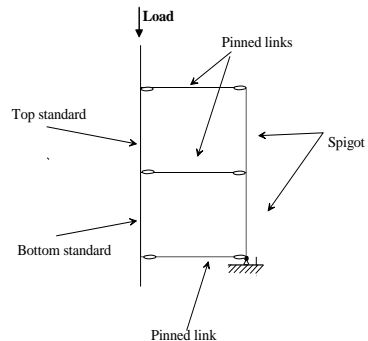


Fig. 4. Schematic of Enright's model [25]

André conducted experiments on both new and used Cuplok® spigot connections testing them in the normal manner reserved for baseplates [21, 22]. This method was also adopted for the tests conducted in this paper and is described in more detail below. André found little difference between the stiffnesses of new and used connections but his results could be due to the fact the specimens were donated by Harsco who manufactured them and only donated new and slightly used connections. In processing his results André used the same multilinear model of moment-curvature presented by Chandrangsu et al [23, 24] and shown in Fig. 5. Note that this 4-step model was created by Chandrangsu to enable an accurate numerical modelling of full-scale scaffolds undertaken in Sydney. For many analyses only one or two rotational stiffnesses are required. Note that the rotational stiffnesses in clockwise and anti-rotations of a connection are usually different, especially for system scaffolds but also for some tube and fitting scaffold connections. BS EN 12811-3 [26] states that the average could be used if the differences in stiffness between the two directions is less than 10%.

Fig. 5 clearly demonstrates the looseness that occur within the section. André was unable to develop a theoretical model for the spigot connection but for each of the 4 stiffness values he produced a statistical model enabling the stiffness to be found for a given axial load. The statistical model showed that the rotational stiffnesses were dependent upon the axial load in the connection but that this could be approximated by three regions defined by the ratio of axial load (kN) divided by the applied transverse moment (i.e. kN/M). The regions are- stiffnesses (a) below 20 N/M; (b) between 20 – 50 N/M; and (c) above 50

N/M.).

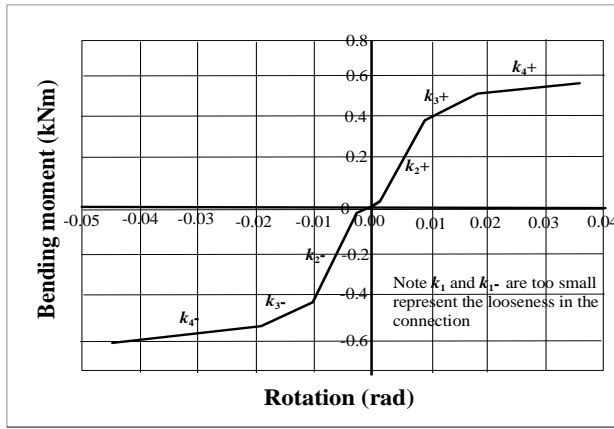


Fig. 5. Approximation of the M - θ curves (André, [19])

An example is given in Fig. 6. This statistical model enabled the analyses conducted by André to be more accurate than those undertaken by Chandrangsu [10, 24]. It is not normally necessary to determine four rotational stiffnesses for design analyses. The European code BS EN 12811-3:2002 [26] only requires a tri-linear curve with two initial stiffnesses, one from zero up to the design working load followed by the stiffness between the design working load and the design maximum load. The third line is simply the design maximum load until failure. Prabhakaran [10, 27] showed that the bi-linear model in the storage rack code BS EN 15512 [20] gave the same results and is probably more useful in design as it easier to apply.

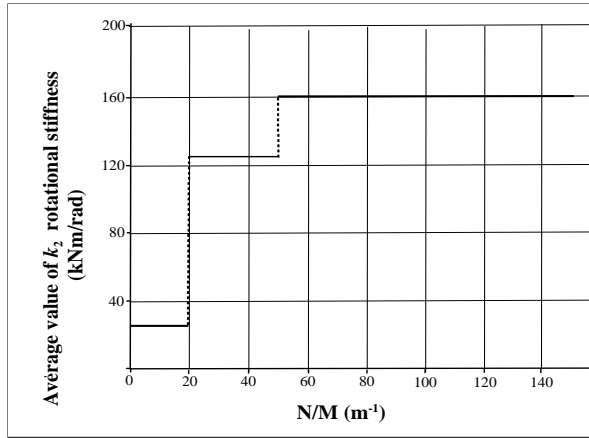


Fig. 6. k_2 stiffness as a function of N/M ratio (André, [19])

However, the objective of this paper is conduct finite element detailed calculations of the connection and verify them against experimental tests of the connection behaviour.

2. Experimental procedure

2.1. Introduction

The experimental configuration to determine the rotation stiffness of spigot connections is identical to that of the baseplate test defined in the European standard for baseplates of racking structures [20] with the exception that there is no need for a block of concrete or other material between two sections of standard. In each test a fixed axial load was first applied to the standards and then the side load was applied incrementally to the connection. A schematic of the test is shown in Fig. 7. An example of a spigot under test undertaken by is shown in Fig. 8.

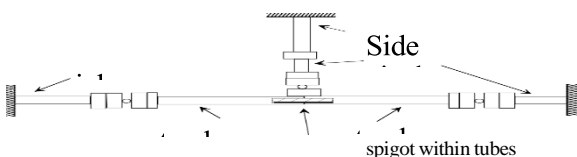


Fig. 7. Schematic of the test procedure for spigots



Fig. 8. Spigot under test

In order to get an estimate of the maximum capacity of a connection under a fixed side load a pilot test was undertaken for each axial load loading to failure. Previous researchers had not determined the looseness of spigot connections. Therefore at least three tests were undertaken with the side load cycled between 60% of the pilot load failure and zero. The side load jack was unable to apply tensile loads to the specimen as this would have meant applying a collar around the connection which would have prevented the spigot deforming (as seen in Fig. 8) and so the normal BS EN 12811- 3 [26] procedure of cycling through zero and including tensile as well as compressive side loads was unable to be undertaken. However, as spigot connections are symmetric the tensile and negative loosenesses were likely to be similar it was considered that cycling between zero transverse load to 60% of the maximum pilot transverse load would give a reasonable estimate of looseness. Note that it is impossible to determine looseness in monotonic tests as hysteresis loops do not return to zero rotation when the side load is unloaded to zero. From Figs. 11 and 12 below it can clearly be seen that the initial loading path is different to reloading paths which tend to be close together. The looseness is derived from the difference between zero and linearly extrapolating the third reloading curve to obtain the rotation at zero axial load. Ideally, if it was possible to fully cycle between positive and negative rotations the looseness would be taken as half the difference between the positive looseness and the negative looseness. Looseness must be determined as all real structures are subject to dynamic loads, particularly wind but occasionally earthquake. Blackmore [28] recorded several incidences where wind load caused scaffold systems to collapse and Beale and Godley [17] showed that lateral wind loads for Northern Scotland could be of the order of 50% of the total vertical imposed and dead loads on a scaffold structure and used these results when producing and validating the load tables for the National Access Scaffold Confederation in NASC TG20:13 [29].

A series of tests was undertaken with different axial loads with the two types of spigot connection to see if there was any difference in performance. The two types of spigot connection were: (i) the spigot welded to one standard and bolted to the other, called a welded spigot connection in the remainder of the paper and (ii) the spigot bolted to both standards, called a bolted spigot connection for the remainder of the paper.

From Fig. 8 it can be seen that 4 LVDTs (Linear variable differential transducers) were used to measure the rotation of the standard. The rotation at time step t , θ_t , is given by Eq. 1:

$$\theta_t = \frac{d_{t,2} - d_{t,1}}{L_d} + \frac{d_{t,3} - d_{t,4}}{L_d} \quad (1)$$

where $d_{t,1}$, $d_{t,2}$, $d_{t,3}$, $d_{t,4}$ are the displacements of transducers 1 to 4 at load increment i as shown in Fig. 9 and L_d is the spacing between the transducers on each side. Note that they were placed close to the spigot connection so that bending rotation in the standards was neglected. In the tests each section of standards was 490 mm long and the transducers were placed 50 mm apart. The transducer locations are clearly visible in the photograph, Fig. 8 above.

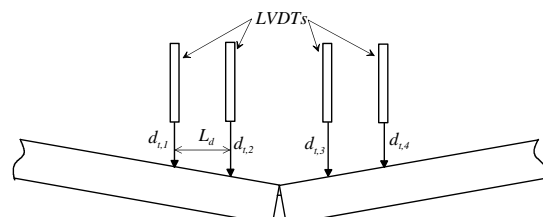
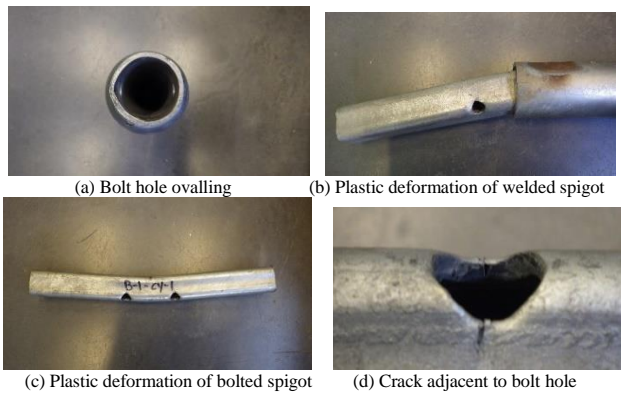


Fig. 9. Schematic showing LVDT nomenclature

Examples of the common failures are shown in Fig. 10.

**Fig. 10.** Examples of failed specimens

The material properties of the samples were determined by tensile tests on tubes and spigots and by Vickers Hardness tests on the bolts and welds. It is notable that several recent papers imply that the only material testing required is the material of the tube and do not test the connection material, for example the paper by Lie et al [15]. The material used for the tubes and spigots was according to the Chinese specification for high strength low alloy structural steel GB/T1591-2008 [30]. Material results are presented in Table 1. It is notable that the material used in the bolts and welding had higher ultimate yield stresses than the material used for the tubes and spigots. Hence all failures occurred with either distortion of the tube or plastic failure of the spigot.

Table 1
Material properties of the test components

Component	Modulus of Elasticity (GPa)	2% Yield Strength (YS) (MPa)	Ultimate Yield Strength (UTS) (MPa)	Test procedure
scaffold tubes	206	385	457	tensile test
spigots	211	442	535	tensile test
weld			649	hardness test
bolt			867	hardness test

2.2. Experimental results

Pilot tests on spigot connections were undertaken without any side load and by simply applying an axial load. The resulting failure loads were 142 kN for the double bolted spigot connection and 152 kN for the welded spigot connection. Hence the original design was to conduct tests on the connections with axial loads up to 120 kN.

The moment-rotation curves for the cyclic tests are given in Figs. 11 and 12.

Table 2 shows the results of the experiments. The code used in the results are: test number – as performed – but rearranged in the table in order to make the results easier to analyse and understand. The letter B or W at the beginning of the test name was to distinguish between spigots have one end welded and the other bolted (W) from those where both ends were bolted (B). The letter P refers to pilot tests with no transverse load. The letters CY referred to cyclic tests which were performed on specimens before the same specimens were tested to failure where a letter L was then appended. From the test results shown in Table 2 it can be seen that the cyclic behaviour was only reliable for axial loads up to 90 kN. Tests were conducted at axial loads of 110 kN for bolted spigots and 120 kN for both bolted and welded spigots. However, in many cases, as recorded in Table 2 the tests had large scatter and the results were unreliable. Examples of the scatter are shown in W-120-CY tests shown Fig. 12.

The looseness in each test was determined by plotting a regression straight line from the lowest part of the third loading cycle and determining its intercept with the x axis. The regression line was only accepted if its correlation coefficient, r^2 , was greater than 0.95. See Fig. 13.

From the test results shown in Table 2 it can be seen that the cyclic behaviour was only reliable for axial loads up to 90 kN. Tests were conducted at axial loads of 110 kN for bolted spigots and 120 kN for both bolted and welded spigots. However, in many cases, as recorded in Table 2 the tests had large scatter and the results were unreliable. Examples of the scatter are shown in W-120-CY tests shown Fig. 12.

The looseness in each test was determined by plotting a regression straight line from the lowest part of the third loading cycle and determining its intercept with the x axis. The regression line was only accepted if its correlation coefficient, r^2 , was greater than 0.95. See Fig. 13.

Table 2
Summary of experimental results

Test No.	Name	Max side load (kN)	Description	Looseness
1	B-C1		Pilot test, axial load only; failed at 142 kN	
2	B-P-B1	5.84	Pilot test, side load only, spigot failed with side load 5.84 kN	
3	W1-BP		Pilot test, immediate failure with tube slipping, slight tube ovaling	
3R	WC-1P		Pilot test, no side load, failed 152 kN	
4	B-30-LF	4.614	Pilot test, large deflection, spigot failure	
5	B-60-LF	3.794	Pilot test, tubes ovalled	
6	B-90-LF	3.699	Pilot test, tubes ovalled slightly	
7	B-120-LF	3.775	Pilot test, small tube ovalling, spigot bent	
8	B-140-LF		Pilot test, test failed under 135 kN axial load, no side load	
9	WB-30-LF	4.957	Pilot test, slight ovaling, small tearing at bolt hole	
10	WB-60-LF	4.245	Pilot test, slight ovaling, small tearing at bolt hole, spigot bent	
11	WB-90-LF	3.606	Pilot test, bolted tube went under welded tube	
12	WB-120-LF	1.529	Pilot test, early failure	
13	WB-140-LF		Pilot test, failed at 137 kN, no side load	
26	W-1-CY-1	3.33	Test successful	0.0008
26L	W-1-CY-1L	5.20	Spigot bent, tube ovalling, bolt thread cutting into bolt hole	
27	W-1-CY-2	3.32	Test successful	0.0180
27L	W-1-CY-2L	5.37	Spigot bent, tube ovalling, load dropped during test with no reason apparent, specimen then fell out of rig	
28	W-1-CY-3	3.33	Test successful	0.0058
28L	W-1-CY-3L	5.28	No description recorded	
52	W-1-CY-4	3.33	Test successful, large scatter in data points	0.0055
52L	W-1-CY-4L	5.18	Spigot bent, ovaling of non-welded tube	
14	W-30-CY-1	2.88	Test successful	0.0021
14L	W-30-CY-1L	5.01	Spigot bent, tube ovalling	
15	W-30-CY-2	2.87	Test successful	0.0027
15L	W-30-CY-2L	5.36	Spigot bent, tube ovalling	
16	W-30-CY-3	2.88	Test successful	0.0033
16L	W-30-CY-3L	4.50	Spigot bent, slight elongation and ovaling of the tube	
50	W-30-CY-4	2.87	Test successful, large scatter in data but terminating at same looseness	0.0096
50L	W-30-CY-4L	4.63	Spigot bent, ovaling of non-welded tube	
17	W-60-CY-1	2.47	Test successful, slight on rotation measurements	0.0009
17L	W-60-CY-1L	3.91	Spigot bent, small ovaling of tubes	
18	W-60-CY-2	2.48	Test successful	-0.0002
18L	W-60-CY-2L	4.12	Spigot bent, small ovaling of tubes	
19	W-60-CY-3	2.47	Test successful, large scatter in measurements, slight drift between cycles	0.0019
19L	W-60-CY-3L	3.89	Spigot bent, small ovaling of tubes	
51	W-60-CY-4	2.46	Unable to determine looseness as too much scatter between cycles, possible instrument fault	
51L	W-60-CY-1L		Spigot bent, ovaling of non-welded tube	
20	W-90-CY-1	2.04	Test successful but sample close to failure, increasing deflection between cycles and large hysteresis	0.0192
20L	W-90-CY-1L	6.64	Lower than cyclic	

Test No.	Name	Max side load (kN)	Description	Looseness	Test No.	Name	Max side load (kN)	Description	Looseness
21	W-90-CY-2	2.66	Load not cycled, displacements show problems with instrumentation, looseness not determined		36	B-60-CY-2	2.23	Test successful	0.0004
21L	W-90-CY-2L	4.24	Test failed with downward displacement; local elongation of tube in line with bolt, bolt bent, tearing and crushing around bolt hole		36L	B-60-C3-2L	4.12	Spigot bent, elongation and ovaling of the tubes	
22	W-90-CY-3	2.07	Test successful	0.0012	37	B-60-CY-3	2.22	Test successful	0.0020
22L	W-90-CY-3L	5.54	Spigot bent, small ovaling of tubes		37L	B-60-CY-3L	3.89	Spigot bent, elongation and ovaling of the tubes	
44	W-90-CY-4	2.13	Test successful, initial rotation jump removed	-0.0012	49	B-60-CY-4	2.23	Test successful, plot shows large scatter in individual points, looseness result low r^2 correlation of 0.89	0.0008
44L	W-90-CY-4L	2.00	Sample failed downwards, spigot bent, tearing at bolthole		49L	B-60-CY-4L	3.42	Spigot bent, ovaling of tubes	
46	W-90-CY-5	2.08	Test successful	-0.0015	38	B-90-CY-1	2.13	Test successful	0.0020
46L	W-90-CY-5L	5.25	Spigot bent, ovaling of tubes		38L	B-90-CY-1L	6.64	Spigot bent, small ovaling of tubes, note specimen recovered after removal of side load, test results anomalous and ignored	
23	W-120-CY-1	0.74	Test successful in that 3 cycles completed, unable to determine looseness due to wide scatter in results		39	B-90-CY-2	2.12	Sample lifted when side load applied; increasing deflections on each cycle (approx. 0.1 per cycle)	0.0099
23L	W-120-CY-1L	4.24	Spigot bent, small ovaling of tubes		39L	B-90-CY-2L	1.59	Both tubes ovaling, slight tear at bolt holes into spigot, bolt thread cutting into spigot	
24	W-120-CY-2	0.73	Test successful in that 3 cycles completed, unable to determine looseness due to wide scatter in results		40	B-90-CY-3	2.12	Sample lifted when side load applied; increasing deflections on each cycle (approx. 0.05 per cycle)	0.0073
24L	W-120-CY-2L	4.24	Spigot bent, small ovaling of tubes		40L	B-90-CY-3L	1.95	Both tubes ovaling, slight tear at bolt holes into spigot, bolt thread cutting into spigot	
25	W-120-CY-3	0.73	Test successful in that 3 cycles completed, unable to determine looseness due to wide scatter in results		45	B-90-CY-4	2.14	Test successful; data scattered, displacements increased on each cycle, low r^2 0.85	0.0115
25L	W-120-CY-3L	1.98	Test failed with upward displacement; ovaling of tube spigot bent, tearing around bolt hole		45L	B-90-CY-4L	2.00	correlation Spigot bent, ovaling of tubes	
29	B-1-CY-1	3.32	Test successful	0.0255	53	B-110-CY-1		Failed at 87 kN axial load	
29L	B-1-CY-1L	5.65	stopped as displacement control jack reached limit.; spigot bent; elongation and ovaling of tubes		54	B-110-CY-2		Failed at 92 kN axial load	
30	B-1-CY-2	3.33	Test successful	0.0388	55	B-110-CY-3		Failed at 104 kN axial load	
30L	B-1-CY-2L	5.11	Sample twisted in rig, test stopped before LVDTs damaged; spigot bent, elongation and ovaling of the tubes		56	B-110-CY-4	2.13	Test successful but deflections increased with each cycle (0.01 between cycles, 2 only completed)	0.0072
31	B-1-CY-3	3.33	Test completed	0.0307	56L	B-110-CY-4L		Test failed below cyclic load	
31L	B-1-CY-3L	4.99	Sample rotated out, LVDTs 3 and 4 became disconnected, end bearing jumped out of end socket; spigot bent, elongation and ovaling of the tubes		41	B-120-CY-1		Sample moved sideways when axial load applied, unable to reach axial load of 120 kN, spigot bent, no cycles performed	
47	B-1-CY-4	2.62	Test successful, displacements increasing on successive cycles	0.0059	42	B-120-CY-2		Failed at an axial load of 110 kN, no cycles performed, tear round both bolt holes, ovaling of both tubes	
47L	B-1-CY-4L	5.00	Spigot bent, ovaling of one tube, crushing on opposite side		43	B-120-CY-3	2.13	Test successful	0.0020
32	B-30-CY-1	3.33	Test successful	0.0001	43L	B-120-CY-3L	2.91	Spigot slightly bent, small ovaling of tubes, note specimen recovered after removal of side load	
32L	B-30-CY-1L	4.72	Elongation and ovaling of the tubes, spigot bent and torn around one of the bolt holes, thread of one bolt cutting into spigot		56	B-110-CY-4	2.13	Test successful but deflections increased with each cycle (0.01 between cycles, 2 only completed)	0.0072
33	B-30-CY-2	2.62	Test successful, deflections slightly increasing on each cycle	0.0045	56L	B-110-CY-4L		Test failed below cyclic load	
33L	B-30-CY-2L	4.73	Spigot bent, ovaling of tubes		41	B-120-CY-1		Sample moved sideways when axial load applied, unable to reach axial load of 120 kN, spigot bent, no cycles performed	
34	B-30-CY-3	2.63	Test successful, deflections slightly increasing on each cycle	0.0017	42	B-120-CY-2		Failed at an axial load of 110 kN, no cycles performed, tear round both bolt holes, ovaling of both tubes	
34L	B-30-CY-3L	4.92	Spigot bent, ovaling of tubes		43	B-120-CY-3	2.13	Test successful	0.0020
48	B-30-CY-4	2.62	Test successful	0.0008	43L	B-120-CY-3L	2.91	Spigot slightly bent, small ovaling of tubes, note specimen recovered after removal of side load	
48L	B-30-CY-4L	4.25	Spigot bent, ovaling of tubes						
35	B-60-CY-1	2.24	Test successful	0.0008					
35L	B-60-CY-1L	3.91	Spigot bent, elongation and ovaling of the tubes						

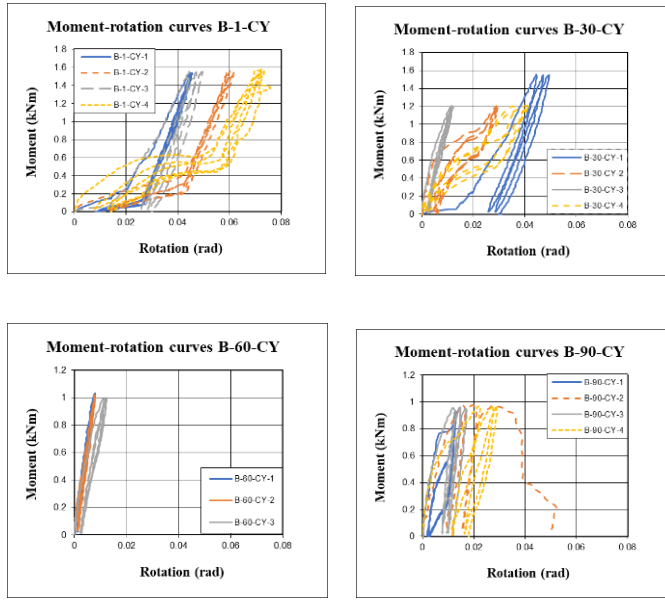


Fig. 11. Moment-rotation curves for the cyclic tests with bolted spigot

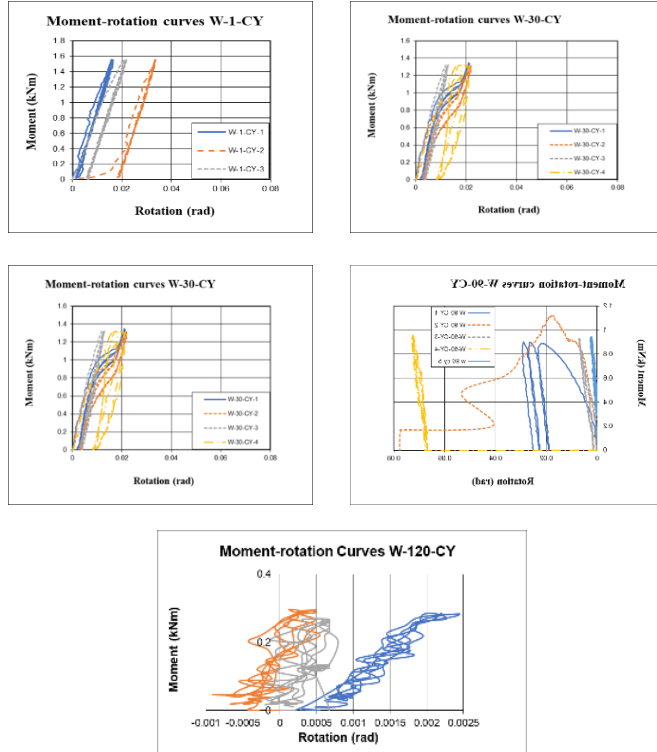


Fig. 12. Moment-rotation curves for the cyclic tests with welded spigot

Mean and standard deviation values were determined as shown in Table 3. In test B-30-CY-1 a correction to remove initial exceptional looseness was made. The looseness for bolted spigots was greater than that of the welded spigots with an overall mean looseness of 0.0088 radians for the double bolted spigots as opposed to 0.0049 radians for the spigots with one end welded and the other end bolted. The standard deviations were respectively 0.0114 radians for the double bolted spigots and 0.0061 radians for the welded spigots. Note

that these values were determined from the original data and not the simplified tables. The size of the looseness in both tests was small but it obvious that all spigots should be welded at one end to reduce the average looseness. The work by Prabhakaran [10] shows that even a small rotational looseness can have deleterious effects on unbraced or poorly braced structures.

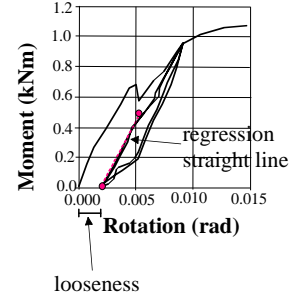


Fig. 13. Determination of looseness

Mean and standard deviation values were determined as shown in Table 3. In test B-30-CY-1 a correction to remove initial exceptional looseness was made. The looseness for bolted spigots was greater than that of the welded spigots with an overall mean looseness of 0.0088 radians for the double bolted spigots as opposed to 0.0049 radians for the spigots with one end welded and the other end bolted. The standard deviations were respectively 0.0114 radians for the double bolted spigots and 0.0061 radians for the welded spigots. Note that these values were determined from the original data and not the simplified tables. The size of the looseness in both tests was small but it obvious that all spigots should be welded at one end to reduce the average looseness. The work by Prabhakaran [10] shows that even a small rotational looseness can have deleterious effects on unbraced or poorly braced structures.

Table 3
Results of looseness calculations under different axial loads

Test group	Mean Looseness	Standard deviation (rad)	Mean cycle Maximum moment (kNm)	Comments
B-1-CY	0.0267	0.0113	1.5481	
B-30-CY	0.0065	0.0085	1.2932	
B-60-CY	0.0012	0.0007	1.0125	
B-90-CY	0.0077	0.0042	0.9566	
B-110-CY	0.0072		0.9930	No standard deviation as only 1 successful test
B-120-CY	0.0020		0.9428	No standard deviation as only 1 successful test
W-1-CY	0.0075	0.0074	1.5562	
W-30-CY	0.0044	0.0035	1.2932	
W-60-CY	0.0012	0.0007	1.0125	
W-90-CY	0.0058	0.0089	0.8479	
W-120-CY			0.2808	No looseness due to large scatter of results

Once a cyclic test had been completed the connection was then tested to failure by increasing the side load. Fig. 14 shows the moment rotation curves of successful tests. In some cases when the test was conducted with a high axial load the specimen then failed prematurely at loads below the cyclic load as detailed in Table 2. Some of the scatter in the results was attributed to the manufacturing tolerances used to enable users of connections to easily fix one standard on top of a second. This scatter could occur when the standards are connected in full structures and therefore the results must be treated with caution.

The lowest stiffnesses were determined putting a regression linear curve through the first straight part of the curve and the logarithmic mean used to determine the stiffness of the curves. The second stiffness was then determined, again by putting a regression linear curve through the next part until the curvature changed significantly. The results were accepted when the regression curves both had an $R^2 > 0.95$. Table 4 shows the mean maximum moments and the mean stiffnesses with a commentary as to why certain tests were removed.

The results show that, as expected, spigots which are doubly bolted to standards have lower capacity in resisting moments than do standards where the spigots are welded at one end.

Table 4

Rotational stiffness results and maximum applied side moment

Test group	Initial stiffness (kNm/rad)	Second stiffness (kNm/rad)	Mean Maximum moment (kNm)	Standard deviation	Comments
B-1-CY	9.90	106.53	2.49	0.14	
B-30-CY	112.50	33.94	2.31	0.09	Too much scatter in B-30-CY-3L and B-30-CY-4L to get stiffnesses
B-60-CY	113.64	160.49	1.81	0.15	Too much scatter in B-60-CY-3L and B-60-CY-4L to get stiffnesses
B-90-CY	153.19	107.37	0.85	0.12	
B-110-CY			0.26		1 curve only so no standard deviation and too much scatter to get stiffnesses
B-120-CY	127.78		1.37		No standard deviation as only 1 successful test and second stiffness could not be calculated
W-1-CY	130.26	107.36	2.49	0.04	
W-30-CY	136.92	51.78	2.32	0.19	Too much scatter in W-30-CY-3L and W-30-CY-4L to get stiffnesses
W-60-CY	132.42	51.01	2.03	0.31	Too much scatter in W-30-CY-3L and W-30-CY-4L to get stiffnesses
W-90-CY	96.24	69.65	1.62	0.50	Too much scatter to determine second stiffness in W-90-CY-3L
W-120-CY	-133.60	74.53	2.21	0.36	

Note that if looseness is properly measured when stiffnesses are determined in accordance with the Eurocode the total looseness is found by adding the initial looseness recorded in Table 3 with the half the difference between the intersects of the regression straight lines of the third loading curve and last cyclic unloading curve with the zero moment axis. These can then be used to obtain a reduced stiffness of the initial slope.

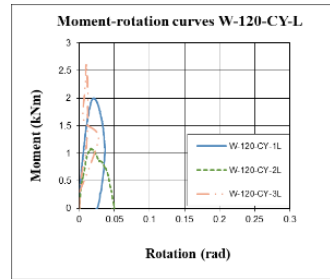
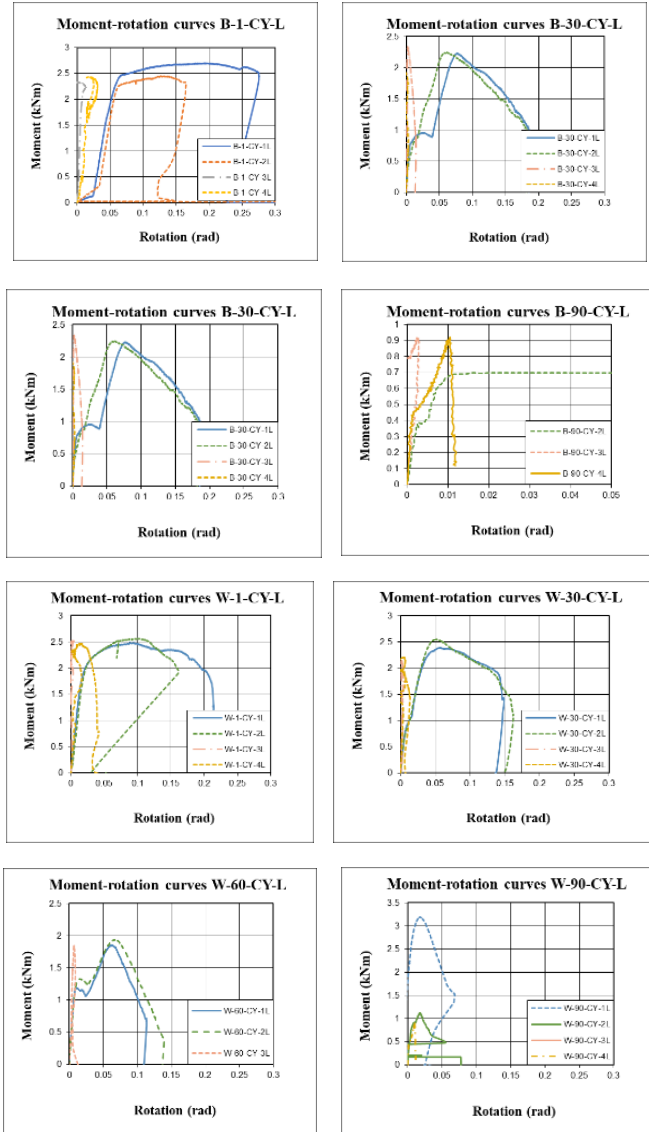


Fig.14 Moment-rotation curves of the connections with different axial loads loaded to failure

The results show that, as expected, spigots which are doubly bolted to standards have lower capacity in resisting moments than do standards where the spigots are welded at one end.

Note that if looseness is properly measured when stiffnesses are determined in accordance with the Eurocode the total looseness is found by adding the initial looseness recorded in Table 3 with the half the difference between the intersects of the regression straight lines of the third loading curve and last cyclic unloading curve with the zero-moment axis. These can then be used to obtain a reduced stiffness of the initial slope.

3. Finite element analysis

3.1. Finite element model

The system was modelled using SolidWorks and a static structural nonlinear analysis was performed using ANSYS [31]. Five tests were conducted. Each test represented a different axial load level. For each axial load level, the transverse force causing bending was increased until failure of the joint assembly. The finite element model was used to determine the connection stiffness and its maximum capacity.

The two tubes and the spigot were exported from solid works. The three parts were assembled into one system.

Since the objective of the analysis was to determine connection stiffness and its maximum capacity the structural analysis included the elastoplastic region as well as a pure elastic region. Hence the bilinear hardening model in ANSYS was used and the tangent modulus was required.

The bilinear hardening model in ANSYS requires two slopes. One slope is the Young's modulus in the elastic region and the second slope is the plastic tangent modulus. The tangent modulus quantifies the "hardening" of material that generally occurs when it begins to yield.

The tangent modulus was obtained using Eq. 2.

$$\text{tangent modulus} = \frac{\text{UTS} - \text{YS}}{\text{Strain at the UTS} - \text{Strain at the YS}} \quad (2)$$

where the UTS is the Ultimate Tensile Strength and the YS is the yield strength.

In the finite element model the automatic procedure in ANSYS generated a constant strain tetrahedral mesh. A simulation using coarse and fine mesh sizes were undertaken. Changing the mesh type to hex dominant failed because the system was loaded dynamically. Hex dominant mesh types in ANSYS are applicable for bodies that do not sweep [16].

Therefore, a mesh sensitivity was done by decreasing the minimum edge

length until a convergence of the von Mises stress of 3% was reached in all the elements. The minimum edge length was 4mm in all simulations. The final mesh had 16203 elements and is shown in Figs. 15 and 16. Unfortunately, the separation between the two tubes of 1 mm is not shown in the Figs. of meshes.

Two options were studied concerning the connection between the spigot and the tubes. Option one studied the case where the spigot was bolted to the tube at one end and bolted at the other end and option two studied the case where the upper surface of the spigot was welded to the inner surface of the tube on one end. The following boundary conditions were applied:

- At the right side of the tube where the axial compression was applied, a roller Boundary Condition is applied.
- At the left side of the tube where the axial compression is applied, a pinned boundary condition was used.

Contact properties

- Tube and tube: Frictionless since they are both connected through the spigot
- Bolted option: Bolts are in contact with the pipe and spigot. See Fig. 16.
- Welded option: The outer surface of the spigot is fully bonded to the inner surface of the tube to simulate the welded connection case. See Fig.15.

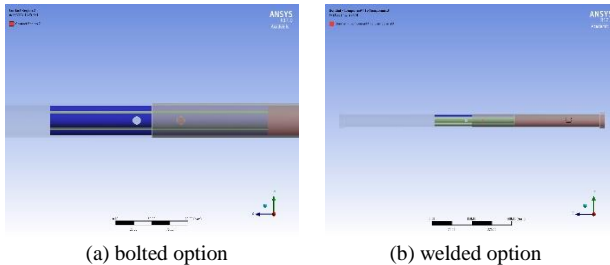


Fig. 15. The connection between the spigot and the tube where the blue segments represent the welding at all surfaces between the spigot and the tubes and the red circle the contact with the bolts

Five different load cases were considered. For each axial load level, a displacement control was applied. The five axial loads were 0KN, 30KN, 60KN, 90KN and 120KN. Since these loads were uniformly distributed, a conversion to axial pressure was undertaken.

For example, the axial pressure for the 30KN force is given in Eq 3.

$$\sigma = \frac{\text{Force}}{\text{Area}} = \frac{30}{\pi \times (50^2 - 48.5^2)/4} = 258 \text{ MPa} \quad (3)$$

Table 5 shows the axial pressure applied at the end of the system.

Table 5
Pressures applied for different axial loads

Load (kN)	Pressure (MPa)
0	Free displacement
30	258.53
60	517.05
90	775.58
120	1034.10

The transverse loading was applied in the middle of the system by a displacement control in the y axis. A ramp function was applied in the y direction fixing the x and z direction. The maximum displacement was chosen such that the maximum ultimate strength was attained during the time frame of the simulation.

A static structural analysis was performed in ANSYS Workbench. The geometry developed using SolidWorks was imported and the material properties as defined above were assigned to the corresponding parts. The aforementioned boundary conditions and loads were input into the ANSYS model to obtain the desired results.

The analysis was carried out for zero compression and a mesh sensitivity was undertaken until convergence occurred. Simulations were conducted when the total deformation and maximum stresses converged to less than 3%. The convergence was reached when the edge length was 4 mm.

Fig. 16 displays the resulting stress for the bolted connection and Fig. 17

shows corresponding results for the welded connection.

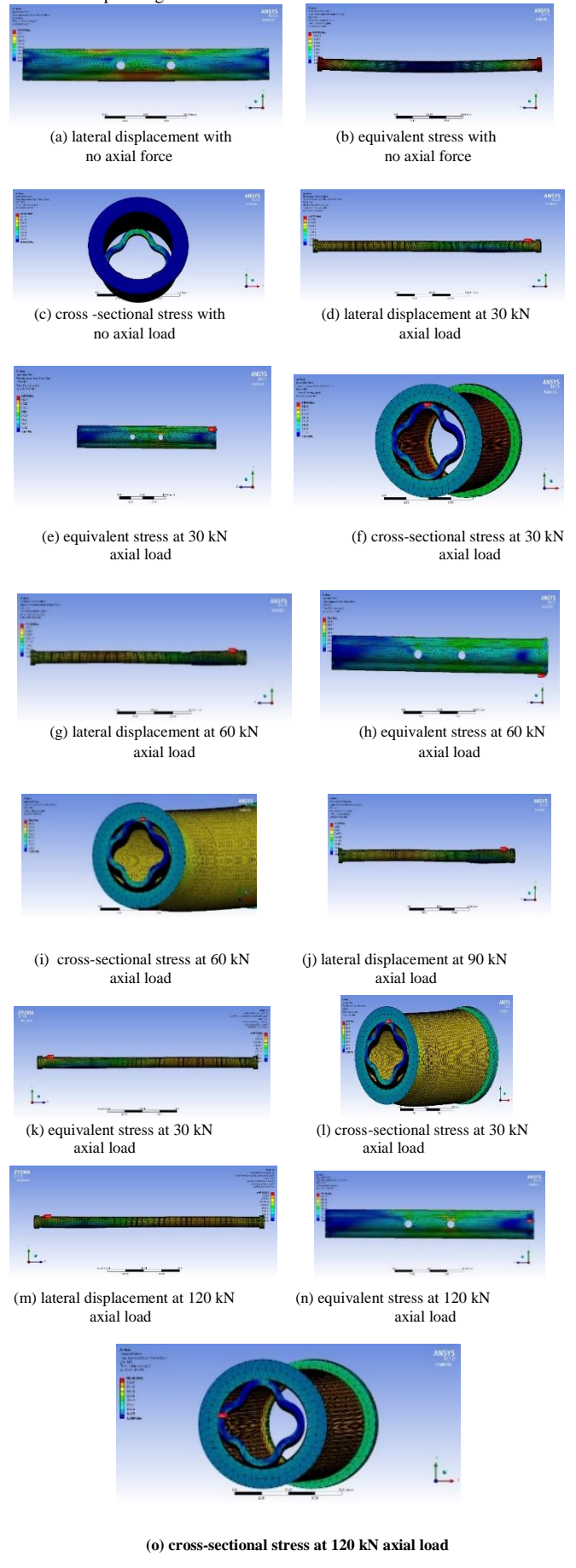


Fig. 16. Plots of displacement and stress for the double bolted connection under different axial load

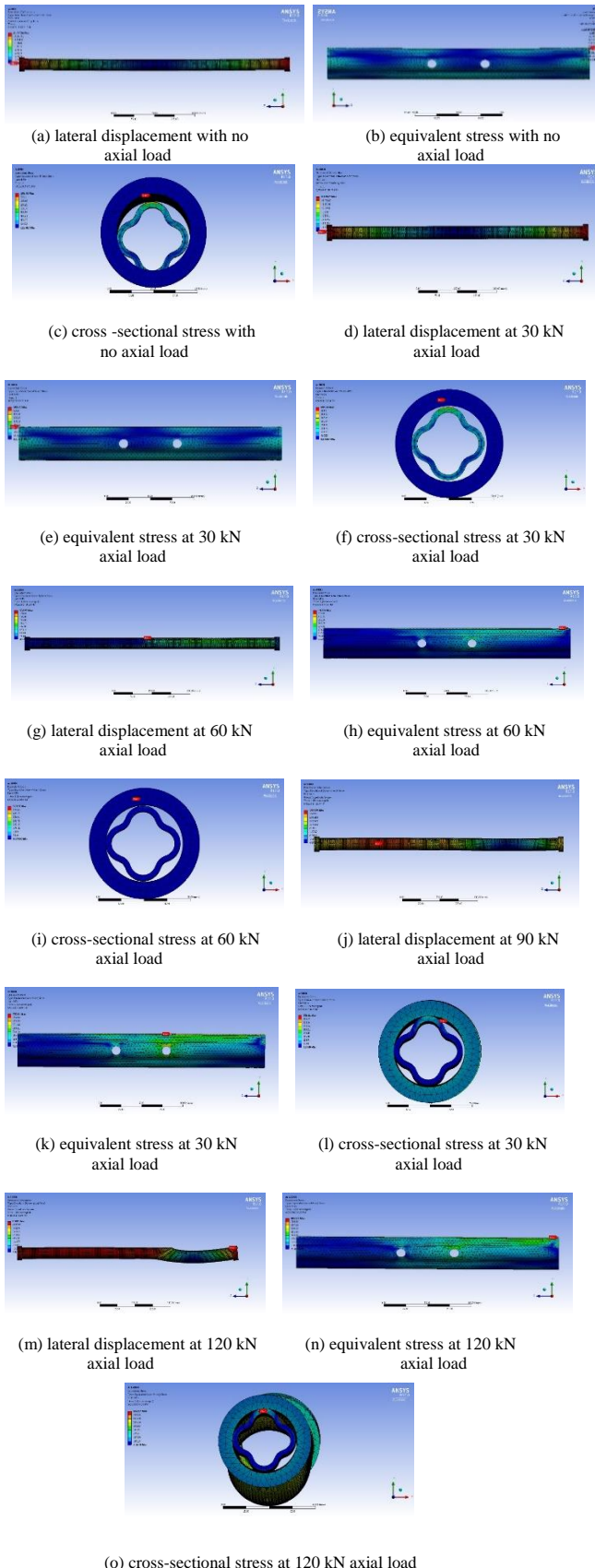


Fig. 17. Plots of displacement and stress for the spigot connection welded at one end bolted at the other under different axial loads.

3.2. Finite element results

The moment-rotation curves for the finite element curves were calculated in exactly the same way as those determined from the experiments, i.e. the displacements at 40 and 50 mm from either side of the centre of the spigot and total rotation of the connection determined. The results are shown in Fig. 18. The analyses were continued until either a convergence fail occurred at a given increment and the load could not be increased or a

collapse was observed.

From the curves the initial stiffness of the spigot connection for each axial load was determined by fitting a regression straight line through the data up to the point of maximum applied side moment. The stiffnesses are presented in Table 6. The program was not accurate enough to be able to obtain two stiffnesses and so a single stiffness was produced. These results show that the stiffness of the double bolted connection was usually less than that of the welded connection but that maximum moments were similar. These moments are attributed to plastic hinge formation in the spigot and crushing at the point where the two standards rotated into contact.

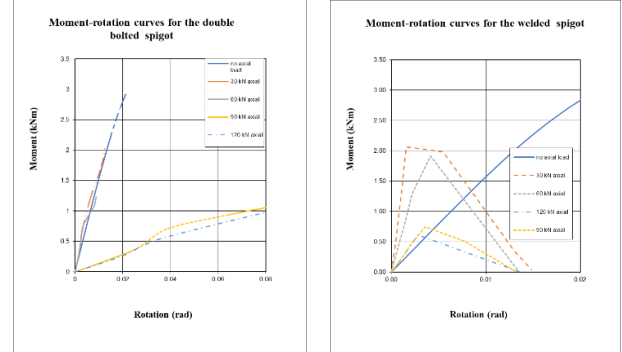


Fig. 18. Moment-rotation curves determined by finite element calculations

Table 6
Initial stiffnesses determined by finite element calculations

Model Group	Initial stiffness (kNm/rad)	Maximum moment (kN)
Bolted – no axial load	145.76	2.922
Bolted – 30 kN axial load	165.97	2.082
Bolted – 60 kN axial load	145.14	1.227
Bolted – 90 kN axial load	14.57	1.532
Bolted – 120 kN axial load	12.02	1.229
Welded – no axial load	148.23	2.914
Welded – 30 kN axial load	1268.17	2.062
Welded – 60 kN axial load	497.81	1.917
Welded – 90 kN axial load	211.34	0.747
Welded – 120 kN axial load	216.30	0.613

4. Comparisons between theory and experiment

Both theory and experiment show that the maximum moment that the connections can carry decreases with increasing axial load. In general, the stiffness of the welded connection is higher than that of the bolted connection. The ANSYS program was not able to model the looseness but as Table 3 shows the looseness is in general small with a double bolted connection having twice the looseness of the welded connection. The authors would recommend applying a looseness of approximately 0.009 radians for the double bolted connection, except for the case where there is no axial load where higher values should be used and 0.005 radians for the welded connection. The large variations in the looseness found in the experiments are due to the fact that the connections are manufactured with large tolerances, particularly so that the spigot can easily go into the tubes. In addition, the cutting of tubes to get different tubes was not perfect and often had a burr. This means that frequently the two tubes do not have a perfect join but that the looseness shown in Fig. 2 occurs, and this affects the performance of the connection.

The initial stiffnesses of the double bolted connections determined experimentally were lower than those determined by the FEA for the cases of 1 kN, 30 kN and 60 kN. This is attributed to effects of looseness and to the accuracy of the FE simulation. For the double bolted and welded connections the FE analysis showed that the statistical result described by André [19, 20] that stiffnesses were unchanged over a range of axial loads and that there were step changes in stiffness at high axial loads. This result mirrored the experimental results although there was significant scatter in the experiments, especially at high axial loads.

The experiments showed a general reduction in moment capacity with increased axial loads. There was good agreement at low axial loads between FE and experimental maximum loads.

5. Conclusions

A combined experimental and theoretical analysis of spigot connections used to enable the tubes used scaffold and falsework structures to be joined together has been conducted. Reasonable agreement has been made between an ANSYS model of the connection and experimental studies. Two types of connection were tested. Firstly, a set where the spigot insert between the two tubes was bolted to both tubes and secondly where the spigot connection was bolted at one end and spliced at the other end.

Previous studies by other researchers have ignored looseness and this paper presents some results for the first time, namely for the double bolted connection that the looseness was approximately 0.009 radians and for the connection with one end welded and the other bolted was 0.005 radians.

The experiments and the FE calculations showed that at high axial loads that such connections are unstable and can only take a limited amount of side moment.

The theoretical and experimental procedures have validated André's statistical model [19, 20] that for a large range of axial loads the rotational stiffnesses can be considered constant but there are differences at low and high axial loads.

Acknowledgements

The authors would like to thank The University of Jordan for funding the experiments and Oxford Brookes University for providing the facilities to enable the experiments to be conducted.

References

- [1] Bragg S.L., "Final report of the Advisory Committee on Falsework", Her Majesties Stationary Office, London, 1975.
- [2] BS 5975, "Code of practice for falsework", British Standards Institution, London, UK, 1996.
- [3] Lightfoot E. and Le Messurier A., "Instability of space frames having elastically-connected and offset members". Proceedings of the Second International Conference on Space Structures, Guildford, UK, 143-149, 1977.
- [4] Lightfoot E. and Oliveto G., "The collapse strength of tubular steel scaffold assemblies", Proceedings of the Institution of Civil Engineers, 63, 311-329, 1977.
- [5] Beale R. G., "Scaffold research – a review", Journal of Constructional Steel Research, 98(1), 188-200, 2014.
- [6] Beale E. and André J., "Design solutions and innovations in temporary structures", IGI Global, Hershey, PA, USA, 2017.
- [7] BS EN 12811-1:2003, "Temporary works equipment, Part 1: scaffolds-performance requirements and general design", British Standards Institution, London, UK, 2003.
- [8] BS EN 74-1, "Couples, spigot pins and baseplates for use in falsework and scaffolds – Part 1: couples for tubes - requirements and test procedures", British Standards Institution, London, UK, 2005.
- [9] Abdel-Jaber M.S., Beale R.G., Godley M.H.R. and Abdel-Jaber M., "Rotational strength and stiffness of tubular scaffold connectors", Proceedings of the Institution of Civil Engineering Structures and Buildings, 162, 391-403, 2009.
- [10] Prabhakaran U., Beale R.G. and Godley M.H.R.G., "Analysis of scaffolds with connections containing looseness", Computers and Structures, 89, 1944-1955, 2011.
- [11] Cimellaro G.P. and Domaneschi M., "Stability analysis of different types of steel scaffolds", Engineering Structures, 152, 535-548, 2017.
- [12] Sevim B., Bekiroglu S and Arsan G., "Experimental evaluation of tie-bar effects on structural behaviour of suspended scaffold systems", Advanced Steel Construction - an International Journal, 13, 62-77, 2017.
- [13] Peng J.L., Ho C.M., Chan S.L. and Chen W.F., "Stability study on structural systems assembled by system scaffolds", Journal of Constructional Steel Research, 137, 135-181, 2017.
- [14] Peng J.L., Wang C.S., Wu C.W. and Chen W.F., "Experiment and stability analysis on heavy-duty scaffold systems with top shores", Advanced Steel Construction - an International Journal, Advanced Steel Construction - an International Journal, 13, 293-317, 2017.
- [15] Liu H., Wen S., Liu Q., Wang G. and Chen Z., "Experimental and theoretical studies on the stability of steel tube-coupler scaffolds with different connection joints", Engineering Structures, 106, 80-95, 2016.
- [16] Milojkovic, "Factors of safety for standard scaffold structures", PhD Thesis, Oxford Brookes University, Oxford, UK, 1999.
- [17] Beale R.G. and Godley M.H.R., "Numerical modelling of tube and fitting access scaffold systems", Advanced Steel Construction - an International Journal, 2, 199-223, 2006.
- [18] Beale R.G. and Godley M.H.R., "The analysis of scaffold structures using LUSAS", Proceedings of LUSAS 95, Tewkesbury, UK, 10-24, 1995.
- [19] Godley M.H.R., Beale R.G. and Feng X., "Rotational stiffnesses of semi-rigid baseplates", Proceedings of the fourteenth International Speciality Conference on Cold-Formed Steel Structures, St. Louis, USA, 323-334, 1998.
- [20] BS EN 15512:2009, "Steel static storage systems – adjustable pallet racking systems – principles for structural design", British Standards Institution, London, UK, 2009.
- [21] André J., "Determination of the main parameters affecting the performance of bridge falsework systems", PhD Thesis, Oxford Brookes University, Oxford, UK, 2014.
- [22] André J., Beale R.G. and Baptista A.M., "Experimental and theoretical investigation of Cuplok® Spigot Connections, Proceedings of the eighth International Conference on Steel and Aluminium Structures ICSAS 2016, Hong Kong, 49, 16, 2016.
- [23] Chandrangsu T. and Rasmussen K.J.R., "Full-scale tests and advanced structural analysis of formwork assemblies", Proceedings of the sixth International Conference on Advances in Steel Structures, Hong Kong, 1083-1090, 2009.
- [24] Chandrangsu T. and Rasmussen K.J.R., "Structural modelling of support scaffold systems", Journal of Constructional Steel Research, 67, 866-875, 2011.
- [25] Enright J., Harris R. and Hancock G.J., "Structural stability of braced scaffolding and formwork with spigot joints", Proceedings of the fifteenth International Speciality Conference on Cold-Formed Steel Structures, Orlando, USA, 357-376, 2000.
- [26] BS EN 12811-3:2002, "Temporary structures equipment – Part 3: load testing", British Standards Institution, London, UK, 2012.
- [27] Prabhakaran U., "Nonlinear analysis of scaffolds with semi-rigid connections", PhD Thesis, Oxford Brookes University, Oxford, UK, 2011.
- [28] Blackmore P.A., "The history of wind damage in the UK", Proceedings of the Conference into Wind Loading on Temporary Structures, Buxton, UK, 17-32, 1994.
- [29] National Access and Scaffolding Confederation (NASC), "NASC TG20:13: Guide to Good Practice for Scaffolding with Tubes and Fittings", London, UK, 2013.
- [30] GB/T1591-2008, "High Strength Low Alloy Structural Steel", National Standards of the Peoples Republic of China, 2009.
- [31] ANSYS, "ANSYS Customer Support", <http://www.ANSYS.com>, accessed 26 June 2017.

BEHAVIOR OF CFST-COLUMN TO STEEL-BEAM JOINTS IN THE SCENARIO OF COLUMN LOSS

Shan Gao^{1,2}, Man Xu^{3,*}, Lan-Hui Guo⁴ and Su-Mei Zhang⁴

¹ Shaanxi Key Laboratory of safety and durability of concrete structures, Xijing University, Xian 710000, China

² Postdoctoral Station of Civil Engineering, Chongqing University, Chongqing 400030, China

³ School of Civil Engineering, Northeast Forestry University, Harbin 150090, China

⁴ School of Civil Engineering, Harbin Institute of Technology, Harbin 150090, China

* (E-mail: xuman@nefu.edu.cn)

ABSTRACT

As a connecting component in structures, the mechanical property of joint is one of the critical factors, especially to prevent progressive collapse. In the scenario of column loss, the joints are subjected to bending moment combined with tension to redistribute loads, which is different from the behavior of joint in an undamaged structure. According to this specific loading condition, two concrete-filled steel tubular column-steel beam joints under bending moment combined with tensile force were tested. In the test, new kind of semi-rigid joint was proposed, whilst an outer-ring configuration was adopted in a rigid joint for comparison. Meanwhile a finite element model of the new joint was developed by using ABAQUS. The results show that new semi-rigid joint possesses good rotation capacity under pure bending moment. The initial stiffness and moment resistance of the new joint are both smaller than those of the outer-ring joint. The moment-tension relationship of new joint keeps linear. The behavior of joint under moment combined with tensile force may be uniformly described by a power function correlation expression. The influence of width of short-limb connected to tube wall and the limb thickness on the initial stiffness and strength of new joint is obvious whilst the influence of width of long-limb connected to beam flange is not evident.

Copyright © 2019 by The Hong Kong Institute of Steel Construction. All rights reserved.

1. Introduction

Progressive collapse in high-rise building structures will result in significant casualties and property loss. The partial collapse of Ronan Point apartment is deemed as a milestone of structural progressive collapse. The notorious terrorism attack of World Trade Center in 2001 triggered more interests on the progressive collapse resistance of building structures. As a connecting component of structural members, the mechanical property of joint is one of the critical factors, especially to prevent progressive collapse.

Once an internal column is damaged and loses its load-carrying capacity, vertical loads would seek another load path to distribute and normally are sustained by the beams connected to the damaged column. The vertical loads would cause large deflection of two-span beam and require the above joint to bridge over the damaged column. The load-carrying mechanism of the joint would transfer from lumped plastic hinge action to catenary action. In this condition, the joint should bear additional tensile force besides moment to transfer the vertical loads to the remaining structure, after tensile catenary action is triggered at the beams. Meanwhile, the joints would undergo large deformation without any significant reduction in strength. During the transition of load-carrying mechanism, the joints at the damaged column and the adjacent columns should be capable of carrying reverse bending moments and additional tensile forces at the same time. The increasing tensile force would influence the bending resistance of the joint. These features are seldom to encounter in conventional design but essential for preventing progressive collapse in structure under column loss. It is crucial to study the performance of the joint in this transition of load-carrying mechanism.

Alternative Load Path method is widely adopted in various national codes and standards (BS [1], GSA [2], DoD [3]) to analyze progressive collapse resistance of structures. Redundancy and ductility of joints are required specifically in Alternative Load Path method, in order to dissipate energy and avoid brittle damage of joint. In addition to moment resistance and initial stiffness, the ability of load-carrying mechanism transformation of joints is more concerned. The joints should undergo tensile loads without any significant reduction in strength and rotation capacity. Large deformation in the damaged part of structure is allowed, as long as progressive collapse is prevented (Haremza et al. [4]). Compared with rigid connection, semi-rigid connection can optimize the bending moment distribution in the connected beams. More importantly, compared with rigid joints, semi-rigid joints possess better rotation capacity which is beneficial for activating "catenary action" in the system of preventing progressive collapse.

ARTICLE HISTORY

Received: 15 April 2017
Revised: 18 December 2017
Accepted: 27 December 2017

KEY WORDS

concrete-filled steel tubular;
progressive collapse;
bending moment combined with tension;
semi-rigid;
beam-column joint

So far, many numerical and analytical studies have been carried out on the behavior of whole structure and the joint in the scenario of internal column removal (Buscemi et al. [5], Gerasimidis et al. [6], Izzuddin et al. [7], Iribarren et al. [8], Khandelwal et al. [9], Li et al. [10], Stylianidis et al. [11], Xu et al. [12], Yu et al. [13]). A significant development of theory, mechanical model and design method about progressive collapse have been proposed. However, more convincing experiments still need to be performed. Yi et al. [14] tested a 1/3-scaled 3-story RC frame with 4 bays in the scenario of middle column loss. The results showed that the RC frame under middle column loss would undergo 4 stages including elastic stage, elastic-plastic stage, plastic stage and catenary stage. Demonceau et al. [15] conducted a static test of a steel frame with RC floor slab in the scenario of internal column removal. Flush endplate beam-column connections were adopted in the steel frame. The registered curves confirmed the development of tying force in the beams. Sadek et al. [16] tested various steel joints and RC joints in the scenario of progressive collapse. Portions of structural framing systems were designed as the boundary condition of the joints. The experimental results presented the behavior and failure modes of steel joints and RC joints. Li and Wang et al. [17] conducted two full-scale tests on steel beam-to-tubular column moment connections with outer-diaphragm under a column removal scenario. Two types of flexural failure modes, namely a continuous flexural failure throughout the section and an interrupted flexural failure without the fracture extending upwards were observed from the tests. Yang et al. [18] conducted an experimental test to estimate the progressive collapse resistance of composite frame under a middle column loss. The experimental results indicated that more reinforcing bars should be used in composite slab and the effectiveness of the enhanced tie forces was investigated. Qian et al. [19] proposed a simple approach which can be used to evaluate the progressive collapse vulnerability of RC buildings under multiple column removal scenarios. Guo and Gao et al. [20–21] performed a series of research project to investigate the behavior of steel structure with RC slab under an internal column-removal scenario. This research work involved a series of tests on steel frame and steel joints with RC slab, finite element study of joint and structure behavior, and development of mechanical models.

Previous studies have been attracted into steel structures and reinforced concrete structures, few attentions are paid on composite structures. In this paper, experimental study and theoretical analysis had been performed on the moment-tension performance of concrete-filled steel tubular (CFST) column to steel-beam joints. A new type of semi-rigid connection was proposed and studied in detail. In addition, parametric analysis on the behavior of the new joint was also conducted by ABAQUS. The influence of angle on the behavior of new joint was analyzed.

2. Experimental program

2.1. Design and fabrication of specimen

According to the experimental set-up, two 1/3-scale specimens of CFST-column to steel-beam joints were designed and fabricated. Outer-ring connection was adopted as rigid joint whilst a new type connection was applied as semi-rigid joint, which can be easily assembled.

The dimension of the rigid joint is shown in Fig. 1. The width and thickness of square steel tube used in CFST column were 160 mm and 5 mm respectively. The profile section of steel beam was H200×100×5.5×8 [H-overall depth×flange width×web thickness×flange thickness]. Two outer-ring plates and a shear plate were welded to the wall of square tube by using fillet weld. The thickness of outer ring plate and shear plate was both 10mm. The flanges of steel beam were welded to the outer-ring plate whilst the web of steel beam was welded to a shear plate on the column. Connection plates which were used to apply tensile forces were welded to the ends of steel beams. A pair of stiffeners was welded to steel beam at the position of hinge support.

Normally, rigid joints such as outer-ring and inner-ring connection are usually adopted in practical buildings with CFST columns. Due to the relatively complicated configuration, semi-rigid joints are not widely used in public building structures, even though semi-rigid joints can optimize the bending moment distribution in the connected beams. As aforementioned, it is also especially beneficial for the system of preventing progressive collapse.

As typical semi-rigid joint, end-plates joints are usually adopted to connect steel-beam to the rectangular section columns. The solutions shown in Fig. 2(a) (Hoang [22]) are usually adopted in the construction, namely use of special bolts or use of intermediate elements. These solutions are adopted to overcome the difficulty of placing bolts in the closed column section. However, the two above joint solutions have some disadvantages in their cost and their generally low bending stiffness and resistance. Meanwhile the mechanical behavior of the mentioned joint is mainly governed by the bolts, which presents generally a rather weak ductility under tensile force. Accordingly, the above joint solutions are normally not suitable to be used for moment resistant frames in seismic and anti-collapse design.

The new joint is shown in Fig. 2(b). Unequal limb angles were employed to accompany this semi-rigid connection. Four short-limbs could circle a close hoop to ensure the effective transformation of loads from beams to column. The new joint could be easily assembled in construction site by welding seams and bolts. Short-limb of angle and shear plate were welded to square steel tube. Meanwhile a stiffener was welded in the middle of the angle to improve the stiffness of the connection. Then the flanges of steel beam were connected to long-limb by high-strength bolts whilst the web of steel beam was connected to a shear plate on tube wall by the same way. The same configuration was adopted in both top flange and bottom flange of steel beam.

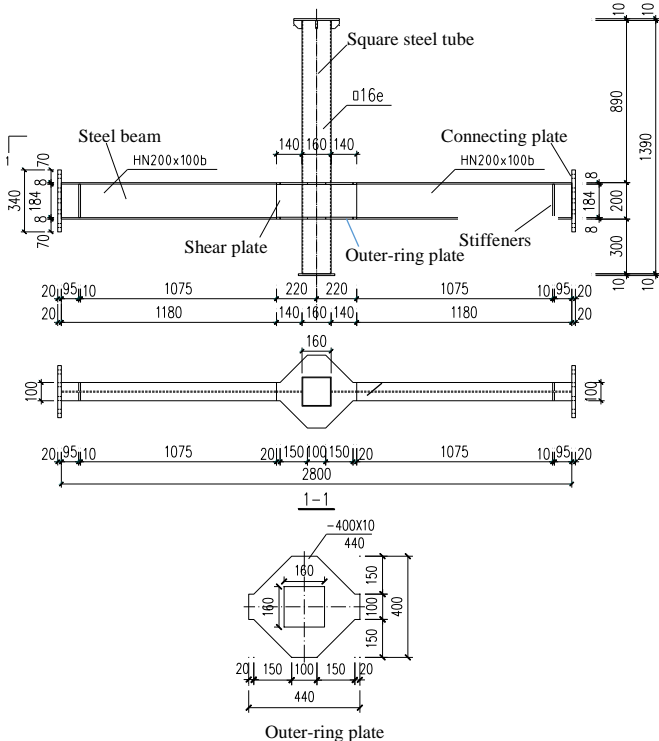
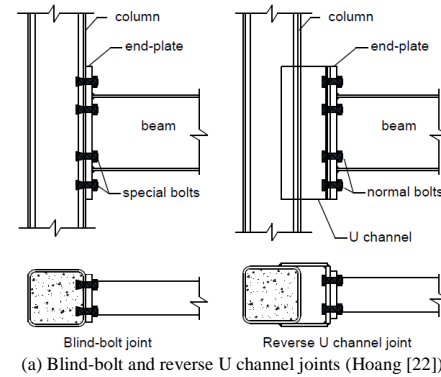


Fig. 1 Dimension of specimens for rigid outer-ring connection (SJ01)



(a) Blind-bolt and reverse U channel joints (Hoang [22])

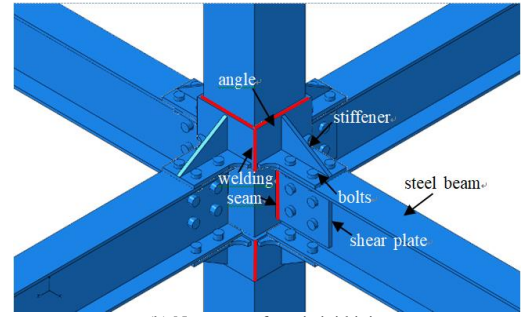


Fig. 3 Steel beam-GEST column joints

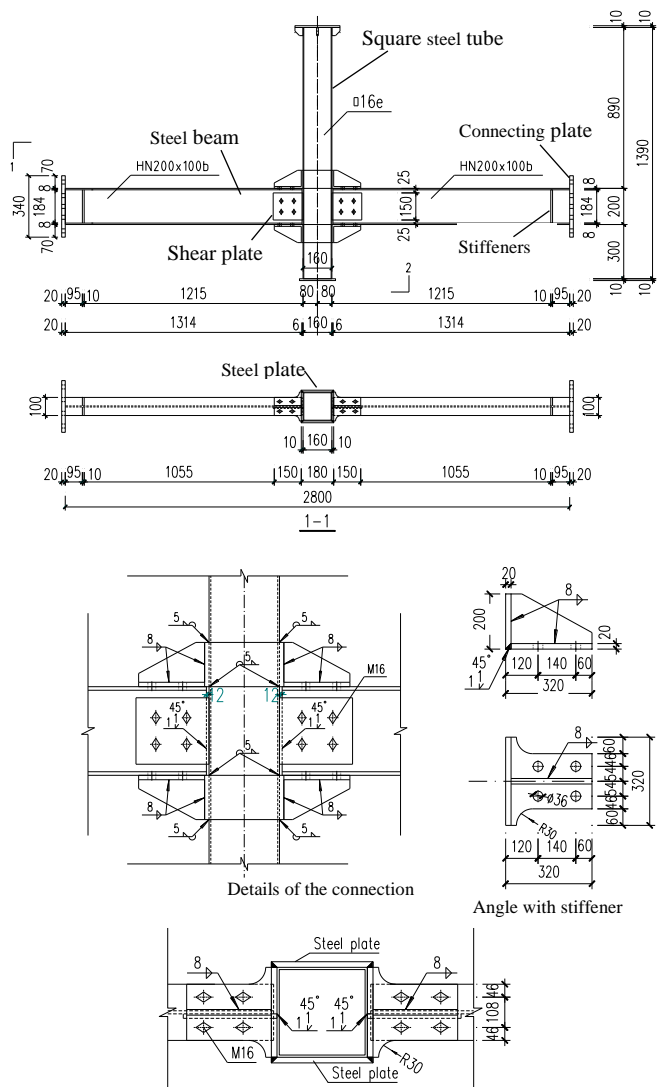


Fig. 3 Dimension of specimens for semi-rigid connections (SJ02)

The dimension of the semi-rigid joints (SJ02) is shown in Fig. 3. Only in-plane connection was designed. To this end, 10 mm steel plates were used to connect the angle on both sides of the joint. The dimensions of square steel tube and steel beam used in specimen SJ02 were identical with SJ01. The thickness of stiffener and shear plate was 10mm. The cross section of angle was $L160 \times 100 \times 10$ [L -Long limb width \times Short limb width \times Limb thickness]. M16 high-strength bolts with grade 10.9 were used in the connections.

2.2. Material properties

In the test, Chinese grade Q235B structural steel was used for all steel members. Standard coupons were cut from each steel member and tested. The material properties of steel are listed in Table 1, where f_y , f_u , E_s are steel yield strength, tensile strength and elastic modulus respectively. Casting of $150 \times 150 \times 150$ mm cubes for concrete strength test and $150 \times 150 \times 300$ mm cylinder for concrete Young's modulus were carried out at the same time. They were cured in similar conditions as the specimen. The average compressive strength of concrete cubes is 33.1 MPa. The Young's modulus of concrete is 2.29×10^4 MPa.

Table 1
Mechanical properties of steel

Se.	t (mm)	f_y (MPa)	f_u (MPa)	E_s (10^5 MPa)
Beam	Flange	7.1	269	401
	Web	5.2	275	411
Square tube	4.8	342	402	1.82
Ring plate/Shear plate	9.2	298	388	1.91

2.3. Loading procedure

In the scenario of column loss, the joint would be under the load combination of bending moment and tensile force during the transition of load-carrying mechanism. Hence the load combination was applied onto the specimens through two steps as shown in Fig. 4:

Step A: Apply vertical load on the column. Through applying vertical load, a bending moment is applied on the joint. After the plastic yield moment of the joint is reached, the vertical jack would be arrested and hold constantly. The beam-ends rotate freely while the vertical load is applied in order to avoid additional tensile force occurring in the beams.

Step B: Apply horizontal tensile force at both ends of the beams. While the rotation of the joint is kept a constant value, the ends of the beams are continuously loaded until the joint fails.

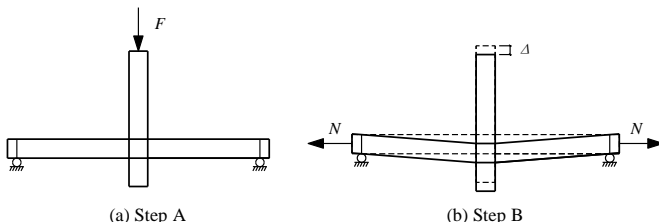


Fig. 4 Loading steps

2.4. Experimental setup

The specimens were tested in the multifunctional loading ring as shown in Fig. 5 (see Guo and Gao et al. [21] for more details). With this loading ring, moment and tensile force could be applied to the joints simultaneously. The details of the experimental setup are illustrated in Fig. 6.

In loading step A, the beam-ends should rotate freely while the vertical load was applied through hydraulic jack (3), in order to avoid additional tensional force occurring in the beam. As shown in Fig. 6, the bottom flange of steel beam where was strengthened by a pair of stiffeners was placed on hinge support (10) to realize boundary condition of simple support. The beam-end was connected to the connecting hinge (9) by high-strength bolts, while the connecting hinge (9) was connected with bolt sleeve (8) by a pivot shaft. This connecting unit could make beam-ends rotate freely while the vertical load was applied. In loading step B, tension rod (7) was screwed into bolt sleeve (8) to transfer the tensile load applied by horizontal jack to the specimen.

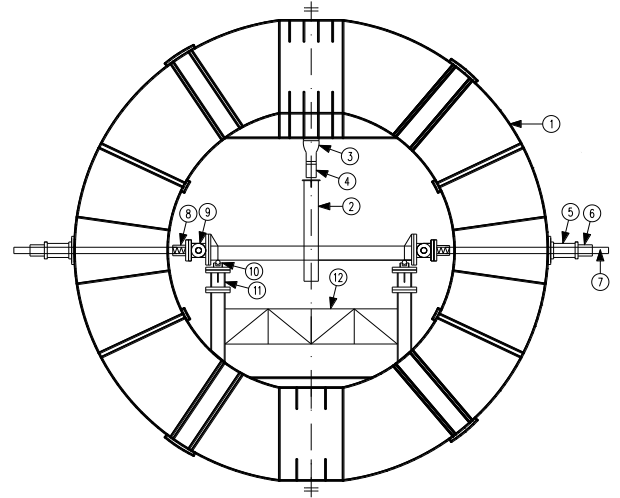


Fig. 5 Experimental setup:

(1) multifunctional loading ring; (2) specimen; (3) 500kN hydraulic jack; (4) load cell; (5) 2500kN hydraulic jack; (6) load cell; (7) 90mm-diameter tension rod; (8) bolt sleeve; (9) connecting hinge; (10) hinge support; (11) support column; (12) column bracing

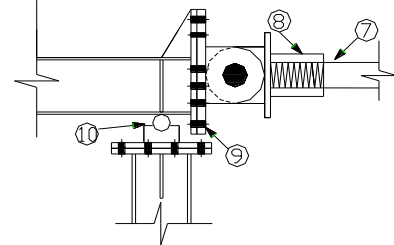


Fig. 6 Hinge support

Linear variable displacement transducers (LVDT) were placed to monitor the displacements of the specimens. The distribution of LVDTs is presented in Fig. 7. The following values were measured: vertical displacement of column (LVDT 1) and beams (LVDT 8-LVDT 9); axial deformation of steel beams (LVDT 2-LVDT 3); horizontal displacement of column (LVDT 4-LVDT 5); support settlement (LVDT 6-LVDT 7). Uniaxial and rosette strain gauges were arranged on the specimen, as shown in Fig. 8.

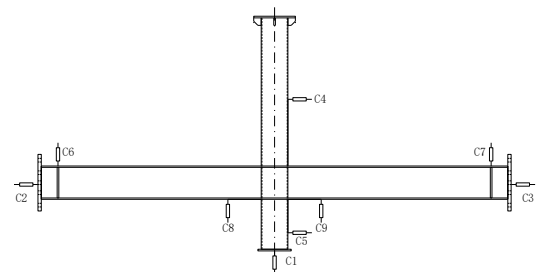


Fig. 7 Distribution of LVDTs

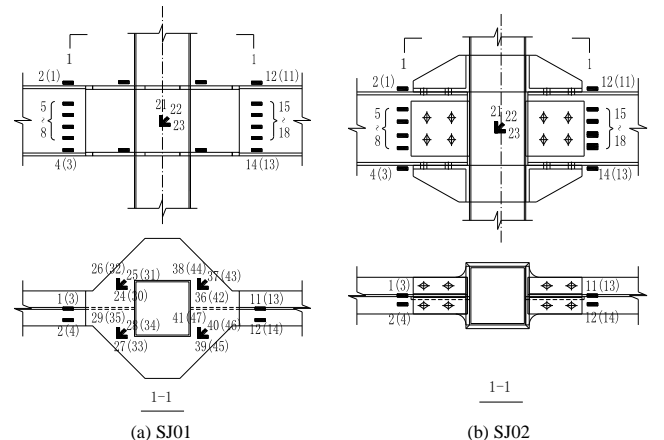


Fig. 8 Distribution of strain gauges

3. Experimental phenomena

3.1. Specimen SJ01

Before the yield load reached, no evident phenomenon was observed in step A. At the end of loading step A, the vertical displacement of specimen SJ01 was only 10 mm. And then horizontal tensile load was applied onto both ends of the beams whereas the vertical load was 80 kN. With the increase of tensile loads, several cracks were appeared on the oxide scale of steel beam. Loading was terminated when the horizontal displacement of steel-beam increased remarkably. Besides the bending deformation of the steel beam, no other phenomenon, such as severe local buckling or fracture, was occurred on the specimen SJ01, as shown in Fig. 9.

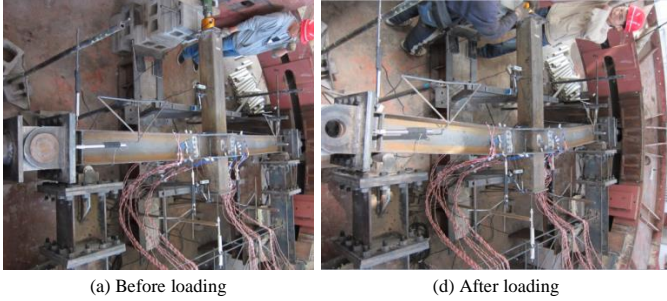


Fig. 9 Phenomena of specimen SJ01

3.2. Specimen SJ02

No evident phenomenon was observed in the joint in loading step A. At the end of loading step A, the vertical load on specimen SJ02 was 60 kN and the corresponding vertical displacement was 12 mm. And then, horizontal tensile load was applied on both ends of steel beams. When the tensile load increased to 480 kN, the tube wall deformed remarkably as shown in Fig. 10(b). With the increase of tensile load, the deformation of tube wall gradually increased. At 625 kN, the loading was terminated due to the fracture of the welding seams between angle and steel plate at the right-side connection as shown in Fig. 10(c-d).

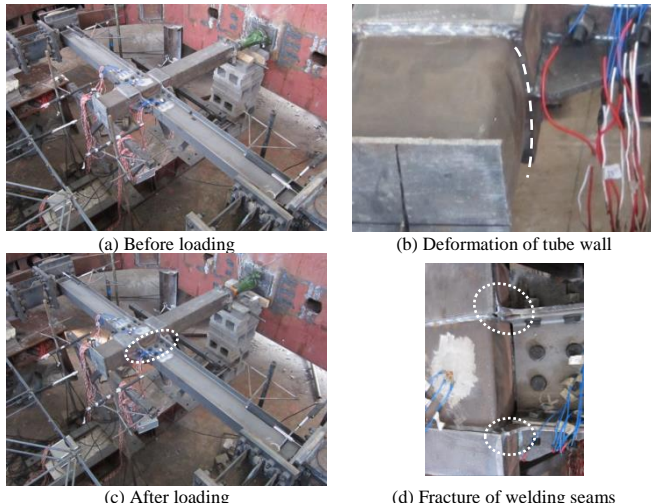


Fig. 10 Phenomena of specimen SJ02

4. Experimental results and discussions

4.1. Relationship between bending moment and tensile force

Fig. 11(a) shows the bending moment-rotation angle curves of specimen SJ01 and specimen SJ02 in loading step A. The bending moment of joints is calculated by using the following expression:

$$M = P / 2 \cdot L \quad (1)$$

where P stands for the vertical load applied at the top of column ; L for the length of beam which is 1.05 m; M for the bending moment.

The rotation angle of the specimens is given as follows:

$$\theta = \Delta / L \quad (2)$$

$$\Delta = u_m - \frac{1}{2}(u_l + u_r) \quad (3)$$

where Δ stands for the vertical displacement of column; u_m for the vertical displacement of column directly obtained from LVDT 1 shown in Fig. 7; u_l and u_r for the left support deformation and right support deformation obtained from LVDT 6 and LVDT 7 respectively.

It can be seen from Fig. 11(a) that the strength and initial stiffness of specimen SJ01 are both greater than those of specimen SJ02. The moment resistance of specimen SJ01 is approximately 1.3 times greater than that of SJ02 and the initial stiffness of specimen SJ01 is 1.2 times greater than that of specimen SJ02. After the moment on specimen SJ02 exceeds 33kN.m, a decline on the stiffness of the joint occurs which is due to the overcoming of frictional force between angle and beam flange as shown in Fig. 12. The frictional force between angle and beam flange can be calculated by using the following expression:

$$V = 4\mu F \quad (4)$$

where F stands for the pre-tighten force in one bolt which is 100kN; μ for the friction coefficient which is 0.4 according to the Chinese Code for Design of Steel Structures [23].

The moment resistance of specimen SJ02 referring to the frictional force between angle and beam flange can be expressed as follows:

$$M_f = VH_{beam} \quad (5)$$

where H_{beam} stands for the depth of steel beam which is 0.2m.

According to the above equations, the moment resistance referring to the frictional force is calculated as 32kN.m which is approximately equal to the experimental value. After the frictional force between angle and beam flange has been overcome, the curve of specimen SJ02 goes into a so-called "elastic-plastic" stage in which the discrepancy of the moment resistance between specimen SJ01 and specimen SJ02 becomes larger. In this stage, the connection deformation of specimen SJ02 under bending moment may already involve the out-of-plane deformation of tube wall.

Fig. 11(b) shows the bending moment-tensile force relationship curves of those two specimens. As above mentioned, tensile force was applied on both beam-ends after the specimen yielded. Due to the vertical deformation of the specimen under bending moment, additional moment would be brought to the specimen. Hence, the moment of the specimen in Step B is given as follows:

$$M = P / 2 \cdot L - N \cdot \Delta \quad (6)$$

where N stands for the tensile force.

It can be seen from Fig. 11(b) that the bending moment of the specimens is descending along with the increase of tensile force. The relationship of moment resistance and tensile force of specimen SJ01 is nonlinear while that of specimen SJ02 is approximately linear. In this case, the relationship of moment resistance and tensile force of specimen SJ01 could be described by the power function correlation equation derived by fitting with the results of parametric analysis (Gao [24]) as follows:

$$\frac{M}{M_p} + \left(\frac{N}{N_p} \right)^2 = 1 \quad (7)$$

where M_p and N_p stand for plastic tensile strength and moment strength of steel beam respectively.

In addition, the behavior of specimen SJ02 under bending moment combined with tensile force could be represented by the linear correlation equation as follows:

$$\frac{M}{M_p} + \frac{N}{N_p} = 1 \quad (8)$$

The correlation equations are validated against the experimental results as shown in Fig. 13. Good agreement is achieved in the comparison of M-N curves. Based on the research in Gao [24], it is worth noticing that the behavior of rigid joint under combined moment and tension could be described by a power function correlation equation, whilst that of semi-rigid joint could be represented by a linear correlation equation. Therefore, the behavior of joint

under combined moment and tension may be uniformly described by the expression as follows:

$$\frac{M}{M_p} + \left(\frac{N}{N_p} \right)^n = 1 \quad (9)$$

where n stands for the coefficient referring to different types of joint.

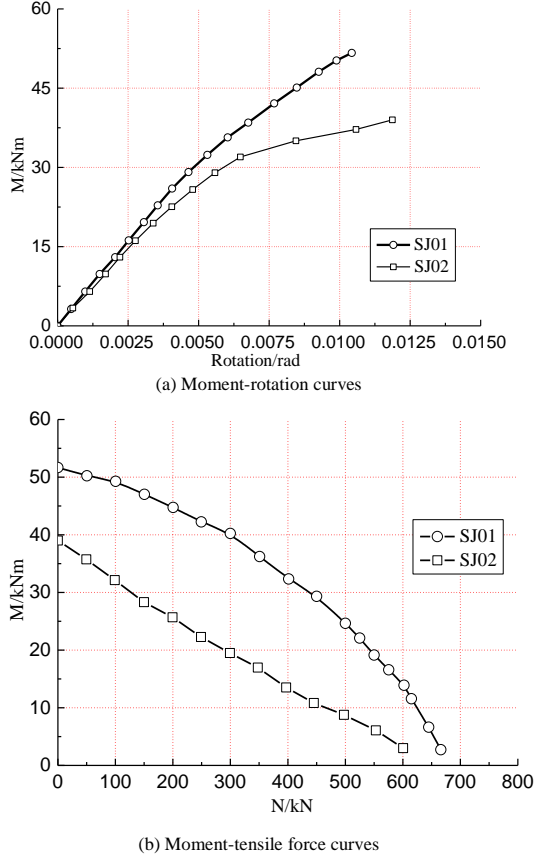


Fig. 11 Experimental results

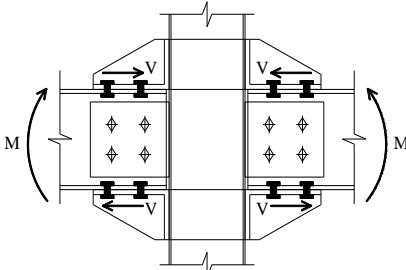


Fig. 12 Frictional force in specimen SJ02

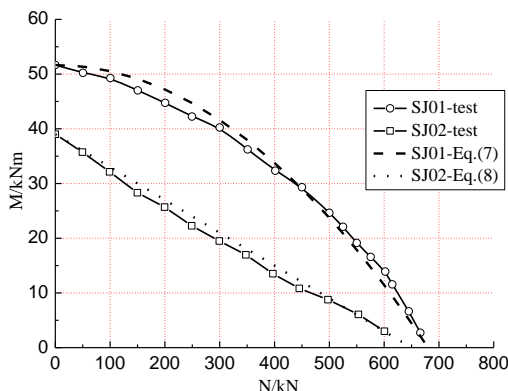


Fig. 13 Comparison of moment-tensile force curves

Fig. 14 shows the horizontal load-vertical displacement relationships in loading Step B. The result of the curves indicates that the vertical displacement of the specimens remains almost constant value with the increase of tensile load.

It verifies that the decrease of moment on the specimen is caused by tensile force and the transition of load-carrying mechanism is undergoing from plastic action to catenary action with the increase of tensile force.

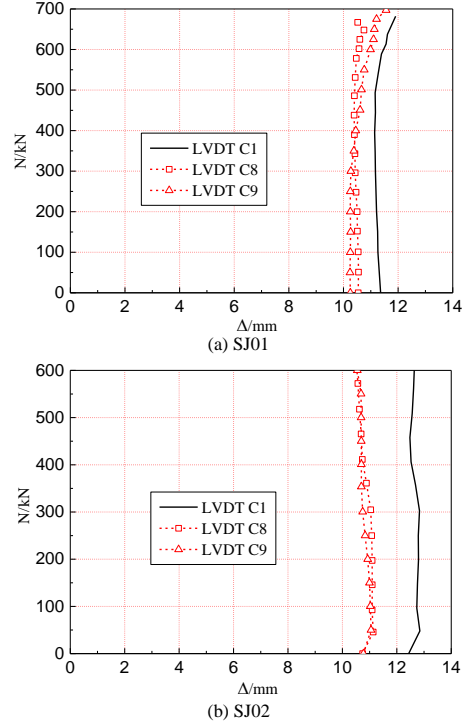


Fig. 14 Horizontal load-vertical displacement relationships in loading Step B

4.2. Analysis of strain gauge data

Fig. 15 shows the strains on steel beams in loading Step A. The detailed location of strain gauges can be found in Fig. 8. The vertical lines in Fig. 15 stand for the yield strain of steel which is about $1334 \mu\epsilon$ in this paper. At the early stage of vertical load applied, the section of steel beam is in accordance with plane cross-section assumption and the neutral axis is located in the middle of the section. At 80kN, the strain on the steel beam of specimen SJ01 has reached plastic yield value while the section of the steel beam in SJ02 is still in elastic stage at 60 kN. It indicates that the decrease of moment resistance of specimen SJ02 in Step B is due to the behavior of connection, rather than steel beam itself.

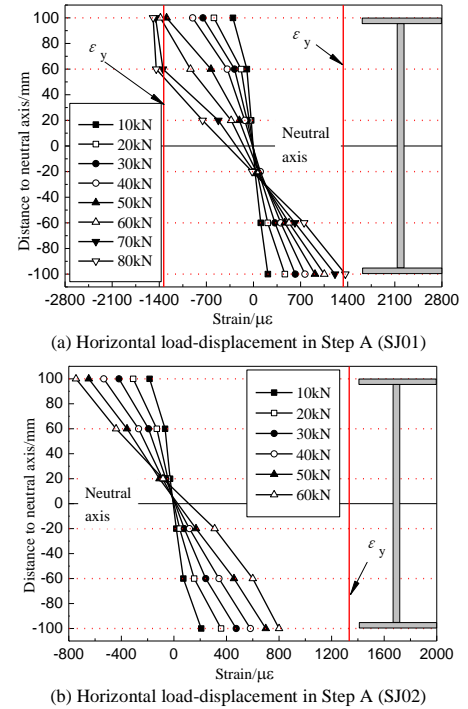


Fig. 15 Strains of steel beam in step A

Fig. 16 shows load-strain relationships in two loading steps. It can be seen from Fig. 16(a-b) that the strain of steel beam increases linearly along with the

increase of vertical load. After tensile loads are applied, the compressive strain of steel beam begins to decrease. At 670 kN, the strain of the whole beam section in specimen SJ01 has reached yield value which means the tensile strength of steel beam has been reached as shown in Fig. 16(c). The test on specimen SJ02 was terminated at 600 kN of tensile load. Even the whole section of steel beam in specimen SJ02 is in tension as shown in Fig. 16(d), part of steel beam has not reached tensile yield strain. It indicates that specimen SJ02 still needs improvement on the mechanical behavior.

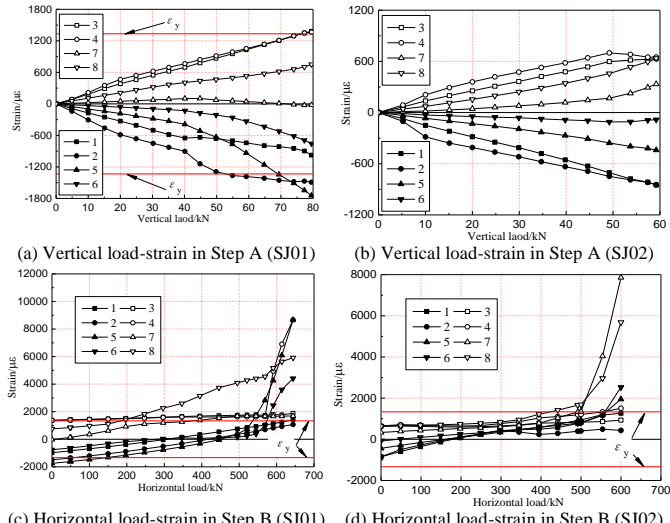


Fig. 16 Load-strain relationships in two loading steps

5. Numerical analysis

5.1. Finite element modeling and model validation

In addition to study and improve the behavior of the new joint, a finite element model using ABAQUS is developed to validate against the experimental results. Solid elements (C3D8R) are used to simulate the core concrete, steel beam, steel column, angle and bolts. The effects of weld seam and weld residual stress are neglected in the model. The angle components are connected to the tube wall by *Tie command. The bolt preloads are applied as the test by using the command of *Bolt load in ABAQUS. The contact between core concrete and column flange is simulated by “surface to surface interaction” in ABAQUS library. The friction coefficient of 0.3 is adopted in surface tangential friction. Due to the symmetrical arrangement of the specimen and test setup, 1/2 model is employed. The finite element model is shown in Fig. 17.

A bi-linear elastic-plastic material model considering stress hardening from ABAQUS is adopted to model the material properties of steel. The stress-strain relationships of steel member and bolts are identical to those in the material test. The concrete damage plasticity model from ABAQUS library is used to model the concrete material. The stress-strain relationships of concrete material from Chinese code for design of concrete structures (GB50010-2010) as shown in Fig. 18 are introduced into ABAQUS to simulate core concrete. The tensile strength of concrete is defined as 10% compressive strength of concrete. The remaining strength after concrete cracking in tension is 0.5 MPa.

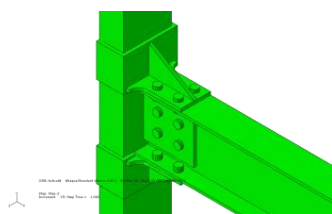


Fig. 17 Finite element model

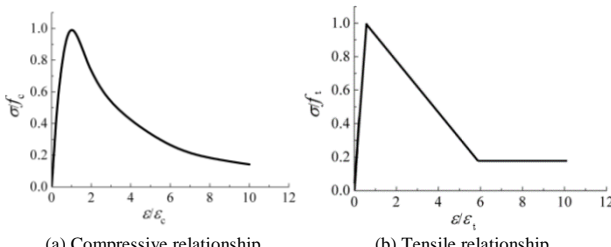


Fig. 18 Stress-strain relationship of concrete

The loading procedure adopted in the simulation is the same as that in the tests. The FE model is validated against the experimental results as shown in Fig. 19. Good agreement is achieved in the simulation of curves. Due to the difficulty in simulation of frictional displacement, a discrepancy occurs after the frictional force has been overcome as shown in Fig. 19(a). The bending moment resistance of the joint descends linearly with the increase of tensional force as shown in Fig. 19(b).

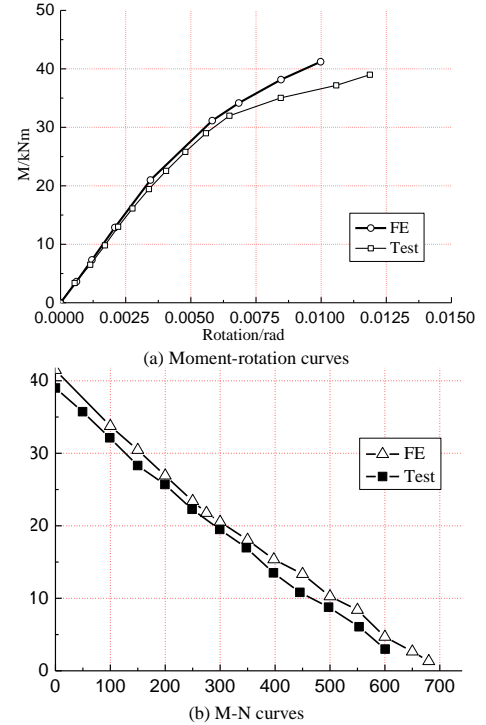


Fig. 19 Validation of FE model

5.2. Parametric analysis

The configuration of angle has effect on the behavior of new joint. Four parameters of angle profile are analyzed as shown in Fig. 20, namely the short-limb width (b_s), short-limb thickness (t_s), long-limb width (b_l) and long-limb thickness (t_l). The cross section of angle in the test was $\square 160 \times 100 \times 10$ [\square - Long-limb width \times Short-limb width \times Limb-thickness]. In the study, only one parameter is changed at each group of analysis. The dimensions and materials of the models in parametric analysis are identical to those of the aforementioned FE model.

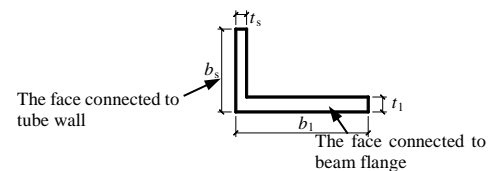
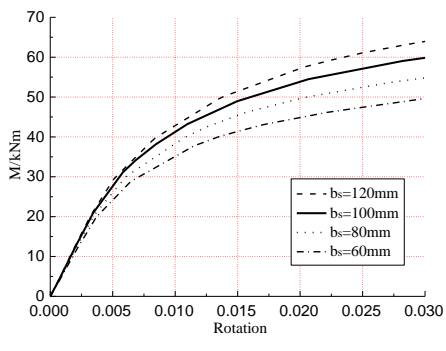


Fig. 20 Unequal-leg angle

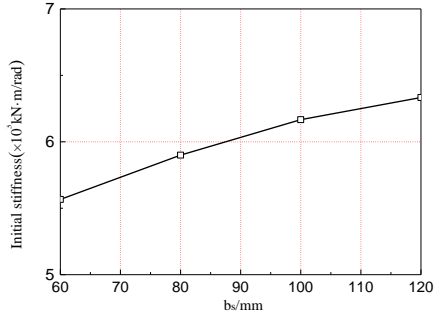
Fig. 21 shows the influence of short-limb width from 60 mm to 120 mm on connection properties. Along with the increase of short-limb width, the moment resistance and initial stiffness of the joint both increase. According to the result of stress distribution, the maximum stress occurs at the welding seams between short-limb and tube wall when the short-limb width is 60 mm and 80 mm. When the short-limb width increases to 100mm and 120mm, the maximum stress occurs at the extreme row of bolt hole. In practice, long short-limb is suggested to enhance the behavior of the joint.

Fig. 22 shows the influence of short-limb thickness from 4 mm to 10 mm on connection properties. Along with the decrease of short-limb thickness, the moment resistance and initial stiffness of the joint both decrease. The increase of short-limb thickness would depress the deformation of tube wall. According to the result of stress distribution, the maximum stress occurs at welding seams between short-limb and tube wall when the short-limb thickness is 4 mm and 6 mm. When the short-limb thickness exceeds 8 mm, the maximum stress relocates from the welding seam between short-limb and tube wall to the

extreme row of bolt hole. In the above test, the fracture of welding seams was observed. Therefore particular attention should be paid on the configuration and construction of the welding seam between short-limb and tube wall.



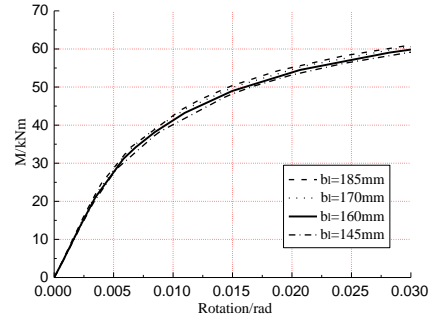
(a) Moment-rotation curves



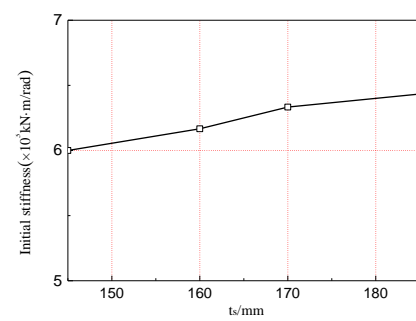
(b) Initial stiffness

Fig. 21 Influence of b_s on connection properties

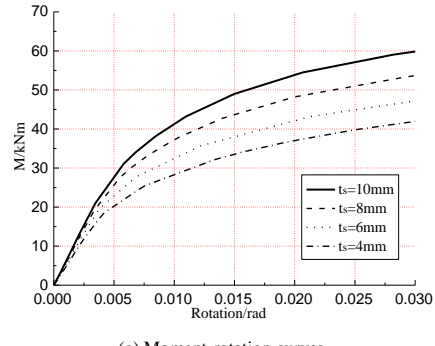
on connection properties. The initial stiffness of the joint increases linearly along with the increase of long-limb thickness. In that case, the shear capacity of bolts group between long-limb and beam flanges would be enhanced by increasing the long-limb thickness. On contrary, the long-limb width shows little influence on the shear capacity of bolts group as described above.



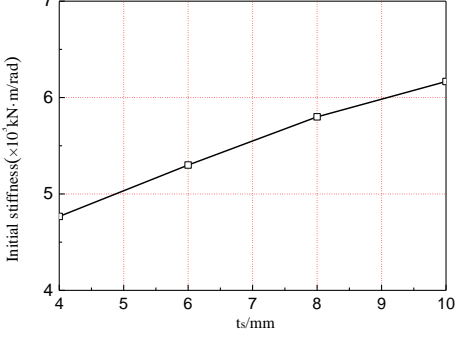
(a) Moment-rotation curves



(b) Initial stiffness

Fig. 23 Influence of b_l on connection properties

(a) Moment-rotation curves



(b) Initial stiffness

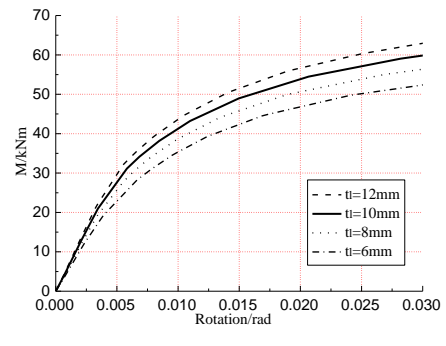
Fig. 22 Influence of t_s on connection properties

6. Conclusions

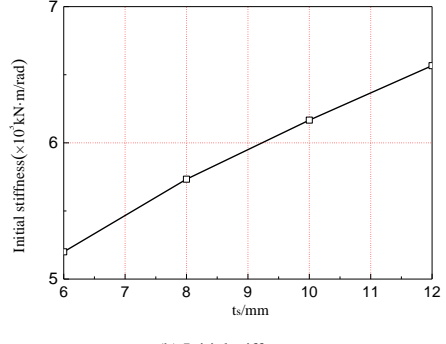
Two CFST column-steel beam joints under bending moment combined with tensile force were tested and studied in detail. In addition, parametric analysis on the new joint was also conducted by using software ABAQUS. Based on the test observations and numerical analysis, the following conclusions are made:

- (1). Under pure bending moment, new semi-rigid joint possesses good

Fig. 24 shows the influence of long-limb thickness from 6 mm to 12 mm



(a) Moment-rotation curves



(b) Initial stiffness

Fig. 24 Influence of t_l on connection properties

rotation capacity. The initial stiffness and moment resistance of the new joint are both smaller than those of rigid joint with outer-ring.

(2). The bending moment capacity of the joints decreases with the increase of tensile force. The bending moment-tensile force relationship of new joint keeps linear. The behavior of rigid and semi-rigid joint under combined moment and tension may be uniformly described by a power function correlation expression.

(3). The numerical analysis result shows that the increase of width of the short-limb connected to tube wall and the limb thickness could enhance the initial stiffness and strength of the new joint whilst the width of the long-limb connected to beam flange shows little influence on the behavior of joint.

Acknowledgments

The research described in this paper was financially supported by National Natural Science Foundation of China (NO. 51408106 and NO. 50878066), Scientific Research Program Funded by Shaanxi Provincial Education Department (17JK1154), Open fund of Shaanxi Key Laboratory of safety and durability of concrete structures (XJKFJJ201803) and Xijing University Special Foundation (XJ17T07) which are gratefully acknowledged.

References

- [1] Office of the Deputy Prime Minister, "The Building Regulations 2000, Part A, Schedule 1:A3, Disproportionate Collapse", London, UK, 2004.
- [2] General Services Administration, "Progressive collapse analysis and design guidelines for new federal office buildings and major modernization projects", Washington (DC), USA, 2003.
- [3] Department of Defense, "Unified Facilities Criteria: Design of Building to Resist Progressive Collapse", New York, USA, 2013.
- [4] Haremeza C., Satiago A., Demonceau J.F., Jaspart J.P. and Simoes da Silva L., "Composite joints under M-N at elevated tempertures", Journal of Constructional Steel Research, 124, 173-186, 2016.
- [5] Buscemi N. and Marjanishvili S., "SDOF model for progressive collapse analysis", Proceedings of the 2005 Structures Congress, New York, USA, 2005, April.
- [6] Gerasimidis S. and Sideri J., "A new partial-distributed damage method for progressive collapse analysis of steel frames", Journal of Constructional Steel Research, 119, 233-245, 2016.
- [7] Izzuddin B.A., Vlassis A.G., Elghazouli A.Y. and Nethercot D.A., "Progressive collapse of multi-storey buildings due to sudden column loss-Part 1: Simplified assessment framework", Engineering Structures, 30(5), 1308-1318, 2008.
- [8] Iribarren S.B., Berke P., Bouillard Ph., Vantomme J. and Massart T.J., "Investigation of the influence of design and material parameters in the progressive collapse analysis of RC structures", Engineering Structures, 33, 2805-2820, 2011.
- [9] Khandelwal K. and El-Tawil S., "Collapse behavior of steel special moment resisting frame connections", Journal of Structural Engineering, 133(5), 646-655, 2007.
- [10] Li Y., Lu X.Z., Guan H. and Ye L.P., "An improved tie force method for progressive collapse resistance design of reinforced concrete frame structures", Engineering Structures, 33, 2931-2942, 2011.
- [11] Stylianidis P.M. and Nethercot D.A., "Modelling of connection behaviour for progressive collapse analysis", Journal of Constructional Steel Research, 113, 169-184, 2015.
- [12] Xu G.Q. and Ellingwood B.R., "An energy-based partial pushdown analysis procedure for assessment of disproportionate collapse potential", Journal of Constructional Steel Research, 67, 547-555, 2011.
- [13] Yu X.H., Lu D.G., Qian K. and Li B., "Uncertainty and sensitivity analysis of reinforced concrete frame structures subjected to column loss", Journal of Performance of Constructed Facilities, No. 04016069, 1-14, 2016.
- [14] Yi W.J., He Q.F. and Xiao Y., "Collapse performance of RC frame structure", Journal of Building Structures, 28(5), 104-117, 2007.
- [15] Demonceau J.F. and Jaspart J.P., "Experimental test simulating a column loss in a composite frame", Advanced Steel Construction, 6, 891-913, 2010.
- [16] Sadek F., Main J.A., Lew H.S. and Bao Y.H., "Testing and analysis of steel and concrete beam-column assemblies under a column removal scenario", Journal of Structural Engineering, 9, 881-892, 2011.
- [17] Li L., Wang W., Chen Y.Y. and Lu Y., "Experimental investigation of beam-to-tubular column moment connections under column removal scenario", Journal of Constructional Steel Research, 88(5), 244-255, 2013.
- [18] Yang B., Tan K.Y., Xiong G. and Nie S.D., "Experimental study about composite frames under an internal column-removal scenario", Journal of Constructional Steel Research, 121, 341-351, 2016.
- [19] Qian K., Li B. and Zhang Z.W., "Influence of multicolumn removal on the behavior of RC floors", Journal of Structural Engineering, 142(5), 04016006, 2016.
- [20] Guo L.H., Gao S., Wang Y.Y. and Zhang S.M., "Tests of rigid composite joints subjected to bending moment combined with tension", Journal of Constructional Steel Research, Vol. 95, 44-55, 2014.
- [21] Guo L.H., Gao S. and Fu F., "Structural performance of semi-rigid composite frame under column loss", Engineering Structures, 95, 112-126, 2015.
- [22] Hoang V.L., Jaspart J.P., Demonceau J.F., "Extended end-plate to concrete-filled rectangular column joint using long bolts", Journal of Constructional Steel Research, 113, 156-168, 2015.
- [23] Ministry of Construction, "Code for Design of Steel Structures". Beijing, China, 2003.
- [24] Gao S., "Progressive collapse behavior of planar steel frame with composite beam", Ph.D. Dissertation, Harbin Institute of Technology, Harbin, 2014.

EXPERIMENTAL VS. THEORETICAL DESIGN APPROACHES FOR THIN-WALLED COLD-FORMED STEEL BEAM-COLUMNS

Nadia Baldassino¹, Claudio Bernuzzi² and Marco Simoncelli^{2,*}

¹ Department of Civil, Environmental and Mechanical Engineering, University of Trento, Trento, Italy

² Department of Architecture, Built Environment and Construction Engineering, Politecnico di Milano, Milano, Italy

(Corresponding author: E-mail: marco.simoncelli@polimi.it)

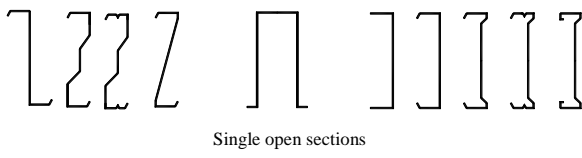
ABSTRACT

The response of thin-walled cold-formed (TWCF) members is significantly influenced by local and distortional buckling phenomena as well as by their interactions with overall instability. Furthermore, because of the frequent use of mono-symmetric cross-section members, their design is often complex and laborious engineering calculations are required, independently of the adopted provisions. With reference to the European (EU) and United States (US) design standards, which are the most commonly adopted worldwide, different alternatives can currently be used: a direct comparison between the predicted load carrying capacities should hence be of great interest for structural engineers and manufacturing technicians. This issue is discussed in the paper, which is focused on isolated TWCF beam-columns. In particular, 5 EU and 2 US alternatives have been discussed focusing attention on the pure theoretical approaches to evaluate the member performance. The applicative part proposes a direct comparison between the associated axial force bending-moment domains investigating the influence of the member slenderness as well as of the moment distribution. Furthermore, these alternatives have been applied to predict the strength of members tested in laboratory for which the behavior of an adequate number of nominally identical specimens has been thoroughly investigated. The proposed statistical re-elaboration of test data, which is comprised of 8 practical cases differing for cross-section sizes, materials and length, for a total of 112 compression tests, allows for defining the experimental design performance to be directly compared with the corresponding one associated with the considered design approaches.

Copyright © 2019 by The Hong Kong Institute of Steel Construction. All rights reserved.

1. Introduction

The use of thin-walled cold-formed (TWCF) members has recently increased throughout the more industrialized Countries for a great amount of applications [1-3] because it offers an efficient load capacity-to-weight ratio, associated with a great economy in production, transportation and handling. As a consequence, labor cost and worker fatigue are significantly reduced by guaranteeing, at the same time, great flexibility in design, high productivity and competitive levels of product standardization. Owing to these advantages, more slender and complex TWCF cross-section types (Fig. 1) are nowadays proposed to the market, which exacerbate the influence of local, distortional and global buckling phenomena and their interaction on the performance of the profiles [4-7]. In addition to a complete lightweight structural solution for residential buildings (Fig. 2), these elements are also frequently and conveniently employed as purlins and supports of roofs, cladding systems and partitions in the case of the more conventional civil and industrial steel buildings with skeleton frames made of hot-rolled profiles.



Single open sections



Built-up sections

Fig. 1 Typical TWCF cross-sections

As a result of the rapid world globalization and of the quite modest transportation costs, in recent years design, fabrication and erection sites of a growing number of TWCF solutions are often separated by few thousands of kilometers. Therefore, a general overview of the design procedures adopted by different countries should be of great interest for researchers and designers.

A recent study on conventional moment-resisting frames made of hot-rolled members [8,9] demonstrated non-negligible discrepancies among the predicted design alternatives allowed by the European (EU) [10] and United States (US) [11] provisions. In this paper, the attention is focused on isolated

ARTICLE HISTORY

Received: 03 October 2017
Revised: 20 December 2017
Accepted: 23 December 2017

KEY WORDS

Thin-walled cold-formed (TWCF) members; Effective geometric properties; Beam-column design domains; Experimental compression tests; Design approach accuracy

TWCF members and on the most common design approaches adopted in Europe and USA. In total, seven different alternatives, 5 related to the EU and 2 to the US design practice, are briefly discussed and compared, pointing out similarities and differences. Furthermore, their application is addressed to draw the bending moment-axial load resistance domains of beam-columns by considering different member slenderness and moment distributions. Finally, attention is focused on the prediction of the resistance of members tested under compression and differing for cross-section sizes, steel grade and effective length. The great amount of experimental data (in total 112 tests related to eight different cases) allows for a statistical re-elaboration of test data according to the limit states design philosophy. The experimental design performances so obtained are directly compared with those associated with the considered design approaches to assess their effective reliability for practical design purposes.



Fig. 2 Typical TWCF steel solution (courtesy of COGI s.r.l.)

2. On the assessment of the effective geometric properties

As already mentioned, TWCF member behaviour is significantly affected by buckling phenomena (local, distortional, global and their mutual interactions). From a practical point of view, design is generally based on geometric parameters (e.g. mainly area, section moduli and second moments of area) lower than the ones associated with the gross cross-section and determined

by means of methods based on the well-known effective width concept [12,13]. The generic cross-section is considered composed by sets of internal and outstand (unstiffened) elements, that are indicated as A and B components in Fig. 3, and suitable rules are proposed by codes of practice to evaluate the parts conventionally considered resisting to compressive stresses when local buckling takes place.

In the case of internal plates, the regions adjacent to the supported edges are considered to be effective in carrying compressive stresses while the ones far from supports are considered completely ineffective in resisting compression (Fig. 4a). Similarly, in case of outstand plates (Fig. 4b), the zone close to the free edge is considered not resisting, i.e. non-effective. This concept was initially introduced by von Karman et al. [14], which defined the effective width, b_e , as:

$$b_e = \left(\sqrt{\frac{\sigma_{cr}}{f_y}} \right) \cdot b \quad (1)$$

where b is the plate width, f_y is the yield stress of the material and σ_{cr} represents the critical elastic buckling stress accounting for the restraints and the compressive stress distribution.

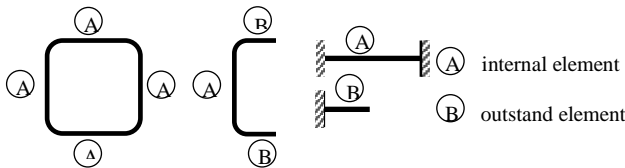


Fig. 3 Typical components of the TWCF cross-sections

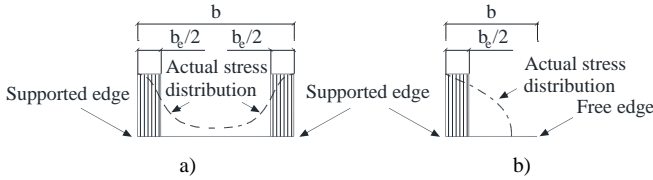


Fig. 4 Effective width for internal (a) and outstand (b) compressed plate

In 1946, Winter [15] improved this expression to also account for the effects of geometrical and mechanical imperfections and proposed to estimate the effective width by accounting for the actual stress distribution, which in case of constant stresses is defined as:

$$b_e = \left[\sqrt{\frac{\sigma_{cr}}{f_y}} \left(1 - 0.22 \cdot \sqrt{\frac{\sigma_{cr}}{f_y}} \right) \right] \cdot b \leq b \quad (2)$$

Recently, the effective width method has been improved to account for the presence of the distortional buckling, also known as "stiffener buckling" or "local-torsional buckling". This mode is characterized by the rotation of the flange at the flange/web junction in members with edge stiffened elements (Fig. 5) and may be directly studied by finite strip analysis, finite element models or, for practical applications, by using the equations proposed by the standard codes for a few cross-section types.

According to Eurocode 3 part 1-3 [16] as well as to the AISI S100 specifications [17], with reference to TWCF mono-symmetric cross-section members, different effective cross-sections (Fig. 6) have to be evaluated to assess the structural performances: one for the axial force N_{Ed} , one for the bending moment along the symmetry axis $M_{y,Ed}$ and two ($M_{z,Ed+}$ or $M_{z,Ed-}$) for bending moment along the non-symmetry axis, to be alternatively used depending on the part under compression.

Design rules for TWCF beam-columns, like the ones for the more conventional hot-rolled members, are based on approaches which combine the resistance of members under axial force with those corresponding to the cases of pure flexure along both principal cross-section axes. Verification checks are developed by using the superposition principle: on the basis of the generalized set of forces arising from the structural analysis output, the effects of N_{Ed} , $M_{y,Ed}$ and $M_{z,Ed}$ are directly added to evaluate the safety index (SI), i.e. the coefficient of utilization ranging from 0 to 1 (achievement of the limit conditions), expressed, in general terms, as:

$$SI = SI_N(N_{Ed}) + SI_M(M_{y,Ed} + \Delta M_{y,Ed}) + SI_M(M_{z,Ed+} + \Delta M_{z,Ed+}) \leq 1 \quad (3)$$

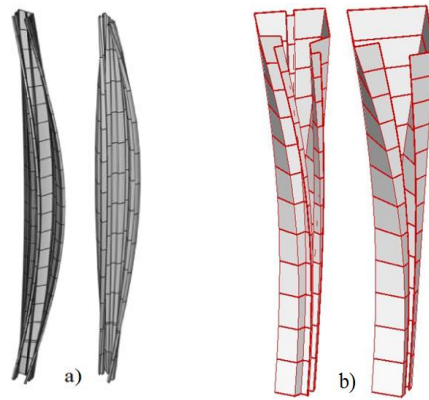


Fig. 5 Typical buckling modes for a compressed simply-supported (a) and cantilever (b) beams (obtained by means of Šiva software, courtesy of prof. A. Gobetti – University of Pavia)

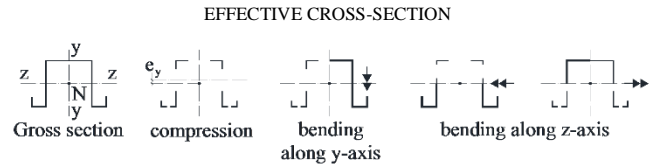


Fig. 6 Effective cross-sections to be considered for the design verification checks

where $SI_K(K_{Ed})$ represents the safety index for the generalized K force, i.e. neglecting the possible interactions with the other design components, and ΔM indicates additional secondary bending moments due to the shift between the gross and the effective centroid of the cross-section (e_y and e_z), with $\Delta M_{y,Ed} = N_{Ed}e_z$ and $\Delta M_{z,Ed} = N_{Ed}e_y$.

It should be noted that TWCF members, because of the cold-forming production process, often present a single axis of symmetry (indicated in the following as y-axis) and hence the non-coincidence between the shear center and the cross-section centroid, the coupling between bending and torsion and the warping torsion could generate an additional state of stress with normal (σ_w) and tangential (τ_w) components. These warping stresses cannot be captured by means of the traditional theory of structures, as already stated few decades ago, when thin-walled beam theory was well-established [18-20] and consequently proposed for routine design. Nevertheless, in all the TWCF design codes, with the sole exception of the Australian provisions for pallet racks [21], the presence of the bi-moment (B_{Ed}) is actually ignored, despite recent studies [22-25] have clearly indicated that also the contribution $SI_B(B_{Ed})$ should be necessarily included in eq. 3) to reach the goal of a safe and reliable structural design. Despite the importance of this issue, in the following reference is made to code requirements that are currently in use, hoping in suitable improvements of the design rules in a near future.

3. Design alternatives for TWCF members

As previously mentioned, attention is herein focused on members having a single axis of symmetry (y-axis) and hence only the additional contribution $\Delta M_{z,Ed}$ has to be considered, since only the shift of the effective geometric cross-section centroid along the y-axis is presented (i.e. $e_z=0$ and hence $\Delta M_{y,Ed} = N_{Ed}e_z = 0$). More in details, making reference to eq. 3), term SI_N depends on the effective cross-section area, A_{eff} , while term SI_{Mj} , with j indicating y- or z-axis, depends on the effective section modulus $W_{eff,j}$.

3.1. Design according to the EU alternatives

As far as design according to European TWCF provisions is concerned, the following alternatives can be considered to assess the member performance:

- a) the EC3-1-3 approach (1-3);
- b) the EC3-1-1 general method (GEM);
- c) the ENV approach (ENV);
- d) the EC3-1-1 according to method A (1-1A);
- e) the EC3-1-1 according to method B (1-1B).

In the following, a brief overview of these methods is presented.

The EC3-1-3 approach. Part 1-3 of Eurocode 3 [16] is the main European reference standard for designing TWCF members. With reference to the buckling verification checks of beam-columns, in section 6.2.5 it is declared

that "the interaction between axial force and bending moment may be obtained from a second-order analysis of the member as specified in EN 1993-1-1, based on the properties of the effective cross-section". As an alternative, the use of the following interaction formula is allowed:

$$\left(\frac{N_{Ed}}{N_{b,Rd}} \right)^{0.8} + \left(\frac{M_{y,Ed}}{M_{by,Rd}} \right)^{0.8} \leq I \quad (4a)$$

where $N_{b,Rd}$ is the design buckling resistance of a compression member according to the criteria based on the actual buckling mode (i.e. the minimum between flexural, torsional and torsional–flexural buckling load) and $M_{by,Rd}$ is the lateral buckling design strength along the y-axis that are defined as:

$$N_{b,Rd} = \chi_{min} \frac{A_{eff} \cdot f_y}{\gamma_M} \quad (5a)$$

$$M_{by,Rd} = \chi_{LT} \frac{W_{eff,y} \cdot f_y}{\gamma_M} \quad (5b)$$

where f_y is the material yield strength, γ_M is the material safety factor, A_{eff} and $W_{eff,y}$ are the effective area and the effective section modulus, respectively, and the reduction factor χ_{min} and χ_{LT} (indicated, for the sake of simplicity, as $\chi_{min/LT}$) are given by the expression:

$$\chi_{min/LT} = \frac{I}{\varphi_{min/LT}^2 + \sqrt{\varphi_{min/LT}^2 - \bar{\lambda}_{min/LT}^2}} \leq I \quad (6a)$$

with $\varphi_{min/LT}$ defined as:

$$\varphi_{min/LT} = 0.5 \cdot \left[I + \alpha(\bar{\lambda}_{min/LT} - 0.2) + \bar{\lambda}_{min/LT}^2 \right] \quad (6b)$$

where α is the imperfection coefficient associated with the stability curve and the relative slenderness $\bar{\lambda}_{min}$ (pure compression) and $\bar{\lambda}_{LT}$ (only bending moment) are defined as:

$$\bar{\lambda}_{min} = \sqrt{\frac{A_{eff} \cdot f_y}{N_{cr}}} \quad (7a)$$

$$\bar{\lambda}_{LT} = \sqrt{\frac{W_{eff,y} \cdot f_y}{M_{cr}}} \quad (7b)$$

where N_{cr} and M_{cr} are the buckling axial load and the elastic critical bending moment for lateral buckling, respectively.

It is worth noting that the use of eq. 4a) is limited to the case of mono-axial flexure. By considering the general case of a mono-symmetric cross-section member belonging to a spatial frame, this approach (herein identified as 1-3) can be directly extended to cover the general case of compressive force and bi-axial bending moments, defining the associated safety index SI_{1-3}^{EU} as:

$$SI_{1-3}^{EU} = \left(\frac{N_{Ed}}{N_{b,Rd}} \right)^{0.8} + \left(\frac{M_{y,Ed}}{M_{by,Rd}} \right)^{0.8} + \left(\frac{M_{z,Ed} + \Delta M_{z,Ed}}{M_{z,Rd}} \right)^{0.8} \leq I \quad (4b)$$

where the flexural resistance along the z-axis, $M_{z,Rd}$, is defined as:

$$M_{z,Rd} = \frac{W_{eff,z} \cdot f_y}{\gamma_M} \quad (5c)$$

The GEM approach. Eurocode 3 in its part 1-1 [10] proposes an innovative design approach [26–28], that is the so-called *general method* (GEM), appropriate also for structural components having geometrical and loading irregularities and complex support conditions. The overall buckling resistance of the whole skeleton frame is guaranteed when:

$$SI_{GEM}^{EU} = \frac{\gamma_M}{\chi_{op} \alpha_{ult}} \leq I \quad (8)$$

where α_{ult} is the minimum load multiplier evaluated with regards to the resistance of the most highly stressed cross-section, χ_{op} is the buckling reduction factor referred to the overall structural system and γ_M is the material safety factor.

Ultimate load multiplier for resistance, α_{ult} is determined as:

$$\frac{I}{\alpha_{ult}} = \frac{N_{Ed}}{N_R} + \frac{M_{y,Ed}}{M_{y,R}} + \frac{M_{z,Ed} + \Delta M_{z,Ed}}{M_{z,R}} \quad (9a)$$

where N_R is the squash load and $M_{y,R}$ and $M_{z,R}$ are the resistance moments evaluated with reference to the effective cross-section and neglecting the presence of the material safety factor γ_M .

Term χ_{op} is the reduction factor to be evaluated by using eqs. 6a) and 6b) that depends on the relative overall slenderness $\bar{\lambda}_{op}$ defined as:

$$\bar{\lambda}_{op} = \sqrt{\frac{\alpha_{ult}}{\alpha_{cr,op}}} \quad (9b)$$

where $\alpha_{cr,op}$ is the critical elastic buckling load multiplier.

The ENV approach. The previous ENV version of EC3 [29] proposed an approach to verify beam-column (herein identified as ENV approach) that has been removed from the updated EN version [10] but it is still contained in the EN 1512 [30], that is the European design standard for pallet rack design. In particular, once the effective member capacity for compression force ($N_{b,Rd}$ from eq. 5a) and for bending moments ($M_{by,Rd}$ from eq. 5b) and $M_{z,Rd}$ from eq. 5c) are defined, the associated safety index SI_{ENV}^{EU} has to meet the condition:

$$SI_{ENV}^{EU} = \frac{N_{Ed}}{N_{b,Rd}} + k_{LT} \frac{M_{y,Ed}}{M_{by,Rd}} + k_z \frac{M_{z,Ed} + \Delta M_{z,Ed}}{M_{z,Rd}} \leq I \quad (10)$$

where k_{LT} and k_z are suitable moment coefficients depending on the slenderness of the member as well as on the distribution of the bending moments along the member.

The EC3-1-1 approaches according to the A and B methods. As already mentioned, European TWCF design provisions, i.e. part 1-3 of the EC3 states that also part 1-1 [10] could be considered for member verification checks as an alternative to eqs. 3), even though the flexural-torsional buckling mode for compressed members is ignored because in the general part of EC3 attention is paid only to bi-symmetric cross-section members. The extension of this approach to members with a sole axis of symmetry is suggested by the upcoming version of the European rack design code [31], which is now in the phase of public enquiry. With reference to this extension proposal, which is of course of great interest providing practical indications to apply also the approach proposed in EC3 part 1-1 to mono-symmetric cross-section members, beam-columns have to satisfy the following conditions:

$$\frac{N_{Ed}}{N_{b,Rd}} + k_{yy} \frac{M_{y,Ed}}{M_{by,Rd}} + k_{yz} \frac{M_{z,Ed} + \Delta M_{z,Ed}}{M_{z,Rd}} \leq I \quad (11a)$$

$$\frac{N_{Ed}}{\chi_z \frac{A_{eff} \cdot f_y}{\gamma_M}} + k_{zy} \frac{M_{y,Ed}}{M_{by,Rd}} + k_{zz} \frac{M_{z,Ed} + \Delta M_{z,Ed}}{M_{z,Rd}} \leq I \quad (11b)$$

where χ_z is the reduction factors due to flexural buckling along the non-symmetry (z) axis.

The interaction factors k_{yy} , k_{yz} , k_{zy} and k_{zz} depend on the approach, which can be selected from two alternatives: method 1 (1-1A) and method 2 (1-1B), which are addressed in Annex A and Annex B of EN 1993-1-1, respectively. As to the use of these methods, the prEN pallet rack design provisions suggest only the 1-1B approach. Furthermore, it is worth underlining, as clearly stated by Boissonade et al. [32], that the 1-1B formulation, proposed by Austrian and German researchers, is generally less complex, quicker and simpler than the 1-1A developed by a team of French and Belgian researchers. Once the approach (i.e. the method A or B) to assess the k_{jk} coefficients is selected, the associated safety index, i.e. SI_{1-1A}^{EU} or SI_{1-1B}^{EU} , is defined as the maximum value from those deriving from eqs. 11a) and 11b).

3.2. Design according to the US approaches

Two approaches can be considered for which concerns the US design cold-formed design code [17], that are identified in the following as the effective width method (EWM) and the direct strength method (DSM).

The EWM approach. The first approach proposed by US design provisions for TWCF members, deriving directly by the Winter studies, is the effective width method (EWM). Like the EU alternatives previously presented, the evaluation of the effective cross-section properties under compression and bending is required. Accounting for the different US symbols to identify the cross-section principal axes, i.e. x and y instead of y and z , respectively, on the basis of the values of the design axial load (P , corresponding to N_{Ed} according to EU notation) and bending moments M_x and M_y (corresponding to $M_{y,Ed}$ and $M_{z,Ed}$, respectively), it is required that:

$$SI_{EWM}^{\text{US}} = \frac{P}{0.9 \cdot P_n} + \frac{M_x}{0.9 \cdot M_{nx}} + \frac{M_y}{0.9 \cdot M_{ny}} \leq 1 \quad (12)$$

where P_n is the nominal compression member capacity and M_{nx} and M_{ny} are the nominal bending flexural capacities, along the principal cross-section axes.

The nominal column resistance (P_n) is expressed as:

$$P_n = A_{\text{eff}} \cdot F_n \quad (13)$$

where F_n is the critical stress depending on the slenderness factor $\bar{\lambda}_c$ defined as:

$$\bar{\lambda}_c = \sqrt{\frac{F_y}{F_{cre}}} \quad (14)$$

with F_y representing the tensile yield stress of the virgin material and F_{cre} is the least of the elastic (global flexural, torsional or flexural-torsional) buckling stresses evaluated with reference to the gross cross-section properties.

In particular:

$$\cdot \text{ if } \bar{\lambda}_c \leq 1.5 \quad F_n = \left(0.658 \bar{\lambda}_c^2 \right) F_y \quad (15a)$$

$$\cdot \text{ if } \bar{\lambda}_c > 1.5 \quad F_n = \left(\frac{0.877}{\bar{\lambda}_c^2} \right) F_y \quad (15b)$$

The beam moment resistance (M_{ny}) accounting for lateral buckling is evaluated as:

$$M_n = (S_{\text{eff}} \cdot F_n) \quad (16)$$

where S_{eff} is the effective section modulus along the x -axis (symmetry) and F_n is the global flexural stress depending by the critical elastic lateral-torsional buckling stress, F_{cre} , and by the yield stress, F_y , by means of the following relationships:

$$\cdot \text{ if } F_{cre} \geq 2.78F_y \quad F_n = F_y \quad (17a)$$

$$\cdot \text{ if } 2.78F_y > F_{cre} > 0.56F_y \quad F_n = \frac{10}{9} F_y \left(I - \frac{10F_y}{36F_{cre}} \right) \quad (17b)$$

$$\cdot \text{ if } F_{cre} \leq 0.56F_y \quad F_n = F_{cre} \quad (17c)$$

The beam moment resistance along the y -axis (non-symmetry axis) is given by the expression:

$$M_{ny} = (S_{\text{eff},y} \cdot F_y) \quad (18)$$

where $S_{\text{eff},y}$ is effective section modulus.

US-DSM. Schafer and Pekoz [33] proposed the DSM approach, that is addressed in the AISI S100 Specifications [17]. In more detail, DSM includes a linear eigenvalue analysis of the elastic buckling behaviour based on the well-known finite strip method [34,35] (comprising of local, distortional and global buckling modes). Unlike all previously presented approaches, it is not required

to evaluate the effective cross-section geometric properties, i.e. the DSM method is applied directly to the gross cross-section. Actually, DSM has been proposed only for elements under pure compression or pure flexure and, in the following a linear relationship for the beam-column domains in the bending moment-axial force reference system is assumed, owing to the lack of practical indications in the code. In the case of compressed elements, the resistance is given by the minimum value between the global buckling resistance (P_{ne}), the local buckling resistance (P_{nl}) and the distortional buckling resistance (P_{nd}).

The global buckling resistance is defined similarly to eq. 13). In particular, once evaluated the squash load (P_y) and the overall critical load (P_{cre}), the overall buckling resistance, P_{ne} , is defined as:

$$\cdot \text{ if } \bar{\lambda}_c \leq 1.5 \quad P_{ne} = \left(0.658 \bar{\lambda}_c^2 \right) P_y \quad (19a)$$

$$\cdot \text{ if } \bar{\lambda}_c > 1.5 \quad P_{ne} = \left(\frac{0.877}{\bar{\lambda}_c^2} \right) P_y \quad (19b)$$

being the slenderness factor $\bar{\lambda}_c$ defined as:

$$\bar{\lambda}_c = \sqrt{\frac{P_y}{P_{cre}}} \quad (19c)$$

The axial strength for local buckling (P_{nl}) depends on the local slenderness factor $\bar{\lambda}_l$ defined as:

$$\bar{\lambda}_l = \sqrt{\frac{P_{ne}}{P_{crl}}} \quad (20a)$$

and

$$\cdot \text{ if } \bar{\lambda}_l \leq 0.776 \quad P_{nl} = P_y \quad (20b)$$

$$\cdot \text{ if } \bar{\lambda}_l > 0.776 \quad P_{nl} = \left[1 - 0.15 \left(\frac{P_{crl}}{P_{ne}} \right)^{0.4} \right] \left[\left(\frac{P_{crl}}{P_{ne}} \right)^{0.4} \cdot P_{ne} \right] \quad (20c)$$

where P_{crl} is the elastic critical load for local buckling.

The nominal axial strength for distortional buckling (P_{nd}) depends on the distortional slenderness factor $\bar{\lambda}_d$ defined as:

$$\bar{\lambda}_d = \sqrt{\frac{P_y}{P_{cnd}}} \quad (21a)$$

and

$$\cdot \text{ if } \bar{\lambda}_d \leq 0.561 \quad P_{nd} = P_y \quad (21b)$$

$$\cdot \text{ if } \bar{\lambda}_d > 0.561 \quad P_{nd} = \left[1 - 0.25 \left(\frac{P_{cnd}}{P_{ne}} \right)^{0.6} \right] \left[\left(\frac{P_{cnd}}{P_{ne}} \right)^{0.6} \cdot P_{ne} \right] \quad (21c)$$

where P_{cnd} is the elastic critical load for distortional buckling.

The overall (P_{cre}), local (P_{crl}) and distortional (P_{cnd}) critical buckling loads, can be easily obtained by using the tools available [36-38] for the study of TWCF members. Fig. 7 shows the typical relationship between the critical load and the half-wave length by considering all the relevant buckling modes, obtained by means of the CUFSM software developed and freely offered by Schafer [36].

Similarly, in the case of elements subjected to bending, the flexural resistance is given by the minimum value between the beam moment resistance (M_{nx}) accounting for lateral buckling (M_{ne}), local (M_{nl}) and distortional buckling flexural (M_{nd}) resistance.

For the global buckling resistance (M_{ne}), the following relationships have to be considered:

$$\cdot \text{ if } M_{cre} \geq 2.78M_y \quad M_{ne} = M_y \quad (22a)$$

- if $2.78M_y > M_{cre} > 0.56M_y$ $M_{ne} = \frac{10}{9}F_y \left(I - \frac{10M_y}{36M_{cre}} \right)$ (22b)

- if $M_{cre} \leq 0.56M_y$ $M_{ne} = M_{cre}$ (22c)

where M_{cre} is the elastic critical moment for global buckling and M_y is the yield moment.

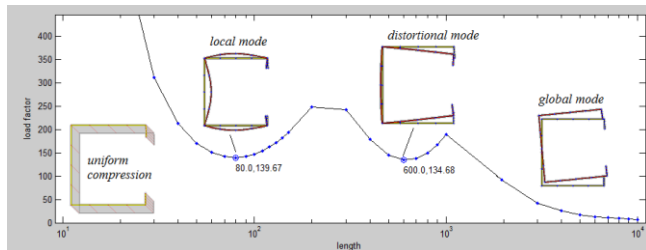


Fig. 7 Evaluation of local and distortional buckling loads for an element under compression (obtained by using CUFSM software by prof. Schafer [36])

In case of elements in bending, the flexural resistance for local buckling (M_{nl}) depends on the local slenderness factor $\bar{\lambda}_l$ defined as:

$$\bar{\lambda}_l = \sqrt{\frac{M_{ne}}{M_{crl}}} \quad (23a)$$

and

- if $\bar{\lambda}_l \leq 0.776$ $M_{nl} = M_{ne}$ (23b)

- if $\bar{\lambda}_l > 0.776$ $M_{nl} = \left[1 - 0.15 \left(\frac{M_{crl}}{M_{ne}} \right)^{0.4} \right] \left(\frac{M_{crl}}{M_{ne}} \right)^{0.4} \cdot M_{ne}$ (23c)

where M_{crl} is the elastic critical moment for local buckling.

The nominal flexural strength for distortional buckling (M_{nd}) depends on the associated slenderness factor $\bar{\lambda}_d$ defined as:

$$\bar{\lambda}_d = \sqrt{\frac{M_y}{M_{crd}}} \quad (24a)$$

and

- if $\bar{\lambda}_d \leq 0.673$ $M_{nd} = M_y$ (24b)

- if $\bar{\lambda}_d > 0.673$ $M_{nd} = \left[1 - 0.22 \left(\frac{M_{crd}}{M_y} \right)^{0.5} \right] \left(\frac{M_{crd}}{M_y} \right)^{0.5} \cdot M_y$ (24c)

where M_{crd} is the elastic critical moment for distortional buckling.

Also in this case, the critical elastic moments for global (M_{cre}), local (M_{crl}) and distortional (M_{crd}) buckling modes can be easily obtained by finite strip analysis. Fig. 8 can be considered as an example of the relationship between the critical moment versus the half-wave length accounting for the relevant buckling modes.

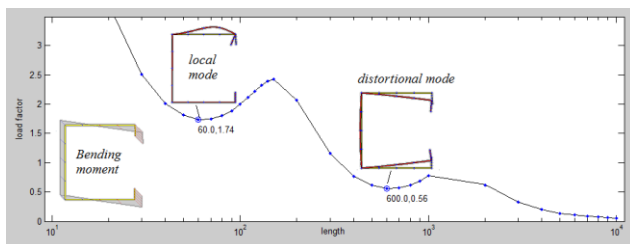


Fig. 8 Evaluation of local and distortional buckling moments for an element under bending (obtained by using CUFSM software by prof. Schafer [36])

Furthermore, it is worth mentioning that the DSM approach will probably be included among the European alternatives to design TWCF members in the next

few years, as attested by the recent attention paid in Europe by researchers [39,40]. Finally, in the Authors' opinion, DSM seems also very promising if applied to the design of steel storage uprights, i.e. TWCF perforated members that are the vertical elements of the skeleton frame directly supporting goods and materials, as demonstrated by the recent researches of Casafont et al. [41], VijayaVengadesh [42], VijayaVengadesh and Arul Jayachandran [43] and Moen [44].

4. Comparison between the different approaches

Table 1

Similarities and differences related to the EU and US approaches for TWCF members

	EU approaches					US approaches	
	1-3	GEM	ENV	1-1A	1-1B	EWM	DSM
Effective geometric properties	Y	Y	Y	Y	Y	Y	N
Secondary bending moments due to the shift of the centroids	Y	Y	Y	Y	Y	Y	N
Equivalent moment coefficient	N	N	Y	Y	Y	Y	Y
Direct interaction between different buckling modes	N	N	N	N	N	Y	Y
M-N linear domain	N	N	N	N	N	Y	Y
Mandatory code alternative	Y	Y	N	N	N	Y	Y

N= No; Y=Yes

As discussed in the previous sections, EU and US standards offer to designers different options for the verification checks of isolated members subjected to axial force and bending moments. The main similarities and differences are pointed out in Table 1. In particular, it is worth noting that:

- all the approaches are based on the theoretical assessment of the effective geometric properties under compression and bending, with the sole exception of the US-DSM;
- a quite complex evaluation of the equivalent moment coefficients is required only by ENV, 1-1A and 1-1B approaches. Otherwise, the maximum value of the bending moment on the member along each principal axis have to be considered;
- all the approaches need complex calculations with the exception of the DSM method which requires the definition of the complete buckling curve considering all the possible critical buckling modes, including the local and distortional ones. In this case, suitable free tools are however offered to engineers for routine design;
- only the EC3-1-3, GEM, EWM and DSM approaches are presently mandatory.

The interest is hence to investigate how these similarities and differences could eventually reflect in the member resistance. Attention has consequently been focused on simply supported beam-columns under moment gradient, which are frequently encountered in routine design. Both cases of equal and opposite bending end moments along the axis of symmetry have been investigated by considering the presence of a constant bending moment in the symmetry plane accounting for the gross-to-effective centroid shift. The cross-section is a typical lipped channel with a stiffened web made of steel grade S355 [45], with yield and ultimate nominal strength of 355 N/mm² and 490 N/mm², respectively. Owing to the confidentiality required by the steel manufacture, the geometry of this cross-section cannot be herein directly presented. However, it is worth noting that the domains proposed in the following and the associated outcomes are, in general, adequately representative for any type of TWCF members, independently of the cross-section type and slenderness of its plates.

At first, attention is focused on the domains drawn according with the European approaches, which are proposed in Figs. 9 and 10. They are related to the cases of equal and opposite end moments, respectively, by considering quite stocky and slender members, corresponding to a relative minimum slenderness for axial buckling (eq. 7a) of $\bar{\lambda}_{min} = 0.6$ (solid lines) and $\bar{\lambda}_{min} = 1.5$ (dashed lines), respectively. For the limit case of a beam, i.e. a member under mono-axial flexure, lacking the axial force and hence the associated secondary moment due to the centroid shift, all the approaches lead to similar values of flexural resistance: differences are within 5% and are mainly due to the absence of the equivalent moment factor in the GEM and 1-3 approaches. For what concerns member response to pure compression (and secondary bending along the symmetry plane), the load carrying capacities are practically equal if the 1-3, 1-1A, 1-1B and GEM approaches are compared (difference within 2%): the 1-3 approach is slightly more conservative than the others and differences are up to 17%, owing to the presence of the exponent (0.8) in the interaction domain in eq. 4b). As far as the beam-column domains are concerned, the interaction formula associated with the ENV approach defines a linear domain between the

axial force and the bending moment. Furthermore, the most conservative approach is the 1-3, which always defines a convex domain, independently of the member slenderness and of the bending moment distribution. In case of constant moment (Fig. 9), no significant differences can be detected between the 1-1A, 1-1B, ENV and GEM approaches: a moderate difference is observed if these four domains are compared with those of the 1-3 approach defining a slightly concave (and hence, in general, more severe) domain.

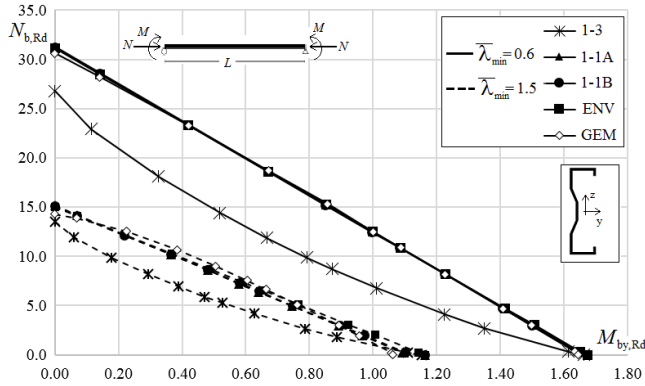


Fig. 9 Typical beam-column EU domains for the case of constant bending moment

In the case of moment gradient (Fig. 10), the previous remarks on the limit cases of beams and columns are confirmed, while, in case of beam-columns, the differences between the considered approaches are more evident with respect to the case of constant end moments, especially by comparing the 1-1A, GEM and ENV domains. The least conservative performances are guaranteed by the 1-1B approach, especially for the greatest value of slenderness while the most severe is again associated with the 1-3 approach.

As to the US domains, owing to the need to focus attention on the key innovative issues of the research, it has been decided to consider only the DSM approach, considering that EWM is based on the evaluation of the effective geometric parameters like all the EU methods. In particular, the same practical cases already discussed for the EU alternatives have been considered. Figs. 11 and 12, corresponding to Figs. 9 and 10, respectively, present the DSM domains compared with those of the 1-3 and GEM approaches, which are the most commonly adopted in practical design according to the EU alternatives.

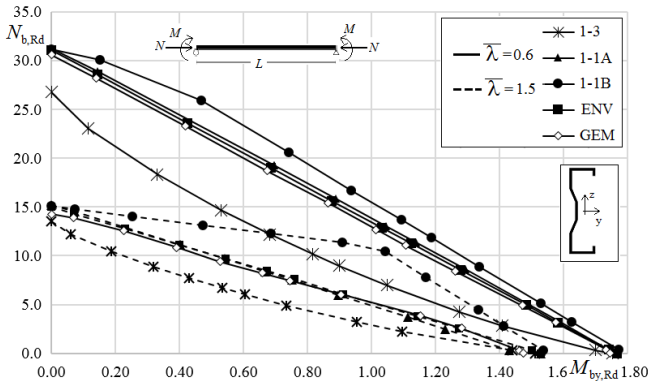


Fig. 10 Typical beam-column EU domains for the case of opposite end bending moments

As to the ideal cases of columns, it can be noted that the DSM approach leads to a less conservative assessment of the load carrying capacity if compared to the 1-3 approach, up to 6% and 10%, for $\bar{\lambda}_{min} = 0.6$ and $\bar{\lambda}_{min} = 1.5$, respectively. Otherwise, DSM is slightly more conservative than GEM but differences are however not greater than 3%. As to beams, non-negligible differences are observed independently of the member slenderness and bending moment diagram: the DSM approach is the most conservative, up to 30% and 34% with respect to 1-3 and GEM approaches, respectively. As to the beam-column domains, the DSM trend has been assumed to be linear and only for high values of the applied axial force, DSM appears to be less conservative than 1-3; otherwise, increasing the value of the bending moments, DSM becomes the most conservative approach.

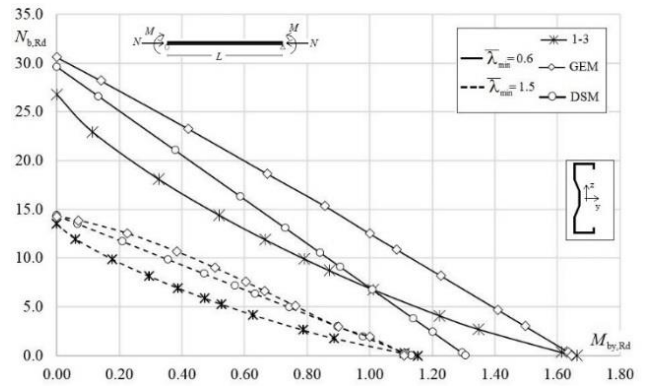


Fig. 11 Typical beam-column EU and US domains for constant bending moment

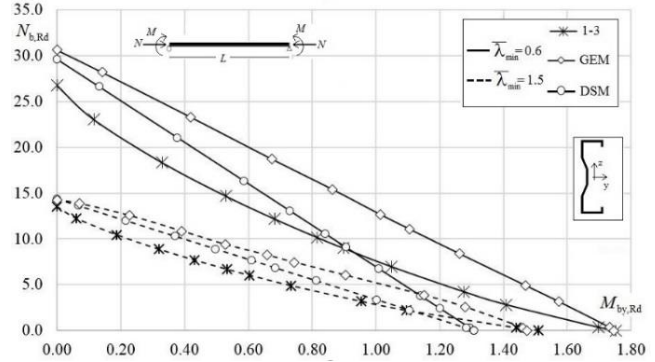


Fig. 12 Typical beam-column EU and US domains for opposite bending moments

A summary of the Figs. 9–12, which are of great interest for practical design purposes, is proposed in Table 2, where selected values of the couple axial force-bending moment have been considered, in terms of load carrying capacity (LCC), which is identified via the α_{ecc} angle representing the angle between the vertical (axial) axis and a generic straight line through the origin (Fig. 13). In case of columns and beams, the LCC coincides with the axial and flexural resistance, respectively.

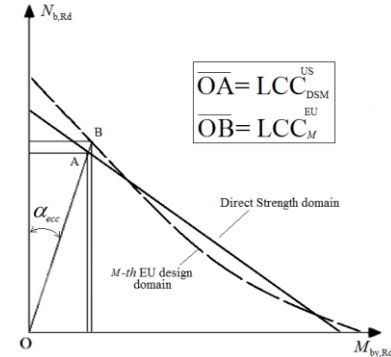


Fig. 13 Details for the identification of the cases considered in Table 3

The following values of α_{ecc} have been considered: 0° (only axial force and secondary bending moment along the non-symmetry axis), $2^\circ, 5^\circ, 30^\circ, 45^\circ, 75^\circ$ and 90° (pure flexure along both axes). These values have been selected to obtain a representative approximation of the whole domain. In order to allow for a direct comparison, the load carrying capacities associated with the considered EU alternatives have been divided by the one obtained via the US-DSM approach, that is the sole method based on the gross cross-section geometry. In the Table 2, for each set of data defining the domain, the mean (*mean*), the maximum (*Max*) and the minimum (*min*) values are reported together with the standard deviation (*dev.*) evaluated according to eq. 31) by assuming the number of data equal to seven. From those data, it appears that the differences in terms of LCC are not negligible for practical design purposes. In case of the 1-3 approach, which is the most conservative among the EU alternatives, the ratio $LCC_{1-3}^{EU}/LCC_{DSM}^{US}$ ranges from 0.88 and 1.34 for stocky members while it is comprised between 0.83 and 1.15 for slender members.

Table 2

Load carrying capacity of the EU alternatives over the DSM one

$\bar{\lambda}_{min}$ [deg]	α_{ecc}	Bending moment distribution type									
		Equal end moments			Opposite end moments						
		$\frac{LCC_{1-3}^{EU}}{LCC_{DSM}^{US}}$	$\frac{LCC_{GEM}^{EU}}{LCC_{DSM}^{US}}$	$\frac{LCC_{ENV}^{EU}}{LCC_{DSM}^{US}}$	$\frac{LCC_{1-1A}^{EU}}{LCC_{DSM}^{US}}$	$\frac{LCC_{1-1B}^{EU}}{LCC_{DSM}^{US}}$	$\frac{LCC_{1-3}^{EU}}{LCC_{DSM}^{US}}$	$\frac{LCC_{GEM}^{EU}}{LCC_{DSM}^{US}}$	$\frac{LCC_{ENV}^{EU}}{LCC_{DSM}^{US}}$	$\frac{LCC_{1-1A}^{EU}}{LCC_{DSM}^{US}}$	$\frac{LCC_{1-1B}^{EU}}{LCC_{DSM}^{US}}$
0.6	0°	0.90	1.03	1.05	1.06	1.05	0.90	1.03	1.05	1.06	1.05
	2°	0.88	1.14	1.14	1.14	1.14	0.90	1.15	1.17	1.18	1.26
	5°	0.96	1.20	1.20	1.20	1.19	0.99	1.22	1.24	1.26	1.31
	30°	1.07	1.24	1.24	1.24	1.24	1.12	1.29	1.30	1.31	1.34
	45°	1.12	1.25	1.25	1.25	1.25	1.17	1.31	1.32	1.32	1.35
	75°	1.25	1.26	1.27	1.27	1.27	1.31	1.34	1.34	1.34	1.37
	90°	1.27	1.26	1.28	1.28	1.28	1.34	1.34	1.35	1.35	1.35
	mean	1.07	1.20	1.21	1.21	1.20	1.11	1.24	1.25	1.26	1.29
	dev.	0.1575	0.0830	0.0838	0.0808	0.0811	0.1814	0.1135	0.1100	0.1068	0.1101
	Max	1.27	1.26	1.28	1.28	1.28	1.34	1.34	1.35	1.35	1.37
	Min	0.88	1.03	1.05	1.06	1.05	0.90	1.03	1.05	1.06	1.05
1.5	0°	0.94	0.99	1.05	1.06	1.05	0.94	0.99	1.05	1.06	1.05
	2°	0.83	1.08	1.04	1.03	1.03	0.86	1.06	1.08	1.08	1.28
	5°	0.83	1.05	1.03	1.01	1.01	0.88	1.09	1.11	1.10	1.52
	30°	0.88	0.99	1.03	0.99	1.00	0.95	1.15	1.14	1.11	1.33
	45°	0.90	0.98	1.03	0.99	0.99	0.99	1.16	1.15	1.11	1.28
	75°	0.99	0.95	1.02	0.98	0.99	1.12	1.14	1.17	1.11	1.20
	90°	1.02	0.98	1.03	1.03	1.03	1.15	1.13	1.17	1.17	1.17
	mean	0.91	1.00	1.03	1.01	1.01	0.99	1.10	1.12	1.11	1.26
	dev.	0.0750	0.0459	0.0080	0.0286	0.0230	0.1129	0.0597	0.0470	0.0342	0.1473
	Max	1.02	1.08	1.05	1.06	1.05	1.15	1.16	1.17	1.17	1.52
	Min	0.83	0.95	1.02	0.98	0.99	0.86	0.99	1.05	1.06	1.05

The GEM approach results on average 22% less conservative than the DSM one for $\bar{\lambda}_{min} = 0.6$ and 5% for $\bar{\lambda}_{min} = 1.5$. No great differences can be observed for the remaining alternatives, with the exception of the 1-1B approach, that has been already identified as the least conservative. In this case, the associated ratio reaches the value of 1.52 for opposite moment on the slender elements, significantly higher than the ones corresponding to the other approaches, never greater than 1.17. It can hence be preliminarily concluded that these alternatives are not equivalent to each other and these different values of the LCC are expected to have a great impact on the design and consequently on the cost and the competitiveness of the products on the market.

5. Experimental assessment of the TWCF member performance

With the exception of the DSM approach, as already mentioned, the other procedures considered in this paper require to theoretically assess the effective resisting cross-sections. Two weakness points associated with the effective width method are i) its field of applicability, which is limited only to few typical cross-section types (i.e. mainly lipped channels and zed, owing to the difficulties of defining the local/distortional buckling interaction), and ii) the ambiguity in few statements, found in codes, that can be interpreted in different ways, as already observed [46,47]. In order to overcome these problems, a “design assisted by testing” procedure could be alternatively adopted, according, as an example, to the general requirements of Appendix D (“Design assisted by testing”) of EN1990 [48] and to the indications addressed in Appendix A (“Testing procedure”) of EN 1993-1-3 [16]. In particular, the key step is the definition of the characteristic value of the considered design performance. To this end, two alternatives are prescribed, depending on the number of tests on nominally equal specimen is small or large. In the former case, the number of specimens is limited to three. The characteristic parameter of interest R_k associated in case of a sole individual test R_i , eventually adjusted/corrected for thickness and yield stress, can be estimated as:

$$R_k = 0.9 \cdot \eta_k \cdot R_i \quad (25)$$

where η_k depends strictly on failure modes such as yielding failure ($\eta_k = 0.9$), gross deformation ($\eta_k = 0.9$), local buckling (from $\eta_k = 0.8$ to $\eta_k = 0.9$ depending on effects on global behavior in tests) and overall instability ($\eta_k = 0.7$).

For a family of two or three tests, provided that each R_i value is within $\pm 10\%$ of the mean value R_m of all the test results, R_k is defined as:

$$R_k = \eta_k \cdot R_i \quad (26)$$

In case of a large number of specimens, i.e. when the number of tests (n) on nominally equal specimens is not less than three, R_k can be assessed as:

$$R_k = R_m - k_s \cdot s \quad (27)$$

where R_m is the mean value of the adjusted test results, k_s is the well-known coefficient based on 95% fractile at a confidence level of 75% (Table 3) and s is the standard deviation defined as:

$$s = \sqrt{\frac{1}{n-1} \sum_{i=1}^n (R_i - R_m)^2} \quad (28)$$

Table 3Values of the k_s coefficients

n	3	4	5	6	8	10	20	30	∞
k_s	3.37	2.63	2.33	2.18	2.08	1.92	1.76	1.73	1.64

If design assisted-by-testing is adopted to assess directly the axial or the flexural resistance, by means of stub column tests (Fig. 14), compressive tests or bending tests, the design values can be obtained directly by using the material safety coefficient γ_M reducing the characteristic value obtained by means of eqs. 28)-30).



Fig. 14 Collapse of lipped angle specimen for interaction between local and distortional buckling

6. Experimental validation of the design procedures

An open question of outstanding interest from the practical point of view is

associated with the evaluation of the actual level of safety of the design approaches discussed in the previous sections: in other words, if the EU-1-1A approach is on the safe side, all the others, and especially the EU-1-3 and US-DSM approach, should result greatly conservative. Otherwise, if the US-DSM, or the EU-1-3 are unconservative, a fortiori, the others lead to a design that should be dangerously unsafe. Experimental results could hence be really useful to define the actual degree of accuracy of the different design alternatives but in many researches, only one or at least two nominally equal specimens have been tested. Test results are in general directly compared by researchers with the results associated with one design approach without any rigorous definition of the characteristic and design experimental values. The sole exception is represented by few experimental campaigns that were carried out on a large number of nominally equal specimens, which have been considered in the present study. The final aim is to compare the experimental load carrying capacity suitably assessed via a statistical re-elaboration of the experimental data according to eq. 30) with the performance estimated by using the discussed design alternatives. In the following, reference is made to four experimental studies [49-54] characterized by tests on three or more nominally equal specimens, i.e. on a more than adequate number of tests for a statistical analysis matching the limit state design philosophy.

A summary of the considered cross-sections is shown in Table 4 where the slenderness of the web (h/t), of the flanges (b/t) and of the lip (c/t) are reported together with the length of the tested specimens and the ratio between the distance (d_g) between the gross-section centroid and the web over the distance between the effective cross-section centroid and the web (d_{eff}). In the case of lipped channels, the d_g/d_{eff} ratio is lower than unity, ranging between 0.842 and 0.987: secondary bending moments induce tension on the web. Otherwise, with plane channels as well as with lipped channels with stiffened web the effective cross-section centroid moves close to the web, inducing a non-negligible secondary moment with compression on the web.

Table 4
The considered cross-section type

ID	h/t	b/t	c/t	L_o [mm]	d_g/d_{eff}	Cross-section	Reference
U2	48.00	24.00	7.00	370	0.946		[49]
U1.2	80.00	41.33	12.33	360	0.916		
U0.8	120.00	63.00	19.00	360	0.896		
UNLIP1	66.79	40.91	-	400	3.763		
UNLIP2	66.11	40.56	-	398	3.724		[50,51]
UNLIP3	64.63	38.33	-	398	3.585		
LIP1	81.34	43.61	13.89	400.2	0.985		
LIP2	84.08	45.08	14.36	398	0.987		
LIP3	83.09	44.59	13.43	402.5	0.984		[50,51]
LIP4	84.12	44.92	13.66	400	0.987		
C1 - C3	76.42	73.58	11.32	2850	0.818		
C4 - C6	70.09	60.75	10.28	2350	0.851		[52]
A100	100.00	57.00	4.90	300 - 550	1.239		
B100	83.33	47.50	4.08	300 - 550	1.215		
A150	150.00	57.00	4.90	350 - 650	1.294		
B150	125.00	47.50	4.08	350 - 650	1.277		
A200	200.00	57.00	4.90	450 - 750	1.183		
B200	166.67	47.50	4.08	450 - 750	1.234		[53,54]

In particular, useful data have been derived from the following researches:

- in 1992, Pu et al. [4,9] investigated the behavior of solid and perforated lipped channels, focusing attention on the prediction of the ultimate load capacity. Several specimens were tested differing for the presence and position of perforations as well as for their geometry. Referring to the cases of solid cross-sections, which is of interest for the present paper, 3 different thicknesses (2mm, 1.2mm and 0.8mm) have been considered and for each of them 3 nominally equal specimens have been tested;
- in 2003, Feng et al. [50,51] analyzed the influence of the temperature on the response of plain as well as lipped channel columns. Only data related to ambient temperature tests are herein considered and in particular, 3 tests on plain channels and 4 tests on lipped channels;
- in 2012, dos Santos et al. [52], focused attention on stainless steel lipped channels and tested two series of specimens, differing for the materials and for the procedure adopted to ensure fixed column end supports. Two sets of results, each of them related to three nominally equal specimens, have been considered in the present study;
- in 2014, Baldassino et al. [53,54] executed stub column tests on 6 different lipped channel cross-sections with stiffened web. Three cross-section types

have been considered, differing for the web height (i.e. 100mm, 150mm and 200mm). For each of them, two different thicknesses were considered: 1mm and 1.2mm were used for A and B specimens, respectively. For each web height and for each thickness, three set of stub-column tests on different column length were carried out on five nominally equal specimens. It is worth noting that Figs. 9-12 are related to the A200 cross-section type.

For all these specimens, the theoretical load carrying capacity has been evaluated according to the European 1-3, GEM, ENV, 1-1A and 1-1B and United States DSM approaches. It can be noted that all the considered specimens satisfy the requirements for the applicability of the considered design approaches.

Two different alternatives can be adopted to assess the degree of accuracy of the design approaches on the basis of experimental data. The first is to compare directly the load carrying capacity associated with the generic M -th approach according to the L -code (LCC_M^L) with the single test result, indicated in the following as LCC_{EXP} , and this is the way most commonly adopted by researchers. In this way it is not possible however to assess the reliability of the method with respect to the requirements associated with the semi-probabilistic limit state design methods. The second, is to compare LCC_M^L with the associated experimental design value (LCC_{DES}^{DES}), obtained by means of a statistical re-elaboration of test data, according to the procedures previously discussed. In the following, according to EC3-1-3 $\gamma_M=1$ has been assumed, i.e. the design value is coincident with the characteristic one.

Figs. 15 and 16 present the results related to the LCC_M^L/LCC_{DES}^{DES} and LCC_M^L/LCC_{EXP} ratios grouping the 1-1A, 1-1B, GEM and ENV results in the first and the DSM and 1-3 results in the second Fig.. In both Figs., straight lines in correspondence of unity allow to appraise directly when the theoretical method is on the safe or unsafe side, i.e. the ratio is lower or greater than 1, respectively. Furthermore, a red box, grouping the $LCC_M^L/LCC_{DES}^{DES} > 1$ and $LCC_M^L/LCC_{EXP} < 1$ points, identifies the cases where the theoretical method is safe only with respect to a direct comparison with the experimental data, i.e. the experimental design performance is lower than the theoretical one.

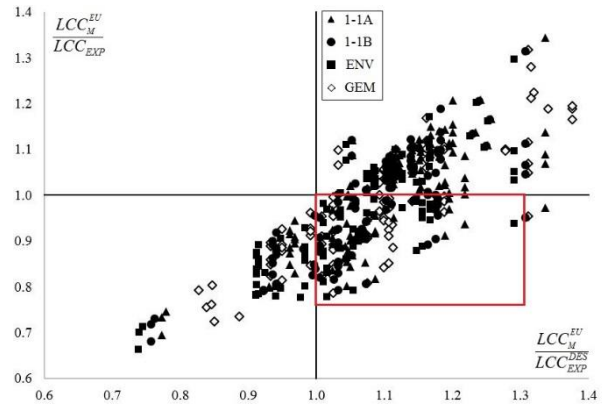


Fig. 15 LCC_M^L/LCC_{DES}^{DES} versus LCC_M^L/LCC_{EXP} ratio for the 1-1A, 1-1B, GEM and ENV approaches

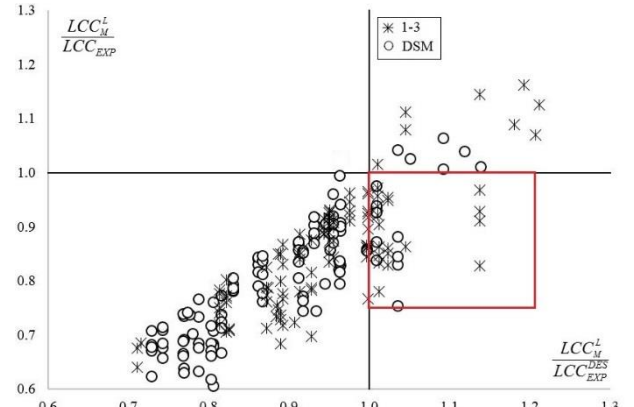


Fig. 16 LCC_M^L/LCC_{DES}^{DES} versus LCC_M^L/LCC_{EXP} ratio for the 1-3 and DESM approaches

By considering the first set of approaches (i.e. 1-1A, 1-1B, ENV and GEM) in 17% of the cases both LCC_M^L/LCC_{DES}^{DES} and LCC_M^L/LCC_{EXP} values are lower than unity, while in 48% they both exceed unity. In the remaining cases, (approximately 35% of the total cases) the direct use of the experimental data reflects the mistaken belief that the method is on the safe side. Otherwise, by

considering Fig. 16, which is related to the 1-3 and DSM approaches, it can be observed that unity is exceeded or not by both the ratios in 6% and 80% of the cases, respectively. The data in the red box are mainly related to the 1-3 approach, considering that points representative of the DSM is quite limited (only 14% of the total points within the box). Independently of the method to assess the structural performance, a non-negligible discrepancy between the experimental result and the predicted theoretical one clearly appears.

Furthermore, to compare directly these design alternatives with reference to the two approaches to deal with experimental data, Fig. 17 proposes the cumulative density function (CDF) of the LCC_M^L/LCC_{EXP}^{DES} (solid line) and LCC_M^L/LCC_{EXP} (dashed line) ratios related to the sole 1-3, GEM and DSM approaches, which are the most commonly adopted. According to the limit state design philosophy reference can be made to the 95% fractile value that is directly boxed in the Fig.: this characteristic value ranges from 0.99 to 1.20 and from 1.04 to 1.33 if reference is made to the experimental and to the design experimental strength, respectively. It is confirmed that, in general, the most conservative approach is the DSM, even though in a number of cases that is non-negligible for practical design purposes the strength is overestimated.

Finally, focusing attention on the sole LCC_M^L/LCC_{EXP}^{DES} ratio, which is, in the Authors' opinion, the most consistent with the limit states design philosophy, reference can be made to Table 5. For each set of data as well as for all results grouped together, the mean, maximum and minimum values are reported with the associated standard deviation. It can be observed that only in a very limited number of cases, the DSM is on the unsafe side: otherwise it underestimates on average quite moderately the experimental design values, up to of 22%. As far as the other EU approaches, only the 1-3 approach seems of interest for practical design purposes, despite the fact that for few families, the design experimental value of the strength is however overestimated, up to 25%.

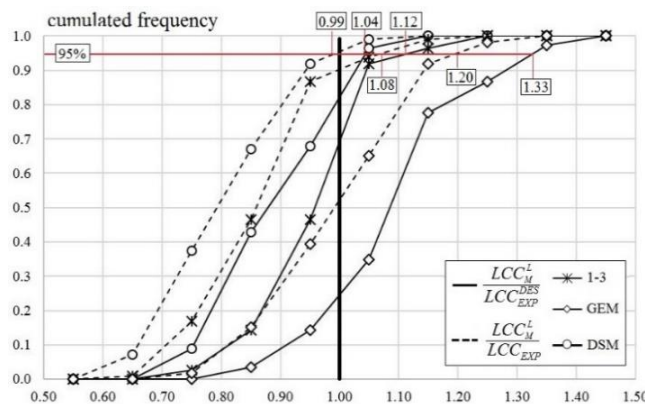


Fig. 17 Cumulative density function of the LCC_M^L/LCC_{EXP}^{DES} and LCC_M^L/LCC_{EXP} ratios

7. Concluding remarks

Alternative approaches can be adopted to design TWCF steel beam-columns according to the EU and US standard codes and, in the present paper, 7 different alternatives have been considered discussing their similarities and differences. The design domains, which have been proposed in terms of relationships between axial and flexural resistances along the symmetry axis, are significantly different from each other, reflecting, from the practical point of view, in different values of the load carrying capacity, or, equivalently, in non-comparable degrees of competitiveness of the members on the market. Owing to the interest in investigating the actual degree of safety of these alternatives, the axial resistance of compressed members has been evaluated, for which the data related to experimental results are available in literature. In particular, attention has been focused on experimental studies which comprised tests on three or more nominally equal specimens, in order to allow for a statistical evaluation of the experimental load carrying capacity. A direct comparison between the predicted values and the experimental one (expressed by the ratio LCC_M^L/LCC_{EXP}) attests that, especially the methods requiring the assessment of the effective width are unsafe. By considering the design experimental resistance obtained via a statistical treatments of test data, the value of the LCC_M^L/LCC_{EXP}^{DES} ratio increases, becoming significantly greater than 1, also for the DSM approach, which however is the most conservative.

As a further activity [55], the Authors also intend to extend this study to a small family test in order to calibrate a suitable safety factor to be adopted in routine design in addition to those already recommended.

Table 5

Values of the LCC_M^L/LCC_{EXP}^{DES}

Cross-section (spec. number)	$\frac{LCC_{EU_1-3}^L}{LCC_{EXP}}$	$\frac{LCC_{EU_GEM}^L}{LCC_{EXP}}$	$\frac{LCC_{EU_INV}^L}{LCC_{EXP}}$	$\frac{LCC_{EU_A/B}^L}{LCC_{EXP}}$	$\frac{LCC_{EU_1B}^L}{LCC_{EXP}}$	$\frac{LCC_{US_TWCF}^L}{LCC_{EXP}}$
9 lipped channels [49]	mean	0.96	1.23	1.01	1.02	1.01
	dev.	0.0999	0.1535	0.0712	0.0658	0.0690
	Max	1.05	1.38	1.06	1.07	1.00
3 plain channel [50,51]	min	0.83	1.03	0.91	0.93	0.92
	mean	0.71	0.84	0.74	0.77	0.76
	dev.	0.0026	0.0115	0.0034	0.0037	0.0034
4 lipped channel [50,51]	Max	0.72	0.85	0.74	0.78	0.76
	min	0.71	0.83	0.74	0.77	0.77
	mean	1.20	1.32	1.24	1.25	1.24
3 lipped channels [52]	dev.	0.0143	0.0121	0.0115	0.0107	0.0111
	Max	1.21	1.34	1.25	1.26	1.26
	min	1.18	1.32	1.23	1.23	1.09
3 lipped channels [52]	mean	0.88	0.86	0.93	1.04	0.99
	dev.	0.0064	0.0255	0.0092	0.0087	0.0088
	Max	0.89	0.89	0.94	1.04	1.00
	min	0.87	0.84	0.92	1.03	0.98
3 lipped channels [52]	mean	0.89	1.11	0.96	1.06	1.01
	dev.	0.0119	0.0011	0.0170	0.0148	0.0158
	Max	0.91	1.11	0.98	1.07	1.03
	min	0.89	1.11	0.95	1.05	1.00
30 lipped channels [53,54]	mean	0.87	1.00	0.98	1.02	1.00
	dev.	0.0409	0.0490	0.0533	0.0458	0.0506
	Max	0.93	1.07	1.05	1.09	1.07
	min	0.81	0.93	0.91	0.96	0.94
30 lipped channels [53,54]	mean	0.96	1.12	1.10	1.16	1.12
	dev.	0.0232	0.0224	0.0319	0.0247	0.0295
	Max	1.01	1.16	1.17	1.20	1.18
	min	0.94	1.09	1.07	1.12	1.10
30 lipped channels [53,54]	mean	1.01	1.14	1.15	1.21	1.17
	dev.	0.0670	0.0986	0.0762	0.0679	0.0748
	Max	1.14	1.31	1.29	1.34	1.31
	min	0.91	0.99	1.04	1.11	1.05
112 tests: 109 lipped channels + 3 plain channels	mean	0.94	1.08	1.01	1.06	1.04
	dev.	0.1389	0.1688	0.1528	0.1465	0.1465
	Max	1.21	1.38	1.29	1.34	1.31
	min	0.71	0.83	0.74	0.77	0.76

Appendix A: List of symbols

Latin upper case letters

A_{eff} = effective cross-section area.

B_{Ed} = Bimoment .

F_{cre} = the least elastic global buckling stress.

F_{el} = elastic buckling stress.

F_n = critical stress.

F_y = yielding strength.

LCC_{EXP} = load carrying capacity associated with the design value.

LCC_{EXP}^{DES} = load carrying capacity associated with the experimental design value.

LCC_M^L = load carrying capacity associated with the L-code and the M- approach.

L_0 = member length.

$M_{by,Rd}$ = bending resistance accounting for global lateral instability.

M_{cr} = elastic critical bending moment.

M_{crd} = elastic critical moment for distortional buckling.

M_{cre} = bending strength for global buckling.

M_{crl} = elastic critical moment for local buckling.

$M_{Ed}, M_{y,Ed}, M_{z,Ed}$ = design bending moment.

$M_{y,R}, M_{z,R}$ = bending resistance along y or z- axis.

M_{ne} = overall buckling resistance for bending.

M_n, M_{nx}, M_{ny} = nominal bending resistance.

M_{nd} = bending strength for distortional buckling.

M_{nl} = bending strength for local buckling.

M_y = yield moment.

$M_{z,Rd}$ = bending resistance along z-axis.

N, N_{Ed} = member axial load.

N_{Rd} = axial stability resistance.

N_{cr} = critical load for the i -member.

N_R = axial resistance.

P = required axial strength.

P_{crd} = elastic critical load for distortional buckling.

P_{cre} = overall critical load.

P_{crl} = elastic critical load for local buckling.

P_n = nominal compression member capacity.

P_{rd} = distortional buckling resistance.

P_{ne} = overall buckling resistance for compression.

P_{nl} = local buckling resistance.

P_y = squash load.

R_i = i -th experimental results.

R_k = characteristic value.
 R_m = mean value of the family results.
 $S_{eff}, S_{eff,y}$ = effective section modulus.
 SI_j^I = safety index associated with the j -code and the k - approach.
 SI, SI^{EU}, SI^{US} = design safety index.
 $SI_K(K_{Ed})$ = safety index associated to the generalized K force.
 $W_{eff}, W_{eff,y}, W_{eff,z}$ = effective cross-section modulus.

Latin lower case letters

b = plate width.
 b_e = effective plate width.
 c = dimension of the lipped.
 d_{eff} = distance between the effective cross-section centroid and the web.
 $dev.$ = standard deviation.
 d_g = distance between the gross cross-section centroid and the web.
 e_y = eccentricity along y axis.
 e_z = eccentricity along z axis.
 f_y = yield stress.
 h = section height.
 k_s = coefficient to determine the characteristic value.
 $k_x, k_y, k_{LT}, k_{xy}, k_{zy}, k_{yz}, k_{zz}$ = bending interaction factor.
 Max = maximum value.
 $mean$ = mean value.
 min = minimum value.
 n = number of tests.
 s = standard deviation.
 t = thickness.

Greek case letters

α = imperfection coefficient associated with the relevant stability curve.
 $\alpha_{cr,op}$ = buckling overall frame multiplier obtained via a finite element buckling analysis.
 α_{ecc} = angle between the vertical axis and a generic straight line through the origin in the M-N domain.
 α_{alt} = minimum load multiplier evaluated with reference to the most stressed cross-section.
 $\Delta M, \Delta M_{y,Ed}, \Delta M_{z,Ed}$ = secondary bending moment.
 χ_{LT} = reduction factor due to lateral buckling.
 χ_{min} = minimum reduction factor.
 χ_{op} = buckling reduction factor referred to the overall structural system.
 χ_z = reduction factor for the relative buckling around z-axis.
 γ_M = material safety factor.
 η_k = coefficients depending on the specimen failure mode.
 φ_{LT} = value to determine the reduction factor χ_{LT}
 φ_{min} = value to determine the reduction factor χ_{min}
 λ_{min} = minimum value of element relative slenderness for pure compression.
 $\bar{\lambda}_d$ = relative slenderness related to distortion buckling.
 $\bar{\lambda}_{LT}$ = relative slenderness related to lateral torsional buckling for bending moment.
 $\bar{\lambda}_l$ = relative slenderness related to local buckling.
 $\bar{\lambda}_c$ = relative slenderness.
 $\bar{\lambda}_{op}$ = relative slenderness of the whole structure.
 σ_c = critical elastic buckling stress.
 σ_w = normal warping stress.
 τ_w = tangential warping stress.

References

- [1] Godley M.H.R., "Design of Cold-formed Steel Members", Rhodes ed., 361-399, 1991.
- [2] Accorti M., Baldassino N., Zandonini R., Scavazza F. and Rogers C.A., "Response of CFS sheathed shear walls", Structures, 7, 100-112, 2016.
- [3] Dubina D., Ungureanu V. and Landolfo R., "Design of Cold-formed Steel Structures, Eurocode 3: Design of Steel Structures, Part 1-3 – Design of Cold-formed Steel Structures", 1st edition, Wiley-Blackwell, Hoboken, NJ, 654, 2012.
- [4] Schafer B.W., "Local, Distortional, and Euler Buckling in Thin-walled Columns", Journal of Structural Engineering, ASCE, 128(3), 289-299, 2002.
- [5] Martins A. D., Camotim D., Dinis P.B. and Young B., "Local-Distortion Interaction in Cold-formed Steel Columns: Mechanics, Testing, Numerical Simulation and Design", Structures, 4, 38-57, 2015.
- [6] Torobian S., Zheng B. and Schafer B.W., "Experimental response of cold-formed steel lipped channel beam-columns", Thin Walled Structures, 89, 152-168, 2015.
- [7] Dinis P.B., Camotim D. and Silvestre N., "FEM-based analysis of the local-plate/distortion mode interaction in cold-formed steel lipped channel columns", Computer and Structures, 85(19-20), 1461-1474, 2007.
- [8] Bernuzzi C., Cordova B. and Simoncelli M., "Unbraced steel frames design according to EC3 and AIS/C provisions", Journal of Constructional Steel Research, 114, 157-177, 2015.
- [9] Arduino V., Bernuzzi C. and Simoncelli M., "Design rules for steel portal frames according to EC3 and AIS/C 360 Provisions", Structural Magazine, 203(07), 1-9, March 2016.
- [10] CEN, "Eurocode 3 – Design of Steel Structures – Part 1-1: General rules and rules for buildings", European Committee for Standardization, Brussels, 91, 2005.
- [11] ANSI/AISC 360-10: "Specification for Structural Steel Buildings", American Institute of Steel Construction, 552, 2010.
- [12] Winter G., "Performance of Compression plates as part of Structural members, Research, Engineering Structures Supplement", Colston Paper, vol. II, Butlerwont, London, 179-184, 1949.
- [13] Winter G., "Thin walled structures-theoretical solutions and test results", Preliminary Publication, 8th Congress IABSE, New York, N.Y., 101-112, 1968.
- [14] Von Karman T., Sechler E.E. and Donnel L.H., "The Strength of Thin Plates in Compression", Transactions A.S.M.E., 54, 53-57, 1932.
- [15] Winter G., "Strength of Thin Steel Compression Flanges", Transactions A.S.C.E., paper n. 2305, 527-576, February 1946.
- [16] CEN, "Eurocode 3 – Design of Steel Structures – Part 1-3: Design of cold formed members", European Committee for Standardization, Brussels, 130, 2005.
- [17] AISI S100-16, "North American specification for the design of cold-formed steel structural members", American Iron and Steel Institute, Washington, 136, 2016.
- [18] Timoshenko S.P. and Gere J.M., "Theory of elastic stability", 2nd ed., McGraw Hill, New-York, 541, 1961.
- [19] Vlasov V.Z., "Thin walled elastic beams", 2nd ed., Israel Program for Scientific Transactions, Jerusalem, 493, 1961.
- [20] Chen W.F. and Atsuta T., "Theory of Beam-Columns. Volume 2: Space behaviour and design", Mc Graw Hill, NY, 732, 1977.
- [21] AS 4084, "Steel Storage Racking", Australian Standards, Australia, 110, 2012.
- [22] The L.H., Hancock G.J. and Clarke M.J., "Analysis and design of double-sided high-rise steel pallet rack frames", Journal of Structural Engineering, 130, 1011-1021, 2004.
- [23] Bernuzzi C., Gobetti A., Gabbianni G. and Simoncelli M., "Warping Influence on the Resistance of Uprights in Steel Storage Pallet Racks", Journal of Constructional Steel Research, 101, 224-241, 2014.
- [24] Bernuzzi C. and Simoncelli M., "EU and US design approaches for steel storage pallet racks with mono-symmetric cross-section uprights", Thin Walled Structures, 113, 181-204, 2017.
- [25] Bernuzzi C., Gabbianni G., Gobetti A. and Rosti A., "Beam design for steel storage racks", Journal of Constructional Steel Research, 116, 156-172, 2016.
- [26] Bijlard F., Feldmann M., Naumes J. and Sedlacek G., "The "General Method" for assessing the out-of-plane stability of structural members and frames in comparison with alternative rule in EN 1993 – Eurocode 3- part 1-1", Steel Construction, 3(1), 19-33, 2010.
- [27] Szalai, J., "The General Method of EN 1993-1-1", New Steel Construction, 30-31 April 2011.
- [28] Papp, F., "Global stability analysis using General Method", www.consteelssoftware.com /files/sharedUploads/Pdf/General_stability_analysis.pdf, accessed in 2017.
- [29] ENV 1993-1-1, "Eurocode 3 - Design of steel structures, Part 1-1: General rules and rules for building", European Committee for Standardization, 325, 1992.
- [30] CEN, "EN 15512, Steel static storage systems - Adjustable pallet racking systems – Principles for structural design", European Committee for Standardization, 137, 2009.
- [31] CEN, prEN "15512, Steel static storage systems - Adjustable pallet racking systems – Principles for structural design", European Committee for Standardization, 288, 2017.
- [32] Boissonnade N., Greiner R., Jaspart J.P. and Lindner J., "Rules for Member Stability in EN 1993-1-1 Background documentation and design guidelines", ECCS-European Convention for Structural Steelworks, Publication n°119, 259, 2006.
- [33] Schafer B.W. and Pekoz T., "Direct strength prediction of cold-formed steel members using numerical elastic buckling solutions", Proceedings of the 14th International Specialty Conference on Cold-Formed Steel Structures, St. Louis, Missouri USA, October 15-16, 69-76, 1998.
- [34] Cheung Y.K., "Finite Strip Method in Structural Analysis", Pergamon Press, New York, USA, 244, 1976.
- [35] Baldassino N., Bontempi F. and Malerba P., "Strips and prisms of infinite lengths", Proceedings of the International Conference on Education, Practice and Promotion of Computational Methods in Engineering using Small Computers, Macau, 1-3, 539-548, August 1990.
- [36] Schafer B.W., "CUFSM: Elastic Buckling Analysis of thin-walled members by the finite strip method". (Open Source Software), 2005. Link: www.ce.jhu.edu/bschafer/cufsm, accessed in 2017.
- [37] Li Z. and Schafer B.W., „Buckling analysis of cold-formed steel members with general boundary conditions using CUFSM: conventional and constrained finite strip methods“, Proceedings of the 20th International Specialty Conference on Cold-Formed Steel Structures, St. Louis, MO, November, 17-31, 2010.
- [38] Thin-Wall, Centre for Advanced Structural Engineering, University of Sidney, http://www.sydney.edu.au/engineering/civil/research/case/software/#thin-wall, accessed in 2017
- [39] Brune B. and Peköz T., "Design of cold-formed steel members - Comparison of EN 1993-1-3 and Direct Strength Method", Steel Construction, 6(2), 82-94, 2013.
- [40] Dubina D., "Direct strength method for buckling design of thin walled sections", Meeting of the Working group CEN TC250 SC3 WG EN 1993-1-3, Madrid, 16-17 February, 2015.
- [41] Casafont M., Pastor M.M., Roura F., Bonada J. and Peköz T., "Design of Steel Storage Rack Columns via the Direct Strength Method", Journal of Structural Engineering, 139(5) 669-679, 2013.
- [42] VijayaVengadesh Kumar J., "Buckling behaviour of cold-formed steel rack uprights", PhD thesis Indian Institute of Technology Madras, 207, 2016.
- [43] VijayaVengadesh Kumar J. and Arul Jayachandran S., "Experimental investigation and evaluation of Direct Strength Method on beam-column behavior of uprights", Thin-Walled Structures, 102, 165-179, 2016.
- [44] Moen C.D., "Direct strength design of cold-formed steel members with perforations", PhD thesis, Johns Hopkins University, 551, 2009.
- [45] CEN, "EN 10025-1: Hot rolled products of structural steels. Part 2: Technical delivery conditions for non-alloy structural steel", European Committee for Standardization, Brussels, 34, 2005.
- [46] Chou S. M., Seah L. K. and Rhodes J., "The Accuracy of Some Codes in Predicting the Load Capacity of Cold-formed Columns", Journal of Constructional Steel Research, 37(2), 137-172, 1996.
- [47] Bernuzzi C. and Rugarli P., "A Unified Approach for the Design of Columns and Beam-Columns cold-formed members. Part 1: The Approach", Costruzioni Metalliche, 5, 38-47, 2009.
- [48] CEN, "EN 1990 Eurocode - Basis of structural design", European Committee for Standardization, Brussels, 87, 2002.
- [49] Pu Y., Godley R. M. H. R., Beale G. and Lau H.H., "Prediction of the Ultimate Capacity

- of Perforated Lipped Channels”, Journal of Structural Engineering ASCE, 125(5), 510-514, 1999.
- [50] Feng M., Wang Y.C. and Davies J.M., “Structural behaviour of cold-formed thin walled short steel channel columns at elevate temperature. Part 1: Experiments”, Thin-Walled Structures, 41, 543-570, 2003.
- [51] Feng M., Wang Y.C. and Davies J.M., “Structural behaviour of cold-formed thin walled short steel channel columns at elevate temperature. Part 2: Design calculations and numerical analysis”, Thin-Walled Structures, 41, 571-594, 2003.
- [52] Dos Santos E.S., Batista E.M. and Camotim D., “Experimental investigation concerning lipped channel columns undergoing local-distortional-global buckling mode interaction”, Thin-Walled Structures, 4, 19-34, 2012.
- [53] Baldassino N. and Zandonini R., “SteelMAX: Experimental and numerical analysis of the structural performances of members, components and subassemblies of cold-formed profile under combined action”, University of Trento, Department of Civil, Environmental and Mechanical engineering, Research report, 253, 2014.
- [54] Baldassino N., Torresani G. and Zandonini R., “Instability of thin walled stiffened C-sections: an experimental study”, in preparation for Thin-Walled Structures.
- [55] Baldassino N., Bernuzzi C. and Simoncelli M., “A proposal to improve the TWCF steel member European design approaches”, Proceedings of the 8th International Conference on Thin-Walled Structures (ICTWS), Lisbon, Portugal, July 24-27, paper no. 185, 2018.

DETERMINATION OF THE BUCKLING LOADS OF IRREGULARLY SHAPED PLATES USING A NEW DESIGN APPROACH

Hesham Ahmed¹, John Durodola² and Robert G. Beale^{3*}

¹ Ingenieur Buero, Rainfarnstr. 25, 80935 Munich, Germany

²Professor, Faculty of Design, Technology and Environment, Oxford Brookes University, Oxford, UK;

³ Visiting Research Fellow, Faculty of Design, Technology and Environment, Oxford Brookes University, Oxford, UK

* (Corresponding author: Email: rgbeale@brookes.ac.uk)

ABSTRACT

Although elastic buckling has been researched for decades there is still a need to develop fast and comprehensive procedures that will reduce product design time especially during the pre-sizing stage. This paper presents a novel equation and parameters for the buckling analysis of plates that accounts for the interaction of geometry parameters, boundary conditions and different load distributions. The method covers geometrical plate shapes such as triangular, trapezoidal, and slightly curved plates. In the place of classical methods the procedure combines a number of concepts in a novel heuristic manner to achieve a comprehensive solution.

The procedure extends the Euler column buckling boundary condition coefficients to different plate edge boundary condition combinations. Geometry parameters reflect the combined effect of plate aspect ratio and the number of buckle waves. A load parameter introduces a factor that allows the effect of different load distributions to be included in the equation. The method is tested for flat plates of different planar shapes and for slightly curved plates with cylindrical geometries. Eighteen combinations of free, simple support and clamped edge boundary conditions are considered together with uniform and linearly varying edge stress loading conditions. The results are compared with analytical and finite element analyses.

Copyright © 2019 by The Hong Kong Institute of Steel Construction. All rights reserved.

ARTICLE HISTORY

Received: 20 April 2017
 Revised: 15 January 2018
 Accepted: 29 January 2018

KEY WORDS

Plates; stability;
 trapezoidal;
 cylindrical;
 triangular;
 buckling

1. Introduction

Following the pioneering work by Bryan [1] in 1890 who determined the buckling load of simply supported rectangular plates, research into two-dimensional plated structures has been carried out by many people and is summarised in standard textbooks such as Timoshenko and Gere [2], Bleich [3], Gerard and Becker [4], Gerard [5] and Bulson [6]. Modern design and analysis of these structures either requires use of the textbooks, such as those in references [2–6] or the use of finite element procedures which require different models when plates of different aspect ratios are analysed or advanced numerical modelling procedures [7–10]. In 2008, Bradford and Roufegarinejad [11] analysed fully clamped rectangular plates under linearly varying axial edge compression. They showed that small variations in the models used for buckling analyses from different investigators for square plates in pure compression gave rise to predictions of the buckling loads varying by up to 30% (in most cases less than 5%). In particular, a model by Liew and Wang [12] using the Rayleigh-Ritz method gave a prediction which was 30% different to the exact solution. The authors in 2013 [14] presented a simple design method to obtain the buckling loads of rectangular plates under a variety of boundary conditions, the results in most cases being within 5% of the exact values. The objective of this paper is to extend the procedure from rectangular plates to planar triangular and trapezoidal plates and to cylindrical rectangular plates. Full details can be found in [15]. Fig. 1 shows the plates considered. The results of the design procedure are compared with those found by the use of MSC/NASTRAN [15] and the German HSB Design Manual [16].

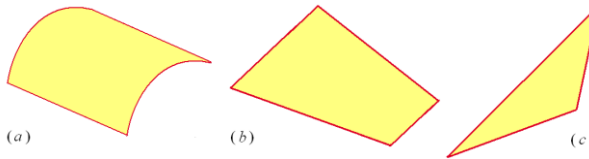


Fig. 1 Irregular plates (a) cylindrical, (b) trapezoidal, (c) triangular

Note that the HSB website [17] states that “The Handbuch Struktur Berechnung [HSB] is a comprehensive reference to procedures, methods, data and tools for the demonstration of sufficient structural integrity of aerospace structures. The manual contains numerous tables, charts, illustrations, and virtually every equation an aerospace design and stress engineer needs. The contents of the manual are updated continuously. The HSB is published by the members of the LTH IASB working group (industry committee for structural analysis documents).”

2. The design procedure for a rectangular plate

The kernel of the procedure is Eq. 1 where the plate buckling equation is given by Eq. 1:

$$\sigma_{cr} = [\sigma_{rel}] [\beta] [\lambda] [\eta] \quad (1)$$

where σ_{cr} is the critical buckling stress, σ_{rel} is a plate relative buckling stress parameter; λ is the applied load shape parameter; β is the plate edge support configuration parameter and η is the plate geometry parameter. A schematic of the scope of the methodology is shown in Fig. 2. Note that λ , β and η are dimensionless whereas σ_{rel} has the dimensions of stress (N/mm²).

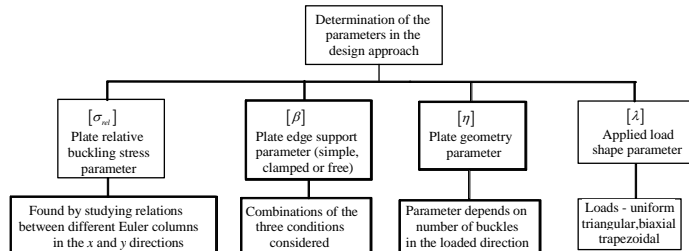


Fig. 2 A schematic of the design methodology

The σ_{rel} term comprises of two terms, $\sigma_{rel,x}$ and $\sigma_{rel,y}$ where these are defined by Eq. 2 and Eq. 3:

$$\sigma_{rel,x} = \left(\frac{\pi}{bt} \right)^2 \left(\frac{EI_y}{a^2} \right) \quad (2)$$

$$\sigma_{rel,y} = \left(\frac{\pi}{at} \right)^2 \left(\frac{EI_x}{b^2} \right) \quad (3)$$

where a and b are the dimensions of a rectangular plate; E , Young's Modulus of Elasticity; t , its thickness; I_x and I_y are the second moments of area of the plate about axes through the centroid of the plate. In determining the plate edge support parameter, β , the four edges of a plate are numbered as shown in Fig. 3 and using the edge boundary combinations shown in Fig. 4 to give the values of β_x and β_y listed in Table 1. Here 's' denotes a simply supported edge, 'c' a clamped edge and 'f' an unsupported or 'free' edge.

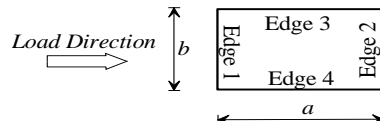


Fig. 3 Edge orientation

Group 1	$ssff$	$s \boxed{f}$	$\boxed{10} s$	$ssfs$	$s \boxed{f}$	$\boxed{18} s$	$ssfc$	$s \boxed{f}$	$\boxed{17} s$	ss
Group 2	$scff$	$s \boxed{f}$	$\boxed{12} c$	$csfs$	$c \boxed{f}$	$\boxed{13} s$	$scfc$	$s \boxed{f}$	$\boxed{16} c$	sc
Group 3	$ccff$	$c \boxed{f}$	$\boxed{11} c$	$ccfs$	$c \boxed{f}$	$\boxed{15} c$	$ccfc$	$c \boxed{f}$	$\boxed{14} c$	cc
Group 1	$ssss$	$s \boxed{s}$	$\boxed{01} s$	$sssc$	$s \boxed{s}$	$\boxed{05} s$	$sscc$	$s \boxed{c}$	$\boxed{07} s$	ss
Group 2	$csss$	$c \boxed{s}$	$\boxed{06} s$	$scsc$	$s \boxed{s}$	$\boxed{03} c$	$secc$	$s \boxed{c}$	$\boxed{08} c$	sc
Group 3	$ccss$	$c \boxed{s}$	$\boxed{04} c$	$ccsc$	$c \boxed{s}$	$\boxed{09} c$	$cccc$	$c \boxed{c}$	$\boxed{02} c$	cc

Fig. 4 Edge support combinations

Table 1

Table 1 Values of the edge boundary parameters β_x and β_y for all the plate cases 01 to 18

Values of the edge boundary parameters β_x and β_y for all the plate cases of 10–18									
Case	01	02	03	04	05	06	07	08	09
Edge	ssss	cccc	scsc	ccss	sssc	csss	sscc	sccc	ccsc
β_x	1.000	3.007	1.696	3.007	1.000	1.696	1.000	1.696	3.009
β_y	1.000	1.738	1.369	1.000	1.369	1.000	1.738	1.738	1.369
Case	10	11	12	13	14	15	16	17	18
Edge	ssff	ccff	scff	csfs	ccfc	ccfs	scfc	ssfc	ssfs
β_x	0.763	2.770	1.459	1.496	2.876	2.807	1.565	0.869	0.800
β_y	0.000	0.000	0.000	0.119	0.250	0.119	0.250	0.250	0.119

Table 2

Values of the geometry parameters η_x and η_y

α	0.300	0.375	0.500	0.625	0.750	0.875	1.000	1.125	1.250	1.375	1.500	1.625	1.750	1.875	2.000
ηx	1.271	1.364	1.526	1.715	1.887	2.058	2.198	2.332	2.443	2.555	2.453	2.290	2.155	2.040	1.954
ηy	0.381	0.512	0.763	1.072	1.415	1.800	2.198	2.624	3.054	3.513	3.679	3.721	3.771	3.825	3.907

The aspect ratio is defined to be $\alpha = a/b$. The plate geometry parameter η relates the relative stress, σ_{rel} , to the plate dimensions, i.e. length a and width b . The parameter η has two components or terms, η_x in the plate x -direction, and η_y in the plate y -direction.

The values of η_s and η_l are given in Table 2 and their derivation is given in references [13] and [14]. The coefficients were derived so that the design procedure produces the exact values for the buckling coefficients of a plate simply supported on all four sides [2]. Note that above an aspect ratio of 2.0, that for design purposes, the buckling coefficient can be considered as a constant.

The load distribution parameter λ is used to extend the procedure from uniform axial loading into triangular and trapezoidal loading. Fig. 5 shows triangular loading and Fig. 6 trapezoidal loading where $\sigma_1 > \sigma_2 > 0$.

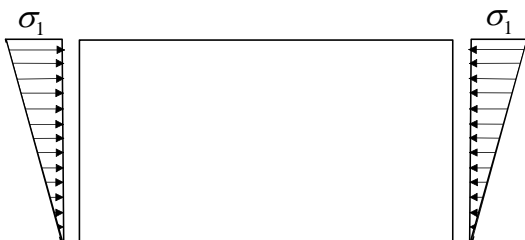


Fig. 5 Triangular loading

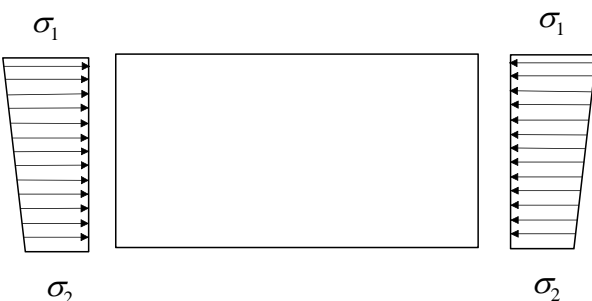


Fig. 6 Trapezoidal loading

The load distribution parameter λ was developed in [13, 14] for triangular, trapezoidal and biaxial distributions. The load distribution for triangular loads is given by λ_m for different stress taper forms and boundary conditions in Fig. 7. Note that in Fig. 7 a solid line for an edge implies that the edge is either simply-supported or clamped and a dotted line that the edge is free.

	α				
	(a)				
	(b)				
	(c)				
	(d)				
1.21	1.21	1.35	1.51	0.300	
1.28	1.28	1.43	1.59	0.375	
1.34	1.34	1.50	1.67	0.500	
1.34	1.34	1.50	1.67	0.625	
1.34	1.34	1.50	1.67	0.750	
1.34	1.34	1.50	1.67	0.875	
1.34	1.34	1.50	1.67	1.000	
1.34	1.34	1.50	1.67	1.125	
1.34	1.34	1.50	1.67	1.250	
1.34	1.34	1.50	1.67	1.375	
1.34	1.34	1.50	1.67	1.500	
1.34	1.34	1.50	1.67	1.625	
1.34	1.34	1.50	1.67	1.750	
1.34	1.34	1.50	1.67	1.875	
1.34	1.34	1.50	1.67	2.000	

Fig. 7 Values of λ_{tri} for different edge boundary conditions

λ_{trap} for trapezoidal loading is given by Eq. 4:

$$\lambda_{trap} = \left(1 + 0.5 \frac{(\sigma_1 - \sigma_2)}{\sigma_1} \right) \quad (4)$$

Before considering plates of triangular, parallelogram or cylindrical shapes let us consider three examples:

2.1. Illustrative example 1

Determine the buckling load of a rectangular aluminium plate with uniform stress applied having a thickness $t = 2.5$ mm, length $a = 90$ mm, width $b = 120$ mm, Young's Modulus of Elasticity $E = 70000$ N/mm 2 and Poisson's ratio $\nu = 0.3$. The plate is fixed in the loading direction and simply-supported in the transverse direction.

Based on the data, $\alpha = 90/120 = 0.75$; $I_y = br^3/12 = 120 \times 2.5^3/12 = 156.25 \text{ mm}^4$ and $I_x = at^3/12 = 90 \times 2.5^3/12 = 117.19 \text{ mm}^4$, then using Eq. 2 and Eq. 3 we obtain

$$\sigma_{rel,x} = 44.423 \text{ N/mm}^2, \text{ and } \sigma_{rel,y} = 24.988 \text{ N/mm}^2.$$

From Eq. 4, for a uniformly distributed load where $\sigma_1 = \sigma_2$ then $\lambda=1.0$.

From Table 1 and for Case 04 we have $\beta_x = 3.007$ and $\beta_y = 1.000$.

From Table 2 $\eta_x = 1.887$ and $\eta_y = 1.415$. Finally substituting into Eq. 5 which is the expanded form of Eq. 1.

$$[\sigma_{cr}] = [\sigma_{rel}][\beta][\lambda][\eta] = (\sigma_{rel,x}\beta_x\lambda_x + \sigma_{rel,y}\beta_y\lambda_y) \quad (5)$$

gives $\sigma_{cr} = 287.43 \text{ N/mm}^2$.

Buckling loads are usually compared with a reference stress, σ_{ref} given by Eq. 6 (which is the Euler buckling load for a rectangular plate simply-supported on all 4 sides):

$$\sigma_{ref} = \frac{\pi^2 E}{12(1-\nu^2)} \left(\frac{t}{b} \right)^2 \quad (6)$$

where ν is Poisson's ratio. For this example, $\sigma_{ref} = 27.46 \text{ N/mm}^2$. The buckling load factor, k , in this case is $k = 287.42/27.46 = 10.47$. This compares with values from a Finite Element Analysis using MSC Nastran [15] of 9.36 and DLUBAL [18] of 9.35.

Fig.8 shows the buckling coefficients (k) for the complete range of aspect ratios together with comparisons with FE calculations. The abbreviation for the new design procedure used in Fig. 8 and others is PBA (Parametric Buckling Analysis).

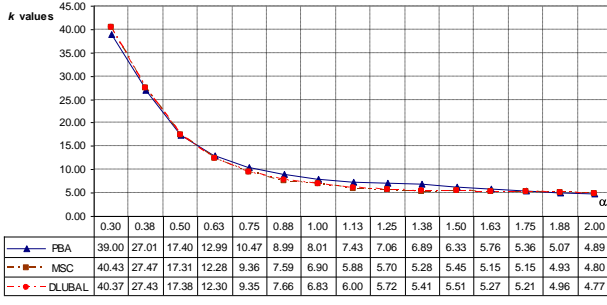


Fig. 8 k -values for a plate with clamped edges loaded and side edges simply-supported

2.2. Illustrative example of a plate subjected to triangular loading

Determine the buckling load factor of a rectangular steel plate with a triangular stress applied having a thickness $t = 5.0 \text{ mm}$, length $a = 2000 \text{ mm}$, width $b = 1500 \text{ mm}$, Young's Modulus of Elasticity $E = 210 \text{ kN/mm}^2$ and Poisson's ratio $\nu = 0.3$. The plate is simply-supported on three sides and fixed on the loading edge.

As before $\alpha = 2000/1500 = 1.333$.

Hence, using Eq. 2 and Eq. 3 $\sigma_{rel,x} = 1.0795 \text{ N/mm}^2$ and $\sigma_{rel,y} = 1.9191 \text{ N/mm}^2$.

From Table 1 and for Case 06 we have $\beta_x = 1.696$ and $\beta_y = 1.000$.

From Table 2, $\eta_x = 2.518$ and $\eta_y = 3.360$ (using linear interpolation for an aspect ratio between two of the tabulated values).

From Table 3 $\lambda_{tri} = 1.67$.

Substituting into Eq. 1 and treating the terms as vectors

$$[\sigma_{cr}] = [\sigma_{rel}][\beta][\lambda][\eta] = (\sigma_{rel,x}\beta_x\lambda_{tri}\eta_x + \sigma_{rel,y}\beta_y\lambda_{tri}\eta_y) \quad (7)$$

$$= (1.0795 \times 1.696 \times 1.67 \times 2.518 + 1.9191 \times 1.000 \times 1.67 \times 3.36) = 18.466 \text{ N/mm}^2$$

As given in example 1, buckling loads are usually compared with the reference stress, given in Eq. 6:

$$\sigma_{ref} = \frac{\pi^2 210000}{12(1-0.3^2)} \left(\frac{5}{1500} \right)^2 = 2.109 \text{ N/mm}^2$$

Hence, the buckling load factor, k , in this case is $k = 18.466/2.109 = 8.76$. This compares with values from a Finite Element Analysis using MSC Nastran [15] of 8.29 and DLUBAL [18] of 8.33. Fig. 9 gives the buckling load factors for the complete range of aspect ratios for this load case with comparisons against finite element calculations.

$$[\sigma_{cr}] = [\sigma_{rel}][\beta][\lambda][\eta] = (\sigma_{rel,x}\beta_x\lambda_{trap}\eta_x + \sigma_{rel,y}\beta_y\lambda_{trap}\eta_y) \quad (9)$$

$$= (1.2282 \times 1.000 \times 1.375 \times 2.453 + 2.7635 \times 1.000 \times 1.375 \times 3.679)$$

$$= 18.122 \text{ N/mm}^2$$

The reference stress, σ is given in Eq. 6:

$$\sigma_{ref} = \frac{\pi^2 210000}{12(1-0.3^2)} \left(\frac{4}{1000} \right)^2 = 3.037 \text{ N/mm}^2$$

Hence, the buckling load factor, k , in this case is $k = 18.1225/3.037 = 5.97$. This compares with values from a Finite Element Analysis using MSC Nastran [15] of 5.96 and DLUBAL [18] of 5.92. See Fig. 10 for a range of aspect ratios for buckling under trapezoidal load with $\sigma_2/\sigma_1 = 0.25$

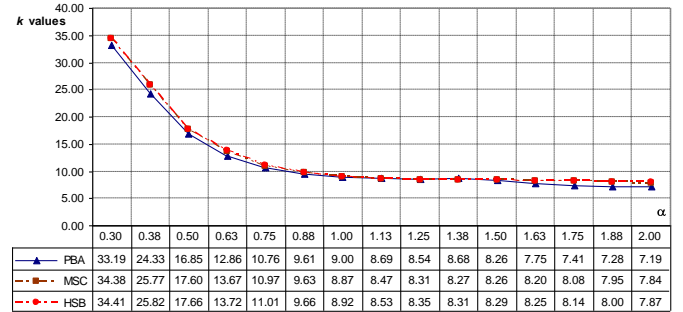


Fig. 9 Buckling load factors for case 06 under triangular loading

2.3. Illustrative example for a plate subjected to trapezoidal loading

Determine the buckling load factor of a rectangular steel plate with uniform stress applied having a thickness $t = 4.0 \text{ mm}$, length $a = 1500 \text{ mm}$, width $b = 1000 \text{ mm}$, Young's Modulus of Elasticity $E = 210 \text{ kN/mm}^2$ and Poisson's ratio $\nu = 0.3$. The plate is fixed on all sides and the ratio of axial force is $\sigma_1/\sigma_2 = 0.25$.

$\alpha = 1500/1000 = 1.5$; and hence $\sigma_{rel,x} = 1.2282 \text{ N/mm}^2$, and $\sigma_{rel,y} = 2.7635 \text{ N/mm}^2$.

From Table 1 and for Case 01 we have $\beta_x = 1.000$ and $\beta_y = 1.000$.

From Table 2, $\eta_x = 2.453$ and $\eta_y = 3.679$.

From Table 3. tri = 1.67.

Using Eq. 4:

$$\lambda_{trap} = \left(1 + 0.5 \frac{(1.0 - 0.5)}{1.0} \right) = 1.250 \quad (8)$$

Finally substituting into Eq. 1 and treating the terms as vectors

$$[\sigma_{cr}] = [\sigma_{rel}][\beta][\lambda][\eta] = (\sigma_{rel,x}\beta_x\lambda_{trap}\eta_x + \sigma_{rel,y}\beta_y\lambda_{trap}\eta_y) \quad (9)$$

$$= (1.2282 \times 1.000 \times 1.375 \times 2.453 + 2.7635 \times 1.000 \times 1.375 \times 3.679)$$

$$= 18.122 \text{ N/mm}^2$$

The reference stress, σ_{ref} is given in Eq. 6:

$$\sigma_{ref} = \frac{\pi^2 210000}{12(1-0.3^2)} \left(\frac{4}{1000} \right)^2 = 3.037 \text{ N/mm}^2$$

Hence, the buckling load factor, k , in this case is $k = 18.1225/3.037 = 5.97$. This compares with values from a Finite Element Analysis using MSC Nastran [15] of 5.96 and DLUBAL [18] of 5.92. See Fig. 10 for a range of aspect ratios for buckling under trapezoidal load with $\sigma_1/\sigma_2 = 0.25$.

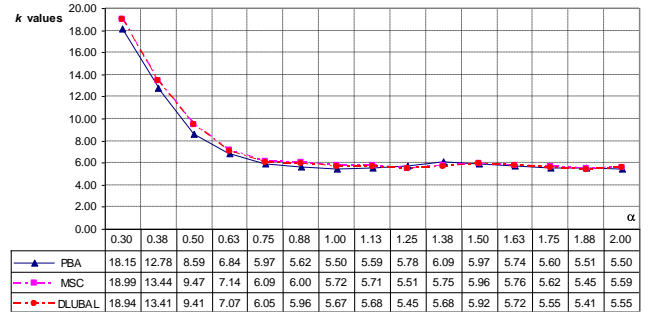


Fig. 10 Buckling load factors for case 01 under trapezoidal loading for $\sigma_1/\sigma_2 = 0.25$

3. Evolutive plates

Eq. 5 describes only the case of rectangular plates. To extend the geometry based plate stability analysis method to include non-rectangular plates a modification of the plate relative buckling stress parameter σ_{rel} is required. Fig. 11 shows the evolutive plate used in this analysis. The analysis below allows for two different direct stresses, σ_1 acting normal to side length b_1 and σ_2 acting normal to side length b_2 . Depending on the choice of σ_1 , b_1 , σ_2 and b_2 reactive normal and shear stresses may occur on the adjacent to sides of b_1 , and b_2 stress. The corresponding out of balance forces are supported by boundaries adjacent to b_1 , and b_2 . The aspect ratios relative to the dimensions of the two ends of the plate, α_1 and α_2 , are given by $\alpha_1 = a/b_1$ and $\alpha_2 = a/b_2$ plates a modification of the plate relative buckling stress parameter σ_{rel} is required. Fig. 11 shows the evolutive plate used in this analysis. The analysis below allows for two different direct stresses, σ_1 acting normal to side length b_1 and σ_2 acting normal to side length b_2 . Depending on the choice of σ_1 , b_1 , σ_2 and b_2 reactive normal and shear stresses may occur on the adjacent to sides of b_1 , and b_2 stress. The corresponding out of balance forces are supported by boundaries adjacent to b_1 , and b_2 . The aspect ratios relative to the dimensions of the two ends of the plate, α_1 and α_2 , are given by $\alpha_1 = a/b_1$ and $\alpha_2 = a/b_2$.

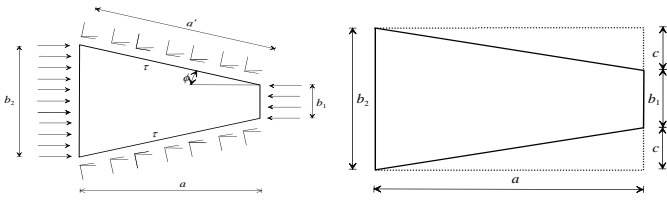


Fig. 11 Evolutive plate

Relating the problem of the evolutive plate to that of the full plate in Fig. 12 by projecting to the left or to the right, it is possible to find a square portion where $a = b_2 = 1$. This gives aspect ratios, $\alpha_1 = 1/b_1$ and $\alpha_2 = 1/b_2$. The change in the longitudinal plate relative buckling stress $\sigma_{rel,x}$ of the plate is related to the change of the aspect ratio from the long edge b_2 to the short edge b_1 of the trapezoidal plate.

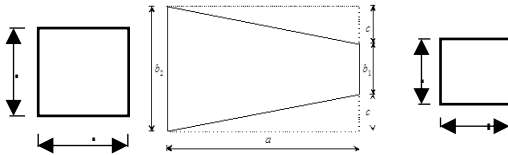


Fig. 12 Evolutive plate and its equivalent rectangular plate

The modification parameter, δ_x is written as:

$$\delta_x = \alpha_1 \cdot \alpha_2 = 1/b_1 \quad (10)$$

The plate's lateral y -direction has width b variable. The lateral plate relative buckling stress parameter δ_y is determined from the plate lateral variation of the evolutive plate.

The area of the evolutive plate in Fig. 12 is A_e and the area of the triangles A_t are given in Eq.11 and Eq. 12.

$$A_e = (b_1 + c) \quad (11)$$

$$A_t = ca \quad (12)$$

Converting the evolutive plate in Fig.11 into square plates in Fig. 12 with an aspect ratio α the areas A_e and A_t have edge lengths l_e and l_t which are given in Eq. 13 and Eq. 14 after applying $\alpha = 1.0$ in the plate x - direction and taking the square root of the area.

$$l_e = \sqrt{b_1 + c} \quad (13)$$

$$l_t = \sqrt{c} \quad (14)$$

The lateral plate relative buckling stress parameter δ_y is given in Eq. 15.

$$\delta_y = l_e + l_t = \sqrt{b_1 + c} + \sqrt{c} \quad (15)$$

The values of δ_x and δ_y for the cases $b_1/b_2 = 0.4$, $b_1/b_2 = 0.6$, $b_1/b_2 = 0.8$ and $b_1/b_2 = 1.0$ at the load condition $\sigma_1/\sigma_2 = 1$ are presented in Table 3. Note that σ_1 and σ_2 are the applied stresses along edges b_1 and b_2 respectively.

Table 3

Values of δ_x and δ_y for $\sigma_1/\sigma_2 = 1.0$

σ_1/σ_2	c	b_1/b_2	δ_x	δ_y
1.0	0.30	0.40	= 1.00 / 0.4	= 1.00 + $\sqrt{0.3}$
	0.20	0.600	= 2.50	= 1.548
	0.10	0.8	= 1.00 / 0.6	= 1.00 + $\sqrt{0.2}$
			= 1.67	= 1.447
			= 1.00 / 0.8	= 1.00 + $\sqrt{0.1}$
			= 1.25	= 1.316

Values of δ_x and δ_y for the cases, $b_1/b_2 = 0.4$, $b_1/b_2 = 0.6$, $b_1/b_2 = 0.8$ and $b_1/b_2 = 1.0$ are calculated by relating the load condition $\sigma_1/\sigma_2 = 1.0$ to the load conditions $\sigma_1/\sigma_2 = 0.8$ and $\sigma_1/\sigma_2 = 1.2$.

Now, let the parameter relating the stress ratio $\sigma_1/\sigma_2 = 0.8$ to the regular stress ratio $\sigma_1/\sigma_2 = 1.0$ be $\mu_{0.8}$, the parameter relating the stress ratio $\sigma_1/\sigma_2 = 1.2$ to the regular stress ratio $\sigma_1/\sigma_2 = 1.0$ be $\mu_{1.2}$, and the parameter representing $\sigma_1/\sigma_2 = 1.0$ is $\mu_{1.0}$. The increment values for both cases $\mu_{0.8}$ and $\mu_{1.2}$ relative to $\mu_{1.0}$ are given in Eq. 16.

$$\Delta\mu = \pm 0.1\mu_{1.0} \quad (16)$$

The sign for the load condition $\mu_{0.8}$ is positive. This is because the plate is subjected to less loads and consequently the plate critical stress would increase. Whilst, the negative sign is for the load condition $\mu_{1.2}$, because the applied stresses are higher and consequently the plate critical stress will be lower. The values of μ for $\sigma_1/\sigma_2 = 0.8$ and $\sigma_1/\sigma_2 = 1.2$ are calculated from Eq. 17 and Eq. 18, respectively.

$$\mu_{0.8} = (1.0 + 0.1)\mu_{1.0} \quad (17)$$

$$\mu_{1.2} = (1.0 - 0.1)\mu_{1.0} \quad (18)$$

The values of μ for the values of b_1/b_2 and σ_1/σ_2 are put together in Table 4 where the value ± 0.1 is modified according to the value of b_1/b_2 .

Table 4

Values of μ

σ_1/σ_2	b_1/b_2	$\Delta\mu$	μ
0.8	0.40	+0.1x0.4 = +0.4	1.04
	0.60	+0.1x0.6 = +0.6	1.06
	0.80	+0.1x0.8 = +0.8	1.08
	1.00	+0.1x1.0 = +1.0	1.10
1.2	0.40	-0.1x0.4 = -0.4	0.96
	0.60	-0.1x0.6 = -0.6	0.94
	0.80	-0.1x0.8 = -0.8	0.92
	1.00	-0.1x1.0 = -1.0	0.90

The change of the plate relative buckling stress $\sigma_{rel,y}$ in the lateral direction is governed by the lateral change in area of the square and trapezoidal plates, i.e. the plate with trapezoidal edges is converted into an equivalent square plate. See Fig. 12. The difference in area, ΔA , is equated to a square plate and the edge length is added to the width of the trapezoidal plate. Accordingly, the area removed equals:

$$\Delta A = 2(0.5c \cdot 1) \quad (19)$$

The change in edge length, Δb equals

$$\Delta b = \sqrt{c} \quad (20)$$

Hence

$$b_2' = 1 + \sqrt{c} \quad (21)$$

δ_y is taken equal to the new value of b_2' . Values of δ_x and δ_y for the cases $b_1/b_2 = 0.4$, $b_1/b_2 = 0.6$, $b_1/b_2 = 0.8$ and $b_1/b_2 = 1.0$ at the load condition $\sigma_1/\sigma_2 = 1$ are given in Table 3.

$$\sigma_{cr} = \mu (\sigma_{rel,x} \beta_x \eta_x \delta_x \lambda_x + \sigma_{rel,y} \beta_y \eta_y \delta_y \lambda_y) \quad (22)$$

3.1. Illustrative case for an evolutive plate

Determine the buckling load of a simply supported evolutive aluminium plate, which is 2.5 mm thick, length 600 mm and has widths $b_1 = 160$ mm and $b_2 = 400$ mm and with $\sigma_1/\sigma_2 = 0.8$.

$$b_1/b_2 = 0.4;$$

$$c = (b_2 - b_1)/2b_2 = 0.3;$$

$$\alpha = 600/400 = 1.5;$$

$$I_y = bt^3/12 = 400 \times 2.5^3/12 = 520.83 \text{ mm}^4 \text{ and}$$

$$I_x = at^3/12 = 600 \times 2.5^3/12 = 781.25 \text{ mm}^4.$$

Therefore

$$\sigma_{rel,x} = \left(\frac{\pi^2}{bt} \right) \left(\frac{EI_y}{a^2} \right) = 0.9995 \text{ N/mm}^2$$

$$\sigma_{rel,y} = \left(\frac{\pi^2}{at} \right) \left(\frac{EI_x}{b^2} \right) = 2.2489 \text{ N/mm}^2$$

From Table 1, $\beta_x = \beta_y = 1.000$, for uniform loading, $\lambda_x = \lambda_y = 1.000$

From Table 2, $\eta_x = 2.453$ and $\eta_y = 3.679$.

From Table 3, $\delta_x = 2.5$ and $\delta_y = 1.548$, and from Table 4, $\mu = 1.04$.

Substituting all these values into Eq. 22 gives $\sigma_{cr} = 19.693 \text{ N/mm}^2$.

From Eq. 6, $\sigma_{ref} = 2.471 \text{ N/mm}^2$. Therefore, the buckling coefficient $k = 19.693/2.471 = 7.97$.

A set of buckling coefficients for an evolutive plate with $\sigma_1/\sigma_2 = 0.8$ and with different b_1/b_2 ratios is presented in Fig. 13 where comparisons are given with the design procedure and the results found from the HSB design code [16]. Other curves are found in Ahmed [14].

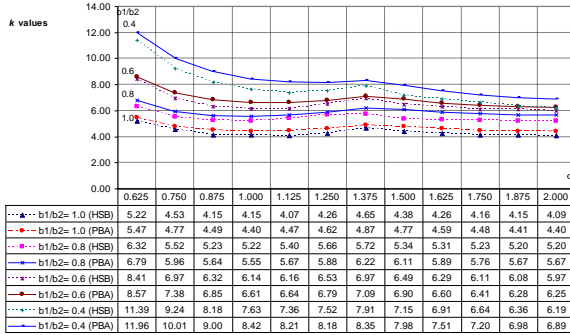


Fig. 13 Comparison of buckling values of a simply-supported evolutive plate with different b_1/b_2 ratios for $\sigma_1/\sigma_2 = 0.8$

4. Triangular Plates

To determine the critical buckling stress for a triangular plate subjected to normal uniform stress σ on all edges, the geometry of a triangular plate will be related to the geometry of a rectangular plate, as has been done for evolutive plates. The analysis assumptions considered in Section 2 are not completely applicable in this section because b_1 equals zero and consequently $1/b_1 \rightarrow \infty$. The plate shown in Fig. 14 is related to a square plate with length a and width $b = a$. Let the modification parameter, as before, be δ and its components in the x and y directions be δ_x and δ_y , respectively.

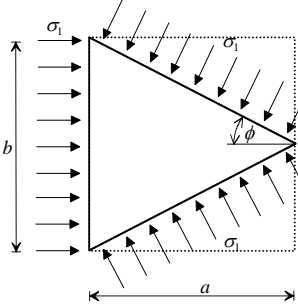


Fig. 14 Triangular plate and the equivalent rectangular plate

In the longitudinal i.e. x direction, the plate length a is constant, whilst the plate aspect ratio α increases with increasing α , i.e., the buckling coefficient k decreases. The parameter δ_x has to increase since the lateral edges move closer and stiffen the plate. The parameter δ_x is therefore related directly to the area of the rectangular plate and the triangular plates, and is given in Eq. 23.

$$\delta_x = \frac{\text{Area rectangular plate}}{\text{Area triangular plate}} = \frac{a \times b}{0.5 \times a \times b} = 2.0 \quad (23)$$

The parameter δ_y in the lateral direction has to decrease due to the additional stress $\Delta\sigma$ arising in the lateral y direction.

From Fig. 12, $\phi = \tan^{-1}(b/2a)$ and the value of $\Delta\sigma_y$ is calculated by Eq. 24.

$$\Delta\sigma_y = \sigma_1 \cos \phi \quad (24)$$

The parameter δ_y in the lateral y direction is related to the stress component in the y direction $\Delta\sigma_y$ and is given in Eq. 25.

$$\delta_y = \cos \phi \quad (25)$$

The general equation for a triangular plate is shown in Eq. 26 (note that the stress ratio $\mu = 1.0$ in this case).

$$\sigma_{cr} = \sigma_{rel,x} \beta_x \eta_x \delta_x \lambda_x + \sigma_{rel,y} \beta_y \eta_y \delta_y \lambda_y \quad (26)$$

To check the equilibrium of the applied loads, the inclined lateral length a' is given in Eq. 27.

$$a' = \frac{a}{\cos \phi} \quad (27)$$

The applied lateral stress has two components, one in the x direction, σ_x , and one in the y direction, σ_y . The x component of the applied lateral stress is given in Eq. 28:

$$\sigma_x = \sigma_1 \sin \phi \quad (28)$$

The resultant, R of the stress determined in Eq. 29 is:

$$R = 2a' \sigma_1 \sin \phi = b \sigma_1 \quad (29)$$

The resultant R determined by Eq. 29 equals the resultant of the applied axial stress, or in other words, the plate is in equilibrium under the applied axial and lateral stresses.

4.1. Example to determine the buckling load of a triangular plate

Determine the buckling load of simply-supported, aluminium triangular plate, length 120 mm, width 160 mm, thickness 1.5 mm subjected to a uniform stress on all three sides. As before the aspect ratio and second moments of area α , I_x and I_y are 0.75, 45.00 mm^4 and 33.75 mm^4 , respectively. The relative stresses $\sigma_{rel,x}$ and $\sigma_{rel,y}$ are obtained as 8.995 N/mm^2 and 5.0601 N/mm^2 respectively from Eq. 2 and Eq. 3.

From Table 1, $\beta_x = \beta_y = 1.000$; for uniform loading, $\lambda_x = \lambda_y = 1.000$.

From Table 2, $\eta_x = 1.887$ and $\eta_y = 1.415$.

From Eq. 23 and Eq. 25, $\delta_x = 2.00$ and $\delta_y = 0.83$. Finally, applying Eq. 26, σ_{cr} is 39.91 N/mm^2 .

Also from Eq. 6, σ_{ref} is 5.561 N/mm^2 and the corresponding buckling loading factor, k , is 39.91/5.561 = 7.18. This compares with the value found from finite element calculations of 6.70, about 7.1% different.

Fig. 15 shows a comparison of the buckling loads computed with the new design procedure against finite element [15] and the HSB [16] provisions.

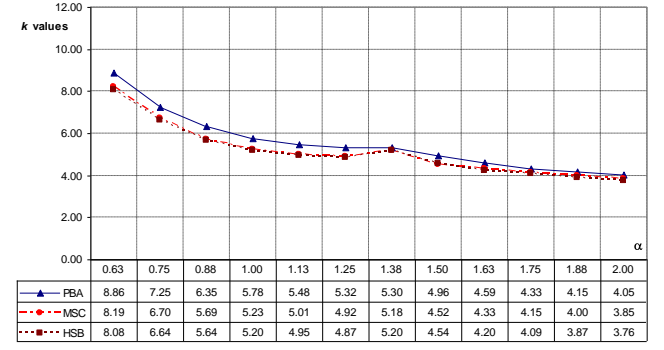


Fig. 15 Buckling coefficients for a triangular plate

5. Shallow cylindrical plates

In the previous section calculations of the critical buckling stresses were considered for flat plates. To extend the method to include shallow cylindrical plates (see Fig. 16) the moment of inertia I_y included in the plate relative buckling stress $\sigma_{rel,y}$ has to be modified for a curved plate, i.e., the displacement of the plate centre of gravity is to be included in the plate's second moment of area.

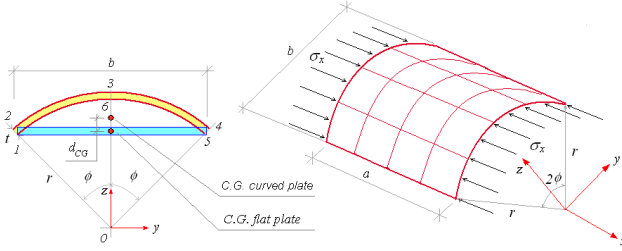


Fig. 16 Geometry of a shallow curved plate

The centre of gravity of a shallow cylindrically curved plate is displaced by an offset distance, d_{CG} , from the centre of gravity of a flat plate. The moment of inertia, I_y , is calculated as for beams with rectangular cross section as given in Eq. 30.

$$I_y = \frac{bt^3}{12} + bt(d_{cg})^2 \quad (30)$$

To calculate the distance, d_{CG} , two virtual circle sectors are constructed. Fig. 16 shows the two circle sectors denoted by the corner points 0234 and 0165. The sector 0234 has the centre of gravity at distance d_1 measured from point 0 in the z direction and the sector has area A_1 . The sector 0165 has the centre of gravity at distance d_2 measured from point 0 in the z direction and the sector has area A_2 . The distance d_{CG} given in Eq. 31 is determined by using Eqs. 32 to 35 [19].

$$d_{cg} = \left(r \cos \phi + \frac{t}{2} \right) - \left(\frac{d_1 A_1 - d_2 A_2}{A_1 - A_2} \right) \quad (31)$$

where:

$$d_1 = \frac{2(r+t)\sin\phi}{2\phi} \quad (32)$$

$$d_2 = \frac{2r\sin\phi}{3\phi} \quad (33)$$

$$A_1 = \frac{2\pi(r+t)^2\phi}{3\phi} \quad (34)$$

$$A_2 = \frac{2\pi r^2\phi}{360} \quad (35)$$

and ϕ is measured in degrees. Comparing the results of the modification with results of other methods such as the one described in HSB Design manual [16], the results are correct as long as d_{cg} is less than the plate thickness; otherwise for d_{cg} greater than the plate thickness, then the results are higher than reality. This is because the value of the term btd_{CG}^2 is greater than the term $bt^3/12$.

In the HSB Design manual [16], there is a limitation for the method based on research summarised by Gerard and Becker [20, 21]. The procedure is applicable if the condition given in Eq. 36 is valid.

$$\frac{100t}{r} \leq 1 \quad (36)$$

The allowable stress for the curved plate equals the allowable stress of the flat plate increased by a value $\Delta\sigma_{cr}$, and $\Delta\sigma_{cr}$ is calculated by Eq. 37.

$$\Delta\sigma_{cr} = 0.2E \left(\frac{t}{r} \right) \quad (37)$$

Consequently, for the new procedure there is also limitation to avoid error due to the term btd_{CG}^2 . Therefore, if the increase in the critical buckling stress calculated using the term btd_{CG}^2 is higher than the value given by Eq. 37, then Eq. 37 must be used.

As an example, determine the buckling load of a simply-supported, aluminium, cylindrical plate, radius of curvature, 10000.0 mm, thickness 4.0 mm, width 200.0 mm, length 200.0 mm subjected to axial compression.

In this case the limitation condition of Eq. 36 is satisfied for all aspect ratios for which the method is applicable (i.e. $\alpha \leq 2$). The half sector angle $\phi = 100/10000 \text{ rad} = 0.773^\circ$.

Applying Eqs. 32–35, $d_1 = 6668.89 \text{ mm}$, $d_2 = 6666.22 \text{ mm}$, $A_1 = 2001733.78 \text{ mm}^2$, $A_2 = 20001333.36 \text{ mm}^2$ and $d_{cg} = 1.333 \text{ mm}$.

According to Eq. 32 the moment of inertia of the flat plate about the y axis

is $I_y = 1066.67 \text{ mm}^2$; increment $\Delta I_y = 1422.49 \text{ mm}^2$ and $I_x = 1066.67 \text{ mm}^2$.

Using Eq. 1:

The plate relative stress in axial direction with ΔI_y is $\sigma_{rel,x} = 53.74 \text{ N/mm}^2$, the plate relative stress in the lateral direction, $\sigma_{rel,y} = 23.03 \text{ N/mm}^2$, the plate geometry terms $\sigma_{rel,x} = 53.74 \text{ N/mm}^2$, $\eta_x = 2.198$ and $\eta_y = 2.198$, the critical buckling stress with ΔI_y , $\sigma_{cr} = 174.32 \text{ N/mm}^2$, the critical buckling stress without ΔI_y , $\sigma_{cr} = 101.228 \text{ N/mm}^2$.

The increase of the critical buckling stress due to the curvature of the plate determined using the design method equals $\Delta\sigma_{cr} = 174.32 - 101.28 = 73.04 \text{ N/mm}^2$.

The increase of the critical buckling stress due to the curvature of the plate determined using the HSB design procedure (Eq. 37 equals $\Delta\sigma_{cr} = 174.32 \text{ N/mm}^2$). Hence, the value determined using the HSB procedure is selected.

Hence $\sigma_{ref} = 174.32 \text{ N/mm}^2$ is given by

$$\sigma_{ref} = \frac{\pi^2 E}{12(1-\nu^2)} \left(\frac{t}{b} \right)^2 = 25.30 \quad (38)$$

The revised buckling load factor is therefore given by Eq. 39.

$$k = \frac{101.28 + 5.60}{25.30} = 4.22 \quad (39)$$

The results for all plates from the three methods, the new design procedure method, the classical method [16], and the FEM eigenvalue method [18], are put together in Fig. 17.

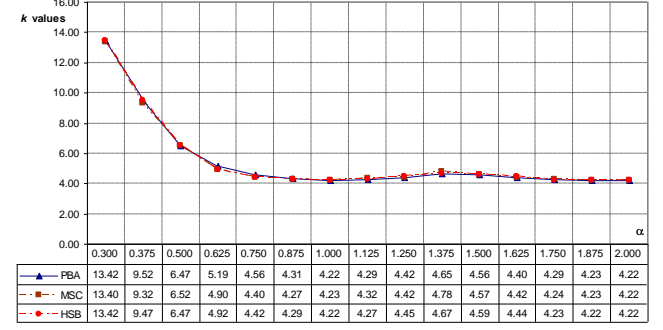


Fig. 17 Buckling coefficients for a simply-supported curved plates

6. Validation

To ensure that the calculations are correct two different methods were used to validate the results; namely by undertaking an eigenvalue analysis or by using a classical theoretical analysis method.

To determine the plate buckling stresses, the MSC/NASTRAN FEM software [15] with the CQUAD4 element and the DLUBAL/RSTAB FEM software [18] with the MITC4 shell element were used. Both elements have 6 degrees of freedom at each node (3 displacement and three rotational) was used to undertake a Mindlin/Reissner analysis [22]. The MSC/NASTRAN was able to analyse all possible plate geometries, i.e., rectangular, non-rectangular, and curved plates. DLUBAL/RSTAB, however, was only able to analyse rectangular flat plates.

To determine the plate buckling stresses based on the classical theoretical method, the literature presented by Bulson [6] and the HSB design manual [16, 17] were used.

A convergence analysis was carried out on different models with different mesh densities. A square plate simply supported on all edges was used to study the convergence of the analysis results. The plate width was 200 mm and the plate thickness was 10 mm. The loaded edge had a uniformly distributed axial stress of 0.05 N/mm² applied to it. To investigate convergence the plate was analysed using 4, 16, 20, 80, 400 and 1280 elements. Results of the analyses using MSC/NASTRAN are collected in Table 5 and results from the analyses using DLUBAL/RSTAB are shown in Table 6.

Analysis showed that the results provided by the model with 400 elements were only marginally different from the results of the model with 1280 mesh elements. However, the analysis was carried out using elements with a length of 10 mm. All other plates using a similar mesh spacing.

Table 5

Results of the convergence analyses using MSC/NASTRAN

No. of Elements	4	16	20	80	400	1280
Critical buckling stress, σ_{cr}	784.7	670.5	670.7	642.3	634.0	633.0
Reference stress, σ_{ref}	158.2	158.2	158.2	158.2	158.2	158.2
Buckling coefficient, k	4.961	4.239	4.241	4.061	4.008	4.002

Table 6

Results of the convergence analyses using DLUBAL/RSTAB

No. of Elements	4	16	20	80	400	1280
Critical buckling stress, σ_{cr}	639.2	637.2	636.3	642.3	634.2	633.0
Reference stress, σ_{ref}	158.2	158.2	158.2	158.2	158.2	158.2
Buckling coefficient, k	4.041	4.029	4.023	4.017	4.010	4.008

Figs. 8-10, 13, 17, 7-9, 12, 15, 17 above show the results using the new design procedure and the corresponding curves using the finite element analyses or the exact theoretical results from the reference texts [6, 15-17].

During the validation process seven errors were investigated and their influence recorded. The errors were load offset (there is a small offset between the centre of gravity of a triangular load and that of a uniform load), deviation in the estimation of the load parameter λ (trapezoidal, biaxial and triangular loads are not exactly modelled in the derivation of λ), estimation of σ_{cr} for uniform stress (trapezoidal, biaxial and triangular loads are not exactly modelled in the derivation of σ_{cr}), estimation of the plate edge parameter β , (the curves developed by the approximations for β_x and β_y do not precisely follow the theoretical curves), estimation of the parameter η (determination of η is based on curve for plate configuration 01 which is not identical for those for cases 02 to 18), the number of buckling waves (for plates under uniform stress with aspect ratios 0.3 and 2.0 where more than two waves can occur as the assumption only allow for 2 waves) and a basic assumption that the overall procedure does not work (this occurs when combinations of plate configurations 05 and 07).

In general, the errors produce an overall discrepancy between the design load and the finite element derivation of less than 4% which is suitable for preliminary design purposes. A full description of each derived curve and its errors is given in the Ahmed's thesis [14]. Slightly larger errors of the order of 10% occurred for free edge boundary conditions.

7. Conclusions

The new design procedure presented in [13, 14] by the authors has been extended to cover evolutive, triangular and cylindrical plates. The general procedure for the implementation of the method has been presented. The method has been validated against FEA and Code book predictions. The procedure is capable of determining buckling loads with very high accuracy of the order of 4% in most cases and about 10% different from FEA and design standards in the worst cases. The method can be implemented in a spreadsheet which makes its application to be faster than FEA methods. The method is particularly useful during design pre-sizing stages.

References

- [1] Bryan G.H. "On the stability of a plane plate under thrusts in its own plane, with applications to the Buckling of the Sides of a Ship", Proceedings of the London Mathematical Society, 22, 54-67, 1890.
- [2] Timoshenko S. and Gere J. "Theory of elastic stability", McGraw-Hill, 1961.
- [3] Bleich F., "Buckling strength of metal structures", McGraw-Hill, 1952.
- [4] Gerard G. and Becker H., "Handbook of structural stability, Part 1 – buckling of flat plates", N.A.C.A. Technical Note 3781, US, 1957.
- [5] Gerard G., "Introduction to structural stability theory", McGraw Hill, 1962.
- [6] Bulson P.S., "The stability of flat plates", Chatto and Windus Ltd., 1962.
- [7] Dayyani I., Moore M. and Shahidi A., "Unilateral buckling of point-restrained triangular plates", Thin-Walled Structures, 66, 1-8, 2013.
- [8] Tran K.L., Douthé C., Sab K., Dallot J. and Davaine L., "Buckling of stiffened curved panels under axial compression", Journal of Constructional Steel Research, 103, 140-147, 2014.
- [9] Martins J.P., Simões da Silva L. and Silverte N., "Energy-based analytical model to predict the elastic buckling of curved panels", Journal of Constructional Steel Research, 127, 165-175, 2016.
- [10] Kim J-H., Park J-S., Lee K-H., Kim J-H., Kim M-H. and Lee K-M., "Computational analysis and design formula development for the design of curved plates for ships and offshore structures", Structural Engineering and Mechanics, 49, 6, 705-726, 2014.
- [11] Bradford M.A. and Roufegarnejad A., "Unilateral and bilateral local buckling of thin-walled plates with Built-in Edges", Proceedings of the Fifth International Conference on Thin-walled Structures, Brisbane, 15- 28, 2008.
- [12] Liew K.M. and Wang C.M., "Elastic buckling of regular polygonal plates", Thin-Walled Structures, 21, 163-173, 1995.
- [13] Ahmed H., Durodola J. and Beale R.G., "A new design approach for the determination of the buckling load of rectangular plates", Proc. Inst. Mech Eng., Part C, J. Mech. Eng. Sci., 227, Issue July, 1417-1428, 2013.
- [14] Ahmed H., "A new parametric buckling analysis approach for plates", PhD Thesis, Oxford Brookes University, Oxford, UK, 2013.
- [15] MSC Nastran. <http://www.mscsoftware.com>, accessed 21:02:2011.
- [16] HSB, "Handbuch Struktur Berechnung", Prepared by L. Schwarmann and J. Ribke, LTH committee, Germany, part 45, 1975.
- [17] HSB, <http://www.fatec-engineering.com/2017/02/17/hsb-structural-analysis-manual/>, Accessed 19:03:2017.
- [18] RSTAB 7.xx, "Dlubal Ing. Software", <http://www.ng.dlubal.com>, accessed 21:02:2011.
- [19] Murray, S. and Liu, J., "Schaums mathematical handbook of formulas and tables", McGraw-Hill, 2003.
- [20] Gerard G. and Becker H., "Handbook of structural stability part 1 – buckling of flat plates", NACA TN 3781, 1957.
- [21] Gerard G. and Becker H., "Handbook of structural stability part 3 – buckling of curved plates and shells", NACA TN 3783, 1957.

- [22] Mindlin R.D., "Influence of rotatory inertia and shear on flexural motions of isotropic, elastic plates," ASME Journal of Applied Mechanics, 18, 31–38, 1951.

STUDY ON DYNAMIC BEHAVIORS AND VIBRATION REDUCTION TECHNIQUES ON CABLE-SUPPORTED RIBBED BEAM COMPOSITE SLAB

Wen-Tao Qiao^{1,*}, Dong Wang², Qi An³ and Hai-Ying Zhang⁴

¹Associate Professor, School of Civil Engineering, Shi JiazhuanTiedao University, China

²PE, TRC Engineering, Inc, LA, United States

³Lecturer, School of Civil Engineering, Qingdao University of Technology, China

⁴Master Candidate, School of Civil Engineering, Shi JiazhuanTiedao University, China

*(*Corresponding author: E-mail:tottyer@126.com)*

ABSTRACT

Based on the cable-supported structure system, a new-style, highly-efficient and long-span pre-stressed floor structure, namely the cable-supported ribbed beam composite slab (CBS) was put forward. The research on dynamic behaviors of CBS was performed with both FEM and experimental methods. The research results indicate that the base frequency of CBS is low and the distribution of CBS's natural vibration frequencies is uniform and concentrated, the low-order modes are mainly vertical vibrations. Four important parameters of CBS were investigated, and the results show that the influence of the slab thickness and cable diameter on CBS's natural frequency is weak. The base frequency will be enhanced by increasing the sag-span ratio, but this effect is insignificant when the sag-span ratio exceeds 0.05. Increasing the depth of ribbed beam can boost the natural vibration frequencies, and this can improve the integral rigidity of CBS. Moreover, the low base frequency of CBS is within the frequency range of the pedestrian excitation loads, five pedestrian loads were used in the analysis, and the results indicate that the vibration comfort problem is significant. The tuned mass dampers (TMD) were used to reduce the structural vibration, when the parameters, numbers and locations of TMD are well designed, the pedestrian-induced vibration is reduced significantly and the reduction efficiency is 68.62%~84.21%.

Copyright © 2019 by The Hong Kong Institute of Steel Construction. All rights reserved.

ARTICLE HISTORY

Received: 5 June 2017

Revised: 12 October 2017

Accepted: 22 January 2018

KEY WORDS

Cable-supported ribbed beam;
composite slab;
Cable-supported structure;
Dynamic behavior;
Vibration reduction;
TMD

1. Introduction

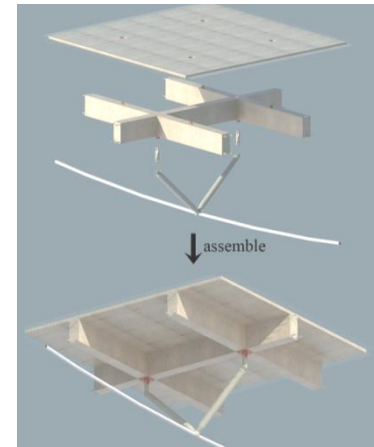
For traditional floor structures, such as reinforced concrete floor, steel-concrete composite floor [1-3], pre-stressed concrete floor [4], reinforced concrete space grid floor [5], the span range is limited. With the development of the social economy, the demands of the large space buildings, such as stadiums, exhibition centers, airport terminals and so on, keep growing, especially the demand of the multi-story large space buildings. To feed the demands, based on the concept of cable-supported structure [6], a new type of pre-stressed long span floor structure, cable-supported ribbed beam composite slab (CBS) is introduced. Fig. 1 shows CBS is a highly efficient space structure which is composed of bottom cables, middle struts and top reinforced concrete ribbed beams. The cable and strut support the slab on top, while the pre-stressed cable gives high stiffness for the whole system. Thus, CBS can reach a longer span.

The reference [7] studies the static properties of CBS, and gives a rational method to determine the initial value of the cable pre-stress. The reference [8] studies the mechanics behaviors of CBS during construction, and introduces a practical construction procedure for CBS. The span of CBS is usually very long, and this makes the global stiffness of CBS low. Thus, pedestrian excitations may cause the strong vibration of CBS which discomforts the occupants. So far, there is very few studies about CBS's dynamic properties, and there is none for the pedestrian-induced vibration comfort problem of CBS. Therefore in this study, firstly both the numerical simulation and experimental methods are used to research the dynamic properties of CBS. Secondly, the univariate analysis of several key parameters is performed to study their influence on CBS's dynamic properties with the FEM model. Finally, a rational vibration reduction method for CBS is studied.

2. Numerical analysis on features of free vibration of CBS

2.1. FEM model

CBS is a new-style long span floor structure which has not been used in the practical project. Based on an actual project using cable supported beam structure-concrete slab composite floor system, the original floor design is updated to a new floor system using CBS. The modified floor design includes 14 pre-stressed cables, and Fig. 2 shows the major dimensions. The precast RC slab is 100 mm thick, and the ribbed beam size is 250 mm × 400 mm. Because the ribbed beam section near the cable anchor takes larger force, the beam size is increased to 500 mm × 500 mm. Concrete grade C30 is used for both the slabs and ribbed beams. The V-shape struts are placed at the joining



(b) Whole floor structure

Fig. 1 CBS rendering

locations of ribbed beams. The strut section is 159×10, and its material grade is Q235B. The cable diameter is 100 mm, and its material grade is strand 1570.

In this study, MIDAS/Gen is used for the numerical analysis. Plate element is used for the precast RC slabs. Beam element is used for the ribbed beams. Beam element with end in-plane bending restrain released is used for the V-shape struts. Tension only element is used for the cables. To simulate the deformation compatibility condition between the ribbed beams and slabs, the

beams and slabs are connected with rigid links. To focus on the dynamic properties of long span floor, the model only includes floor system. Boundary conditions are assumed based on the surrounding members. One end of the span is as rollers, and the other is as pin support. From the columns, only the vertical restraints are considered. Fig. 3 shows the FEM model.

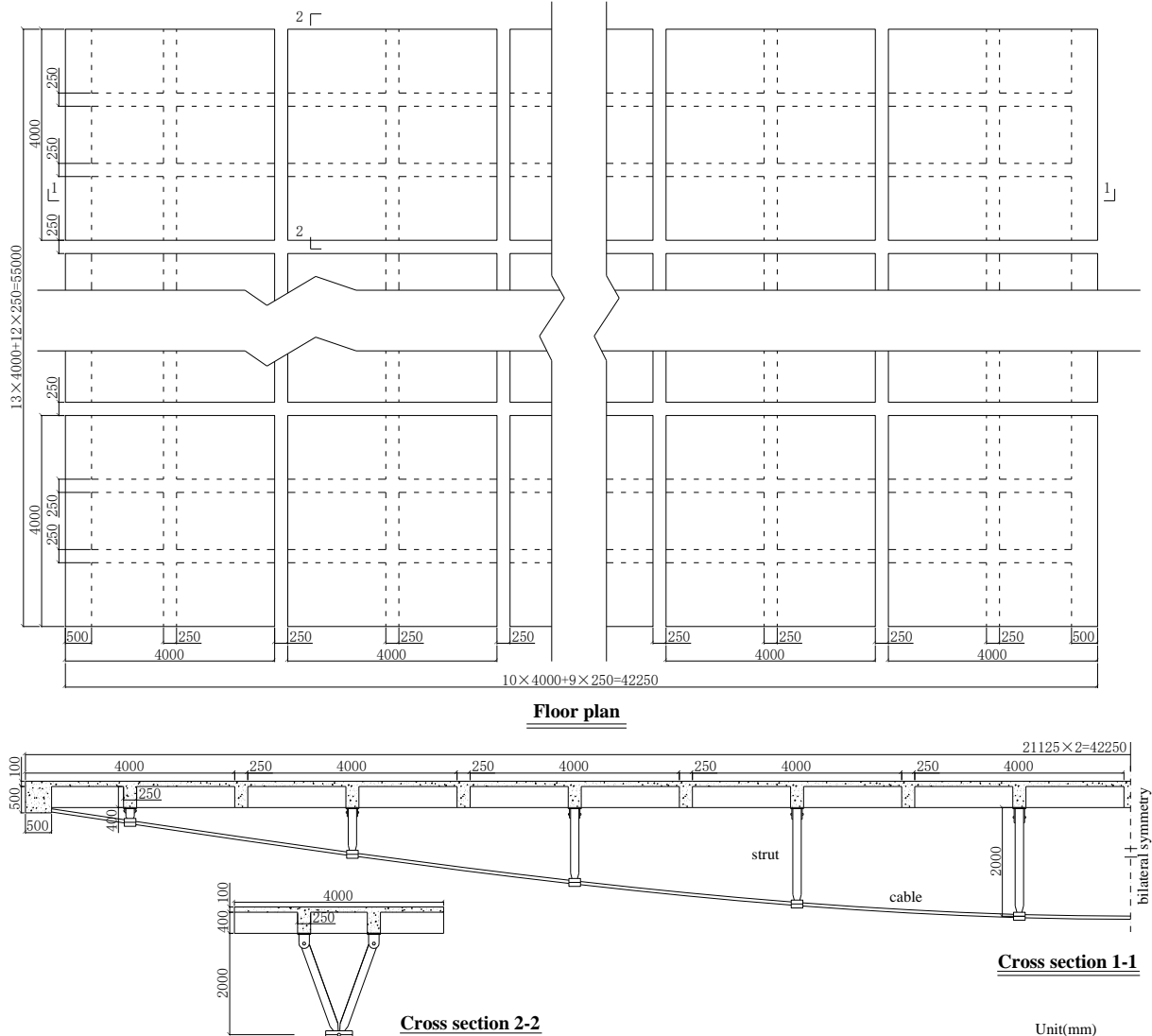


Fig. 2 Model's major dimensions

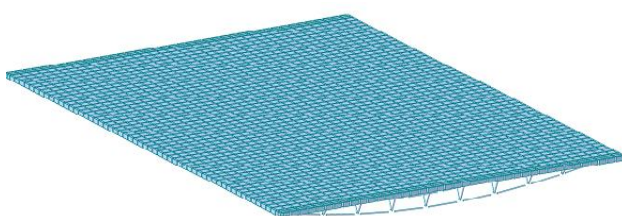


Fig. 3 FEM model of CBS

2.2. Numerical analysis

The initial tension force is determined as 1900 kN with the static equilibrium method [7]. Considering the structure self-weight and the pre-stress, the eigenvalue analysis was performed with the subspace iteration method. The 1st to 30th free vibration frequencies and modes are determined. Fig. 4 plots the 1st to 30th free vibration frequencies.

From Fig. 4:

(1) The structure base frequency is low. The 1st frequency is 2.42 Hz.

(2) Looking at the frequency spectrum, the range of the variation is only 12.76 Hz. Especially the frequency increase from 20th to 30th is only 3.07 Hz. This tells that the distribution of CBS's free vibration frequencies is concentrated.

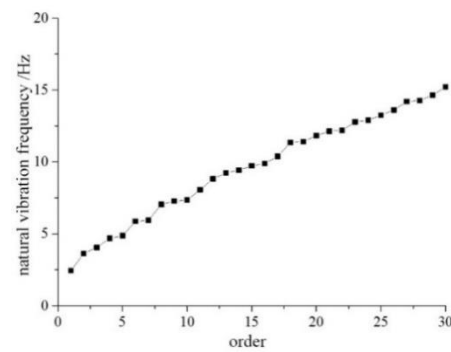


Fig. 4 The first 30 natural vibration frequencies of CBS

The 1st to 3rd free vibration modes are shared in Fig. 5. The free vibration modes reflect the stiffness distribution of the structure.

(1) The 1st mode is the vertical vibration at mid-span. This means the vertical stiffness at mid-span is the weakest.

(2) The 2nd mode shows one cycle of the waveform of vertical deformation along the span, and the 3rd mode shows one and a half cycles. This reflects CBS behaves as a plane in free vibration.

(3) Most of the other modes are symmetric or anti-symmetric vertical vibrations, and only very few are torsional or horizontal vibrations. This tells

CBS has high torsional and horizontal stiffness.

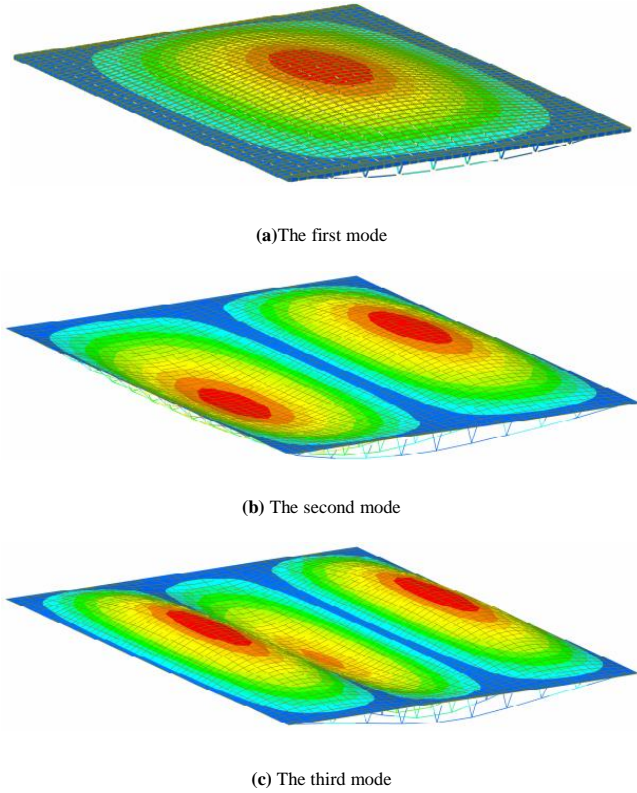


Fig. 5 The first 3 order modes

3. Experimental study on features of free vibration

3.1. Test model

To verify the reliability of the FEM model and the analysis results, the experimental study was performed. Hammer test was performed on a scaled CBS model to determine its free vibration modes and frequencies of the first three orders.

Based on the dimensions of the CBS floor design in section 2, a 1:5 scaled test model with three CBS units (spans) was made. According to the rule of

scaled model for engineering experiments, the scaled test model's major dimensions are listed as follows. Span length is 8 m. Cable sag is 0.4 m. RC precast slab length and width are the same as 800 mm (this does not include length of the doweling rebar). Slab thickness is 20 mm. Concrete grade is C30. The slab transverse rebar is 4 mm diameter and is spaced as 50 mm. The dowel rebar extends 25 mm from the slab. Four 40 mm diameter holes were casted at four corners of the slab. The section of precast RC beam is 50 mm × 80 mm and the concrete grade is C30. Two 6 mm diameter grade HRB400 through longitudinal rebar were placed at the top and bottom of the section. The dowel rebar extends 25 mm from the beam. The beam stirrups were spaced at 40 mm, and the diameter of stirrup is 1.8 mm. M5 bolts were used as shear connector between the beams and slabs, and were embedded at the top of the beam where is corresponding to the hole locations in the slab. 34 mm × 2.5 mm Q235B steel pipe were used as V-shape struts. Steel plates were placed between the struts and beams, and each steel plate was welded with two steel plates with a hole. The struts were attached to the steel plates with a hole using M14 bolts. Each V-shape strut system has two steel pipes, and the two pipes are connected together on a steel plate using M14 bolt. One 42.5 mm × 2.5 mm steel pipe was welded at the bottom of the plate, and the cable ran through the pipe. Φs15.2 (7Φ5) high strength (≥ 200 MPa) steel strand was used for pre-stress cables. See the scaled model in Fig. 6.

3.2. Configurations of measure points and excitation points

Hammer test was used for CBS's free vibration properties. Acceleration transducers, broadband amplifier and data recorder were used in the test. The impact responses of the measure points were recorded using signal data process technique. The free vibration properties of the test model can be determined through analyzing the recorded responses. Fig. 7 show the major equipment used in the test.

FEM model analysis shows that the vertical deformation dominates CBS free vibration modes, so only vertical measure points for acceleration were used which can reveal test model's vertical and torsional vibration. Based on measure point layout principle, nine 941B type vibration pickup sensors were used in this test (see Fig. 8). For each CBS unit, three vibration pickup sensors were placed at span middle and quarter points. Each sensor was attached at the top of the slab using bond particles. For better excitation of hammer impact, the impact location was set at one third point of the middle CBS unit span.

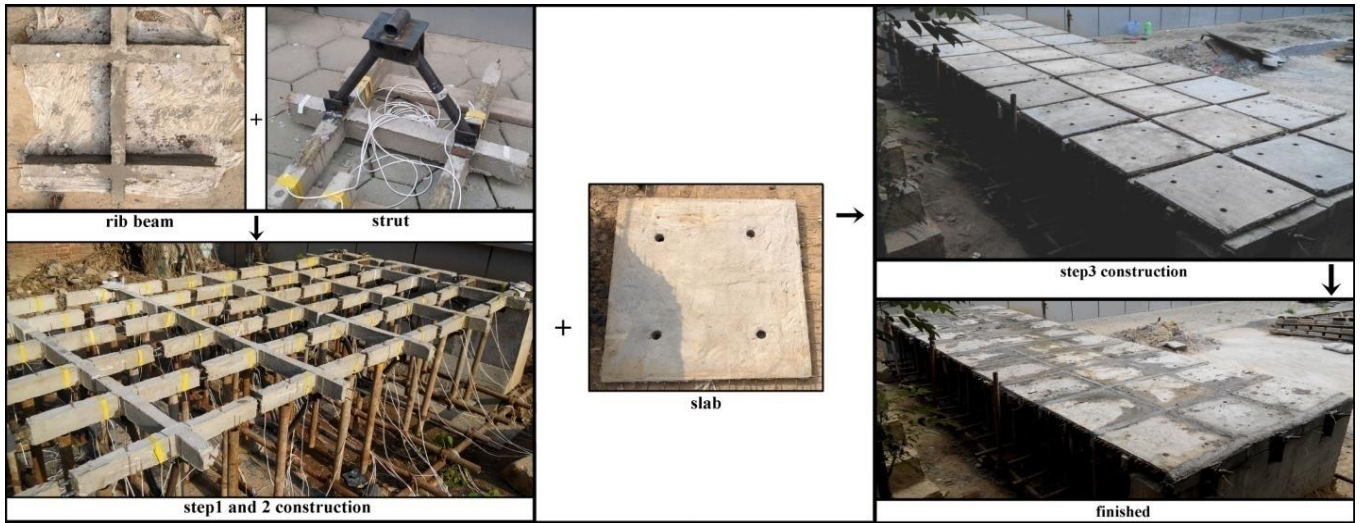


Fig. 6 Scaled test model



(a) 941B vibration sensor



(b) 3018C data recorder



(c) 941 type amplifier



(d) DFC elastic hammer

Fig. 7 Test instruments

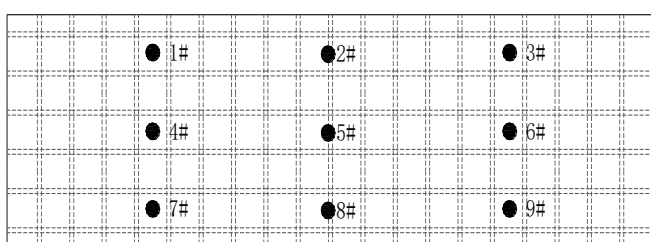


Fig. 8 Measure points distribution

3.3. Experimental results

In the hammer test, the vibration signals from vibration pickup sensors were

recorded using automatic signal acquisition unit DASP. DASP recorded the typical wave shapes of each measure point, and the spectrum of the test model under hammer impact was generated using frequency analysis. Peak value method was used to determine the free vibration frequencies of the test model. The high modes' frequencies were not recognizable due to the environmental interferences. Through auto-spectrum analysis and cross-spectrum analysis, the first three modes and frequencies of the test model were obtained (See table 1).

Based on calculation principal of scaling factor of the scaled model, the scaling factor of the frequency between test model and FEM model is $\sqrt{5}:1$ considering the facts that models used same material and length scaling factor was 1:5.

Table 2 shows the first mode frequency difference between test model and FEM model is 13.2%, while the difference is only 1.1% for the third mode. Table 2 also shows the frequency values from FEM model are all slightly bigger than the experimental values. The mode shapes matched well for the first three modes. The 1st mode shows a half wave shape of vertical deformation. The 2nd mode shows a whole cycle of waveform and the 3rd mode shows one and a half cycles. In a word, the first three modes' frequencies and shapes match well between the test model and the FEM model, and this verifies the reliability of the FEM model and the analysis method used.

Table 1

Test results of free vibration of CBS

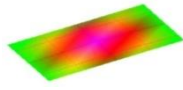
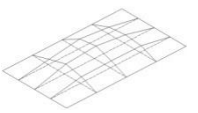
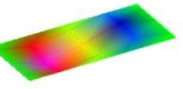
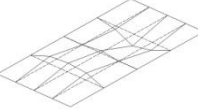
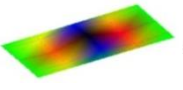
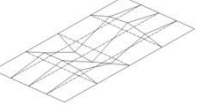
Order	Frequencies(Hz)	Mode shape
1	4.71	 
2	5.90	 
3	9.72	 

Table 2

The first 3 free vibration frequencies comparison

Order	Free vibration frequencies		
	Calculated value(Hz)	Analysis value(Hz)	Error(%)
1	2.42	4.71(2.10)	13.2
2	3.00	5.90(2.64)	12
3	4.39	9.72(4.34)	1.1

Note: the values in parenthesis are calculated from test results according to scaled modeling theory; error = (analysis result-calculated value)/analysis result.

4. Free vibration features parametric study

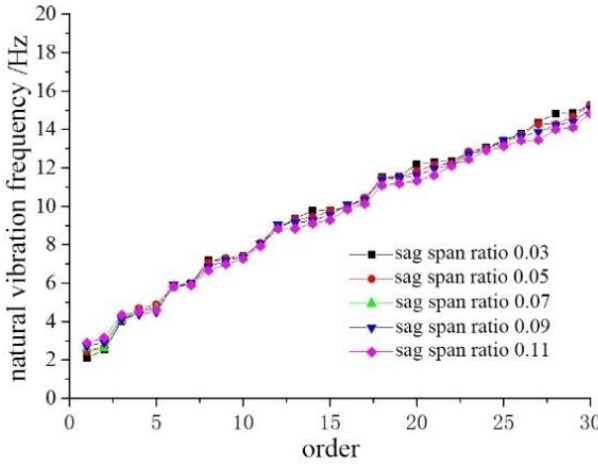
There are four major control parameters in CBS design, sag-span ratio, slab thickness, ribbed beam depth and cable diameter. Using the FEM model, the univariate analysis of the control parameters was performed. To study their influence on CBS's dynamic properties, five typical values were used for each parameter.

The 1st to 30th free vibration modes' frequencies were obtained in the analysis. Fig. 9 shows the frequency changes due to variance of each control parameter.

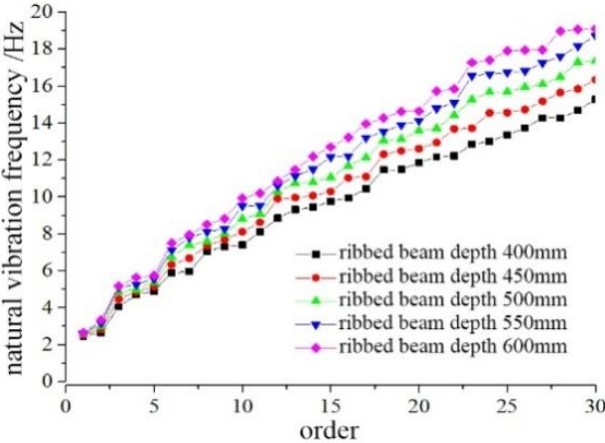
Fig. 9(a) shows the sag-span ratio affects the base frequency significantly, but for 2nd to 30th modes the sag-span ratio variance only slightly affects the frequencies. Thus, the sag-span ratio doesn't have significant influence on frequencies. Fig. 9(b) shows the ribbed beam depth doesn't affect the base frequency. However, it significantly affects the higher order frequencies. Especially from 10th mode to above, the frequency of each mode increases with the increase of the beam depth. Fig. 9(c) and 9(d) show that the slab thickness and cable diameter have very limited influences on frequencies. Also, the free vibration mode shape stays the same (as showed in Fig. 5) with the parameter variance.

In summary, Fig. 9 shows: (1) Base frequency increases significantly with the sag-span ratio increase. However, when sag-span ratio is bigger than 0.05, the influence of sag-span ratio becomes very little. This means increasing sag-

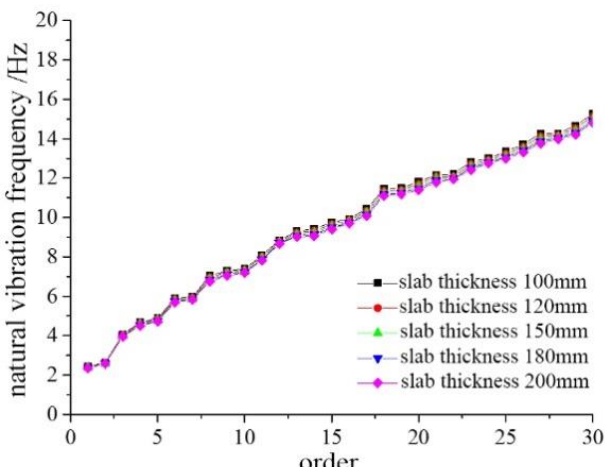
span ratio improves the global stiffness of the CBS, but this improvement is limited once the ratio is bigger than 0.05. Thus, 0.05 is recommended to be used for the sag-span ratio. (2) Under the conditions of adequate structure strength and permitted deformations, increasing ribbed beam depth can improve CBS global stiffness. (3) The influences on global stiffness from slab thickness and cable diameter are negligible. Therefore, the thinner slab and smaller cable can be used to save the cost in practical project.



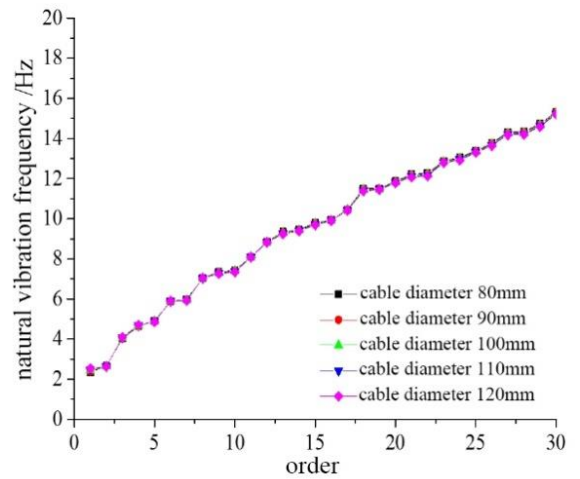
(a) Sag-span ratio influence on free vibration frequencies



(b) Ribbed beam depth influence on free vibration frequencies



(c) Slab thickness influence on free vibration frequencies



(d) Cable diameter influence on free vibration frequencies

Fig. 9 Parameter influence on free vibration frequencies

5. Study on vibration reduction

5.1. Vibration comfort

The study on CBS's free vibration characteristics shows that its lower order vibration modes are vertical vibrations and its base frequency is very low. The base frequency of CBS is very close to the pedestrian excitation frequency which is from 1.5 to 3.5 Hz (walking frequency 1.6~2.5Hz, running frequency 2.0~3.5Hz, jumping frequency 1.8~3.4Hz) [9]. Therefore, the pedestrian load will cause resonance of CBS. This resonance of CBS may dissatisfy the vibration comfort requirements on the floor, so the vibration reduction method needs to be investigated for CBS.

5.1.1. Vibration comfort criteria

In 1997, AISC issued the design criteria for floor vibration. AISC-11 criteria limit the floor vibration acceleration, and its method is currently considered to be one of the most reasonable methods. Fig. 10 shows the human acceptable floor accelerations for different frequencies and different floor usage. Fig. 10 is a double logarithmic plot.

The CBS described in section 2 is used as subject in this section to study the vibration comfort issue of CBS. The structure was assumed to be a sports complex. The AISC-11 criterion is adopted, and the CBS sports complex belongs to the AISC-11 category sports complex with rhythmic activities.

5.1.2. Model parameter selection

Elastic modulus of concrete under dynamic loads is bigger than that under static loads. Thus, the modulus of concrete in FEM model is set as 1.2 times of that specified in design code [9]. Structure damping is another critical parameter for structure dynamic analysis. For the CBS floor, referring to ATC 1999 design guidance and considering the influence from the occupancies and activities, the damping ratio is taken as 0.05. Dead loads considered include structure self-weight and 1.0 kN/m² floor load. Cable pre-tension load is taken as 1900 kN. The effective floor live load is taken as 1.0 kN/m² which is 1/4~1/6 of the floor live load for normal usage based on engineering experience. The other model parameters, like densities, strengths, are taken as in section 2.

From modal analysis in section 2.2, the 1st to 3rd free vibration frequencies are 2.42Hz, 3.00Hz and 4.39Hz, and the first three modes are all primarily vertical vibrations. Although the first three vibration frequencies are all close to pedestrian excitation frequency 1.5~3.5Hz, the 1st modal participating mass ratio is 69.87%, while it is 3.04% for 2nd mode and 11.12% for 3rd mode. The vibration energy in first mode is much more than that in other modes, therefore, the 1st mode shape is used as the main vibration mode of CBS under pedestrian excitation.

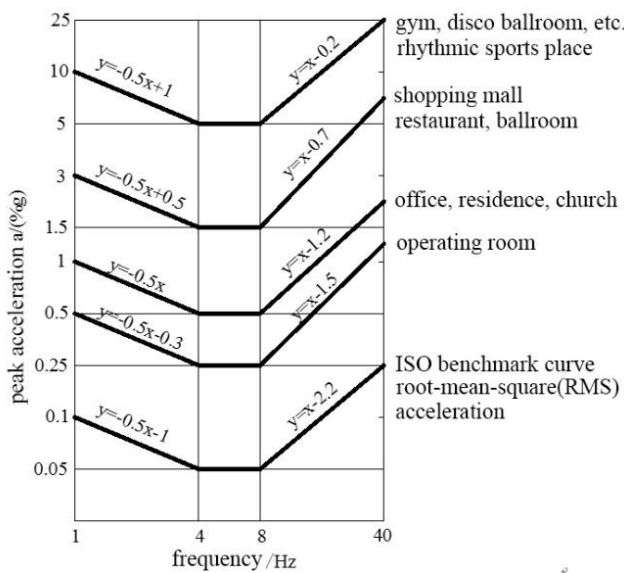


Fig. 10 AISC-11 evaluation criteria

5.1.3. Pedestrian load cases

Considering all possible activities in a sport complex, five pedestrian excitation load cases were used in the analysis.

Load case I: Single pedestrian walking. Fourier series load model defined by IABSE was used for single pedestrian walking load (see Eq. 1).

$$F(t) = G \left[1 + \sum_{i=1}^3 \alpha_i \sin(2i\pi f_s t + \varphi_i) \right] \quad (1)$$

Where, G —body weight, 0.7kN is a common value to use; α_i —the i^{th} order load frequency dynamic factor, $\alpha_1=0.4+0.15(f_s-2)$, $\alpha_2=\alpha_3=1$; f_s —pedestrian walking frequency; φ —initial phase angle, $\varphi_1=1$, $\varphi_2=\varphi_3=0.5\pi$.

To maximize the floor's vibration response, the walking frequency f_s is taken as 2.42Hz, which is the 1st free vibration frequency of the CBS floor. Fig. 11 shows time-history graph of the load.

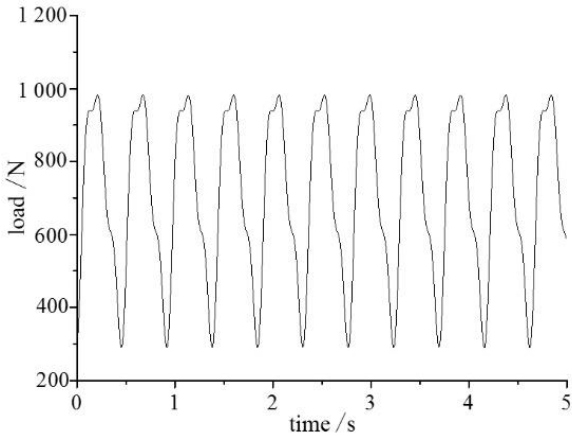


Fig. 11 Load time history curve of case I

Load case II: Single pedestrian running. Based on the actual data of the single pedestrian running from Wheeler [10], half sine load curve was used to simulate this load. The running load frequency is taken as 2.42Hz the same as the first free vibration frequency of CBS. See Eq. 2 for load expression. Fig. 12 shows the time-history curve of this load.

$$F(t) = \alpha \cdot G \cdot |\sin(\pi t/f_s)| \quad (2)$$

Where, G —body weight, uses 0.7kN; α —dynamic factor, 2.6; f_s —running load frequency.

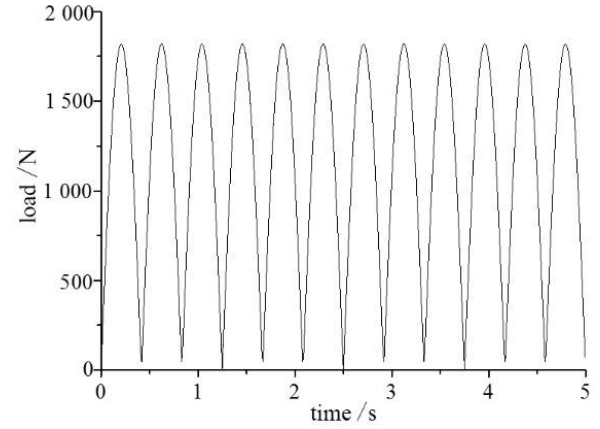


Fig. 12 Load time history curve of case II

Load case III: Single pedestrian jumping. There are few studies on the pedestrian jumping excitation load. The load model defined in BS6399-(1996) is usually used for jumping excitation simulation (see Eqs. 3, 4). 2.42Hz was used as the jumping frequency. Fig. 13 shows time-history curve of this load.

$$F(t) = \begin{cases} k_p \cdot G \cdot \sin(\pi t/T_p) & t \leq T_p \\ 0 & T_p \leq t \leq T_p \end{cases} \quad (3)$$

$$F(t) = G \left[1 + \sum_{i=1}^3 \alpha_i \sin(2i\pi f_s t + \varphi_i) \right] \quad (4)$$

Where, k_p —impact load amplification factor; G —body weight, use 0.7kN; t_p —duration of foot on the ground in each jumping cycle; T_p —jumping cycle period; α —contact ratio, $\alpha=t_p/T_p$, use $\alpha=1/3$ for normal jumping.

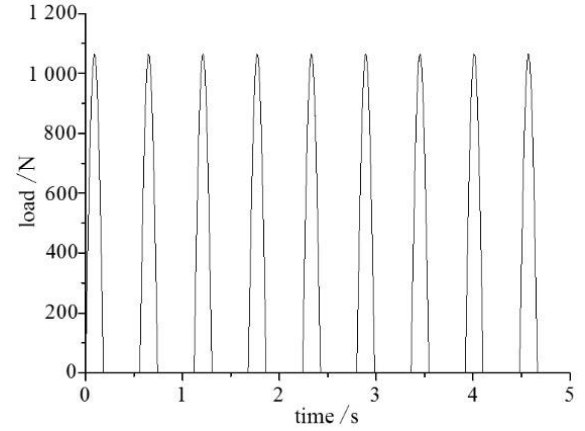


Fig. 23 Load time history curve of case III

Load case IV: Crowd walking. Crowd walking load is very complex because many uncertain factors, such as walking frequencies, phase angles, crowd size and location, individual differences and so on. In most of the studies, the single pedestrian walking load with a crowd factor is used to simulate crowd walking load (see Eq. 5).

$$F(t) = m f(t) \quad (5)$$

where, $F(t)$ —crowd walking load; $f(t)$ —single walking load; m —crowd factor.

To determine the crowd factor, with the assumptions that pedestrian distribution in a crowd accords with Poisson's distribution and the individual walking phase angle is random, the reference [11] derived the expression of crow factor as Eq. 6.

$$m = \sqrt{n} \quad (6)$$

Where, n means number of individuals in the crowd.

Assume the crowd is very dense as one person per square meter. Based on the floor dimensions showed in Fig. 2, a crowd of 2324 persons can walk on

the floor. This gives crowd factor m as 48. The crowd walking frequency is assumed the same as the base frequency of the CBS floor. Fig. 14 shows the time-history curve of this load.

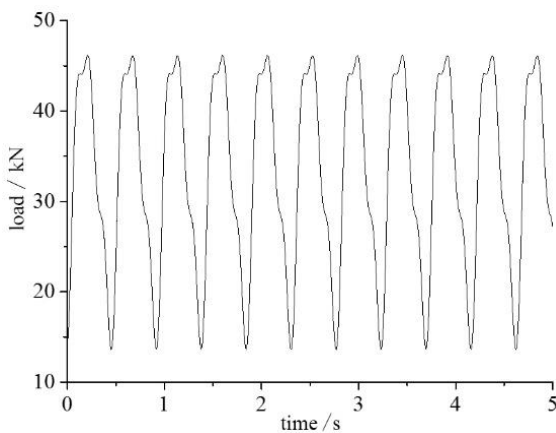


Fig. 14 Load time history curve of case IV

Load case V: Rhythmic activities. The load caused by rhythmic activities can be expressed with a series of simple harmonic waves (see Eq. 7).

$$F(t) = w_p [1 + \sum \alpha_i \cos(2\pi f_i t + \varphi_i)] \quad (7)$$

where, w_p —equivalent uniform load, see table 3; α_i —the i^{th} order load dynamic factor; f_i —the i^{th} order load frequency; φ_i —the i^{th} order load phase angle, $\varphi_1=1$, $\varphi_2=\varphi_3=0.5\pi$.

To maximize the floor vibration response, f_i is taken as the base frequency of the CBS floor as 2.42Hz. Fig. 15 shows the time-history curve of this load.

Table 3
Equivalent uniform loads and dynamic load factors

Dance	Aerobic exercise	Concert sports meeting			
$W_p(\text{kN})$	α_i	$W_p(\text{kN})$	α_i	$W_p(\text{kN})$	α_i
1.2	0.5	0.2	0.6	1.5	0.05(0.15)

Where there is no fixed seat in accordance with the value in bracket.

5.1.4. Comfort analysis

For the first four load cases, the load was applied at the mid-span as a nodal load. The rhythmic activity load was applied on the floor as a uniform load. The FEM dynamic analysis was performed using MIDAS/Gen, and the maximum accelerations at mid-span for each load case obtained are listed in table 4.

Table 4

Maximum acceleration under each load case

Load cases	Case I	Case II	Case III	Case IV	Case V
Acceleration($\text{m} \cdot \text{s}^{-2}$)	0.011	0.015	0.038	0.621	1.144

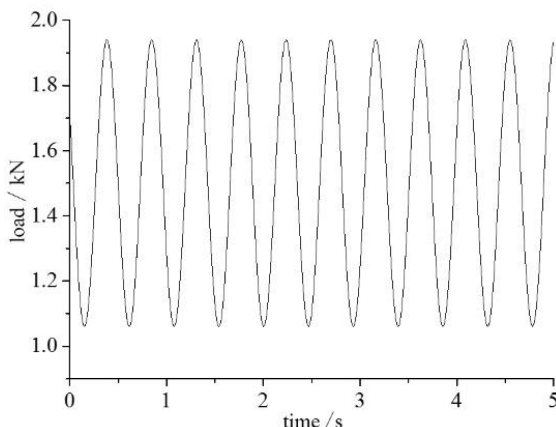


Fig. 15 Load time history curve of case V

The acceleration limit is determined as 0.53 m/s^2 corresponding to the 2.42 Hz base frequency of the floor based on AISC-11 floor comfort criteria. For table 4, accelerations caused by single walking, single running and single jumping are much smaller than the limit. For crowd walking and rhythmic activities, the accelerations are bigger than 0.53 m/s^2 . Thus, the comfort issue of CBS under pedestrian excitations is significant and certain vibration reduction method should be applied.

5.2. Study on vibration reduction

Tuned mass damper (TMD) is one kind of passive vibration reduction device attached on the main structure (master control member) under control. TMD consists of three parts of mass, spring and energy dissipation damper. The mass is connected with main structure through the spring and damper, which form the main structure-TMD system. Usually the base frequency of the structure is used as master control frequency. If the free vibration frequency of TMD is close to the base frequency of the structure, under dynamic load the mass will move due to inertia force, and the master control member will take the counterforce from the TMD. Therefore, the dynamic response on the structure caused by excitation can be reduced.

Because the floor vibration under pedestrian loads is mainly vertical vibration, the suspended TMD device is installed at the bottom of the ribbed beams to control the floor vertical vibration. The mass is usually made of lead blocks in steel case or steel plates. Either pneumatic spring or normal spring can be used which is set symmetrically in the device. The mass weight and spring stiffness are selected to reach the desired frequency. Viscous damper is used as the energy dissipation damper. The damping can be adjusted by change the piston area or the type of viscous material.

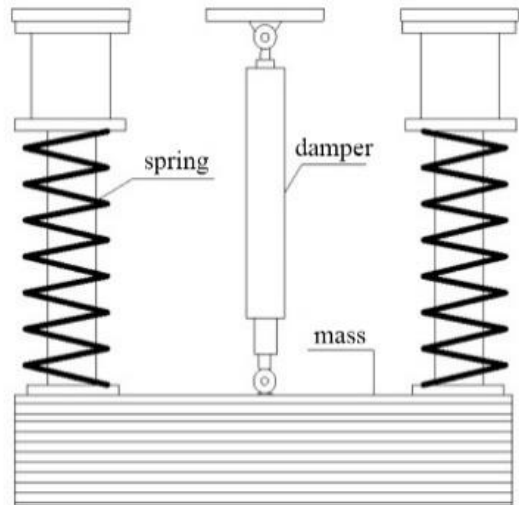


Fig. 16 Suspended-TMD sketch

The advantages of TMD include low cost, easy to install, aesthetically friendly and small space occupancy. As early as in 1966, Lenzen used TMD device as weight as 2% of the whole structure weight, and the expected vibration reduction was achieved [12]. In 1992, Setare and Haason used TMD to control the floor vibration caused by dancing, and the on-site monitoring verifies the effectiveness of the TMD [13]. In 2008 Beijing Olympics, the conference center in Olympic park has a 60m span steel truss roof. The modal analysis shows this long span floor's base frequency is very close to the pedestrian load frequency. The resonant issue can be very significant for the floor. To resolve this issue, 72 TMD devices are used for vibration reduction and they are very effective [14]. For one project using the cable-supported beam and steel composite floor, 24 TMD devices were used on the 40 meter span to reduce the pedestrian-induced vibration and they significantly increase the comfort of the floor [15]. Based on these results from previous studies and projects, TMD was adopted to reduce the pedestrian-induced vibration of the CBS floor in this study.

With reference to the vibration reduction design methods in the previous studies [9, 16-18], DH parameter adjustment method was used to simplify and optimize TMD calculation equations. The optimal stiffness and optimal damping equations for TMD are as follow:

TMD optimal stiffness:

$$k_2 = \omega_2^2 M_2 = (2\pi f_2)^2 M_2 \quad (8)$$

$$C_2 = 2\zeta_2 M_2 \omega_2 = 4\pi f_2 M_2 \zeta_2 \quad (9)$$

$$f_2 = \frac{f_1}{1+u} \quad (10)$$

$$\zeta_2 = \sqrt{\frac{3u}{8(1+u)^3}} \quad (21)$$

$$\mu = \frac{M_2}{M_1} \quad (32)$$

Where, C_2 —TMD damping, f_1 —master control structure's base frequency, f_2 —TMD free vibration frequency, K_2 —TMD stiffness, M_1 —main control structure mass, M_2 —TMD mass, ζ_2 —TMD damping ratio, μ —mass ratio.

From Eqs. 10 and 11, both TMD free vibration frequency f_2 and the damping ratio ζ_2 are related to the mass ratio μ . To perform the optimal design of TMD parameters, the mass ratio μ is determined first, and then the TMD optimal stiffness and optimal damping are calculated with Eqs. 8 and 9. To reach better vibration reduction result, several trials for different μ were performed to figure out the most reasonable value of μ . On the one hand, bigger value of μ is preferred for better load-induced vibration reduction. On the other hand, TMD device is extra weight attached on the structure and it is usually connected at the locations where have less local stiffness and resonant deformation. TMD installment may introduce too much extra weights and this will affect the serviceability of the structure. Therefore, the weight of TMD device should be limited. Based on previous studies and projects, the value of μ should be within 0.005 to 0.06. To maximize the vibration control effect, TMD devices were mounted at the locations showing peak deformations in the 1st free vibration mode of free vibration. Therefore, TMD were placed at the mid-span of the floor. Totally 44 devices were used in 4 rows (see Fig. 17).

The 1st mode participation mass of the CBS model in section 2.2 is about 1030807 kg. 12 values of mass ratio μ were used, from 0.005 to 0.06 with the increment of 0.005. Each TMD's mass was set as $M_1 \cdot \mu / 44$. The worst load case (rhythmic activities) was used in the analysis. The Fig. 18 shows the plot of mass ratios μ versus the mid-span maximum acceleration.

Fig. 18 tells that the vibration reduction effect gets better along with increasing the mass of TMD. However, this influence becomes insignificant when the value of μ is bigger than 0.04. Therefore, μ as 0.04 is recommended in this study. Table 5 shows the major design parameters of TMD. Fig. 19 shows the curves of mid-span dynamic responses with/without the TMD for different load cases. Table 6 shows the comparison on the peak accelerations with/without TMD devices.

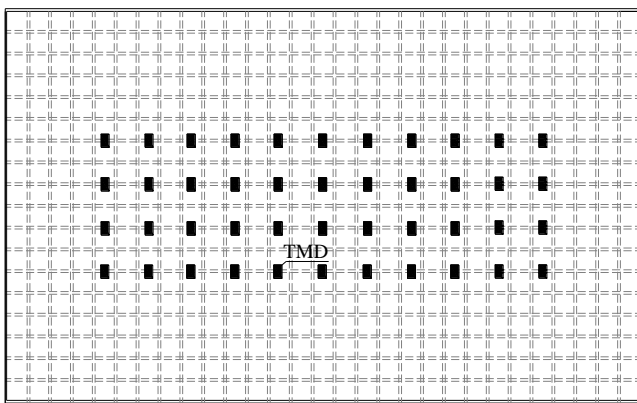


Fig. 17 Layout of TMD

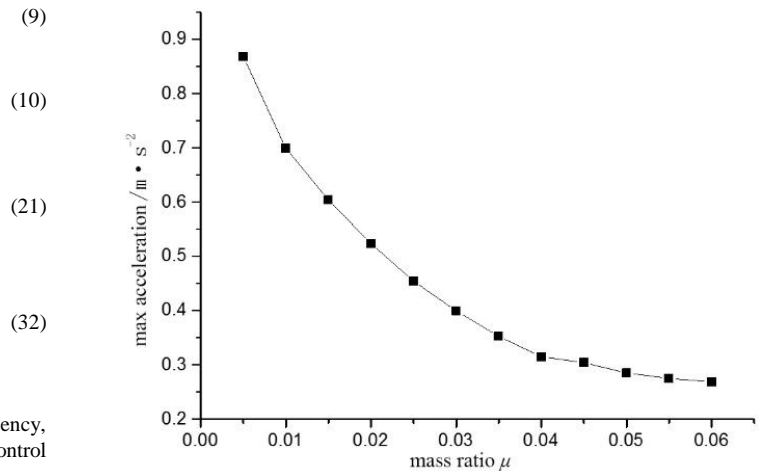


Fig. 18 Max acceleration with different mass ratios

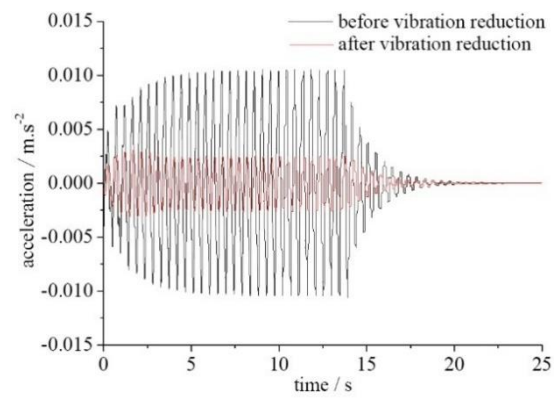
Table 5
TMD parameters

Mass ratio	Mass weight (kg)	Spring stiffness (kN·m ⁻¹)	TMD damping(kN·s·m ⁻¹)
0.04	937	159	2.82

Table 6
Max acceleration before and after vibration reduction

Load cases	Max acceleration before vibration reduction (m/s^2)	Max acceleration after vibration reduction (m/s^2)	Vibration reduction efficiency (%)
Case I	0.011	0.0031	71.82
Case II	0.015	0.0029	80.67
Case III	0.038	0.006	84.21
Case IV	0.621	0.1949	68.62
Case V	1.144	0.352	69.23

Table 6 shows the vibration reduction effect of TMD devices on CBS floor structure is significant. The vibration reduction efficiency is from 68.62% to 84.21%. The max accelerations of CBS floor with TMD are all less than 0.53 m/s^2 , and the floor comfort requirement is satisfied.



(a) Load case I

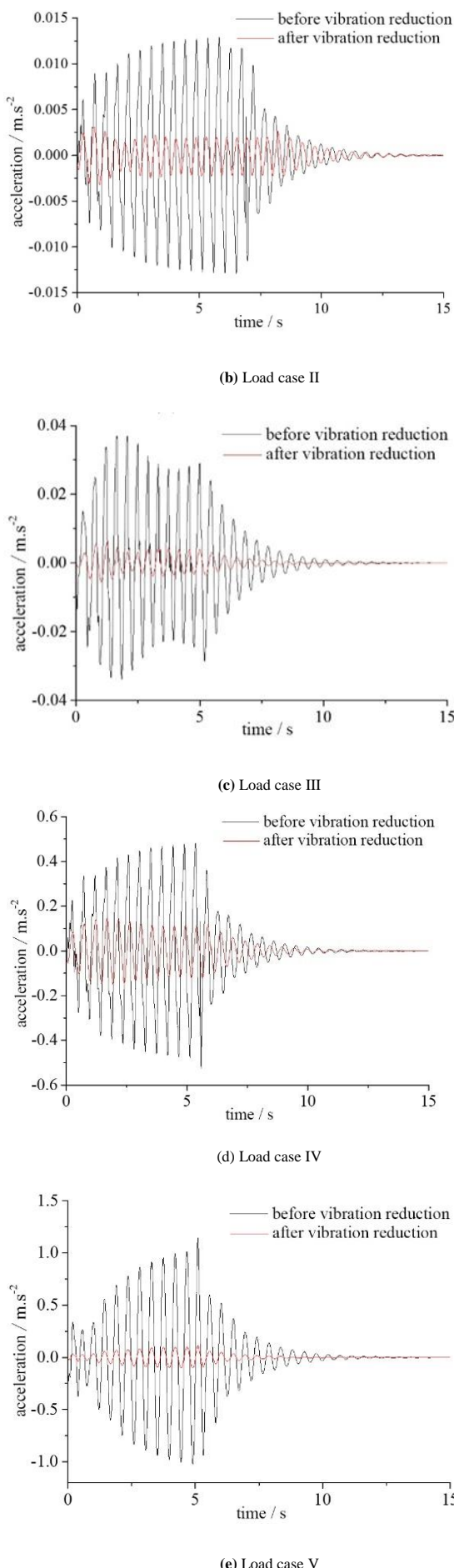


Fig. 19 Vibration response curve before and after vibration reduction

6. Conclusions

In this paper, the CBS floor system's dynamic properties and vibration reduction technique are studied using both numerical analysis and experimental method. The conclusions are as follows:

(1) The base frequency of CBS floor is relatively low. The frequencies increase uniformly from lower mode to higher mode and concentrate in a small range. The lower modes are mainly vertical vibrations, and then the torsional vibrations show up in the higher modes. There is rarely horizontal vibration in vibration modes. This tells that the vertical stiffness of the CBS is the lowest, the torsional stiffness is relatively high and horizontal stiffness is the highest.

(2) Parametric analysis shows the slab thickness and the cable diameter have little effect on CBS dynamic properties. The base frequency increases along with increasing sag-span ratio, but this influence is limited. Sag-span ratio of 0.05 is recommended. The depth of the ribbed beam has little effect on the base frequency, but its influence on higher mode's frequencies is significant. Increasing ribbed beam depth can improve the global stiffness of CBS floor. The variance of different parameters doesn't change the vibration modes.

(3) The stiffness of CBS floor is relatively low, and the vibration comfort issue is serious. TMD devices are adopted to limit the vertical vibration of CBS floor. TMD is designed using HD parameter adjustment method. Numerical simulation shows the vibration reduction of TMD on CBS floor is very effective, and the reduction efficiency is from 68.62% to 84.21% for different load cases. Therefore, the vibration comfort issue of CBS floor is solved by using TMD devices.

Acknowledgements

The research described in this paper was sponsored by National Natural Science Fund (51208317), Natural Science Foundation of HeBei Province (E2016210052), Science and Technology Research Key Project in Higher Institutions of Hebei Province (ZD2018250) and especially supported by Large Infrastructure Disaster Prevention and Mitigation Collaborative Innovation Center of Hebei Province.

References

- [1] José G.S.D.S., Sebastio A.L.D.A. and Elvis D.C.L., "Parametric modelling of the dynamic behavior of a steel-concrete composite floor", *Journal of Engineering Structures*, 75(75), 327–339, 2014.
- [2] Mello A.V.A., Silva D.J.G.S., Vellasco S.D.P.C.G., Andrade D.S.A.L. and Lima D.L.R.O., "Dynamic analysis of composite systems made of concrete slabs and steel beams", *Journal of Constructional Steel Research*, 64(10), 1142–1151, 2008.
- [3] Lee K., Lee S.H., Kim G.C. and Woo S.S., "Global vertical resonance phenomenon between steel building and human rhythmic excitations", *Journal of Constructional Steel Research*, 92(1), 164–174, 2014.
- [4] Pavic A., Reynolds P., Waldron P. and Bennett K., "Dynamic modelling of post-tensioned concrete floors using finite element analysis", *Journal of Finite Element in Analysis & Design*, 37(4), 305–323, 2001.
- [5] Chanaka M.A., David P.T. and Nimal J.P., "Dynamic performance characteristics of an innovative Hybrid Composite Floor Plate System under human-induced loads", *Journal of Composite Structure*, 2013, 96(4), 590–600.
- [6] Sun G.J., Chen Z.H. and Longman R.W., "Numerical and experimental investigation of the dynamic characteristics of cable-supported barrel vault structures", *Journal of Mechanics of Materials and Structures*, 8(1), 1–13, 2013.
- [7] Qiao W.T., Li Y., and Deng Y.Z., "Study on mechanical behaviors of cable-supported ribbed beam composite slab structure", *Proceedings of the 14th World Conference on Modern Structural Engineering*, Tianjin, 520–525, 2014.
- [8] Qiao W.T., An Q., Wang D. and Zhao M.S., "Study on mechanical behaviors of cable-supported ribbed beam composite slab structure during construction phase", *Journal of Steel Composite Structure*, 21(1), 177–194, 2016.
- [9] Lou Y., Huang J., and Lv Z.C., "The vibration comfort design of floor system", Beijing: Science Press.
- [10] Wheeler J.E., "Prediction and control of pedestrian induced vibration in footbridges", *Journal of Structural Division-ASCE*, 108(9), 2045–2065, 1982.
- [11] Matsumoto Y. and Griffin M.J., "Mathematical models for the apparent masses of standing subjects exposed to vertical whole-body vibration", *Journal of Sound & Vibration*, 260(3), 431–451, 2003.
- [12] Lenzen K.H., "Vibration of steel joist-concrete slab floors", *AISC Engineering Journal*, 3(3), 133–136, 1966.
- [13] Setareh M. and Hanson R.D., "Tuned mass dampers for balcony vibration control", *Journal of Structural Engineering*, ASCE, 118(3), 723–740, 1992.
- [14] Zhu M., Zhang Z.Q., Ke C.H., et al., "Study on improving people's comfortableness on large-span steel floor structures", *Journal of Building Structure*, 38(1), 72–76, 2008.
- [15] An Q., Chen Z.H., Ren Q.Y., Liu H.B., et al., "Control of human-induced vibration of an innovative CSBS-CSCFS", *Journal of Constructional Steel Research*, 115, 359–371, 2015.
- [16] Wendell D.V. and Ronaldo C.B., "Control of vibrations induced by people walking on large span composite floor decks", *Journal of Engineering Structure*, 33(9), 2485–2494, 2011.
- [17] Caetano E., Cunha Á., MoutinhoC. and MagalhãesF., "Studies for controlling human-induced vibration of the Pedro e Inês footbridge, Portugal. Part 2: Implementation of tuned mass dampers", *Journal of Engineering Structure*, 32(4), 1082–1091, 2015.
- [18] Lee S.H., Lee K.K., Woo S.S. and Cho S.H., "Global vertical mode vibrations due to human group rhythmic movement in a 39 story building structure", *Journal of Engineering Structure*, 57(4), 296–305, 2013.

TURBULENT WIND FIELD SIMULATION OF WIND TURBINE STRUCTURES WITH CONSIDERATION OF THE EFFECT OF ROTATING BLADES

Tao Huo^{1,2,3}, Le-Wei Tong^{1,2*} and Fidelis R. Mashiri⁴

¹State Key Laboratory of Disaster Reduction in Civil Engineering, Tongji University, Shanghai 200092, China

²College of Civil Engineering, Tongji University, Shanghai 200092, China

³East China Architectural Design & Research Institute Co., Ltd, Shanghai 200011, China

⁴School of Computing, Engineering and Mathematics, Western Sydney University, Sydney, NSW 2751, Australia

(* Corresponding author: E-mail: tonglw@tongji.edu.cn)

ABSTRACT

In order to achieve the wind-induced vibration response analysis and fatigue analysis, this study conducts the wind field simulations around tubular tower and rotating blades of typical pitch-controlled 1.25MW wind turbine structures, respectively. Based on field test data, there is a large difference between the turbulent wind spectrum for the rotating blades and classic wind spectrum adopted by the non-rotating blades and tubular tower. In this study, first, the auto and cross-rotational Fourier spectrums are deduced based on the physical mechanism, with particular focus on the influences of the rotational effect and the correlation between different points located on the same and different blades. Then, the Davenport type coherence function is optimized. The high accuracy of the rotational Fourier spectrum model is verified by comparing with the real data. Relevant parameter analysis of the rotational Fourier spectrum is conducted. Finally, turbulent wind fields around the tubular tower based on the Kaimal spectrum and the rotating blades based on the rotational Fourier spectrum are simulated by means of the harmony superposition method. The results indicate that the calculated wind spectrums have good agreement with the target wind spectrums. Therefore, the proposed approach in this study is feasible for the turbulent wind field simulation of wind turbine structures.

Copyright © 2019 by The Hong Kong Institute of Steel Construction. All rights reserved.

1. Introduction

As more and more public concern and awareness about energy and environmental issues has increased, wind power, which is a renewable source of energy, has gained prominence and has been extensively developed [1,2]. In recent years, large-scale wind turbine structures have been widely used around the world, with the characteristics of large moment of inertia, broad range of working wind speed and high-rise towers [3,4]. It is worth noting that cyclic loadings, which are exerted on the rotating blades, and fluctuating wind load can inevitably bring about fatigue failure of the wind turbine tubular tower [5]. In general, the fatigue issue of tubular towers is not only related to the fatigue strength, but also dependent on the load effect (see Figure 1). While continuous progress has been made looking into the fatigue strength of the various materials, relevant investigations on the load effect induced by the cyclic loading of rotating blades and fluctuating wind load are generally insufficient. Therefore, in order to guarantee the fatigue reliability of the wind turbine tubular towers, it is essential to analyze wind-induced dynamic responses. To achieve this purpose, wind field simulations around the wind turbine structure are necessary, especially for the fluctuating component.

It is worth mentioning that due to the rotational effect of blades, the turbulent wind field model of wind turbine structures is quite different from that of the ordinary wind-sensitive structures such as high-rise buildings and bridges [6]. Field tests confirmed that compared with the turbulent wind spectrum of the non-rotating blades, energy distribution of turbulent wind from rotating blades produces fundamental change, especially in high frequency components [7]. Moreover, wind-induced fatigue loads obtained through considering rotational effect of blades are obviously greater than the corresponding values caused by the non-rotating state, which could lead to unsafe fatigue life prediction [8]. Therefore, rotational effect of blades should be considered to accurately obtain the aerodynamic loads and carry out the wind-induced fatigue analysis of wind turbine structures. However, many researchers still adopt the classical turbulent wind spectrum models [3,9], such as the Von Karman and the Kaimal wind spectrums, to simulate the wind field around the blades, and relevant studies on rotational spectrum models of blades are still insufficient. Therefore, it is necessary to take an in-depth look into the theoretical rotational sampled wind spectrum to consider the impact of the blade rotational effect on turbulent wind field of wind turbine structures.

ARTICLE HISTORY

Received: 31 January 2018
Revised: 12 July 2018
Accepted: 25 July 2018

KEY WORDS

Wind turbine structures;
Turbulent wind field simulation;
Rotational Fourier spectrum;
Coherence function;
optimization;
Parameter analysis;
Harmony superposition method

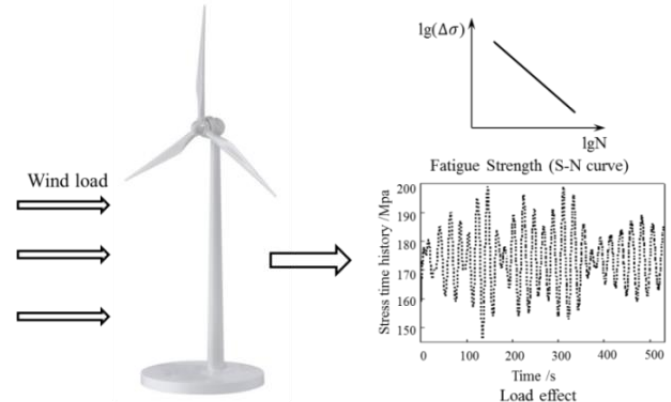


Fig.1 Fatigue calculation diagram

At present, there are two fundamental rotationally sampled wind spectrum models, namely, the Pacific Northwest Laboratory (PNL) model [5,8,10-13] and the Sandia National Laboratory (SNL) model [14,15]. With regard to the PNL model, Connell [7] found that there are significant differences between turbulent wind spectrum for the rotating blades and wind spectrum for the non-rotating blades, and that the energy redistribution is obvious. In order to describe the wind speed of rotating blades at a theoretic level, Connell [10] established a mathematical model of the rotational sampled wind spectrum in a rotating coordinate system. Powell [11] compared the theoretical model results to the measured data to validate the correctness of PNL model. Parameter analysis results show that turbulent wind speed variance and turbulent integral scales in longitudinal and lateral directions are important input parameters. Based on the PNL model, Powell and Connell [12] simulated the wind field of wind turbine structures and obtained the fluctuating wind speed taking the rotating effect of blades into account. However, only auto-spectrum was applied in the wind field simulation without considering correlation between the different fluctuating wind speeds. Based on the research findings proposed by Connell [10], Burton *et al.* [16] deduced the rotational cross-spectrum model that considered the correlation of different points located in the same blade. However, the correlation between the different points located on the different blades was not considered in the model. It is worth mentioning that the rotationally sampled spectrum of PNL model, which is an analytical formula, is generated through Fourier transformation of an autocorrelation function taken from Von Karman

spectrum (*one type of origin spectrum*). For origin spectrum, this requirement, which influences further popularization and application, is extremely strict.

Veers [14] adopted a rotational sampling method to develop another theoretically rotational spectrum model, namely, the SNL model. Phase lag terms were introduced to consider the rotational effect of blades. Veers [15] presented that through improving two kinds of variables, the differences between calculated results and measured results can be controlled because of open origin spectrum and coherence function. Kelley [17] successfully extended the velocity components of the SNL model from the longitudinal direction to three dimensions. However, the SNL model has the limitations of time-consuming, dissatisfying with Navier-Stokes equation, and artificially defining the coherence function [14,15].

He [18] put forward a rotational Fourier spectrum of wind turbine structures based on the physical mechanism, however, the derivation process was relatively complex and no comparison with the measured results was conducted.

Therefore, it is essential to establish a theoretically rotational wind spectrum model in this study, which has the advantages of a simple derivation process, clear physical mechanism, open origin function and reliable simulated results, to simulate the wind field of wind turbine structures.

In order to conduct the wind-induced response analysis in time domain, numerical simulation algorithm of wind field based on Monte-Carlo theory should be developed. At present, the main methods adopted in the fluctuating wind speed simulation are Linear Filter Method [19], Harmony Superposition Method [20], and Wavelet Analysis Method [21]. Based on the linear filtering technique, Linear Filter Method uses Auto-Regressive algorithm (*AR*), Moving Average algorithm (*MA*) and Auto-Regressive Moving Average algorithm (*ARMA*) to describe the stationary random process. Wavelet Analysis Method adopts good localization characteristics of the wavelet and inverse wavelet transform to simulate random processes. Compared with other methods, Harmony Superposition Method, which is widely used in design standards and professional software of wind turbine structures, has its merits of high accuracy, simple algorithm, and strict mathematical deduction. Veers [14] firstly applied this method to the wind turbine structure.

In light of the above, based on the theoretical rotational spectrum proposed by He [18], a simpler and more accurate rotational Fourier spectrum model optimized by the current authors is established to consider the influence of blade rotating effect and the correlation between different points located on the same and different rotating blades in this study. Based on the optimized coherence function, a comparison between the rotational Fourier spectrum model and real data is conducted to confirm high accuracy of the rotational Fourier spectrum model. Moreover, parameter analyses are carried out in details. Finally, turbulent wind fields around the tubular tower using the Kaimal spectrum and the rotating blades adopting rotational Fourier spectrum are simulated based on the Harmony Superposition Method.

2. Rotational Fourier spectrum model

2.1. Physical mechanism

With blades rotating, the spatial position of any point located on the blade varies. Hence, the wind speed of any point on the blade rotational plane not only reflects the fluctuating property of wind speed itself but also involves the wind speed fluctuation induced by periodic variation of a spatial point coordinate. To accurately describe the wind speed time series of rotating blades, the Cartesian coordinate system should be transformed into the rotating coordinate system first, and then the sampling points are regularly selected on the rotating plane of the rotor, as shown in Figure. 2. When the blade rotates to the sampling point, the wind speed of sampling point at this time should be extracted. According to the time sequence, a set of wind speed time series are obtained. Finally, the rotational Fourier spectrum is generated through Fourier transformation of the new wind speed time series. In fact, the greatest advantage of rotational Fourier spectrum is that the kinematic problem of rotating blades can be transformed into a static problem.

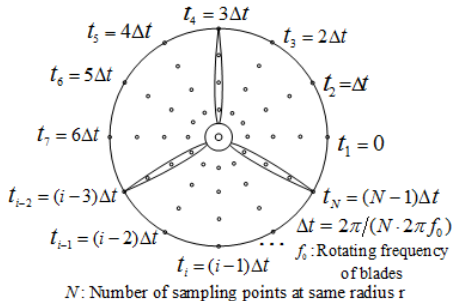


Fig.2 Sampling points position in rotating plane

2.2. Rotational Fourier auto-spectrum

In general, it is assumed that the wind field $U(x, y, z, t)$ is uniformly incompressible and isotropic. The mean wind speed is represented as $\bar{U}(z)$, and the fluctuating wind speed, which is represented as $u(x, y, z, t)$, is usually assumed to be a Gauss random process with zero mean value. In addition, for fluctuating wind field around blades, only the longitudinal component has obvious rotational effect, and lateral and vertical components are relatively complex. Herein, it is defined that the blades rotational plane is perpendicular to longitudinal direction, and the lateral direction is parallel to the blades rotational plane. Therefore, only the longitudinal fluctuating wind speed of the blades conducts the rotational Fourier spectrum analysis.

It is assumed that the blades rotate at a constant frequency, f_0 . At any radius, r , u_1 is the wind speed time series at time, t , and u_2 is the wind speed time series at time, $t + \tau$ and radius, r . τ is the time interval. The cross-correlation function between u_1 and u_2 is represented as follows:

$$R_{u_1 u_2} = E[u_1(t)u_2(t + \tau)] \quad (1)$$

According to the Wiener-Khintchine formula [22], the cross-power spectrum density between u_1 and u_2 is as follows:

$$S_{u_1 u_2}(f) = \int_{-\infty}^{+\infty} R_{u_1 u_2}(\tau) \cdot e^{-i2\pi f \tau} d\tau \quad (2)$$

The corresponding inverse Fourier transformation is as follows:

$$R_{u_1 u_2}(\tau) = \int_{-\infty}^{+\infty} S_{u_1 u_2}(f) \cdot e^{i2\pi f \tau} df \quad (3)$$

It is assumed that the fluctuating wind velocity obtained by sampling in the blade rotational plane is isotropic. Therefore, auto-power spectral density is independent of the spatial position of sampling points. The classical fluctuating wind spectrum density, such as the Von Karman wind spectrum [23] and the Kaimal wind spectrum [24, 25], is adopted as auto-power spectrum in this study. The relational expression between the fluctuating wind velocity cross-power spectrum and auto-power spectrum (*origin spectrum*) is represented as follows:

$$S_{u_1 u_2}(f) = \sqrt{S_{u_1 u_1}(f)S_{u_2 u_2}(f)}\gamma(\tau, f) = S_u(f)\gamma(\tau, f) \quad (4)$$

where $\gamma(\tau, f)$ is the coherence function. Dragt [26], Sørensen[27] and Veers [15] suggest the following exponential form [28]:

$$\gamma(\tau, f) = \exp\left(-\frac{a \cdot d(\tau) \cdot f}{\bar{U}_h}\right) \quad (5)$$

In Equation 5, a is the decay constant. The specific value of a , which is obtained by experiment, ranges from 7~20. \bar{U}_h is the mean wind speed at the height of the hub; $d(\tau)$ is the distance between two points during time, τ , as is shown in Figure 3. The calculating equation recommended by Dragt [26] is as follows:

$$d(\tau) = 2r \left| \sin \frac{2\pi f_0 \tau}{2} \right| = 2r \left| \sin \frac{\phi}{2} \right| \quad (6)$$

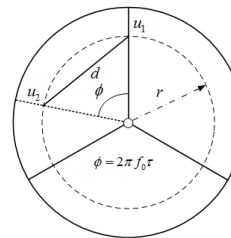


Fig.3 The geometry sketch diagram of rotational Fourier auto-spectrum

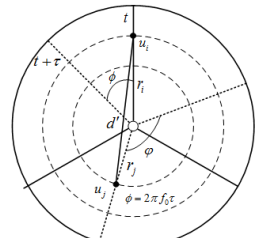


Fig.4 The geometry sketch diagram of rotational Fourier cross-spectrum

According to Taylor frozen hypothesis [29, 30], the cross-correlation function between u_i and u_j can be transformed into the auto-correlation function for any point at different times, namely, $\hat{R}_{uu}(\tau) = R_{u_i u_j}(\tau)$. Therefore, the rotational Fourier auto-spectrum at any point of blades could be obtained through Fourier transformation from auto-correlation function $\hat{R}_{uu}(\tau)$, and the specific formula is as follows:

$$\begin{aligned}\hat{S}_{uu}(f) &= \int_{-\infty}^{+\infty} \hat{R}_{uu}(\tau) \cdot e^{-i2\pi f\tau} d\tau \\ &= \int_{-\infty}^{+\infty} S_u(f') df' \cdot \int_{-\infty}^{+\infty} \gamma(\tau, f') \cdot e^{i2\pi(f'-f)\tau} d\tau\end{aligned}\quad (7)$$

It can be seen in Equation 5 that the coherence function $\gamma(\tau, f)$ belongs to the triangular form of Fourier series and the period is $1/f_0$. Therefore, it can be expanded into the exponential form of the Fourier series as follows:

$$\gamma(\tau, f) = \sum_{n=-\infty}^{+\infty} t_n(f) \cdot e^{i2\pi n f_0 \tau} \quad (8)$$

In Equation 8, f_0 is the rotating frequency of blades; $t_n(f)$ is the complex Fourier coefficient, namely, rotational mode, given in Equation 9.

$$\begin{aligned}t_n(f) &= f_0 \int_0^{1/f_0} \gamma(\tau, f) \cdot e^{-i2\pi n f_0 \tau} d\tau \\ &= \frac{1}{2\pi} \int_0^{2\pi} \gamma(\phi, f) \cdot e^{-i\cdot n \phi} d\phi\end{aligned}\quad (9)$$

The property of Dirac delta function, namely, δ function can be represented as follows:

$$\int_{-\infty}^{+\infty} e^{-i2\pi(f-f'-nf_0)\tau} d\tau = \delta(f - nf_0 - f') \quad (10)$$

Substituting Equation 8 and Equation 10 into Equation 7, the basic equation of rotational Fourier auto-spectrum can be obtained as follows:

$$\hat{S}_{uu}(f) = \sum_{n=-\infty}^{+\infty} t_n(f - nf_0) \cdot S_u(f - nf_0) \quad (11)$$

Furthermore, Substituting Equation 9 into Equation 11, the specific formula of the rotational Fourier auto-spectrum is obtained in the following form:

$$\hat{S}_{uu}(f) = \frac{1}{2\pi} \sum_{n=-\infty}^{+\infty} \int_0^{2\pi} \gamma(\phi, f - nf_0) \cdot \cos(n\phi) d\phi \cdot S_u(f - nf_0) \quad (12)$$

2.3. Rotational Fourier cross-spectrum

In light of the above, the PNL model does not consider the correlation of fluctuating wind speed at different points on rotating blades. In addition, the SNL model considers the correlation of wind speed at different points through directly adopting the coherence function to construct the rotational power cross-spectrum in the Cartesian coordinate system. It is worth noting that due to the rotational effect of blades, the method of employing the product of rotational power auto-spectrum and coherence function does not work. Herein, the correlation of the fluctuating wind speed at different points on the rotating blades is deduced in the rotating coordinate system.

It is assumed that u_i represents the wind speed time series of any point at time, t and radius, r_i ; u_j is the wind speed time series of another point at time, $t + \tau$ and radius, r_j . $d'(\tau)$ is the distance between two points, as shown in Figure 4. The equation for determining d' is given in Equation 13.

$$d'(\tau) = \sqrt{r_i^2 + r_j^2 - 2r_i r_j \cos(2\pi f_0 \tau + \varphi)} \quad (13)$$

In this equation, φ is the initial phase angle of the blade; when two points

are on the same blade, $\varphi = 0$, and the rotational Fourier cross-spectrum is described as the cross-spectrum between different points on the same blade. When two points are located on the different blades, $\varphi = 2\pi/N$, where N is the number of blades. For the wind turbine structures applied in this study, $\varphi = 2\pi/3$, and the rotational Fourier cross-spectrum is expressed as the cross-spectrum between different points on the different blades. Therefore, through introducing the initial phase angle φ , the rotational Fourier cross-spectrum truly considers the correlation of the fluctuating wind speed on the blades rotating plane.

The derivation of rotational Fourier cross-spectrum is similar to the rotational Fourier auto-spectrum, and only the coherence function $\gamma'(\tau, f)$ transforms into the following form:

$$\gamma'(\tau, f) = \sum_{n=-\infty}^{+\infty} t'_n(f) \cdot e^{i\cdot n(2\pi f_0 \tau + \varphi)} \quad (14)$$

The corresponding complex Fourier coefficient, namely, the rotational mode can be expressed into the following equation:

$$\begin{aligned}t'_n(f) &= f_0 \int_0^{1/f_0} \gamma'(\tau, f) \cdot e^{-i\cdot n(2\pi f_0 \tau + \varphi)} d\tau \\ &= \frac{1}{2\pi} \int_0^{2\pi} \gamma'(\phi, f) \cdot e^{-i\cdot n(\phi + \varphi)} d\phi\end{aligned}\quad (15)$$

Finally, the basic and detailed forms of the rotational Fourier cross-spectrum are given in Equation 16 and Equation 17, respectively.

$$\hat{S}_{u_i u_j}(f) = \sum_{n=-\infty}^{+\infty} t'_n(f - nf_0) \cdot S_u(f - nf_0) \cdot e^{i\cdot n\cdot \varphi} \quad (16)$$

$$\hat{S}_{u_i u_j}(f) = \frac{1}{2\pi} \sum_{n=-\infty}^{+\infty} \int_0^{2\pi} \gamma'(\phi, f - nf_0) \cdot \cos(n\phi) d\phi \cdot S_u(f - nf_0) \quad (17)$$

It can be seen from Equation 11 and Equation 16 that the rotating Fourier spectrum is superposed of infinitely classical fluctuating wind origin spectrum, obtained by translating to integer times of rotating frequency f_0 , multiplied by corresponding rotational mode. Therefore, it is not accurate to apply the classic fluctuating wind speed spectrum (*auto-power spectrum*) such as the Von Karman spectrum and the Kaimal spectrum for predicting the extreme loads and fatigue loads.

It is worth mentioning that when the order of the Fourier series, n is sufficiently large, both Equation 12 and Equation 17 involve the integral of high oscillatory functions. In order to avoid the occurrence of Runge oscillation, the classical Filon method [31] is applied to solve this type of integral.

2.4. The Comparison between Origin Spectrum and Rotational Fourier Spectrum

In order to compare the difference between the origin spectrum and rotational Fourier spectrum, the measured wind turbine structure at Clayton in New Mexico, conducted by Connell [11], is taken as a case. In the case provided by Connell, the height of the hub is 30.5m. The radius of the blades is 19m. The mean wind speed at the height of the hub is 8.21m/s. The rotating frequency of blades is 0.667Hz. The longitudinal turbulence standard deviation is 0.79m/s. The ground roughness length is 0.005m. The longitudinal turbulence integral scale is 112m. The lateral turbulent integral scale is 45m. In addition, the Von Karman fluctuating wind spectrum is adopted as the origin spectrum of the rotational Fourier spectrum. The specific equation is as follows [23]:

$$\frac{f \cdot S_u(f)}{\sigma_u^2} = \frac{4f \cdot L_u / V_{hub}}{\left[1 + 70.8(fL_u / V_{hub})^2\right]^{5/6}} \quad (18)$$

In this equation, V_{hub} represents the mean wind speed at the height of hub; σ_u represents the longitudinal turbulence standard deviation; L_u represents the longitudinal turbulence integral scale.

Based on the parameters provided above, a program was created by using MATLAB software [32]. The calculated results are shown in Figure 5 through Figure 6.

As shown in Figure 5(a), with an increase in the order n (*integer multiple of rotational frequency*) of the origin spectrum, the spectrum peak is translated to the position which corresponds to n times of rotating frequency, and each peak value is equal. Moreover, the peak values of n -order rotational mode are observed at the integer multiple of the rotating frequency, and with increase in order n , the peak values gradually decrease (*see Figure 5(b)*).

Compared with the Von Karman spectrum, the energy distributions of the rotational Fourier spectrum, which transfer from the low frequency range to high frequency range, produce fundamental change, as shown in Figure 6. In addition, the spectrum peak values appear at the integer multiples of the rotating frequency.

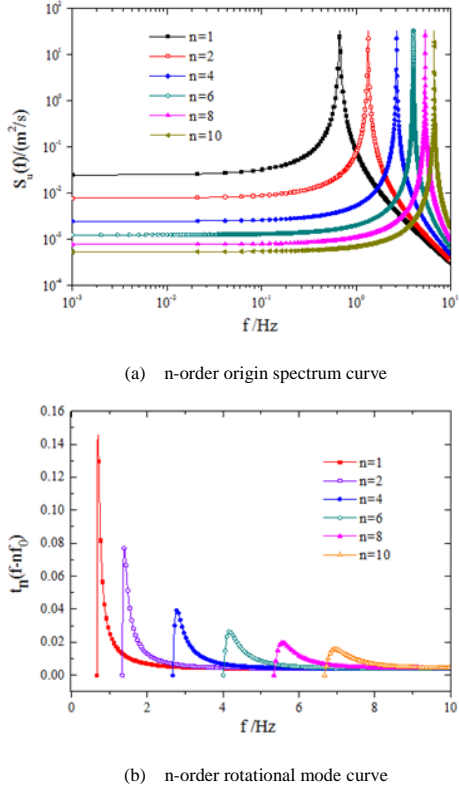


Fig.5 The translated origin spectrum and rotational mode curve

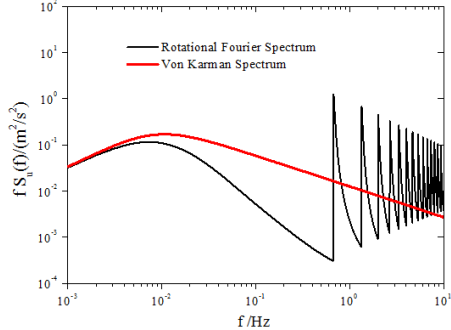


Fig.6 Comparison between Von Karman spectrum and rotational Fourier spectrum

2.5. Optimization of Coherence Function

It can be observed from Equation 12 and Equation 17 that the coherence function has a key influence on the rotational Fourier spectrum. Generally, the coherence function adopts Davenport exponential form. Firstly, the coherence function type in Equation 5 and Equation 6, recommended by Dragt [26], is explored. It can be observed in Figure 5(b) that the frequency of each order rotational mode only starts from the corresponding integer multiples of the rotating frequency. The reason for this is that in order to guarantee the coherence function satisfying the equation $0 \leq \gamma(\phi, f - nf_0) \leq 1$, the frequency must meet $f > n \cdot f_0$ based on the positive decay constant.

As shown in Figure 5(b), the rotational modes appear as stepped variations at the integer multiples of the rotational frequency, the case that is unreasonably held by Dragt [26]. In order to investigate the essential cause of this variation, the first-order coherence function and rotational mode varying with rotating angle ϕ near the rotating frequency f_0 are taken as an example, as drawn in Figure 7.

It can be seen from Figure 7 that when $f = f_0 = 0.667$, the integral of the first-order rotational mode and coherence function values in the interval $[0, 2\pi]$ are always equal to 0 and 1, respectively. When the frequencies f stay away from the rotating frequency f_0 , the integral values of the first-order rotational mode, which are greater than 0, increase first and decrease afterwards

as rotating angle ϕ increases. In addition, the coherence function, which is obviously smaller than the corresponding values when $f = f_0 = 0.667$, decreases first and increases afterwards.

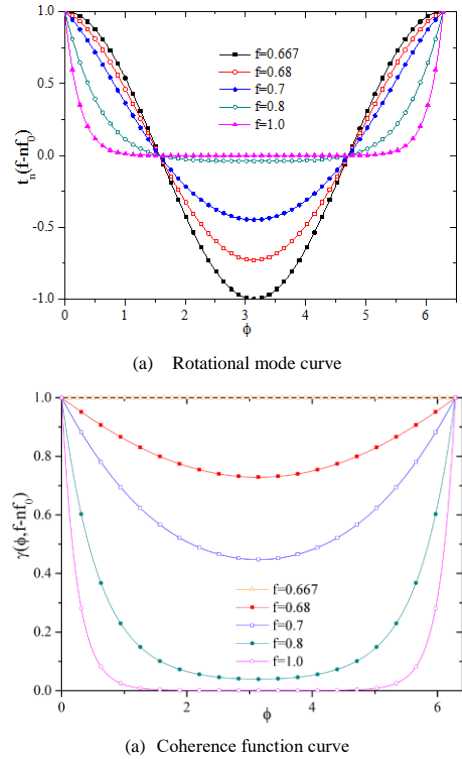


Fig.7 Rotational mode and coherence function varying with rotating angle

On the whole, the reason why the rotational Fourier spectrum appear as stepped variations at the integer multiples of the rotational frequency is because the coherence function values are always equal to 1 when $f = nf_0$, leading to the results that each order rotational mode is always equal to 0 when $f = nf_0$. In fact, the δ function and constant, 1 are conjugate functions of a pair of Fourier transformations. When the frequency, f is equal to nf_0 , the coherence function values are always equal to 1, hence the rotational mode function is equal to the δ function. According to the property of Dirac delta function, only when n is equal to 0, this function is not equal to 0, which contradicts the fact that each order rotational mode value is greater than 0 except when the frequency f is equal to nf_0 . In addition, the frequency cannot cover the whole frequency ranges. Consequently, the exponential form of coherence function proposed by Dragt [26] and Veers [15] is unreasonable, and the reasonable function form should be reconstructed.

According to the above analysis, the reconstructed coherence function should be less than 1. Therefore, the traditional Davenport type should be modified through adding minor items. The modified coherence function suggested by IEC61400-1:1999 [33] and Burton [16] is as follows:

$$\gamma(\phi, f) = \exp(-8.8 \cdot d(\phi) \cdot \sqrt{\left(\frac{f}{V_{hub}}\right)^2 + \left(\frac{0.12}{L_u}\right)^2}) \quad (19)$$

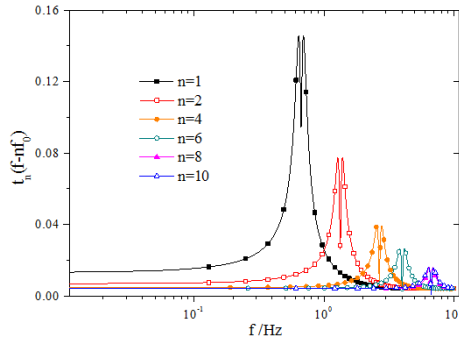
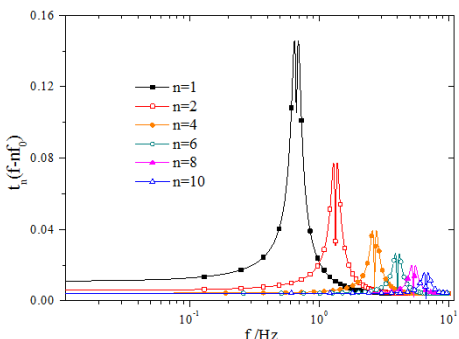
Furthermore, the modified coherence function model is put forward by IEC61400-1:2005[25] and GBT 18451.1-2012 [34]. The specific formula takes the following form:

$$\gamma(\phi, f) = \exp(-12 \cdot d(\phi) \cdot \sqrt{\left(\frac{f}{V_{hub}}\right)^2 + \left(\frac{0.12}{L_u}\right)^2}) \quad (20)$$

where L_u is equal to $8.1\Lambda_u$ and Λ_u represents the turbulent scale parameter. Here, values of Λ_u at the height of hub are described as follows [25, 34]:

$$\Lambda_u = \begin{cases} 0.7z & z \leq 60m \\ 42m & z \geq 60m \end{cases} \quad (21)$$

The definitions of other parameters have been described earlier.

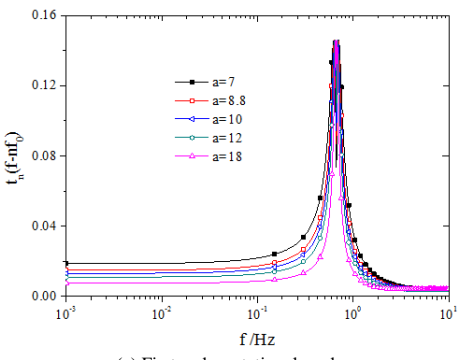
(a) Each order rotational mode when a is equal to 10(b) Each order rotational mode when a is equal to 12**Fig.8** Each order rotational mode when a is equal to 10 and 12

As is shown in Equation 19 and Equation 20 and compared with coherence function form shown in Equation 6 and Equation 7, the modified formulas not only add minor terms, but also gradually adjust the decay coefficient a . In general, the value of a ranges are from 7 to 20. The variation laws between each order rotational mode and frequency when a is equal to 10 and 12 are provided in Figure 8.

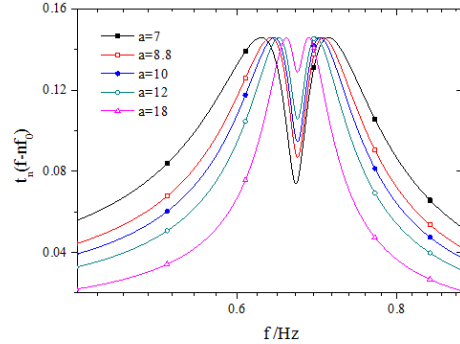
It can be shown in Fig.8 that being different from the coherence function form shown in Equation 6 and Equation 7, each order rotational mode after adopting the modified coherence function, which distributes over the whole frequency range, are all greater than 0 when $f = nf_0$ even if $n = 10$. Moreover, when the same decay coefficient a is employed, stepped variation values induced by adopting the modified coherence function are smaller than the corresponding values caused by the traditional Davenport type of coherence function (see Figure 5(b) and Figure 8(a)). Therefore, the modified coherence function, through adding minor items is reasonable. Apart from this, it is necessary to investigate the influence of the decay coefficient on the rotational mode and rotational Fourier spectrum. Herein, based on the modified coherence function form, a is selected as 7, 8.8, 10, 12 and 18 to study this influence, respectively.

2.5.1. Impact on Rotational Mode and Rotational Fourier Spectrum

The impact of the decay constant on the rotational mode function is explored first. The rotational mode values at rotating frequency f_0 , corresponding to different decay constant are provided in Figure 9(a). Due to numerous data points at rotating frequency f_0 , the locally enlarged drawings at rotating frequency f_0 are provided to clearly show the influence of the decay constant, as illustrated in Figure 9(b).



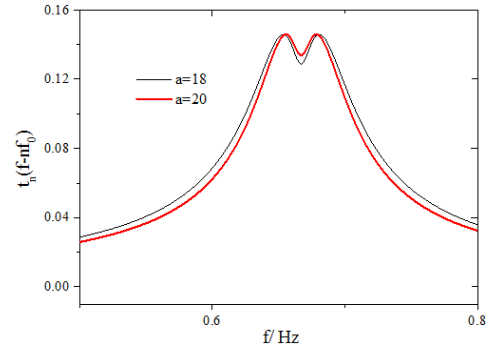
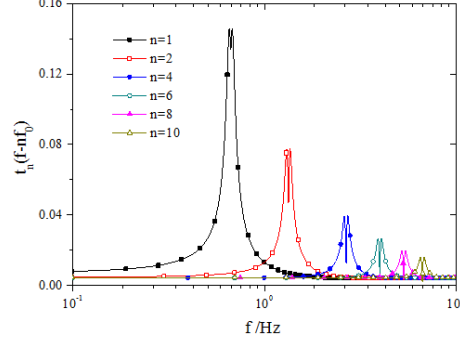
(a) First-order rotational mode



(b) locally enlarged drawings at the rotating frequency

Fig.9 First-order rotational mode corresponding to different decay

According to Figure 9, within the range staying away from f_0 , the decay constant can decrease the rotational mode values. Moreover, the decay coefficient could lead to higher rotational mode values near f_0 . It is worth noting that when the decay constant reaches the extreme value of 20, the drop-off phenomenon is least significant near f_0 (see Figure 9 and Figure 10(a)). Also, Figure 10(b) shows each order of rotational mode function when a is equal to 20. It is clearly seen that compared with the decay constant adopted by IEC61400-1:2005[25] ($a=12$), each order value of rotational mode is dramatically increased near nf_0 when a is equal to 20 (see Figure 8(a) and Figure 10(b)).

(a) First-order rotational mode when a is equal to 18 and 20(b) Each order rotational mode when a is equal to 20**Fig.10** Rotational mode values when a is equal to 18 and 20

In general, the increased decay constant gives each order rotational mode the tendency to be sharp, and increases the energy at the integer times of the rotating frequency. In other words, with increase in decay constant, the drop-off phenomenon can be further eliminated.

Furthermore, the influence of the decay constant on the rotational Fourier spectrum needs to be studied, as detailed in Figure 11. Being similar to the results of rotational mode, the increased decay constant makes the energy transfer from the low frequency ranges to high frequency ranges. Based on Equation 11 and Equation 16, each rotational mode has a drop-off phenomenon at the integer times of the rotating frequency, which eventually brings about the same case for rotational Fourier spectrum. In addition, the drop-off phenomenon is least evident at the integer times of the rotating frequency when a is equal to 20.

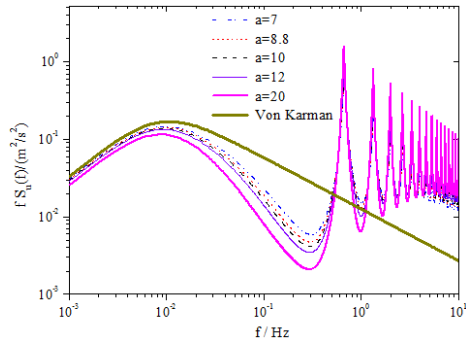


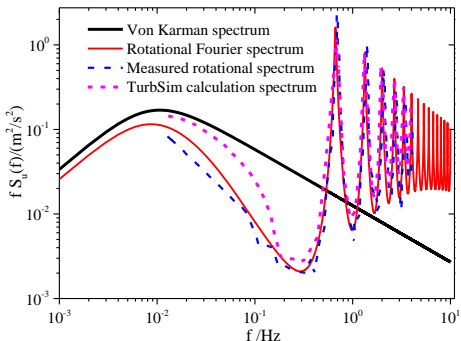
Fig.11 Rotational Fourier spectrum corresponding to different decay constant

Overall, the selection of decay constant has a great influence on the rotational mode function and rotational Fourier spectrum. The increased decay constant makes the wind field energy around blades generate redistribution, and further weakens the drop-off phenomenon. Therefore, considering that the decay constant ($a=12$), which is applied by IEC61400-1:2005[25], still lead to significant drop-off phenomenon, the upper limit of decay constant $a=20$ is recommended and adopted in the next section.

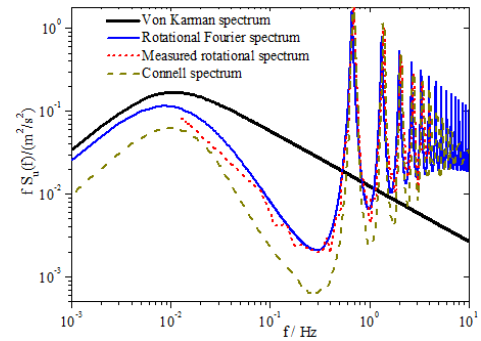
2.5.2. Comparison with measured data

According to Equation 12 and the optimized coherence function, the rotational Fourier spectrum is programmed, and then the calculated results are compared to the measured rotational spectrum conducted by Connell [11]. It is worth mentioning that the measured rotational spectrum only takes the first five harmonic frequencies. This is possibly due to the fact that Nyquist frequency (*half of the sampling frequency*) must exceed the highest frequency of sampled signal to ensure the reconstruction of the original continuous signal. Compared results are provided in Figure 12(a). As indicated in Figure 12(a), the rotational Fourier spectrum values based on proposed model in this study and optimized decay constant have better agreement with measured rotational spectrum values.

In order to further verify the accuracy of the rotational Fourier spectrum model, this spectrum model is compared with the Connell spectrum (*PNL model*) as well as TurbSim calculation spectrum (*based on the modified SNL model*) [35], as shown in Figure 12. It can be clearly seen that the deviation values of the PNL model from the measured rotational spectrum in the wave trough are relatively larger, compared with the proposed rotational Fourier spectrum in this study. The rotational Fourier spectrum has good agreement with the TurbSim calculation spectrum, especially in the high frequency range which is important for rotational sample. This apparent difference in the low frequency range between TurbSim calculation spectrum and rotational Fourier spectrum is attributed to that the Von Karman spectrum used as origin spectrum of SNL model has lower accuracy when the frequency is smaller than the rotating frequency of blades [15]. Therefore, the rotational Fourier spectrum around the blades can accurately predict the extreme load and fatigue load of wind turbine structure.



(a) Comparison with measured rotational spectrum and TurbSim calculation spectrum



(b) Comparison with Connell spectrum (PNL model)
Fig.12 Comparison between the proposed rotational Fourier spectrum and the different rotational spectrum models

2.6. Parameter analysis of Rotational Fourier Spectrum

The rotational Fourier spectrum model is related to the calculated radius of the blade, rotating frequency of blades, mean wind speed at the height of hub, and the fluctuating wind speed correlations of different points. This study considers a typical pitch-controlled 1.25MW wind turbine structure, based on which parameter analyses of rotational Fourier spectrum are carried out to explore their influence laws.

In this study, it is considered that the diameter of blades is 64.35m; the rated rotating speed of blades is 17.8r/min; the height of the hub is 63.342m; the mean wind speed at the height of hub V_{hub} is 12 m/s and ground roughness length is 0.005m. The origin spectrum of the rotational Fourier spectrum adopts the Kaimal wind spectrum recommended by IEC61400-1:2005[25] where the detailed formula is as follows:

$$f S_u(f) = \frac{4f(L_u/V_{hub})}{(\sigma_u^2(1+6f(L_u/V_{hub}))^{5/3})} \quad (22)$$

According to the IEC standards [25], the longitudinal turbulence standard deviation σ_u is 1.752m/s and the longitudinal turbulence integral scale, L_u is 340.2m. The coherence function uses the optimized exponent form, and the specific equation is as follows:

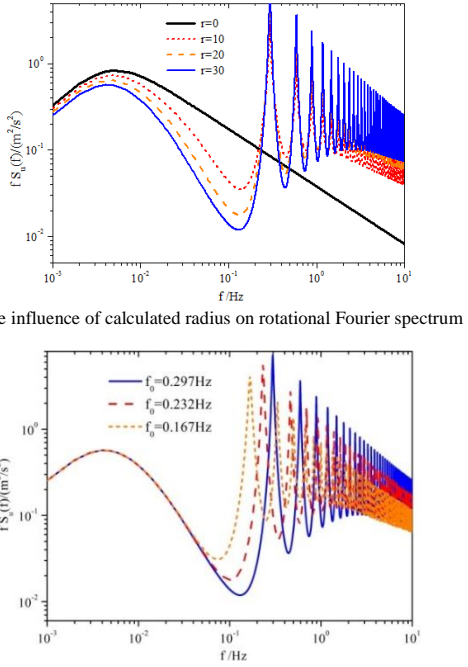
$$\gamma(\phi, f) = \exp(-20 \cdot d(\phi) \cdot \sqrt{\left(\frac{f}{V_{hub}}\right)^2 + \left(\frac{0.12}{L_u}\right)^2}) \quad (23)$$

where $d(\phi)$ represents the distance between two points. For the rotational Fourier auto-spectrum, $d(\phi) = 2r \left| \sin\left(\frac{\phi}{2}\right) \right|$ and for the rotational Fourier cross-spectrum, Equation 13 is adopted.

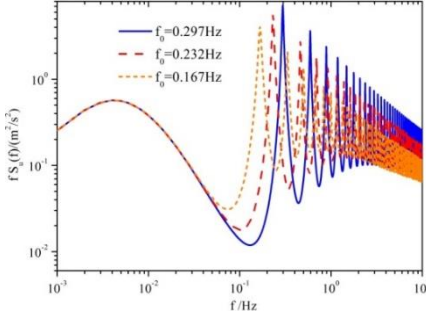
2.6.1. Calculated radius of blades

As can be seen from Equation 23, the calculated radius r on the blade is closely related to the coherence function, which further influences the rotational Fourier spectrum. In this study, r is taken as 0, 10, 20 and 30m to investigate this influence. The analysis results are provided in Figure 13(a).

It is clearly seen in Figure 13(a) that when the calculated radius is equal to 0, the calculated point locates at the height of hub, and the rotating effect disappears, indicating that the rotational Fourier spectrum degenerates into the Kaimal spectrum of fixed points. Moreover, within low frequency components staying away from nf_0 , the increased calculated radius can decrease the rotational Fourier spectrum values. For high frequency components near nf_0 , the increased radius could lead to larger rotational Fourier spectrum values. This implies that the energy transfers from the low frequency to high frequency gradually, and high frequency oscillation becomes more and more severe. It is worth noting that when the calculated radius reaches 30m, the energy redistribution phenomenon is most significant.



(a) The influence of calculated radius on rotational Fourier spectrum



(b) The influence of rotating frequency on rotational Fourier spectrum

Fig.13 The influence of radius and blades rotating speed on rotational spectrum

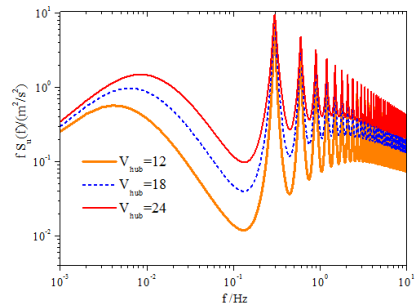
2.6.2. Rotating speed of blades

According to Equation 12, the rotational Fourier spectrum is closely related to the rotating frequency of the blades. For the 1.25MW wind turbine structure studied in this study, the working speed of the rotor is 9.6~17.8 r/min, and therefore the corresponding rotational frequency range is 0.16~0.30 Hz. To study the influence of the rotating speed on the rotational Fourier spectrum, the rotating frequencies are chosen as 0.167 Hz, 0.232 Hz and 0.297Hz and the corresponding calculated results are given in Figure 13(b).

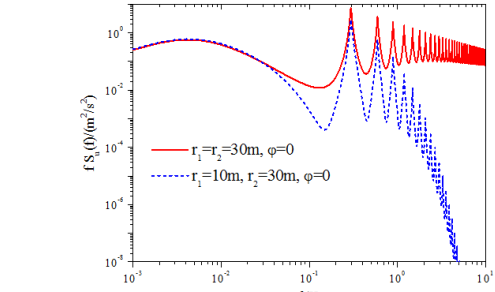
According to Figure 13(b), the increased rotating frequency can result in larger rotational Fourier spectrum peak values, which indicates that the rotating effect of the blades becomes more significant. In addition, with an increase in the rotating frequency, the peak values of the rotational Fourier spectrum near ηf_0 translate to the high frequency range side.

2.6.3. Mean wind speed

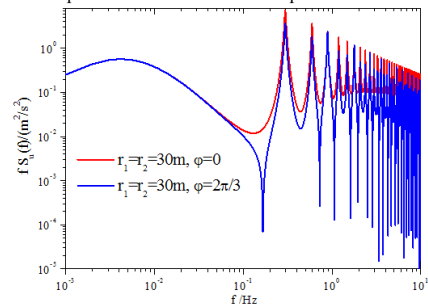
For the wind turbine structures in service discussed in this study, the cut-in wind speed (*minimum wind speed of electrical generation*) is 4m/s, the rated wind speed (*corresponding to the rated power*) is 16m/s, and the cut-out wind speed (*maximum wind speed of electrical generation*) is 25m/s. To deeply understand the influence of the mean wind speed at the height of the hub on the rotational Fourier spectrum, the mean wind speed is selected as 12, 18, and 24m/s. The analysis results are shown in Figure 14(a). It is clearly seen that the increased mean wind speed increases the rotational Fourier spectrum values and leads to significant rotating effect of the blades.



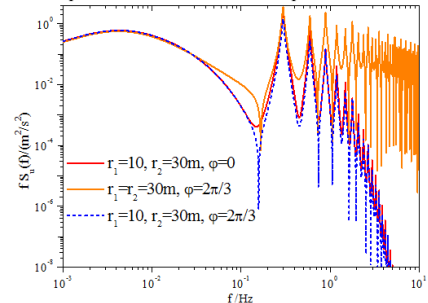
(a) The influence of mean wind speed on rotational Fourier spectrum



(b) The comparison of rotational Fourier spectrum for the same blade



(c) The comparison of rotational Fourier spectrum for the same radius



(d) The comparisons for different rotational Fourier cross-spectra

Fig.14 The influence of mean speed and correlation between different points on rotational Fourier spectrum

2.6.4. Correlation between different points

The influence of the correlation between different points on the wind-induced responses and fatigue issues is significant. The rotational Fourier spectrum model proposed in this study not only considers the correlation between different points located on the same blade, but also considers those located on different blades. Therefore, the rotational Fourier auto-spectrum $r_1 = r_2 = 30\text{m}, \varphi = 0$, rotational Fourier cross-spectrum including $r_1 = 10\text{m}, r_2 = 30\text{m}, \varphi = 0$, $r_1 = r_2 = 30\text{m}, \varphi = 2\pi/3$ and $r_1 = 10, r_2 = 30\text{m}, \varphi = 2\pi/3$ are considered to investigate the impact of the correlation. The corresponding calculated results are given in Figure 14(b) through Figure 14(d). As can be seen from Figure 14(b), for the same blade, the rotational Fourier auto-spectrum values are obviously greater than the rotational Fourier cross-spectrum values corresponding to different radii, especially within the high frequency ranges. Under the condition of the same radius, the rotational Fourier auto-spectrum values are almost the same as the rotational Fourier cross-spectrum values corresponding to different blades. However, the initial phase angle of the blade, φ brings about a significant influence on the rotational Fourier spectrum values (see Figure 14(c)). In addition, for the rotational Fourier cross-spectrum, the amplitude of the rotational Fourier cross-spectrum corresponding to the same radius and different blades is largest, and the rotational Fourier cross-spectrum corresponding to different blades and radii leads to the smallest amplitude (see Figure 14(d)).

3. Wind field simulation of wind turbine structure

Owing to the strongly nonlinear property of wind turbine structures, the time-domain method is used to directly understand the dynamic characteristics and obtain more information about fatigue issues compared with the frequency-domain method. Moreover, dynamic time history analysis of wind turbine structures requires time series data of the wind speed. In general, the artificial wind field simulation method, which is economical, fast and accurate, is widely used to obtain the accurate wind speed series data.

3.1. The application scope of turbulent wind spectrum

According to the kinetic property, parts of the wind turbine structures can

be classified into two types: the fixed part such as tower and the periodic rotating parts such as the blades. As mentioned previously, the wind field around the tower is essentially different from that around the blades. For any point on the tower, wind speed is only a function of time, so its turbulent wind spectrum is the same as that of high-rise buildings. In this study, the Kaimal wind spectrum recommended in IEC61400-1:2005 [25] is adopted to simulate the turbulent wind field of the tower. For any point attached to the rotating blade, the wind speed is not only related to the time, but also the periodic variations of the spatial position coordinate. Therefore, the turbulent wind spectrum of the blades needs to consider the rotational effect. This study uses the rotational Fourier spectrum deduced in the previous section to simulate the wind field of the blades. The illustrated diagram is given in Figure 15.

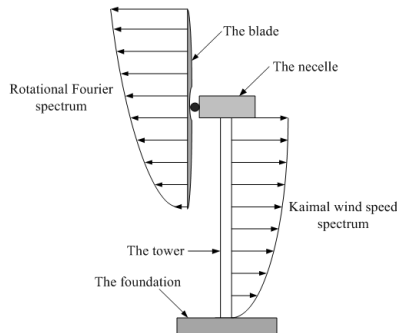


Fig. 15 Turbulent wind field model of wind turbine structures

3.2. Wind field simulation of tubular tower

Generally, for any point on the wind turbine structure, the wind speed consists of two parts: mean wind speed and fluctuating wind speed. The fluctuating wind field can be deemed as a four dimensional univariate random field. Furthermore, if the fluctuating wind field can be divided into the fluctuating wind field at each discrete spatial point, the fluctuating wind field can be assumed to be a multi-dimensional and multivariate stationary Gauss random process.

For mean wind speed, the exponential model describing the wind shear effect is widely used in the research field of wind turbine structures.

For wind turbine structures, the random characteristics of fluctuating wind speed at any point on the tubular tower can be described by the wind speed spectrum. As mentioned previously, the Kaimal wind spectrum is used to simulate the wind field of the tower, and shown in Equation 22. Moreover, the correlation between two points is reflected by the cross-power spectrum. Therefore, the cross-power spectrum can be described as follows:

$$S_{uv}(f) = \sqrt{S_{uu}(f)S_{vv}(f)} \cdot Coh(f) \quad (24)$$

At this time, the Davenport correlation function, presented by Davenport, is used for the calculation of the correlation between different spatial points on the tower. The detailed expression is as follows [37]:

$$Coh(f) = \exp\left(-\frac{f[C_y^2(y_1 - y_2)^2 + C_z^2(z_1 - z_2)^2]^{1/2}}{2[U(z_1) + U(z_2)]}\right) \quad (25)$$

Where f represents fluctuating wind frequency; y_i, z_i ($i=1,2$) represents the lateral and vertical coordinates of any two points on the tubular tower, and the line of two points is perpendicular to the direction of the mean wind speed; C_y, C_z represents the lateral and vertical exponent decay coefficient, the values of which are recommended as 16 and 10 respectively. $U(z_1), U(z_2)$ represents the mean wind speed at the height of z_1 and z_2 . In general, under the fixed fluctuating wind frequency, the correlation between two points on the tower becomes smaller with increase in distance between the two points.

3.3. Wind field simulation of the blades

The most significant difference between the wind field around the blades and the wind field of the tower is that the influence of the rotating effect on the wind field around the blades must be considered when the wind turbine structure is in operation. In addition, the mean wind speed for any point on the blade shows a periodic variation with the rotation of the blade.

3.3.1 Mean wind speed

As mentioned previously, when blades are in operation, the height of any point on the blade exhibits periodic harmonic variations. Based on the exponential model, the mean wind speed for any point at the radius r of the blade can be obtained as follows:

$$\bar{U}(r) = \bar{U}(z_h) \left(\frac{z_h + r \cos \phi}{z_h} \right)^\alpha \quad z = z_h + r \cos \phi \quad (26)$$

In this equation, r represents the radius of calculated point on the blade, i.e. the distance between the center of hub and the calculated point along the radial direction; $\phi = 2\pi f_0 t + \varphi$ is the azimuth angle of blades at the time, t in the vertical rotating plane; φ is the initial phase angle, and the location where the blade coincides with the opposite direction of gravity is defined as 0° azimuth angle. It is noted that the blades rotate along the anti-clockwise direction. z_h represents the height of hub; α represents the ground roughness coefficient.

3.3.2. Fluctuating wind speed

The random characteristics of fluctuating wind speed for any point on the blades can be reflected by the rotational Fourier spectrum model, which consists of the rotational Fourier auto-spectrum model and the rotational Fourier cross-spectrum model. The rotational Fourier auto-spectrum is shown in Equation 11. Moreover, the rotational Fourier cross-spectrum model is given in Equation 16. In addition, the Kaimal wind velocity spectrum is recommended to become the origin spectrum of the rotational Fourier spectrum.

3.4. Harmony superposition method

The time series of the incoming wind speed for the tower and the blades are simulated through the harmony superposition method proposed by Shinozuka [38]. The time series of the fluctuating wind speed can be simulated using the following equation:

$$u_j(t) = 2\sqrt{\Delta\omega} \sum_{k=1}^j \sum_{l=1}^N |H_{jk}(\omega_{kl})| \cos[\omega_{kl}t - \theta_{jk}(\omega_{kl}) + \phi_{kl}] \quad (27)$$

In this equation, $H_{jk}(\omega_l)$ represents elements of the lower triangular matrix $\mathbf{H}(\omega_l)$, which are acquired by the Cholesky decomposition of wind spectrum matrix $\mathbf{S}(\omega_l)$. The spectrum matrix $\mathbf{S}(\omega_l)$ consists of auto-power spectrum, which can be obtained using Equation 22 and Equation 11 for the tower and blades respectively, and cross-power spectrum which can be calculated using Equation 24 and Equation 16 for the tower and blades, respectively. ω_{kl} represents the double index frequency. ϕ_{kl} is the random phase angle. N represents the sampling points. $\Delta\omega = \omega_{up}/N$ is the frequency increment; ω_{up} is the upper bound cutoff frequency.

3.5. Case analysis and results

A typical pitch-controlled 1.25MW wind turbine structure with three blades is taken as the case to carry out the wind field simulation. The height of the hub is 63.342m. The diameter of the blade is 64.35m. The mean wind speed at the height of hub is assumed as 12m/s. The rotating frequency of blade is 0.297Hz. In order to input the aerodynamic loads acting on the wind turbine structures in the wind-induced vibration response analysis, three uniformly distributed lumped points along the radial direction of the blade are chosen as load input points and seven non-uniform distributed lumped points on the tubular tower are taken as the load input points. Therefore, the lumped points mentioned above are adopted to simulate the wind field of the wind turbine structures. The simplified dynamic analysis model of wind turbine structure is shown in Figure 16.

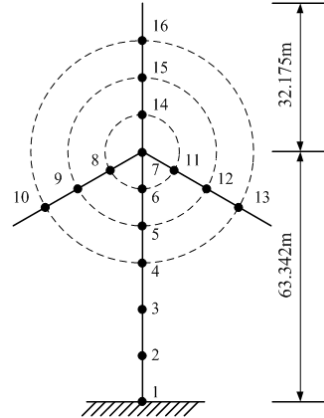


Fig. 16 Dynamic analysis model of wind turbine structure

3.5.1. Simulated results of the tower

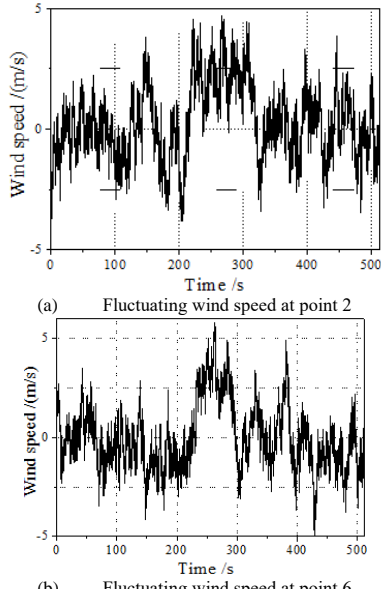
As mentioned above, the mean wind speeds of the tubular tower at point 1 through point 7 are given in Table 1.

Table 1

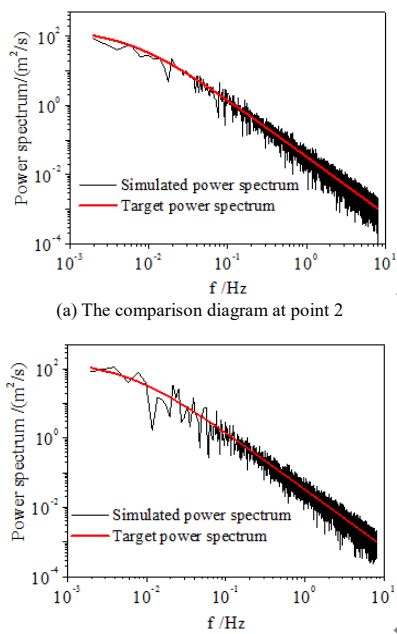
The mean wind speed of the tower at each calculated point

Number	Calculated height (m)	Mean wind speed (m/s)
7	63.342	12.00
6	55.298	11.71
5	47.255	11.49
4	39.211	11.23
3	26.141	10.70
2	13.070	9.85

In addition, based on the FFT technology, the fluctuating wind speed time series of the tubular tower at each calculated point are obtained through the MATLAB program [32]. Based on the harmony superposition method, the upper bound cutoff frequency, ω_{up} is set to be 8Hz in the process of computing. The number of the frequency sampling points, N is 4096, and the time increment, Δt is equal to 0.0625s. The duration, t is equal to 512s. The fluctuating wind speeds of the tubular tower at point 2 and point 6 (*selected as a representative*) are shown in Figure 17.

**Fig. 17** Fluctuating wind speed of tubular tower

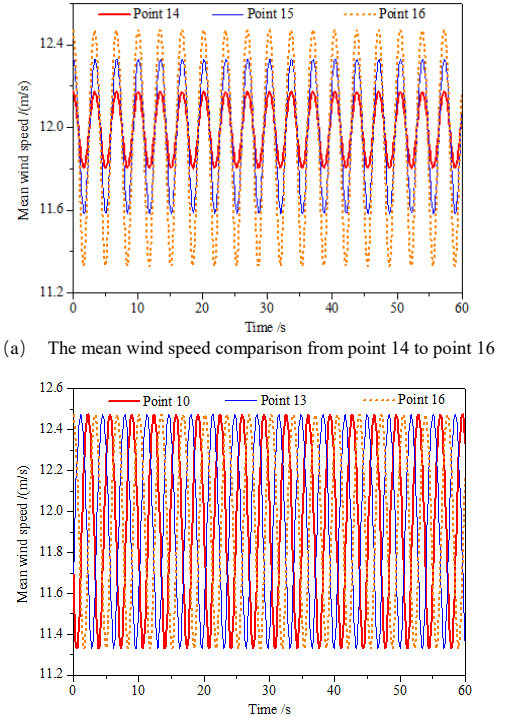
As indicated in Figure 17, the statistical characteristics of the simulated data are consistent with the assumptions. In order to verify the validity and reliability of the simulation method, comparative analyses between the calculated spectrum acquired through the spectrum analysis of the simulated wind speed time history, and the target wind spectrum (Equation 22) are carried out. The comparisons of wind spectrum at simulation point 2 and point 6 (*selected as a representative*) are shown in Figure 18.

**Fig. 18** Comparison of simulated spectrum and target spectrum of tubular tower

It is clearly seen in Figure 18 that the spectral trend line of the simulated wind spectrum is consistent with that of the target wind spectrum, and the mean value of the spectral line has good agreement with the target wind spectrum. Therefore, the method adopted in this study is effective to simulate the fluctuating wind speed of the tubular tower. Moreover, the parameters used in this study are reasonable and practical.

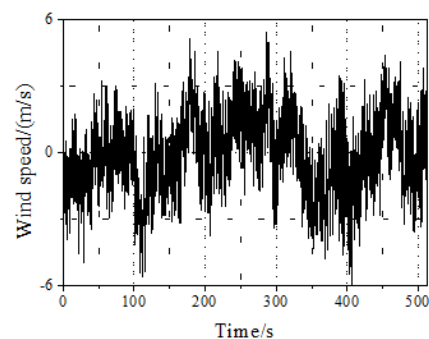
3.5.2. Simulated results of blades

According to Equation 26 and parameters given for the case, the mean wind speed at the calculated points of blades can be determined. As the period of the mean wind speed in China is 10min, only the first 60s duration are selected to clearly show the wind speed variation law against time. The reason for this is that periodic variation law of the blade mean speed is identical with those in the remaining duration. Comparisons of mean wind speed time history at different radii of the same blade are given in Figure 19(a). Comparisons of mean wind speed at the same radius of different blades are shown in Figure 19(b).

**Fig. 19** The mean wind speed comparison of the blades

It can be seen from Figure 19 that being different from the mean wind speed of calculated points on the tower, the mean wind speed of the calculated points on the blades shows a periodic variation, the varying frequency of which is rotating frequency of blades. In addition, with increasing calculated radius, the mean wind speed of calculated points on the same blade gradually increase. For the calculated points on the same radius of different blades, there is a phase difference, the value of which is $2\pi/N_b$, between the different blades. N_b represents the number of blades. For the case investigated in this study, the phase difference is $2\pi/3$.

Based on the harmony superposition theory and FFT computing technology, the program code developed in MATLAB [32] is used to acquire the fluctuating wind speed of uniformly distributed calculated points on the blades. The simulated parameters are identical to those adopted in the tubular tower. Similarly, the fluctuating wind speed of calculated point 9,12 and 15 (*selected as a representative*) on the blades are provided in Figure 20.

**(a)** Fluctuating wind speed at point 9

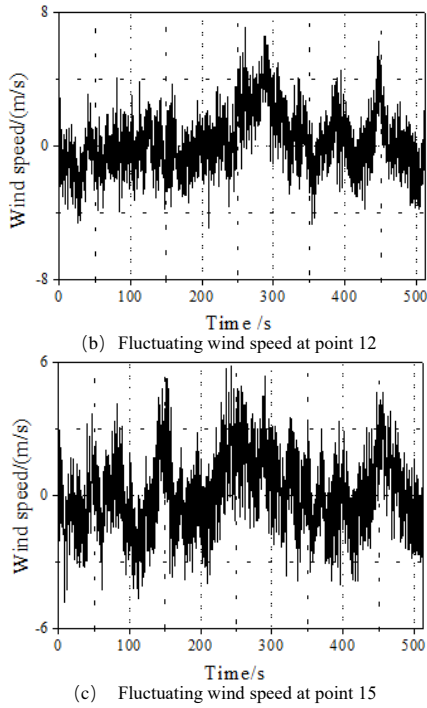


Fig. 20 Fluctuating wind speed of blades based on rotational Fourier spectrum

Similarly, the statistical analysis results of fluctuating wind speed are consistent with the theoretical hypothesis (see Figure 20).

Moreover, the calculations of fluctuating wind speed for corresponding points based on the Kaimal wind spectrum [3,9] are carried out, in order to consider the rotating effect of blades, as shown in Figure 21.

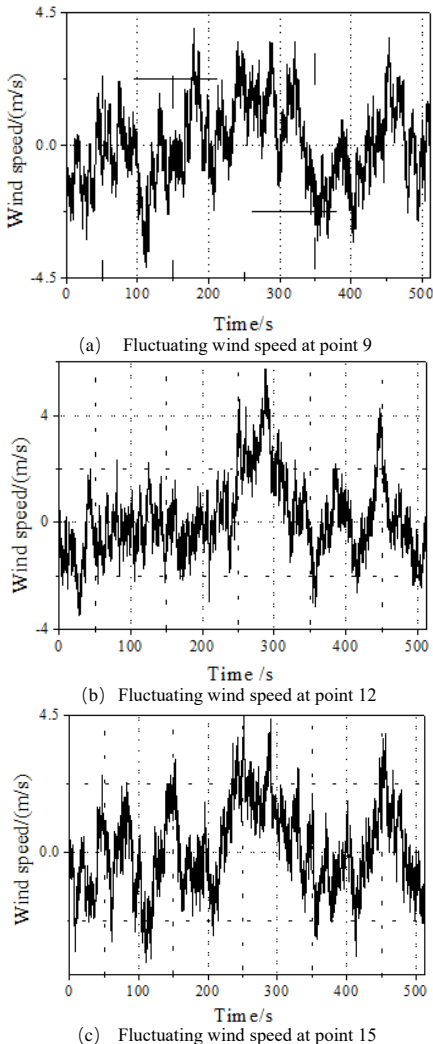


Fig. 21 Fluctuating wind speed of blades based on the Kaimal spectrum

As can be illustrated in Figure 21, compared with the fluctuating wind

speed without considering the rotating effect of blades, the fluctuating wind speed amplitude and vibration frequency based on rotational Fourier spectrum significantly increase. The reason for this is that after considering the rotating effect of blades, the fluctuating wind speed not only reflects the fluctuating characteristics against the time, but also exhibits the spatial variation property induced by the periodic coordinate variation of calculated point on the blade. In summary, the increased amplitude and vibration frequency of fluctuating wind speed inevitably have a significant influence on the extreme load and fatigue load of the wind turbine structures. This is the essential purpose of the rotational Fourier spectrum study.

In order to confirm the effectiveness and reliability of the simulated method, the comparisons between the calculated rotational Fourier spectrum obtained by spectrum analysis of simulated fluctuating wind speed on the blades and the target rotational Fourier spectrum (Equation 12) are conducted, and the corresponding results are shown in Figure 22.

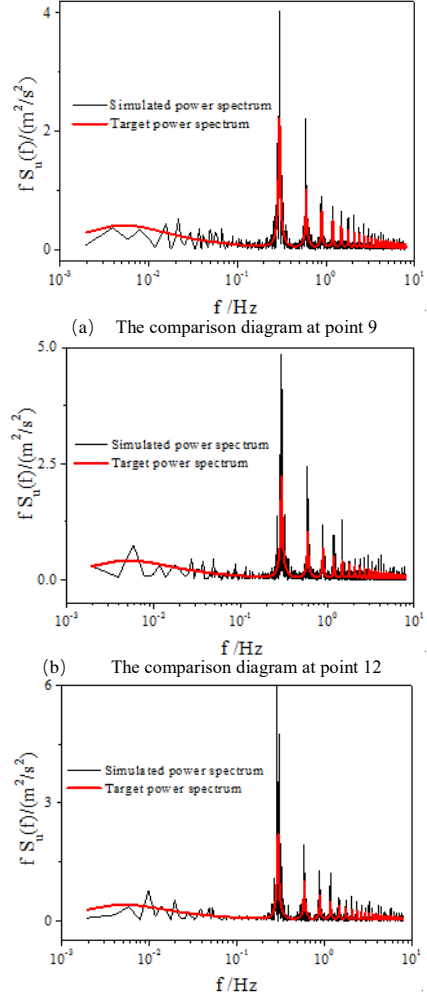


Fig. 22 Comparison between the simulated spectrum and target spectrum

Comparative results from Figure 22 also show that the calculated wind spectrums give good agreement with the target rotational Fourier spectrum. In general, the fluctuating wind speed is considered as a stochastic process. As a statistical variable, the comparison between different rotational spectrums, rather than between different fluctuating wind speed time series, can be regarded more reasonable. Both Connell [11,13,39] and Veers [15] pointed out that the accuracy of their own proposed rotational spectrum model should be verified by the comparison with other rotational spectrum models or measurement data. Besides, this approach can ensure the accuracy of prediction of wind speed by guaranteeing the same statistical characteristics [13]. The rotational Fourier spectrum proposed in this study for simulating the fluctuating wind speed of blades is made comparison with the measured rotational spectrum and other important rotational spectrums, which has verified high accuracy of the proposed rotational Fourier spectrum model. From the interpretation of the findings of this study, it can be deduced that the theory and method provided in this study can accurately predict wind speed of rotating blades which can be considered as a complex phenomenon.

4. Conclusions

In this study, the analytical expressions of the simpler and more accurate rotational Fourier auto-spectrum and rotational Fourier cross-spectrum were systematically deduced. The optimization analysis of the coherence function and

parameter analysis were conducted, and wind field simulation of the wind turbine structures based on the harmony superposition method were carried out. According to the analytical results, the main conclusions are noted as follows:

(1) The modified rotational Fourier spectrum model not only deals with the rotating effect of blades based on the physical mechanism, but also reflects the correlation between different points located on the same and different rotating blades. Therefore, compared with the classical wind spectrum model (*origin spectrum*), the rotational Fourier spectrum model presented in this study is more accurate to predict the extreme loads and fatigue loads.

(2) Compared with the Von Karman spectrum, energy distributions of the rotational Fourier spectrum are significant, especially within the high frequency ranges. Moreover, the spectrum peak values appear at the integer multiples of the rotating frequency.

(3) The optimized coherence function can not only further weaken the drop-off phenomenon of the rotational mode and the rotational Fourier spectrum, but also bring about more significant energy redistribution. In addition, compared with the PNL model, adopting the proposed rotational Fourier spectrum model and optimized coherence function can result in better agreement with the measured rotational spectrum.

(4) The increased calculating radius and rotating frequency of the blades can induce more significant energy redistribution phenomenon. Additionally, the increased mean wind speed can lead to higher spectrum values. The correlations between different points of blades are quite different.

(5) The simulations of the wind field around a tubular tower based on the Kaimal wind spectrum recommended in IEC61400-1:2005 and blades based on the rotational Fourier spectrum are reasonable and effective, by means of the harmony superposition method.

Acknowledgement

The authors wish to thank the Ministry of Science and Technology of China for financially supporting the research in the study through the Grant No. SLDRCE14-B-04.

References

- [1]. Bilgili M., Yasar A. and Simsek E., "Offshore wind power development in Europe and its comparison with onshore counterpart", Renewable and Sustainable Energy Reviews, 15(2), 905-915,2011.
- [2]. Heistermann C., Pavlović, M., Veljković, M., et.al. "Influence of execution tolerances for friction connections in circular and polygonal towers for wind converters", Advanced Steel Construction, 13(4), 343-360, 2017.
- [3]. Ke S.T., Ge Y. J. and Wang T. G., "Wind field simulation and wind-induced responses of large wind turbine tower-blade coupled structure", The Structural Design of Tall and Special buildings, 24(8), 571-590, 2015.
- [4]. Huo T., Tong L.W., and Zhang Y. F., "Dynamic response analysis of wind turbine tubular towers under long-period ground motions with the consideration of soil-structure interaction", Advanced Steel Construction, 14(2), 227-250, 2018.
- [5]. Shan W. and Shan M., "Fatigue load estimation and reduction for wind turbine", EWEA 2015 Europe's Premier Wind Energy Event, Paris, France, 2015.
- [6]. Rosenbrock H.H., "Vibration and stability problem in large turbines having hinged blades", British Electrical and Allied Industries Research Association, 1955.
- [7]. Connell J.R., "Turbulence spectrum observed by a fast-rotating wind-turbine blade", Report No. PNL-3426, Battelle Pacific Northwest Labs., Richland, WA (USA), 1980.
- [8]. Powell D.C. and Connell J.R., "Verification of Theoretically Computed Spectra for a Point Rotating in a Vertical Plane", Solar Energy, 39(1), 53-63, 1987.
- [9]. Ke S.T., Wang T.G., Ge Y.J., et.al. "Aeroelastic response of ultra large wind turbine tower-blade coupled structures with SSI effect", Advances in Structural Engineering, 18(12), 2075-2087, 2015.
- [10]. Connell J.R., "The spectrum of wind speed fluctuations encountered by a rotating blade of a wind energy conversion system", Solar Energy, 29(5), 363-375,1982.
- [11]. Powell D.C., Connell J.R. and George, R.L., "Verification of theoretically computed spectra for a point rotating in a vertical plane", Report No. PNL-5440, Pacific Northwest Laboratory, Richland, WA (USA), 1985.
- [12]. Powell D.C. and Connell J.R., "A model for simulation rotational data for wind turbine applications", Report No. PNL-5857, Battelle Pacific Northwest Laboratory, Richland,WA (USA), 1986.
- [13]. Powell D.C. and Connell J.R., "Review of wind simulation methods for horizontal-axial wind turbine analysis", Report No. PNL-5903, Battelle Pacific Northwest Laboratory, Richland,WA (USA), 1986.
- [14]. Veers P.S., "Modeling stochastic wind loads on vertical-axis turbines", Report No. SAND83-1909, Sandia National Laboratories, Albuquerque, New Mexico (USA), 1984.
- [15]. Veers P.S., "Three-dimensional wind simulation", Report No. SAND88-0152, Sandia National Laboratories, Albuquerque, New Mexico (USA), 1988.
- [16]. BurtonT., Sharpe D. and Jenkins, N., Wind energy handbook, 2nd section, John Wiley & Sons, New York, 2011.
- [17]. Kelley N.D., "Full Vector (3-D) Inflow Simulation in Natural and Wind Farm Environments Using an Expanded Version of the SNLWIND (Veers) Turbulence Code", Report No. NREL/TP-442-5225, National Renewable Energy Laboratory, 1992.
- [18]. He G.L., "Rotational Fourier Spectrum of Wind Turbine Systems: A Physical Model", Advanced Materials Research, 243, 730-734, 2011.
- [19]. Erdem E. and Shi J., "ARMA based approaches for forecasting the tuple of wind speed and direction", Applied Energy, 88(4), 1405-1414,2011.
- [20]. Schueller G. I. and Shinozuka M., Stochastic methods in structural dynamics, Martinus Nijhoff Publishers, Dordrecht, 1987.
- [21]. Kitagawa T. and Nomura T., "A wavelet-based method to generate artificial wind fluctuation data", Journal of wind engineering and industrial aerodynamics, 91(7), 943-964, 2003.
- [22]. Kittel C., Elementary Statistical Physics, John Wiley & Sons, New York, 1958.
- [23]. Von Karman T., "Progress in the statistical theory of turbulence", Proceedings of the National Academy of Sciences of the United States of America, 34(11), 530-539, 1948.
- [24]. Kaimal J.C., Wyngaard J.C., Izumi Y., et al. "Spectral characteristics of surface-layer turbulence", Quarterly Journal of the Royal Meteorological Society, 98(417), 563-589, 1972.
- [25]. IEC61400-1, Wind Turbines Part 1:Design requirements:, International Electrotechnical Commission, Geneva, 2005.
- [26]. Dragt J.B., "Load fluctuations and response of rotor systems in turbulent wind fields", Report No. ECN-172, Netherlands Energy Research Foundation, Petten, 1985.
- [27]. Sørensen P., Hansen A.D., Rosas P.A.C., "Wind models for simulation of power fluctuations from wind farms", Journal of Wind Engineering and Industrial Aerodynamics, 90(12), 1381-1402, 2002.
- [28]. Smilden E., Sørensen A. and Eliassen L., "Wind Model for Simulation of Thrust Variations on a Wind Turbine", Energy Procedia, 94, 306-318, 2016.
- [29]. Taylor G.I., "The spectrum of turbulence", Proceedings of the Royal Society of London A:Mathematical, Physical and Engineering Sciences, 164(919), 476-490, 1938.
- [30]. Arany L., Bhattacharya S., Macdonald J., et al. "Simplified critical mudline bending moment spectra of offshore wind turbine support structures", Wind Energy, 18(12), 2171-2197, 2015.
- [31]. Filon L.N.G., "On a Quadrature Formula for Trigonometric Integrals", Proceedings of the Royal Society of Edinburgh, 49(1), 38-47, 1928.
- [32]. Mathworks Inc., Matlab User's Guide, Natick, MA, 2016.
- [33]. IEC61400-1, Wind Turbine Generator Systems Part 1: Safety Requirements, International Electrotechnical Commission, Geneva, 1999.
- [34]. GB/T 18451.1, Wind turbine generator systems-Design requirements, Standardization Administration of the People's Republic of China, Beijing, 2012. (in Chinese).
- [35]. Jonkman J. and Kilcher L., Turbsim User's Guide, National Renewable Energy Laboratory, 2012.
- [36]. Liu Y., Qian H.L. and Fan F., "Reflector wind load characteristics of the large all-movable antenna and its effect on reflector surface precision", Advanced Steel Construction, 13(1), 1-29, 2017.
- [37]. Davenport A.G., "The dependence of wind load on meteo-logical parameters", Proceedings of the International Research Seminar on Wind Effects on Building and Structures , University of Toronto, Ottawa,1967.
- [38]. Shinozuka M. and Jan C.M., "Digital Simulation of random processes and its applications", Journal of sound and vibration, 25(1), 111-128, 1972.
- [39]. Connell J.R., "Turbulence spectrum observed by a fast-rotating wind-turbine blade", Report No. PNL-4083, Battelle Pacific Northwest Labs., Richland, WA (USA), 1981.

INFLUENCE OF RANDOM GEOMETRICAL IMPERFECTION ON THE STABILITY OF SINGLE-LAYER RETICULATED DOMES WITH SEMI-RIGID CONNECTION

Zhong-Wei Zhao¹, Hai-Qing Liu¹, Bing Liang² and Ren-Zhang Yan^{3,*}

¹ School of Civil Engineering, Liaoning Technical University, Fuxin 123000, China

² School of Mechanics and Engineering, Liaoning Technical University, Fuxin 123000, China

³ School of Civil Engineering, Chongqing Jiaotong University, Chongqing 400074, China

* (Corresponding author: E-mail: yrzssuper@126.com)

ABSTRACT

Single-layer reticulated domes are commonly used structural layouts due to their large span capacity and novel appearance. Such structures contain a large number of members, which inevitably lead to imperfection. In this study, a numerical method considering the initial curvature of members, nodal installation error, and joint stiffness was proposed. The randomness of the initial curvature direction, initial curvature magnitude, and joint stiffness could be considered simultaneously. The influence of random geometrical imperfection on the stability of two types of latticed shell structures was investigated. The proposed method could be performed based on general finite element software, and its applicability could be ensured.

Copyright © 2019 by The Hong Kong Institute of Steel Construction. All rights reserved.

1. Introduction

Single-layer reticulated domes are commonly used structural layouts due to their large span capacity and novel appearance. Such structures usually contain hundreds of members and joints, which inevitably lead to imperfections, such as lack of fit [1].

In most analyses, members in latticed shells are assumed to be perfectly straight. However, the imperfection of structural members is inevitable, which may cause negative influence on the structural mechanic performance [2]. In view of the combined influence of shear deformation and member imperfection, Li and Liu [3] developed an accurate beam element stiffness matrix for the nonlinear analysis of planar steel frames. Adman and Afra [4] obtained an accurate displacement shape function for beam elements with imperfection under any boundary conditions. López et al. [5] indicated that the rigidity of joint requires further study because it significantly affects the behavior of the structures. Chan [6–13] conducted a systematical nonlinear analysis on semi-rigid steel frames. The use of stability functions that allow initial imperfections in place of cubic Hermite element was proposed to conduct the second-order analysis for the design of glass-supporting and pre-tensioned trusses [6]. In the analysis, the member was assumed to be pinned or rigidly connected. However, semi-rigid connection and installation error cannot be considered simultaneously.

Producing a precise single-layer assembly of reticulated domes is virtually impossible. Initial curvature and nodal installation error are the most common geometrical imperfection for latticed shell structures. In this regard, several investigations have been conducted [14–17], each include one or several random variables.

El-sheikh [18] investigated the effect of geometric imperfections on the capacity and failure mechanism of single-layer barrel vaults, and presented that geometrical imperfections decrease the load bearing capacity. Zhao et al. [19] investigated the effects of random geometrical imperfections on concentrically braced frames. Kato et al. [20] discussed buckling collapse and its analytical method of steel reticulated domes with semi-rigid ball joints. Spring element was adopted to simulate semi-rigid joints, and four types of geometrical imperfections were studied. The magnitude of maximum nodal imperfection was set to 50 mm and 100 mm. Bruno et al. [21] investigated the sensitivity of the global and local stability of a hybrid single-layer grid shell to a set of equivalent geometric nodal imperfections, which represents the actual structure and construction imperfections.

In the present work, a numerical method considering member initial curvature, nodal installation error, and joint stiffness was proposed. The influence of random geometrical imperfection on the stability of two types of latticed shell structures was investigated. The proposed method could be executed based on general finite element software, and its applicability could be ensured.

ARTICLE HISTORY

Received: 20 July 2017
Revised: 1 January 2018
Accepted: 29 January 2018

KEY WORDS

Member initial curvature;
Nodal installation error;
Latticed shell structure;
Buckling capacity;
Semi-rigid connection

2. Establishment of random geometrical imperfection

2.1. Establishment of initial member curvature

General finite element software ANSYS was used to establish imperfect elements. In traditional analysis, straight line was generated and meshed to simulate the components of the latticed shell. Member imperfection cannot be considered in this case. In this study, a straight line was replaced by a curved line through “BSPLIN” command. The magnitude of imperfection was set in the middle of the component. In most analysis, the imperfection is deemed to be of a half-wave sinusoid, which can be achieved by adding an imperfection value at other points to make the b-spline close to the half-wave sinusoid, as shown in Fig. 1. To set the imperfection value conveniently, a local coordinate system was set up. The x-axis is in the member direction, whereas the y-axis is in the vertical direction. Imperfection value can be generated by adopting the sine function in ANSYS. All imperfect members can be generated through looping statements. The entire process can be performed easily and is easy for engineers to master. The accuracy of this method had been validated in existing literature [22].

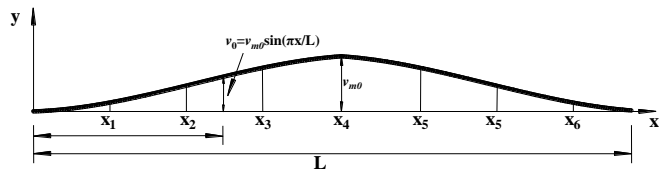


Fig. 1 Imperfection member and local coordinate system

The method of establishing imperfect members has not been considered in the randomness of imperfection direction. Thus, the method was developed in the present work. A random constant θ ranging from 0 Rad to 2π Rad was generated. The local coordinate system was generated according to nodes located at the two sides of components. Then, the local coordinate system was rotated around the x-axis. The random constant satisfied a uniform distribution. Then, the imperfection direction could be randomly distributed all throughout.

To incorporate the influence of joint stiffness, imperfect elements with semi-rigid joints were adopted in this study. Detailed information can be derived from existing literature [22–24]. Two types of latticed shell structures were analyzed.

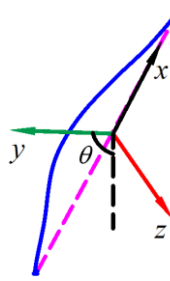


Fig. 2 Rotation of local coordinate system

2.2. Establishment of nodal installation error

Random parameters Δx , Δy , and Δz were introduced to represent nodal installation error. The magnitude of nodal installation error is $E_{\max} = \sqrt{\Delta x^2 + \Delta y^2 + \Delta z^2}$. The random constants Δx , Δy , and Δz satisfy a uniform distribution. The value range of Δx , Δy , and Δz are $(-E_{\max}, E_{\max})$, $(-$

$\Delta y = \sqrt{E_{\max}^2 - \Delta x^2}$, $\Delta y = \sqrt{E_{\max}^2 - \Delta x^2}$), and $(-\Delta z = \sqrt{E_{\max}^2 - \Delta x^2 - \Delta y^2}$, $\Delta z = \sqrt{E_{\max}^2 - \Delta x^2 - \Delta y^2}$). The nodal installation error was considered by adding random parameters to the nodal coordinate.

3. Analyzed structures

Schwedler and Kewitte domes with an increase of 0.1 of their span were analyzed to investigate the influence of geometrical imperfection on different types of reticulated structures. Two Kewitte domes were analyzed to investigate the influence of geometrical imperfection on the buckling capacity of Kewitte domes with different rise-span ratio, as shown in Figs. 3 and 4. The surface of the dome is in the shape of a sphere. The Young's modulus and yield strength are 2.1×10^5 MPa and 345 MPa, respectively.

In the analysis, loads were applied uniformly on the nodes of the dome, that is, 200 KN per node for the Schwedler and Kewitte domes. Every member was meshed by 20 elements. Parametric analysis was conducted to investigate the influence of the initial curvature and nodal installation error on the stability of different types of latticed shell structures.

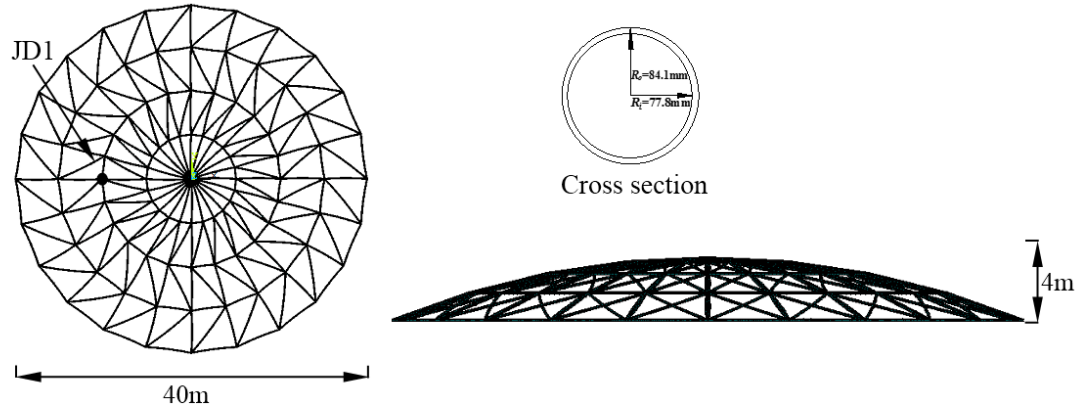
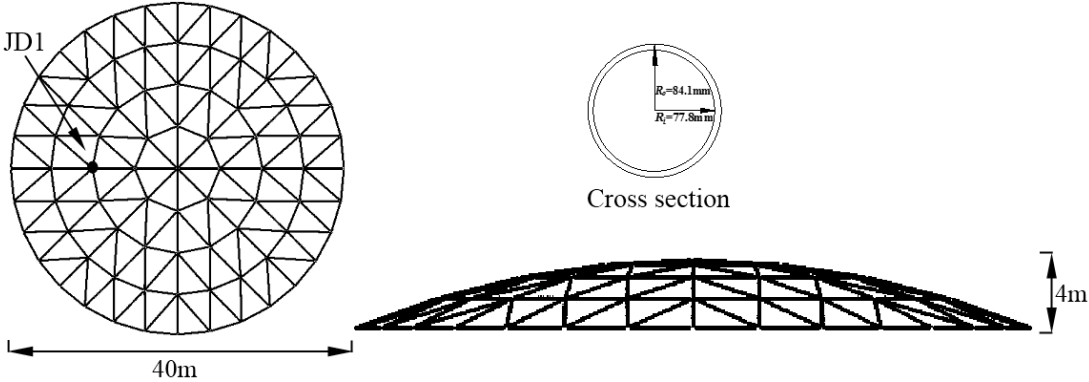
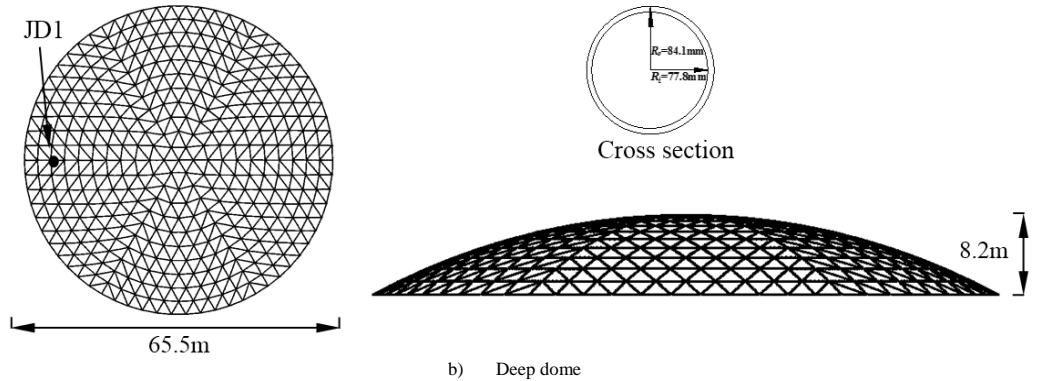


Fig. 3 Schwedler dome



a) Shallow dome



b) Deep dome

Fig. 4. Kewitte dome

4. Influence of member imperfection on stability

4.1. Influence of member imperfection amplitude

In this section, parametrical analysis was conducted on the influence of the magnitude of initial curvature (v_{m0}) on structural buckling capacity. A numerical

model with $v_{m0}=15l/1000$ is shown in Fig. 5.

In view of the randomness of member imperfection, 100 computations were performed for each joint stiffness factor. v_{m0} was set as different values. The probabilistic model of v_{m0} satisfied a uniform distribution because only the variation range of the buckling load was considered.

Fig. 6 shows the influence of member imperfection on the buckling load

factor of Schwedler latticed shell when the joint stiffness was set to different values. Generally, the buckling load capacity of the Schwedler latticed shell increases with the joint stiffness. The results show that when the joint stiffness was 0.1 and v_{m0} was $l/1000$, the buckling load factor of the ideal structure was 0.49. The buckling load factor of the defective structure changed from 0.29 to 0.49. When v_{m0} was set to $5l/1000$, $10l/1000$, and $15l/1000$, the buckling load factor of the defective structure changed from 0.29 to 0.35, 0.28 to 0.33, and 0.27 to 0.29, respectively. In addition, the buckling load was insensitive to the variation of v_{m0} when the joint stiffness was set to 0.1. The shell could be assumed as pinned joint in this condition.

The buckling load factor of the ideal structure was 0.6 when the joint stiffness was 1.0 and v_{m0} was $l/1000$. The buckling load factor changed from 0.58 to 0.6. When v_{m0} was set to $5l/1000$, $10l/1000$, and $15l/1000$, the buckling load factor changed from 0.55 to 0.6, 0.54 to 0.57, and 0.52 to 0.57, respectively. Buckling capacity decreased with the increase of v_{m0} , and the variation range of buckling load factor was almost not influenced by v_{m0} .

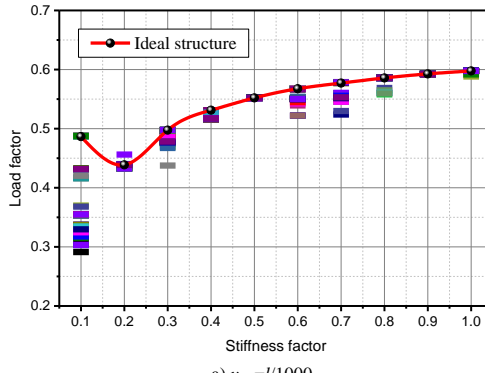
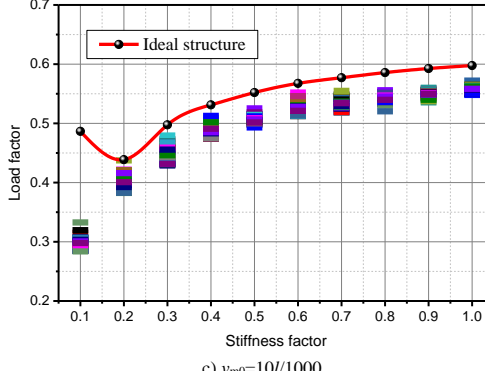
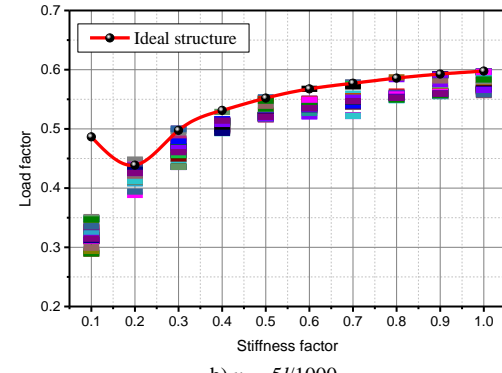
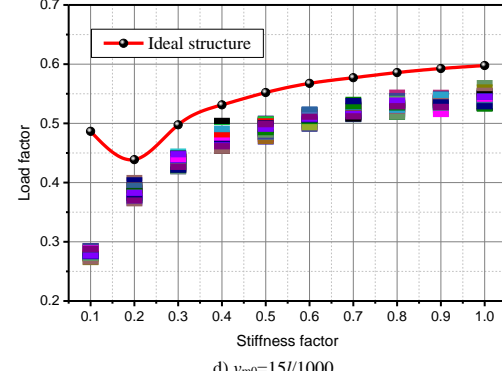
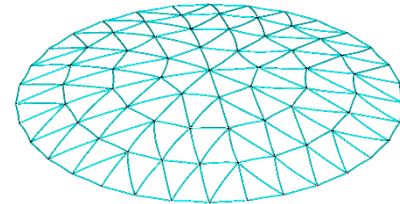
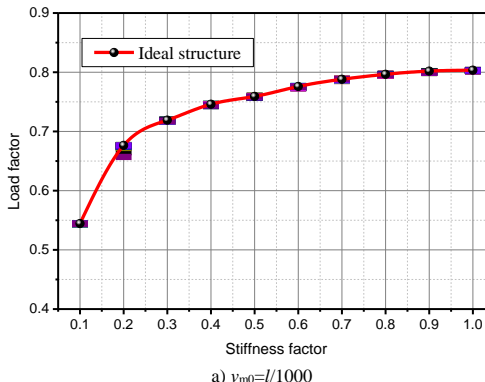
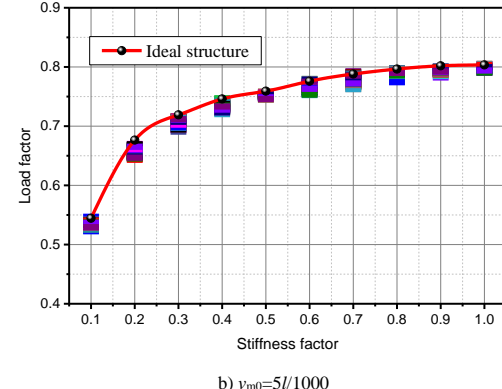
a) $v_{m0}=l/1000$ c) $v_{m0}=10l/1000$ b) $v_{m0}=5l/1000$ d) $v_{m0}=15l/1000$

Fig. 6 Influence of member imperfection on Schwedler latticed shell

The changing rule of the buckling load of shallow K8 latticed shell along with joint stiffness factor and v_{m0} is shown in Fig. 7. The buckling load capacity was almost not influenced when v_{m0} was set to $l/1000$. The variation range of the buckling load factor increased with v_{m0} , and the peak value remained as the buckling load factor of the ideal structure, which was different from the Schwedler latticed shell.

The changing rule of the buckling load of deep K8 along with joint stiffness factor and v_{m0} is shown in Fig. 8. The variation range of the load factor of shallow K8 is larger than that of deep K8. This finding indicates that the sensitivity of the changing range of loading capacity to the initial curvature

The influence of the initial curvature on the semi-rigid connected Schwedler latticed shell would change with the stiffness factor. The change tendency of the load factor of a defective structure along with joint stiffness factor was almost the same with that of the ideal structure.

Fig. 5 Numerical model with $v_{m0}=15l/1000$ a) $v_{m0}=l/1000$ b) $v_{m0}=5l/1000$

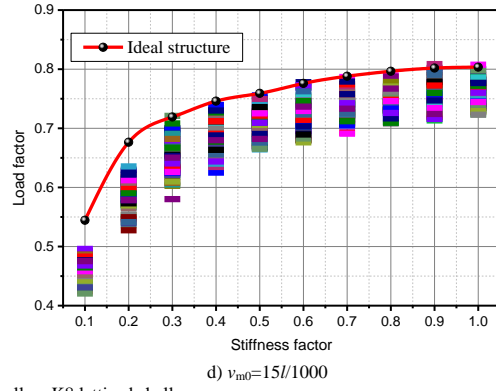
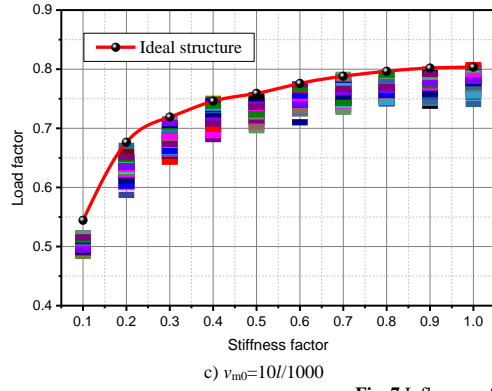


Fig. 7 Influence of member imperfection on shallow K8 latticed shell

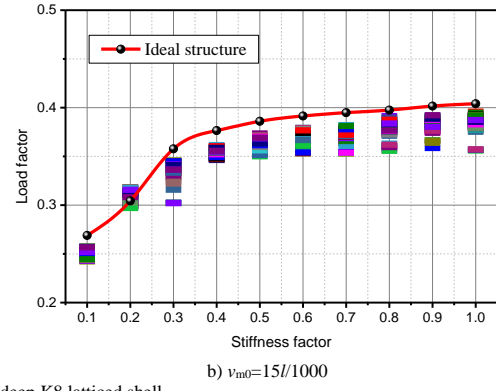
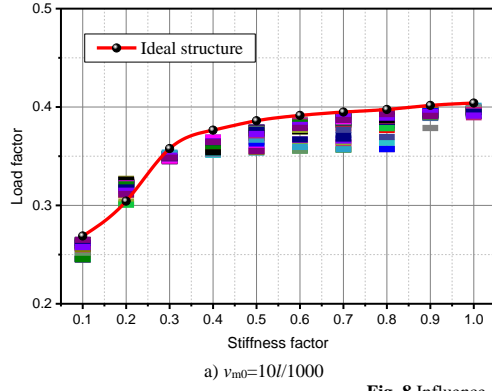


Fig. 8 Influence of member imperfection on deep K8 latticed shell

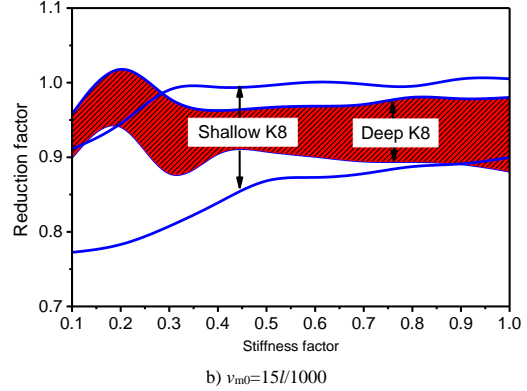
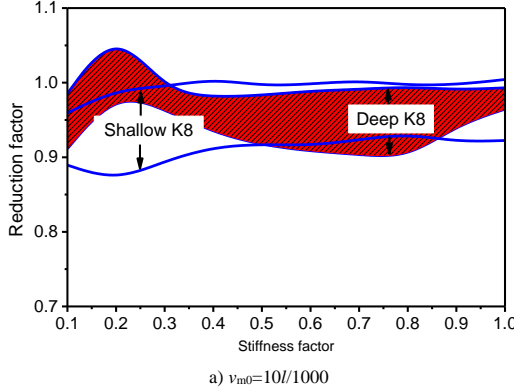


Fig. 9 Change of reduction factor along with stiffness factor (initial curvature)

4.2. Influence of initial curvature direction

Initial curvature may be in random direction in the actual project, and its direction may influence structural capacity. The influence of initial curvature direction is discussed in this section. The magnitude of initial curvature remained constant at $l/1000$ with joint stiffness of 0.1 and 1. The results in Fig.

10 indicate that the initial curvature direction almost has no influence on the structural buckling capacity when the joint stiffness factor was set to 0.1. The influence on structural buckling capacity remained within 1% when the joint stiffness factor was to 1.0. Thus, the influence of the initial curvature direction on K8 latticed shell could be neglected.

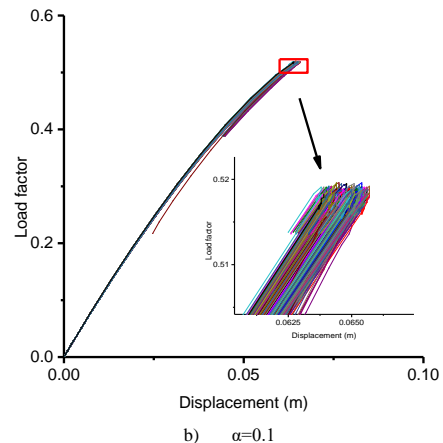
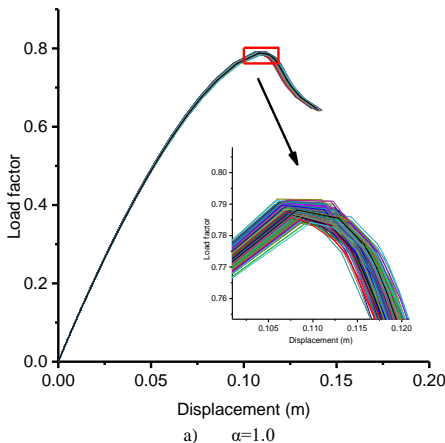


Fig. 10 Influence of initial curvature direction on shallow K8 latticed shell

5. Influence of nodal installation error on stability

Imperfections are determined using the eigenmode imperfection method in most of the numerical analysis of buckling capacity. However, this imperfection distribution mode was not consistent with the actual condition.

The nodal installation error was assumed to satisfy a uniform distribution in the present work. The magnitude of the nodal installation error (E_{\max}) was set as different values. The numerical model with nodal installation error is shown in Fig. 11. The results are shown in Fig. 12.

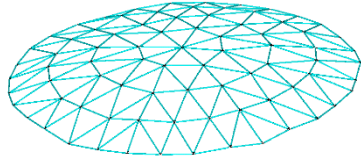


Fig. 11. Numerical model with $E_{\max}=400$ mm

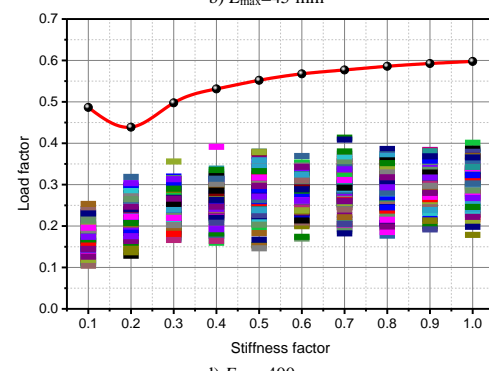
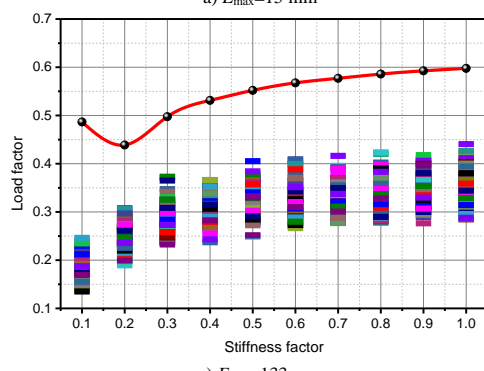
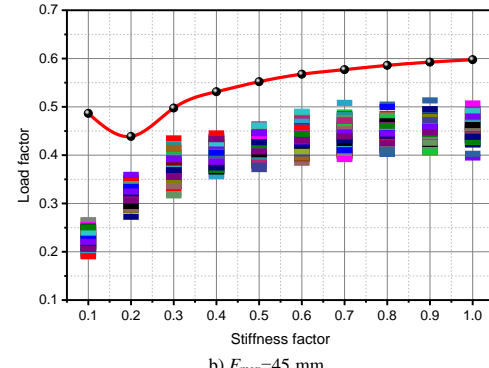
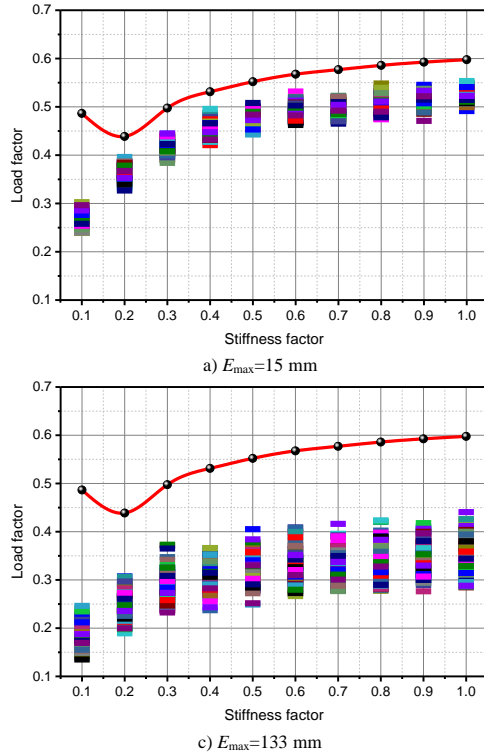
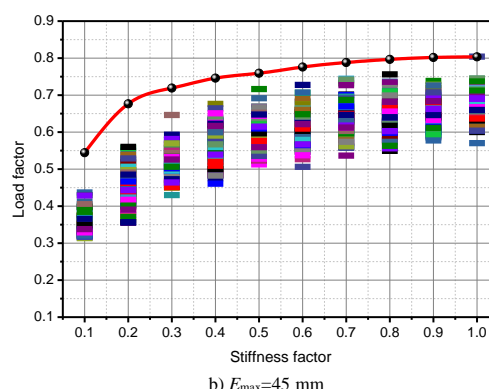
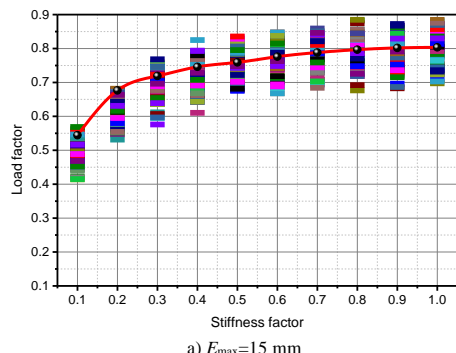


Fig. 12 Influence of installation error on Schwedler latticed shell

Fig. 13 shows the influence of nodal installation error on the buckling load factor of the shallow K8 latticed shell when the joint stiffness is set as different values. The results in Fig. 13(a) indicate that the buckling capacity of the shallow K8 latticed shell with nodal installation error may be larger than that of the ideal structure, which is different from the Schwedler latticed shell. The influence of nodal installation error on the K8 latticed shell was less than the Schwedler latticed shell.

The influence of nodal installation error on the deep K8 latticed shell is depicted in Fig. 14. The results show that the changing range of the loading factor of the deep K8 is small, that is, the sensitivity of the loading factor to nodal installation error was weak for deep K8. The loading capacity of imperfect structures was compared to that of the ideal structures to investigate the change of reduction factor along with stiffness factor. Findings indicate that minimal

Fig. 12 shows the influence of nodal installation error on the buckling load factor of the Schwedler latticed shell when the joint stiffness was set as different values. Generally, the buckling load capacity of the Schwedler latticed shell increase with the joint stiffness. The results indicate that when the joint stiffness was 0.1 and $E_{\max}=15$ mm, the buckling load factor of the ideal structure was 0.49. The buckling load factor of the defective structure changed from 0.24 to 0.3. When E_{\max} was set to 45, 133, and 400 mm, the buckling load factor of the defective structure changed from 0.19 to 0.26, 0.13 to 0.25, and 0.1 to 0.25, respectively. In addition, the influence of nodal installation error on the buckling capacity of the Schwedler latticed shell was larger than that of the initial curvature. The variation ranges of the buckling load factor increased with the installation error E_{\max} . The buckling capacity of the Schwedler latticed shell with nodal installation error was definitely lower than that of the ideal structure.



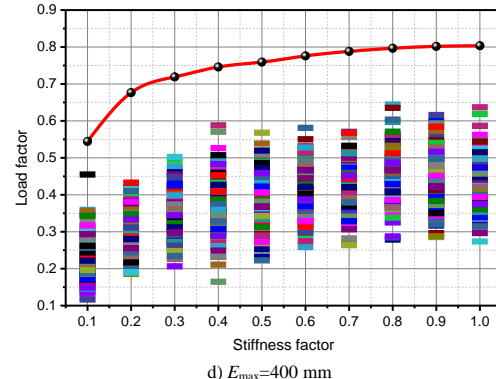
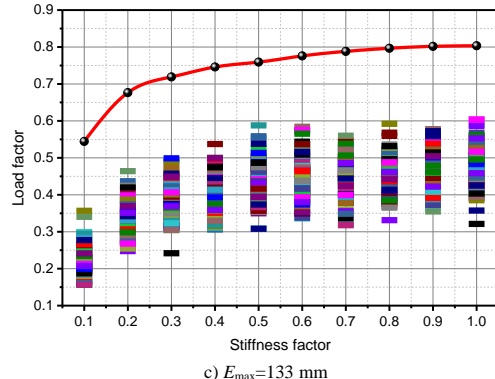


Fig. 13 Influence of installation error on shallow K8 latticed shell

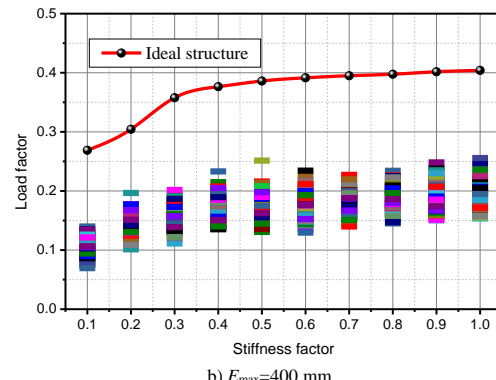
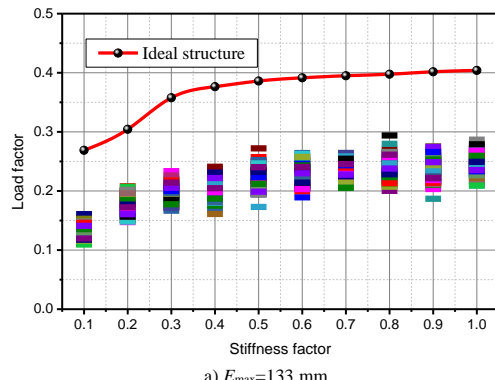


Fig. 14 Influence of installation error on deep K8 latticed shell

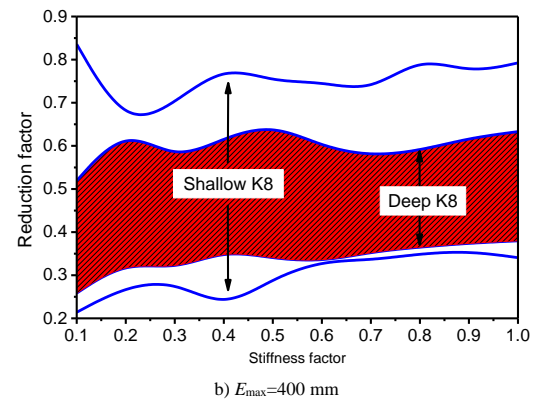
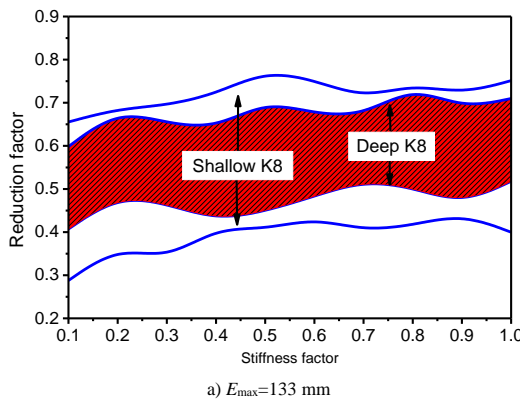


Fig. 15 Change of reduction factor along with stiffness factor (nodal installation error)

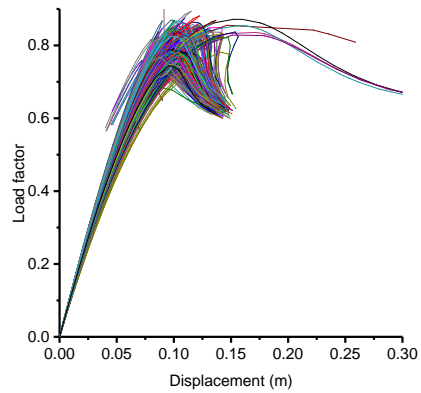
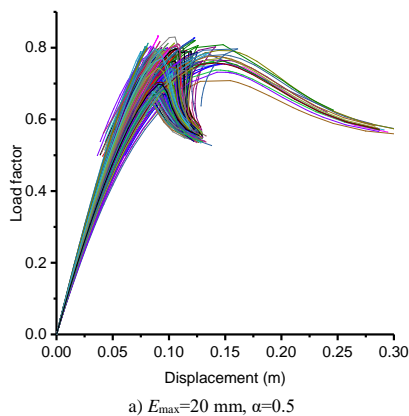


Fig. 16 Load-deflection curves of shallow K8 latticed shell

6. Conclusions

A numerical method considering random member initial curvature and

nodal installation error was proposed in this study. The randomness of the direction and magnitude of the initial curvature could be considered simultaneously, as well as the joint stiffness. The proposed method could also

be adopted for inelastic analysis, and it was proposed based on general finite element software. Hence, tedious programming work could be avoided, and the method could be conveniently utilized by researchers and workers.

Influences of member initial curvature and nodal installation error on the buckling capacity of Schwedler and K8 latticed shells were analyzed. The influence of structure size was further investigated. The influence of the initial curvature direction on the K8 latticed shell could be neglected. The influence of the initial curvature and nodal installation error were related to joint stiffness. Different from the influence of initial curvature, the changing range of reduction factor caused by nodal installation error was positively related to structural size.

Acknowledgments

The work presented in this paper was financially supported by the State Key Research Development Program of China (Grant Nos. 2016YFC0801404 and 2016YFC0600704) and the Project Funded by China Postdoctoral Science Foundation (Grant No. 2017M621156).

References

- [1] El-Sheikh A., "Effect of member length imperfections on triple-layer space trusses", *Engineering structures*, 19(7), 540-550, 1997.
- [2] Zhou Z., Wu J. and Meng S., "Influence of member geometric imperfection on geometrically nonlinear buckling and seismic performance of suspen-dome structures", *International Journal of Structural Stability and Dynamics*, 14(3), 1-20, 2014.
- [3] Li G.Q. and Liu Y.S., "A nonlinear beam element considering initial imperfection", *Chinese Journal of Computational Mechanics*, 22(1), 69-72, 2005.
- [4] Adman R. and Afra H., "Exact shape functions of imperfect beam element for stability analysis", *Advances in Engineering Software*, 38(8-9), 576-585, 2007.
- [5] López A., Puentet I. and Serna M.A., "Numerical model and experimental tests on single-layer latticed domes with semi-rigid joints", *Computers and Structures*, 85(7), 360-374, 2007.
- [6] Chan S.L. and Zhou Z.H., "Second-order elastic analysis of frames using single imperfect element per member", *Journal of Structural Engineering*, 121(6), 939-945, 1995.
- [7] Chan S.L. and Gu J.X., "Exact tangent stiffness for imperfect beam-column members", *Journal of Structural Engineering, ASCE*, 126(9), 1094-1102, 2000.
- [8] Chan S.L. and Zhou Z.H., "Second-order elastic analysis of frames using single imperfect element per member", *Journal of Structural Engineering, ASCE*, 121(6), 939-945, 1995.
- [9] Chan S.L. and Cho S.H., "Second-order analysis and design of angle trusses Part 1: Elastic analysis and design", *Engineering Structures*, 30, 616-625, 2008.
- [10] Chan S.L. and Cho S.H., "Second-order analysis and design of angle trusses Part 2: Plastic analysis and design", *Engineering Structures*, 30, 626-631, 2008.
- [11] Chan S.L., Huang H.Y. and Fang L.X., "Advanced analysis of imperfect portal frames with semi-rigid base connections", *Journal of Applied Mechanics, ASCE*, 131(6), 633-640, 2005.
- [12] Chan S.L. and Cho S.H., "Second-order P-D-d analysis and design of angle trusses allowing for imperfections and semi-rigid connections", *International Journal of Advanced Steel Construction*, 1(1), 157-172, 2005.
- [13] Chan S.L. and Chui P.P.T., "Non-Linear Static and Cyclic Analysis of Steel Frames with Semi-Rigid Connections", Elsevier Science, 2002.
- [14] Chen G.B., Hao, Z., Kim, J.R. Rasmussen and Fan, F., "Modeling geometric imperfections for reticulated shell structures using random field theory", *Engineering Structures*, 126, 481-489, 2016.
- [15] Liu H.J., Wei, Z. and Hao, Y., "Structural stability analysis of single-layer reticulated shells with stochastic imperfections", *Engineering Structures*, 124, 473-479, 2016.
- [16] Zhao Z., Zhu H. and Chen Z., "Investigations on buckling behavior of single-layer reticulated shell with emphasis on considering welding residual stress", *Welding in the World*, 60(6), 1181-90, 2016.
- [17] Zhao Z., Chen Z., Liu H., Zhao B., "Investigations on influence of erection process on buckling of large span structures by a novel numerical method", *International Journal of Steel Structures*, 16(3), 789-798, 2016.
- [18] El-Sheikh, A.L., "Effect of geometric imperfections on single-layer barrel vaults", *International Journal of Space Structures*, 17(4), 271-283, 2002.
- [19] Zhao J., Zhang Y. and Lin Y., "Study on mid-height horizontal bracing forces considering random initial geometric imperfections", *Journal of Constructional Steel Research*, 92, 55-66, 2014.
- [20] Kato S., Mutoh I. and Shomura M., "Collapse of semi-rigidly jointed reticulated domes with initial geometric imperfections", *Journal of Constructional Steel Research*, 48(2), 145-168, 1998.
- [21] Bruno L., Sassone M. and Venuti F., "Effects of the equivalent geometric nodal imperfections on the stability of single layer grid shells", *Engineering Structures*, 112, 184-199, 2016.
- [22] Zhao Z.W., Chen, Z.H., Yan, X.Y. and Xu, H., "Simplified numerical method for latticed shells that consider member geometric imperfection and semi-rigid joints", *Advances in Structural Engineering*, 19(4), 689-702, 2016.
- [23] Zhao Z.W. and Chen Z.H., "Analysis of door-type modular steel scaffolds based on a novel numerical method", *International Journal of Advanced Steel Construction*, 12(3), 316-327, 2016.
- [24] Zhao Z.W., Liu H.Q. and Liang B., "Novel numerical method for the analysis of semi-rigid jointed lattice shell structures considering plasticity", *Advances in Engineering Software*, 114, 208-214, 2017.
- [25] Sheidai M.R. and Gordini M., "Effect of random distribution of member length imperfection on collapse behavior and reliability of flat double-layer grid space structures", *Advances in Structural Engineering*, 18(9), 1475-1485, 2015

SEISMIC OPTIMIZATION ANALYSIS OF VERTICAL STIFFENER CONNECTION TO L-CFST COLUMN

Wang Zhang^{2,5}, Zhi-Hua Chen^{1,2,3}, Qing-Qing Xiong^{2,5} and Ting Zhou^{4,*}

¹ State Key Laboratory of Hydraulic Engineering Simulation and Safety, Tianjin, China

² Department of Civil Engineering, Tianjin University, Tianjin, China

³ Key Laboratory of Coast Civil Structure Safety of China Ministry of Education, Tianjin University, China

⁴ Department of Architecture, Tianjin University, Tianjin, China

⁵ School of Civil Engineering, Shijiazhuang Tiedao University, Shijiazhuang, China

* (Corresponding author: E-mail: zhouting1126@126.com)

ABSTRACT

In this paper, 14 models in two series were designed and numerically analysed based on the results of quasi-static tests of vertical stiffener connections to L-CFST columns. For the fracture problem of the beam flange connecting plate at the end of the vertical stiffener, four optimization methods were proposed and compared in the H300 series: tapered vertical stiffener, flush vertical stiffener with beam flange, reduction beam section and thickened beam flange connecting plate. For the problem of the vertical stiffener fracture along the column flange, the effect of the vertical stiffener sectional area and width-to-thickness ratio were considered and analysed in the H400 series. The skeleton curves, Von Mises stress distribution and fracture index of each model in the two series were compared. The crack propagation on the beam flange connecting plate and vertical stiffener can be reduced and even eliminated using a thickened connecting plate and a minor width-to-thickness ratio, respectively. A calculation method for the flexural capacity of the vertical stiffener connection to the L-CFST column was proposed. Good consistency was observed between the theoretical and test results of both yield and ultimate flexural capacity. Finally, a design example of the flexural capacity of the connection is provided to guide the engineering practice.

Copyright © 2019 by The Hong Kong Institute of Steel Construction. All rights reserved.

1. Introduction

The special-shaped column frame system has attracted increasing attention in the residential construction industry because of its advantages such as the prominent absence of columns, large usable space in buildings and convenience of furniture layouts. Because of the weak seismic behaviour of the frame structure system with the special-shaped reinforced concrete column, the height of this structure system has strict limitations in earthquake-prone areas [1]. Meanwhile, the concrete-filled steel tubular column has been studied by many scholars because of its beneficial seismic behaviour, high bearing capacity, fire-proofing qualities and economic benefits [2-7]. The research background of this paper is the frame structure system of a special-shaped column composed of concrete-filled steel tubes (S-CFST column), which can be applied to high-rise steel residential buildings particularly with braces or shear walls. Special-shaped columns composed of concrete-filled steel tubes are divided into L-, T- and cross-shapes and can be wrapped inside the wall, as shown in Fig. 1. However, in engineering designs, L-shaped columns composed of concrete-filled steel tubes (L-CFST columns) are the ideal member forms for economic reasons [8, 9] because the stiffness and strength of L-CFST columns can be increased by extending the length or increasing the thickness of the boundary mono columns or vertical steel plates. The L-CFST column with vertical stiffener connections is shown in Fig. 2.

At present, scholars have paid more attention to the seismic behaviour of different connections to concrete-filled rectangular steel tubular columns and their flexural and shear capacity calculation methods. These connections include external-diaphragm connections [10], through-diaphragm connections [11], internal-diaphragm connections [12-14] and vertical stiffener connections [15-18]. However, there are relatively few experimental and theoretical studies of the special-shaped column frame joints. The seismic performance of L-, T- and cross-shaped steel-tube columns with internal-diaphragms was studied by Xue et al. [19]. However, the internal diaphragm is not conducive to welding construction in connection regions and concrete pouring in steel tubes, particularly for small-size steel-tube sections in residential buildings. Xu et al. [20] experimentally studied the external diaphragm connections between T- and cross-shaped columns with steel beams. However, this type of connection requires more steel and affects the living space and aesthetics. Ma et al. [21] conducted cyclic loading tests of two full-scale flange-reinforced connection specimens, which are similar to the vertical stiffener connection in this paper. The test result showed that the cracking of the steel beam flanges in two specimens occurred at the end of the reinforcement, and the deformation of the panel zone was not obvious.

ARTICLE HISTORY

Received: 9 August 2017
Revised: 4 March 2018
Accepted: 1 April 2018

KEY WORDS

L-shaped column composed of concrete-filled steel tubes; vertical stiffener connection; optimization analysis; crack; flexural capacity

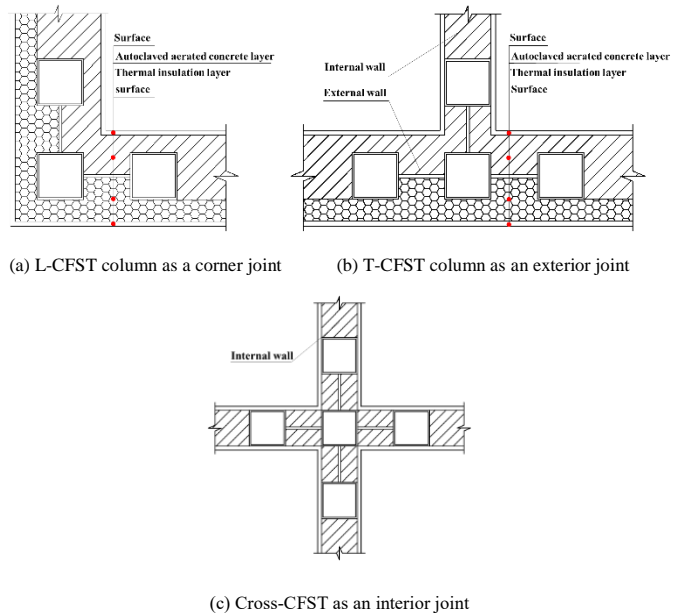


Fig. 1 Layout of S-columns with different sections

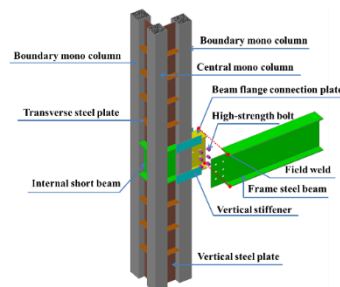


Fig. 2 Installation diagram of the vertical stiffener connection between an L-CFST column and a frame steel beam

To study the seismic behaviour of the vertical stiffener connection to the L-CFST column, the presence of concrete, width-to-thickness ratio of the vertical stiffener, internal extending length of the vertical stiffener, and section area of the vertical stiffener were analysed in five specimens [8]. The dimension details of Specimen H300-2 are shown in Fig. 3, and the other specimens were adjusted only in the local component size, as shown in Table 1.

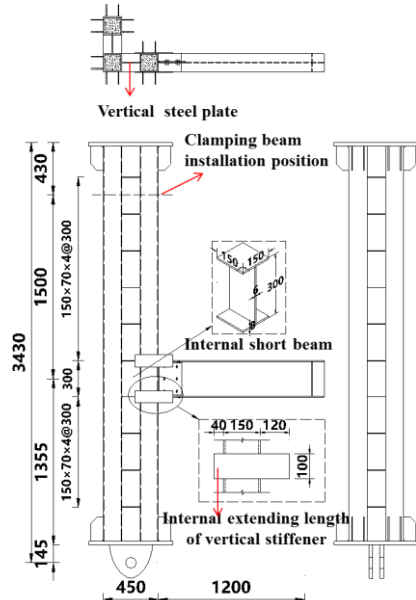


Fig. 3 Details of Specimen H300-2

Table 1
Summary of the test specimens

Specimen No.	B × t (mm)	Concrete	Internal extending length of vertical stiffener (mm)
H300-0	100×6	Filled	0
H300-1	75×8	Filled	0
H300-2	100×6	Hollow	40
H400-0	100×6	Filled	40
H400-1	100×12	Filled	40

Specimens H300-0, H300-1 and H300-2 had similar failure process and final damage results. Only minor cracks were generated at the beam flange connecting plate at the end of the vertical stiffener when the loading at the end of the steel beam was small. With the increase in loading, the crack length of the upper and lower flange connecting plates in the diagonal position quickly increased. Finally, the cracks extended to the shear plate, and the steel beam developed serious torsion. There was a slight heave at the column flange, and the deformation and cracks in the panel zone of the joint were not observed.

When the force increased at the steel beam end, the upper south and lower north vertical stiffeners in Specimen H400-0 were broken. Then, the displacement of the beam end rapidly increased, whereas the bearing capacity decreased sharply. However, the failure began with the weld cracking between the vertical stiffeners and the beam flange connecting plate in Specimen H400-1. In the loading process, continuous distinctive sounds emitted from it, and the weld between the vertical stiffener and the beam flange connecting plate completely cracked. Then, the column flange cracked. After the test, the weld of the internal extending part of the vertical stiffener cracked, and dislocation also occurred between the vertical stiffeners and internal short beam flange.

Considering the unreasonable phenomenon in the test, 14 analytic models in two series with different configurations were designed and optimized by the finite-element method to improve the seismic performance. By analysing the bearing capacity of the analytic models, Von Mises stress distribution and rupture index, this paper provides the experimental support and design basis to apply and generalize this structural system.

2. Model parameters and result verification of FEM

2.1. Model parameters

Since the centroid and shear centre of L-CFST columns do not coincide,

under the seismic action, L-CFST columns easily twist around the shear centre of the cross section, as shown in Fig. 4, which aggravates the cracking of the beam flange connecting plate at the end of the vertical stiffener. Simultaneously, the rupture risk of the vertical stiffener at the column flange increases under the dual action of the tension of the steel beam flange and cross-sectional shear moment around the L-CFST column. Existing quasi-static test results on the T-shaped stiffener-steel beam connection show that the rupture of the steel beam flange at the end of the vertical stiffener is the root cause of the poor performance of many test specimens in terms of plasticity and bearing capacity [16, 21-22]. Thus, some scholars have investigated the cracking of the steel beam flange caused by reinforcement at both sides of the column flange [23].

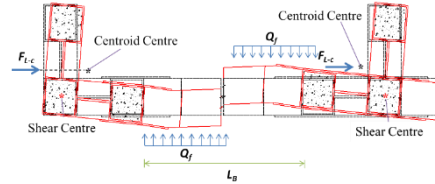


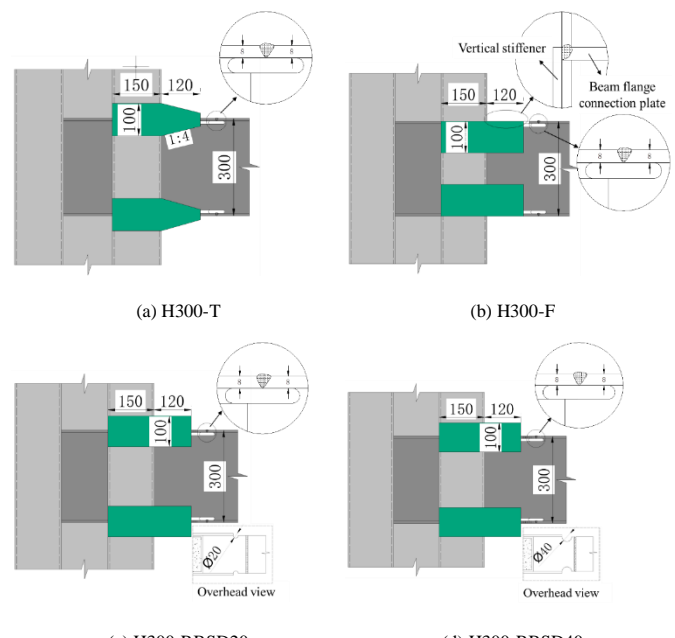
Fig. 4 Plane deformation and force diagram of the L-CFST column framework

In this section, 14 analytic models in two series (H300 and H400) were designed for the rupture of the beam flange connecting plate in the test with the 300-mm-high beam and the rupture of the vertical stiffener in the test with the 400-mm-high beam.

In the H300 series, Specimen H300-0 was used as the basic contrast model. The tapered vertical stiffener model (H300-T), flush vertical stiffener with the beam flange model (H300-F), reduction beam section model (H300-RBSD20 and H300-RBSD40) and models (H300-BFCPT10 and H300-BFCPT12) with the thickness of the beam flange connecting plate increasing by 2 mm and 4 mm were used for the optimization analysis. The specific naming and detailed parameters are shown in Fig. 5 and Fig. 6.

H300 series	H300-0	Specimen CJ-H300-3 (Base object in H300 series)
	H300-T	Tapered vertical stiffener
	H300-P	Vertical stiffener flushed with beam flange
	H300-RBSD20	Arc chamfer with 20 mm diameter at vertical stiffener end
	H300-RBSD40	Arc chamfer with 40 mm diameter at vertical stiffener end
	H300-BFCPT10	Thickness of flange connection plate is 10 mm
	H300-BFCPT12	Thickness of flange connection plate is 12 mm
H400 series	H400-0 (VSA/W-600/100)	Specimen CJ-H400-2 (Base object in H400 series)
	H400-VSA/W-800/100	Dimension of vertical stiffener is 8 × 100 mm
	H400-VSA/W-1000/100	Dimension of vertical stiffener is 10 × 100 mm
	H400-1 (VSA/W-1200/100)	Dimension of vertical stiffener is 12 × 100 mm
	H400-VSA/W-1200/80	Dimension of vertical stiffener is 15 × 80 mm
	H400-VSA/W-1200/120	Dimension of vertical stiffener is 10 × 120 mm
	H400-VSA/W-1200/150	Dimension of vertical stiffener is 8 × 150 mm

Fig. 5 Specific naming convention of all analytic models



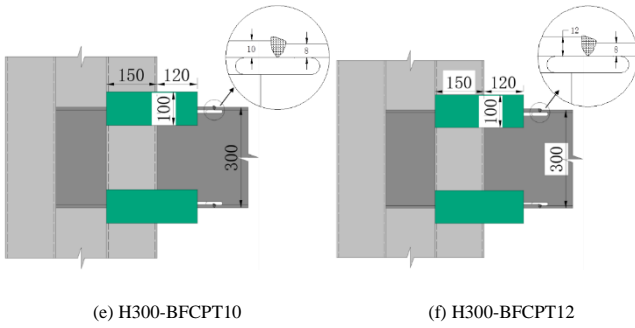


Fig. 6 Detailed parameters of the analytic models in the H300 series

In the H400 series, specimens H400-0 and H400-1 are the basic contrast models, and the sectional area and width-to-thickness ratio of the vertical stiffener were the research objects to design 5 parameterized analytic models: H400-VSA/W-800-100, H400-VSA/W-1000-100, H400-VSA/W-1200-80, H400-VSA/W-1200-120 and H400-VSA/W-1200-150. The seismic performances of the analytic models H400-VSA/W-600-100 (H400-0), H400-VSA/W-800-100, H400-VSA/W-1000-100 and H400-VSA/W-1200-100 (H400-1) were compared when all vertical stiffeners were 100 mm wide and the areas were 600 mm^2 , 800 mm^2 , 1000 mm^2 and 1200 mm^2 , respectively. The seismic performances of the analytic models H400-VSA/W-1200-80, H400-VSA/W-1200-100 (H400-1), H400-VSA/W-1200-120, and H400-VSA/W-1200-150 were compared when the areas of all vertical stiffeners were 1200 mm^2 and the widths were 80 mm, 120 mm, 120 mm and 150 mm, respectively. The specific naming convention is shown in Fig. 5.

2.2. Finite element modelling

The models were analysed using the general finite-element software ANSYS. The concrete filled in the mono column was modelled by element Solid65. The vertical steel plate and transverse steel plate were modelled by element Shell191. Other steels were modelled by element Solid95. The contact element pair Targe 170 and Conta 174 was applied at the contact surfaces. The friction coefficients were equal to 0.4, 0.1 and 0.4 between connecting stiffener and beam web, between bolt shank and bolt hole, and between steel tube and concrete, respectively.

Three reference points were established at the plane centroid point of the top and bottom of the L-CFST column for constraining and the cross-sectional centroid point of the steel beam end for loading. The specific boundary conditions of the models are shown in Fig. 7.

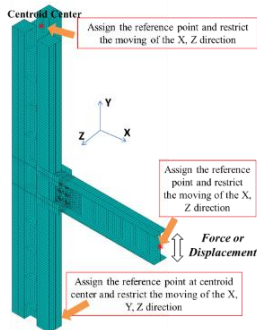


Fig. 7 Typical meshing, boundary condition and loading on the models

2.3. Results verification of FEM

The finite-element results of Specimen H300-0 are shown in Fig. 8. Since the effect of the welding residual stress of the specimen and the gradual cracking of the steel beam flange at the end of the vertical stiffener were not considered, the peak bearing capacity obtained by the finite-element model was 152.6 kN, which is approximately 19.7% higher than the test value of 127.4 kN. This result occurred because the beam flange connecting plate gradually cracked at the end of the vertical stiffener in the loading process, which decreased the tension cross-section of the steel beam flange and made the bearing capacity fail to reach the theoretical value. Because of the crack of the beam flange connecting plate, the bearing capacity could not be given full play. Fig. 8 (d) shows that the stress of the lower steel beam flange on the place at a distance from the end of the vertical stiffener was large, and the steel beam flange bent. In Fig. 8 (e), the strain at the junction area of the vertical stiffener and beam flange connecting

plate was large, and the maximum Von Mises strain of 0.385 occurred on the beam flange connecting plate at the end of the vertical stiffener, which was 208 times higher than the yield strain of the beam flange connecting plate.

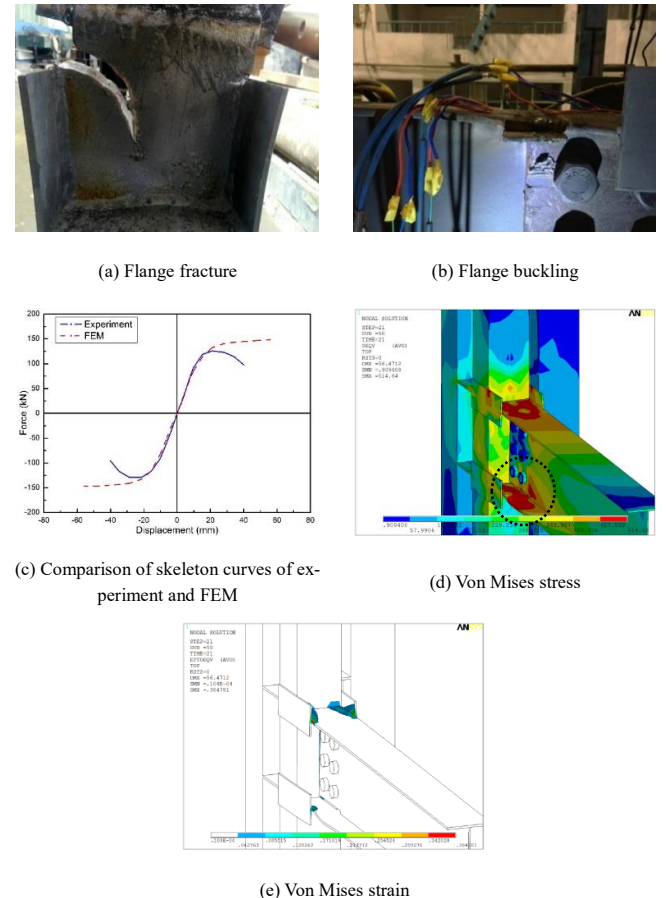


Fig. 8 Comparison of the finite-element analysis results with the experimental results

The finite-element analysis of Specimen H400-0 is shown in Fig. 9. Since the sudden rupture of the vertical stiffener was not considered in the finite-element model, the finite element obtained a skeleton curve with superior ductility compared to the test. Simultaneously, the forces of the test and finite-element method (FEM) at the peak loading point were 318.4 kN and 329.5 kN, respectively. The error was approximately 3.5%. In Fig. 9 (c), Von Mises value of the connection was maximal at the junction of the column flange and vertical stiffener. The stress at the junction of the vertical stiffener and beam flange connecting plate was also large. In Fig. 9 (d), the maximum Von Mises strain was on the vertical stiffener and distributed along the column flange, which is notably consistent with the rupture phenomenon of the vertical stiffener in the testing process.

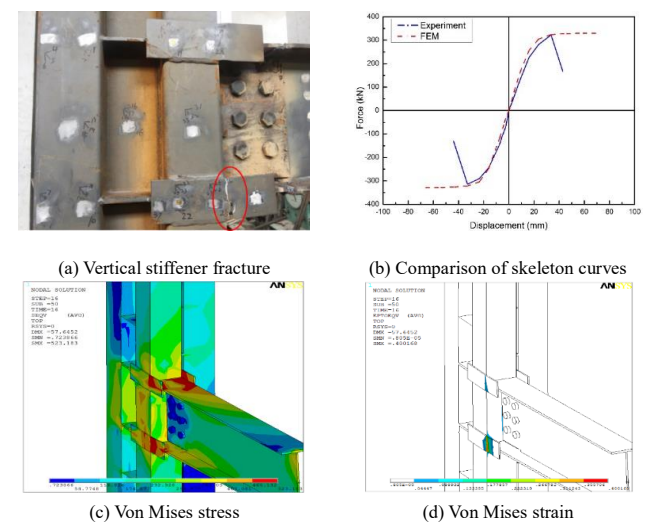


Fig. 9 Numerical results of Specimen H400-0

The analysis results illustrate the feasibility of predicting the seismic performance of the analytic models in the H300 series and H400 series using the finite-element method.

3. Seismic performance analysis

3.1. Skeleton curves

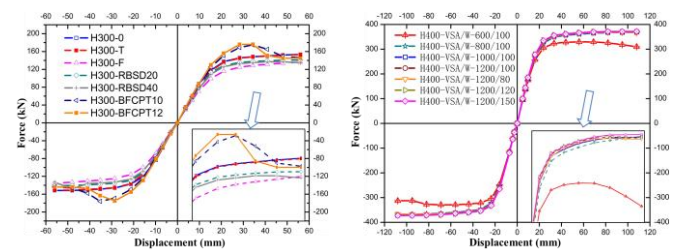
The skeleton curves of 7 analytic models in the H300 series are shown in Fig. 10 (a). According to the Fig., except for H300-BFCPT10 and H300-BFCPT12, the bearing capacities of all other analytic models decreased compared to H300-0, where the bearing capacity of the analytic model H300-T reduced by approximately 0.8%, which indicates that the effect of the vertical stiffener form on the decrease in bearing capacity is negligible. The bearing capacity of model H300-F decreased by 11% because the decrease in effective tensile area of the vertical stiffener blocked the full performance of its bearing capacity. The bearing capacity of this construction form can be increased by welding the cover plates on the upper and lower beam flanges [23]. The bearing capacities of models H300-RBSD20 and H300-RBSD40 decreased by 7.7% and 12.2%, respectively. In the high-rise steel structure housing system in the paper, because of the restriction on the width of the steel beam flange, using this type of structure will sacrifice considerable bearing capacity of the connection. For analytic models H300-BFCPT10 and H300-BFCPT12 with beam flange connecting plates thickened by 2 mm and 4 mm, respectively, all bearing capacities increased by 15%; hence, increasing the thickness of the beam flange connecting plate can significantly increase the bearing capacity of the connection in a certain range. However, the force rapidly decreased when analytic model H300-BFCPT12 reached the peak force, which indicates that the ductility decreases when the thickness of the beam flange connecting plate significantly increases.

The skeleton curves of 7 analytic models in H400 series are shown in Fig. 10 (b). After a comparison among the analytic models H400-VSA/W-600/100, H400-VSA/W-800/100, H400-VSA/W-1000/100 and H400-VSA/W-1000/120, with the increase in area of the vertical stiffener to 800 mm², the bearing capacity of the connection no longer increased. Simultaneously, after comparing H400-VSA/W-1200/80, H400-VSA/W-1200/100, H400-VSA/W-1200/120 and H400-VSA/W-1200/150, if the area of the vertical stiffener is unchangeable, with the decrease in width-to-thickness ratio of the vertical stiffener, the bearing capacity of the connection slightly reduced but only by 1.2% compared between H400-VSA/W-1200/80 and H400-VSA/W-1200/150. Thus, the width-to-thickness ratio of the vertical stiffener hardly affects the bearing capacity of the connection. Because a large width-to-thickness ratio will cause the corner exposure of the stiffener and affect the indoor aesthetics of the high-rise steel structure house, a small width-to-thickness ratio should be used, if possible.

Table 2

Comparison of the bearing capacity of analytic models in the H300 and H400 series

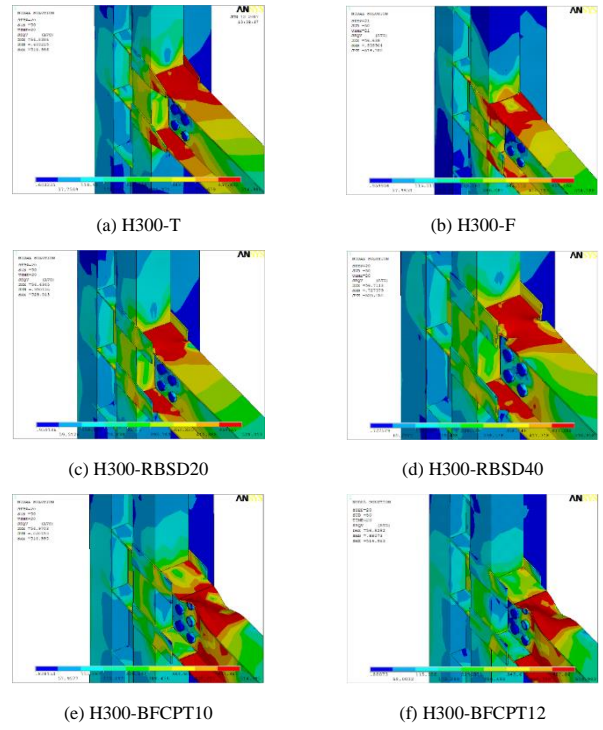
Series	Analytic model No.	Average bear capacity (kN)	Error (%)
H300	H300-0	152.6	-
	H300-T	152.0	-0.8
	H300-F	136.0	-11.0
	H300-RBSD20	140.8	-7.7
	H300-RBSD40	134.0	-12.2
	H300-BFCPT10	175.5	15.0
	H300-BFCPT12	175.5	15.0
H400	H400-0	311.3	-
	H400-VSA/W-800/100	370.3	19.0
	H400-VSA/W-1000/100	370.5	19.0
	H400-VSA/W-1200/100	369.0	18.5
	H400-VSA/W-1200/80	367.7	18.1
	H400-VSA/W-1200/120	369.5	18.7
	H400-VSA/W-1200/150	372.2	19.6



(a) H300 series (b) H400 series
Fig. 10 Skeleton curves of the analytic models

3.2. Von mises stress distribution

Von Mises stress distributions of the analytic models in the H300 series with the beam end displacement of 56.6 mm are shown in Fig. 11. For analytic model H300-T, the stress in the beam flange connecting plate region in the vertical stiffener was large and evenly distributed. The beam flange did not obviously bend. The beam flange connecting plate region had a notably different stress distribution from the basic analytic model H300-0 (as shown in Fig. 8 (d)). Hence, the tapered vertical stiffener promoted the bearing capacity of the beam flange connecting plate to give full play. For analytic model H300-F, near the column flange, the stress in the middle of the beam flange connecting plate was small; however, the stresses at both ends were large, so the vertical stiffener had little contribution to the bearing capacity of the connection in this form of construction. On the vertical stiffener, it was easy to form a large stress concentration at the beam flange connecting plate and the column flange, which was adverse to the seismic performance of the connection. The stress distribution of the vertical stiffener end chamfering of analytic models H300-RBSD20 and H300-RBSD40 shows that the stress in the beam flange connecting plate region in the vertical stiffener was evenly distributed, and the local bending formed at the arc chamfer and extended to the column flange. For this type of structure, since the arc chamfer was at the end of the vertical stiffener and near the column flange, the local bending of the beam flange can easily destroy the panel zone. For this type of construction, the extended part of the vertical stiffener should be appropriately lengthened to protect the panel zone. For analytic models H300-BFCPT10 and H300-BFCPT12, the stress in the area inside the vertical stiffener gradually reduced with the increase in thickness of the beam flange connecting plate, but an obvious plastic hinge formed on the steel beam flange. Thus, this type of construction can well protect the panel zone and form an energy dissipation section, which was conducive to the seismic performance of the connection.



(a) H300-T (b) H300-F
(c) H300-RBSD20 (d) H300-RBSD40
(e) H300-BFCPT10 (f) H300-BFCPT12
Fig. 11 Von Mises stress of analytic models in the H300 series

The Von Mises stress distributions of the analytic models in the H400 series

with the beam end displacement of 110 mm are shown in Fig. 12. According to Figs. 12 (a), (b) and (c), with the increase in area of the vertical stiffener, the bending degree of the steel beam at the end of the stiffener increased. However, when the area of the vertical stiffener was 1000 mm², its bending degree of the steel beam flange no longer changed. According to Figs. 12 (c), (d), (e) and (f), when the area of the vertical stiffener was fixed (1200 mm²), with the increase in width-to-thickness ratio of the vertical stiffener, the bending degree of the steel beam flange slightly changed, but the maximum Von Mises stress was narrowly distributed through the entire cross section of the lower vertical stiffener under the tension. This analysis explains that the flexural capacity of the vertical stiffener connection to L-CFST column was directly related to the area of the vertical stiffener but barely affected by its width-to-thickness ratio.

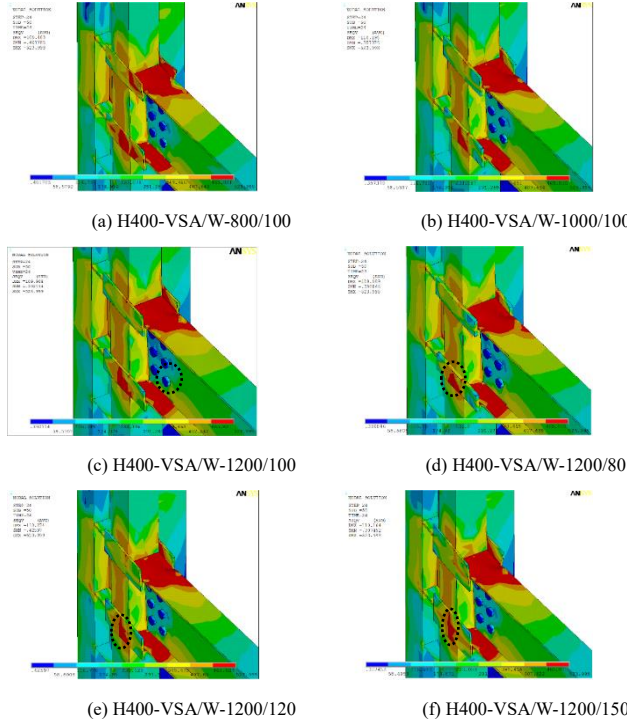


Fig. 12 Von Mises stress of analytic models in the H400 series

3.3. Rupture evolution analysis

The rupture index was introduced by Hancock and Mackenzie [24] for the equivalent plastic rupture strain of steel for different stress triaxiality conditions. To compare the rupture degrees of the connections in different forms of improvement at the beam flange connecting plate at the end of the vertical stiffener, the method was used in this paper to assess the rupture risk. It has been used by many scholars, and its correctness has been verified [23-27]. The rupture index (RI) is expressed in Eq. (1). A greater RI indicates higher rupture risk.

$$RI = \frac{\varepsilon_{epv}^{pl}/\varepsilon_y}{\exp(-1.5 \frac{\sigma_m}{\sigma_{eff}})} \quad (1)$$

where ε_{epv} , ε_y , σ_m , and σ_{eff} are the equivalent plastic strain, yield strain, hydrostatic stress, and Von Mises stress, respectively.

The ratio of the hydrostatic stress to the Von-Mises stress (i.e., σ_m/σ_{eff}), which appears in the denominator of Eq. (1), is called the Triaxiality Ratio (TR), as shown in Eq. (2). El-Tawil et al. [28] reported that TR values less than -1.5 could cause brittle fracture, whereas values between -0.75 and -1.5 usually resulted in a large decrease in rupture strain of the metal.

$$TR = \frac{\sigma_m}{\sigma_{eff}} \quad (2)$$

The ratio of the equivalent plastic strain to the yield strain in the numerator of Eq. (1) is called the plastic equivalent strain (PEEQ) index. The PEEQ is a measure of the local inelastic strain demands, which can be useful in evaluating and comparing the performance of different connection configurations. The PEEQ index is computed by Eq. (3),

$$PEEQ = \frac{\varepsilon_{eqv}^{pl}}{\varepsilon_y} = \frac{\int \sqrt{\frac{2}{3} d\varepsilon_{ij}^p d\varepsilon_{ji}^p}}{\varepsilon_y} \quad (3)$$

where ε_{ij}^p is the plastic strain rate tensor components in directions i, and j; ε_y is the yield strain of the beam flange connecting plate.

For the analytic models in the H300 series, the rupture critical points a and b of the beam flange connecting plate at the end of the vertical stiffener along the width direction were determined (as shown in Fig. 13 (a)). The obtained values of the PEEQ index, triaxiality index and rupture index are plotted along the beam flange at the peak force state in Fig. 14. In addition, TR, PEEQ and RI of the analytic models at critical points a and b are listed in Table 3.

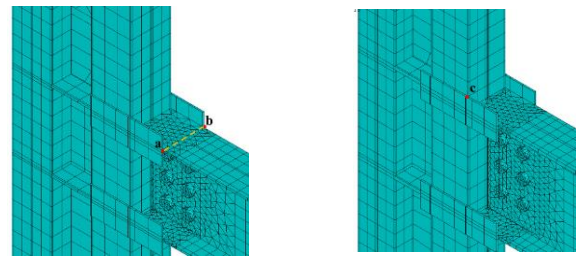


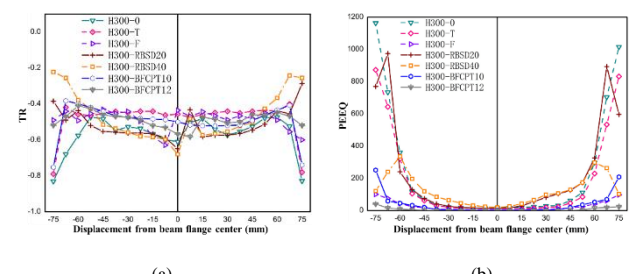
Fig. 13 Analytic models of the two series and their critical points

Fig. 14 shows that at the peak force state, TR, PEEQ and RI of the analytic models significantly varied with the range of 15 mm from either side of the beam flange connecting plate to the end of the vertical stiffener, but those values were basically similar at other positions. Thus, different optimization measures have remarkable effect on the rupture of the beam flange connecting plate at the end of the vertical stiffener.

Fig. 14 (a) and Table 3 show that the analytic models with improvement at the critical points had larger TR indices (above -0.8) than the basic model H300-0. The reduction beam section models H300-RBSD20 and H300-RBSD40 had the smallest TR values, which were above -0.4. Hence, those improvement measures might have certain effects on improving the brittle rupture of the beam flange connecting plate.

The equivalent plastic strain index diagram indicates the plastic strain demand at the critical points; therefore, an increase in this parameter can indicate an increase in probability of rupture at the mentioned points. From Fig. 14 and Table 3, except for the analytic model H300-BFCPT12 at the critical points, which had the minimal value, all PEEQ values of other models exceeded 120. In addition, the PEEQ values of the analytic models H300-RBSD20, H300-T and H300-0 were larger than 596.9 at the critical points, and those of the basic model H300-0 were greater than 1000. In addition, the PEEQ values of the analytic models H300-RBSD20 and H300-RBSD40 with the arc chamfering at the end of the vertical stiffener showed an increasing trend. Thus, the improvement measure can reduce the equivalent plastic strain of the beam flange connecting plate at the critical point, but the presence of the arc chamfering increases the equivalent plastic strain in the middle of the beam flange connecting plate.

According to Fig. 14(c), the RI values of the analytic models significantly differed at the critical points. The analytic model H300-RBSD20 had an RI value above 388.4, but H300-BFCPT12 had the minimum RI of 18.6. The RI values of the other analytical models were 2.6-23 times larger than that of H300-BFCPT12. Thus, the analytic model with the beam flange connecting plate thickened by 4 mm most significantly decreases the brittle rupture of the steel beam flange at the end of the vertical stiffener. In addition, in Table 3, the RI value at the critical point a was larger than that of b, which indicates that the twist of the L-CFST column exacerbated the rupture of the beam flange connecting plate at the end of the vertical stiffener.



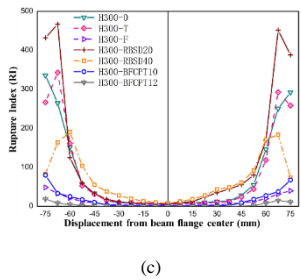


Fig. 14 TR, PEEQ, and RI along the beam flange connecting plate at peak force state in the H300 series

Table 3

TR, PEEQ and RI of the beam flange connecting plate at the end of vertical stiffeners in the H300 series

Analytic model	TR		PEEQ		RI	
	Point a	Point b	Point a	Point b	Point a	Point b
H300-0	-0.83	-0.83	1163.2	1015.3	335.9	292.3
H300-T	-0.79	-0.78	872.7	832.2	266.8	258.3
H300-P	-0.49	-0.6	100.8	98.0	48.6	40.0
H300-RBSD20	-0.39	-0.29	770.1	596.9	432.2	388.4
H300-RBSD40	-0.26	-0.22	121.7	102.6	83.0	73.5
H300-BFCPT10	-0.76	-0.75	251.2	208.8	80.0	67.5
H300-BFCPT12	-0.52	-0.51	40.54	24.05	18.6	11.04

For the H400 series, this paper studies the changes in TR, PEEQ and RI of the vertical stiffeners at the vertical stiffener at critical point c with the beam end displacement. Fig. 15 presents the change trend of the analytic models at critical point c for different unilateral vertical stiffener areas (600 mm^2 , 800 mm^2 , 1000 mm^2 and 1200 mm^2). According to the Fig., with the increase in vertical stiffener area, the absolute values of TR, PEEQ and RI at critical point c decreased sharply, which indicates that the brittle rupture of the vertical stiffener is directly related to its area. Thus, to ensure the bearing capacity and ductility of the L-CFST column connection, a sufficient bearing capacity of the vertical stiffener is required.

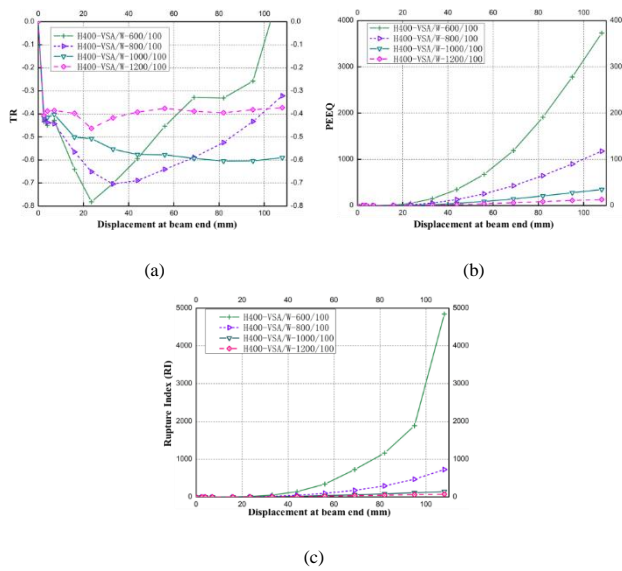


Fig. 15 TR, PEEQ, and RI at critical point (c) with beam end displacement for different vertical stiffener areas in the H400 series

To ensure the flexural capacity of the connection, the analytic models H400-VSA/W-1200/80, H400-VSA/W-1200/100, H400-VSA/W-1200/120 and H400-VSA/W-1200/150 with a unilateral vertical stiffener area of 1200 mm^2 were used as the research objects; the width-to-thickness ratios were 5.3, 8.3, 12 and 37.5, respectively. Fig. 16 presents the variation trend of the TR, PEEQ and RI indices of these four analytic models at critical point c with the beam end displacement. With the increase in width-to-thickness ratio of the vertical stiffener, the TR index significantly decreased. For the analytic model

H400-VSA/W-1200/150, the minimum TR value was close to -0.6, which indicates that a greater width-to-thickness ratio of the specimen corresponds to a more obvious degree of its stress concentration at characteristic point c. Similarly, as shown in Fig. 16 (b), for the model H400-VSA/W-1200/80 with the width-to-thickness ratio of 5.3, PEEQ and RI were approximately 1/10 and 1/8 of those of the other analytic models. Its rupture risk at critical point c obviously decreased. In Fig. 17, when the width-to-thickness ratio was less than 10, the RI value at the peak force state significantly decreased. When the width-to-thickness ratio was 5.3, the RI value was minimal. Thus, in the connection design, to ensure that the vertical stiffeners do not protrude beyond the wall, the width-to-thickness ratio of the vertical stiffener can be appropriately reduced to prevent the vertical stiffener from a sudden rupture at characteristic point c.

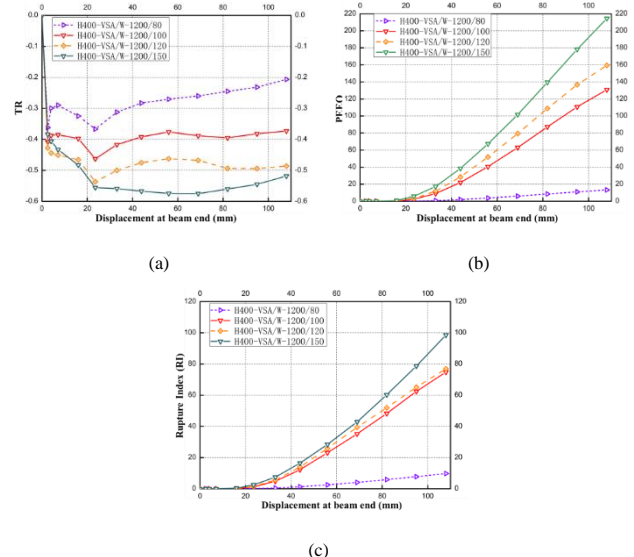


Fig. 16 TR, PEEQ, and RI at critical point c with beam end displacement for different vertical stiffener width-to-thickness ratios in the H400 series

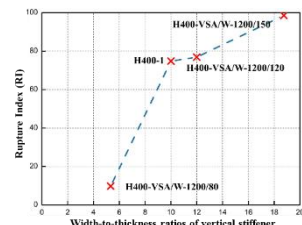


Fig. 17 RI at critical point c with vertical stiffener width-to-thickness ratios in the H400 series at the peak force state

3.4 Flexural capacity calculation method

Fig. 18 shows a typical span in the design of the L-CFST column frame system. The steel beam was under the uniformly distributed load q and concentrated load p . According to existing research [29], for the flange-reinforced connection, the location easily formed a plastic hinge at Position 1 located at $1/4 H_B$ from the end of the vertical stiffener. Position 2 checked the flexural capacity of the panel zone considering the twisting effect of the L-CFST column and fillet weld strength between the vertical stiffener and the beam flange connecting plate.

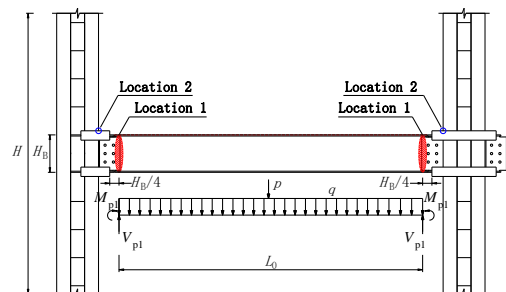


Fig. 18 Anti-seismic analysis model of the connection to the L-CFST column

The yield flexural capacity of the vertical stiffener connection to the

rectangular CFST column based on the theory of yield line can be calculated using Eq. (4), [30]

$$M_Y = \beta \left(2h_{vs}t_{vs}f_{vyy} + t_{mc} \left(t_{bfcp} + \sqrt{D_0 t_c} \right) f_{mcy} + 4D_0 m_p \frac{1}{\sqrt{D_0 t_c}} \right) \times (H_B - t_{bf}) \quad (4)$$

where M_Y is the yield flexural capacities of the panel zone; h_{vs} is the width of the vertical stiffener; t_{vs} is the thickness of the vertical stiffener; f_{vyy} is the yield strength of the vertical stiffener; t_{mc} is the thickness of the mono steel tube connected with the steel beam; t_d is the thickness of the steel beam connecting plate; D_0 is the width of the weld between the steel beam connecting plate and the beam flange; t_{bf} is the thickness of the steel beam flange; $m_p = f_y \cdot t_c^2 / 4$ is the yield bending moment of the column wall per unit length; H_B is the height of the steel beam; β is the adjustment coefficient based on the previous test results. The yield and ultimate bearing capacity are calculated to be 0.8 and 0.7, respectively.

The torsional stress of the vertical stiffener can be calculated using Eq. (5),

$$\tau_T = \frac{T}{W_t} \quad (5)$$

where T is the torque of the cross section at the column flange, and W_t is the torsion resistant cross-sectional modulus of the L-CFST column in Eqs. (6) and (7), respectively,

$$T = F_{L-C} \times e = \frac{M_{pb}}{H_B - t_{bf}} \times e \quad (6)$$

$$W_t = \frac{I_p}{\rho_{max}} \quad (7)$$

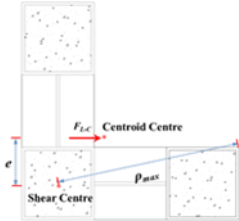


Fig. 19 A schematic diagram of shear stress calculation

Table 4

Comparison of the experimental and predictive values for the end plate connections

Specimen	Test		DB/T29-186-2011				Proposed formula			
	M_{TY} (kN·m)	M_{TU} (kN·m)	M_Y (kN·m)	M_U (kN·m)	$\frac{M_Y}{M_{TY}}$	$\frac{M_U}{M_{TU}}$	M_{PY} (kN·m)	M_{PU} (kN·m)	$\frac{M_{FY}}{M_{TY}}$	$\frac{M_{FU}}{M_{TU}}$
H400-0	231.4	301.3	185.1	214.2	0.80	0.71	191.3	299.5	0.83	0.99
H400-1	303.5	435.6	306.0	377.7	1.00	0.87	304.2	440.6	1.0	1.01
Average					0.90	0.79			0.92	1.0
Standard Deviation					0.1	0.08			0.08	0.01

3.5 Design Example

In the L-CFST column frame system, the design steps of the flexural capacity of the vertical stiffener connection are shown in Table 5. The used parameters are related to Fig. 18 and Eqs. (4)-(10). The material strength is the design value. The vertical stiffener connection details are the following geometry and properties.

where e is the vertical distance from the centroid centre to the shear centre; I_p is the polar moment of inertia of the L-CFST column section; ρ_{max} is the distance from the column flange corner to the shear centre of the L-CFST column.

The effect from the tensile force from the fillet welds between the vertical stiffeners and the beam flange connecting plates must be considered when the flexural capacity is calculated. This strength can be obtained using Eq. (8),

$$F_{hwy} = 4f_v^w a_e (L_1 - 2h_f) \quad (8)$$

where F_{hwy} is the yield tensile force provided by the fillet welds; f_v^w = design strength of fillet welds; a_e is the calculated thickness of weld; L_1 is the extending length of the vertical stiffener; h_f is the fillet weld size.

Previous studies [31] indicate that the ultimate flexural capacity of the connections can be calculated using the ultimate strength of steel instead of the yield strength of steel in the proposed formulas. As a result, the yield and ultimate flexural capacities of the connection considering the twist of the L-CFST column and the tensile force from the fillet welds between the vertical stiffener and the beam flange connecting plate can be calculated as shown in Eqs. (9) and (10),

$$M_{PY} = \left(\min \left(2h_{vs}t_{vs} \left(f_{vyy} - \frac{T}{W_t} \right), 4f_v^w a_e (L_1 - 2h_f) \right) + \left(t_{mc} \left(t_{bfcp} + \sqrt{D_0 t_{mc}} \right) f_{mcy} + 4D_0 m_p \frac{1}{\sqrt{D_0 t_{mc}}} \right) \right) \times (H_B - t_{bf}) \quad (9)$$

$$M_{PU} = \left(\min \left(2h_{vs}t_{vs} \left(f_{vyy} - \frac{T}{W_t} \right), 4Kf_v^w a_e (L_1 - 2h_f) \right) + \left(t_{mc} \left(t_{bfcp} + \sqrt{D_0 t_{mc}} \right) f_{mcy} + 4D_0 m_p \frac{1}{\sqrt{D_0 t_{mc}}} \right) \right) \times (H_B - t_{bf}) \quad (10)$$

where $K=2.23$, safety factor of fillet weld [32].

The specimens H400-0 and H400-1, whose panel zone failed in the experiment, are selected as examples to verify the above formulas. The comparison of the test results, existing methods and proposed theoretical formulas for the yield and ultimate flexural capacity of the connections is presented in Table 4.

Table 4 shows that the proposed predicted yield M_{PY} and ultimate flexural capacity M_{PU} are closer to the experimental results than the calculation method of DB/T29-186-2011. The standard deviations of the proposed formulas are also acceptable.

The H-shaped steel beam: $B_{bf}=150$ mm, $H_B=300$ mm, $t_{bf}=8$ mm, $t_w=6$ mm; $f_b=345$ MPa; $W_{pb}=471384$ mm³; The beam flange connecting plate: $t_{bfcp}=12$ mm; The steel tube of mono column: $B_{mc}=150$ mm, $t_{mc}=6$ mm, $f_{mc}=345$ MPa; The vertical steel plate: $B_{vsp}=150$ mm, $t_{vsp}=6$ mm; The vertical stiffener: $h_{vs}=100$ mm; $t_{vs}=6$ mm; The torque: $T=556.9 \times 99.35=55328$ kN·mm; The torsion resistant cross sectional modulus of the L-CFST column: $W_t=11366800.2$ mm³; The strength of fillet weld: $f_v^w=200$ MPa.

Table 5

Summary of the vertical stiffener design

Design step	Calculations
1- Determining the thickness of beam flange connecting plate	$t_{bfcp} = t_{bf} + 4 \text{ mm} = 12 \text{ mm}$
2- Beam design moment	$M_p = W_{pb} \times f_b = 471384 \times 345 = 162627 \text{ kN}\cdot\text{mm}$
3- Axial force in the beam flange	$F_{bf} = M_p / (H_b - t_{bf}) = 162627 / (300 - 8) = 556.9 \text{ kN}$
4- Controlling the dimension of vertical stiffener	$h_{vs} t_{vs} = \frac{F_{bf} - t_{mc} (t_{bfcp} + \sqrt{D_0 t_{mc}}) f_{mc} - 4 D_0 m_p \frac{1}{\sqrt{D_0 t_{mc}}}}{2(f_{vs} - \frac{T}{W_t})}$ $= \frac{556900 - 6 \times (12 + \sqrt{138 \times 6}) \times 345 - 4 \times 138 \times \frac{1}{4} \times 6^2 \times 345 \times \frac{1}{\sqrt{138 \times 6}}}{2 \times (345 - \frac{55328000}{11366800.2})}$ $\approx 600 \text{ mm}^2$
5- Controlling the double fillet weld between the beam flange connecting plate and the vertical stiffener	$L_1 = \frac{h_{vs} t_{vs} f_{vs}}{2 f_v^w a_e} + 2 h_f = \frac{100 \times 6 \times 345}{2 \times 200 \times 0.7 \times 7} + 2 \times 7 \approx 120 \text{ mm}$
6- Controlling the sides fillet welds between vertical stiffener and column flange	$L_{mc} = \frac{h_{vs} t_{vs} f_{vs}}{f_v^w a_e} + 2 h_{vs} = \frac{100 \times 6 \times 345}{200 \times 0.7 \times 7} + 2 \times 7 = 119.6 \text{ mm} < B_{mc} - 2 t_{mc} = 138 \text{ mm}$
7- Determining the section of vertical stiffener	The cross section of 60 mm × 10 mm can be selected, whose h_{vs}/t_{vs} is 6. According to Fig. 17, the section satisfies the design requirements.

4. Conclusion

In this paper, the parameterized finite element optimization analysis was carried out in two series of connection models according to the test results. Comparisons were made in the skeleton curve, Von Mises stress distribution and rupture index at the critical position. Then, the flexural capacity of the L-CFST column considering the twist and the tensile force from the fillet welds between the vertical stiffener and beam flange connecting plate was given. The main conclusions as follows:

(1) Comparison among the models in the H300 series, the construction measure of thickening the beam flange connecting plate had obvious advantages over other optimization methods in the connection bearing capacity, plastic hinge formation and rupture risk at the critical position. When the beam flange connecting plate was thickened by 4 mm, the bearing capacity no longer increased obviously, and the rupture index of the critical position reduced to the acceptable scope. Therefore, it was most economic and reasonable to adopt the construction measure of thickening the beam flange connecting plate by 4 mm to improve the seismic performance of the connection.

(2) It could be obtained from the comparison of the analytic models in the H400 series that the bearing capacity of the connection increased with the area of the vertical stiffener to a certain extent, but when the bending resistant bearing capacity of the connection exceeded the plastic flexural capacity of the entire plastic cross section of the steel beam, the increase of the vertical stiffener area contributed little to the bearing capacity of the connection. Meanwhile, when the vertical stiffener area was the same, with the increase of the width-to-thickness ratio of the vertical stiffener, the rupture risk of the critical position of the vertical stiffener increased. Therefore, in the case of meeting the flexural capacity of the panel zone and the maximum thickness difference in the fillet weld connection between the steel tube and the vertical stiffener, the width-to-thickness ratio of the vertical stiffener should be small to avoid the sudden rupture of the vertical stiffener.

(3) In a comparison of experimental results, the results of the proposed calculation methods exhibited excellent consistency with the experimental results for both the yield and ultimate flexural capacity. For the convenience of engineering application, a design example is given which adopting the experimental and numerical results in this paper.

5. Acknowledgement

This work was sponsored by the National Key Research and Development Program of China (Grant No. 2017YFC0703802) and the Key Project of Hebei Natural Science Foundation, China (Grant No. E2017202278).

References

- [1] JGJ 149-2017. Technical specification for concrete structures with specially shaped columns. Ministry of Housing and Urban-Rural Development of the People's Republic of China, China, 2017. (in Chinese)
- [2] Yu F., He S. and Niu D., "Study on unified bearing capacity of rectangular concrete-filled steel tubular column subjected to axial compression", Advanced Steel Construction, 8(1), 95-111, 2012.
- [3] Hu J.W., Park J. and Leon R.T., "Advanced analysis and performance based evaluation of concrete filled tube (CFT) columns", Advanced Steel Construction, 6(4), 1019-1033, 2010.
- [4] Wang H.Y. and Zha X.X., "Axial strength of CFST columns considering concrete age", Advanced Steel Construction, 139-150, 2(10), 2014.
- [5] Guler S., Çopur A. and Aydogan M.A., "A comparative study on square and circular high strength concrete-filled steel tube columns", Advanced Steel Construction, 10(2), 234-247, 2014.
- [6] Li G.C., Di C.Y., Tian L. and Fang C., "Nonlinear finite element analysis on long columns of high-strength concrete-filled square steel tube with inner CFRP circular tube under axial load", Advanced Steel Construction, 9(2), 124-138, 2013.
- [7] Chen Z.Y. and Shen Z.Y., "Behavior of L-shaped concrete-filled steel stub columns under axial loading: Experiment", Advanced Steel Construction, 6(2), 688-697, 2010.
- [8] Zhang W., Chen Z.H., Xiong Q.Q. and Zhou T., "Experimental seismic behavior of vertical stiffener connections to L-CFST columns", Steel and composite structure, 26(6), 793-808, 2018.
- [9] Zhou T., Xu M.Y., Chen Z.H., Wang X.D. and Wang Y.W., "Eccentric loading behavior of L-shaped columns composed of concrete-filled steel tubes", 12(3), 227-244, 2016.
- [10] Lee S.H., Yang I.S. and Choi S.M., "Structural characteristics of welded built-up square CFT column-to-beam connections with external diaphragms", Steel and Composite Structures, 10(3), 261-279, 2010.
- [11] Qin Y., Chen Z.H., Wang X.D. and Zhou T., "Seismic behavior of through-diaphragm connections between CFRT columns and steel beams-experimental study", Advanced Steel Construction, 10(3), 351-371, 2014.
- [12] Chen Z.H., Qin Y. and Wang X.D., "Development of connections to concrete-filled rectangular tubular columns", Advanced Steel Construction, 11(4), 408-426, 2015.
- [13] Kang L., Leon R.T. and Lu X., "Shear strength analyses of internal diaphragm connections to CFT columns", Steel and Composite Structures, 18(5), 1083-1101, 2015.
- [14] Guo Y. and Yao X., "Seismic performance and design of reduced steel beam section with concrete filled square tubular column", Advanced Steel Construction, 9(3), 173-189, 2013.
- [15] Kimura J., Choi S., Matsui C. and Chung J., "Structural characteristics of H-shaped beam-to-square tube column connection with vertical stiffeners", International Journal of Steel Structures, 5(2), 109-117, 2005.
- [16] Shin K.J., Kim Y.J. and Oh Y.S., "Seismic behaviour of composite concrete-filled tube column-to-beam moment connections", Journal of Constructional Steel Research, 64(1), 118-127, 2008.
- [17] Kang C.H., Kim Y.J., Shin K.J. and Oh Y.S., "Experimental investigation of composite moment connections with external stiffeners", Advances in Structural Engineering, 16(10), 1683-1700, 2013.
- [18] Kang C.H., Shin K.J., Oh Y.S. and Moon T.S., "Hysteresis behavior of CFT column to H-beam connections with external T-stiffeners and penetrated elements", Engineering Structures, 23(9), 1194-1201, 2001.
- [19] Xue J.Y., Chen X., Zhou P., Ge H.P. and Zeng F.S., "Shear capacity of joints between concrete-filled square steel tubular special-shaped columns and steel beams", Journal of Building Structures, 33(8), 51-57, 2012. (in Chinese)
- [20] Xu C.X., Wan B. and Zhang J.C., "Experimental research on seismic behavior of interior joints in the composite frame consisting of CFST cross-section columns and steel beams", Journal of Building Structures, 42(3), 80-83, 2012. (in Chinese)
- [21] Ma R.Q., Ban H.Y., Zhao Y.Z., Wang Y.Q., Li Q. and Liu M., "Experimental study on seismic behavior of steel beam to wide-flange specially-shaped composite column connections", Journal of Building Structures, 38(6), 105-111, 2017. (in Chinese)

- [22] Ghobadi M.S., Mazroi A. and Ghassemieh M., "Cyclic response characteristics of retrofitted moment resisting connections", Journal of Constructional Steel Research, 65(3), 586-598, 2009.
- [23] Ghobadi M.S., Ghassemieh M., Mazroi A. and Abolmaali A., "Seismic performance of ductile welded connections using T-stiffener", Journal of Constructional Steel Research, 65(4), 766-775, 2009.
- [24] Hancock J.W. and Mackenzie, A.C., "On the mechanisms of ductile failure in high strength steels subjected to multi-axial stress states", Journal of the Mechanics and Physics of Solids, 24(2), 147-69, 1976.
- [25] Mao C., Ricles J.M., Lu L.W. and Fisher J.W., "Effect of local details on ductility of welded moment connections", Journal of Structural Engineering, 127(9), 1036-1044, 2001.
- [26] Atashzaban A., Hajirasouliha I., Jazany R.A. and Izadinia M., "Optimum drilled flange moment resisting connections for seismic regions". Journal of Constructional Steel Research, 112, 325-338, 2015.
- [27] Roudsari M.T., Abdollahi F., Salimi H., Azizi S. and Khosravi A.R., "The effect of stiffener on behavior of reduced beam section connections in steel moment-resisting frames", International Journal of Steel Structures, 15(4), 827-834, 2015.
- [28] El-Tawil S., Mikesell T., Vidarsson E. and Kunath S. "Strength and ductility of FR welded bolted connections", Report No. SAC/BD-98/01, Sacramento, CA: SAC Joint Venture, 1998.
- [29] Wang Y., Feng S. and Wang Y.T., "Experimental study on hysteretic behavior for rigid-reinforced connections", China Civil Engineering Journal, 44(5), 57-68, 2011. (in Chinese)
- [30] DB/T29-186-2011. Technical specification for connection in CRFT structure of Tianjin, Tianjin Urban & Rural Construction Commission, Tianjin, China, 2011.
- [31] Nie J.G., Qin K. and Cai C.S., "Seismic behavior of composite connections - flexural capacity analysis", Journal of Constructional Steel Research, 65(5), 1112-1120, 2009.
- [32] Dai G.X. "Study and Evaluation Reliability of Steel Structural Buildings", Chongqing University, 2004.

METHOD FOR EVALUATING THE PROGRESSIVE COLLAPSE RESISTANCE OF LONG-SPAN SINGLE-LAYER SPATIAL GRID STRUCTURES

Li-Min Tian^{1,*}, Jian-Peng Wei¹ and Ji-Ping Hao¹

¹ School of Civil Engineering, Xi'an University of Architecture and Technology, Xi'an, China
*(Corresponding author: E-mail: tianlimin@xauat.edu.cn)

ABSTRACT

In recent years, researchers have increasingly reported the progressive collapse of long-span spatial grid structures. However, research on long-span spatial grid structures, especially single-layer spatial grid structures, remains limited. Thus, this study conducted an incremental dynamic analysis to develop a suitable method for evaluating single-layer spatial grid structures. The method uses a quantitative evaluation index called the collapse margin ratio. Engineering cases were analysed to validate the proposed method. For instance, the proposed method was used to evaluate the progressive collapse of the main stadium of the Shenzhen Universiade Sports Centre. The results showed that the roof of the structure has good resistance against progressive collapse from the perspective of quantitative analysis, even though the cantilever length reached 51.9–68.4 m at some locations, and the novel method is not restricted by the structural form. Thus, the method can be used to quantitatively evaluate a structure's resistance to collapse.

ARTICLE HISTORY

Received: 31 August 2017
Revised: 21 February 2018
Accepted: 28 March 2018

KEY WORDS

Single-layer spatial grid structure;
Progressive collapse;
Evaluation method;
Incremental dynamic analysis;
Vulnerability curve;
Collapse margin ratio

Copyright © 2019 by The Hong Kong Institute of Steel Construction. All rights reserved.

1. Introduction

Progressive collapse is defined as the spread of an initial local failure from element to element, which eventually results in the collapse of the entire structure or a disproportionately large part of it [1, 2]. Since the collapse of the Romexpo Pavilion in Bucharest, Romania (which was comprised of a single-layer spherical reticulated shell with a span of 93.5 m and rise of 19.1 m) in 1961 and the destruction of the Hartford Civic Centre (which was comprised of a space truss structure with a span of 110 m) in 1978, the traditional concept that the progressive collapse of a spatial grid structure following the loss of one important member can be prevented by a large degree of redundancy has been changing [3, 4]. Cases about the progressive collapse of long-span spatial grid structures have been reported more frequently than ever because of the widespread use of such structures in public buildings, which has enhanced socioeconomic development [5, 6, 7].

Studies regarding the progressive collapse have mostly focused on the frame structure [8, 9, 10]. Researchers have conducted several progressive collapse experiments for a single-column removal scenario [11] and have compared various modelling approaches for steel frames [12]. Moreover, engineers have developed design specifications for steel frames for the prevention of progressive collapse [13, 14, 15]. However, research on long-span spatial grid structures, especially single-layer spatial grid structures, has been rather limited [16, 17, 18]. A new beam–column element was presented [19] and adopted in a second-order direct analysis of a long-span single-layer roof [20]. The collapse of a single-layer spatial grid structure, which occurs due to the accumulation of node failures and member buckling, is different from that of a frame, wherein a sufficiently plastic hinge is formed in the structure and induces progressive collapse. The load-carrying mechanism of a single-layer spatial grid structure relies heavily on its structural shape. Therefore, evaluation methods that are appropriate for frames cannot be used directly for single-layer spatial grid structures [21]. Thus, a new method must be developed to evaluate single-layer spatial grid structures specifically.

Incremental dynamic analysis (IDA) considers several types of random factors to evaluate the structural seismic performance without being limited by the structural form [22]. The progressive collapse induced by member removal is different from that in the case of an earthquake. Based on the principle of IDA, this study developed a suitable method for evaluating single-layer spatial grid structures. The seismic waves were replaced by the failure of a different member in order to conduct a series of dynamic and time-history analyses. Moreover, vulnerability analysis was conducted to describe the probability of the exceedance of collapse states. A quantitative evaluation index called the collapse margin ratio (CMR) was derived. The proposed method was validated by analysing several engineering cases, and the influence of an initial geometric imperfection was analysed. The evaluation method was then utilised in a computer simulation of the main stadium for the Shenzhen Universiade Sports Centre and was found to provide accurate and reliable results for the progressive collapse of a long-span single-layer spatial grid structure. The finite element

(FE) analysis performed in this study was validated by conducting an experiment on the progressive collapse of a single-layer latticed dome [4].

2. Evaluation method based on an incremental dynamic analysis

2.1. Basic principle of evaluation method

IDA can be regarded as an improvement over static pushover analysis, wherein the ground motion intensity measure (IM) is continuously increased to obtain the corresponding damage measure (DM). A curve is plotted with the DM and IM along the horizontal and vertical axes, respectively. Multiple DM–IM curves can be drawn for various seismic waves to evaluate the ability of a structure to resist collapse.

Although the specific causes of collapse differ in the case of an earthquake and the loss of an important member, they are similar in that both are dynamic processes that occur due to an accidental event. Thus, the principle of IDA can be used for evaluating single-layer spatial grid structures. Unlike a seismic wave, the failure of a different member is considered a cause of structural vibration. To consider the influence of various loads, the combined load is increased such that the intensity is changed until the progressive collapse of the structure occurs. The potential ability of a single-layer spatial grid structure to resist progressive collapse and its performance for various combined loads can be obtained, and its resistance to progressive collapse can be quantitatively evaluated.

2.2. Evaluation procedure

A suitable method for evaluating single-layer spatial grid structures was developed based on the principle of IDA. The main steps are given below.

(1) A certain number of important members are selected through a *multiple-response evaluation method based on the primary scope* [7]. The maximum displacement that directly produces a damaged condition for the structure is chosen as the DM, and the combined load that reflects the vibration strength is chosen as the IM. These are used to derive a load–displacement curve in a manner that is similar to a pushdown analysis.

(2) The loss of one important member is considered. An *alternate load path method along with the consideration of the construction effect* [7] is used to obtain the DM when the IM is increased or decreased through a change in the live load without changing the dead load. This may cause the DM to increase significantly with a slight increment in the IM. The DM–IM curve is then plotted. It should be noted that the load increment should be reduced in order to capture the change in the DM–IM curve more clearly during the plastic development process. The two reasons why only the single-member failure condition was considered in this study are that member failure is a small-probability event, and the removal of a single member can reflect the ability to form other load paths.

(3) Step (2) is repeated using different important members to obtain more DM–IM curves.

(4) The DM–IM curves are processed according to the evaluation standard

to evaluate the resistance of the structure to progressive collapse.

The method is called *evaluation of progressive-collapse resistance based on IDA*, and the basic process is presented in Fig. 1. This method can be regarded as a series of dynamic and time-history analyses in which the alternate load path method along with the consideration of the construction effect are applied.

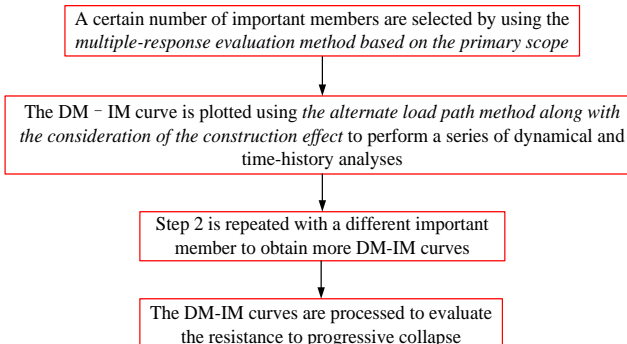


Fig. 1 Basic procedure of the evaluation method

2.3. Evaluation standard

To demonstrate the structural performance of anti-collapse, a statistical method is required to address the discrete DM-IM curves. The 16%, 50%, and 84% quantile curves for qualitative analysis can be obtained to characterise the average level and discreteness of the curves [23]. The specific procedure is as follows (Fig. 2):

(1) The fitting method of a spline or polynomial curve can be imposed on discrete data points to obtain DM-IM curves. Regardless of the fitting method used, the fitting result should be precisely consistent with the DM-IM curves.

(2) DM-IM curves can be summarised using parametric or nonparametric methods. The former assumes that each DM-IM curve obeys an exponential distribution. Regression analysis is used to obtain the exponential model parameters for plotting the DM-IM curve. For the latter, the mean value and logarithmic standard deviation of the IM are calculated at certain DMs to obtain the curves of $(DM, \mu e^{-\delta})$, (DM, μ) , and $(DM, \mu e^{+\delta})$, which represent the 16%, 50%, and 84% quantile curves, respectively. The calculation method is the same as that used for the various IMs.

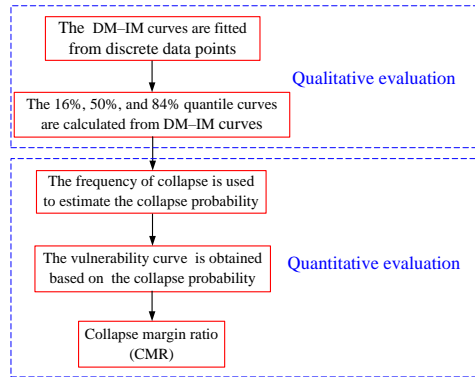


Fig. 2 Evaluation standard

A quantitative analysis is also necessary. A structural vulnerability curve that reflects the probability of progressive collapse for accidents with various intensities can be depicted using the IM parameters for the collapse point of each DM-IM curve [24, 25]. The CMR of the structure can then be calculated based on the vulnerability curve. The specific procedure is as follows (Fig. 2):

(1) The frequency of collapse is used to estimate the collapse probability for different IMs:

$$P[C|IM = im] = N_c/N \quad (1)$$

where $P[C|IM = im]$ is the collapse probability of the structure when $IM = im$, and N is the number of important members for which N_c important members cause the progressive collapse of the structure.

(2) A logarithmic normal distribution model is adopted for the vulnerability function, and the vulnerability curve in Eq. 2 can be fitted to the collapse probability of each IM:

$$P[C|IM = im] = \Phi[\ln(im/m) / \beta] \quad (2)$$

where m and β are the mean value and logarithmic standard deviation,

respectively, of the structure's ability to resist progressive collapse.

(3) $IM_{50\%}$ corresponds to a 50% collapse in probability and was adopted as the resistance index of progressive collapse. The accidental events were the main reason for a progressive collapse, which has a lower probability of occurring. The dead load was in a dominant position, and thus, the live load was reduced, and the wind load was ignored. Consequently, IM_o was set to 1.2 times the dead load and 0.5 times the live load ($1.2DL+0.5LL$, [13, 14]). The combined load is used to determine the ability of a structure to resist collapse. The ratio of $IM_{50\%}$ to IM_o is the CMR:

$$CMR = IM_{50\%}/IM_o \quad (3)$$

2.4. Collapse standard

Based on the characteristics of a single-layer spatial grid structure, its progressive collapse after partial destruction occurs due to the accumulation of node failures and member buckling, which diminish the overall stiffness of the structure. Therefore, the collapse point in a DM-IM curve is defined as the point at which the overall stiffness is reduced to 20% of K_e , where K_e is the initial slope of the curve and indicates the original stiffness of the structure [26]. It should be noted that a single-layer spatial grid structure with few members may collapse without a decrease in stiffness. In this situation, the actual collapse point is adopted.

3. Verification of finite element analysis

3.1. Analysis model

To validate the FE analysis performed in this study, a single-layer latticed dome was tested, as shown in Fig. 3. The span and rise were 4.2 and 0.7 m, respectively, and the meridians were equally divided on the horizontal projection plane. In addition, the edge supports were set as fixed ideal pins to make this experimental program a benchmark for the validation of the FE analysis. A two-node space beam element [27] was employed for each member, and the members were connected by rigid joints. To accurately simulate the collapse process, material and geometric nonlinearity were considered. This modelling approach was adopted for the subsequent case studies and engineering applications. Further details regarding this test model are provided by Zhao *et al.* [4].

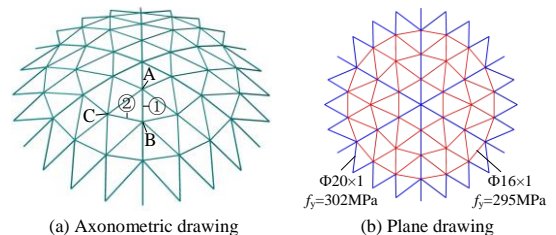


Fig. 3 Test model

The test model was subjected to a point load of 0.8 kN using weights. For a beam element with virtual density, the mass centre and stiffness centre were coincided with the linked joint to avoid the application of torsion at each joint, as shown in Fig. 4. Member 1 was eliminated by a member-breaking device after static loading. Fig. 5 presents the decreased ratio of the axial force in member 1; the axial force decreased quickly and was reduced to zero in 0.26 s. Therefore, the axial force of member 1 in the FE analysis was plotted along the curve shown in Fig. 5 until it reached zero.

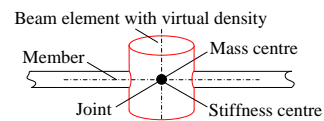


Fig. 4 Beam element with virtual density

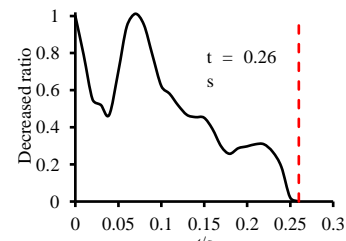
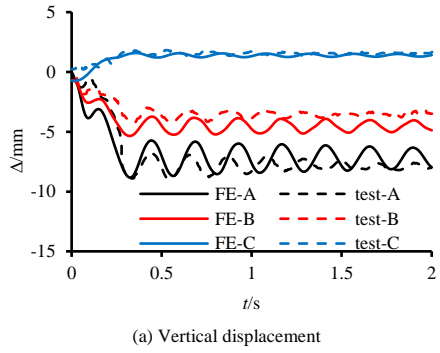


Fig. 5 Decreased ratio of axial force in member 1

First, an implicit time integration analysis (Newton–Raphson iteration algorithm) was performed to obtain the initial static condition of the intact dome. Second, the deformed mesh and material state of the dome without member 1 were imported into the explicit time integration solver (central difference method) for the dynamic analysis of progressive collapse. A damping ratio of 0.02 [28] was considered as the Rayleigh damping, but the stiffness damping was ignored in the explicit time integration solver to eliminate the requirement for calculating a stiffness matrix and to reduce the computational costs.

3.2. Results

Fig. 6 presents the displacements of joints near member 1 and the strain of member 2 near joint B. A good agreement was observed between the FE and test results; the values for the maximum displacement and strain matched well. In addition, the balance state was regained after member 1 was eliminated, which matched the test observation. Therefore, it was verified that the FE analysis used in this study provides efficient and accurate results.



(a) Vertical displacement

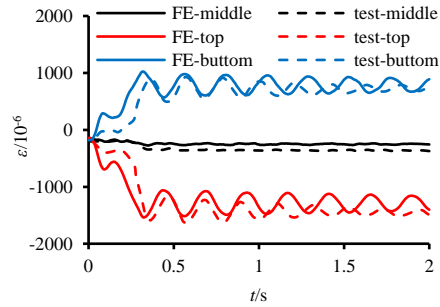
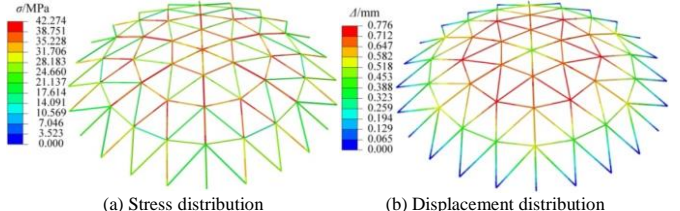


Fig. 6 Comparison between FE and test results

Fig. 7 shows the initial state with a point load of 0.8 kN. The maximum stress was 42.3 MPa, and the displacement was negligible. Fig. 8 plots the distributions of the stress and displacement when member 1 was eliminated and the peak values were reached. The maximum values were concentrated in the local area next to joint B, which showed considerable resistance to an

unbalanced load. The maximum displacement remained low, and the stress was less than the yield stress of the dome. Thus, progressive collapse was prevented.



(a) Stress distribution (b) Displacement distribution

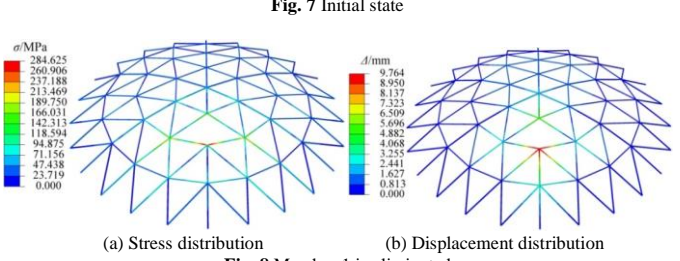


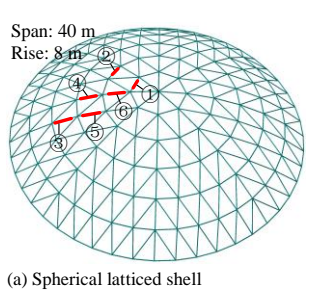
Fig. 8 Member 1 is eliminated

4. Verification of the evaluation method

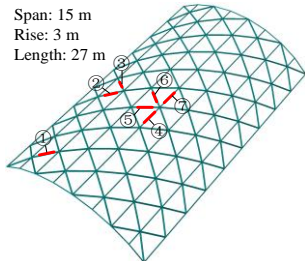
4.1. Engineering Cases

To validate the evaluation method, three typical single-layer spatial grid structures [28] representing latticed shells with nonnegative, zero, and negative Gaussian curvatures were analysed. The specific arrangements of the members and structural geometric parameters are shown in Fig. 9. The boundary conditions were determined based on the practical conditions of the structures. The surrounding nodes of the spherical latticed shell were considered as solid joints. For the cylindrical latticed shell, fixed hinge supports were used on two longitudinal edges, and the rest of the edges only restricted the in-plane displacement. For the hyperbolic paraboloid latticed shell, the vertical displacement of the edge nodes was limited except in the case of four corner nodes with fixed hinge supports.

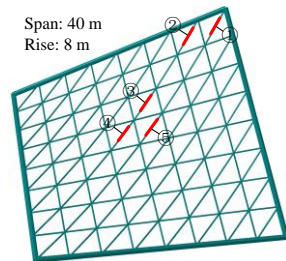
A circular steel pipe was used in the three single-layer spatial grid structures. The specific member sizes are listed in Table 1. A greater stiffness was required for the boundary members of the hyperbolic paraboloid latticed shell than for the rest of members. A cross-section of $\Phi 630 \text{ mm} \times 16 \text{ mm}$ was adopted, which is approximately eight times larger than that of the chord members. The members were made of the material Q235 with a standard yield strength of 235 MPa, and a bilinear isotropic constitutive model that considers the material reinforcement was selected to examine the dynamic collapse process. The member weights were automatically calculated using the FE software, and the node weights were estimated to have 25% of the member weights imposed. The roof material (1.5 kN/m^2) and live load (0.5 kN/m^2) were applied to the nodes of the shells using an equivalent calculation.



(a) Spherical latticed shell



(b) Cylindrical latticed shell



(c) Hyperbolic paraboloid latticed shell

Fig. 9 Three typical single-layer spatial grid structures

4.2. Quantile curves analysis

The multiple-response evaluation method based on the primary scope [7] was applied to the three single-layer spatial grid structures in order to determine the distribution of the important members, as shown in Fig. 9. The resistance to progressive collapse was evaluated using IDA. Fig. 10 shows the progressive collapse of the three single-layer spatial grid structures when member 1 was eliminated and the ultimate load condition was achieved. The structures as well as other important members lost bearing capacity and collapsed completely in 3 s.

Table 1

Member sizes

Structural form	Member location	Cross-section
Spherical latticed shell	Meridian and parallel member	$\Phi 121 \times 3.5$
	Diagonal member	$\Phi 114 \times 3$
Cylindrical latticed shell	Longitudinal and short edge member	$\Phi 89 \times 4$
	Diagonal member	$\Phi 140 \times 6$
Hyperbolic paraboloid latticed shell	Chord member	$\Phi 180 \times 7$
	Boundary member	$\Phi 630 \times 16$

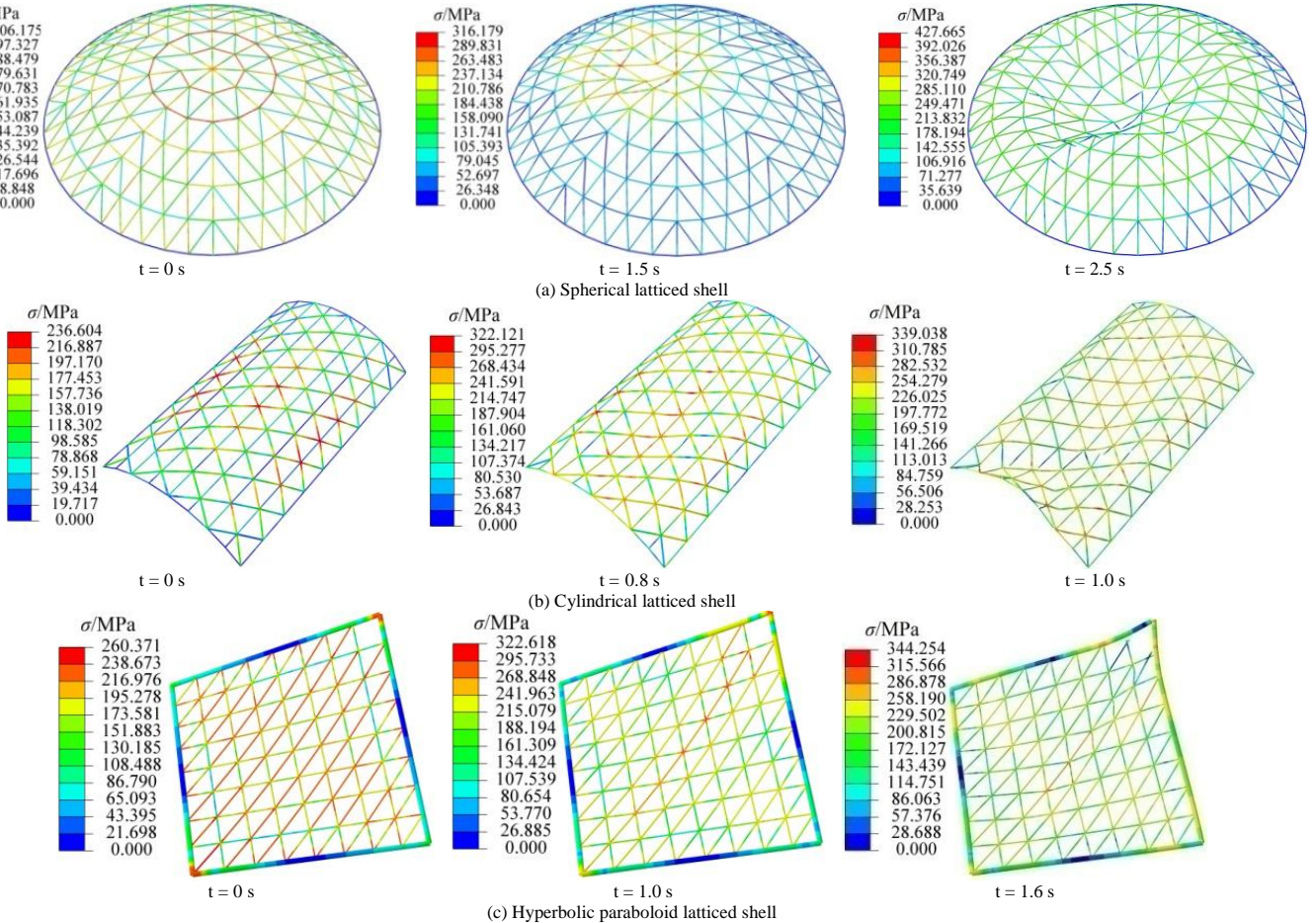


Fig. 10 Progressive collapse of structures

Fig. 11 presents the DM–IM curves of the original model after each important member failure. The partial coefficient of the live load γ was chosen as the vertical axis because the partial coefficient of the dead load was fixed at 1.2 [13, 14]. Fig. 12 presents the DM–IM curves when an initial geometric imperfection was considered based on the consistent mode imperfection method. The imperfection distribution was the same as the first-order buckling mode

under a vertical load. The magnitude of the initial imperfection was $l/300$, where l is the span of the structure [28]. Therefore, the initial imperfections were set as 50 mm for the cylindrical latticed shell and 133 mm for the other two latticed shells. The nonparametric method was used to calculate the 16%, 50%, and 84% quantile curves for each DM, as shown in Figs. 13 and 14.

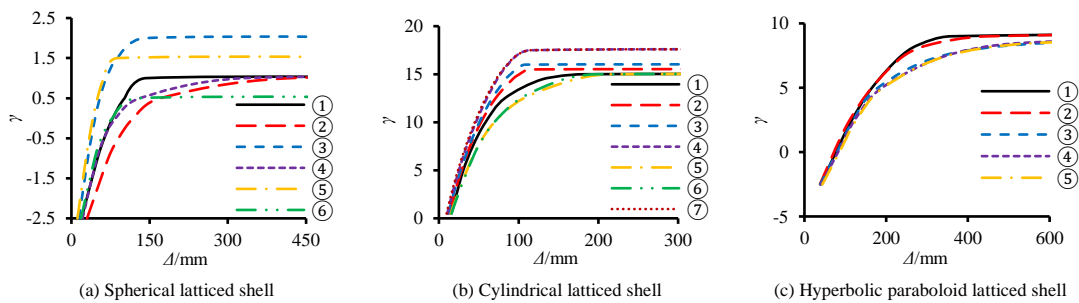


Fig. 11 DM–IM curves of the original model

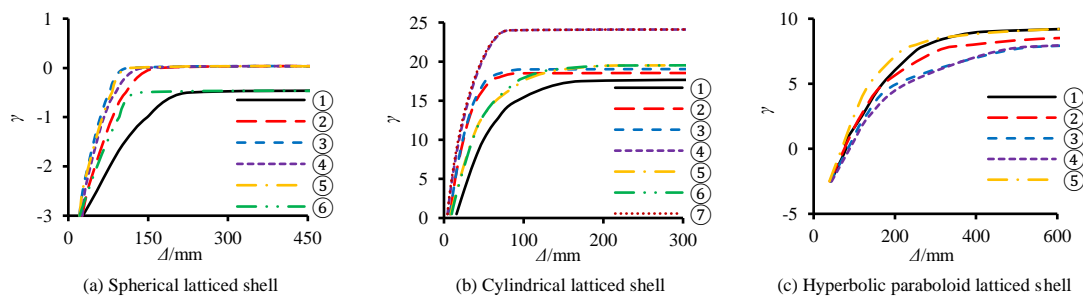


Fig. 12 DM–IM curves considering the initial geometric imperfection

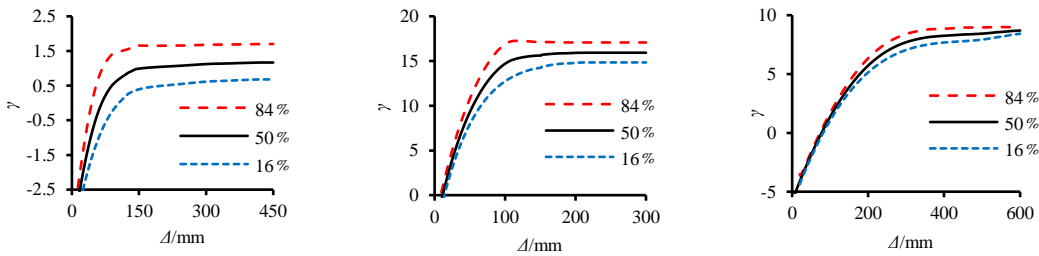


Fig. 13 Quantile curves of the original model

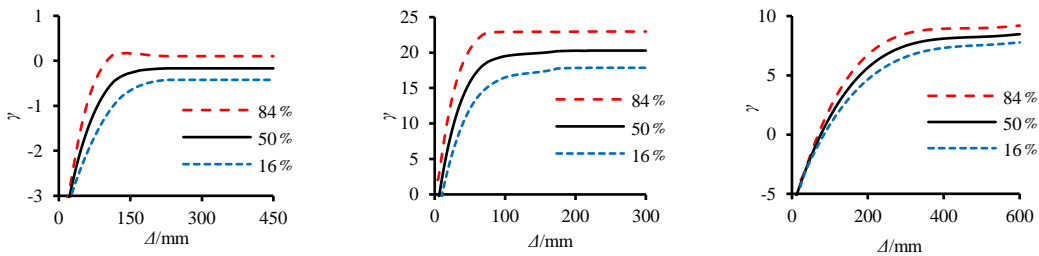


Fig. 14 Quantile curves considering the initial geometric imperfection

The analysis showed that the performance level of the structure can be divided into two stages. First, the slope of the curve remains nearly constant in the initial stage, wherein the entire structure stays in an elastic state as the members deform elastically. Second, as members yield or buckle with an increasing live load, the slope of the curve clearly decreases until the ultimate load condition is finally reached. Therefore, the collapse point is obtained when the slope of the curve is reduced to 20% of K_e .

In the case of the spherical and cylindrical latticed shells, the effects of the initial geometric imperfection were more serious than for the hyperbolic paraboloid latticed shell. This is because the majority of the members experienced compression. Based on the obtained results, the bearing capacity of the spherical latticed shell decreased when the initial geometric imperfection was considered, while the bearing capacity of the cylindrical latticed shell increased considerably due to shape distortion.

The quantile curves revealed the discreteness of the results. Thus, the difference in the importance of the members can be recognised, and the weak

links of a structure can be identified. After the initial geometric imperfection was imposed, the discreteness of the results for the cylindrical and hyperbolic paraboloid latticed shells increased. This indicates that considering an initial geometric imperfection increases the difference in importance of the members and highlights weak links.

4.3. Vulnerability curves analysis

These curves only allow for a qualitative analysis of collapse resistance. The cylindrical latticed shell showed the best resistance to progressive collapse among the structures in terms of bearing capacity and was followed by the hyperbolic paraboloid latticed shell. The spherical latticed shell could not even bear the dead load. Hence, a quantitative analysis is proposed to calculate the relationship between the collapse probability and IM parameters, which is shown in Figs. 15 and 16. The CMR can then be obtained based on the vulnerability curves, whose results are listed in Table 2.

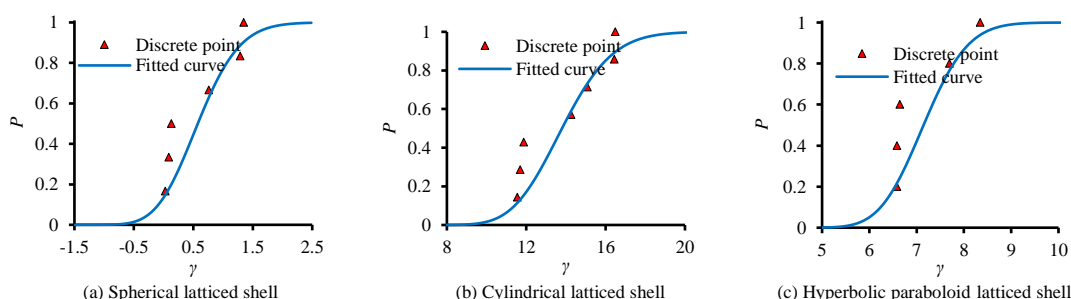


Fig. 15 Vulnerability curves of the original model

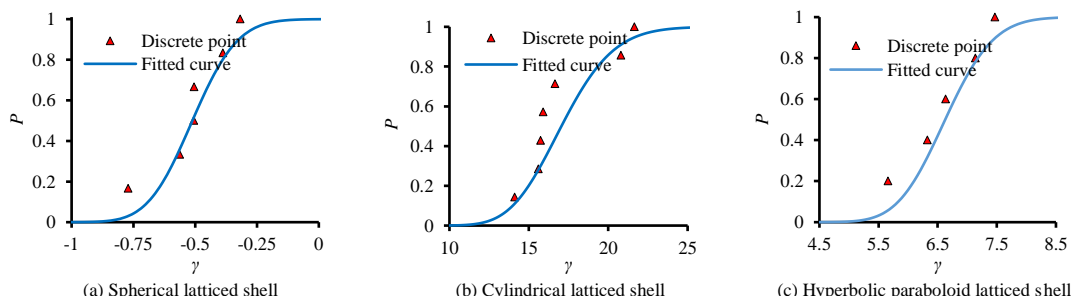


Fig. 16 Vulnerability curves considering the initial geometric imperfection

Table 2
Results of CMR

Structural form	Spherical latticed shell	Cylindrical latticed shell	Hyperbolic paraboloid latticed shell
Original model	1.01	3.55	2.27
Initial geometric imperfection considered	0.80	4.81	2.17

The vulnerability curves indicated that the resistance to progressive collapse can be described comprehensively, and the corresponding collapse probability can be determined for various combined loads. As compared to the cylindrical and hyperbolic paraboloid latticed shells, the collapse points of the spherical latticed shell were more concentrated. This illustrates that the differences in mechanical performance of the important members were small

and that the overall structure was uniformly forced.

Table 1 indicates that the CMR can be used as a unified evaluation index to quantitatively evaluate a structure's resistance against progressive collapse. For the original model, the CMR of the cylindrical latticed shell was 3.52 times greater than that of the spherical latticed shell, which had a CMR of 1.01. When the initial geometric imperfection was considered, the CMRs of the three latticed shell structures changed. The CMR of the cylindrical latticed shell increased by 35.5%, while those of the other two latticed shells decreased. In particular, the CMR of the spherical latticed shell was less than 1. Thus, the structure's safety margin of resistance to progressive collapse was insufficient, and thus, there existed a severely higher risk of collapse after the failure of a single member.

The above analysis showed that the *evaluation of progressive-collapse resistance based on IDA* is not restricted by the structural form and that the structural performance in terms of resistance to collapse can be quantitatively evaluated. Moreover, the initial geometric imperfection should be considered; otherwise, incorrect or even dangerous evaluation results may be obtained.

5. Engineering application

5.1. Project profile

The roof of the main stadium for the Shenzhen Universiade Sports Centre has a single-layer folded-plane latticed shell structure system. The structural system is comprised of 20 units of similar shapes, and the dimensions of the architectural plane are 274 m × 289 m, as shown in Fig. 17. The sections of the main members are circular, and their diameters range from 700 to 1400 mm. The materials used for the main members are Q390 and Q420.

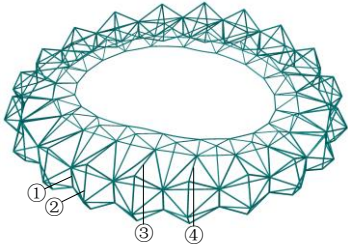


Fig. 17 Structural system of the main stadium

5.2. Qualitative evaluation

The important members were chosen from a quarter of the structure because of its symmetry using the multiple-response evaluation method based on the primary scope, which was employed by Tian et al. [7], as shown in Fig. 17. Decreasing the number of important members such that non-important members are eliminated is a conservative approach. Therefore, only four important members were evaluated.

Fig. 18 presents the DM–IM curves after the failure of each important member. The nonparametric method was used to calculate the 16%, 50%, and 84% quantile curves for each DM, as shown in Fig. 19. First, the increase in the maximum displacement accelerated until a progressive collapse was finally triggered. At the collapse point, the displacement–span ratio was 1/30, and the combined load was greater than 1.2DL+0.5LL. Consequently, the main stadium for the Shenzhen Universiade Sports Centre was found to have a good resistance to progressive collapse. The entire structure has relatively good ductility. Second, the DM–IM curves of members 2 and 4 were identical, and thus, eliminating either of these two important members had a similar effect on the structure. However, because of the existence of member 1, the discreteness of the quantile curves increased under a large displacement. Third, the structure was significantly weakened by the failure of member 1, which makes the importance of member 1 evident. Thus, threats and damage to member 1 should be avoided.

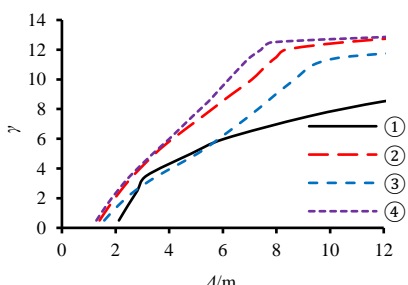


Fig. 18 DM–IM curves for the project

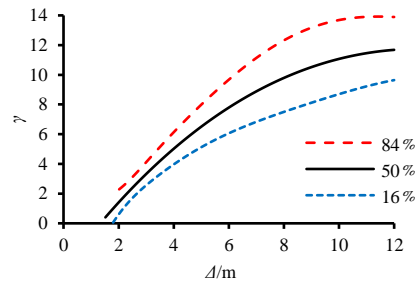


Fig. 19 Quantile curves for the project

5.3. Quantitative evaluation

Fig. 20 shows the vulnerability curves of the main stadium for the Shenzhen Universiade Sports Centre with a CMR of 1.68. According to the quantitative analysis, the main stadium showed good resistance to progressive collapse even though its cantilever length reached 51.9–68.4 m at some locations. The potential ability of the structure to resist progressive collapse was evaluated and expressed in the form of probability.

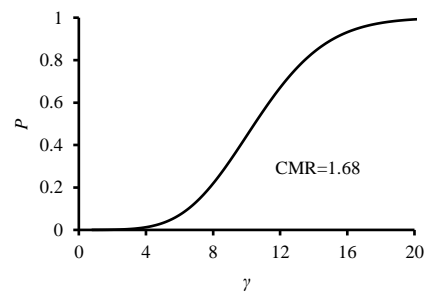


Fig. 20 Vulnerability curves for the project

Fig. 21 shows the collapse modes when the ultimate load condition is achieved. The deformation was concentrated in the structural unit that contained the failure member, and the fractures of the members were distributed around the failure member. This part of the structure is not appropriate for bearing the load, while the rest of the structural units are less affected by the failure member. Hence, dividing the structural units in the main stadium for the Shenzhen Universiade Sports Centre can effectively suppress the occurrence of progressive collapse. Three ring beams (i.e., bottom of the shoulder, bottom of the crown, and inner ring [29, 30]) connect the entire structure, and the effect of them working together is apparent.

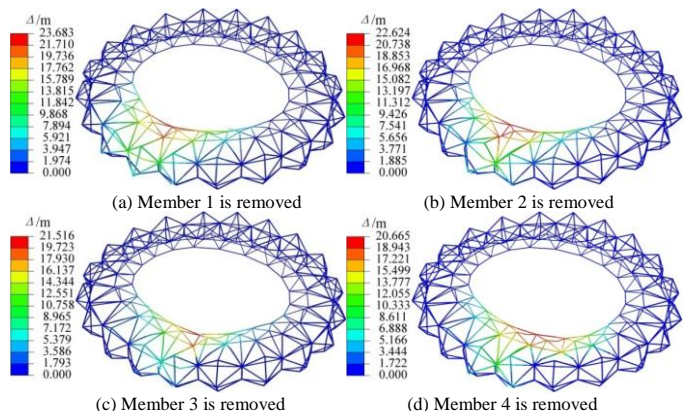


Fig. 21 Displacement distribution

6. Conclusions

A method of evaluating structural seismic performance known as IDA was intensively studied and used to develop a new method for evaluating the resistance to progressive collapse of long-span single-layer spatial grid structures. The proposed method was validated using three engineering case analyses and utilised in a computer simulation of the main stadium of the Shenzhen Universiade Sports Centre. The following conclusions were drawn:

(1) A suitable method for evaluating single-layer spatial grid structures called the *evaluation of progressive-collapse resistance based on IDA* was introduced. The method is not restricted by the structural form, and the method

can quantitatively analyse the resistance of a structure to collapse.

(2) The displacement and strain responses can be predicted well with the FE model. In addition, the balance state that was regained matched the test observation. Thus, an efficient and accurate approach to studying the progressive collapse of single-layer spatial grid structures was developed.

(3) An initial geometric imperfection should be considered based on the consistent mode imperfection method; otherwise, incorrect or even dangerous evaluation results may be obtained.

(4) The main stadium for the Shenzhen Universiade Sports Centre was found to have good resistance to progressive collapse in the quantitative analysis even though the cantilever length reached 51.9–68.4 m at some locations. The potential ability of the structure to resist progressive collapse was evaluated and expressed in the form of probability.

Acknowledgements

This research was supported by the National Natural Science Foundation of China (Grant No. 51608433), the Science and Technology Co-ordination and Innovation Fund Project of Shaanxi Province of China (Grant No. 2016KTZDSF04-02-02), the Shaanxi Province Youth Science and Technology New Star Program (2018KJXX-20), the Shanghai Rising-Star Program (Grant No. 17QB1402300), and the Natural Science Foundation of Shaanxi Province of China (Grant No. 2018JQ5052). Their financial supports are greatly appreciated.

References

- [1] ASCE 7-10, Minimum Design Loads for Buildings and Other Structures, American Society of Civil Engineers, 2010.
- [2] Rezvani F.H., Yousefi A.M. and Ronagh H.R., "Effect of span length on progressive collapse behaviour of steel moment resisting frames", *Structures*, 3, 81-89, 2015.
- [3] Piroglu F. and Ozakgul K., "Partial collapses experienced for a steel space truss roof structure induced by ice ponds", *Engineering Failure Analysis*, 60, 155-165, 2016.
- [4] Zhao X.Z., Yan S. and Chen Y.Y., "Comparison of progressive collapse resistance of single-layer latticed domes under different loadings", *Journal of Constructional Steel Research*, 129, 204-214, 2017.
- [5] Biegus A. and Rykaluk K., "Collapse of Katowice fair building", *Engineering Failure Analysis*, 16, 1643-1654, 2009.
- [6] Kamari Y.E.I., Raphael W. and Chateauneuf A., "Reliability study and simulation of the progressive collapse of Roissy Charles de Gaulle Airport", *Case Studies in Engineering Failure Analysis*, 3, 88-95, 2015.
- [7] Tian L.M., Wei J.P., Hao J.P. and Wang X.T., "Dynamic analysis method for progressive collapse of long-span spatial grid structures", *Steel and Composite Structures*, 23(4), 435-444, 2017.
- [8] Song B.I. and Sezen H., "Experimental and analytical progressive collapse assessment of a steel frame building", *Engineering Structures*, 56, 664-672, 2013.
- [9] Sagiroglu S. and Sasani M., "Progressive collapse-resisting mechanisms of reinforced concrete structures and effects of initial damage locations", *Journal of Structural Engineering*, 140(3), 04013073, 2014.
- [10] Yang B., Tan K.H., Xiong G. and Nie S.D., "Experimental study about composite frames under an internal column-removal scenario", *Journal of Constructional Steel Research*, 121, 341-351, 2016.
- [11] Demonceau J.F. and Jaspart J.P., "Experimental test simulating a column loss in a composite frame", *Advanced Steel Construction*, 6(3), 891-913, 2010.
- [12] Yu H., Izzuddin B.A. and Zha X.X., "Progressive collapse of steel-framed buildings: influence of modelling approach", *Advanced Steel Construction*, 6(4), 932-948, 2010.
- [13] GSA 2013, Progressive Collapse Analysis and Design Guidelines for New Federal Office Buildings and Major Modernization Projects, Washington DC: General Services Administration, 2013.
- [14] UFC 4-023-03, Design of Buildings to Resist Progressive Collapse, Washington DC: Department of Defense, 2013.
- [15] CECS 392, Code for Anti-collapse Design of Building Structures, China Association for Engineering Construction Standardization, 2015.
- [16] Malla R.B., Agarwal P. and Ahmad R., "Dynamic analysis methodology for progressive failure of truss structures considering inelastic postbuckling cyclic member behavior", *Engineering Structures*, 33, 1503-1513, 2011.
- [17] Thai H.T. and Kim S.E., "Nonlinear inelastic time-history analysis of truss structures", *Journal of Constructional Steel Research*, 67, 1966-1972, 2011.
- [18] Jiang X.F. and Chen Y.Y., "Progressive collapse analysis and safety assessment method for steel truss roof", *Journal of Performance of Constructed Facilities*, 26(3), 230-240, 2012.
- [19] Liu S.W., Bai R., Chan S.L. and Liu Y.P., "Second-order direct analysis of domelike structures consisting of tapered members with I-sections", *Journal of Structural Engineering*, 142(5), 04016009, 2016.
- [20] Liu Y.P., Chan S.L., Du Z.L. and He J.W., "Second-order direct analysis of long-span roof structures", *The 8th European Conference on Steel and Composite Structures*, 1(2&3), 3930-3939, 2017.
- [21] Fascati A., Kunath S.K. and Nisticò N., "Robustness evaluation of RC frame buildings to progressive collapse", *Engineering Structures*, 86, 242-249, 2015.
- [22] Vamvatsikos D. and Cornell C.A., "Incremental dynamic analysis", *Earthquake Engineering and Structural Dynamics*, 31, 491-514, 2002.
- [23] Zhou Y., Lv X.L. and Bo Y., "Application of incremental dynamic analysis to seismic evaluation of hybrid structure", *Journal of Tongji University (natural science)*, 38(2), 183-187, 2010. [in Chinese].
- [24] Shi W., Ye L.P., Lu X.Z. and Tang D.Y., "Study on the collapse-resistant capacity of RC frames with different seismic fortification levels", *Engineering Mechanics*, 28(3), 41-48, 2011. [in Chinese].
- [25] Yu X.H. and Lv D.G., "Seismic collapse fragility analysis considering structural uncertainties", *Journal of Building Structures*, 33(10), 8-14, 2012.
- [26] FEMA-350, Recommended Seismic Design Criteria for New Steel Moment-frame Buildings, Washington D.C: Federal Emergency Management Agency, 2000.
- [27] Wang W.M., Li H.N. and Tian L., "Progressive collapse analysis of transmission tower-line system under earthquake", *Advanced Steel Construction*, 9(2), 161-172, 2013.
- [28] JGJ 7-2010, Technical Specification for Space Frame Structures, Ministry of Housing and Urban-Rural Development of the People's Republic of China, 2010.
- [29] Tian L.M. and Hao J.P., "Nonlinear time-varying analysis algorithms for modeling the behavior of complex rigid long-span steel structures during construction processes", *Steel and Composite Structures*, 18(5), 1197-1214, 2015.
- [30] Tian L.M., Wei J.P., Hao J.P., "Anti-progressive collapse mechanism of long-span single-layer spatial grid structures", *Journal of Constructional Steel Research*, 144, 270-282, 2018.

BEHAVIOUR OF STEEL-CONCRETE-STEEL SANDWICH PLATES UNDER DIFFERENT ICE-CONTACT PRESSURE

Jia-Bao Yan¹, Zhe Wang² and Xuan Wang^{3,*}

¹ Associate Professor; ²M.E. Candidate, School of Civil Engineering / Key Laboratory of Coast Civil Structure Safety of Ministry of Education, Tianjin University, Tianjin 300350, P.R. China

³ Associate Professor, School of Marine Science and Technology, Tianjin University, Tianjin 300072, P.R. China

(*Corresponding author: Email: wangx2010water@126.com)

ABSTRACT

Steel-concrete-steel (SCS) sandwich plate has been developed as the ice-resisting walls in Arctic offshore constructions. This paper investigates the ultimate strength behaviour of SCS sandwich plates under different surface loading area by numerical analysis method. This paper adopted the finite element model that was developed and extensively validated by the test results. Through the 35-case study, the ultimate strength behaviour of the SCS sandwich plate under different surface loading area was investigated. The general load-deflection behaviour of the SCS sandwich plates under different loading area were analysed and summarized. Different failure modes of the SCS sandwich plate under different surface loading area were reported and discussed. The load-transferring mechanism of the SCS sandwich plate under different surface loading area were analysed. Finally, considering the applications of these SCS sandwich plate as the ice-resisting wall in the Arctic offshore constructions, these FE predicted ultimate resistances of the SCS sandwich plates under different surface loading area were compared with the corresponding ice-contact pressure predicted by the design codes. These comparisons confirmed the applicability of developed SCS sandwich plate as the ice-resisting wall in Arctic offshore constructions.

Copyright © 2018 by The Hong Kong Institute of Steel Construction. All rights reserved.

ARTICLE HISTORY

Received: 10 September 2017

Revised: 8 July 2018

Accepted: 15 July 2018

KEY WORDS

Steel-concrete composite structure;
Finite element analysis;
Punching shear resistance;
Numerical analysis;
Ice-contact pressure;
Steel damage

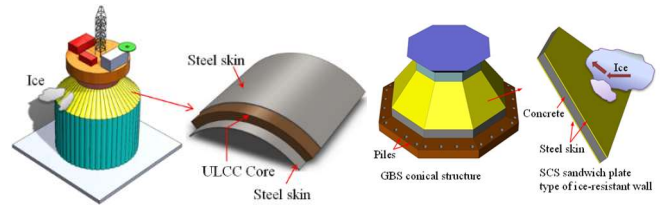


Fig. 1 SCS sandwich plate type of ice-resistant wall in Arctic offshore structure [2]

plate or shell type of ice-resisting walls under patch loads. These literatures showed that previous studies on the ice-resisting walls mainly focused on the normal (or lightweight) reinforced concrete plates or shells. Moreover, all of these studies focused on the structural behaviours of reinforced concrete ice-resisting walls under patch loads. Nojiri et al. [11] reported experimental and analytical studies on the steel-concrete composite ice-resisting walls for the Arctic offshore structures. However, this study mainly tested the SCS composite beams that deemed to be different from the SCS sandwich plate structures. Shukry and Goode [12] and Yan et al. [13] investigated punching shear behaviours of the SCS sandwich shells under patch loads. The ultimate strength behaviour of the SCS plates under patch loads have been reported by Sohel et al. [14], Shanmugam et al. [15], and Yan et al. [16-19]. These reported experimental and analytical works mainly focused on the structural behaviours of the SCS sandwich plate (or shell) under patch loads. The information on the SCS sandwich plate under large loading area so far is still quite limited. Therefore, it is of interest and importance to carry out more studies on the structural behaviours of the SCS sandwich plate under different ice-contact loading areas, which would provide more information to understand their structural performances under these different loading scenarios.

Different numerical models have been developed and offer alternative approaches for the analysis on the SCS sandwich structures [15, 20-22], which provided useful and economic means to investigate the structural behaviours of this type of structures. Foundoukos and Chapman [20] developed 2-D FE model for SCS sandwich beam, and this 2-D model limits the simulation of 3D behaviors of the shear connectors in the SCS sandwich structure. Shanmugam et al. [15] developed a simplified 3-D model by introducing anisotropic element that simplified the concrete with inside embedded headed studs. Though this model could globally capture the structural behaviour of the SCS sandwich plates, it could not simulate well the shear failure of the inside connectors and punching shear failure of the concrete core and steel face plates. Great efforts have been made to develop the FE models to simulate the SCS sandwich composite structures with different types of connectors. Yan et al. [21] and Sohel et al. [22] developed the 3-D FE models for SCS sandwich structure through simplifying a pair of overlapped headed studs or interlocked J-hook connectors into two cylindrical studs linked by the nonlinear spring element. However, this model could not accurately simulate the shear-tension interaction strength and damage failure mechanism of steel face plates or connectors. Yan et al. [23] and Yan and Zhang [24] continued this work and developed detailed FE model that offered accurate and detailed simulations on the stud-concrete interactions in

1. Introduction

The explorations of oil and gas in the Arctic region becomes popular recently due to 30% of the world's undiscovered gas and 13% of the world's undiscovered oil are stored in this region. With such rich resources, the Arctic will be the essential output region of oil and gas in the future. However, the moving ice sheets in the Arctic ocean that were driven by the wind and current critically threat the Arctic offshore structures used for the oil and gas explorations. Various types of engineering constructions have been proposed and used for the Arctic oil and gas explorations, e.g., artificial island, jacket structure, caisson-retained structure, gravity based conical structure, and floating structures. Marshall et al. [1] and Yan et al. [2] have developed gravity based conical structures (GBCSs) with curved and flat steel-concrete-steel (SCS) type of ice-resisting wall, respectively (see Fig. 1). These GBCSs focused on the applications at Arctic locations with the water depth of 10~100 m. The inclined SCS sandwich plate or shell type of ice-resisting wall would raise the impacting ice sheets and fail them in flexural bending rather than crushing that significantly alleviated the ice-contact pressure acting on the structure. The flat SCS sandwich plate type of ice-resistant wall usually consists of two layers of steel plates and a sandwiched concrete core with the bonding measures (e.g., cohesive material or mechanical shear connectors) to form an integrity. This type of structure shows better buckling resistance and superior ductility over the traditional reinforced concrete (RC) structure. Compared with the traditional RC structure, the transparent advantages of the SCS sandwich plates include saving formwork for concrete casting and labour force for site construction, avoiding the detailing and fabricating of the reinforcements, promising modular construction that improves the construction efficiency, and offering external steel skins as blast- or impact-resistant membranes. This type of structure exhibits versatile potential application in civil and offshore constructions, e.g., shear walls, protective structures, decks in bridges and offshore structures, nuclear walls, containments for oil and liquid natural gas, and ice-resistant walls [1-3].

In the ice-resisting wall system, ice-contact pressure produced by the floating ice becomes the main concern [4]. The pressure at the ice-structure interface could be up to more than 15 MPa on a local area and about 2.5 MPa on a large interacting area [4-7]. Therefore, the structural performances of these ice-resisting walls under the patch loads or large area ice-contact pressure need to be understood for the safety purpose of the Arctic offshore construction. Birdy and Bhula [4] experimentally studied the punching shear behaviour of reinforced concrete plates and shells under concentrated loading. Experimental and analytical works on arch-shaped RC ice-resisting wall under patch loads have been reported by Ellis and Macgregor [7]. Long [8], and Mclean [9]. Mclean et al. [10] have reported the reinforced normal and lightweight concrete

the SCS sandwich structure. This developed FE model also considered damage in steel and concrete that proved to be capable of simulating the structural behaviour of the SCS sandwich plates and shells [23-4]. Thus, this model offered useful mean to investigate the behaviour of the SCS sandwich plate under larger surface loading area that significantly reduced the costing and time compared with the testing method.

This paper utilized the finite element model (FEM) with detailed simulation on headed shear studs in the SCS sandwich plate that was developed by the authors. In this numerical model, continuum damage plasticity model was used to simulate the damage evolutions in the steel materials. Moreover, concrete damage plasticity model was also used to model concrete core in the SCS sandwich plate. The headed stud connectors in the SCS sandwich plate were detailed simulated, and contact algorithms were used to model different interactions among the concrete core, headed studs, and steel face plates. The accuracy of the developed FEM was validated by nine large scale tests carried out by the authors. With this validated FEM, ultimate strength behaviours of the SCS sandwich plate under different surface loading area were studied. The failure modes, ultimate resistance, and load-transferring mechanism were reported and analysed based on the FE parametric study. The FE predicted resistances of the SCS sandwich plate were also compared with the ISO predicted ice-contact pressure to further confirm its applicability as the ice-resisting wall in the Arctic offshore construction.

2. Tests on steel-concrete-steal sandwich plate

2.1. SCS sandwich plate and test setup

The SCS sandwich plate usually consists of two external steel face plates and a sandwich concrete core as shown in Fig. 2 [16].

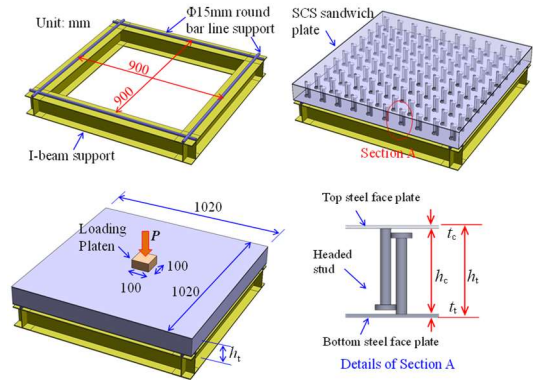


Fig. 2 Details and test setup of SCS sandwich plates [16]

Table 1
Material and geometry details of the tests on SCS sandwich plates

Specimen	h_t (mm)	$t=t_c$ mm	S_a mm	f_{ck} (MPa)	f_t (MPa)	Stud $d \times h_s$ mm ²	E_s (GPa)	f_y (MPa)	f_u (MPa)	E_{sh} (GPa)
SP1	112.0	4	100	65.1	4.1	13×100	202	317.8	472.0	199
SP2	107.7	4	150	65.1	4.1	13×100	202	317.8	472.0	199
SP3	110.9	4	100	46.0	2.9	13×100	202	317.8	472.0	199
SP4	111.8	4	100	54.7	3.4	13×100	202	317.8	472.0	199
SP5	117.5	6	100	65.1	4.1	13×100	204	435.0	538.7	199
SP6	120.2	8	100	65.1	4.1	13×100	200	330.8	486.0	199
SP7	110.9	4	100	62.7	5.1	13×100	202	317.8	472.0	199
SP8	73.8	4	100	68.4	4.2	13×70	202	317.8	472.0	198
SP9	135.0	4	100	68.4	4.2	13×100	202	317.8	472.0	199

Table 1
Continued

Specimen	E_{sh} (GPa)	σ_y (MPa)	σ_y (MPa)	P_1 (kN)	P_2 kN	$P_{1,F}$ (kN)	$\frac{P_{1,F}}{P_1}$	$P_{2,F}$ (kN)	$\frac{P_{2,F}}{P_2}$
SP1	199	418.5	505.5	482.8	618.8	458.8	0.95	609.0	0.98
SP2	199	418.5	505.5	288.0	518.8	264.0	0.92	441.7	0.85
SP3	199	418.5	505.5	427.3	547.9	406.6	0.95	607.8	1.11
SP4	199	418.5	505.5	464.6	520.9	435.0	0.94	613.7	1.18
SP5	199	418.5	505.5	624.5	859.2	670.0	1.07	776.9	0.90
SP6	199	418.5	505.5	811.6	1067.5	771.0	0.95	1062.8	1.00
SP7	199	418.5	505.5	512.6	638.2	459.8	0.90	604.5	0.95
SP8	198	417.0	495.3	284.5	529.9	365.4	1.28	545.9	1.03
SP9	199	418.5	505.5	540.7	583.4	519.7	0.96	607.0	1.04
					u	0.99		1.00	
					COV	0.12		0.10	

h_t denotes total depth of the SCS sandwich plate; t_t, t_c denote thickness of tension and compression steel face plates, respectively; S_a denote spacing of the studs; f_s, f_{ck} denote tensile and compressive strength of the concrete core, respectively; d, h, σ_y, σ_u denote diameter, height, yield and ultimate strength of the stud, respectively; E_{sh}, f_y, f_u denote Young's modulus, yield and ultimate strength of the steel plate, respectively; $P_{1,F}$ and $P_{2,F}$ denotes first and second peak resistance by FEA, respectively

Headed studs were firstly welded to the two external steel faceplates, and after casting of the concrete they were anchored to the concrete core and bond these three layers of materials as an integrity. Nine specimens in total were prepared and tested under patch loads [16]. All the specimens measuring 1020×1020 mm² (length by width) adopted the ultra-lightweight cement composite (ULCC) as the core material. More material and geometric details of the SCS sandwich plates are given in Table 1. As shown in Fig. 2(b), all the specimens were applied by the concentrated loads at the center of top steel face plate through a steel cube measuring $100 \times 100 \times 100$ mm³. The deflections of the plates at middle span were measured by the Linear Varying Displacement Transducers (LVDTs).

2.2. Materials

Ultra-lightweight cement composite (ULCC) with a 28-day compressive strength about 60 MPa and a density of 1450 kg/m³ was adopted as the core materials in the SCS sandwich plate that aims to deliver a lightweight structural solution. The detailed information on the ULCC has been extensively reported by Chia et al. [25], Yan et al. [26], and Wang et al. [27]. Fig. 3(a) and (b), respectively, show the representative compressive and tensile stress-strain curves of the ULCC that were obtained from the material tests. The tensile and compressive strengths of the ULCC for each specimen were listed in Table 1.

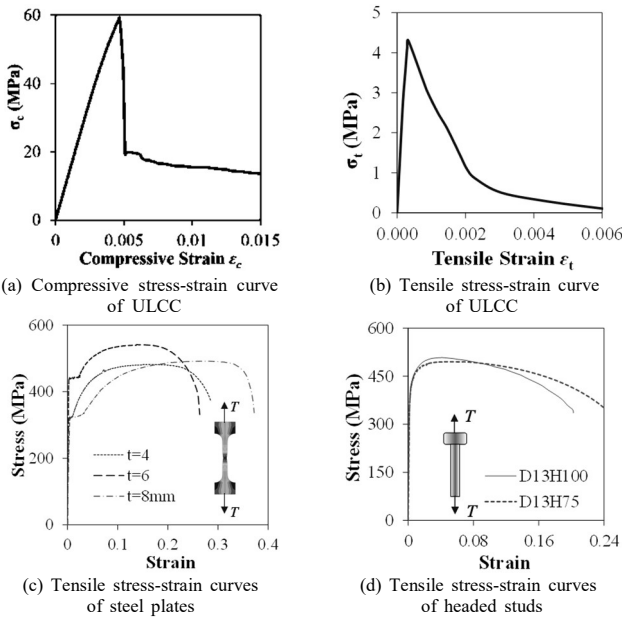


Fig. 3 Stress-strain curves of ULCC, headed studs and steel skin plates [16]

Mild steel plates with different thicknesses of 4, 6, and 8 mm were used to fabricate the SCS sandwich plate. Fig. 3(c) depicts the tensile engineering stress-strain curves of these steel face plates [16]. Headed studs with height of 75 mm and 100 mm were used in this test program. The tensile engineering stress-strain curves of these two types of headed studs are shown in Fig. 3(d) [16]. Table 1 lists all the mechanical properties of the ULCC and the steel materials involved in this test program.

3. Finite element modelling

3.1. General

General finite element code ABAQUS/CAE was used for the FE modelling of the SCS sandwich plate with the headed shear studs [26]. ABAQUS/Explicit type of solver was chosen to overcome the convergence problem during the nonlinear analysis of the SCS sandwich plate.

3.2. Finite element model

The finite element model (FEM) developed by Yan et al. [23-4] provides detailed modelling on the headed studs in the SCS sandwich plate to achieve a successful stud-concrete interacting simulation. Fig. 4 shows the FEM for SCS sandwich plate as proposed by Yan et al. [24]. One quarter of the full size specimen was built in this FEM that considered the symmetric geometry and loading pattern (see Fig. 4). Hundreds of headed studs on both top and bottom steel plate in SCS sandwich plate were detailed modelled as shown in Fig. 4. The holes in the concrete core were also reserved for these headed studs. In order to facilitate the FE modelling, the square section of headed studs was used to replace the circular section through using equivalent cross sectional area and height. This simplification was proved to be efficient in the FE model building and also offered satisfactory simulations on the behaviour of the SCS sandwich plate [23-24].

The FEM adopted three-dimensional eight-node continuum elements (C3D8R) in ABAQUS element library to simulate the different components in the SCS sandwich plate, e.g., headed stud, steel plate, and concrete core. The C3D8R element had eight nodes with three translation degrees of freedom on each node and one integration point.

In order to make a balance of computing efficiency and accuracy, different mesh sizes in the FEM were used. The mesh size of the C3D8R element for the headed stud is $5 \times 5 \times 5$ mm³; the mesh sizes of the elements in the steel face plate near and far away from the headed studs are $5 \times 5 \times 2$ mm³ and $10 \times 10 \times 2$ mm³, respectively; the mesh sizes of the elements in the concrete core near and far away from the headed studs are $5 \times 5 \times 10$ mm³ and $5 \times 10 \times 10$ mm³, respectively. Taking the specimen SP1 for example, there are 10874, 31020, and 10874 elements for the bottom steel plate, concrete core, and top steel plate, respectively.

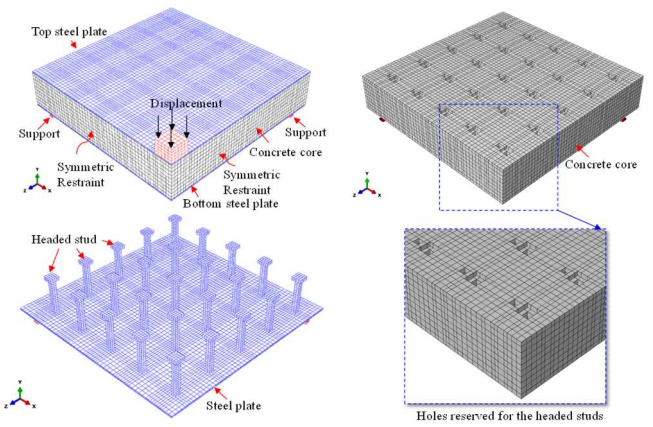


Fig. 4 FE model for SCS sandwich plate

3.3. Loadings and interactions

Since the FEM only built one quarter of the SCS sandwich plate, symmetric restraints have been applied on the surfaces of the sections along the centreline as shown in Fig. 4. Displacement controlled type of loading was applied on the centre of the top steel face plate through a steel cube measuring 100 mm in width. The round bar type of line support was also modelled and hard contact was defined to simulate its interaction with the SCS sandwich plate.

Different interacting pairs among different components (e.g., interaction between studs and concrete core, interaction between steel plates and concrete core, and interaction between loading platen and top steel face plates) adopted surface-to-surface contact algorithm in the FEM. Hard contact algorithm and Coulomb friction model were used to define the contact algorithms in the normal direction and tangent direction to the contact surface, respectively. The hard contact algorithm allows transferring the contact pressure of the surface under compression, and permits separation without transferring pressure once the two interacting surfaces are under tension. In Coulomb friction algorithm, a friction coefficient was used to simulating the friction forces at the interacting surfaces. In this paper, a value of 0.4 was chosen that has been used in this developed FEM for the SCS sandwich plates [24].

3.4. Material model of concrete

The FEM adopted the concrete damage plasticity model (CDPM) in ABAQUS to simulate the mechanical properties of the concrete core. In CDPM model, isotropic tensile and compressive plasticity with isotropic damage was used to describe the inelastic mechanical behaviours of the concrete [28]. The yield function proposed by Lublinear et al. [29] and modified by Lee and Fenves [30] was used to define the evolution of the strength of the concrete under compression and tension. The non-associated potential flow rule and isotropic damage were followed in the CDPM [28].

The CDPM model in ABAQUS used the uniaxial tensile and compressive stress-strain curves to define the constitutive model of the concrete. For the ULCC used in this study the experimental tensile and compressive stress-strain curves were used to calibrate the CDPM model [24].

These uniaxial tensile and compressive engineering stress-strain curves have to be converted to the inelastic strain versus stress curves as specified in ABAQUS material library. In the CDPM, the consideration on the strain-softening of the concrete core was realized through introducing the damage coefficient. Thus, in the CDPM model, the compressive and tensile damage coefficient versus inelastic strain curves were used to specify this strain-softening, i.e., D_c (or D_t) $\sim \varepsilon_c^{in}$ (or ε_t^{in}) curves as defined,

$$\varepsilon_c^{pl} = \varepsilon_c^{in} - \frac{D_c}{(1-D_c)} \frac{\sigma_c}{E_0} \quad (1a)$$

$$\varepsilon_t^{pl} = \varepsilon_t^{in} - \frac{D_t}{(1-D_t)} \frac{\sigma_t}{E_0} \quad (1b)$$

where, ε_c^{pl} and ε_t^{pl} denote true tensile or compressive plastic strain of the concrete, respectively; ε_c^{in} and ε_t^{in} denote inelastic tensile or compressive strain of the concrete, respectively; D_c and D_t denote the compressive and tensile damage ratio, respectively. The D_c (or D_t) can be determined by the following proposed functions as proposed by Wang and Chen [31]

$$D_c = A_c e^{-\varepsilon_c^{in}/t_c} + B_c \quad (2a)$$

$$D_t = A_t e^{-\varepsilon_t^{in}/t_t} + B_t \quad (2b)$$

where $\bar{\varepsilon}_c^{ln}$ and $\bar{\varepsilon}_t^{ln}$ refer to the inelastic compressive and tensile strain against the maximum strain in the stress-strain curves, respectively; t_c and t_t are a constant empirical values; $A_c = \frac{1}{e^{-1/t_c}-1}$; $B_c = -\frac{1}{e^{-1/t_c}-1}$; $A_t = \frac{1}{e^{-1/t_t}-1}$; $B_t = -\frac{1}{e^{-1/t_t}-1}$.

Finally, Fig. 5(a) and (b) show the determined compressive and tensile damage ratio versus inelastic strain curves for CDPM, respectively.

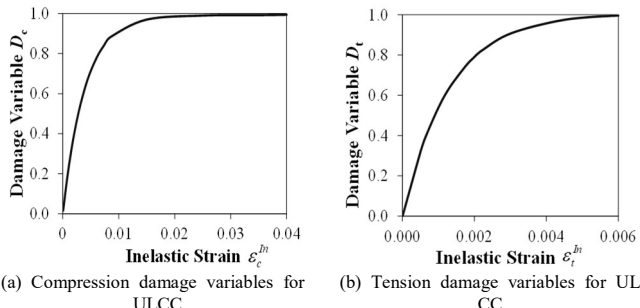


Fig. 5 Definitions of the stress-strain curves and damage variables for CDPM

The other plasticity parameters including flow potential eccentricity of 0.1, ratio of the biaxial/uniaxial compressive strength ratio of 1.16, and the dilation angles of 36° were chosen for the CDPM in the FEM developed in this paper.

3.5. Material model of steel and connector

The proposed FEM [24] adopted the continuum damage model (CDM) for the steel face plates and headed studs. The tensile stress-strain curves that were obtained from the uniaxial tensile tests as shown in Figs. 3(c) and (d) were used in this FE modelling. From these test data, the elastic modulus Es and Poisson's ratio v were determined as 200 GPa and 0.3, respectively.

In the definition of the CDM, the damage initiation criterions, damage evolution laws, and true stress-strain curves of the steel materials were required. This paper follows the methods proposed by Yan et al. [23-4] and detailed information could be found in Refs. [23, 24].

3.6. Validations of the finite element model

The comparisons between the test results and FE analysis proved that the developed FE model could provide satisfactory FE simulations on the load-deflection behaviours, deformation behaviour, the first and second peak resistances of the SCS sandwich plate, and failure modes of the SCS sandwich plate that includes the punching shear in the concrete core and steel face plates [24]. Table 1 compares the FE predicted ultimate resistances with those experimental values. It can be seen that the average test-to-prediction ratio (nine tests) for the first and second peak resistance are 0.99 and 1.00 with corresponding coefficient of variation for the test-to-prediction ratios of 0.12 and 0.10, respectively.

Thus, this validated FE model could be used to investigate behaviour of the SCS sandwich plate under different loading area.

4. Ultimate strength behaviour of SCS sandwich plate under different loading area

4.1. FE parametric studies on SCS sandwich plate under different loading area

Ultimate strength behaviour of the SCS sandwich plate under different loading area was carried out by the validated FEM.

Table 2
Details and results of the FEA cases

FE Case	L_a (m)	A (m ²)	P_{max} (kN)	p (MPa)	Failure mode
SP1A0	0.10	0.01	482.8	48.3	PSC
SP1A1	0.20	0.04	757.2	18.9	FLC
SP1A2	0.45	0.20	977.7	4.8	FLC
SP1A3	0.64	0.40	1365.9	3.4	FLC
SP1A4	0.90	0.81	2106.0	2.6	FLC
SP3A0	0.10	0.01	464.6	46.5	PSC
SP3A1	0.20	0.04	730.0	18.2	FLC
SP3A2	0.45	0.20	956.8	4.7	FLC
SP3A3	0.64	0.40	1350.0	3.3	FLC
SP3A4	0.90	0.81	1944.0	2.4	FLC
SP5A0	0.10	0.01	624.5	62.5	PSC
SP5A1	0.20	0.04	742.6	18.6	FLC
SP5A2	0.45	0.20	967.6	4.8	FLC
SP5A3	0.64	0.40	1356.3	3.4	FLC
SP5A4	0.90	0.81	1944.0	2.4	FLC
SP6A0	0.10	0.01	811.6	81.2	PSC
SP6A1	0.20	0.04	784.9	19.6	FLC
SP6A2	0.45	0.20	1105.9	5.5	FLC
SP6A3	0.64	0.40	1469.2	3.6	FLC
SP6A4	0.90	0.81	2268.0	2.8	FLC

Table 2
Continued

FE case	L_a (m)	A (m ²)	P_{max} (kN)	p (MPa)	Failure mode
SP7A0	0.10	0.01	512.6	51.3	PSC
SP7A1	0.20	0.04	1179.0	29.5	FLC
SP7A2	0.45	0.20	1372.5	6.8	FLC
SP7A3	0.64	0.40	2192.9	5.4	FLC
SP7A4	0.90	0.81	2268.0	2.8	FLC
SP9A0	0.10	0.01	284.5	28.5	PSC
SP9A1	0.20	0.04	488.4	12.2	FLC
SP9A2	0.45	0.20	648.0	3.2	FLC
SP9A3	0.64	0.40	870.2	2.2	FLC
SP9A4	0.90	0.81	1458.0	1.8	FLC
SP10A0	0.10	0.01	540.7	54.1	PSC
SP10A1	0.20	0.04	745.0	18.6	FLC
SP10A2	0.45	0.20	1118.7	5.5	FLC
SP10A3	0.64	0.40	1229.0	3.0	FLC
SP10A4	0.90	0.81	2430.0	3.0	FLC

L_a denotes length of the square patch area; A denotes area of the patch loads; P_{max} and p denote ultimate resistance and pressure, respectively; PSC denotes punching shear failure of the concrete core; FLC denotes flexural failure due to connectors; SP1A0 denotes Loading area size A0; Control specimen SP1

Different surface loading area was considered that simulated the different ice-interacting area on the Arctic offshore structures. Eight specimens as reported in the experimental program, i.e., SP1, SP4~7, and SP9~10 were chosen as the controlling cases in this study. For each specimen, including the test under 100×100 mm² patch loading, four more analyses for each specimen under different loading area A (in mm²) with length L_a (mm) measuring 200, 450, 675, and 900 mm were carried out. Thus, taking specimen SP1 for example, the FE analyses (FEAs) SP1A0~A4 denotes the SCS sandwich plate was applied to square loading area measuring 100×100, 200×200, 400×400, 675×675, and 900×900 mm², respectively. Thus, including the seven tests on the SCS sandwich plates, there are totally 35 results. Fig. 6 shows the details of FEA cases on the SCS sandwich plate under different loading area, and Table 2 lists details of the different FEA cases in this parametric study.

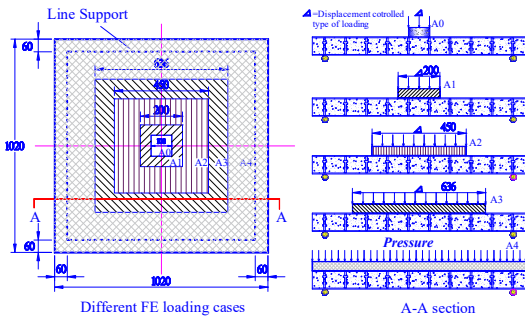


Fig. 6 Illustration on different loading cases in FE parametric study

4.2. Finite element analysis results and discussions

4.2.1. General behavior

Fig. 7 (a)~(h) plots the resultant force versus central deflection curves of the SCS sandwich plate under different loading area. As reflected in Fig. 7, the load-deflection curves of the SCS sandwich plate can be categorized into three types. Fig. 8 shows the generalized load-deflection curves of the SCS sandwich plate under different loading area. The first type is for the SCS sandwich plate under patch loading of $100 \times 100 \text{ mm}^2$. This type of load-deflection curves exhibited two peak resistances. From the experimental studies on SCS sandwich plate under concentrated loading by Yan et al. [16], the first peak resistance was achieved when the concrete core was punched through, and the second peak resistance of the SCS sandwich plate occurred when the region of top steel skin near the patch loading was punched through. The second type of the load-deflection curves occurred to the specimens under medium size of surface pressure. As reflected in Fig. 7, the reaction forces of the SCS sandwich plate increases with the applied displacement type of surface loading until the concrete core was punching through or shear failure mode occurred to the support. The third type of load-deflection curves occurred to the specimens under full surface pressure. As reflected in Fig. 7~8 the specimens belonged to this type exhibit ductile load-deflection behaviour. These figures show that the load carrying capacity of specimens firstly increased linearly with their central deflections. After the elastic limit, the load carrying capacity of the specimens continue increasing with gradually decreased stiffness. And the specimens exhibit certain degree of ductility with a plateau in the load-deflection curves. Finally, these SCS sandwich specimens failed in excessive deflection.

From Fig. 7 and 8, it can be concluded that as the loading area increases the load-deflection behaviours of the SCS sandwich plate changes from the brittle behaviour to the ductile behaviour. Only the SCS sandwich plate under loading area of 100 mm (i.e., La/L ratio equals to about 0.98) exhibited two peak resistances. Except the FE analysis cases under full surface pressure and patch loading of $100 \times 100 \text{ mm}^2$, the rest specimens all exhibited one peak resistance. The FE analysis cases under full surface pressure exhibit ductile behaviour. These differences in the load-deflection behaviours implied that the failure mode at final stage changes as the surface loading area increases.

4.2.2. Ultimate resistances and failure modes

From these load-deflection curves in Fig. 7, the ultimate resistance of the SCS sandwich plate can be easily determined. The ultimate resistance and pressure for different FEA cases are listed in Table 2. With these ultimate resistances, the ultimate pressure for these loading cases could be obtained, and the ultimate pressure versus La (length of the square loading area) relationship are plotted in Fig. 9. From these table and figures, it can be found that the ultimate resisting pressure of the SCS sandwich plate decreases dramatically as the length of the square interacting area increases from 0.1 m to 0.45 m. For the seven SCS sandwich plates with different parameter, the ultimate resisting pressure of the specimens under 0.2 m² surface pressure area was averaged reduced to about 10% of the value for the specimen under 0.01 m² surface pressure loading area. However, this decreasing rate of the ultimate resisting

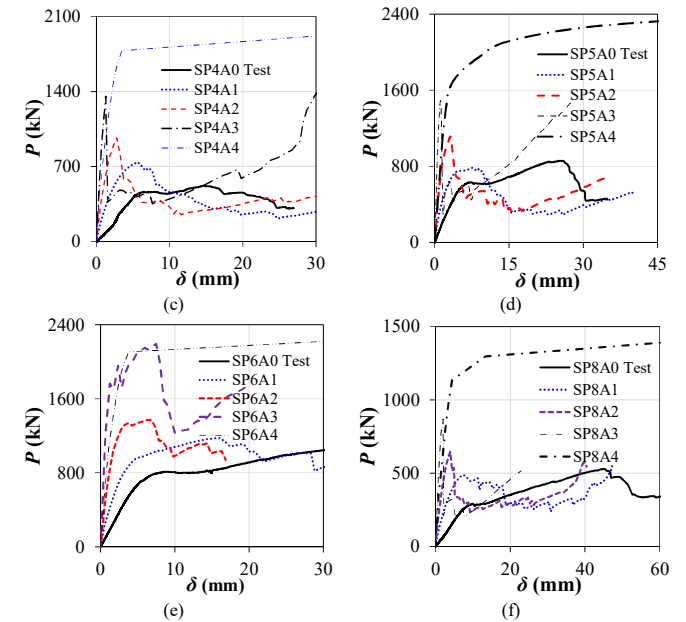
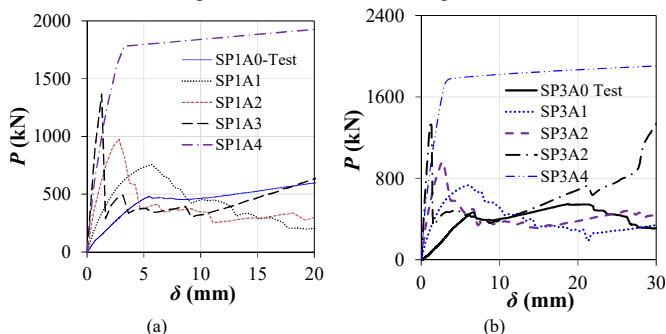


Fig. 7 Load-central deflection curves of SCS sandwich plate under different loading area

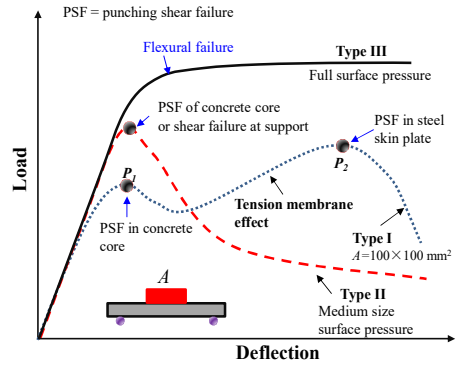


Fig. 8 Illustration on generalized load-deflection curves of SCS sandwich plate under different loading area

pressure acting on the specimen tends to slow down as the square surface loading area increases from 0.2 m² to 0.81 m². As the surface loading area increases about four times from 0.2 m² to 0.81 m², the ultimate resisting pressure of the SCS sandwich plate was only reduced by about 50%.

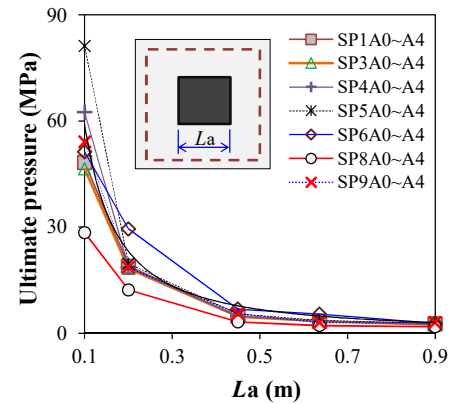


Fig. 9 Ultimate pressure versus loading area relationship for different specimens loading area

Based on these 35 FEA cases, two main types of failure modes were observed, i.e., punching shear failure in the core material and flexural failure mode due to failure of the connectors. Fig. 10(a) depicts the representative contour of the plastic strain distribution in specimen SP1A0. This figure shows a clearly developed punching cone due to large shear deformation. Meanwhile, no plastic strain was observed in both top and bottom steel face plates. Moreover, as reflected in the load-deflection curves in Fig. 7, there are sharp reductions in the load carrying capacity of the SCS sandwich plate. These observations implied that punching shear failure occurred to the core material in specimen SP1A0. This type of failure of occurred to specimens under $100 \times 100 \text{ mm}^2$ square patch loads.

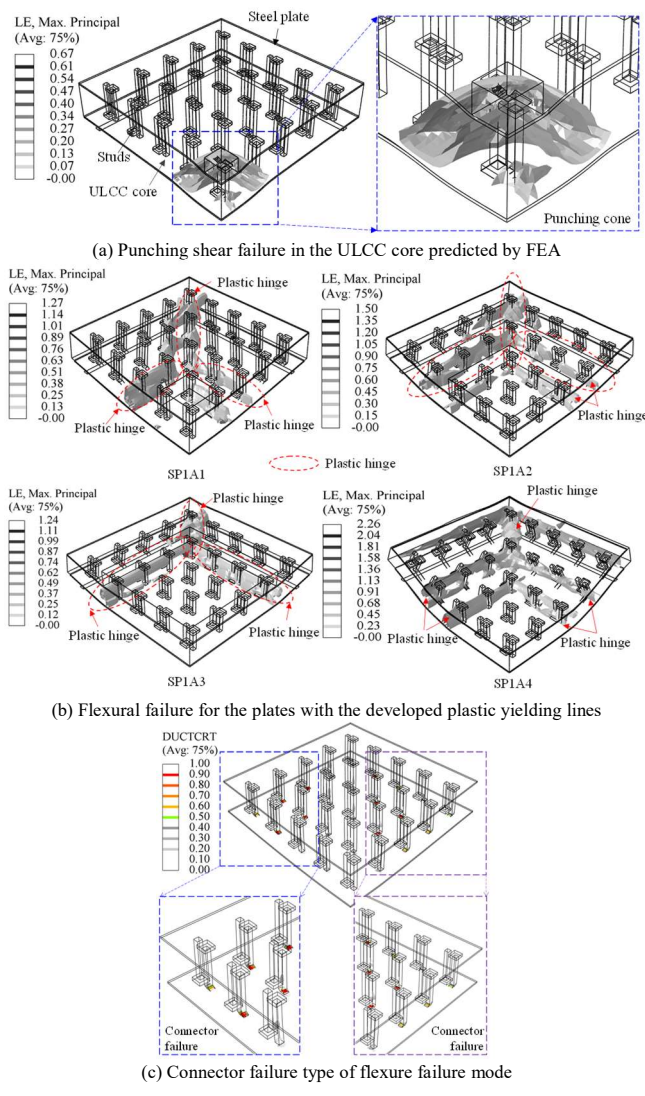


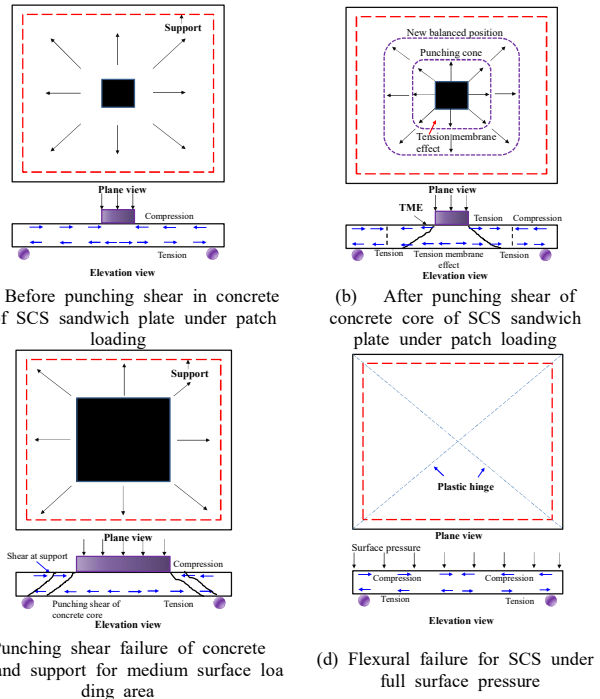
Fig. 10 Different failure modes of the SCS sandwich plate

Fig. 10(b) plots the representative contour of the plastic strain in the specimen SP1A1~4. This figure shows that typical plastic hinges were observed along the edges of the square patch loads and in the diagonal direction that connects the corner of the specimen and corner of the square loading area. These plastic hinges were mainly produced by the excessive rotation. No punching cones were observed in these four specimens. These observations implied that the section along these yielding lines failed in flexural bending. This supports the statement that the specimens under larger loading area failed in flexural bending rather than punching shear mode. There were three types of flexural failure modes that may occur to the SCS sandwich plates, i.e., yielding of the steel face plates, failure of the connectors, or combinations of these two modes. The FEA analyses show that most of the FEA cases failed in the mode due to failure of the connectors as shown in Fig. 10(c). The ultimate resisting force and pressure of each FEA case as well as corresponding failure mode are listed in Table 2.

4.2.3. Load-transferring mechanism

As the surface loading area is small (e.g., patch loading), the applied load is taken by the SCS sandwich plate and transferred to the support in two directions as shown in Fig. 11(a). During this stage, the SCS sandwich plate behaves elastically with the top and bottom steel skin plate under compression and tension, respectively (see Fig. 11(a)). Considering the strain compatibility between the concrete core and steel face plates, the concrete core tends to fail prior to the failure of the steel skin plate. Thus, as shown in Fig. 11(b), punching shear failure of the concrete core tends to occur that corresponds to the first peak resistance on the load-deflection curves (see Fig. 9). After a cone of concrete in the SCS sandwich plate is punched through, the top steel skin plate would continue taking the applied load and transferring the load to the rest undamaged portion of the SCS sandwich plate through the tension membrane effect (see Fig. 11(b)). And a new balanced larger critical perimeter than the size of the punched concrete cone will be formed. Thus, as shown in Fig. 11(b), the top steel skin plate within the scope of the punched concrete cone will be under tension due

to the tension membrane effect whilst the top steel skin plate out of this scope is under compression. The bottom steel skin plate is still under tension due to bending or pushing down effect by the punched concrete cone. For the SCS sandwich plate under medium size of surface loading area, punching shear failure may occur at the support or in the vicinity of the loading area as shown in Fig. 11(c). Once the surface pressure was applied on the top steel skin plate, all the SCS sandwich plats fail in flexural mode. As illustrated in Fig. 11(c) and Fig. 10, it can be found that the plastic “yielding lines” were formed. This observation was also consistent with the experimental results reported by Sohel et al. [14], Yan et al. [17], and Shanmugam et al. [32]. The applied surface pressure was transferred in two ways along the sandwich plate.



(a) Before punching shear in concrete core of SCS sandwich plate under patch loading
 (b) After punching shear of concrete core and support for medium surface loading area
 (c) Punching shear failure of concrete core and support for medium surface loading area
 (d) Flexural failure for SCS under full surface pressure

Fig. 11 Load-transferring mechanism of SCS sandwich plate under different surface loading area

4.2.4. Comparisons of resistances of SCS sandwich plates under different surface loading area with the ice-contact pressure by ISO code

Since the developed SCS sandwich plate was developed as the ice-resisting wall in Arctic offshore structure, its ultimate resistance under different surface ice-contact pressure becomes the main concern. The ice-contact pressure, IP, with varying interaction surface, A, which acts on the Arctic offshore structure may be calculated by ISO/FDIS 19906 [32] as follows:

$$IP = \begin{cases} 7.4A^{-0.7}A \leq 10m^2 \\ 1.48A > 10m^2 \end{cases} \quad (3)$$

where, IP is in MPa; A is in m².

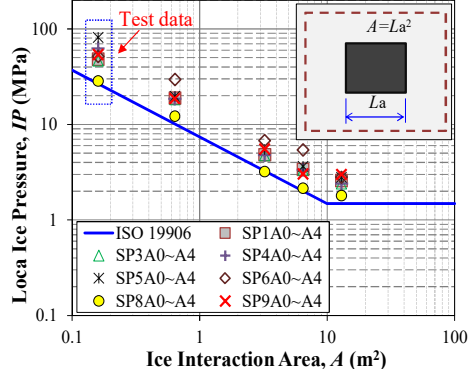


Fig. 12 Comparisons of the resistance of the SCS sandwich plates with the different size of surface ice-contact pressure

Considering that all the tested specimens were 1/4 scaled, the ice-structure interacting area needs to be determined accordingly. Fig. 12 compares the ultimate resisting pressure of the 35 results (seven tests and 28 FEA) with the calculated ice-contact pressure by Eq. 3. This figure shows that the ISO criteria with a reasonable safety factor could be satisfied for all the developed SCS

sandwich plate type of ice-resisting wall under different surface ice contacting area. These comparisons with the ISO ice-contact pressure further confirms that the developed SCS sandwich plate system could be used to resist the ice-contact pressure in the Arctic offshore constructions.

5. Conclusions

This paper utilized the developed a finite element model (FEM) to investigate the ultimate strength behaviour of steel-concrete-steel sandwich plates under different surface loading area. The numerical studies provided valuable information on the ultimate strength behaviour of the SCS sandwich plate under different surface loading area. In addition, the ultimate resistances of the SCS sandwich plate under different loading area were checked by the ice-contact pressure, which was the main concern for the SCS sandwich plate type of ice-resisting wall. Based on these FE investigations, the following observations and conclusions are drawn;

- (1) The CDPM and CDM were successfully applied in the FE analysis of the SCS sandwich plates with ULCC and headed studs. The validations of the FEA against the test results showed that the FEM could simulate well the damage evolution in the steel materials.
- (2) With the validated FEM, the ultimate strength behaviour of the SCS sandwich plate under different surface loading area were studied. The FE parametric studies showed that as the surface loading area ratio (loading area over area of the top surface) increased from 0.1 to 1.0 the failure mode changed from punching shear of the ULCC core to the connector-failed type of flexure mode; the ultimate resistances of the SCS sandwich plate increased, but the surface loading pressure significantly decreased.
- (3) With the FE predicted ultimate resistances of SCS sandwich plate under different surface loading area, it was observed that the ISO criteria with a reasonable safety factor could be satisfied for all the developed SCS sandwich plate type of ice-resisting wall. The comparisons of the resistances of the developed SCS sandwich plate with the ISO ice-contact pressure further confirms that the developed SCS sandwich plate system could be used to resist the ice-contact pressure in the Arctic offshore constructions.

Acknowledgements

The authors would like to acknowledge the research grant 51608358 received from National Natural Science Foundation of China for the works reported herein. The authors gratefully express their gratitude for these financial supports.

Compliance with ethical standards:

Funding: This study was funded by National Natural Science Foundation of China (grant number 51608358).

Conflict of Interest: The authors declare that they have no conflict of interest.

Nomenclature

- D_c =Compressive damage ratio of concrete
- D_i =Damage ratio of steel at load step i
- D_t =Tensile damage ratio of concrete
- D_R =Damage ratio of steel
- E_0 =Initial elastic modulus of concrete
- E_s =Elastic modulus of the steel
- E_{sh} =Elastic modulus of the headed stud
- P_1 =First peak resistance in the load-deflection curves of the SCS sandwich plate
- P_2 =Second peak resistance in the load-deflection curves of the SCS sandwich plate
- S_a =Spacing of the connectors in the SCS sandwich plate
- f_c =Compressive stress at the softening region in the stress-strain curve
- h_c =Thickness of the core material in SCS sandwich plate
- h_t =Depth of the composite section in SCS sandwich plate
- t_c =Thickness of the compressive steel face plate
- t_t =Thickness of the tensile steel face plate
- δ_f =Central deflection of the shell
- σ_c =Uniaxial compressive stress of concrete
- σ_t =Uniaxial tensile stress of concrete
- σ_{cu} =Uniaxial ultimate compressive stress of concrete
- σ_{tu} =Uniaxial ultimate tensile stress of concrete
- δ_f =Uniaxial ultimate tensile stress of concrete
- v =Poisson's ratio

Abbreviations

- CDM= continuum damage model;
- CDPM=concrete damage plasticity model;
- COV=coefficient of variation; FE=finite element;
- FEA=finite element analysis;
- FEM=finite element model;
- HSS=headed shear stud connector.

References

- [1] Marshall P.W., Sohel K.M.A., Liew J.Y.R., Yan J.B., Palmer A. and Choo Y.S., "Development of Steel-Concrete-Steel sandwich composite shell for Arctic Caissons", In: Offshore technology conference, paper no. 23818, Houston, Texas, USA; 3–5 December.
- [2] Yan J.B., Liu X.M., Liew J.Y.R., Qian X. and Zhang, M.H., "Steel-concrete-steel sandwich system in Arctic offshore structure: Materials, experiments, and design. Materials & Design, 91, 111–121, 2016.
- [3] Yan J.B., Liew J.Y.R. and Zhang M.H., "Mechanical properties of normal strength mild steel and high strength steel S690 in low temperature relevant to Arctic environment", Materials & Design, 61, 150-159, 2014.
- [4] Birdy J.N. and Bhula D.N., "Punching resistance of slabs and shells used for Arctic concrete platforms", Offshore Technology Conference, Paper No. 4855, 135–150. 5/6/1985, Houston, Texas, 1985.
- [5] Croasdale K.R., "Ice interaction with structures: recent developments and future trends", Arctic Technology Conference, Calgary, Sept. 1985.
- [6] Palmer A.C. and Croasdale K.R., "Arctic Offshore Engineering", World Scientific, 2012.
- [7] Ellis R.M. and Macgregor J.G., "Tests on arch-shaped ice-resisting walls for offshore structures", ACI Structural Journal, 90(1), 42-51, 1993.
- [8] Long T.P., "Experimental and analytical investigations on punching shear of thick, lightweight concrete plates and shells", PhD thesis, Washington University, 1988.
- [9] McLean D.I., "A study of punching shear strength of curved slabs", Ph.D. Thesis, Cornell University, USA. 1987.
- [10] McLean D.I., Phan L.T., Lew H.S. and White R.N., "Punching shear behavior of lightweight concrete slabs and shells", ACI structural Journal, 7(4), 386-392, 1990.
- [11] Nøjiri Y., Koseki K., Yoshiki T. and Sawayanagi M., "Structural behavior and design method of steel/concrete composite ice walls for Arctic offshore structures", Offshore Technology Conference, Paper No. 5292, 597-604, 1986.
- [12] Shukry M.E.S. and Goode C.D., "Punching shear strength of composite construction", ACI Structural Journal, 87(1), 12-22, 1990.
- [13] Yan J.B., Liew J.Y.R., Zhang M.H. and Li Z.X., "Punching shear resistance of steel-concrete-steel sandwich composite shell structure", Engineering Structures, 117, 470-485, 2016.
- [14] Sohel K.M.A. and Liew J.Y.R., "Steel-Concrete-Steel sandwich slabs with lightweight core-Static performance", Engineering Structures, 33(3), 981-992, 2011.
- [15] Shamugam N.E., Kumar G. and Thevendran V., "Finite element modeling of double skin composite slabs", Finite Elements in Analysis and Design, 38(7), 579-599, 2002.
- [16] Yan J.B., Wang J.Y., Liew J.Y.R. and Qian, X., "Punching shear behavior of steel-concrete-steel sandwich composite plate under patch loads", Journal of Constructional Steel Research, 121, 50–64, 2016.
- [17] Yan J.B. and Liew J.Y.R., "Design and behavior of steel-concrete-steel sandwich plates subject to concentrated loads", Composite Structures, 150, 139-152, 2016.
- [18] Yan J.B., Wang J.Y., Liew J.Y.R., Qian X.D. and Zong L., "Ultimate strength behaviour of steel-concrete-steel sandwich plate under concentrated loads", Ocean Engineering, 118, 41-57, 2016.
- [19] Yan J.B., Wang J.Y., Liew J.Y.R. and Zhang, M.H., "Applications of ultra-lightweight cement composite in flat slabs and double skin composite structure", Construction and Building Materials, 111, 774-796, 2016.
- [20] Foundoukos, N. and Chapman, J.C., "Finite element analysis of steel-concrete-steel sandwich beams", Journal of Constructional Steel Research, 64(9), 947-961, 2008.
- [21] Yan J.B., Liew J.Y.R. and Zhang M.H., "Shear-tension interaction strength of J-hook connectors in steel-concrete-steel sandwich structure", Advanced Steel Construction, 11(1), 72-93, 2015.
- [22] Sohel K.M.A., Liew J.Y.R. and Koh, C.G., "Numerical modelling of lightweight Steel-Concrete-Steel sandwich composite beams subjected to impact", Thin-Walled Structures, 94(9), 135-146, 2015.
- [23] Yan J.B., Qian, X., Liew J.Y.R. and Zong L., "Damage plasticity based numerical analysis on steel-concrete-steel sandwich shells used in the Arctic offshore structure", Engineering Structures, 117, 542-559, 2016.
- [24] Yan J.B. and Zhang W., "Numerical analysis on steel-concrete-steel sandwich plates by damage plasticity model: From materials to structures", Construction and Building Materials, 149, 801-815, 2017.
- [25] Chia K.S., Zhang M.H. and Liew J.Y.R., "High-strength ultra lightweight cement composite -material properties", Proceedings of the 9th international symposium on high performance concrete-design, verification & utility, Rotorua, New Zealand, August, 2011.
- [26] Yan J.B., Wang J.Y., Liew J.Y.R., Qian X. and Zhang, W., "Reinforced ultra-lightweight cement composite flat slabs: Experiments and analysis", Materials & Design, 95, 148-158, 2016.
- [27] Wang J.Y., Chia K.S., Liew J.Y.R. and Zhang M.H., "Flexural performance of fibre-reinforced ultra-lightweight cement composites with low fibre content", Cement Concrete Composite, 43, 39-47, 2013.
- [28] ABAQUS, "ABAQUS Standard User's Manual", Version 6.12. Providence, RI (USA): Dassault Systems Corp; 2012.
- [29] Lubliner J., Oliver J., Oller S. and Oñate, E., "A plastic-damage model for concrete", International Journal of Solids and Structures, 25(3), 299-326, 1989.
- [30] Lee J. and Fenves G.L., "Plastic-damage model for cyclic loading of concrete structures", Journal of Engineering Mechanics, ASCE, 124(8), 892-900, 1998.
- [31] Wang J.C. and Chen Y.K., "Applications of ABAQUS in Civil Engineering (in Chinese)", Press of Zhejiang University, Publication No. C2118999F, China, 2006.
- [32] Shamugam N.E., Kumar G. and Thevendran V., "Finite element modeling of double skin composite slabs", Finite Elem Anal Des, 38(7), 579–99, 2002.
- [33] International Standards Organization. ISO/CDIS 19906: 2010(E). Petroleum and natural gas industries – Arctic offshore structures; 2010.